รายงานวิจัยฉบับสมบูรณ์

โครงการวิจัยเรื่อง: บริเวณรอยต่อเฟสของสารเฟร์โรอิเล็กทริกที่มีโครงสร้างแบบเพอรอฟสไกด์

โดย

ผศ. ดร. นราธิป วิทยากร

สถาบันเทคโนโลยีพระจอมเกล้าเจ้าคุณทหารลาดกระบัง

เมษายน 2554

สัญญาเลขที่ RSA5180002

รายงานวิจัยฉบับสมบูรณ์

โครงการ: บริเวณรอยต่อเฟสของสารเฟร์โรอิเล็กทริกที่มีโครงสร้างแบบเพอรอฟสไกด์

ผศ. ดร. นราธิป วิทยากร

สถาบันเทคโนโลยีพระจอมเกล้าเจ้าคุณทหารลาดกระบัง

สนับสนุนโดยสำนักงานกองทุน สนับสนุนการวิจัย

(ความเห็นในรายงานนี้เป็นของผู้วิจัย สกว.ไม่จำเป็นต้องเห็นด้วยเสมอไป)

กิตติกรรมประกาศ

งานวิจัยนี้สำเร็จได้ด้วยดีเนื่องจากการสนับสนุนจาก สำนักงานกองทุนสนับสนุนการวิจัย (สกว) ขอขอบคุณ คณะวิทยาศาสตร์ สถาบันเทคโนโลยีพระจอมเกล้าเจ้าคุณทหารลาดกระบังที่อำนวยความสะดวกในการใช้เครื่องมือและสถานที่ ขอขอบคุณ วิทยาลัยนาโนเทคโนโลยีพระจอมเกล้าเจ้าคุณทหารลาดกระบัง ที่อำนวยความสะดวกในงานวิจัย ขอขอบคุณ รองศาสตราจารย์ ดร. จิติ หนูแก้ว และ ผู้ช่วยศาสตราจารย์ ดร. รัตติกร ยิ้มนิรัญ ที่คอยให้คำปรึกษา แนะนำ และสนับสนุนในทุกๆ ด้านด้วยดีเสมอมา ขอบคุณผู้ร่วมวิจัย ดร. ธีรชัย บงการณ์ คุณรังสรรค์ เมืองเหลือ และนักศึกษาทุกคนที่ช่วยกันทำงานวิจัยอย่างเต็มที่จนสำเร็จลุล่วงไปด้วยดี สุดท้ายขอบคุณกำลังใจและการสนับสนุนที่มีให้เสมอมาจากจาก พ่อ แม่ ภรรยา ลูก และน้องสาว

(ผู้ช่วยศาสตราจารย์ ดร. นราธิป วิทยากร)
หัวหน้าโครงการ

สารบัญ

หน้า

บทคัดย่อ

1. รหัสโรงการ: RSA5180002

2. ชื่อโครงการ บริเวณรอยต่อเฟสของสารเฟร์โรอิเล็กทริกที่มีโครงสร้างแบบเพอรอฟไกต์

3. ชื่อหัวหน้าโครงการ

ผศ.ดร. นราธิป วิทยากร

ภาควิชา เคมี คณะวิทยาศาสตร์ สถาบันเทคโนโลยีพระจอมเกล้าเจ้าคุณทหารลาดกระบัง ถนนฉลองกรุง เขตลาดกระบัง กรุงเทพฯ 10520

E-mail Address: naratipcmu@yahoo.com, kvnarati@kmitl.ac.th

4. ระยะเวลาดำเนินงาน 3 ปี (1 พฤษภาคม 2551 ถึง 30 เมษายน 2554)

บทคัดย่อ

โครงการวิจัยนี้ได้ทำการศึกษาบริเวณรอยต่อเฟสของสารเฟร์โรอิเล็กทริกในกลุ่มดังต่อไปนี้ $PbZrO_3$-$Pb(Co_{1/3}Nb_{2/3})O_3$ $PbZrO_3$-$Pb(Ni_{1/3}Nb_{2/3})O_3$, $PbZrO_3$-$Pb(Zn_{1/3}Nb_{2/3})O_3$, $PbTiO_3$-$PbZrO_3$-$Pb(Zn_{1/3}Nb_{2/3})O_3$, $PbZrO_3$-$BiAlO_3$, $PbZrO_3$-$Pb(Yb_{1/2}Nb_{1/2})O_3$, $PbZrO_3$-$Pb(Y_{1/2}Nb_{1/2})O_3$, $PbZrO_3$-$Pb(In_{1/2}Nb_{2/3})O_3$ และ $PbZrO_3$-$Pb(Mg_{1/2}W_{1/2})O_3$ โดยสารละลายของแข็งที่ศึกษาเตรียมด้วยกระบวนการโคลัมไบต์ – (วุลแฟรไมต์) ซึ่งใช้เทคนิคการเลี้ยวเบนของรังสีเอกซ์ (X-ray diffraction หรือ XRD) และรามานสเปกโทรสโกปี (Raman spectroscopy) สำหรับการตรวจสอบโรงสร้างผลึกของเซรามิกที่ผ่านการเผาซินเตอร์ (Sintering) แล้ว นอกจากนี้การตรวจสอบทางสัณฐานวิทยา (Morphology) สมบัติทางความร้อน (Thermal properties) การขยายตัวทางความร้อน (Thermal expansion) สมบัติไดอิเล็กทริก (Dielectric properties) และสมบัติเฟอร์โรอิเล็กทริก (Ferroelectric properties) ของเซรามิกเทียบกับสัดส่วนองค์ประกอบนั้น ตรวจสอบโดยใช้กล้องจุลทรรศ์อิเล็กตรอนแบบส่องกราด (Scanning Electron Microscopy หรือ SEM) เครื่องดิฟเฟอเรนเชียลสแกนนิ่งแคลอรีมิเตอร์ (Differential Scanning Calorimeter หรือ DSC) เครื่องไดลาโตมิเตอร์ (Dilatometer) ชุดวัดไดอิเล็กทริก และชุดวัดวงวนฮิสเทอรีซิส P - E ตามลำดับ ความสัมพันธ์ระหว่าง โครงสร้าง และ สมบัติ ถูกศึกษาและเชื่อมโยงให้เห็นในในกลุ่มสารละลายของแข็ง ผสมระหว่าง เฟร์โรอิเล็กทริกแบบปกติ-รีแรกเซอร์-แอนติเฟร์โรอิเล็กทริก

Abstract

Project code: RSA5180002

Project Title: Morphotropic Phase Boundary in Ferroelectric Materials Based on Perovskite Structure

Investigator: Asst. Prof. Dr. Naratip Vittayakorn

E-mail Address: naratipcmu@yahoo.com, kvnarati@kmitl.ac.th

Project Period: 3 years (1 May 2008 - 30 April 2011)

Abstract

The morphotropic phase boundary in many mixed ferroelectric system, such as $PbZrO_3$-$Pb(Co_{1/3}Nb_{2/3})O_3$ $PbZrO_3$-$Pb(Ni_{1/3}Nb_{2/3})O_3$, $PbZrO_3$-$Pb(Zn_{1/3}Nb_{2/3})O_3$, $PbTiO_3$-$PbZrO_3$-$Pb(Zn_{1/3}Nb_{2/3})O_3$, $PbZrO_3$-$BiAlO_3$, $PbZrO_3$-$Pb(Yb_{1/2}Nb_{1/2})O_3$, $PbZrO_3$-$Pb(Y_{1/2}Nb_{1/2})O_3$, $PbZrO_3$-$Pb(In_{1/2}Nb_{2/3})O_3$ and $PbZrO_3$-$Pb(Mg_{1/2}W_{1/2})O_3$ system was investigated in this study. Ceramics were prepared by high temperature solid state reaction involving the use of high-purity starting oxides and columbite-(wolframite) precursor method. Compositions were selected across each solid solution so as to represent all of the phases that occur in the systems with special emphasis on compositions near MPBs and other regions of particular interest. Each composition was synthesized by ball-milling followed by calcining at temperatures ranging from 700-950 ^{o}C. Phase development of the calcined powders and the crystal structure of sintered ceramics were analyzed by X-ray diffraction. The properties of the ceramics were characterized by a combination of dielectric spectroscopy, polarization switching, and x-ray diffraction measurements. This project explores the structure-properties relationship of a number of normal-relaxor - antiferroelectric solid solution systems.

Executive Summary

โครงการวิจัยนี้ได้ทำการศึกษาบริเวณรอยต่อเฟสของสารเฟร์โรอิเล็กทริกในกลุ่มดังต่อไปนี้ $PbZrO_3$-$Pb(Co_{1/3}Nb_{2/3})O_3$ $PbZrO_3$-$Pb(Ni_{1/3}Nb_{2/3})O_3$, $PbZrO_3$-$Pb(Zn_{1/3}Nb_{2/3})O_3$, $PbTiO_3$-$PbZrO_3$-$Pb(Zn_{1/3}Nb_{2/3})O_3$, $PbZrO_3$-$BiAlO_3$, $PbZrO_3$-$Pb(Yb_{1/2}Nb_{1/2})O_3$, $PbZrO_3$-$Pb(Y_{1/2}Nb_{1/2})O_3$, $PbZrO_3$-$Pb(In_{1/2}Nb_{2/3})O_3$ และ $PbZrO_3$-$Pb(Mg_{1/2}W_{1/2})O_3$ รวมถึงการสังเคราะห์ผงผลึกของสารเฟร์โรอิเล็กทริกในกลุ่มเพอร์รอฟสไกด์เช่น $K_{1/2}Na_{1/2}NbO_3$, $KNbO_3$ และ $NaNbO_3$ โดยสามารถแยกได้ดังนี้

1. <u>ผลการศึกษาในระบบ $(1-x)PbZrO_3 – xPb(Co_{1/3}Nb_{2/3})O_3$</u>

เตรียมเซรามิกในระบบ $(1-x)PbZrO_3$-$xPb(Co_{1/3}Nb_{2/3})O_3$ เมื่อ x = 0.00 0.02 0.04 0.06 0.08 0.10 0.20 และ 0.30 ด้วยกระบวนการโคลัมไบต์ ทำการตรวจพิสูจน์เอกลักษณ์ด้วยเทคนิคการเลี้ยวเบนของรังสีเอกซ์ (XRD) และรามานสเปกโทรสโกปี ตรวจสอบพฤติกรรมทางความร้อนด้วยเทคนิค DSC วัดค่าไดอิเล็กทริก ตรวจสอบสมบัติเฟอร์โรอิเล็กทริกโดยการวัดวงฮิสเทอรีซิส P-E และตรวจสอบสัณฐานวิทยาของเซรามิกด้วยกล้องจุลทรรศน์อิเล็กตรอนแบบส่องกราด (SEM) ผลการตรวจสอบโครงสร้างผลึกของเซรามิก PZ - PCoN ด้วยเทคนิค XRD พบว่ามีโครงสร้างเป็นเพอรอฟสไกต์ที่สัดส่วนองค์ประกอบ $0.00 \leq x \leq 0.30$ และไม่พบเฟสไพโรคลอร์ในทุกสัดส่วนองค์ประกอบ โดยพบว่าที่สัดส่วนองค์ประกอบ $0.00 \leq x \leq 0.10$ นั้นมีระบบผลึกเป็นแบบออร์โทรอมบิก และจะเปลี่ยนไปเป็นรอมโบฮีดรอลเมื่อปริมาณของ PCoN เพิ่มสูงขึ้น จากการผลของ DSC พบว่าเกิดการเปลี่ยนเฟสจาก AFE$\rightarrow$FE$\rightarrow$PE ที่สัดส่วนองค์ประกอบ $0.00 \leq x \leq 0.08$ โดยอุณหภูมิในการเปลี่ยนเฟสจากนั้นจะลดลงเมื่อสัดส่วนองค์ประกอบ x สูงขึ้น และช่วงกว้างของอุณหภูมิของเฟส FE จะเพิ่มขึ้นเมื่อปริมาณของ PCoN เพิ่มขึ้น ส่วนที่ $x \geq 0.08$ พบการเปลี่ยนแปลงเพียงช่วงเดียวคือการเปลี่ยนเฟสจาก FE$\rightarrow$PE ส่วนผลจากการวัดค่าคงที่ไดอิเล็กทริกนั้นพบว่าพีคที่สัดส่วนองค์ประกอบ x = 0.00 นั้นจะมีลักษณะเป็นพีคแหลม (Sharp peak) และที่อุณหภูมิประมาณ 237 °C มีการเปลี่ยนเฟสจาก AFE$\rightarrow$PE แต่ที่สัดส่วนองค์ประกอบ $0.02 \leq x \leq 0.06$ นั้นพบการเปลี่ยนแปลง 2 ช่วง โดยที่อุณหภูมิต่ำกว่าเป็นการเปลี่ยนเฟสจาก AFE$\rightarrow$FE ส่วนช่วงที่อุณหภูมิสูงกว่าเป็นพีคที่แสดงการเปลี่ยนเฟสจาก FE$\rightarrow$PE โดยช่วงอุณหภูมิที่เป็น FE นั้นจะกว้างขึ้นเมื่อ x สูงขึ้น ส่วนที่ $x \geq 0.08$ พบการเปลี่ยนแปลงเพียงช่วงเดียวคือการเปลี่ยนเฟสจาก FE$\rightarrow$PE ซึ่งอุณหภูมิในการเปลี่ยนเฟสจะมีแนวโน้มลดลงเมื่อปริมาณของ PCoN เพิ่มสูงขึ้น นอกจากนี้ค่าคงที่ไดอิเล็กทริกสูงสุด ($\varepsilon_{r,\ max}$) มีแนวโน้มสูงขึ้นเมื่อปริมาณของ PCoN เพิ่มขึ้น โดยการเปลี่ยนเฟสที่พบจาก DSC และไดอเล็กทริกนั้นมีความสอดคล้องกัน จากการวัดวงวนฮิสเทอรีซิส P-E จะพบลักษณะวงวนฮิสเทอรีซิสที่สมบูรณ์ที่สัดส่วนองค์ประกอบ $x \geq 0.08$ โดยค่าโพลาไรเซชันอิ่มตัวและโพลาไรเซชันคงเหลือนั้นมีค่าใกล้เคียงกัน และมีค่าเพิ่มขึ้นเมื่อ x เพิ่มขึ้น และจากการ

ตรวจสอบบริเวณรอยหักของเซรามิกในระบบ PZ-PCoN ด้วย SEM พบว่าการหักส่วนใหญ่เกิดขึ้นที่บริเวณขอบเกรน และขนาดเกรนในช่วง $0.00 \leq x \leq 0.10$ มีแนวโน้มเพิ่มขึ้นเมื่อปริมาณ PCoN สูงขึ้น และมีขนาดเล็กลงเมื่อ $x = 0.20$ และ 0.30 ตามลำดับ โดยขนาดเกรนอยู่ในช่วง 0.57-0.59

2. *<u>ผลการศึกษาในระบบ $(1\text{-}x)PbZrO_3 – xPb(Ni_{1/3}Nb_{2/3})O_3$</u>*

เตรียมเซรามิกเพอรอฟสไกต์ในระบบ $(1–x)PbZrO_3–xPb(Ni_{1/3}Nb_{2/3})O_3$ (PZ-PNN) ที่ x เท่ากับ 0.00 0.02 0.04 0.06 0.08 0.10 0.20 0.30 0.40 และ 0.50 ด้วยเทคนิคกระบวนการรีแอกชัน-ซินเทอริง และเทคนิคปฏิกิริยาสถานะของแข็ง ทำการตรวจสอบลักษณะเฟส และโครงสร้างผลึกด้วยเทคนิคการเลี้ยวเบนของรังสีเอกซ์ พบว่าสามารถเตรียมเซรามิกเพอรอฟสไกต์ในระบบ PZ-PNN บริสุทธิ์ได้จากทั้งสองเทคนิค โดยที่สัดส่วน x เท่ากับ 0.00 ถึง 0.08 มีโครงสร้างผลึกเป็นแบบออร์โทรอมบิก เมื่อปริมาณของ x เพิ่มขึ้นเท่ากับ 0.10 ถึง 0.40 โครงสร้างผลึกเปลี่ยนไปเป็นแบบรอมโบฮีดรอล และเปลี่ยนเป็นแบบคิวบิกเสมือนเมื่อ x เท่ากับ 0.50 ทำการตรวจสอบการเปลี่ยนเฟสด้วยเทคนิคดิฟเฟอเรนเชียลสแกนนิงแคลอริเมทรี พบว่าเซรามิกที่เตรียมได้จากทั้งสองเทคนิคที่สัดส่วนของ x เท่ากับ 0.00 ถึง 0.08 มีการเปลี่ยนเฟสเกิดขึ้น 2 ครั้ง โดยที่อุณหภูมิต่ำจะเกิดการเปลี่ยนเฟสจากแอนติเฟอร์โรอิเล็กทริกเฟสไปเป็นเฟอร์โรอิเล็กทริกเฟส และจะเปลี่ยนจากเฟอร์โรอิเล็กทริกเฟสไปเป็นพาราอิเล็กทริกเฟสที่อุณหภูมิสูง ส่วนที่สัดส่วน x เท่ากับ 0.10 ถึง 0.40 มีการเปลี่ยนเฟสเกิดขึ้นเพียงครั้งเดียว คือการเปลี่ยนเฟสจากเฟอร์โรอิเล็กทริกเฟสไปเป็นพาราอิเล็กทริกเฟส และไม่พบการเปลี่ยนแปลงใด ๆ ที่ x เท่ากับ 0.50 นอกจากนี้ยังพบอีกว่าเมื่อปริมาณของ x เพิ่มสูงขึ้น อุณหภูมิการเปลี่ยนเฟสจะลดลงตามลำดับ เมื่อทำการตรวจสอบสมบัติทางไดอิเล็กทริกเทียบกับอุณหภูมิที่ความถี่ต่าง ๆ พบว่าที่ x เท่ากับ 0.00 เกิดพีคแหลมฐานแคบที่อุณหภูมิ 230 องศาเซลเซียส ค่าคงที่ไดอิเล็กทริกที่ได้ไม่ขึ้นกับความถี่ และเมื่อเพิ่มปริมาณของ x มากขึ้นพบว่าพีคที่ได้จะมีความแหลมลดลง ฐานกว้างมากขึ้น ค่าคงที่ไดอิเล็กทริกที่ได้ก็ขึ้นกับความถี่มากขึ้นตามลำดับ ซึ่งเห็นได้ชัดเจนที่สัดส่วน x เท่ากับ 0.50 และอุณหภูมิที่เกิดพีคก็ลดต่ำลงตามลำดับ จากนั้นตรวจสอบสมบัติทางเฟอร์อิเล็กทริกพบว่าที่ x เท่ากับ 0.00 ถึง 0.06 มีสมบัติเป็นแอนติเฟอร์โรอิเล็กทริก ที่ x เท่ากับ 0.08 เกิดวงวนเฟอร์โรฮีสเทอเรซิสที่กว้าง และจะแคบลงเมื่อปริมาณ x เพิ่มสูงขึ้น สุดท้ายทำการตรวจสอบทางสัณฐานวิทยาพบว่าเซรามิกที่เตรียมได้มีความบริสุทธิ์ ไม่พบสิ่งแปลกปลอม ขอบเกรนติดชิดกันดี และมีขนาดเกรนเฉลี่ยอยู่ระหว่าง 0.91 ถึง 6.76 ไมโครเมตร

3. *<u>ผลการศึกษาในระบบ $(1\text{-}x)PbZrO_3 – xPb(In_{1/2}Nb_{1/2})O_3$</u>*

ทำการศึกษาสารละลายของแข็งของเซรามิกในระบบ เลดเซอร์โคเนต-เลดอินเดียมไนโอเบต ($(1\text{-}x)PbZrO_3$ - $xPb(In_{1/2}Nb_{1/2})O_3$; $(1\text{-}x)$PZ-xPIN) โดยทำการศึกษารูปแบบการเกิดเฟสเพ

อรอฟสไกต์ การเปลี่ยนเฟส สมบัติไดอิเล็กทริก และสมบัติเฟอร์โรอิเล็กทริกของเซรามิกที่เตรียมได้ โดยทำการเตรียมผงผลึกของ (1-*x*)PZ-*x*PIN ที่สัดส่วน *x* เท่ากับ 0.00 0.02 0.04 0.06 0.08 0.10 0.20 0.30 0.40 และ 0.50 ด้วยวิธีการเตรียมสารตั้งต้นวูลแฟรไมต์ (Wolframite Precursor Method) โดยใช้สารตั้งต้นเป็นโลหะออกไซด์ที่มีความบริสุทธิ์สูง (> 99.5%) เผาแคลไซน์ที่อุณหภูมิ 850°C เป็นเวลา 2 ชั่วโมง อัตราการขึ้น/ลงอุณหภูมิ 10°C /นาที จากนั้นทำการอัดขึ้นรูปชิ้นงานเป็นรูปแผ่นกลม และเผาซินเตอร์ที่อุณหภูมิ 1200-1250°C เป็นเวลา 2 ชั่วโมง พบว่าเมื่อปริมาณ *x* เพิ่มสูงขึ้นอุณหภูมิซินเตอร์จะลดลง จากการตรวจสอบรูปแบบการเกิดเฟสเพอรอฟสไกต์และโครงสร้างผลึกของเซรามิก (1-*x*)PZ-*x*PIN ด้วยเทคนิคการเลี้ยวเบนของรังสีเอกซ์ (X-ray diffraction; XRD) พบว่าที่ *x* เท่ากับ 0.00 มีรูปแบบการเลี้ยวเบนของรังสีเอกซ์คล้ายคลึงกับรูปแบบการ เลี้ยวเบนรังสีเอกซ์มาตรฐาน(ICDD File no. 75-1607) ของ $PbZrO_3$ ซึ่งมีโครงสร้างผลึกเป็นแบบออร์โทรอมบิก และที่ *x* เท่ากับ 0.02-0.10 ยังคงมีรูปแบบการเลี้ยวเบนของรังสีเอกซ์ใกล้เคียงกับรูปแบบการเลี้ยวเบนรังสีเอกซ์มาตรฐานของ $PbZrO_3$ เมื่อปริมาณ *x* เพิ่มขึ้นถึง 0.20 พบการเปลี่ยนเฟสเกิดขึ้นจากออร์โทรอมบิก เป็นรอมโบฮีดรอล เมื่อทำการตรวจสอบอุณหภูมิการเปลี่ยนเฟส ด้วยผลของค่าคงที่ไดอิเล็กทริก การวัดการขยายตัวทางความร้อน และดิฟเฟอเรนเชียลสแกนนิงแคลอริเมทรี (Differential scanning calorimetry; DSC) พบว่า ที่ x = 0.02-0.4 เซรามิกส์เกิดการเปลี่ยนเฟส 2 ครั้งจากแอนติเฟอร์โรอิเล็กทริกไปเป็นเฟอร์โรอิเล็กทริก และจากเฟอร์โรอิเล็กทริกไปเป็นพาราอิเล็กทริกตามลำดับ ส่วนที่ x = 0.5 เกิดการเปลี่ยนเฟสเพียงครั้งเดียวจากเฟอร์โรอิเล็กทริกไปเป็นพาราอิเล็กทริก และพบว่าอุณหภูมิการเปลี่ยนเฟสที่เกิดขึ้นทั้ง 2 ครั้ง จะลดลงเมื่อปริมาณของ *x* เพิ่มสูงขึ้น นอกจากนี้ที่อุณหภูมิห้องเซรามิกที่สัดส่วน x = 0.2 สามารถวัดวงวนฮีสทีรีซิสได้โดยมีลักษณะคล้ายกับวงวนฮีสทีรีซิสของแอนติเฟอร์โรอิเล็กทริก สัดส่วน x = 0.3-0.5 แสดงสมบัติเฟอร์โรอิเล็กทริก ผลการตรวจสอบโครงสร้างในระดับจุลภาคที่บริเวณรอยหักด้วยกล้องจุลทรรศอิเล็กตรอนแบบส่องกราด (Scanning electron microscope) พบว่าที่บริเวณรอยหักของเม็ดเซรามิกส์ส่วนใหญ่เกิดที่บริเวณขอบเกรน และมีขนาดเกรนในช่วง 2.26 - 3.16 μm

4. <u>เซรามิกในระบบ $(1-x)PbZrO_3 - xPb(Yb_{1/2}Nb_{1/2})O_3$</u>

ทำการศึกษาสารละลายของแข็งของเซรามิกในระบบ เลดเซอร์โคเนต-อิทเทอร์เบียมไนโอเบต ($(1-x)PbZrO_3$ - $xPb(Yb_{1/2}Nb_{1/2})O_3$; (1-*x*)PZ-*x*PYbN) โดยทำการศึกษารูปแบบการเกิดเฟสเพอรอฟสไกต์ การเปลี่ยนเฟส สมบัติไดอิเล็กทริก และสมบัติเฟอร์โรอิเล็กทริกของเซรามิกที่เตรียมได้ โดยทำการเตรียมผงผลึกของ (1-*x*)PZ-*x*PYbN ที่สัดส่วน *x* เท่ากับ 0.00 0.02 0.04 0.06 0.08 0.10 0.20 0.30 0.40 และ 0.50 ด้วยวิธีการเตรียมสารตั้งต้นวูลแฟรไมต์ (Wolframite Precursor Method) โดยใช้สารตั้งต้นเป็นโลหะออกไซด์ที่มีความบริสุทธิ์สูง (> 99.5%) เผาแคลไซน์ที่อุณหภูมิ 900°C เป็นเวลา 2 ชั่วโมง อัตราการขึ้น/ลงอุณหภูมิ 20°C /นาที จากนั้นทำการอัดขึ้นรูป

ชิ้นงานเป็นรูปแผ่นกลม และเผาซินเตอร์ที่อุณหภูมิ 1200-1250°C เป็นเวลา 2 ชั่วโมง จากการตรวจสอบรูปแบบการเกิดเฟสเพอรอฟสไกต์ และโครงสร้างผลึกของเซรามิก (1-*x*)PZ-*x*PYbN ด้วยเทคนิคการเลี้ยวเบนของรังสีเอกซ์ (X-ray diffraction; XRD) พบว่าที่ *x* เท่ากับ 0.00 มีรูปแบบการเลี้ยวเบนของรังสีเอกซ์คล้ายคลึงกับรูปแบบการ เลี้ยวเบนรังสีเอกซ์มาตรฐาน(ICDD File no. 75-1607) ของ ซึ่งมีโครงสร้างผลึกเป็นแบบออร์โทรอมบิก และที่ *x* เท่ากับ 0.02-0.20 ยังคงมีรูปแบบการเลี้ยวเบนของรังสีเอกซ์ใกล้เคียงกับรูปแบบการเลี้ยวเบนรังสีเอกซ์มาตรฐานของ $PbZrO_3$ เมื่อปริมาณ *x* เพิ่มเป็น 0.30-0.50 พบเฟสแปลกปลอมเกิดขึ้น แสดงให้เห็นว่าเซรามิกส์ในระบบ (1-*x*)PZ-*x*PYbN ไม่สามารถเกิดเป็นสารละลายของแข็งที่มีโครงสร้างแบบเพอรอฟสไกต์ที่บริสุทธิ์ได้เมื่อ *x* มากกว่า 0.2 จากนั้นทำการตรวจสอบอุณหภูมิการเปลี่ยนเฟส ด้วยผลของค่าคงที่ไดอิเล็กทริกและดิฟเฟอเรนเชียลสแกนนิงแคลอริเมทรี (Differential scanning calorimetry; DSC) พบว่าอุณหภูมิคูรีลดลง ลักษณะของพีกค่าคงที่ไดอิเล็กทริกจะมีฐานกว้างมากขึ้นเมื่อปริมาณของ *x* เพิ่มสูงขึ้น และที่สัดส่วน *x* = 0.02-0.20 มีการเปลี่ยนเฟสในช่วงอุณหภูมิแคบๆ ก่อนถึงอุณหภูมิคูรี นอกจากนี้ยังพบว่าเซรามิกที่เตรียมได้ทุกสัดส่วน แสดงสมบัติแอนติเฟอร์โรอิเล็กทริกที่อุณหภูมิห้อง

5. *<u>ผลการศึกษาเซรามิกในระบบ (1-x)PbZrO$_3$ – xPb(Y$_{1/2}$Nb$_{1/2}$)O$_3$</u>*

ทำการศึกษาสารละลายของแข็งของเซรามิกในระบบ เลดเซอร์โคเนต-อิทเทียมไนโอเบต ((1-*x*)$PbZrO_3$ - *x*Pb($Y_{1/2}Nb_{1/2}$)O_3; (1-*x*)PZ-*x*PYN) โดยทำการศึกษารูปแบบการเกิดเฟสเพอรอฟสไกต์ การเปลี่ยนเฟส สมบัติไดอิเล็กทริก และสมบัติเฟอร์โรอิเล็กทริกของเซรามิกที่เตรียมได้ โดยทำการเตรียมผงผลึกของ (1-*x*)PZ-*x*PYN ที่สัดส่วน *x* เท่ากับ 0.00 0.02 0.04 0.06 0.08 0.10 0.20 0.30 0.40 และ 0.50ด้วยวิธีการเตรียมสารตั้งต้นวูลแฟรไมต์ (Wolframite Precursor Method) โดยใช้สารตั้งต้นเป็นโลหะออกไซด์ที่มีความบริสุทธิ์สูง (> 99.5%) เผาแคลไซน์ที่อุณหภูมิ 900°C เป็นเวลา 2 ชั่วโมง จากนั้นทำการอัดขึ้นรูปชิ้นงานเป็นรูปแผ่นกลม และเผาซินเตอร์ที่อุณหภูมิ 1200-1300°C เป็นเวลา 2 ชั่วโมง พบว่าเมื่อปริมาณ *x* เพิ่มสูงขึ้นอุณหภูมิซินเตอร์จะลดลง จากการตรวจสอบรูปแบบการเกิดเฟสเพอรอฟสไกต์ และโครงสร้างผลึกของเซรามิก (1-*x*)PZ-*x*PYN ด้วยเทคนิคการเลี้ยวเบนของรังสีเอกซ์ (X-ray diffraction; XRD) พบว่าที่ *x* เท่ากับ 0.00 มีรูปแบบการเลี้ยวเบนของรังสีเอกซ์คล้ายคลึงกับรูปแบบการ เลี้ยวเบนรังสีเอกซ์มาตรฐาน(ICDD File no. 75-1607) ของ ซึ่งมีโครงสร้างผลึกเป็นแบบออร์โทรอมบิก และที่ *x* เท่ากับ 0.02-0.10 ยังคงมีรูปแบบการเลี้ยวเบนของรังสีเอกซ์ใกล้เคียงกับรูปแบบการเลี้ยวเบนรังสีเอกซ์มาตรฐาน(1-*x*)PZ-*x*PYN ของ $PbZrO_3$ แต่เมื่อปริมาณ *x* เพิ่มขึ้นถึง 0.20 พบเฟสแปลกปลอมเกิดขึ้น แสดงว่าสารในระบบ (1-*x*)PZ-*x*PYN สามารถเกิดเป็นสารละลายของแข็งที่มีโครงสร้างเป็นเพอรอฟสไกต์บริสุทธิ์ได้ที่ปริมาณ $x \leq 0.1$ เมื่อทำการตรวจสอบอุณหภูมิการเปลี่ยนเฟสจากแอนติเฟอร์โรอิเล็กทริกไปเป็น

พาราอิเล็กทริก หรือที่เรียกว่า “อุณหภูมิคูรี (Curie temperature; T_C)” ด้วยผลของค่าคงที่ไดอิเล็กทริก การวัดการขยายตัวทางความร้อน และดิฟเฟอเรนเชียลสแกนนิงแคลอริเมทรี (Differential scanning calorimetry; DSC) พบว่า ที่ x = 0.02-0.20 พบว่าอุณหภูมิคูรีลดลงและลักษณะพีกที่เมื่อปริมาณของ x เพิ่มสูงขึ้น นอกจากนี้ยังพบอีกว่าที่อุณหภูมิห้องเซรามิกที่สัดส่วน x = 0.02-0.10 แสดงสมบัติแอนติเฟอร์โรอิเล็กทริก และที่สัดส่วน x = 0.20 แสดงสมบัติเฟอร์โรอิเล็กทริก

6. <u>ผลการศึกษาเซรามิกในระบบ $(1-x)PbZrO_3 - xPb(Zn_{1/3}Nb_{2/3})O_3$</u>

เตรียมเซรามิกส์ $(1-x)PbZrO_3 - xPb(Zn_{1/3}Nb_{2/3})O_3$ ที่ x = 0.0-0.5 ด้วยวิธีโคลัมไบต์ ทำการตรวจพิสูจน์เอกลักษณ์ด้วยเทคนิคการเลี้ยวเบนของรังสีเอ็กซ์ และรามานสเปกโทรสโกปี วัดการขยายตัวเชิงเส้น วัดค่าคงที่ไดอิเล็กทริก วัดวงวนฮิสเทอริซิส P-E และตรวจสอบโครงสร้างในระดับจุลภาค ผลการตรวจสอบโครงสร้างผลึกพบว่า สามารถเตรียมเซรามิกส์ในระบบ PZ-PZN ที่มีโครงสร้างแบบเพอรอฟสไกต์ ในสัดส่วน $0.00 \leq x \leq 0.50$ ได้โดยไม่พบเฟสแปลกปลอม จากผลที่ได้จาก XRD และรามานพบว่าที่สัดส่วน $0.00 \leq x \leq 0.10$ มีระบบผลึกเป็นแบบออร์โธรอมบิก และเกิดการเปลี่ยนเฟสจากออร์โธรอมบิกไปเป็นรอมโบฮีดรอลที่ $x = 0.2$ การตรวจสอบสมบัติไดอิเล็กทริกพบว่าที่ปริมาณ PZN เป็น 0.02-0.06 พบการเปลี่ยนเฟสเกิดขึ้น 2 ครั้ง จาก AFE$\rightarrow$FE$\rightarrow$PE โดยอุณหภูมิการเปลี่ยนเฟสจาก AFE$\rightarrow$FE มีแนวโน้มลดลงเข้าใกล้อุณหภูมิห้องเมื่อปริมาณ PZN เพิ่มขึ้น และอุณหภูมิการเปลี่ยนเฟส FE$\rightarrow$PE มีแนวโน้มลดลงเมื่อ PZN เพิ่มขึ้น และพบว่าช่วงอุณหภูมิของเฟสเฟอร์โรอิเล็กทริกที่อยู่ระหว่างเฟสพาราอิเล็กทริกและแอนติเฟอร์โรอิเล็กทริกของ $PbZrO_3$ จะเพิ่มขึ้นตามความเข้มข้นของ PZN ที่ $0.08 \leq x$ พบการเปลี่ยนเฟสเกิดขึ้นเพียงครั้งเดียวจาก FE$\rightarrow$PE โดยอุณภูมิการเปลี่ยนเฟสมีแนวโน้มลดลงเมื่อปริมาณ PZN เพิ่มขึ้น นอกจากนี้ค่าคงที่ไดอิเล็กทริกสูงสุดจะค่อยๆ เพิ่มขึ้นเมื่อสัดส่วนองค์ประกอบเพิ่มสูงขึ้นถึง $x = 04$ จากนั้นจะกลับมามีค่าลดลงที่ $x = 0.5$ ผลการวัดการขยายตัวเชิงเส้นที่ $0.02 \leq x \leq 0.06$ พบการเปลี่ยนเฟสและแนวโน้มของอุณหภูมิการเปลี่ยนเฟสที่สอดคล้องกับผลการเปลี่ยนเฟสที่พบจากการวัดค่าไดอิเล็กทริก ในการเปลี่ยนเฟสจาก AFE $\rightarrow$ FE จะเกิดการขยายตัวเชิงเส้น ส่วนการเปลี่ยนเฟสจาก FE$\rightarrow$PE จะเกิดการหดตัวของสาร แต่ที่ x = 0.00 ผลที่ได้ขัดแย้งกับผลไดอิเล็กทริกคือพบการเปลี่ยนเฟสเกิดขึ้น 2 ครั้ง ผลการวัดวงวนฮิสเทอรีซิสพบวงวนฮิสเทอริซิสที่สมบูรณ์ที่สัดส่วน $0.08 \leq x \leq 0.50$ และพบลักษณะวงวนคล้ายกับวงวนของเฟอร์โรอิเล็กทริกปกติ ผลการตรวจสอบโครงสร้างในระดับจุลภาคที่บริเวณรอยหักของเม็ดเซรามิกส์พบว่าการหักส่วนใหญ่เกิดที่บริเวณขอบเกรน และขนาดเกรนในช่วง $0.02 \leq x \leq 0.06$ มีแนวโน้มเพิ่มขึ้นตามปริมาณ PZN จากนั้นจะมีขนาดลดงเมื่อเพิ่มขึ้นที่ $x = 0.08$ และ $x = 0.01$ เมื่อปริมาณ PZN เพิ่มขึ้นถึง $0.20 \leq x \leq 0.50$ จะกลับมีแนวโน้มเพิ่มขึ้นตามปริมาณ PZN อีกครั้ง

7. *<u>ผลการศึกษาเซรามิกในระบบ $(1-x)PbZrO_3 - xPb(Mg_{1/2}W_{1/2})O_3$</u>*

โครงสร้างผลึกและการเปลี่ยนเฟสของเซรามิกในระบบ เลดเซอร์โคเนต-เลดแมกนีเซียมทังสเตต ($(1-x)PbZrO_3$-$xPb(Mg_{1/2}W_{1/2})O_3$; PZ-PMW) ที่สัดส่วนขององค์ประกอบ (x) ตั้งแต่ 0.00-0.50 ด้วยเทคนิควุลแฟลมไมท์ (Wolframite precursor method) ทำการเตรียมผงผลึกโดยการเผาแคลไซน์ที่อุณหภูมิ 900°C เป็นเวลา 4 ชั่วโมงจากนั้นทำการตรวจสอบความบริสุทธิ์ด้วยเทคนิคการเลี้ยวเบนของรังสีเอกซ์พบว่า ผงผลึกที่เตรียมได้มีความบริสุทธิ์ ซึ่งเมื่อสัดส่วนขององค์ประกอบอยู่ที่ $0.00 \leq x \leq 0.10$ ผงผลึก PZ-PMW มีรูปแบบการเลี้ยวเบนรังสีเอกซ์สอดคล้องกับรูปแบบการเลี้ยวเบนรังสีเอกซ์ของ $PbZrO_3$ (PZ) จากฐานข้อมูลมาตรฐาน JCPDS เลขที่ 75-1607 แต่ที่สัดส่วนขององค์ประกอบ $0.20 \leq x \leq 0.50$ พบพีกแปลกปลอมเกิดขึ้นซึ่งเมื่อทำการตรวจสอบแล้วพบว่าพีกที่ปรากฏนั้นสอดคล้องกับรูปแบบการเลี้ยวเบนรังสีเอกซ์ของ PMW จากฐานข้อมูลมาตรฐาน JCPDS เลขที่ 75-0004 โดยเมื่อทำการหาปริมาณของ PMW ที่เกิดขึ้นพบว่าปริมาณของ PMW จะเพิ่มขึ้นตามสัดส่วนขององค์ประกอบที่เพิ่มขึ้น จากนั้นนำผงผลึกที่ได้มาทำการอัดขึ้นรูปแล้วนำไปเผาซินเตอร์ที่อุณหภูมิแตกต่างกันพบว่าเมื่อสัดส่วนขององค์ประกอบเพิ่มสูงขึ้น อุณหภูมิในการเผาซินเตอร์จะเพิ่มสูงขึ้นด้วย จากนั้นนำเซรามิกที่เตรียมได้มาทำการตรวจสอบความบริสุทธิ์และโครงสร้างผลึก (Crystal structure) ด้วยเทคนิคการเลี้ยวเบนของรังสีเอกซ์ (X-ray diffractometry; XRD) พบว่าเซรามิกที่เตรียมได้มีความบริสุทธิ์ โดยเมื่อสัดส่วนขององค์ประกอบอยู่ที่ $0.00 \leq x \leq 0.10$ เซรามิก PZ-PMW มีรูปแบบการเลี้ยวเบนรังสีเอกซ์สอดคล้องกับรูปแบบการเลี้ยวเบนรังสีเอกซ์ของ $PbZrO_3$ (PZ) จากฐานข้อมูลมาตรฐาน JCPDS เลขที่ 75-1607 เมื่อเพิ่มสัดส่วนขององค์ประกอบ (x) อยู่ที่ $0.20 \leq x \leq 0.50$ จะแบ่งการพิจารณาออกเป็นทีละสองสัดส่วนองค์ประกอบดังนี้คือ ที่สัดส่วนขององค์ประกอบเท่ากับ 0.20 และ 0.30 พบว่าจากรูปแบบการเลี้ยวเบนของรังสีเอกซ์ที่ได้จากผงผลึกปรากฏพีกของ PMW แยกออกมาแต่เมื่อทำการเผาซินเตอร์แล้วไม่พบพีกดังกล่าวแต่เมื่อสัดส่วนขององค์ประกอบเพิ่มขึ้นเป็น 0.40 และ 0.50 นั้นพบว่ายังคงปรากฏพีกของ PMW แยกออกมาอยู่เช่นเดิมแต่มีปริมาณของ PMW ลดลงและเมื่อทำการพิจารณาถึงโครงสร้างแล้วพบว่ามีแนวโน้มในการเปลี่ยนโครงสร้างจากออโทรอมบิกเป็นรอมโบฮีดรอลเมื่อสัดส่วนขององค์ประกอบ (x) สูงขึ้น จากนั้นทำการตรวจสอบสมบัติไดอิเล็กทริก (Dielectric properties) การขยายตัวทางความร้อน(Thermal expansion) สมบัติการเปลี่ยนแปลงทางความร้อนและยืนยันการเปลี่ยนเฟสด้วยการตรวจสอบสมบัติเฟอร์โรอิเล็กทริก (Ferroelectric properties) พบว่าเซรามิก PZ-PMW ที่สัดส่วนขององค์ประกอบ $0.00 \leq x \leq 0.10$ มีการเปลี่ยนเฟสสองช่วงคือเปลี่ยนจากแอนติเฟอร์โรอิเล็กทริกเป็นเฟอร์โรอิเล็กทริกและเปลี่ยนจากเฟอร์โรอิเล็กทริกเป็นพารา-อิเล็กทริกและเมื่อสัดส่วนขององค์ประกอบ (x) สูงขึ้นพบว่าอุณหภูมิในการเปลี่ยนเฟสลดลง และที่สัดส่วนขององค์ประกอบ $0.20 \leq x \leq 0.50$ มีการเปลี่ยนเฟสช่วงเดียวคือเปลี่ยนจากเฟอร์โรอิเล็กทริกเป็นพาราอิเล็กทริก

8. <u>ผลการศึกษาในระบบ (1-x)PbZrTiO$_3$ – xPb(Zn$_{1/3}$Ta$_{2/3}$)O$_3$</u>

เซรามิกในระบบ PZT-PZnTa เตรียมสารละลายของแข็ง Pb[(1-x)($Zr_{1/2}Ti_{1/2}$)-x($Zn_{1/3}Ta_{2/3}$)]O_3 เมื่อ x = 0.1-0.5 ด้วยกระบวนการโคลัมไบต์และวูลแฟรไมต์ (columbite and wolframite methods) และใช้เทคนิคการเลี้ยวเบนของรังสีเอกซ์ (XRD) กล้องจุลทรรศน์อิเล็กตรอนแบบส่องกราด (SEM) และเครื่องวัดไดอิเล็กทริก (dielectric spectroscopy) สำหรับตรวจสอบโครงสร้างผลึก สัณฐานวิทยา และสมบัติไดอิเล็กทริกของเซรามิก ตามลำดับ จากผลที่ได้พบว่า ปริมาณของเลดซิงค์แทนทาเลต [Pb($Zn_{1/3}Ta_{2/3}$)O_3; PZTa] ในสารละลายของแข็งนั้นส่งผลต่อเสถียรภาพของโครงสร้างเพอรอฟสไกต์ (perovskite) ของเลดเซอร์โคเนตไท [Pb($Zr_{1/2}Ti_{1/2}$)O_3; PZT] และเมื่อปริมาณ PZTa เพิ่มขึ้นจะเกิดการเปลี่ยนเฟสจากเตตระโกนอล (tetragonal) ไปเป็นซูโด-คิวบิก (pseudo-cubic) นอกจากนี้ยังพบว่าที่สัดส่วนองค์ประกอบ x = 0.1 นั้นมีทั้งสองเฟสของเตตระโกนอลและซูโด-คิวบิก และจากค่าคงที่ไดอิเล็กทริกที่ได้พบว่ามีค่าคงที่ไดอิเล็กทริกสูงสุดที่บริเวณรอยต่อเฟส (Morphotropic Phase Boundary; MPB) ซึ่งมีค่าเท่ากับ 19,600 ที่อุณหภูมิ 330 °C

9. <u>ผลการศึกษาเซรามิกในระบบ (1-x)Bi$_{0.5}$K$_{0.5}$O$_3$ – xBaTiO$_3$</u>

ทำการศึกษาสารละลายของแข็ง ของเซรามิกเพียโซอิเล็กทริกไร้สารตะกั่วในระบบ (1-x)$Bi_{0.5}K_{0.5}O_3$ – $x$$BaTiO_3$ (BKT – BT) เมื่อ x = 0.00 0.02 0.04 0.06 0.08 0.10 0.20 0.30 0.40 0.50 0.60 0.70 0.80 0.90 และ 1.00 โดยได้ทำการศึกษาโครงสร้างผลึก การเปลี่ยนเฟส และสมบัติไดอิเล็กทริกของสารระบบนี้ โดยได้ทำการเตรียมผงผลึกที่มีความบริสุทธิ์สูงด้วยเทคนิคปฏิกิริยาสถานะของแข็ง โดยใช้สารตั้งต้นเป็นสารประกอบประเภทออกไซด์หรือคาร์บอเนตที่มีความบริสุทธิ์สูง และทำการเผาแคลไซน์ในช่วงอุณหภูมิ 850 – 1300 องศาเซลเซียส เป็นเวลา 2 ชั่วโมง นำผงผลึกที่ได้ทำการอัดขึ้นรูปชิ้นงานที่มีเส้นผ่านศูนย์กลาง 15 มิลลิเมตร หนา 5 มิลลิเมตร หลังจากนั้นนำไปทำการอัดขึ้นรูปแบบทุกทิศทุกทาง (Isostatic press) ด้วยความดัน 250 MPa ทำการเผาซินเตอร์ในช่วงอุณหภูมิ 1040 – 1350 องศาเซลเซียส เป็นเลา 2 ชั่วโมง จากการศึกษาพบว่าเมื่อปริมาณของ BT เพิ่มขึ้น อุณหภูมิที่ใช้ในการเผาแคลไซน์และซินเตอร์เพิ่มสูงขึ้นตามลำดับ จากการศึกษาความหนาแน่นของเซรามิกที่เตรียมได้ พบว่า ความหนาแน่นของเซรามิกเพิ่มสูงขึ้น ตามปริมาณสัดส่วนของ BT ที่เพิ่มขึ้น จากการตรวจสอบรูปแบบการเกิดเฟส เพอรอฟสไกต์ และโครงสร้างผลึกของเซรามิก BKT – BT ด้วยเทคนิคการเลี้ยวเบนของรังสีเอกซ์ (X-ray diffraction; XRD) พบว่า สามารถเตรียมเซรามิกในระบบ BKT – BT ที่มีโครงสร้าง เพอรอฟสไกต์ที่มีความบริสุทธิ์สูงได้ทุกส่วนองค์ประกอบของสาร โดยที่ x เท่ากับ 0.00 มีรูปแบบการเลี้ยวเบนของรังสีเอกซ์คล้ายคลึงกับรูปแบบการเลี้ยวเบนรังสีเอกซ์มาตรฐาน (ICDD File no. 36-0339) ของ $Bi_{0.5}K_{0.5}O_3$ ซึ่งมีโครงสร้างผลึกเป็นแบบเททระโกนอล และเมื่อทำการเจือ BT เข้าไปในเซรามิก BKT พบว่า ยังคงมีโครงสร้างผลึกเป็นแบบเททระโกนอลทุกสัดส่วนองค์ประกอบของสาร อย่างไร

ก็ตาม เมื่อพิจารณาความเป็นเททระโกนอล (Tetragonality) ของเซรามิก พบว่า ความเป็นเททระโกนอลของเซรามิกมีค่าเพิ่มขึ้น ตามปริมาณสัดส่วนของ BT ที่เพิ่มขึ้น ยิ่งไปกว่านั้นยังพบว่า แลททิสพารามิเตอร์มีขนาดใหญ่ขึ้นตามปริมาณของ BT ที่เพิ่มขึ้นด้วย จากการตรวจสอบการเปลี่ยนเฟสและสมบัติทางไดอิเล็กทริก พบว่า ที่ x เท่ากับ 0.00 พบอุณหภูมิคูรีย์ที่ 400 องศาเซลเซียส ซึ่งเป็นอุณหภูมิการเปลี่ยนเฟสจากเฟสเฟอร์โรอิเล็กทริกแบบเททระโกนอลไปเป็นเฟสพาราอิเล็กทริกที่มีโครงสร้างเป็นแบบคิวบิก และเมื่อทำการเจือ BT มากขึ้น พบว่า อุณหภูมิคูรีย์จะลดลงตามลำดับ นอกจากนี้ยังพบว่า ที่ x เท่ากับ 0.00 กราฟไดอิเล็กตริกมีลักษณะเป็นพีคฐานกว้าง (Broad peak) ซึ่งเป็นลักษณะของการเปลี่ยนเฟสแบบต่อเนื่อง (Diffuse phase transition) และเมื่อปริมาณของ BT เพิ่มขึ้นลักษณะของพีคเริ่มแหลมขึ้น (Shape peak) ซึ่งเป็นลักษณะของการเปลี่ยนเฟสแบบฉับพลัน (First order phase transition)

10. <u>ผลการศึกษาเซรามิกในระบบ (1-x)$PbZrO_3$ – x$BiFeO_3$</u>

ทำการศึกษาสารละลายของแข็ง ของเซรามิกเพียโซอิเล็กทริกไร้สารตะกั่วในระบบ (1-x)$PbZrO_3$ – $x$$BiFeO_3$ (PZ - BF) เมื่อ x = 0.00 0.02 0.04 0.06 0.08 0.10 และ 0.20 โดยได้ทำการศึกษาโครงสร้างผลึก การเปลี่ยนเฟส และสมบัติไดอิเล็กทริกของสารระบบนี้ โดยได้ทำการเตรียมผงผลึกที่มีความบริสุทธิ์สูงด้วยเทคนิคปฏิกิริยาสถานะของแข็ง โดยใช้สารตั้งต้นเป็นสารประกอบประเภทออกไซด์ที่มีความบริสุทธิ์สูง และทำการเผาแคลไซน์ที่อุณหภูมิ 850องศาเซลเซียส เป็นเวลา 2 ชั่วโมง นำผงผลึกที่ได้ทำการอัดขึ้นรูปชิ้นงานที่มีเส้นผ่านศูนย์กลาง 15 มิลลิเมตร ทำการเผาซินเตอร์ในช่วงอุณหภูมิ 1050 – 1250 องศาเซลเซียส เป็นเวลา 2 ชั่วโมง จากการศึกษาพบว่า เมื่อปริมาณของ $BiFeO_3$ เพิ่มขึ้น อุณหภูมิที่ใช้ในการเผาซินเตอร์ลดลงตามลำดับ จากการตรวจสอบรูปแบบการเกิดเฟสเพอรอฟสไกต์ และโครงสร้างผลึกของเซรามิก PZ – BF ด้วยเทคนิคการเลี้ยวเบนของรังสีเอกซ์ (X-ray diffraction; XRD) พบว่า สามารถเตรียมเซรามิกในระบบ PZ – BF ที่มีโครงสร้างเพอรอฟสไกต์บริสุทธิ์ได้สูงสุดที่ 20 %โมล ของ $BiFeO_3$ ที่เจือเข้าไป (รอยืนยันผล XRD x = 0.3 0.4 และเม็ด ได้ 20 เม.ย.) โดยที่ x เท่ากับ 0.00 มีรูปแบบการเลี้ยวเบนของรังสีเอกซ์คล้ายคลึงกับรูปแบบการเลี้ยวเบนรังสีเอกซ์มาตรฐาน (ICDD File no. 75-1607) ของ $PbZrO_3$ ซึ่งมีโครงสร้างผลึกเป็นแบบออร์โธรอมบิก และเมื่อทำการเจือ $BiFeO_3$ เข้าไปในเซรามิก $PbZrO_3$ ที่ x เท่ากับ 0.02 พบว่า ยังคงมีโครงสร้างผลึกเป็นแบบออร์โธรอมบิกอยู่ อย่างไรก็ตาม เมื่อปริมาณของ $PbZrO_3$ เพิ่มมากขึ้นเป็น x = 0.10 กลับไม่พบโครงสร้างผลึกแบบออร์โธรอมบิก และโครงสร้างน่าจะเปลี่ยนเป็นโครงสร้างแบบรอมโบฮีดรอล (รอผล XRD เม็ด) นอกจากนี้ยังพบว่าแลททิสพารามิเตอร์มีขนาดเล็กลงตามปริมาณของ $BiFeO_3$ ที่เพิ่มขึ้นด้วย จากการตรวจสอบการเปลี่ยนเฟสและสมบัติทางไดอิเล็กทริก พบว่า ที่ x = 0.00 พบอุณหภูมิคูรีย์ที่ 230 องศาเซลเซียส ซึ่งเป็นอุณหภูมิการเปลี่ยนเฟสจากเฟสเฟอร์โรอิเล็กทริกแบบออร์โธรอมบิกไปเป็นเฟสพาราอิเล็กทริก

ที่มีโครงสร้างเป็นแบบคิวบิก และเมื่อทำการเจือ $BiFeO_3$ เพิ่มขึ้น พบว่า อุณหภูมิคูรีย์จะลดลงตามลำดับ เมื่อพิจารณาค่าไดอิเล็กทริกสูงสุด (ε_{max}) พบว่า ในช่วงแรก เมื่อปริมาณของ $BiFeO_3$ เพิ่มขึ้น ค่า ε_{max} มีค่าเพิ่มขึ้นตามลำดับ อย่างไรก็ตามเมื่อ $x = 0.08$ กลับพบว่าค่า ε_{max} มีค่าลดลงและลดลงอย่างต่อเนื่องเมื่อปริมาณของเพิ่มขึ้น นอกจากนี้ยังพบว่า ที่ x เท่ากับ 0.00 กราฟไดอิเล็กทริกมีลักษณะเป็นพีคแหลม (Shape peak) ซึ่งเป็นลักษณะของการเปลี่ยนเฟสแบบฉับพลัน (First order phase transition) และเมื่อปริมาณของ $BiFeO_3$ เพิ่มขึ้น พีคเริ่มมีลักษณะฐานกว้าง (Broad peak) มากขึ้นตามลำดับ ซึ่งเป็นลักษณะของการเปลี่ยนเฟสแบบต่อเนื่อง (Diffuse phase transition)

11. <u>ผงผลึกในระบบ $KNbO_3$</u>

ศึกษาการเตรียมผงผลึกไร้สารตะกั่วโพแทสเซียมไนโอเบต ($KNbO_3$) โดยวิธีปฏิกิริยาสถานะของแข็งแบบดัดแปลง โดยการใช้โพแทสเซียมออกซาเลตโมโนไฮเดรตเป็นสารตั้งต้น (แทนโพแทสเซียมคาร์บอเนตที่ใช้ในวิธีดั้งเดิม) โดยทำการศึกษาพฤติกรรมทางความร้อนของสารตั้งต้นโดยเทคนิคเทอร์โมกราวิเมตริกอนาไลซิส (Thermo gravimetric analysis; TGA) และเทคนิคดิฟเฟอร์เรนเชียลเทอร์มอลอนาไลซิส (Differential thermal analysis; DTA). เพื่อหาอุณหภูมิที่เหมาะสมในการเผาแคลไซน์ ผงผลึกที่เตรียมได้ภายหลังจากการเผาแคลไซน์ถูกนำไปตรวจสอบการเกิดเฟสเพอรอฟสไกต์และความบริสุทธิ์โดยเทคนิคการเลี้ยวเบนของรังสีเอกซ์ (X-ray diffraction technique; XRD) และตรวจสอบสัณฐานวิทยาโดยกล้องจุลทรรศน์อิเล็กตรอนแบบส่องกราด (Scanning electron microscope; SEM) พบว่าสามารถสังเคราะห์ผงผลึกไร้สารตะกั่วโพแทสเซียมไนโอเบต ($KNbO_3$) ได้ภายหลังจากการเผาแคลไซน์ที่อุณหภูมิ 550 องศาเซลเซียส เป็นเวลา 20 นาที (หรือมากกว่า) โดยใช้อัตราการขึ้นลงของอุณหภูมิเท่ากับ 20 องศาเซลเซียสต่อนาที โดยผงผลึกที่เตรียมได้มีรูปแบบการเลี้ยวเบนของรังสีเอกซ์สอดคล้องกับรูปแบบการเลี้ยวเบนของรังสีเอกซ์โพแทสเซียมไนโอเบตมาตรฐาน JCPDS no.32-0822 ซึ่งมีโครงสร้างผลึกแบบออโธรอมบิก (Orthorhombic) ผลึกมีรูปร่างคล้ายคลึงกัน ไม่สังเกตพบลักษณะผลึกที่แตกต่างซึ่งแสดงถึงเฟสไพโรคลอร์หรือเฟสแปลกปลอมอื่นใด โดยขนาดผลึกเฉลี่ย (Mean crystalline size; *D*) เมื่อคำนวณจากรูปแบบการเลี้ยวเบนของรังสีเอกซ์ พบว่ามีค่าเท่า 33.15$\pm$9.22 นาโนเมตร ซึ่งเป็นค่าน้อยกว่าขนาดอนุภาคเฉลี่ยที่สังเกตได้จากรูปจากกล้องจุลทรรศน์อิเล็กตรอนแบบส่องกราดที่มีค่าเท่ากับ 222.14$\pm$81.51 นาโนเมตร ทั้งนี้อาจเป็นผลจากการเกาะกลุ่มหรือการจับตัวกันของผงผลึก นอกจากนั้นยังพบว่าอุณหภูมิและเวลาในการเผาแคลไซน์ มีผลต่อการเติบโตของผลึก สังเกตได้จากรูปแบบการเลี้ยวเบนของรังสีเอกซ์เกิดพีกที่สูงขึ้น ค่าแลตทิซพารามิเตอร์และขนาดผลึกเฉลี่ย (*D*) ที่คำนวณได้มีค่าเพิ่มขึ้นเมื่ออุณหภูมิและเวลาในการเผาแคลไซน์เพิ่มขึ้น

12. <u>ผงผลึกในระบบ $NaNbO_3$</u>

ทำการศึกษาการเตรียมผงผลึกไร้สารตะกั่วโซเดียมไนโอเบต ($NaNbO_3$) โดยวิธีการสังเคราะห์แบบเผาไหม้ (Combustion technique) โดยใช้โซเดียมไนเตรท ($NaNO_3$) และไนโอเบียมเพนตะออกไซด์ (Nb_2O_5) เป็นสารตั้งต้น โดยมีไกลซีน (NH_2CH_2COOH) เป็นสารเชื้อเพลิง โดยทำการศึกษาอิทธิพลของอัตราส่วนโดยโมลระหว่างสารตั้งต้นต่อสารเชื้อเพลิง (φ) ที่มีผลต่อการเกิดเฟสเพอรอฟสไกต์ของโซเดียมไนโอเบต และศึกษาอิทธิพลของอุณหภูมิที่ใช้ในการเผาแคลไซน์เมื่ออัตราส่วนระหว่างสารตั้งต้นต่อสารเชื้อเพลิง (φ) คงที่ จากนั้นตรวจสอบเอกลักษณ์ของผงผลึกที่เตรียมได้โดยเทคนิคการเลี้ยวเบนของรังสีเอกซ์ (X-ray diffraction technique; XRD) และเครื่องฟูเรียทรานสฟอร์มอินฟราเรดสเปกโตมิเตอร์ (Fourier transform infrared spectrometer; FTIR) จากนั้นตรวจสอบสัณฐานวิทยาโดยกล้องจุลทรรศน์อิเล็กตรอนแบบส่องกราด (Scanning electron microscope; SEM) จากผลการทดลองส่วนแรกพบว่าที่อัตราส่วน $\varphi < 0.7$ จะไม่เกิดปฏิกิริยาการเผาไหม้ และไม่เกิดเฟสเพอรอฟสไกต์ในผงผลึก เมื่ออัตราส่วน $\varphi \geq 0.7$ จึงเกิดปฏิกิริยาการเผาไหม้และตรวจพบเฟสเพอรอฟสไกต์ของโซเดียมไนโอเบต ที่มีรูปแบบการเลี้ยวเบนของรังสีเอกซ์สอดคล้องกับรูปแบบการเลี้ยวเบนของรังสีเอกซ์มาตรฐาน JCPDS no.82-0606 จากการตรวจสอบสัญฐานวิทยาพบว่า อนุภาคที่เตรียมได้มีลักษณะเป็นทรงลูกบาศก์สี่เหลี่ยมมุมฉาก โดยขนาดอนุภาคเฉลี่ยของผงผลึกที่เตรียมได้มีค่าระหว่าง 55 ถึง 600 นาโนเมตร ทั้งนี้เมื่ออัตราส่วน $\varphi \geq 1.0$ พบว่านอกจากพบเฟสเพอร์รอฟสไกต์แล้ว ยังตรวจพบเฟสแปลกปลอมของไนโอเบียมเพนตะออกไซด์ซึ่งเป็นสารตั้งต้นหลงเหลืออยู่ ซึ่งเฟสดังกล่าวจะมีปริมาณมากขึ้นเมื่ออัตราส่วน φ เพิ่มมากขึ้น จากผลการทดลองส่วนที่สอง เมื่อนำผงผลึกที่เตรียมได้จากวิธีการสังเคราะห์แบบเผาไหม้โดยใช้ $\varphi = 1.0$ ไปผ่านกระบวนการเผาแคลไซน์ที่อุณหภูมิต่างๆ เป็นเวลา 4 ชั่วโมง พบว่าเมื่ออุณหภูมิเพิ่มสูงขึ้น รูปแบบการเลี้ยวเบนของรังสีเอกซ์แสดงถึงการลดลงของปริมาณเฟสแปลกปลอมของไนโอเบียมเพนตะออกไซด์ และแสดงเฟสเพอรอฟสไกต์ของโซเดียมไนโอเบตบริสุทธิ์ เมื่อผงผลึกผ่านการเผาแคลไซน์ที่อุณหภูมิอย่างน้อย 400 องศาเซลเซียส เป็นต้นไป อย่างไรก็ตาม พบว่าอุณหภูมิที่สูงขึ้นจะส่งผลต่อการเพิ่มขึ้นของความเป็นผลึกของผงผลึกด้วย สังเกตจากการสูงขึ้นและการแยกออกของพีกที่เกิดในรูปแบบการเลี้ยวเบนของรังสีเอกซ์

Output จากโครงการวิจัยที่ได้รับทุนวิจัย

1. ผลงานตีพิมพ์ในวารสารวิชาการระดับนานาชาติจำนวนทั้งสิ้น 46 เรื่อง

1 **Naratip Vittayakorn**, Nopsiri Chaiyo, Rangson Muanghlua, Anuchar Ruangphanit and Wanwilai C. Vittayakorn "Effect of annealing on the structure and dielectric properties in PZT-PCoN ceramics" *Advance Materials Research;* Vol. 55-57(2008) pp 49-52

2 Manun Sutapun, Rangson Muanghlua, Chian-Chih Huang, David P. Cann, Wanwilai C. Vittayakorn and **Naratip Vittayakorn** "Influence of Fabrication Processing on Perovskite Phase Formation of KNN-BZT" *Advance Materials Research;* Vol. 55-57(2008) pp 113-116

3 Supamas Wirunchit, Pitak Laoratanakul and **Naratip Vittayakorn** "Effect of Lead Nickel Niobate Substitution on Phase Transitions of Lead Zirconate Ceramics Prepared by the Solid State Reaction Method" *Advance Materials Research;* Vol. 55-57(2008) pp 117-120

4 Wanwimon Banlue, Rangson Muanfhlua, Wanwilai C. Vittayakorn and **Naratip Vittayakorn** "Synthesis, crystal structures, phase transition characterization and thermal properties of the $(1-x)PbZrO_3$-$xPb(Co_{1/3}Nb_{2/3})O_3$ solid solution system" *Advance Materials Research;* Vol. 55-57(2008) pp 121-124

5 Rangson Muanfhlua, Wanwilai C. Vittayakorn and **Naratip Vittayakorn** "Effects of Zr/Ti ratio on the structure and ferroelectric properties in PZT-PZN-PMN ceramics near the morphotropic phase boundary" *Advance Materials Research*; Vol. 55-57(2008) pp 125-128

6 Nopsiri Chaiyo, Rangson Muanghlua, Anuchar Ruangphanit and Wanwilai C. Vittayakorn and **Naratip Vittayakorn** "Synthesis, phase formation and characterization of $Co_4Nb_2O_9$ powders synthesized by solid-state reaction" *Advance Materials Research;* Vol. 55-57(2008) pp 873-876

7 S. Nabunmee, **N Vittayakorn**, D. P. Cann and G. Rujijanagul "Ferroelectric and Mechanical Properties of PZT-PZN-PNN ceramics" *Advance Materials Research;* Vol. 55-57(2008) pp 217-220

8 T. Bongkarn, N Phungjitt and **N. Vittayakorn** "Effect of Calcination Temperatures on Microstructure and Phase Formation of $Ba(Zr_{0.25}Ti_{0.75})O_3$ Powders" *Advance Materials Research;* Vol. 55-57(2008) pp 205-208

9 Wanwimon Banlue, **Naratip Vittayakorn** , Chien-Chih Huang and David P. Cann "Dielectric properties of $Pb[(1-x)(Zr_{1/2}Ti_{1/2})-x(Zn_{1/3}Ta_{2/3})]O_3$ ceramics prepared by columbite and wolframite methods" *Journal of Materials Science,* Volume 43, Number 12 / June, 2008**,** page 4220-4225 Impact factor = 0.99

10 Supamas Wirunchit, Pitak Laoratanakul and **Naratip Vittayakorn** "Physical properties and phase transitions in perovskite $Pb[Zr_{1-x}(Ni_{1/3}Nb_{2/3})_x]O_3$ $(0.0 \leq x \leq 0.5)$ ceramics" *Journal of Physics D: Applied physics* Volume 41 Number 12, page 125406-125413; 21 Jane 2008: Impact Factor = 2.077

11 Supamas Wirunchit and **Naratip Vittayakorn** "Structural transformation in antiferroelectric $PbZrO_3$-relaxor ferroelectric $Pb(Ni_{1/3}Nb_{2/3})O_3$ solid solution system" *Journal of Applied Physics* (2008)104 (2), p.p 024103 Impact factor = 2.2

12 Nopsiri Chaiyo and **Naratip Vittayakorn** "Effect of calcinations conditions on phase formation of microwave dielectric cobalt niobate ($CoNb_2O_6$) powders via a mixed oxide synthesis route" *Journal of Ceramic Processing Research*, Vol. 9 No. 4, 2008 page 381-384, Impact factor = 0.534

13 Wanwimon Banlue and **Naratip Vittayakorn** "Ferroelectric phase stabilization, phase transformations and thermal properties in $(1-x)PbZrO_3$-$xPb(Co_{1/3}Nb_{2/3})O_3$ solid solution" *Applied Physics A: Materials Science and Processing* (2008) 93 (2), pp. 565-569, Impact factor = 2.2

14 Anurak Prasatkhetragarn, **Naratip Vittayakorn**, Supon Ananta, Rattikorn Yimnurun and David P. Cann "Synthesis and Dielectric and Ferroelectric Properties of Ceramics in $(1-x)Pb(Zr_{1/2}Ti_{1/2})O_3$–$(x)Pb(Co_{1/3}Nb_{2/3})O_3$ System" *Japanese Journal of Applied Physics* Vol. 47, No. 2, 2008, pp. 998–1002, Impact factor = 1.13

15 Chien-Chih Huang, **Naratip Vittayakorn**, Anurak Prasatkhetragarn, Brady J. Gibbons, and David P. Cann "Phase Transitions and Dielectric Properties in $Bi(Zn_{1/2}Ti_{1/2})O_3$–$(Na_{1-y}Li_y)NbO_3$ Perovskite Solid Solutions" *Japanese Journal of Applied Physics* 48 (2009) 031401, Impact factor = 1.13

16 W. Qu, X. Tan, **N. Vittayakorn**, S. Wirunchit, and M. F. Besser "High temperature phases in the $0.98PbZrO_3$–$0.02Pb(Ni_{1/3}Nb_{2/3})O_3$ ceramic" *Journal of Applied Physics* (2009) 105, p.p 014106 Impact factor = 2.2

17 Manoon Sutapun, Chien-Chih Huang David P. Cann and **Naratip Vittayakorn** "Phase transitional behavior and dielectric properties of lead free $(K_{0.5}Na_{0.5})NbO_3$-$Bi(Zn_{0.5}Ti_{0.5})O_3$ ceramics" *Journal of Alloy and Compound*. ; Vol. 479 Page 462-466 (2009); Impact Factor 2007:1.455

18 Nopsiri Chaiyo, Anucha Ruangphanit, Rangson Muanghlua, Surasak Niemcharoen, Atchara Sangseub, Saowanee Taopen, Sunanta Leelapattana, Wanwilai C. Vittayakorn, **Naratip Vittayakorn** "Synthesis and Morphology Evolution of Lead-Free Piezoelectric $K_{1/2}Na_{1/2}NbO_3$ Powder at Low Temperature" *Ferroelectrics*, Volume 383, Issue 1 2009 , pages 8 – 14; Impact Factor: 0.427

19 Rangson Muanghlua; Surasak Niemcharoen; Wanwilai C. Vittayakorn; Nattapong Tungsitvisetkul; Pimjan Chinwaro; Anucha Ruangphanit; Nopsiri Chaiyo; **Naratip Vittayakorn** "Preparation and Properties of Lead Free Bismuth Sodium Titanate-Bismuth Zinc Titanate Ceramics" *Ferroelectrics*, Volume 383, Issue 1 2009 , pages 1 – 7; Impact Factor: 0.427

20 Theerachai Bongkarn; Nalinee Phungjitt; **Naratip Vittayakorn** "Effect of Firing Temperatures on Phase Formation and Microstructure of $Ba(Zr_{0.3}Ti_{0.7})O_3$ Ceramics Prepared via Mixed Oxide Method" *Ferroelectrics*, Volume 383, Issue 1 2009 , pages 65 – 72; Impact Factor: 0.427

21 Wanwilai C. Vittayakorn and **Naratip Vittayakorn** "Hysteresis Response of Lead Zirconate —Lead Nickel Niobate Ferroelectric Ceramic Under Compressive Stress" *Ferroelectrics*, Volume 382, Issue 1 2009 , pages 1– 6; Impact Factor: 0.427

22 **Naratip Vittayakorn**; Wanwimon Banlue "Synthesis, Ferroelectric Phase Stabilization, Phase Transition and Thermal Properties in $(1\text{-}x)PbZrO_3$-$xPb(Zn_{1/3}Nb_{2/3})O_3$ Solid Solution" *Ferroelectrics*, Volume 382, Issue 1 2009 , pages 110– 114; Impact Factor: 0.427

23 Manoon Sutapun; **Naratip Vittayakorn** "Phase Transition and Dielectric Properties of Lead Free $(K_{0.5}Na_{0.5})NbO_3$- $Bi(Zn_{0.5}Ti_{0.5})O_3$ Piezoelectric Ceramics" *Ferroelectrics*, Volume 382, Issue 1 2009 , pages 115– 121; Impact Factor: 0.427

24 Wanwimon Banlue; **Naratip Vittayakorn** "Effect of $Pb(Zn_{1/3}Nb_{2/3})O_3$ Additions on Phase Structure, Ferroelectric and Dielectric Properties of $PbZrO_3$ Ceramics" *Ferroelectrics*, Volume 382, Issue 1 2009 , pages 122– 126; Impact Factor: 0.427

25 Supamas Wirunchit; **Naratip Vittayakorn** "Crossover from Antiferroelectric to Normal Ferroelectric Behavior in Lead Zirconate-Lead Nickel Niobate Ceramics Prepared by the Reaction Sintering Process" *Ferroelectrics*, Volume 382, Issue 1 2009 , pages 135– 140; Impact Factor: 0.427

26 Supamas Wirunchit; Rangson Muanghlua; Surasak Niemcharoen; Wanwilai C. Vittayakorn; Pitak Laoratanakul; **Naratip Vittayakorn** "Preparation of Lead Zirconate-Lead Nickel Niobate Ceramics by the Reaction Sintering Process" *Ferroelectrics*, Volume 380, Issue 1 2009 , pages 14– 19; Impact Factor: 0.427

27 G. Rujijanagul; **N. Vittayakorn**; S. Nabunmee "Effect of Annealing Time on Electrical and Mechanical Properties of $0.7(Pb(Zr_{1/2}Ti_{1/2})O_3)$-$0.3(Pb(Zn_{1/2}Nb_{2/3})O_3$ Ceramics" *Ferroelectrics*, Volume 384, Issue 1 2009 , pages 68 – 72; Impact Factor: 0.427

28 B. Boonchom, M. Thongkam, S. Kongtaweelert and **N. Vittayakorn** "A simple route to synthesis new binary cobalt iron cyclotetraphosphate $CoFeP_4O_{12}$ using aqueous and acetone media" *Journal of Alloys and Compounds*, Volume 486, Issues 1-2, 3 November 2009, Pages 689-692 Impact Factor 2007:1.455

29 Nalinee Phungjitt, perapong panya, Theerachai Bongkarn and **Naratip Vittayakorn** "The Structure phase and microstrucutres of perovskite $Ba(Ti_{1-x}Zr_x)O_3$ ceramics using the combustion routre" *Journal Functional Materials Letters* ; Vol. 2 Page 169-174 (2009)

30 Nopsiri Chaiyo, Banjong Boonchom and **Naratip Vittayakorn** "Solid State reaction of Sodium Niobate ($NaNbO_3$) powder at low temperature." *Journal of Materials Science,* Volume 45, 2010 , pages 1443-1447; Impact Factor: 0.99

31 Banjong Boonchom and **Naratip Vittayakorn** "One-step thermal synthesis of binary manganese iron cyclotetraphate $MnFeP_4O_{12}$" *Journal of Materials Science,* Volume 45, 2010 , pages 1443-1447; Impact Factor: 1.4

32 Banjong Boonchom, Montree Thongkam, Samart Kongtaweelert and **Naratip Vittayakorn** "Flower-like micro-particles and novel super paramagnetic properties of new binary $Co_{1/2}Fe_{1/2}(H_2PO_4)_2.2H_2O$ obtained by a rapid solid state route at ambient temperature" *Materials Research Bulletin*, Volume 44, 2009 , pages 2206-2210; Impact Factor: 1.7

33 Banjong Boonchom and **Naratip Vittayakorn** "Synthesis and ferromagnetic property of new binary copper iron pyrophosphate $CuFeP_2O_7$" *Materials letters,* Volume 64, 2010 , pages 275-277; Impact Factor: 1.7

34 Banjong Boonchom and **Naratip Vittayakorn** "Floral-like microarchitectures of cobalt iron cyclotetraphosphate obtained by solid state synthesis" *Powder Technology* Volume 198, 2010, page 25-28; Impact Factor: 1.8

35 **Naratip Vittayakorn**, Piyanut Charoonsuk, Panisara Kasiansin, Supamas Wirunchit,and Banjong Boonchom "Dielectric properties and phase transition behaviors in (1-x)$PbZrO_3$–xPb($Mg_{1/2}W_{1/2}$)O_3 ceramics" *Journal of Applied physics* Volume 106 page 064104, 2009; Impact factor: 2.4

36 Usa Sukkha, Rangson Muanghlua, Surasak Niemcharoen, Banjong Boonchom and **Naratip Vittayakorn** "Antiferroelectric–ferroelectric phase transition in lead zinc niobate modified lead zirconate ceramics: crystal studies, microstructure, thermal and electrical properties" *Applied Physics A: Materials Science & Processing*, 2010, Volume 100, Number 2, Pages 551-559; Impact Factor = 1.595

37 Banjong Boonchom, Rattanai Baitahe, Zongporn Joungmunkong, **Naratip Vittayakorn** "Grass blade-like microparticle $MnPO_4 \cdot H_2O$ prepared by a simple precipitation at room temperature" *Powder Technology*, Volume 203, Issue 2, 10 November 2010, Pages 310-314; Impact Factor = 1.745

38 Banjong Boonchom, Rattanai Baitahe, Samart Kongtaweelert and **Naratip Vittayakorn** "Kinetics and Thermodynamics of Zinc Phosphate Hydrate Synthesized by a Simple Route in Aqueous and Acetone Media" *Industrial & Engineering Chemistry Research*, 2010, 49 (8), pp 3571–3576 ;Impact Factor =1.758

39 Banjong Boonchom and **Naratip Vittayakorn** "Dehydration Behavior of Synthetic $Al_{0.5}Fe_{0.5}PO_4 \cdot 2.5H_2O$" *Journal of Chemical & Engineering Data*, 2010, 55 (9), pp 3307–3311 Impact Factor =1.695

40 Piyanut Charoonsuk, Supamas Wirunchit, Rangson Muanghlua, Surasak Niemcharoen, Banjong Boonchom, **Naratip Vittayakorn** "The phase evolution with temperature in 0.94$PbZrO_3$–0.06Pb($Mg_{1/2}W_{1/2}$)O_3 antiferroelectric ceramic" *Journal of Alloys and Compounds*, Volume 506, Issue 1, 10 September 2010, Pages 313-316; Impact Factor = 2.135

41 Banjong Boonchom and **Naratip Vittayakorn** "Soft synthesis route and characterization of superparamagnetic $Mn_{1/2}Fe_{1/2}(H_2PO_4)_2 \cdot 2H_2O$ and its decomposed product" *Industrial & Engineering Chemistry Research* Volume 50, 2011, pp 2021–2030 ;Impact Factor = 1.758

42 Banjong Boonchom, Chanaiporn Danvirutai and **Naratip Vittayakorn** "A simple synthesis and characterization of binary $Co_{0.5}Fe_{0.5}(H_2PO_4)_2 \cdot 2H_2O$ and its final decomposition product $CoFeP_4O_{12}$" *Journal of Solid State Chemistry*, Volume 13 (2011) 77-81, Impact factor = 2.34

43 **Naratip Vittayakorn** and Banjong Boonchom "Effect of $BiAlO_3$ modification on the stability of antiferroelectric phase in $PbZrO_3$ ceramics prepared by conventional solid state reaction" *Journal of Alloys and Compounds*, Volume 509, 2011, Pages 2304 - 2310; Impact Factor = 2.135

44 Nopsiri Chaiyo, Rangson Muanghlua, Surasak Niemcharoen, Banjong Boonchom and **Naratip Vittayakorn** "Solution combustion synthesis and characterization of lead-free piezoelectric sodium niobate ($NaNbO_3$) powders" *Journal of Alloys and Compounds*, Volume 509, 2011, Pages 2445 - 2449; Impact Factor = 2.135

45 Nopsiri Chaiyo, Anucha Ruangphanit, Rangson Muanghlua, Surasak Niemcharoen, Banjong Boonchom and **Naratip Vittayakorn** "Synthesis of potassium niobate ($KNbO_3$) nano-powder by a modified solid-state reaction" *Journal of Materials Science*, Volume 46 (2011) 1585–1590, Impact Factor = 1.4

46 Rangson Muanghlua, Surasak Niemcharoen, Manoon Sutapun, Banjong Boonchom and **Naratip Vittayakorn** "Phase transition behaviour and electrical properties of lead-free $(K_{0.5}Na_{0.5})$ NbO_3-$LiNbO_3$-$LiSbO_3$ piezoelectric ceramics" *Current Applied Physics*, Volume 11 (2011) 434-437, Impact factor = 1.52

2. การนำเสนอผลงานวิจัยในที่ประชุมวิชาการทั้งสิ้น 30 เรื่อง

1. **Naratip Vittayakorn**, Nopsiri Chaiyo, Rangson Muanghlua, Anuchar Ruangphanit and Wanwilai C. Vittayakorn "Effect of annealing on the structure and dielectric properties in PZT-PCoN ceramics" Smart/intelligent materials and nanotechnology & 2nd International workshop on functional materials and nanomaterials 22-25 April 2008 Chiang Mai ,Thailand

2. Wanwimon Banlue and **Naratip Vittayakorn** "Characterization of the (1-*x*)$PbZrO_3$-*x*$Pb(Co_{1/3}Nb_{2/3})O_3$ ceramics by XRD, SEM, thermal and dielectric properties tests" The Asian Meeting on Electroceramics 22-24 October 2008, Tsukuba, Japan
3. Nabunmee, S., **Vittayakorn, N.**, Cann, D.P., Rujijanagul, G. "Ferroelectric and mechanical properties of PZT-PZN-PNN ceramics" Smart/intelligent materials and nanotechnology & 2nd International workshop on functional materials and nanomaterials 22-25 April 2008 Chiang Mai ,Thailand
4. Sutapun, M., Muanghlua, R., Huang, C.-C., Cann, D.P., Vittayakorn, W.C., **Vittayakorn, N.** "Influence of fabrication processing on perovskite phase formation of KNN-BZT " Smart/intelligent materials and nanotechnology & 2nd International workshop on functional materials and nanomaterials 22-25 April 2008 Chiang Mai ,Thailand
5. Wirunchit, S., Laoratanakul, P., **Vittayakorn, N**. "Effect of lead nickel niobate substitution on phase transitions of lead zirconate ceramics prepared by the solid state reaction method" Smart/intelligent materials and nanotechnology & 2nd International workshop on functional materials and nanomaterials 22-25 April 2008 Chiang Mai ,Thailand
6. Chaiyo, N., Muanghlua, R., Ruangphanit, A., Vittayakorn, W.C., **Vittayakorn, N**. "Synthesis, phase formation and characterization of $Co_4Nb_2O_9$ powders synthesized by solid-state reaction " Smart/intelligent materials and nanotechnology & 2nd International workshop on functional materials and nanomaterials 22-25 April 2008 Chiang Mai ,Thailand
7. Muanghlua, R., Niemchareon, S., Vittayakorn, W.C., **Vittayakorn, N**. "Effects of Zr/Ti ratio on the structure and ferroelectric properties in PZT-PZN-PMN ceramics near the morphotropic phase boundary " Smart/intelligent materials and nanotechnology & 2nd International workshop on functional materials and nanomaterials 22-25 April 2008 Chiang Mai ,Thailand
8. Bongkarn, T., Phungjitt, N., **Vittayakorn, N.** "Effect of calcination temperatures on microstructure and phase formation of $Ba(Zr_{0.25}Ti_{0.75})O_3$ powders" Smart/intelligent materials and nanotechnology & 2nd International workshop on functional materials and nanomaterials 22-25 April 2008 Chiang Mai ,Thailand

9. Banlue, W., Muanghlua, R., Vittayakorn, W.C., **Vittayakorn N.** "Synthesis, crystal structures, phase transition characterization and thermal properties of the (1-*x*)$PbZrO_3$-*x*$Pb(Co_{1/3}Nb_{2/3})O_3$ solid solution system" Smart/intelligent materials and nanotechnology & 2nd International workshop on functional materials and nanomaterials 22-25 April 2008 Chiang Mai ,Thailand
10. Nopsiri Chaiyo Anuchar Ruangphanit and **Naratip Vittayakorn** "Synthesis and Morphology evolution of lead-free piezoelectric $KNbO_3$ powder using a modified solid state reaction" The Twenty-sixth annual conference of the microscopy society of Thailand 28th January 2009 – 30th January 2009
11. C. Chansi, N. Adam, S. Vuttivong N. Chaiyo and **N. Vittayakorn** "Hydrothermal synthesis and characterization of lead-free piezoelectric $KNbO_3$ powders" The Twenty-sixth annual conference of the microscopy society of Thailand 28th January 2009 – 30th January 2009
12. N. Chaiyo, A. Ruangphanit and **N. Vittayakorn** "Effect of calcinations condition on lead-free piezoelectric $NaNbO_3$ powder through a modified solid state reaction synthesis" The Twenty-sixth annual conference of the microscopy society of Thailand 28th January 2009 – 30th January 2009
13. Nopsiri Chaiyo, Anucha Ruangphanit, Rangson Muanghlua, Surasak Niemcharoen, Atchara Sangseub, Saowanee Taopen, Sunanta Leelapattana, Wanwilai C. Vittayakorn, **Naratip Vittayakorn** "Synthesis and Morphology Evolution of Lead-Free Piezoelectric $K_{1/2}Na_{1/2}NbO_3$ Powder at Low Temperature" The Sixth Asian Meeting on Ferroelectric (AMF-6), 2 – 7 Aug. 2008. National Taipei University of Technology, Taipei, Taiwan.
14. Rangson Muanghlua; Surasak Niemcharoen; Wanwilai C. Vittayakorn; Nattapong Tungsitvisetkul; Pimjan Chinwaro; Anucha Ruangphanit; Nopsiri Chaiyo; **Naratip Vittayakorn** "Preparation and Properties of Lead Free Bismuth Sodium Titanate-Bismuth Zinc Titanate Ceramics" The Sixth Asian Meeting on Ferroelectric (AMF-6), 2 – 7 Aug. 2008. National Taipei University of Technology, Taipei, Taiwan.
15. Theerachai Bongkarn; Nalinee Phungjitt; **Naratip Vittayakorn** "Effect of Firing Temperatures on Phase Formation and Microstructure of $Ba(Zr_{0.3}Ti_{0.7})O_3$ Ceramics Prepared via Mixed Oxide Method" The Sixth Asian Meeting on Ferroelectric (AMF-6), 2 – 7 Aug. 2008. National Taipei University of Technology, Taipei, Taiwan.

16. Wanwilai C. Vittayakorn and **Naratip Vittayakorn** "Hysteresis Response of Lead Zirconate —Lead Nickel Niobate Ferroelectric Ceramic Under Compressive Stress" The Sixth Asian Meeting on Ferroelectric (AMF-6), 2 – 7 Aug. 2008. National Taipei University of Technology, Taipei, Taiwan.
17. **Naratip Vittayakorn**; Wanwimon Banlue "Synthesis, Ferroelectric Phase Stabilization, Phase Transition and Thermal Properties in $(1\text{-}x)PbZrO_3\text{-}xPb(Zn_{1/3}Nb_{2/3})O_3$ Solid Solution" The Sixth Asian Meeting on Ferroelectric (AMF-6), 2 – 7 Aug. 2008. National Taipei University of Technology, Taipei, Taiwan.
18. Manoon Sutapun; **Naratip Vittayakorn** "Phase Transition and Dielectric Properties of Lead Free $(K_{0.5}Na_{0.5})NbO_3$- $Bi(Zn_{0.5}Ti_{0.5})O_3$ Piezoelectric Ceramics" The Sixth Asian Meeting on Ferroelectric (AMF-6), 2 – 7 Aug. 2008. National Taipei University of Technology, Taipei, Taiwan.
19. Wanwimon Banlue; **Naratip Vittayakorn** "Effect of $Pb(Zn_{1/3}Nb_{2/3})O_3$ Additions on Phase Structure, Ferroelectric and Dielectric Properties of $PbZrO_3$ Ceramics" The Sixth Asian Meeting on Ferroelectric (AMF-6), 2 – 7 Aug. 2008. National Taipei University of Technology, Taipei, Taiwan.
20. Supamas Wirunchit; **Naratip Vittayakorn** "Crossover from Antiferroelectric to Normal Ferroelectric Behavior in Lead Zirconate—Lead Nickel Niobate Ceramics Prepared by the Reaction Sintering Process" The Sixth Asian Meeting on Ferroelectric (AMF-6), 2 – 7 Aug. 2008. National Taipei University of Technology, Taipei, Taiwan.
21. Supamas Wirunchit; Rangson Muanghlua; Surasak Niemcharoen; Wanwilai C. Vittayakorn; Pitak Laoratanakul; **Naratip Vittayakorn** "Preparation of Lead Zirconate-Lead Nickel Niobate Ceramics by the Reaction Sintering Process" The Sixth Asian Meeting on Ferroelectric (AMF-6), 2 – 7 Aug. 2008. National Taipei University of Technology, Taipei, Taiwan.
22. G. Rujijanagul; **N. Vittayakorn**; S. Nabunmee "Effect of Annealing Time on Electrical and Mechanical Properties of $0.7(Pb(Zr_{1/2}Ti_{1/2})O_3) - 0.3(Pb(Zn_{1/2}Nb_{2/3})O_3$ Ceramics" The Sixth Asian Meeting on Ferroelectric (AMF-6), 2 – 7 Aug. 2008. National Taipei University of Technology, Taipei, Taiwan.
23. Nopsiri Chaiyo, Banjong Boonchom and **Naratip Vittayakorn** "A modified solid-state reaction synthesis and characterization of sodium niobate ($NaNbO_3$) powders " The 3rd

International Symposium on Functional Materials (ISFM2009) 15-18 June 2009, Jinju, KOREA

24. Usa Sukkha, Wanwimon Banlue, Banjong Boonchoma and **Naratip Vittayakorn** "Antiferroelectric-ferroelectric phase transition in lead zinc niobate modified lead zirconate ceramics: Crystal studies, Raman spectroscopy, Thermal expansion and electrical properties" The 3rd International Symposium on Functional Materials (ISFM2009) 15-18 June 2009, Jinju, KOREA

25. Manoon Sutapun, Rangson Muanghlua, Surasak Niemcharoen, Banjong Boonchom and **Naratip Vittayakorn** "Phase transition and dielectric properties of lead – free $(K_{0.5}Na_{0.5})NbO_3$ – $LiNbO_3$ – $LiSbO_3$ piezoelectric ceramics" The 3rd International Symposium on Functional Materials (ISFM2009) 15-18 June 2009, Jinju, KOREA

26. Prapapim Phetnoi, Surasak Niemcharoen, Rangson Muanglua, Manoon Sutapun and **Naratip Vittayakorn** "Preparation of Bismuth Potassium Titanate – Strontium Titanate Ceramics" The 27th Annual Conference of the Microscopy Society of Thailand, 20-22 Jan. 2010. Koh Samui, Surat Thani, Thailand.

27. Usa Sukkha and **Naratip Vittayakorn** "Influence of $Pb(In_{1/2}Nb_{1/2})O_3$ on the Phase transformations, Dielectric and Thermal properties of $PbZrO_3$ ceramic" The 27th Annual Conference of The Microscopy Society of Thailand (MST27), 20 - 22 Jan. 2010. The Fair House Beach Resort & Hotel, Surat Thani, Thailand.

28. Nopsiri Chaiyo, Anucha Ruangphanit, **Naratip Vittaykorn** "Solution Combustion Synthesis of Lead-free Piezoelectric Sodium Niobate (NaNbO3) Powders" The 27th Annual Conference of The Microscopy Society of Thailand (MST27), 20 - 22 Jan. 2010. The Fair House Beach Resort & Hotel, Surat Thani, Thailand.

29. Piyanut Charoonsuk, Panisara Kasiansin, Supamas Wirunchit, Banjong Boonchom and **Naratip Vittayakorn** "Ferroelectric phase transition and microstructure of the $(1-x)PbZrO_3$-$xPb(Mg_{1/2}W_{1/2})O_3$ system" The 27th Annual Conference of The Microscopy Society of Thailand, 20-22 Jan. 2010. Koh Samui, Surat Thani, Thailand.

30. C. Nawanil and **N. Vittayakorn**, "Synthesis of Blended Lead Zirconate ($PbZrO_3$) / Poly(Ethylene Oxide) Nanofibers via Electrospinning" The 27th Annual Conference of The Microscopy Society of Thailand, 20-22 Jan. 2010. Koh Samui, Surat Thani, Thailand.

Reprint

Advanced Materials Research Vols. 55-57 (2008) pp 49-52
online at http://www.scientific.net

Effect of Annealing on the Structure and Dielectric Properties in PZT-PCoN Ceramics

N. Vittayakorn[1,5,a], N. Chaiyo[1], R. Muanghlua[2], A. Ruangphanit[3] and W. C. Vittayakorn[4]

[1] King Mongkut's Institute of Technology Ladkrabang Nanotechnology Research Center(NRC), King Mongkut's Institute of Technology Ladkrabang, Bangkok, Thailand 10520

[2]Electronics Research Center, Faculty of Engineering, King Mongkut's Institute of Technology Ladkrabang, Bangkok Thailand 10520

[3] Department of Physics, Faculty of Science, Chiang Mai University, Chiang Mai, Thailand 50200

[4] Thai Microelectronics Center (TMEC), National Electronics and Computer Technology Center, Nation Science and Technology Development Agency, Ministry of Science and Technology, Chachoengsao 24000, Thailand

[5] Materials Science Research Unit, Department of Chemistry, Faculty of Science, King Mongkut's Institute of Technology Ladkrabang, Bangkok, Thailand 10520

[a] e-mail: naratipcmu@yahoo.com

Keyword: Ferroelectric Materials, Lead Zirconate Titanate, Lead Cobolt Niobate

Abstract The solid solution between the normal ferroelectric $Pb(Zr_{1/2}Ti_{1/2})O_3$ (PZT) and relaxor ferroelectric $Pb(Co_{1/3}Nb_{2/3})O_3$ (PCoN) was synthesized by the solid state reaction method. Sintered PZT-PCoN ceramics were annealed at temperatures ranging from 850 to 1,100°C for 4 h. X-ray diffraction patterns revealed changes of crystalline structure after annealing, which could be correlated to the accompanied changes in dielectric properties. Furthermore, significant improvements in the dielectric responses were observed in this system. After annealing, a huge increase of up to 200% occurred in the dielectric constants, especially near the temperature of maximum dielectric constant.

Introduction

Piezoelectric lead zirconate titanate (PZT) ceramic material has been widely used for transducer applications, due to its excellent piezoelectric properties, and was a candidate in a number of recent investigations [1, 2]. It is well known that PZT material is almost always used with a dopent, modifier or other chemical constituents to improve and optimize its basic properties for a particular application [1, 3]. Lead zirconate titanate ceramics and their solid solution, along with several complex perovskite oxides represented by $Pb(B'B'')O_3$, have been investigated [4-6]. Among the various complex ferroelectric oxide materials, several niobates with transition temperatures below room temperature are $Pb(Mg_{1/3}Nb_{2/3})O_3$, $Pb(Ni_{1/3}Nb_{2/3})O_3$, and $Pb(Co_{1/3}Nb_{2/3})O_3$. Among them, lead cobalt niobate [$Pb(Co_{1/3}Nb_{2/3})O_3$ (PCoN)] is also a typical ferroelectric relaxor material with a transition temperature of -70°C, as reported by Smolenskii *et al.* [7] in 1958 . In this compound, the octahedral sites of the crystal are occupied randomly by Co^{2+} and Nb^{5+} ions. Recently, our previous work has shown promise in producing phase pure perovskite PZT–PCoN ceramics with the solid state reaction method [5, 8]. A morphotropic phase boundary (MPB) between the PCoN-rich pseudo-cubic phase and the PZT-rich tetragonal phase was reported at $0.7Pb(Zr_{1/2}Ti_{1/2})O_3$:$0.3Pb(Co_{1/3}Nb_{2/3})O_3$ [5].

In this study, we emphasized the effect of annealing on the crystal structure, and dielectric properties in PZT–PCoN ceramics. Based on our previous results for the PZT–PCoN system, PZT containing 30 mol% of PCoN was selected as the starting composition, which is close to the rhombohedral MPB in this system. For annealing, the samples were heat treated at 850-1,100°C for

4 hours in a sealed Al_2O_3 crucible, with PbO-rich atmosphere. This paper reports evolution of the perovskite phase, and crystal structure of the PZT–PCoN ceramics. Next, the temperature and frequency dependence of the dielectric constant are given for as-sintered and annealed samples. The results of influence on the post-sintering annealing of these properties are shown in brief.

Experiment

The *0.7*$Pb(Zr_{1/2}Ti_{1/2})O_3$-*0.3*$Pb(Co_{1/3}Nb_{2/3})O_3$ ceramics were prepared by conventionally mixed–oxide processing, in which stoichiometric mixtures of reagent-grade metal oxide powders of 99% + purity (PbO, CoO, TiO_2, ZrO_2 and Nb_2O_5) were used as the starting raw materials. Thermal synthesis of blended and pressed mixture of the starting material was carried out at 900°C for a period of 4 h. Crumbled, milled and sieved material was pressed again in the form of cylinders and then sintered at 1,100°C for 4 h. The sintered pellets were then annealed at various temperatures from 850 to 1,100°C for 4 h. These annealing processes were performed in a double crucible, with interior PbO + ZrO_2 atmosphere, in order to maintain the established composition and, especially, avoid the loss of PbO caused by its sublimation. The Archimedes displacement method with distilled water was employed to evaluate sample density. The ceramic pellets were ground and polished to make parallel surfaces, and densities were determined geometrically. After gold sputtering onto the major faces of the pellets as electrodes, dielectric constants and losses at the frequency decades of 10 kHz were measured, using a computer-interfaced LCR meter.

Results and Discussions

The phase development in the annealed samples was analyzed by XRD and the results are presented in Figure 1. All samples show a single-phase powder diffraction pattern. No secondary reaction phases such as PbO, Pb-based compounds, unreacted oxide and so on, are observed in the pattern.

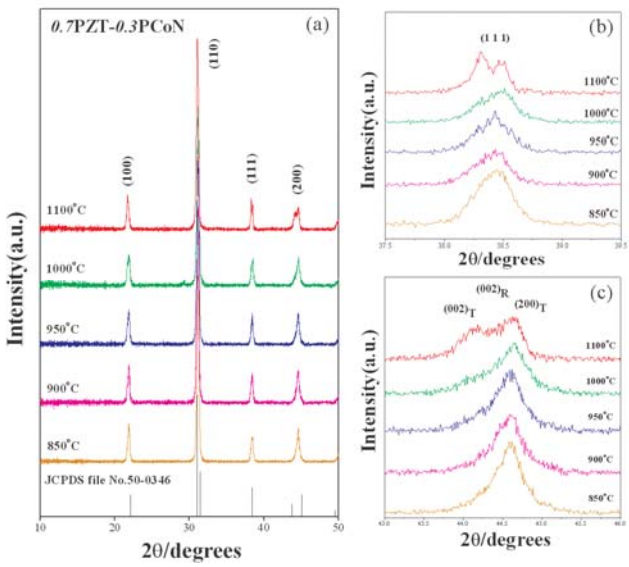

Figure 1 (a) XRD patterns of 0.7PZT-0.3PZN annealed samples at various temperatures for 4 h, (b) XRD pattern of the (1 1 1) peak, (c) XRD pattern of the (2 0 0) peak.

After annealing, a significant change in the crystal structure was observed, especially above an annealing temperature of 1,000°C, where the crystal structure changes from pseudo-cubic to tetragonal and rhombohedral. On the basis of XRD and dielectric experiments, we have identified the MPB in the $(1-x)$PZT–xPCoN system from our previous work. The MPB resides at around $x \sim 0.2$, separating the tetragonal phase for $x \leq 0.2$ from the rhombohedral phase for $x \geq 0.3$. In this study, the XRD data show that splitting of the (200) and (111) peak is not observed in ceramic

samples annealed at temperatures below 1,000°C. These results indicated that the major phase in this ceramic sample had pseudo-cubic symmetry. Splitting of the (200) peak becomes more pronounced as the annealing temperature approaches 1,100°C, thus indicating stabilization of the tetragonal phase. Furthermore, the unambiguous splitting of the (111) peak indicated the coexistence of the rhombohedral and tetragonal phase. The co-existence of the tetragonal and rhombohedral phase is seen clearly when the XRD profile peak splits with increasing annealing temperature. From these results, it is clear that the composition of the annealed sample has shifted very closely to the MPB.

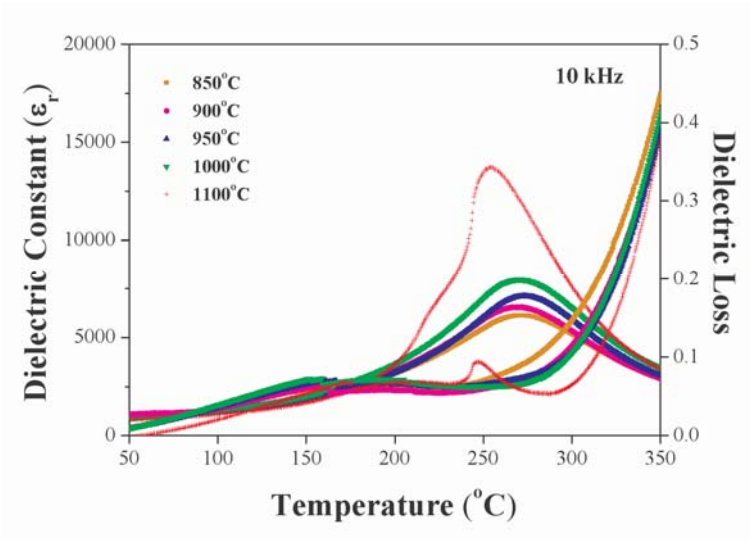

Figure 2 Variation of the dielectric constant (ε_r) and loss tangent (tan δ) with different annealing temperatures at 10 kHz.

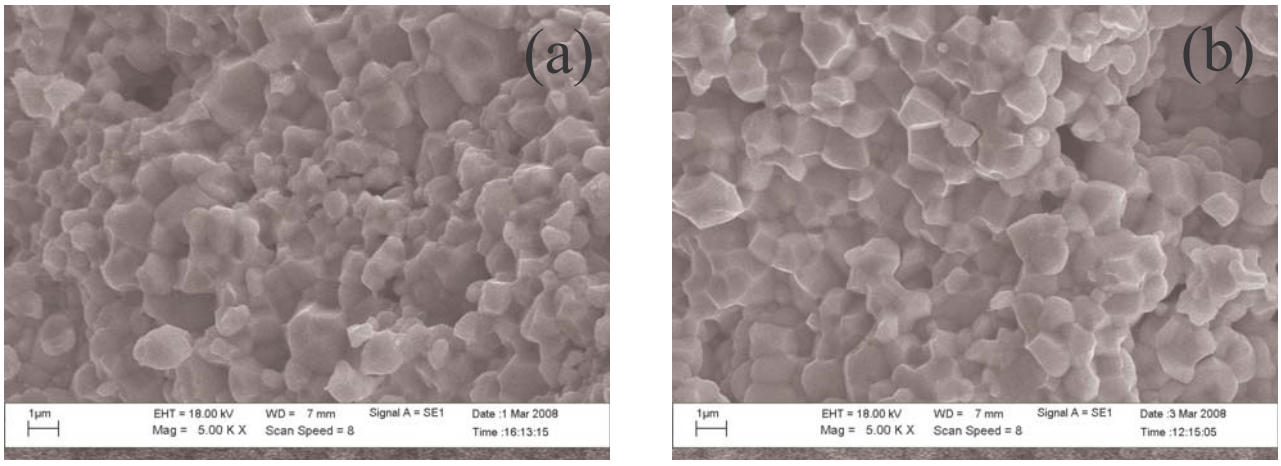

Figure 3 SEM photographs of 0.7PZT-0.3PCoN ceramics (a) as-sintered samples (b) annealing at 1,100°C.

Figure 2 shows the dielectric constant (ε_r) at 10 kHz versus the temperature for *0.7*PZT-*0.3*PCoN ceramics annealed at different temperatures for 4 h. After annealing, a significant improvement in the dielectric constant was observed, especially near the temperature of the maximum dielectric constant (ε_m), where the improvement was up to 200%. This change in behavior might be due to a shift in a chemical composition close to the MPB, caused by thermal annealing. This behavior is consistent with the conclusions of Randall *et al.* [9]and Leite *et al.* [10] in the PMN–PT system. Figure 3 shows scanning electron microscopy (SEM) images of the fractured surfaces of 0.7PZT-

0.3PCoN ceramics before and after annealing at 1,100°C. There was no change in the grain size. The density of the samples decreased from 8.120 to 8.015 g/cm^3 after annealing at 1,100°C for 4 h. Obviously, the decrease in density did not lead to an improvement of electrical responses.

Summary

The dielectric properties of 0.7PZT–0.3PCoN ceramics, formed via the solid state reaction, were investigated. Thermal annealing was seen to be effective at improving the dielectric and piezoelectric responses of PZT-based ferroelectric ceramics. The annealing time was found to have an effect on the electrical properties. After annealing at 1,100°C for 4h in a PbO-rich atmosphere, *0.7*PZT–*0.3*PCoN ceramics with ε_m 14,400 were achieved in this study. The large improvements in dielectric properties after annealing were attributed to a shift in the phase composition to the MPB composition.

Acknowledgements

This work was supported by the Thailand Research Fund (TRF), the Commission on Higher Education (CHE), Thailand Graduate Institute of Science and Technology (TGIST), National Research Council of Thailand (NRCT) and King Mongkut's Institute of Technology Ladkrabang (KMITL).

References

[1] G. H. Haertling: J. Am. Ceram. Soc. Vol. 82 (1999), p. 797.
[2] K. Uchino: *Ferroelectric Devices* (Marcel Dekker,Inc., New York, 2000)
[3] K. Uchino: Solid State Ionics Vol. 108 (1998), p. 43.
[4] N. Vittayakorn, G. Rujijanagul, X. Tan, M. A. Marquardt and D. P. Cann: J. Appl. Phys. Vol. 96 (2004), p. 5103.
[5] N. Vittayakorn and T. Tunkasiri: Phys. Scr. Vol. T129 (2007), p. 199.
[6] N. Vittayakorn, G. Rujijanagul, X. Tan, H. He, M. A. Marquardt and D. P. Cann, J. Electroceramic Vol. 16 (2006), p. 141.
[7] G. A. Smolenskii and A. L. Agranovskaya: Sov. Phys.-Tech. Phys. (1958), p. 1380.
[8] N. Vittayakorn, S. Wirunchit, S. Traisak, R. Yimnirun and G. Rujijanagul: Curr. Appl Phys. Vol. 8 (2008), p. 128.
[9] C. A. Randall, A. D. Hilton, D. J. Barber and T. R. Shrout: J. Mater. Res. Vol. 8 (1993), p. 880.
[10] E. R. Leite, A. M. Scotch, A. Khan, T. Li, H. M. Chan, M. P. Harmer, S.-F. Liu and S.-E. Park: J. Am. Ceram. Soc. Vol. 85 (2002), p. 3018.

Advanced Materials Research Vols. 55-57 (2008) pp 113-116
online at http://www.scientific.net

Influence of Fabrication Processing on Perovskite Phase Formation of KNN-BZT

M. Sutapun[1], R. Muanghlua[2], C-C Huang[3], D. P. Cann[3], W. C. Vittayakorn[4] and N. Vittayakorn[1,a]

[1] Materials Science Research Unit, Department of Chemistry, Faculty of Science, King Mongkut's Institute of Technology Ladkrabang, Bangkok, Thailand 10520

[2]Electronics Research Center, Faculty of Engineering, King Mongkut's Institute of Technology Ladkrabang, Bangkok Thailand 10520

[3]Materials Science, School of Mechanical, Industrial, and Manufacturing Engineering, Oregon State University Corvallis, Oregon, 97331, USA

[4] Department of Physics, Faculty of Science, Chiang Mai University, Chiang Mai, Thailand 50200

[a] e-mail: naratipcmu@yahoo.com

Keywords: Lead-free piezoelectric ceramics; Dielectric properties; perovskites; $(K_{0.5}Na_{0.5})NbO_3$; $Bi(Zn_{0.5}Ti_{0.5})O_3$

Abstract The binary system of $(1\text{-}x)(K_{1/2}Na_{1/2})NbO_3$–$xBi(Zn_{1/2}Ti_{1/2})O_3$; x = 0.0-0.30 ceramics was fabricated by conventionally mixed oxide and two-stage mixed oxide methods. Phase development of calcined powders and the crystal structure of sintered ceramics were analyzed by X-ray diffraction (XRD). The microstructure analyses were undertaken by scanning electron microscopy (SEM). In the conventional method, the perovskite phases were obtained for compositions containing only 10 mol % KNN. For compositions above this amount, a complex mixture of phases was observed. However, the complete solid solution of perovskite phase, prepared by two–stage mixed oxide, was retained up to 20 mole % BZT content. The experiments in this study suggest that the two-stage mixed oxide method helps to stabilize the perovskite phase better, when compared with the conventional method.

Introduction

Piezoelectric materials based on $Pb(Zr_{1-x}Ti_x)O_3$ (PZT) ceramics have been widely used, due to their excellent piezoelectric and dielectric properties at the morphotropic phase boundary(MPB) [1]. However, the use of lead-based ceramics has caused serious environmental problems because of the high toxicity of lead oxide [2]. Alkali niobate $K_{0.5}Na_{0.5}NbO_3$ (KNN), a solid solution of ferroelectric $KNbO_3$ and antiferroelectric $NaNbO_3$, is thought to be a promising candidate for lead-free piezoelectric ceramics because of its high Curie temperature (420 °C) and large electromechanical coupling factors [2]. $Bi(Zn_{1/2}Ti_{1/2})O_3$ (BZT) is a ferroelectric, which has a Zn^{2+} and Ti^{4+} complex on the B-site of ABO_3 perovskite structure, with a tetragonal symmetry [4, 5]. The BZT exhibits a high T_c and tetragonality enhanced through solid solution with $PbTiO_3$[4]. However, BZT is unstable in pure form and can only be stabilized under high pressures or in solid solutions with other perovskite end members [3, 4]. In order to develop lead-free piezoelectric materials, KNN was used for this research to stabilize the BZT perovskite phases in a solid solution. Both the conventionally mixed oxide and two-stage mixed oxide methods have been used in synthesizing the KNN-BZT ceramic. Finally, a comparison of the important dielectric properties was made to identify the optimum processing conditions.

Experimental

The $(1\text{-}x)(K_{1/2}Na_{1/2})NbO_3$–$xBi(Zn_{1/2}Ti_{1/2})O_3$; x = 0.0-0.30 lead-free ceramics were prepared by the conventionally mixed oxide and two-stage mixed oxide methods. Both methods used high purity

AR grade K_2CO_3 (99.0%), Na_2CO_3 (99.5%), Bi_2O_3 (99.5%), Nb_2O_5 (99.9%), ZnO (99.0%) and TiO_2 (99.0%). Alkali carbonates were used as a starting material, which had been treated carefully by a special drying process before use. These powders were placed in an oven at 230°C for 2 days and then stored in a moisture-free vessel. For the conventionally mixed oxide method, KNN-BZT ceramics were prepared by mixing starting reagent powders in the desieved stoichiometry and ball-milling in polyethylene, with ethanol and stabilized zirconia (YTZ) media, for 18 h After drying, the mixture was calcined at 850°C for 4 h. For the two-stage mixed oxide method, $(K_{0.5}Na_{0.5})NbO_3$ (KNN) powders were prepared first, followed by a reaction with Bi_2O_3, Nb_2O_5 and TiO_2 to form the KNN-BZT solid solution. Uncalcined powders were weighed according to the following chemical reaction equation and characterized by TG-DTA (Perkin Elmer). The microstructure analyses were undertaken by scanning electron microscopy (SEM, Leo 1455VP). The calcined powders, with polyvinyl alcohol (PVA) added as binder, were pressed into pellets of 15 mm diameter and ~ 2 mm thickness, and sintered at 1,000°C in KNN-atmosphere for 2 h in a closed alumina crucible. For dielectric measurement, sample surfaces were polished and painted with silver paste. Dielectric properties were measured using an LCR meter (HP-4284, Hewlett–Packard Inc.).

Results and Discussion

TG-DTA curves are given in Figure 1(a) and (b) for the conventional method (K_2CO_3, Na_2CO_3, Bi_2O_3, Nb_2O_5, ZnO and TiO_2) and two-stage method (KNN, Bi_2O_3, ZnO and TiO_2), respectively. The TGA curve, showing overall weight loss, was equal to 32.5% for the conventional method and ~24.5% for the two-stage method. The DTA curve showed an endothermic peak positioned at around 114-197°C and 115-179°C for the conventional method and two-stage method, respectively, which associated with the decomposition of water molecules. Furthermore, the TGA curve showed a 4.37 % and 3.51% weight loss at between 400°C and 600°C for the conventional method, which associated with the decarbonation of K_2CO_3 and Na_2CO_3, respectively. However weight loss was not observed at all in the same temperature for the two-stage method. The endothermic peaks, appearing at 850°C for both methods, should be correlated to the phase transition of perovskite structure because there was no weight loss on the TGA curves. These data were used to define the calcined temperature of the perovskite phase.

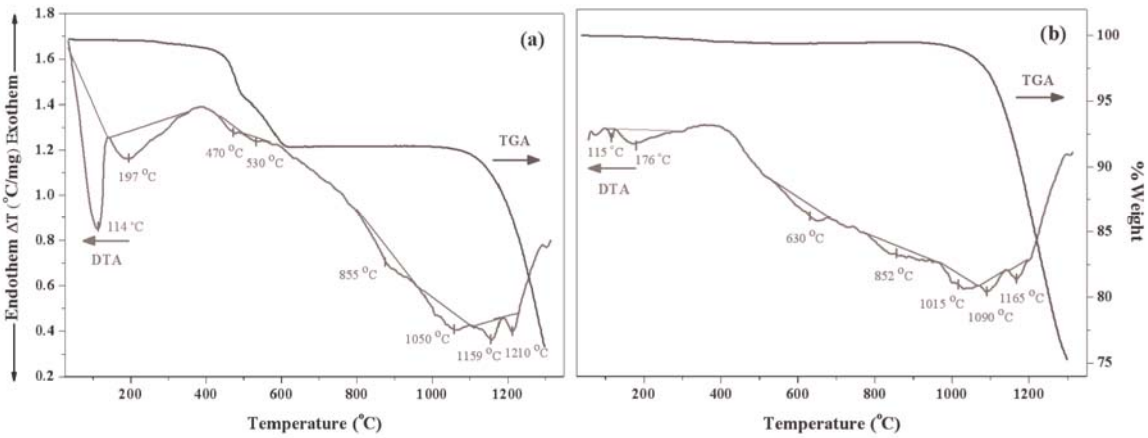

Figure 1 TG-DTA curves for the powder mixture of the starting reagent for (a) the conventionally mixed oxide method and (b) the two−stage mixed oxide method.

XRD patterns of the sintered (*1-x*) KNN – *x*BZT ceramics for both methods are shown in Figure 2(a) and (b). In the conventional method, the perovskite phases were obtained for compositions containing only 10 mol % KNN. For compositions above this amount, a complex mixture of phases was observed. However the complete solid solution of perovskite phase prepared by two stages was retained up to 20 mole% BZT content. The experiments in this study suggest that the two-stage method helps to stabilize the perovskite phase better, when compared to the conventional method.

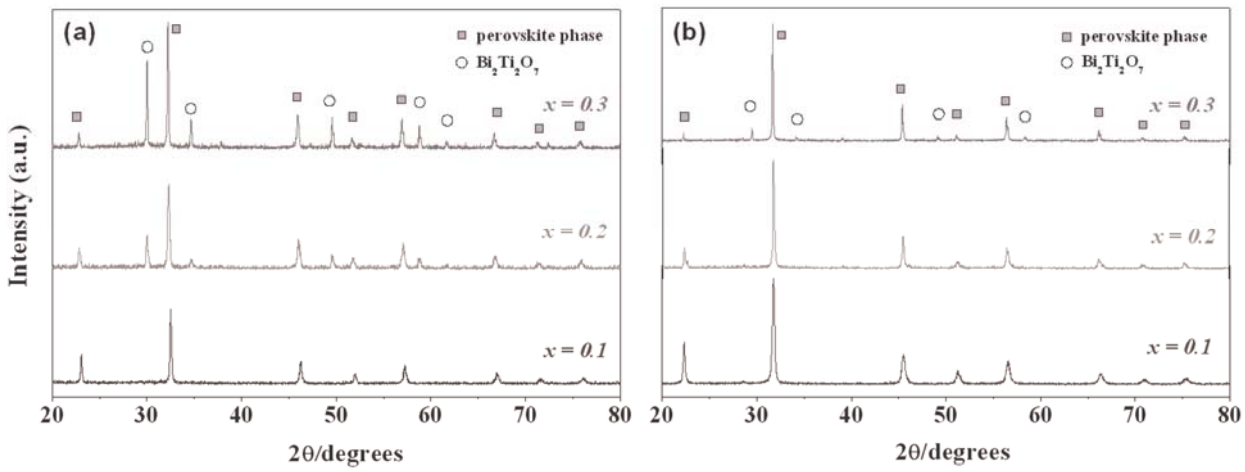

Figure 2 XRD patterns of the (*1-x*)KNN – *x*BZT powders calcined at 850 °C for 4 h, obtained by (a) the conventional mixed oxide method and (b) the two-stage mixed oxide method.

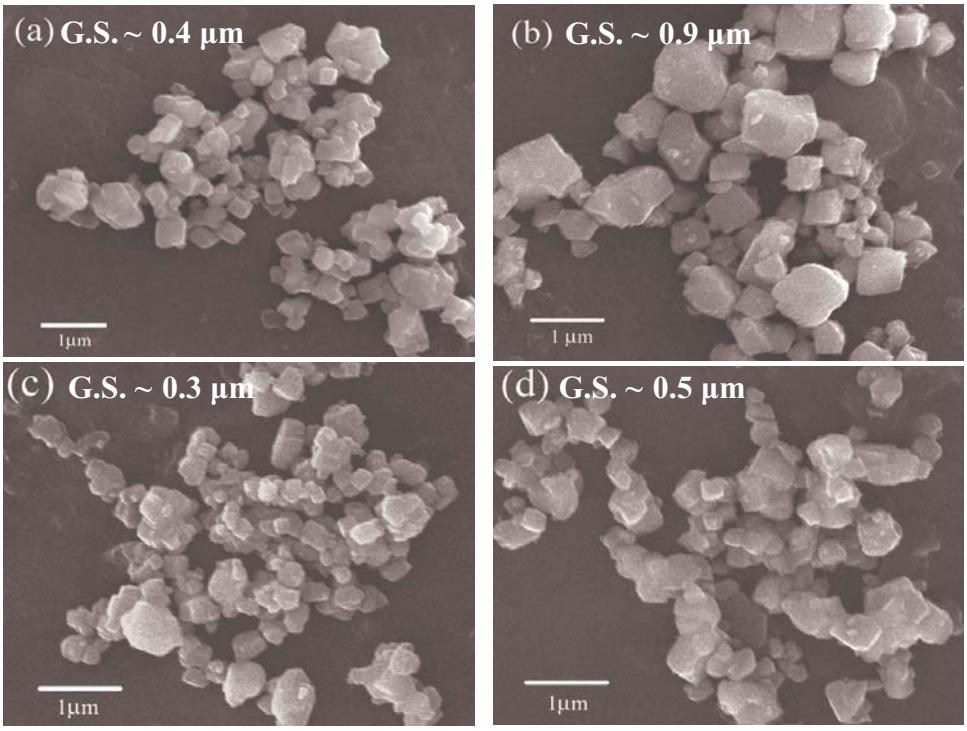

Figure 3 SEM micrographs of the (*1-x*)KNN – *x*BZT powders calcined at 850 °C for 4 h, obtained by the conventional mixed oxide method with (a) $x = 0.1$, (b) $x = 0.2$, and two-stage mixed oxide method with (c) $x = 0.1$ and (d) $x = 0.2$.

Figure 3 (a), (b), (c) and (d) show SEM micrographs of KNN-BZT powders for both methods, in which the average particle size was seen to increase with increasing BZT. However, there were no significant changes in grain size in the different preparation methods. Dielectric constant (ε_r) and loss tangent (tan (δ) at room temperature in both methods are shown in Figure 4. When compared to the conventional method, the two-stage method produces a slightly higher dielectric constant as well as a lower loss tangent. This may be attributed to the heterogeneous composition of ceramics synthesized by the conventional method. These results indicated that the two-stage method helps to

stabilize the perovskite phase and produces ceramics with better dielectric properties when compared to the conventional method.

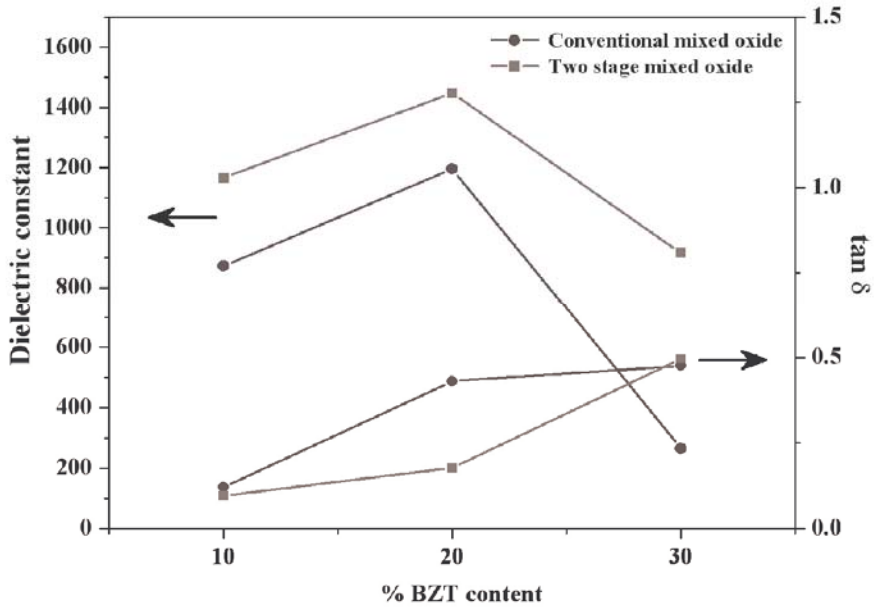

Figure 4 Dielectric constant (ε_r) and loss tangent (tan (δ)) of (1-*x*)KNN–*x*BZT ceramics at room temperature.

Summary

The properties of (1-*x*)KNN-*x*BZT; *x* = 0.0-0.3 ceramics prepared by conventional and two–stage methods were investigated. Perovskite phase formation behavior and dielectric properties were found to depend on the the methods of preparation. In the conventional method, the perovskite phases were obtained for compositions containing only 10 mol % KNN. For compositions above this amount, a complex mixture of phases was observed. However the complete solid solution of perovskite phase prepared by two–stage mixed oxide was retained up to 20 mole % BZT content. A better dielectric property was found for the ceramics synthesized by the two-stage method. The higher chemical homogeneity in ceramics synthesized by the two-stage method is the main reason for the higher dielectric constant.

Acknowledgements

This work was supported by the Thailand Research Fund (TRF), the Commission on Higher Education (CHE), National Research Council of Thailand (NRCT) and King Mongkut's Institute of Technology Ladkrabang (KMITL).

References

[1] G. H. Haertling: J. Am. Ceram. Soc. Vol. 82 (1999), p. 797.
[2] T. Takenaka and H. Nagata: J. Eur. Ceram. Soc. Vol. 25 (2005), p. 2693.
[3] M. R. Suchomel and P. K. Davids: Appl. Phys. Lett. Vol. 86 (2005), p. 262905.
[4] M. R. Suchomel, A. M. Fogg, M. Allix, H. Niu, J. B. Claridge and M. J. Rosseinsky: Chem. Mater. Vol.18 (2006), p. 4987.

Advanced Materials Research Vols. 55-57 (2008) pp 117-120
online at http://www.scientific.net

Effect of Lead Nickel Niobate Substitution on Phase Transitions of Lead Zirconate Ceramics Prepared by the Solid State Reaction Method

S. Wirunchit[1], P. Laoratanakul[2] and N. Vittayakorn[1,a]

[1]Materials Science Research Unit, Department of Chemistry, Faculty of Science, King Mongkut's Institute of Technology Ladkrabang, Bangkok, Thailand 10520

[2]National Metal and Materials Technology Center (MTEC), Pathumthani 12120, Thailand

[a]naratipcmu@yahoo.com

Keyword: Antiferroelectric Materials, Ferroelectric, Lead Zirconate

Abstract The solid solution between the antiferroelectric, $PbZrO_3$ (PZ), and relaxor ferroelectric, $Pb(Ni_{1/3}Nb_{2/3})O_3$ (PNN), was synthesized by the columbite method. The phase structure and phase transition of $Pb(Zr_{1-x}(Ni_{1/3}Nb_{2/3})_xO_3$ (PZNN), where $x = 0.0 \leq x \leq 0.50$, were investigated. The samples were kept at the calcination temperature of 900°C for 4 h and at the sintering temperature of 1,150°C for 2 h. Phase formation and phase transition of PZNN were investigated by x-ray diffraction (XRD) and thermal analysis, respectively. It was found that the structure of sintered pellets is orthorhombic for $0.0 \leq x \leq 0.10$, rhombohedral for $0.20 \leq x \leq 0.30$ and pseudo-cubic for $x = 0.5$. DSC measurement shows that in the antiferroelectric (AFE) phase – ferroelectric (FE) phase and FE to paraelectric (PE) phase; phase transformation temperatures decrease with increasing PNN concentration. The AFE–FE phase transformation was detected for compositions $0.00 \leq x \leq 0.08$.

Introduction

Lead zirconate, $PbZrO_3$ (PZ), is considered to be an excellent candidate as a key material of antiferroelectric ceramics [1-3]. At room temperature, PZ has an orthorhombic structure, with a = 5.87 Å, b = 11.74 Å and c = 8.20 Å [4], and an antiferroelectric (AFE) phase. It undergoes the AFE to a paraelectric (PE) phase and transforms from an orthorhombic structure to a cubic structure at 236°C [4]. It is reported that a ferroelectric (FE) phase exists over a very narrow temperature range (230-233°C) [5-8]. Lead nickel niobate ($Pb(Ni_{1/3}Nb_{2/3})O_3$;PNN) has a perovskite structure and typical relaxor ferroelectric properties. It exhibits a diffuse phase transition at around -120°C, with a much lower peak permittivity of about 4000 [9]. The crystal structure of PNN at room temperature is cubic (*Pm3m*), with a lattice parameter of 4.03 Å [9]. PNN based systems, such as $Pb(Ni_{1/3}Nb_{2/3})O_3$- $Pb(Fe_{1/2}Nb_{1/2})O_3$ [10] and $Pb(Ni_{1/3}Nb_{2/3})O_3$- $Pb(Mg_{1/2}W_{1/2})O_3$- $PbTiO_3$ [11], have been evaluated to possess low sintering temperatures and high dielectric constants. Thus, mixing PNN with PZ is expected to decrease the sintering temperature of PZ-based ceramics, a desirable move towards lower-cost electrodes [12].

In this work, the columbite precursor method was used to synthesize the $Pb(Zr_{1-x}(Ni_{1/3}Nb_{2/3})_xO_3$ (PZNN) with $x = 0.0 – 0.5$. The effect of PNN substitution on the phase transformation behavior of PZ was investigated. Phase structure, phase transitions and the related properties were studied by a differential scanning calorimeter.

Experimental

The perovskite structure of lead zirconate – lead nickel niobate ceramic, $Pb(Zr_{1-x}(Ni_{1/3}Nb_{2/3})_xO_3$ (PZNN), was prepared by the columbite precursor method via the ball-milling technique. The columbite structure ($NiNb_2O_6$) was synthesized first. Stoichiometric amounts of the precursor (NiO, Nb_2O_5) were mixed and milled in ethyl alcohol for 18 h. The mixture was dried and calcined at 1,100°C for 4 h. Then, $NiNb_2O_6$ and ZrO_2 were mixed with PbO, according to the composition of $Pb(Zr_{1-x}(Ni_{1/3}Nb_{2/3})_xO_3$ (PZNN), $0.0 \leq x \leq 0.5$, with an excessive content of 2 mol% PbO. After re-milling and drying, the mixtures were calcined at 850°C for 4 h in a closed alumina crucible. Pellets

of 15 mm in diameter were pressed using 5% PVA. The binder was burnt out by slowly heating to 500°C over 2 h. The samples were sintered at temperatures ranging from 1,100°C to 1,150°C for 6 h. Phase formation and phase transition of PZ-PNN were investigated by x-ray diffraction (XRD) and a differential scanning calorimeter (DSC).

Results and Discussion

The XRD patterns of $Pb(Zr_{1-x}(Ni_{1/3}Nb_{2/3})_xO_3$, $(0.0 \leq x \leq 0.5)$ ceramics, sintered at 1,150°C, are shown in Figure 1. From the patterns, PZ powder was identified as a single-phase material with a perovskite structure having orthorhombic symmetry, which could be matched with ICDD file no. 75-1607. The XRD patterns of the PZNN compositions showed a combination between PZ and PNN patterns, which indicated a perovskite structure having a symmetry that varied from orthorhombic to pseudo-cubic types. The ICDD file no. 34-0103 for PNN, with a cubic structural symmetry, showed a better comparison. The $Pb(Zr_{1-x}(Ni_{1/3}Nb_{2/3})_xO_3$ was orthorhombic, rhombohedral and pseudo-cubic for compositions where $x = 0.00 \leq x < 0.10$, $x = 0.10 \leq x \leq 0.40$ and $x = 0.50$, respectively.

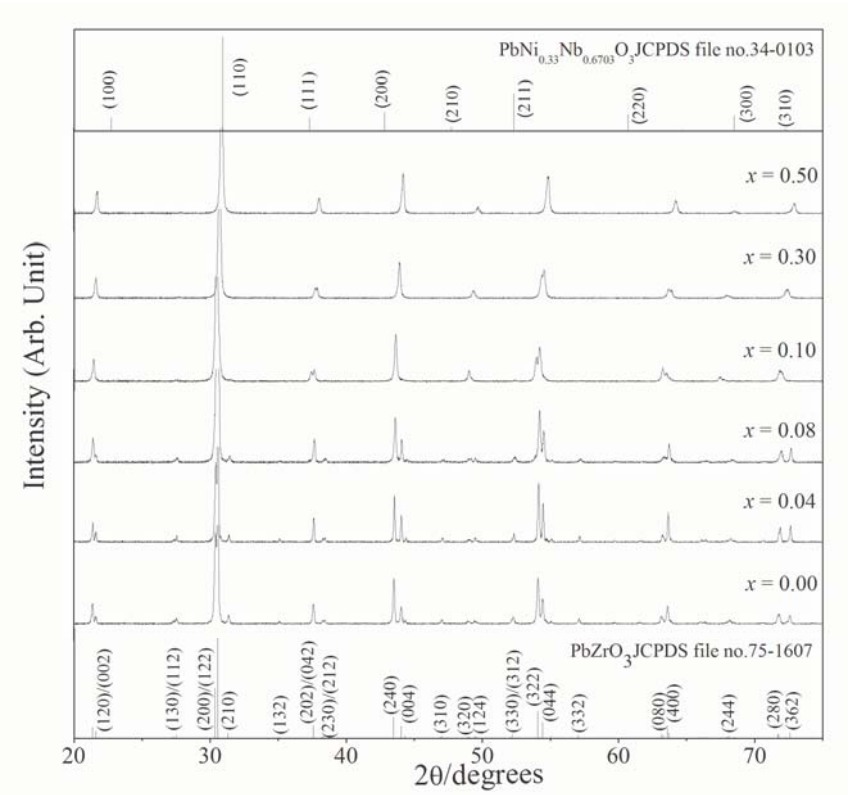

Figure 1 XRD patterns of $Pb(Zr_{1-x}(Ni_{1/3}Nb_{2/3})_xO_3$ ceramics.

The DSC was used to investigate the phase transition in the $Pb(Zr_{1-x}(Ni_{1/3}Nb_{2/3})_xO_3$ system. AFE-FE phase transition temperatures, enthalpy and paraelectric (PE) transitions are summarized in Table I. Figure 2 shows results of the DSC analysis of the PZNN ceramics. Two distinct endothermic peaks were observed for $Pb(Zr_{1-x}(Ni_{1/3}Nb_{2/3})_xO_3$ samples with $0.0 \leq x < 0.08$. The lower temperature corresponds to the transition temperature of the AFE → FE phase transition, while the higher temperature corresponds to the FE→PE phase transition.

Table 1 Phase transition temperatures of $Pb(Zr_{1-x}(Ni_{1/3}Nb_{2/3})_xO_3$ ceramics (R, Rhombohedral; O, Orthorhombic; C, pseudo-cubic)

Composition (x)	Crystal Structure	Phase transition Temperature (°C)		Enthalpy (J/g)	
		AFE→FE	FE→PE	AFE→FE	FE→PE
0.00	O	229.5	235.5	1.53	2.34
0.04	O	150.1	220.8	1.33	2.89
0.08	O	55	205.5	0.29	2.44
0.10	R	-	200.2	-	1.88
0.30	R	-	149.0	-	0.16
0.50	C	-	-	-	-

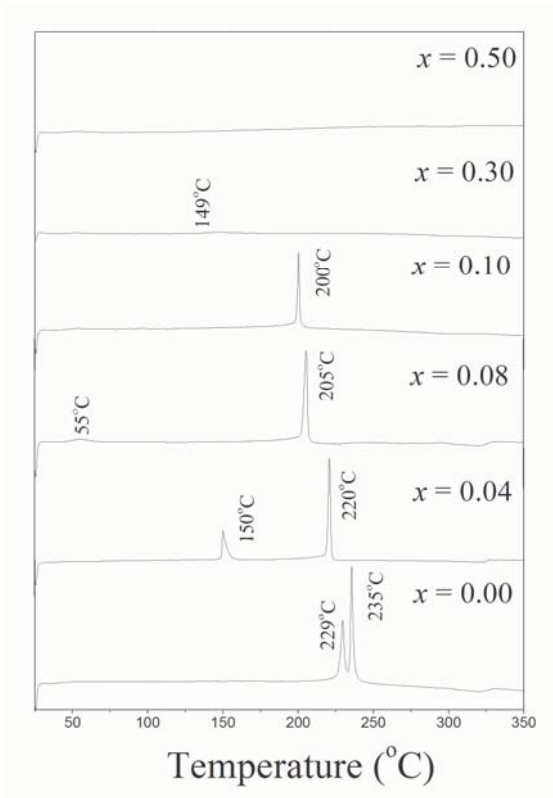

Figure 2 DSC thermographs of $Pb(Zr_{1-x}(Ni_{1/3}Nb_{2/3})_xO_3$ ceramics.

Based on the results of XRD, and DSC data, the ferroelectric phase diagram for the $Pb(Zr_{1-x}(Ni_{1/3}Nb_{2/3})_xO_3$ binary system has been established, as shown in Figure 3. The transition temperature decreases at approximate linearity with x. The phase diagram consists of three distinct crystallographic phases in this system; high temperature paraelectric cubic (*Pm3m*), rhombohedral (*R3m*), and ferroelectric orthorhombic [*P2cb* (no. 32)]. At low concentrations of PNN $x \leq 0.08$, the symmetry can be defined as orthorhombic. The orthorhombic symmetry transforms into rhombohedral at a composition near $x = 0.08$.

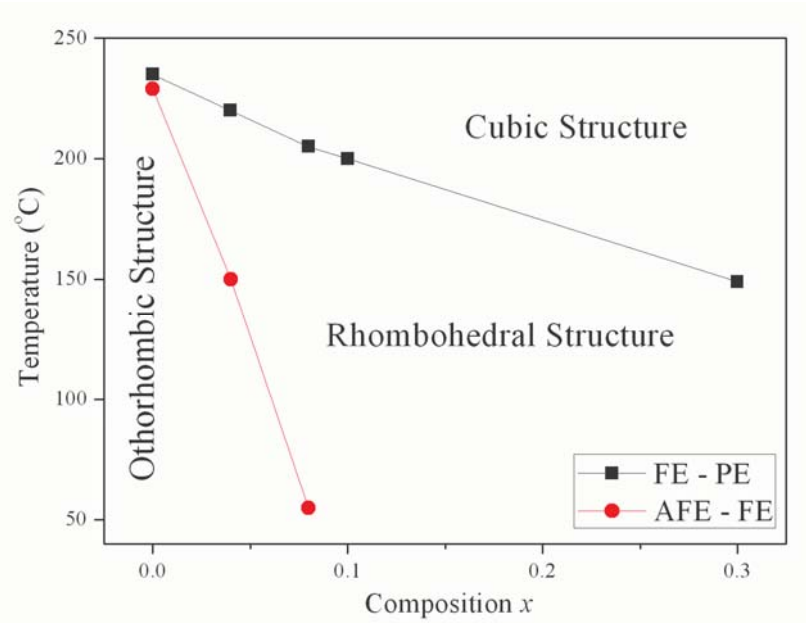

Figure 3 Phase diagram of the $Pb(Zr_{1-x}(Ni_{1/3}Nb_{2/3})_xO_3$, x = 0.0-0.5 binary system.

Summary

The Structure of $Pb(Zr_{1-x}(Ni_{1/3}Nb_{2/3})_xO_3$ (PZNN) is orthorhombic, rhombohedral and pseudo-cubic for compositions where $x = 0.00 \leq x < 0.10$, $x = 0.10 \leq x \leq 0.40$ and $x = 0.50$, respectively. In the antiferroelectric (AFE) phase – ferroelectric (FE) phase and FE to paraelectric (PE) phase, phase transformation temperatures decrease with increasing PNN concentration. The AFE–FE phase transformation is detected for compositions $0.00 \leq x \leq 0.08$.

Acknowledgment

This work was supported by the Thailand Research Fund (TRF), the Commission on Higher Education (CHE), Thailand Graduate Institute of Science and Technology (TGIST) and King Mongkut's Institute of Technology Ladkrabang (KMITL).

References

[1] E. Sawaguchi, G. shirane and S. Hosshino: Phys. Rev. Vol. 83 (1951), p. 1078.
[2] E. Sawaguchi, G. shirane and Y. Takagi: J. Phys. Jpn. Soc. Vol. 6 (1951), p. 333.
[3] N. Vittayakorn and S. Wirunchit, Smart Mater. Struct. Vol. 16 (2007), p. 851.
[4] S. Roberts, J. Am. Ceram. Soc. Vol. 33 (1953), p. 63.
[5] L. Goulpeau: Sov. Phys. Solid State. Vol. 8 (1967), p. 1970.
[6] V. J. Tennery: J. Am. Ceram. Soc. Vol. 49 (1966), p. 483.
[7] B. A. Scott and G. Burns: J. Am. Ceram. Soc. Vol. 55, (1972), p. 331.
[8] R. W. Whatmore and A. M. Glazer: J.Phys. C: Solid state Physc. Vol. 12 (1979), p. 1505.
[9] V. A. Bokov and I. E. Myl'nikova: Sov. Phys. Solid State. Vol. 3 (1961), p. 631.
[10] T. R. Shrout, S. L. Swartz and J. M. Haun: Am. Ceram. Soc. Bull. Vol. 63 (1984), p. 808.
[11] M. Yonezawa, Ferroelectrics. Vol. 68 (1986), p. 181.
[12] Y. Xu, *Ferroelectric Materials and Their Application* (Elsevier Science Publishers B.V., 1991).

Advanced Materials Research Vols. 55-57 (2008) pp 121-124
online at http://www.scientific.net

Synthesis, Crystal Structures, Phase Transition Characterization and Thermal Properties of the (*1–x*)$PbZrO_3$-*x*$Pb(Co_{1/3}Nb_{2/3})O_3$ Solid Solution System

W. Banlue[1], R. Muanghlua[2], W. C. Vittayakorn[3] and N. Vittayakorn[1,a]

[1]Materials Science Research Unit, Faculty of Science, King Mongkut's Institute of Technology Ladkrabang, Bangkok, Thailand 10520

[2]Electronics Research Center, Faculty of Engineering, King Mongkut's Institute of Technology Ladkrabang, Bangkok Thailand 10520

[3] Department of Physics, Faculty of Science, Chiang Mai University, Chiang Mai, Thailand 50200

[a] naratipcmu@yahoo.com

Keyword: Antiferroelectric Materials, Ferroelectric, Lead Zirconate

Abstract The phase transition behavior of the (1–*x*) $PbZrO_3$-*x*$Pb(Co_{1/3}Nb_{2/3})O_3$ (PZCN) solid solution system ($0 \leq x \leq 0.30$) has been investigated by X-ray diffraction and DSC. In the solid solution, for $x \leq 0.20$, the transition shows a first-order phase transition behavior and its antiferroelectric (AFE) crystal structure is orthorhombic. The transition temperature gradually decreases with increased Co^{2+}/Nb^{5+} concentration. On the composition range $0.20 \leq x \leq 0.30$, a typical relaxor-like behavior is displayed. The low temperature crystal structure is pseudo-cubic in this composition range. With these data, the ferroelectric phase diagram between PZ and PCoN has been established.

Introduction

Lead zirconate [$PbZrO_3$, abbreviated as PZ] is an antiferroelectric ceramic with a Curie temperature of 230°C [1, 2]. PZ is a parent compound of $PbZr_{1-x}Ti_xO_3$ (PZT) solid solutions, which are of high scientific and technological interest for their ferroelectricity and piezoelectricity observed over a wide range of compositions [3]. It is reported that the antiferroelectric (AFE) to ferroelectric transition (under the application of a strong electric field to the ceramic in the antiferroelectric state) leads to significant energy storage for the DC field [4]. This feature of $PbZrO_3$ makes it a candidate material for energy storage applications [3]. Lead cobolt niobate [$Pb(Co_{1/3}Nb_{2/3})O_3$, abbreviated as PCoN] is a relaxor ferroelectric, characterized by frequency-dependent dielectric maxima and a diffuse phase transition [5, 6]. The diffuse phase transition characteristic of the PCoN was first explained by Smolenskii and Agranovskaya on the basis of local compositional fluctuations on a microscopic scale [6, 7]. PCoN-based ceramics are considered to possess low sintering temperatures. Therefore, these materials can be applied for fabricating multilayer capacitors with low-temperature melting inner electrodes [8]. There have been many studies concerning the solid solution of PZ and other perovskite materials such as $PbTiO_3$ [9], $BaZrO_3$, [4, 10] $PbSnO_3$ [11] and $SrZrO_3$ [9]. However, to the best of the authors' knowledge, no work has been done on the solid solution between PZ and PCoN. Therefore, the objective of our present study is to investigate phase transition of (1–*x*)$PbZrO_3$ – *x*$Pb(Co_{1/3}Nb_{2/3})O_3$ (PZ – PCoN) with $x = 0.00 – 0.30$ as a function of composition and temperature.

Experimental

The (*1–x*)$PbZrO_3$ – *x*$Pb(Co_{1/3}Nb_{2/3})O_3$ ceramics, where $x = 0.00, 0.02, 0.04, 0.06, 0.08, 0.10, 0.20$ and 0.30, were prepared by a columbite precursor. First, a columbite ($CoNb_2O_6$) precursor was prepared using reagent-grade CoO and Nb_2O_5 in stoichiometric proportions. The powders were thoroughly mixed in a ball mill for 18 h, using ethanol as a grinding medium, and the mixed powder was calcined at 1,100°C for 4 h to obtain the columbite precursor. Single-phase formation of the

precursor was confirmed by X-ray diffraction. The columbite precursor was mixed with PbO (99% purity), and ZrO_2 (99% purity) in different proportions for making different compositions, and each mix was calcined at 900°C for 4 h to acquire the desired composition of $(1-x)$PZ–xPCoN. Two mol percent of excess PbO was added to all the compositions to compensate for the lead loss during sintering. Single-phase formation was verified by powder XRD. Powders were compacted in disk form with a diameter of 15 mm and thickness of 2–3 mm. These disks were sintered in PbO-rich atmosphere at 1,150°C for 2 h. The densities of the sintered samples were measured to ~ 95% of the theoretical values. The crystal structure of the sintered pellets was determined by X-ray diffraction (XRD). The phase transition temperatures and enthalpy (ΔH) of the phase transitions were determined by DSC. This was operated from room temperature to 250◦C with a heating rate of 10◦C/min.

Results and Discussion

Figure 1 illustrates the XRD patterns of $(1\text{-}x)$PZ-xPCoN sintered pellets for $0.00 \leq x \leq 0.30$. It can be seen that the sintered pellets are single-phase: all the lines in each XRD pattern could be indexed with a perovskite cell. The diffraction peaks move gradually towards higher angles with increasing PCoN contents, indicating smaller cell parameters.

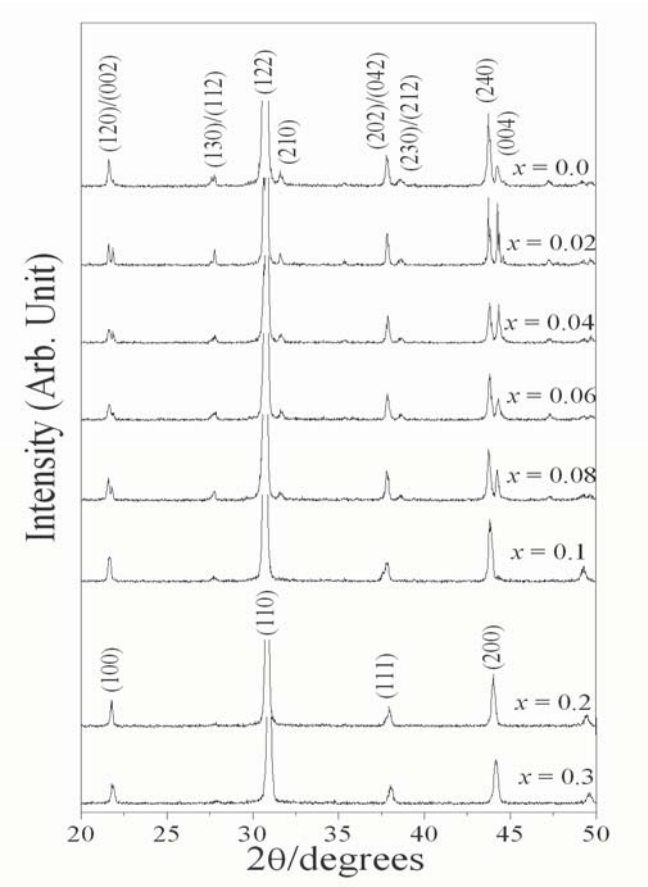

Figure 1 XRD patterns of $(1-x)PbZrO_3 - xPb(Co_{1/3}Nb_{2/3})O_3$ sintered pellets.

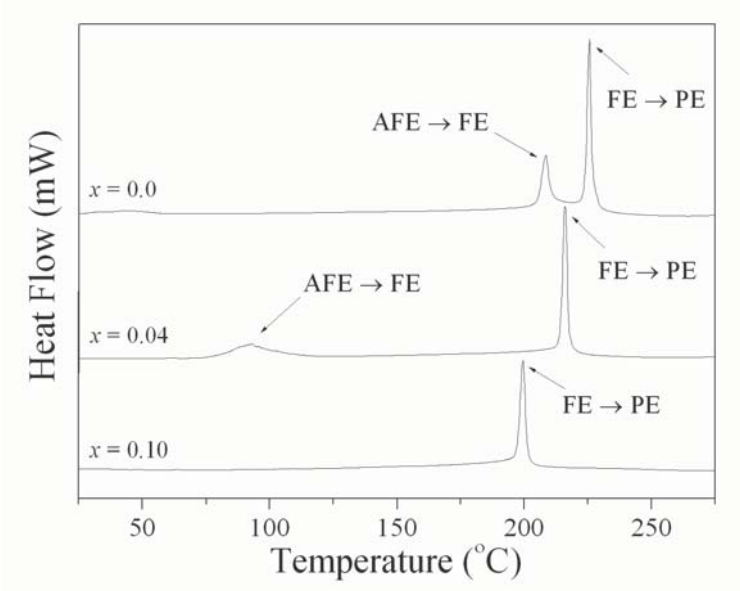

Figure 2 DSC thermographs of PZ-PCoN samples for: (a) $x = 0$, (b) $x = 0.04$ and (c) $x = 0.10$.

For the composition $0.00 \leq x \leq 0.10$, superstructure lines along with strong peaks are clearly observed, indicating that this composition belongs to the AFE orthorhombic phase. Furthermore, the samples with $x = 0.1$, 0.2 and 0.3 had a split (1 1 1) and (2 2 0) reflection and single (2 0 0) reflection, confirming that the crystal structure of the samples with $x = 0.1$, 0.2 and 0.3 is a rhombohedral perovskite. The DSC technique was used to investigate the phase transition of PZ-PCoN ceramics, with increasing PCoN concentration. A typical result of the DSC of PZ-PCoN for the composition $x = 0$, 0.04 and 0.10 is presented in Figure 2(a)-(c). Two distinct endothermic peaks observed for PZ at about 208.4 and 225.6°C are shown in Figure 2(a). The lower temperature corresponds to the transition temperature of the AFE→FE phase transition, while the higher temperature corresponds to the FE→PE phase transition. In Figure 2(b), two endothermic peaks are shown at 92.8 and 216.1°C for the composition, $x = 0.04$. The AFE→FE phase transition was found in the compositions of $0.00 \leq x \leq 0.10$. The peaks shift to lower temperatures, with a higher composition of x. This result corresponds to a decreasing AFE phase, with increasing amounts of PCoN content. Table 1 gives the transition temperature, including AFE→FE and FE→PE transitions of different PZ-PCoN compositions observed from DSC. The temperature range width of the FE phase increases progressively with PCoN content. After accumulating all these data, the ferroelectric phase diagram of $(1\text{-}x)$PZ–xPCoN has been finally established as a function of temperature and composition, as shown in Figure 3.

Table 1 Phase transitions temperature of $(1\text{-}x)$PZ-xPCoN ceramics

Composition	Phase transition temperature (°C)	
x	AFE→FE	FE→PE
0.00	208.4	225.6
0.02	145.2	220.9
0.04	92.8	216.1
0.06	33.3	209.9
0.08	-	204.6
0.10	-	199.4
0.20	-	182.0
0.30	-	158.2

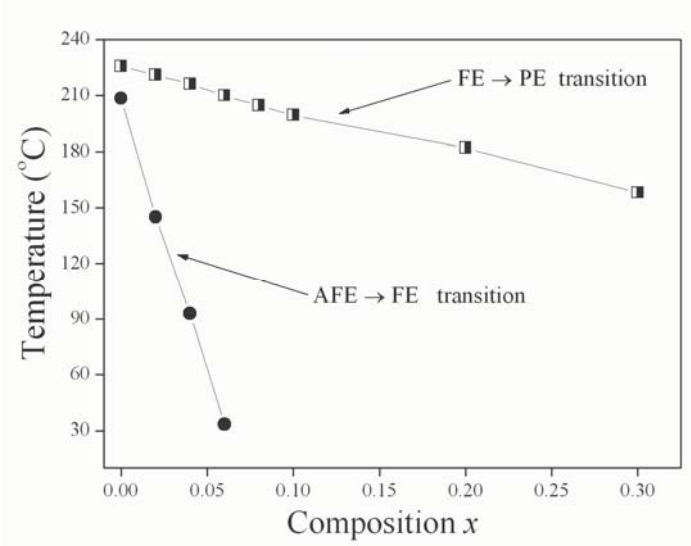

Figure 3 Ferroelectric phase diagram of the (*1-x*)PZ –*x*PCoN, *x* = 0.0-0.30 binary system.

The transition temperature decreases linearly with *x*, from approximately T_c = 235°C for *x* = 0.0 to 158.2°C for *x* = 0.3. At room temperature, the phase boundary between the orthorhombic, antiferroelectric and rhombohedral ferroelectric phases was observed near *x* = 0.08. The phase diagram consists of three distinct crystallographic phases in this system; high temperature paraelectric cubic, rhombohedral, and ferroelectric orthorhombic.

Summary

Relaxor ferroelectric PCoN has been found to strongly influence crystal structure and thermal properties of PZ ceramics. The crystal structure data obtained from XRD indicate that the solid solution (*1-x*)PZ - *x*PCoN, where *x* = 0.0-0.3, successively transforms from orthorhombic to rhombohedral symmetry with increased PCoN concentration. The AFE→FE phase transition is found in compositions of $0.0 \leq x \leq 0.08$. The AFE→FE phase transition shifts to lower temperatures with higher compositions of *x*. The temperature range width of the FE phase increases with increased PCoN.

Acknowledgment

This work was supported by the Thailand Research Fund (TRF), the Commission on Higher Education (CHE), and King Mongkut's Institute of Technology Ladkrabang (KMITL).

References

[1] E. Sawaguchi, G. Shirane and S. Hoshino: Phys. Rev. Vol. 83 (1951), p. 1078.
[2] F. Jona, G. Shirane, F. Mazzi and R. Pepinsky: Phys. Rev. Vol. 105 (1957), p. 849.
[3] G. H. Haertling: J. Am. Ceram. Soc. Vol. 82 (1999), p. 797.
[4] B. P. Pokharel and D. Pandey: J. Appl. Phys. Vol. 86 (1999), p. 3327.
[5] K. Uchino: Ferroelectrics Vol. 151 (1994), p. 321.
[6] G. A. Smolenskii and Isupov: Sov. Phys. doklady. Vol. 9 (1954), p. 653.
[7] N. Setter and L. E. Cross: J. Appl. Phys. Vol. 51 (1980), p. 4356.
[8] A. Halliyal, U. Kumar, R. E. Newham and L. E. Cross: Am. Ceram. Soc. Bull. Vol. 66 (1987), p. 671.
[9] B. Jaffe and W. R. Cook: *Piezoelectric ceramic* (R.A.N. Publishers, 1971).
[10] B. P. Pokharel and D. Pandey, Phys. Rev. B. Vol. 65 (2002), p. 214108.
[11] Y. Xu, *Ferroelectric Materials and Their Application* (Elsevier Science Publishers B.V., 1991).

Advanced Materials Research Vols. 55-57 (2008) pp 125-128
online at http://www.scientific.net

Effects of Zr/Ti Ratio on the Structure and Ferroelectric Properties in PZT-PZN-PMN Ceramics Near the Morphotropic Phase Boundary

R. Muanghlua[1], S. Niemchareon [1], W. C. Vittayakorn[2] and N. Vittayakorn[3,a]

[1]Electronics Research Center, Faculty of Engineering, King Mongkut's Institute of Technology Ladkrabang, Bangkok Thailand 10520

[2] Department of Physics, Faculty of Science, Chiang Mai University, Chiang Mai, Thailand 50200

[3]Materials Science Research Unit, Faculty of Science, King Mongkut's Institute of Technology Ladkrabang, Bangkok, Thailand 10520

[a] e-mail: naratipcmu@yahoo.com

Keyword: Ferroelectric Materials, Lead Zirconate titanate, Morphotropic phase boundary

Abstract The piezoelectric ceramics of $Pb(Zr_xTi_{1-x})O_3$ – $Pb(Zn_{1/3}Nb_{2/3})O_3$ – $Pb(Mn_{1/3}Nb_{2/3})O_3$; PZT-PZN-PMN with Zr/Ti ratios of 48/52, 50/50 and 52/48 were fabricated in order to investigate the effect of compositional modifications on the ferroelectric properties of PZT-PZN-PMN ceramics. The phase structure of ceramics sintered at 1,150°C was analyzed. Results show that the pure perovskite phase was in all ceramic specimens, and the phase structure of PZT-PZN-PMN piezoelectric ceramics transformed from tetragonal to rhombohedral, with the Zr/Ti ratios increased in the system. The PZT-PZN-PMN ceramics with a Zr/Ti ratio of 50/50 exhibited the most promising properties including high remanent polarization and low coercive field of 25.95 μC cm^{-2} and 12.5 kV cm^{-1}, respectively. Furthermore, the transition temperature decreased when the Zr/Ti ratio increased in the system.

Introduction

Lead zirconate titanate (PZT) is one of the most commonly used ferroelectric ceramic materials. The material has been studied intensively since discovery of the miscibility of lead titanate and lead zirconate in the 1950s. Due to their excellent dielectric, pyroelectric, piezoelectric and electro optic properties, they have a variety of applications in high energy capacitors, non-volatile memories (FRAM), ultrasonic sensors, infra red detectors, electro optic devices, and step-down multilayer piezoelectric transformers for AC–DC converter applications. Until now, many ternary and quaternary systems, such as PNW–PMN–PZT [1], PMN–PZN–PZT [2], PZT–PNN–PZN [3], and PZT–PFW–PMN [4] have been synthesized by modifications or substitutions to satisfy the requirements of the multilayered piezoelectric transformers. In this work, we studied influences of the Zr/Ti ratio on the crystal structure, and piezoelectric and dielectric properties of $Pb(Zr_xTi_{1-x})O_3$ – $Pb(Zn_{1/3}Nb_{2/3})O_3$ – $Pb(Mn_{1/3}Nb_{2/3})O_3$; PZT-PZN-PMN ceramics for multilayered piezoelectric transformer applications.

Experimental

The powders and ceramics with compositions of $Pb_{0.97}Sr_{0.03}[(Mn_{1/3}Nb_{2/3})_{0.07}(Zn_{1/3}Nb_{2/3})_{0.06}(Zr_{(1-x)}Ti_x)_{0.87}]O_3$ were prepared via a conventional mixed-oxide process, where x = 0.48, 0.50 and 0.52. Reagent-grade oxide powders PbO (99.0%), ZrO_2 (99.0%), TiO_2 (99.5%), Nb_2O_5 (99.5%), ZnO(99.9%) and MnO_2 (99.0%) were mixed, consecutively. The mixtures were milled in ethanol using zirconium ball as media in a polyethylene jar for 18 h. The mixed slurry was dried at 80°C and calcined at 850°C for 4 h. Then, the calcined powders were ground again under the same condition in order to obtain fine uniform powders. After drying, the powders were added to 5 wt.% polyvinyl alcohol (PVA) solution, and then pressed into15 mm diameter plates under a pressure of 100 MPa. The pressed plates were sintered at 950–1,100°C for 6 h in a sealed alumina crucible with lead atmosphere. The sintered ceramics were examined by X-ray diffractometry (XRD, D8

Advance) to determine the phase structure. Subsequently, the sintered disks were polished, and silver-paste electrodes were fired at 850°C. In addition, the polarization (P) was measured as a function of electric field (E), using a ferroelectric tester system (Radiant Technologies, Inc., PT66A).

Results and Discussion

Figure 1 (a) and (b) show the XRD patterns of $Pb_{0.97}Sr_{0.03}[(Mn_{1/3}Nb_{2/3})_{0.07}(Zn_{1/3}Nb_{2/3})_{0.06}(Zr_{(1-x)}Ti_x)_{0.87}]O_3$ sintered pellets for x = 0.48, 0.50 and 0.52. The sintered pellets can be seen as a single-phase: all the lines in each XRD pattern could be indexed with a perovskite cell. No secondary reaction phases, such as PbO, Pb-based compounds, unreacted oxide and so on, are observed in the pattern.

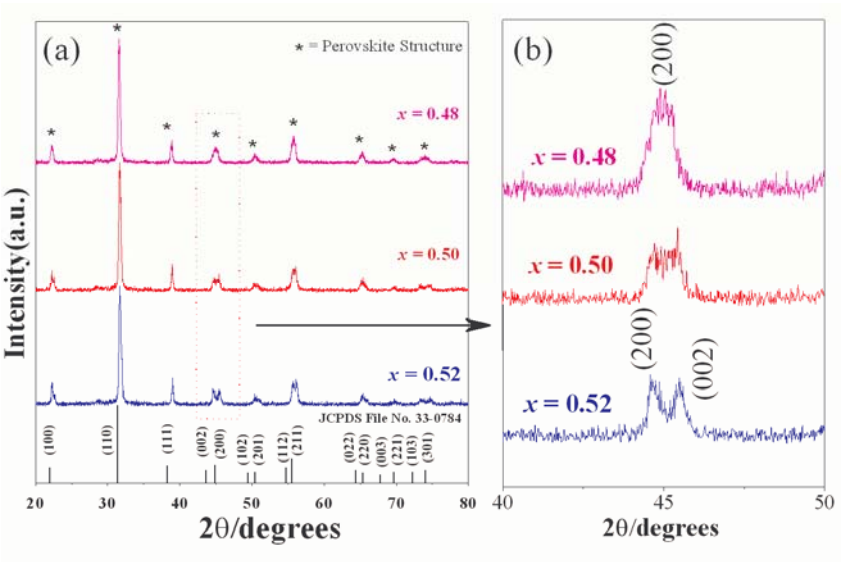

Figure 1 XRD patterns of $Pb_{0.97}Sr_{0.03}[(Mn_{1/3}Nb_{2/3})_{0.07}(Zn_{1/3}Nb_{2/3})_{0.06}(Zr_{(1-x)}Ti_x)_{0.87}]O_3$ sintered pellets.

Based on the careful XRD study of (2 0 0) reflections in Figure 1(b), we found that a phase transformation from the pseudo-cubic structure to the tetragonal structure occurs with increasing x content. The ceramics with $x = 0.48$ exist as a pseudo-cubic phase revealed by the single $(2\ 0\ 0)_R$ peak. At $x = 0.50$, the ceramics coexist as a tetragonal and pseudo-cubic phase revealed by the coexistence of $(0\ 0\ 2)_T$ and $(2\ 0\ 0)_R$ peaks in the 2θ range of 43.5° to 45.5°. The ceramics exist as a tetragonal phase when indicated by the splitting of (0 0 2) and (2 0 0) peaks in the 2θ range of 43.5° to 46.5° at $x = 0.52$.

Table 1 Characteristics of $Pb_{0.97}Sr_{0.03}[(Mn_{1/3}Nb_{2/3})_{0.07}(Zn_{1/3}Nb_{2/3})_{0.06}(Zr_{(1-x)}Ti_x)_{0.87}]O_3$ ceramics with optimized processing conditions

Composition x	Crystal structure	Theoretical Density (%)	Grain Size (μm)
0.48	PC	94.05	2.84
0.50	PC+T	94.03	2.72
0.52	PC	95.21	2.94

In the first approximation, it could be said that the composition between $x = 0.50$ is close to the morphotropic phase boundary (MPB) of this system, where the structure of the $Pb_{0.97}Sr_{0.03}[(Mn_{1/3}Nb_{2/3})_{0.07}(Zn_{1/3}Nb_{2/3})_{0.06}(Zr_{(1-x)}Ti_x)_{0.87}]O_3$ compositions is gradually changing from pseudo-cubic to tetragonal. The physical properties do not vary significantly with the ceramic compositions, as listed in Table 1.

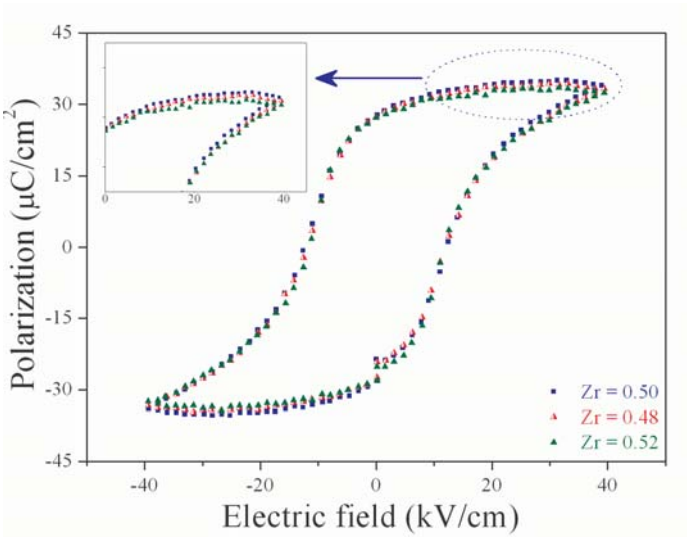

Figure 2 Hysteresis loops of the $Pb_{0.97}Sr_{0.03}[(Mn_{1/3}Nb_{2/3})_{0.07}(Zn_{1/3}Nb_{2/3})_{0.06}(Zr_{(1-x)}Ti_x)_{0.87}]O_3$ ceramics with $x = 0.48$, 0.50 and 0.52 measured at 40 kV/cm.

Figure 2 illustrates the *P–E* curves of the samples, with $x = 0.48$, 0.50 and 0.52 measured at 25 kV/cm. All compositions show symmetry in shape and reveal rectangular hysteresis loops, which is typical of a phase that contains long-range cooperation between dipoles. No evidence of pinning effect or asymmetric loop was detected in any electric field strengths. From the fully saturated loops, the remanent polarization P_r and coercive field E_c were determined. The values of P_r and E_c for composition $x = 0.50$ are 25.95 μC/cm^2 and 12.5 kV/cm, respectively, whereas the remanent polarization P_r is 25.7 μC/cm^2 for composition $x = 0.48$. Maximum remanent polarization was observed in the ceramic with composition $x = 0.5$. It has been seen that the samples with compositions $x = 0.5$ exhibit the highest saturation and remnant polarization among all the ceramics studied. As indicated by the above XRD, the composition with $x = 0.5$ contains both tetragonal and pseudo-cubic phases, so it should favor a strong ferroelectric effect. This is due to the increased ease of reorientation during poling by the transformation of a number of 180° domains into 90° ones. Also revealed from these results, the MPB coexisting in the tetragonal and pseudo-cubic phases in the present system is a broad composition region of $x = 0.5$, which exhibits high ferroelectric properties around the center of the MPB.

Summary

The Zr/Ti ratio has been found to influence crystal structure and ferroelectric properties of $Pb_{0.97}Sr_{0.03}[(Mn_{1/3}Nb_{2/3})_{0.07}(Zn_{1/3}Nb_{2/3})_{0.06}(Zr_{(1-x)}Ti_x)_{0.87}]O_3$ ceramics. The crystal structure data obtained from XRD indicate that the solid solution $Pb_{0.97}Sr_{0.03}[(Mn_{1/3}Nb_{2/3})_{0.07}(Zn_{1/3}Nb_{2/3})_{0.06}(Zr_{(1-x)}Ti_x)_{0.87}]$, where $x = 0.48$, 0.50 and 0.52, successively transforms from pseudo-cubic to tetragonal symmetry with increased x concentration. More interestingly, XRD analysis and ferroelectric property measurements indicated the existence of the MPB composition at between $x = 0.50$.

Acknowledgment

This work was supported by the Thailand Research Fund (TRF), the Commission on Higher Education (CHE), and Faculty of Engineering, King Mongkut's Institute of Technology Ladkrabang and King Mongkut's Institute of Technology Ladkrabang (KMITL).

References

[1] Z. Yang, R. Zhang, L. Yang and Y. Chang: Materials Research Bulletin. Vol. 42 (2007), p. 2156.
[2] J. Yoo, K. Kim, C. Lee, L. Hwang, D. Paik, H. Yoon and H. Choi: Sensors and Actuators A: Physical. Vol. 137 (2007), p. 81.
[3] N. Vittayakorn and D. P. Cann; Appl. Phys. A. Vol. 86 (2007), p. 403.
[4] Z. Yang, X. Chao, C. Kang and R. Zhang: Materials Research Bulletin. Vol. 43 (2008), p. 38.

Advanced Materials Research Vols. 55-57 (2008) pp 873-876
online at http://www.scientific.net

Synthesis, Phase Formation and Characterization of $Co_4Nb_2O_9$ Powders Synthesized by Solid-State Reaction

N. Chaiyo[1], R. Muanghlua[2], A. Ruangphanit[3], W. C. Vittayakorn[4] and N. Vittayakorn[1,5,a]

[1] King Mongkut's Institute of Technology Ladkrabang Nanotechnology Research Center (NRC), King Mongkut's Institute of Technology Ladkrabang, Bangkok, Thailand 10520

[2]Electronics Research Center, Faculty of Engineering, King Mongkut's Institute of Technology Ladkrabang, Bangkok Thailand 10520

[3] Thai Microelectronics Center (TMEC), National Electronics and Computer Technology Center,

Nation Science and Technology Development Agency, Ministry of Science and Technology, Chachoengsao 24000, Thailand

[4] Department of Physics, Faculty of Science, Chiang Mai University, Chiang Mai, Thailand 50200

[5] Materials Science Research Unit, Department of Chemistry, Faculty of Science, King Mongkut's Institute of Technology Ladkrabang, Bangkok, Thailand 10520

[a] e-mail: naratipcmu@yahoo.com

Keywords: $Co_4Nb_2O_9$; Calcinations; Powder synthesis; Microwave dielectric

Abstract. A corundum-type structure of cobalt niobate ($Co_4Nb_2O_9$) has been synthesized by a solid-state reaction. The formation of the $Co_4Nb_2O_9$ phase in the calcined powders was investigated as a function of calcination conditions by differential thermal analysis (DTA) and X-ray diffraction (XRD) techniques. Morphology and particle size have been determined by scanning electron microscopy (SEM). It was found that the minor phases of unreacted Co_3O_4 tend to form together with the columbite $CoNb_2O_6$ phase at a low calcination temperature and short dwell time. It seems that the single-phase of $Co_4Nb_2O_9$ in a corundum phase can be obtained successfully at the calcination conditions of 900°C for 60 min, with heating/cooling rates of 20°C /min.

Introduction

A variety of microwave dielectric ceramics have been utilized for microwave dielectric applications including the filters and resonators in the wireless communication system [1]. There are three important properties required, i.e., a high dielectric constant ε_r, high quality factor $Q \times f$ and low temperature coefficient of resonant frequency τ_f., in order to miniaturize the size of the microwave dielectric resonator and reach suitability for application at high frequency, and the resonant frequency must be stable at various operating temperatures. A high $Q \times f$ value of more than 30,000 GHz is required to withstand high electric loads, especially for microwave dielectric ceramics used in the base stations of mobile phones. However, still higher $Q \times f$ – value materials are required for new digital systems [2]. Over the past few years, the demand for smaller, lighter and temperature stable devices has increased. Cobalt niobate $CoNb_2O_6$ is one of the best known microwave dielectric materials, which recently gained considerable attention. In general, production of single-phase $CoNb_2O_6$ is not straightforward, as a minor concentration of $Co_4Nb_2O_9$ sometimes forms alongside the major phase of $CoNb_2O_6$. The crystal structure of $Co_4Nb_2O_9$ ceramic is known to have a corundum-type structure. The oxygen ions are located at the lattice sites of a hexagonal closed-packed unit cell. In the HCP crystal structure, as in the FCC structure, there are as many octahedral interstitial sites as there are atoms in the unit cell. In recent study, the microwave dielectric properties of a corundum-type structure such as $Mg_4Nb_2O_9$ ceramic was reported to have a high $Q \times f$ value, which was comparable to that of Al_2O_3. Thus far, although $Co_4Nb_2O_9$ is identical

in stoichiometry to $Mg_4Nb_2O_9$, it has not been synthesized to the corundum-type structure. Interestingly, the mixed oxide route for the production of $Co_4Nb_2O_9$ powders has not received detailed attention, and the effects of calcination conditions have not yet been studied extensively. The objective of this work was to study the reaction between the starting cobalt oxide and niobium oxide precursors, phase formation and microstructure of corundum-type structure cobalt niobate powder.

Experimental

Reagent-grade oxides of Co_3O_4 (99.99 %, Aldrich, USA) and Nb_2O_5 (99.9%, Aldrich, USA) were used in this study. $Co_4Nb_2O_9$ powders were synthesized by the solid-state reaction of Co_3O_4 and Nb_2O_5 powders that were homogenized by ball milling with ethyl alcohol in the required stoichiometric ratio. The mixed slurry was dried at 80°C. The reactions of the uncalcined $Co_4Nb_2O_9$ powder, taking place during heat treatment, were investigated by differential thermal analysis (DTA; Perkin-Elmer 7 series) using a heating rate of 10°C /min in air from room temperature to 1,350 °C. According to the DTA results, various calcination conditions (i.e. temperatures ranging from 700 – 1,100°C and dwell times from 15 to 240 min) were applied, with a heating/cooling rate of 20°C/min in order to investigate the formation of $Co_4Nb_2O_9$. Calcined powders were subsequently examined by room temperature X-ray diffraction (XRD; Bruker D8 Advance) using Ni-filtered CuK_α radiation to identify the phase formed and optimum calcination condition for the formation of $Co_4Nb_2O_9$ powders. Powder morphologies and grain size were directly imaged using scanning electron microscopy (LEO, LEO 1455VP, Cambridge, England).

Results and Discussion

The DTA curve for the powder mixed in the stoichiometric proportions of $Co_4Nb_2O_9$ is shown in Figure 1. Three endothermic peaks centered at 121°C, 294°C and 837°C were observed. The first and second endothermic peaks should correspond to the evaporation of water molecules and decomposition of the organic species from the milling process, respectively [3, 4]. The third endothermic peak, at 837 °C, was assigned to the formation of $Co_4Nb_2O_9$ by combination reactions of Co_3O_4 and Nb_2O_5. Based on the DTA measurements, these data were used to define the range of calcination temperature at between 700 to 1,100 °C for XRD investigation.

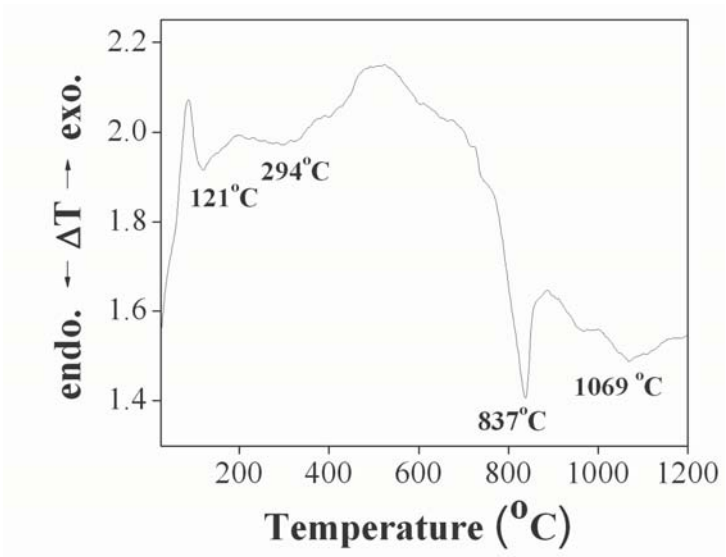

Figure 1. DTA curve for the mixture of Co_3O_4-Nb_2O_5 powder.

XRD patterns of all calcined powders are given in Figure 2. At a clacination temperature as low as 800°C, the strongest reflections were apparent in the majority of the XRD patterns, which indicated the formation of a columbite phase of $CoNb_2O_6$ (A) that could be matched with JCPDS file numbers 32-0304. The minor phase of unreacted cubic-Co_3O_4 (Y), which could be matched with JCPDS files No 78-1969, were found. As the calcination temperature increased to 900°C, intensity of the corundum $Co_4Nb_2O_9$ peaks was enhanced further and became the monophasic phase. This $Co_4Nb_2O_9$ phase was indexable according to a hexagonal corundum-type structure, with a lattice parameter of a = 517 pm and c = 1412 pm, and space group *P3c1* (no. 165), consistent with JCPDS file numbers 38-1457. Upon calcinations at 1,000 and 1,100 °C, an essentially monophasic phase of $Co_4Nb_2O_9$ was obtained. However, in this work, there were no significant differences between the powders calcined at temperatures ranging from 900 to 1,100 °C.

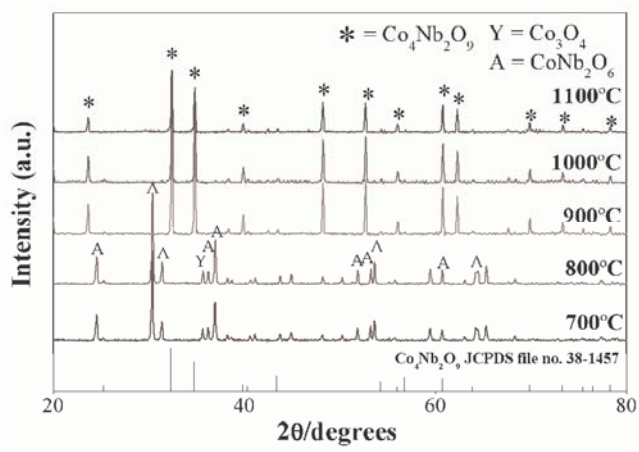

Figure 2. XRD patterns of $Co_4Nb_2O_9$ powder calcined at various temperatures for 4 h with heating/cooling rates of 20 °C /min.

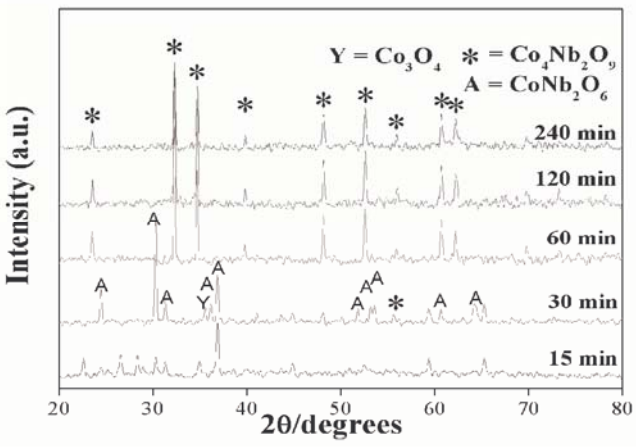

Figure 3. XRD patterns of $Co_4Nb_2O_9$ powder calcined with heating/cooling rates of 20 °C /min at 900 °C for 15-240 min.

After obtaining the optimum calcination temperature, dwell times ranging from 15 min to 120 min, with a constant heating/cooling rate of 20°C/min were applied at 900 °C, as shown in Figure 3. It was observed that the single-phase of $Co_4Nb_2O_9$ (yield of 100% within the limitations of the XRD technique) powder was possible in powders calcined at 900°C, with a dwell time of 60 min or more applied. Observation that the dwell time effect may also play an important role in obtaining a single-phase product is also consistent with other systems [5, 6].

The average grain sizes were determined from the XRD pattern according to the Scherrer's equation

$$D = \frac{k\lambda}{\beta \cos \theta_B}$$

where D is the average grain size, k is a constant equal to 0.89, θ_B is the (3 1 1) peak angle, λ is the X-ray wavelength equal to 1.5406 Å and β is the half peak width. The average grain size of $Co_4Nb_2O_9$ powders was about 280 nm at 900 °C, with a dwell time of 60 min. The morphology of the calcined $Co_4Nb_2O_9$ powders was investigated by scanning electron microscopy (SEM), which is illustrated in Figure 4(a) and 4(b). In general, the particles are agglomerated and basically irregular in shape, with a substantial variation in particle size and morphology. The particle size can be estimated in the range of 300-400 nm from SEM micrographs. A detailed study at higher

magnification [Fig. 5(b)] shows that the particles had spherical secondary particles, composed of nano-sized primary particulates.

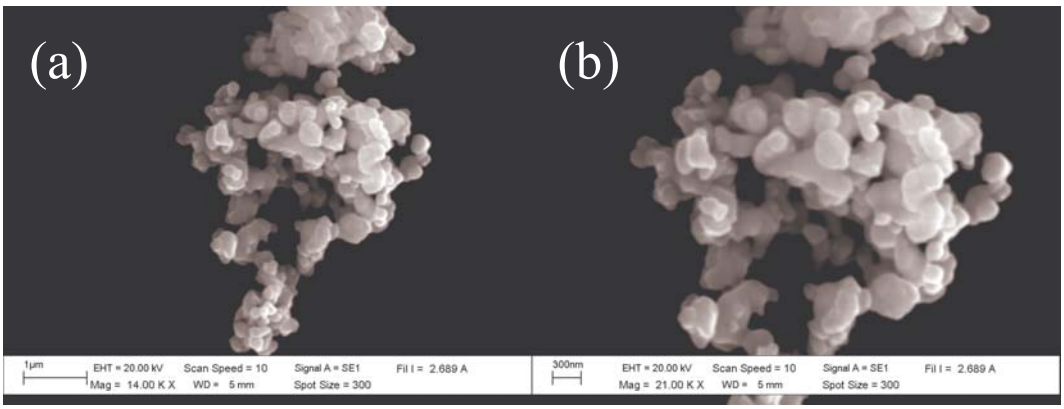

Figure 4. Scanning electron micrographs of the $Co_4Nb_2O_9$ powders calcined at 900 °C for 60 min, with a heating/cooling rate of 20 °C /min.

Summary

The corundum-structure, $Co_4Nb_2O_9$, was synthesized by solid state reaction using oxides as starting materials. The content of the impurity phases decreased with increasing calcination temperature and dwell time. Evidence has been obtained of a 100% yield of $Co_4Nb_2O_9$ at a calcination temperature of 900°C for 60 min, with heating/cooling rates of 20°C/minute. XRD showed the compound to have a corundum structure, with hexagonal lattice parameters of a = 5.1669(± 0.0014) and c = 14.1248 (± 0.0072). The particle size can be estimated in the range of 300-400 nm from SEM micrographs.

Acknowledgements

This work was supported by the Thailand Research Fund (TRF), the Commission on Higher Education (CHE), Thailand Graduate Institute of Science and Technology (TGIST), National Research Council of Thailand (NRCT) and King Mongkut's Institute of Technology Ladkrabang (KMITL).

References

[1] A. Kan, H. Ogawa, A. Yokoi and Y. Nakamura: J. Euro. Ceram. Soc. Vol. 27 (2007), p. 2977.
[2] A. J. Moulson and J. M. Herbert: *Electroceramics: Materials, Properties, Appications* (Chapman and Hall, New York, 1990)
[3] S. Ananta, Mater. Lett. Vol. 58 (2004), p. 2530.
[4] R. Wongmaneerung, T. Sarakonsri, R. Yimnirun and S. Ananta: Materials Science and Engineering: B. Vol. 130 (2006), p. 246.
[5] R. Wongmaneerung, R. Yimnirun and S. Ananta: Mater. Lett. Vol. 60 (2006), p. 2666.
[6] S. Wongsaenmai, R. Yimnirun and S. Ananta: Mater. Lett. Vol. 61 (2007), p. 2426.

Advanced Materials Research Vols. 55-57 (2008) pp 217-220
online at http://www.scientific.net

Ferroelectric and Mechanical Properties of PZT-PZN-PNN Ceramics

S. Nabunmee, N. Vittayakorn, D. P. Cann and G. Rujijanagul*

Department of Physics, Faculty of Science, Chiang Mai University, Chiang Mai 50200, Thailand

*rujijanagul@yahoo.com

Keywords: Dielectric permittivity, Phase transition, PZT-PZN-PNN ceramics

Abstract. Ceramics in the system $0.05(Pb(Zn_{1/3}Nb_{2/3})O_3$-$0.15Pb(Ni_{1/3}Nb_{2/3})O_3$-$0.8Pb(Zr_{1/2}Ti_{1/2})O_3$ (0.05PZN-0.15PNN-0.8PZT) were synthesized via the columbite method. Ferroelectric properties of the samples prepared by different sintering conditions were investigated. The mechanical property of the ceramics was also determined. The best ferroelectric properties were observed for the sample sintered at 1250°C.

Introduction

In the last decade, normal ferroelectric such as lead zirconate titanate [$PbZr_{1-x}Ti_xO_3$, PZT] has become an important commercially produced piezoelectric materials.[1-3] Excellent piezoelectric properties of PZT have been observed in compositions close to the morphotropic phase boundary(MPB Zr:Ti ,52:48). [1-3] Locating the MPB for the ferroelectric materials is very important for making the phase diagram and for obtaining excellent electrical properties. Therefore, most commercial PZT and other ferroelectric ceramics are thus designed in the vicinity of the MPB with various dopings in order to achieve high properties.

Lead-based relaxor perovskites, such as $Pb(Zn_{1/3}Nb_{2/3})O_3$ (PZN) and $Pb(Ni_{1/3}Nb_{2/3})O_3$ (PNN), having the general formula $Pb(B'B'')O_3$ have received significant attention since the 1970s because of their peculiar dielectric and piezoelectric behavior. These materials have been applied in many areas such as electrostrictive actuators, transducers, and multilayer ceramic capacitors. [4-9]

Recently, binary or ternary systems containing a combination of relaxor ferroelectrics with rhombohedral symmetry and normal ferroelectric tetragonal symmetry near the MPB have attracted particular attention owing to their high dielectric and piezoelectric properties. The excellent electrical properties can be applied to many areas such as multilayer ceramic capacitors, electrostrictive transducers, sensors, and actuators. [10-12] In the present work, solid solution of 0.05PZN-0.15PNN-0.8PZT ternary system was synthesized via a columbite method. Various sintering temperature were carried out, to find out the optimum processing condition.

Experimental

The ternary system of 0.05PZN-0.15PNN-0.8PZT was synthesized by a columbite method. The wolframite precursor $ZrTiO_4$ was formed by reaction between ZrO_2 with TiO_2 at 1400 °C for 4 h. The columbite precursor $ZnNb_2O_6$ was prepared from the reaction between ZnO and Nb_2O_5 at 975 °C for 4 h. The precursors $ZrTiO_4$, $ZnNb_2O_6$ were then mixed with PbO (99.9%) according to the stoichiometric ratio for the desired compositions with 2 mol% excess PbO added. The mixed powders were calcined at temperatures ranging, 900°C at a dwell time of 2 h in a double crucible configuration with a heating rate of 20 °C/min. The calcined powders were isostatically cold pressed into pellets at a pressure of 100 MPa. Sintering occurred between 1100 and 1350 °C with a dwell time of 2 h at 500°C with heating rate 1°C/min and 2 h at 1250°C with heating rate 5°C/min. The perovskite phase was examined by x-ray diffraction (XRD). The density of the sintered samples was measured by Archimedes' method with distilled water as the fluid medium. The polarization-Electric field (P-E) property and mechanical property of the sintered samples were measurement.

Results and Discussion

The perovskite and pyrochlore phase formation at different sintering temperatures in 0.05PZN-0.15PNN-0.8PZT ceramics were studied and analyzed by XRD.

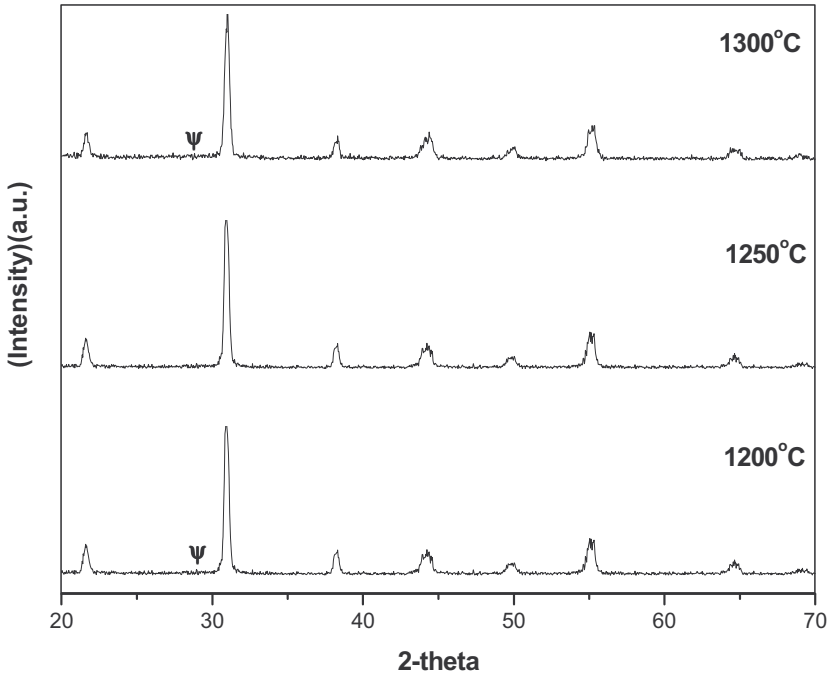

Figure 1. XRD patterns at room temperature of 0.05PZN-0.15PNN-0.8PZT ceramics.

Fig. 1 illustrates XRD patterns from this system. The pyrochlore-type structure was found in the sample sintered at 1200 and 1300°C, as indicated by ψ. In the other hand, pure peroskite was observed for the 1250 °C sintered sample. The formation of pyrochlore phase may be due to reaction between PbO and the columbite precursors or due to lead lose at high temperature.

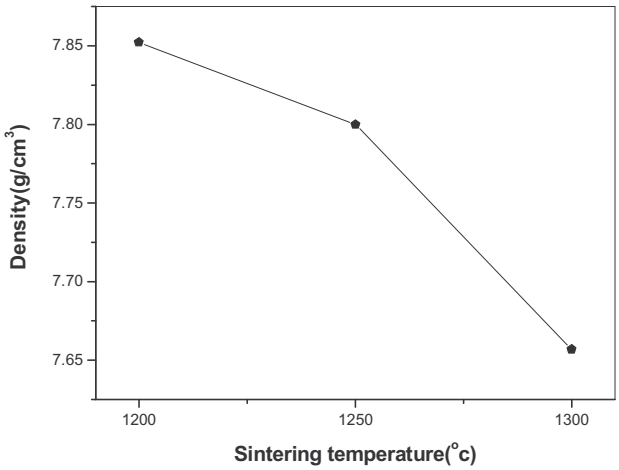

Figure 2. Density as a function of sintering temperature of 0.05PZN-0.15PNN-0.8PZT ceramics.

Fig. 2 shows the typical sintered densities of 0.05PZN-0.15PNN-0.8PZT ceramics for various sintering temperature. Although the pure perovskite phase was found at 1250°C, the density of the sample was observed to decrease with increasing sintering temperature. The decreasing in density may be due to the PbO evaporation at high temperature.

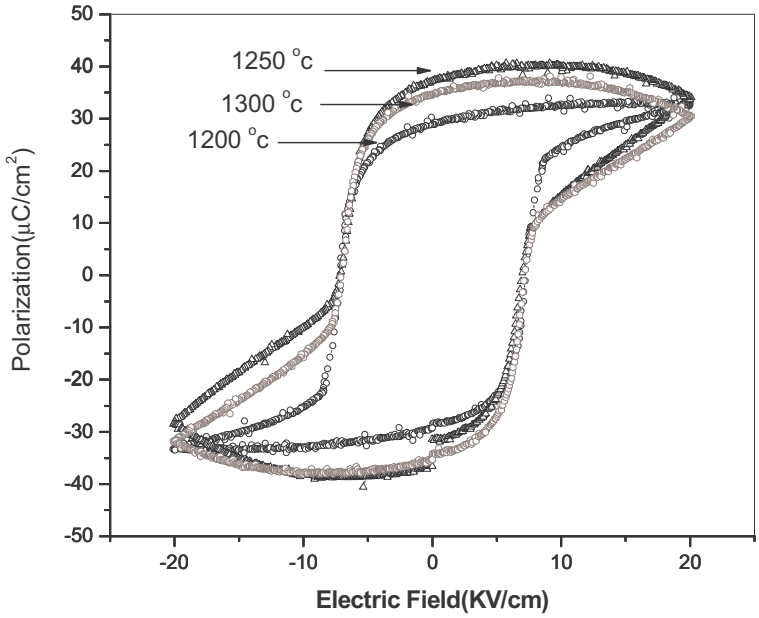

Figure 3. Polarization vs. electrical field for 0.05PZN-0.15PNN-0.8PZT ceramics.

The result of polarization-field (*P-E*) measurements for the ceramics sintered at various temperatures is shown in Fig. 3. All samples showed normal ferroelectric behavior with a rectangular loop. High polarization was observed for all samples. The optimum ferroelectric with higher remanent polarization (*P*r) of 40 μC/cm^2 was observed for the sample sintered at 1250°C, as expected. The lower remanent polarization in other sintering conditions may due to the formation of pyrochlore phase in the samples which made the ceramics have lower ferroelectric behavior. However, coercive field (E_c) was ~ 7.2 kV/cm for all sintering conditions.

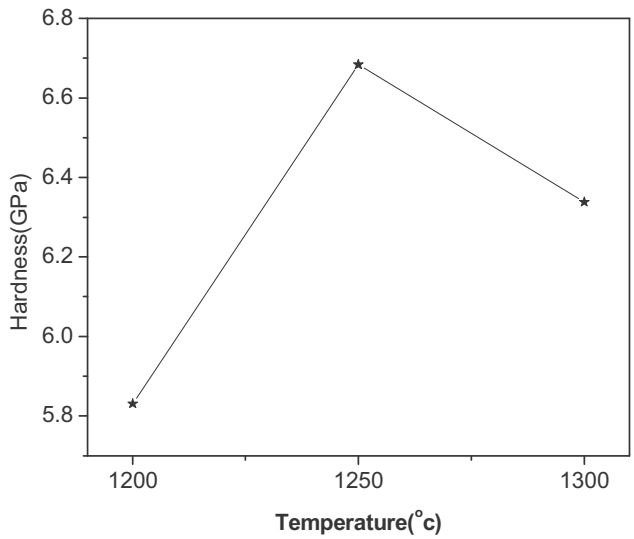

Figure 4. The 1250°C sintered sample displayed a higher hardness than the other samples.

The results of hardness measurements are shown in Fig. 4. The higher hardness value was 6.7 GPa. In the present work, the grain size of the system was found to increase with increasing the sintering temperature. Therefore, the existent of pyrochlore phase may result in the lower mechanical property of the samples.

Summary

In this work, 0.05PZN-0.15PNN-0.8PZT ceramics were synthesized via a columbite method. The sintering temperature of 1250°C was selected as the optimum sintering condition for preparation of the 0.05PZN-0.15PNN-0.8PZT ceramics. Pyrochlore phase was found to effect on the ferroelectric and mechanical properties of the ceramics.

Acknowledgements

This work was supported by The Thailand Research Fund (TRF), National Metal and Materials Technology Center (MTEC), Faculty of Science and Graduate School Chiang Mai University, and Commission on Higher Education (CHE) Thailand. The authors would like to thank Prof. Dr. Tawee Tunkasiri for his help in many facilities.

References

[1] K. Uchino: *Ferroelectric Devices* (Marcel Dekker, New York, 2000).
[2] A. J. Moulson and J. M. Herbert : *Electroceramics Materials Properties and Applications* (Chapman and Hall, New York, 1990).
[3] K. Uchino: Solid State Ionics Vol. 108 (1998), p. 43.
[4] L.E. Cross: Ferroelectrics Vol.76 (1987), p. 241.
[5] T.R. Shrout and A. Halliyal: Journal of American Ceramics Society Bull. (1987).
[7] K. Uchino: Ferroelectrics Vol.151 (1994), p. 321.
[8] K. Uchino: Solid State Ionics Vol.108 (1998), p. 43.
[9] K. Uchino: *Piezoelectric Actuators and Ultrasonic Motors* (Kluwer Academic Publishers, Boston, MA, 1996).
[10] N. Vittayakorn, C. Puchmark, G. Rujijanagul, X. Tan, and D. P. Cann: J. Appl. Phys. Vol.6 (2006), p. 303.
[11] N. Vittayakorn, G. Rujijanagul, X. Tan, M. A. Marquardt, and D. P. Cann: J. Appl. Phys. Vol. 96 (2004), p. 5103.
[12] S. Nabunmee, G. Rujijanagul, N. Vittayakorn, D. P. Cann: J. Appl. Phys. Vol.102 (2007), p. 094108.

Advanced Materials Research Vols. 55-57 (2008) pp 205-208
online at http://www.scientific.net

Effect of Calcination Temperatures on Microstructure and Phase Formation of $Ba(Zr_{0.25}Ti_{0.75})O_3$ Powders

T. Bongkarn[1,a*], N. Phungjitt[2,b] and N. Vittayakorn[3,c]

[1]Department of Physics, Faculty of Science, Naresuan University, Phitsanulok, Thailand

[2]Department of Physics, Faculty of Science, Uttaradit Rajabhat University, Uttaradit, Thailand

[3]Department of Chemistry, Faculty of Science, King Mongkut's Institute of Technology Ladkrabang, Bangkok,Thailand

[a]reseachcmu@yahoo.com, [b]nalinee_amp@hotmail.com, [c]naratipcmu@yahoo.com

Keywords: Barium zirconate titanate, Microstructure, Phase formation, Solid state reaction

Abstract. In this work, the effect of calcination temperatures on the microstructure and phase formation of $Ba(Zr_{0.25}Ti_{0.75})O_3$ (BZT) powders were investigated. The BZT powders were prepared via the solid state reaction method under various calcination temperatures. It was found that the second phases such as $BaCO_3$, ZrO_2, $BaZrO_3$ and Ba_2ZrO_4 existed in samples with calcination temperature below 1200 ^oC. Homogeneity and a highly pure perovskite phase of the BZT powders were obtained with calcination condition at 1300 ^oC for 4 h. Lattice parameter *a* and the percentage of cubic perovskite phase tended to increase with increasing calcination temperatures. The TG-DTA results corresponded to the XRD investigation. The microstructures of calcined powders exhibited an almost-spherical morphology and had a porous agglomerated form in all samples. The average particle sizes were increased from 0.2 to 1.1 μm when calcination temperatures were increased from 800 to 1350 ^oC.

Introduction

Barium titanate ($BaTiO_3$; BT) is well known as a fundamental ferroelectric perovskite oxide and is often used in multilayer ceramic capacitors (MLCs) due to its high dielectric constant [1,2]. $BaTiO_3$ displays dielectric anomalies at 130, 0, and -90 ^oC with respective transformations in symmetry from cubic to tetragonal, from tetragonal to orthorhombic, and from orthorhombic to rhombohedral. Those anomalies are accompanied by a high dielectric constant near the phase transition [3]. Barium zirconate titanate $Ba(Zr_xTi_{1-x})O_3$ is obtained by substituting ions at the B site of $BaTiO_3$ with Zr ions. This substitution results were in a decrease of the temperature and a broadening of the permittivity maximum [4-6]. At a Zr/Ti ratio greater than 0.10, the three dielectric constant peaks coalesce into a single broad maximum [7]. Moreover, the transition temperature of BZT shifts to a lower temperature region with the increase of the Zr content. The dielectric study of the $[Ba(Zr_xTi_{1-x})O_3]$ ceramics with x=0.20 and 0.25 showed a normal ferroelectric with weak diffuse phase transition behaviors [8]. The diffuse phase transition and a relaxor-like behavior were found at higher Zr contents (x=0.30 and 0.35). The high tunability and the value of figure of merit (FOM) of the $[Ba(Zr_xTi_{1-x})O_3]$ with x=0.25 ceramic measured at room temperature under the biasing field 20 kV/cm are 58% and 135, respectively [8,9]. This makes $[Ba(Zr_xTi_{1-x})O_3]$ ceramic a promising material for tunable capacitor applications. Successfully, $[Ba(Zr_xTi_{1-x})O_3]$ ceramics were prepared via sol-gel process and mixed oxide method [8,9]. However, the detail of calcined temperatures affected crystal structure and morphology evolution of $[Ba(Zr_xTi_{1-x})O_3]$ powders, which synthesis by solid state reaction method have been reported yet. Therefore, in the present work, the effect of calcination temperatures on microstructure and the phase formation of $[Ba(Ti_{0.75}Zr_{0.25})O_3$; BZT] powders prepared via a solid state reaction method was studied.

Experimental

The starting materials were commercially available barium carbonate; $BaCO_3$ (99%), titanium (IV) oxide; TiO_2 (99%) and zirconium (IV) oxide; ZrO_2 (99%). Barium zirconate titanate [$Ba(Zr_{0.25}Ti_{0.75})O_3$, BZT] powder was synthesized by the solid state reaction of thoroughly ground mixtures of $BaCO_3$, TiO_2 and ZrO_2 powders that were by a ball milling procedure (zirconia milling media under ethanol for 24 h). Drying was carried out at 120 ^oC for 4 h. After sieving, various calcination temperatures, ranging from 800 to 1350 ^oC, with a dwell time of 4 h and a heating /cooling rate of 5 ^oC/min, were performed. The reaction of the uncalcined BZT powders taking place during heat treatment were investigated by thermogravimetric and differential thermal analysis (TG-DTA) using a heating rate of 10 ^oC/min from room temperature up to 1350 ^oC. Calcined powders were subsequently examined at room temperature by X-ray diffraction (XRD; Philip PW3040/60 X' Pert Pro) to identify the phase formed and the optimum calcination temperature of BZT powders. Powder morphologies and particle sizes were directly imaged, using scanning electron microscopy (SEM; LEO 1455 VP).

Results and discussion

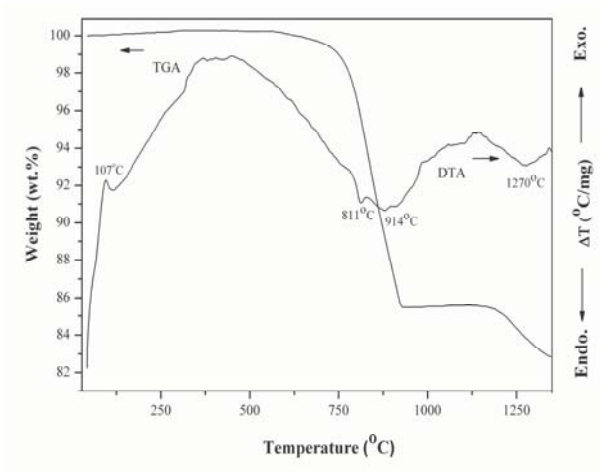

Figure 1. The DTA-TGA curve for the mixture of BZT powders.

The TG-DTA curves recorded at a heating rate of 10 ^oC/min in air for an equimolar mixture in the stoichiometric proportion of BZT is displayed in Fig. 1. The TG curve shows two distinct weight losses. The first weight loss occurs around 780 ^oC and the second one above 1190 ^oC. The sample shows a small exothermic peak in the DTA curve ~107 ^oC. This DTA peak can be attributed to the vaporization of water. No anomaly was observed from the TG pattern at this temperature. This may indicate that the small amount of vaporization of water could not be detected by the TG measurement. The first weight loss is attributed to the transition from witherite orthorhombic $BaCO_3$ to the rhombohedral phase [10]. In the second fall of specimen weight, a solid state reaction between $BaCO_3$, TiO_2 and ZrO_2 was observed. The broad endothermic characteristic of the DTA curve showed that these chemicals reacted most strongly at a minimum peak of 914 ^oC. Moreover, another endothermic peak with a minimum at 1270 ^oC was also observed in this profile. These data were used to define the range of optimum calcination temperatures from 800 to 1350 ^oC.

To further study the phase development with increased calcination temperatures in the powders, they were calcined for 4 h in normal air at various temperatures up to 1350 ^oC, followed by phase analysis using XRD. XRD patterns of the BZT powders formed with different calcinations temperatures are given in Fig. 2. After calcination at 800 ^oC, the crystalline phase of BZT was accompanied with $BaCO_3$ and ZrO_2 as separate phases, whose X-ray peak matched with the JCPDS file number 41-0373 and 24-1165. As the temperature increased to 1000 ^oC, the peaks corresponding to the raw materials disappeared, while the intensity of the $BaZrO_3$, $BaTiO_3$ and Ba_2ZrO_4 peaks become minor phases, which can correlate with JCPDS file number 41-0726 and 24-0130, respectively. After calcination at 1250 ^oC, the peaks corresponding to $BaZrO_3$ and Ba_2ZrO_4 were not detectable, whereas the $BaTiO_3$ phase remained. Evidently, a single phase of BZT is formed by calcination at 1300 ^oC. This observation agrees well with those derived from the TG-DTA results.

The strong reflections in the majority of the XRD patterns indicate the formation of the BZT perovskite phase, which can be matched with the JCPDS file number 36-0019. To a first approximation, this phase has a cubic perovskite type structure in the space group Pm-3m (no.221)

with a cell parameter a = 4.0520 Å. The lattice parameter a as a function of calcination temperatures of this study is shown in Fig. 3. The lattice parameter was increased with the increasing of calcinations temperatures. This indicated that the calcination temperatures have a direct significance on lattice parameter and unit cell volume. The relative amount of perovskite and impurity phases were determined by measuring the major XRD peak intensities of the perovskite and impurity phases. Fig. 4 shows the percentage of the BZT perovskite phase as a function of calcination temperatures. The percentage of the BZT perovskite phase was increased with increasing calcination temperatures. The calcined powders, ranging from 800 to 1250 ^{o}C, were not achieved 100% of the time. The single phase of perovskite of the calcined samples at higher temperatures than 1300 ^{o}C is formed.

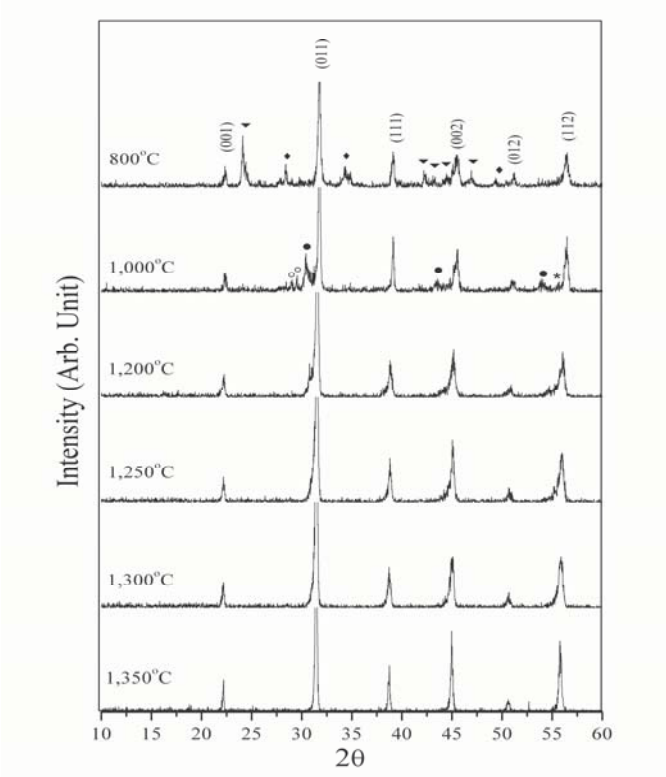

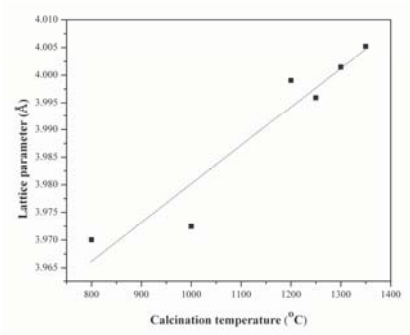

SEM photographs of BZT powders calcined at 1000 and 1300 ^{o}C are shown in Fig. 5. These powders exhibited an almost spherical morphology and have a porous agglomerated form. As the temperatures increased, more agglomerate particles could be observed. The average particle size tended to increase as calcination temperatures increased. The average particle size was 0.2, 0.3, 0.6, 0.8, 0.9 and 1.1 μm for the powders calcined at 800, 1000, 1200, 1250, 1300 and 1350 ^{o}C, respectively.

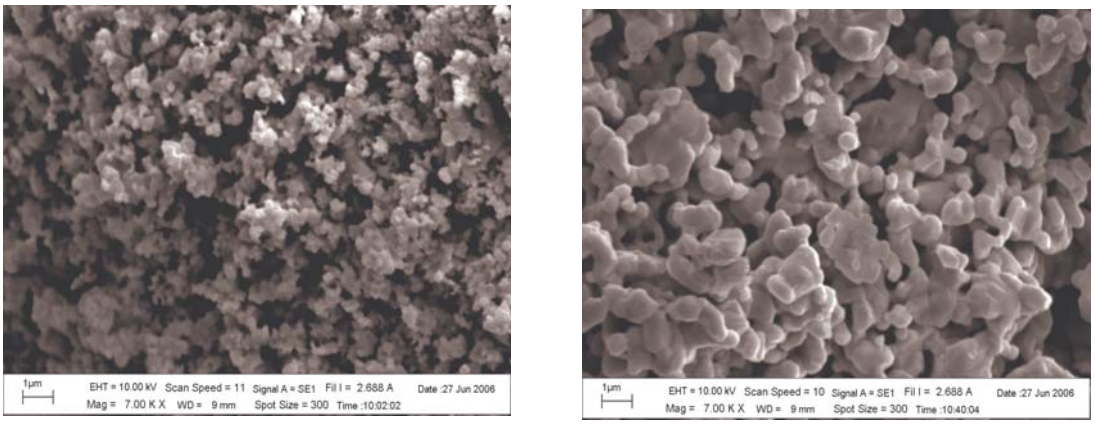

(a) (b)

Figure 5. SEM photomicrographs of BZT powders calcined at (a) 1000 ^{o}C and (b) 1300 ^{o}C.

Summary

It has been shown that the pure perovskite phase of $Ba(Ti_{0.75}Zr_{0.25})O_3$ powders can be formed through the reaction of barium carbonate, titanium (IV) oxide and zirconium (IV) oxide with calcined temperatures at 1300 ^{o}C. Evidence of the formations of minor phases of $BaZrO_3$, $BaTiO_3$ and Ba_2ZrO_4, which coexists with the perovskite phase, is found at calcinations temperatures ranging from 1000-1250 ^{o}C. The calcination temperatures have a strong influence on the crystal structure, homogeneity and the unit cell volume of the calcined powders. The resulting microstructure of the BZT powders were more agglomerated as the calcination temperatures increased.

Acknowledgments

This work was supported financially by the Thailand Research Fund (TRF), Commission on Higher Education (CHE), and Naresuan University. Thanks also to the Uttaradit Rajabphat University and King Mongkut's Institute of technology, Ladkrabang (KMITL) for supporting facilities. Acknowledgement is also given to Mr. Don Hindle, for his helpful comments and correction of the manuscript.

References

[1] W.S. Clabaugh, R. Swiggard and R.Gilchrist: J. Res. Nat. Bur. Stds. Vol. 56 (1956), p. 289.
[2] Y. Sakabe, K. Minai and K.Wakino: Jpn. J. Appl. Phys. Suppl. Vol. 20 (1981), p.147.
[3] B. Jaffe, J. Cook and H. Jaffe: *Piezoelectric Ceramics* (Academic Press, London, U.K., 1997).
[4] E. J. Brajer: U.S. Patent 2, 708, 243. (1955).
[5] F. Kulscar: U.S. Patent 2, 735, 024. (1956).
[6] W. Ulrich, G. Georg B. Ulrich, W. Sophie, H. Detlev and W. Rainer: J. Am. Ceram. Soc. Vol. 84 (2001), p. 759.
[7] D. Hennings, A. Schnell and G. Simon: J. Am. Ceram. Soc. Vol. 65 (1982), p. 539.
[8] X.G. Tang, K.H. Chew and H.L.W. Chan: Acta Mater. Vol. 52 (2004) , p. 5177.
[9] R. Liang, X. Dong, Y. Chen, F. Cao and Y. Wang: Ceram. Int. Vol. 33 (2007), p. 957.
[10] A. S. Seveyrat, A. Hajjaji, Y. Emziane, B. Guiffard and D. Guyomar: Ceram. Int. Vol 35 (2007), p. 35.

J Mater Sci (2008) 43:4220–4225
DOI 10.1007/s10853-008-2610-5

Dielectric properties of $Pb[(1-x)(Zr_{1/2}Ti_{1/2})-x(Zn_{1/3}Ta_{2/3})]O_3$ ceramics prepared by columbite and wolframite methods

Wanwimon Banlue · Naratip Vittayakorn · Chien-Chih Huang · David P. Cann

Received: 15 January 2008 / Accepted: 24 March 2008 / Published online: 9 April 2008

Abstract Polycrystalline samples of $Pb[(1-x)(Zr_{1/2}Ti_{1/2})-x(Zn_{1/3}Ta_{2/3})]O_3$, where $x = 0.1$–0.5 were prepared by the columbite and wolframite methods. The crystal structure, microstructure, and dielectric properties of the sintered ceramics were investigated as a function of composition via X-ray diffraction (XRD), scanning electron microscopy (SEM), and dielectric spectroscopy. The results indicated that the presence of $Pb(Zn_{1/3}Ta_{2/3})O_3$ (PZnTa) in the solid solution decreased the structural stability of overall perovskite phase. A transition from tetragonal to pseudo-cubic symmetry was observed as the PZnTa content increased and a co-existence of tetragonal and pseudo-cubic phases was observed at a composition close to $x = 0.1$. Examination of the dielectric spectra indicated that PZT–PZnTa exhibited an extremely high relative permittivity at the MPB composition. The permittivity showed a ferroelectric to paraelectric phase transition at 330 °C with a maximum value of 19,600 at 100 Hz at the MPB composition.

Introduction

Lead zirconate titanate $Pb(Zr_{1-x}Ti_x)O_3$ perovskite solid solutions (PZT) are normal ferroelectric ceramic materials with many important practical applications including piezoelectric devices, ferroelectric memories, high ε capacitors, and infrared pyroelectric detectors, by utilizing their excellent piezoelectric, ferroelectric, and pyroelectric properties [1, 2]. The anomalous piezoelectric properties of PZT ceramics near the morphotropic phase boundary (MPB) separating two ferroelectric phases, namely, rhombohedral and tetragonal phases at low and high Ti contents, respectively [3]. Recently, the new free energy formulation automatically predicts equilibrium PZT phase diagram with two-phase region replacing the linear MPB and satisfying the Gibbs phase rule [4]. Identifying the MPB in the phase equilibria in ferroelectric systems is very important in order to obtain the optimum electrical properties. Therefore, most commercial ferroelectric ceramics are designed in the vicinity of the MPB with various doping schemes in order to take advantage of the superior dielectric and piezoelectric properties [5, 6].

Recently, many piezoelectric ceramic materials have been developed from binary systems containing a combination of normal ferroelectrics with tetragonal symmetry and relaxor ferroelectrics with rhombohedral symmetry near the MPB. These systems can yield high dielectric permittivities such as in PMN–PT [7] and PZN–PT [8], excellent piezoelectric coefficients such as in PZN–PZT [9] and PSN–PT [10], and high pyroeletric coefficients such as in PNN–PT–PZ [11]. The low phase-transition temperature of some members of the lead-based tantalate family $Pb(B_{1-x}Ta_x)O_3$, in which B is Zn^{2+}, Mg^{2+} and Ni^{2+}, make them important candidates for utilization in devices such as low-temperature capacitors and actuators for space applications [12]. Lead zinc tantalate $Pb(Zn_{1/3}Ta_{2/3})O_3$ solid solutions (PZnTa) possess the perovskite structure and exhibit relaxor ferroelectric behavior. Nevertheless, synthesis of perovskite lead zinc tantalate $Pb(Zn_{1/3}Ta_{2/3})O_3$

W. Banlue · N. Vittayakorn (✉)
Materials Science Research Unit, Department of Chemistry, Faculty of Science, King Mongkut's Institute of Technology Ladkrabang, Bangkok 10520, Thailand
e-mail: naratipcmu@yahoo.com

C.-C. Huang · D. P. Cann
Materials Science, School of Mechanical, Industrial, and Manufacturing Engineering, Oregon State University, Corvallis, OR 97331, USA

(PZnTa) has been unsuccessful until now [13]. It is well-known that during the phase-formation process of lead-based perovskite materials a pyrochlore-type phase ($A_2B_2O_{7-\delta}$) with low dielectric permittivity precedes the formation of the perovskite phase. The failure can be attributed to the higher covalency of Zn^{2+} and Ta^{5+} as well as to the somewhat larger ionic size of Zn^{2+} as compared to the sixfold lattice sites formed by the oxygen octrahedra. A columbite–wolframite process was then introduced to promote the development of the perovskite phase and to suppress the formation of the pyrochlore phase [13–15].

Since both PZT and PZnTa have the perovskite structure, it is suggested that PZnTa can be alloyed with PZT in order to stabilize and optimize the PZnTa ceramics. Recently our previous work [9, 16] has shown promise in producing phase-pure perovskite solid solutions based on $Pb(Zr_{1/2}Ti_{1/2})O_3$–$Pb(Zn_{1/3}Nb_{2/3})O_3$ (PZT–PZN) via the columbite method. The binary system of $(1 - x)$PZT $- x$PZN exhibited two MPBs at the compositions $x = 0.5$ and $x \sim 0.2$–0.3. The maximum value of d_{33} (>600 pC/N) and the highest k_p ($\sim$0.7) were recorded for the composition $x = 0.3$. In addition, Nb and Ta belong to the same group in the periodic table and the have the same ionic radii. It is expected that excellent properties can be obtained from ceramics in PZT–PZnTa system. So far, there have been no systematic studies on the structural and dielectric properties over the entire range of PZT–PZnTa solid solutions. In the present study, PZT and PZnTa were chosen as end components to prepare solid solutions via a columbite–wolframite precursor method. Crystal structure and microstructure were investigated by XRD and SEM analysis, respectively. Finally, the dielectric properties of PZT–PZnTa ceramics were determined as a function of temperature and frequency to establish structure–property relationships.

Experimental

The perovskite-phase powders were synthesized using a columbite–wolframite precursor method in order to avoid the formation of a pyrochlore phase. Powders of ZnO (99.9%), Ta_2O_5 (99.9%), PbO (Fluka, >99% purity), TiO_2 (99.8%), and ZrO_2 (99%) were used as the starting materials. The following reaction sequences are proposed for the formation of PZT–PZnTa:

$$ZnO_{(s)} + Ta_2O_{5(s)} \rightarrow ZnTa_2O_{6(s)} \quad (1)$$

$$ZrO_{2(s)} + TiO_{2(s)} \rightarrow ZrTiO_{4(s)} \quad (2)$$

$$PbO_{(s)} + (1-x)/2\ ZrTiO_{4(s)} + x/3\ ZnTa_2O_{6(s)} \rightarrow Pb\left[(1-x)\left(Zr_{1/2}Ti_{1/2}\right) - x\left(Zn_{1/3}Ta_{2/3}\right)\right]O_{3(s)} \quad (3)$$

The columbite precursor $ZnTa_2O_6$ was prepared from the reaction between ZnO and Ta_2O_5 at 1,100 °C for 4 h and then ZrO_2 was reacted with TiO_2 at 1,400 °C for 4 h to form $ZrTiO_4$. The precursors $ZnTa_2O_6$, $ZrTiO_4$ and PbO (with 2 mol% excess PbO) were weighed according to the compositions of $Pb[(1 - x)(Zr_{1/2}Ti_{1/2}) - x(Zn_{1/3}Ta_{2/3})]O_3$ with $x = 0.1$–0.5. Each mixture of the starting powders was milled and mixed in a ball mill, as well as wet-homogenized with ethanol using nylon-coated YTZ zirconia milling as media for 18 h. After drying, the mixtures were calcined at 700–950 °C for 4 h in an alumina crucible and configured with a heating rate of 20 °C/min. The calcined powders were milled for 3 h in order to reduce the particle size. After grinding and sieving, the calcined powders were mixed with 5 wt% polyvinyl alcohol binder and uniaxially pressed into pellets. Binder burnout occurred by slowly heating to 500 °C and holding for 2 h. Sintering occurred between 1,100 and 1,250 °C with a dwell time of 4 h. To mitigate the effects of lead loss during sintering, the pellets were sintered in a closed alumina crucible containing $PbZrO_3$ powder. PZT–PZnTa ceramics were subsequently examined by room temperature X-ray diffraction (XRD; Philips PW 1729 diffractometer), using Ni-filtered CuK_α radiation to identify the perovskite structure. The relative amounts of perovskite and pyrochlore phase were then determined by measuring the primary X-ray peak intensities of the perovskite and pyrochlore phase. The density of the sintered PZT–PZnTa pellets was measured by the water immersion method (Archimedes method). The relative density of all the sintered pellets in this study was approximately 94–96% of the theoretical density. To determine the dielectric properties, the maximum density sample for each composition samples was ground on both surfaces and silver electrodes were applied using a low-temperature silver paste by firing at 500 °C for 30 min. The capacitance was measured with a HP4284A LCR meter in connection with a sample holder (Norwegian Electroceramics) capable of high temperature measurement. The relative permittivity (ε_r) was calculated using the geometric area and thickness of the discs.

Result and discussion

The XRD patterns of $(1 - x)$PZT $- x$PZnTa ceramics with various x values are shown in Fig. 1. The patterns show a single-phase perovskite for the compositions $x = 0.1$ and 0.2. A cubic pyrochlore phase $Pb_{1.83}(Zn_{0.29}Ta_{1.71})O_{6.39}$ (Powder diffraction Files No. 34-395), identified with "*", began to develop at $x = 0.3$ and increased in intensity with increasing PZnTa concentration. No evidence of a cubic phase of $Pb_{1.49}Ta_2O_{6.28}$ (Powder diffraction Files No. 84-1732) was found. These results indicate that the presence of PZnTa in the solid solution decreased the structural stability of the PZT perovskite phase due to its tolerance factor and electronegativity [13]. It is interesting to note that the pure

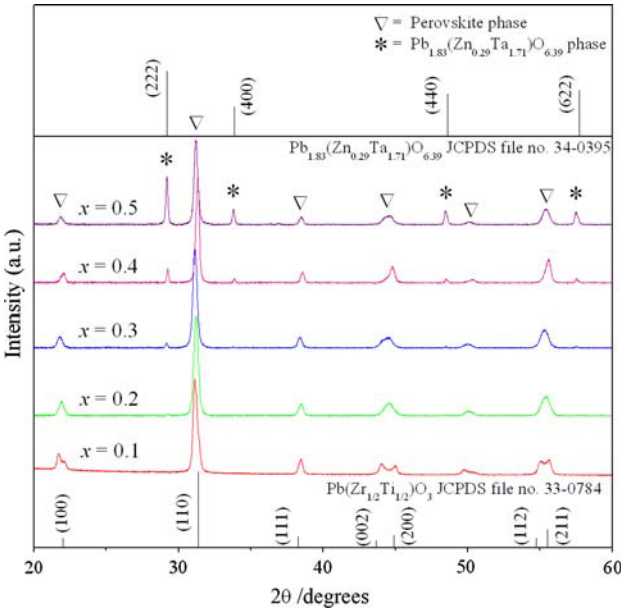

Fig. 1 XRD patterns of $(1 - x)$PZT $- x$PZnTa ceramics prepared by columbite–wolframite method as a function of composition

perovskite phase in $(1 - x)$PZT $- x$PZnTa can only be obtained for $x \leq 0.2$. This is a significant contrast to the $(1 - x)$PZT $- x$Pb$(Zn_{1/3}Nb_{2/3})O_3$ system in which the perovskite phase can be obtained up to $x \leq 0.5$. The results indicate that it is more difficult to obtain a pure perovskite phase in tantalate systems than in niobates.

Although Nb and Ta belong to the same periodic group, Ta^{5+} has stronger covalent properties [17]. It is well known that an increase in covalent bond strength decreases the thermodynamic stability of the perovskite structure [13]. This is likely the main reason it is difficult to obtain the perovskite phase in the tantalate system. Studies on the stabilization of the perovskite phase in solid solutions of PZN and PZnTa with BT, PMN and PMT also showed an easier stabilization of the perovskite structure in PZN, due to the higher ionic strength of Nb–O bonds [18].

SEM micrographs of a fractured surface of PZT–PZnTa ceramics are shown in Fig. 2a and b, respectively. The micrograph of 0.9PZT–0.1PZnTa (Fig. 2a) shows a highly homogeneous microstructure. These micrographs indicate that average grain size was in the range of 1.27 μm, and the fracture occurred mostly by intergranular mechanisms. The 0.5PZT–0.5PZnTa ceramic showed a very heterogeneous microstructure (Fig. 2b) with a large amount of pyrochlore phase, as XRD patterns also indicated.

The $PbZrO_3$–$PbTiO_3$ phase diagram predicts that at room temperature $Pb(Zr_{1/2}Ti_{1/2})O_3$ falls within the tetragonal phase field near the MPB. The crystal symmetry for PZnTa-based perovskite is cubic at room temperature. Below the phase transition temperature the symmetry changes to rhombohedral. Since PZnTa has a low phase

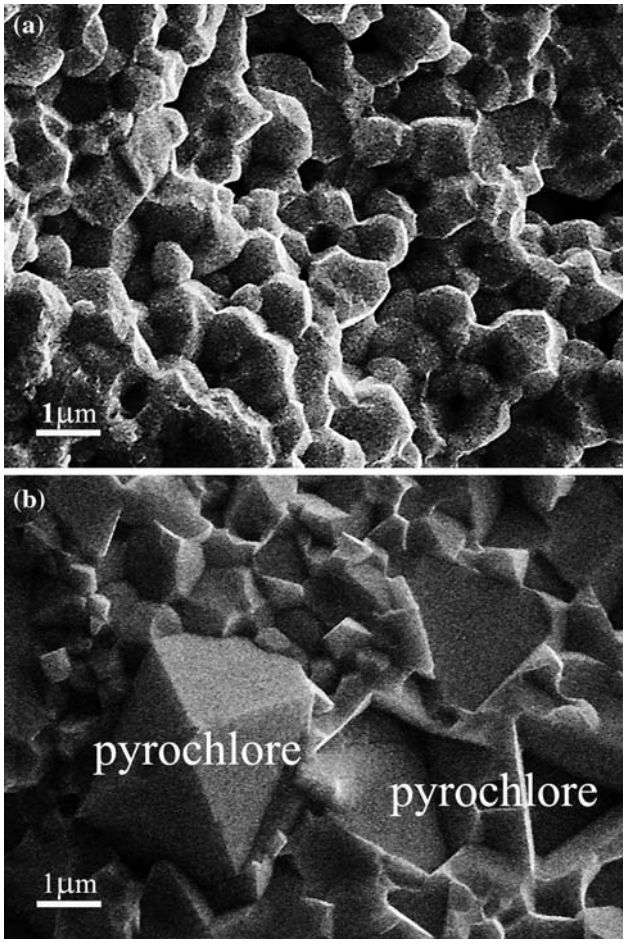

Fig. 2 SEM images of the grain morphology in $(1 - x)$PZT $- x$PZnTa ceramics for (**a**) $x = 0.1$ and (**b**) $x = 0.5$

transition temperature, with increasing x the crystal symmetry should change due to the decrease in phase transition temperature. It is well known that in the pseudo-cubic phase the {2 0 0} profile will show a single narrow peak because all the planes of {2 0 0} share the same lattice parameters, while in the tetragonal phase the {2 0 0} profile should be split into two peaks with the intensity height of the former being half of the latter because the lattice parameters of (2 0 0) and (0 2 0) are the same but are slightly different from those of (0 0 2).

Figure 3 shows the evolution of the (2 0 0) peak as a function of composition. At low PZnTa concentrations, the XRD pattern shows strong (200) peak splitting which is indicative of tetragonal symmetry. As the PZnTa concentration increased, the (2 0 0) reflection transformed to a single peak which suggests pseudo-cubic symmetry. To a first approximation, it could be said that the composition with $x = 0.1$ is close to the MPB, where the structure of the PZT–PZnTa compositions gradually shifts from tetragonal to pseudo-cubic symmetry as the PZnTa content increased. Dielectric data described later further supports this

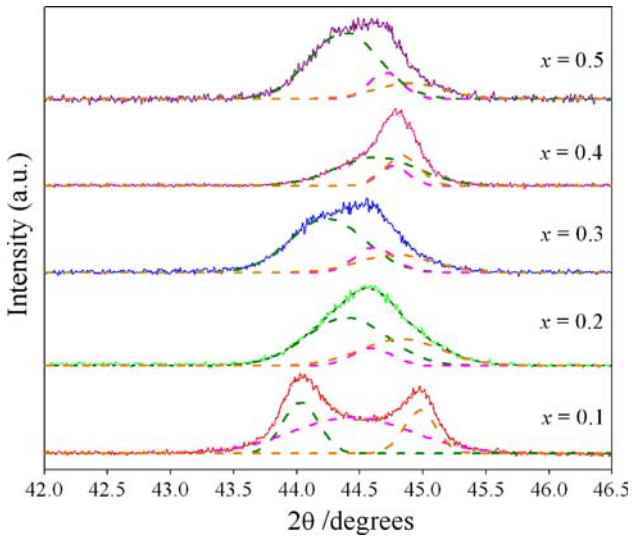

Fig. 3 XRD pattern of the (200) peak of $(1 - x)$PZT $- x$PZnTa ceramics, for $x = 0.0$–0.5

assumption. It is interesting to note that the influence of the addition of PZnTa on the phase transition of $Pb(Zr_{1/2}Ti_{1/2})O_3$ is similar to that of the $Pb(Zr_{1/2}Ti_{1/2})O_3$–$Pb(Ni_{1/3}Nb_{2/3})O_3$, $Pb(Zr_{1/2}Ti_{1/2})O_3$–$Pb(Co_{1/3}Nb_{2/3})O_3$, and $Pb(Zr_{1/2}Ti_{1/2})O_3$–$Pb(Zn_{1/3}Nb_{2/3})O_3$ systems [9, 19–21].

The characteristic temperature dependence of the dielectric constant at 100 Hz for $(1 - x)$PZT $- x$PZnTa, where $x = 0.1$–0.5, is shown in Fig. 4. The transition temperatures and maximum dielectric constants of the 0.9PZT–0.1PZnTa ceramics in this work were 330 °C and 19,600, respectively. The frequency dependence of dielectric properties for $x = 0.1$ and 0.5 ceramics are shown in Fig. 5a and b. For 0.9PZT–0.1PZnTa (Fig. 5a), the dielectric constants peak is sharp and approaches19,600. The dielectric properties of 0.9PZT–0.1PZnTa ceramic change significantly with

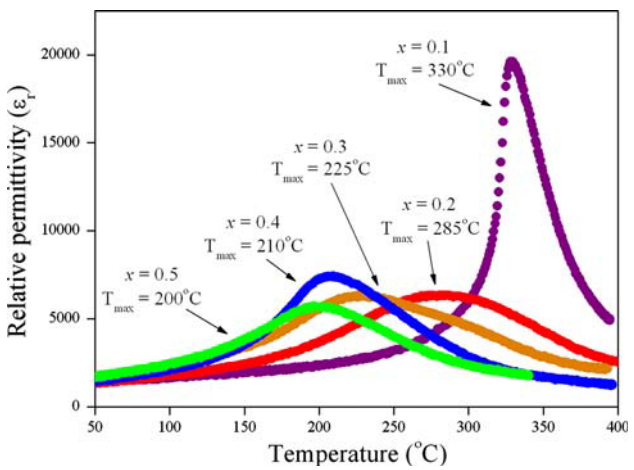

Fig. 4 Variation of the dielectric constant with temperature for $(1 - x)$ PZT $- x$PZnTa ceramics at 100 Hz

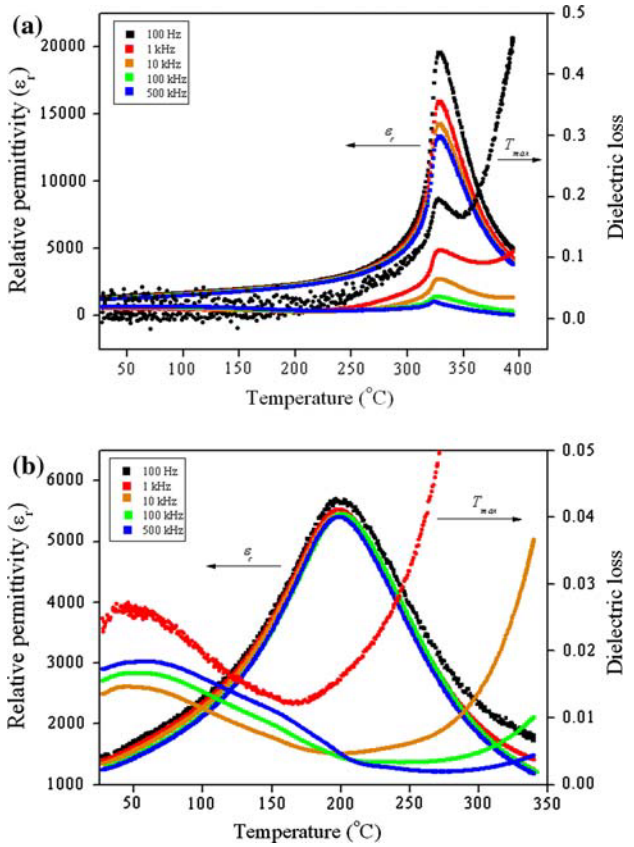

Fig. 5 Temperature and frequency dependence of the dielectric properties for: (**a**) $x = 0.1$ and (**b**) $x = 0.5$ ceramics

temperature, but are nearly independent of frequency, except in the vicinity of the phase transformation temperature [22, 23]. This is a typical characteristic of ferroelectric ceramics with a long-range ordered structure. It is well known that PZT exhibits normal ferroelectric behavior and PZnTa is a relaxor ferroelectric material as a result of a short-range ordered structure with a nanometer scale compositional heterogeneity [24]. The nature of the homogeneously polarized states is believed to be primarily controlled by the concentration of PZnTa. When PZnTa is added to form the binary system with PZT, a clear shift of the transition temperature to lower temperatures was observed. Furthermore, the dielectric peak broadened indicating an increase in the diffuseness of the phase transition. It should also be noted here that, in all compositions, the dielectric properties increased significantly at high temperatures as a result of thermally activated space charge conduction. The variation in the transition temperature with composition and other dielectric data is listed in Table 1. The Curie temperature significantly decreased with increasing PZnTa content up to 30 mol%. However, for the compositions $0.3 \leq x \leq 0.5$, transition temperature remained at a nearly constant value between 200 and 225 °C. This is consistent with the X-ray

diffration findings that indicated the co-existence of a pyrochlore phase for these compositions.

A modified Curie–Weiss law can be used to model the dielectric behavior of a normal ferroelectric in solid solution with a relaxor ferroelectric with a diffuse phase transition. The formulation is as follows:

$$\frac{\varepsilon'_{\mathrm{m}}}{\varepsilon'(f,\ T)} = 1 + \frac{(T - T_{\mathrm{m}}(f))^{\gamma}}{2\delta_{\gamma}^{2}} \tag{4}$$

where $1 \leq \gamma \leq 2$. When $\gamma = 1$, Eq. 4 simplifies to the Curie–Weiss law; when $\gamma = 2$ this equation describes the ideal relaxor behavior with a quadratic dependence. The

Table 1 Dielectric properties of $(1 - x)$PZT $- x$PZnTa ceramics at 100 Hz

PZTa content (x)	ε_r at room temp.	tan δ at room temp.	$T_{\max}$ (°C)	ε_r at $T_{\max}$	tan δ at $T_{\max}$	δ_γ (°C)	γ
0.1	1,430	0.0102	330	19,600	0.193	13.51	1.74
0.2	1,280	0.0429	285	6,310	0.081	22.36	1.98
0.3	1,500	0.0282	225	6,290	0.066	21.11	1.89
0.4	1,340	0.0289	210	7,410	0.072	12.57	1.80
0.5	1,520	0.0163	200	5,690	0.039	11.87	1.72

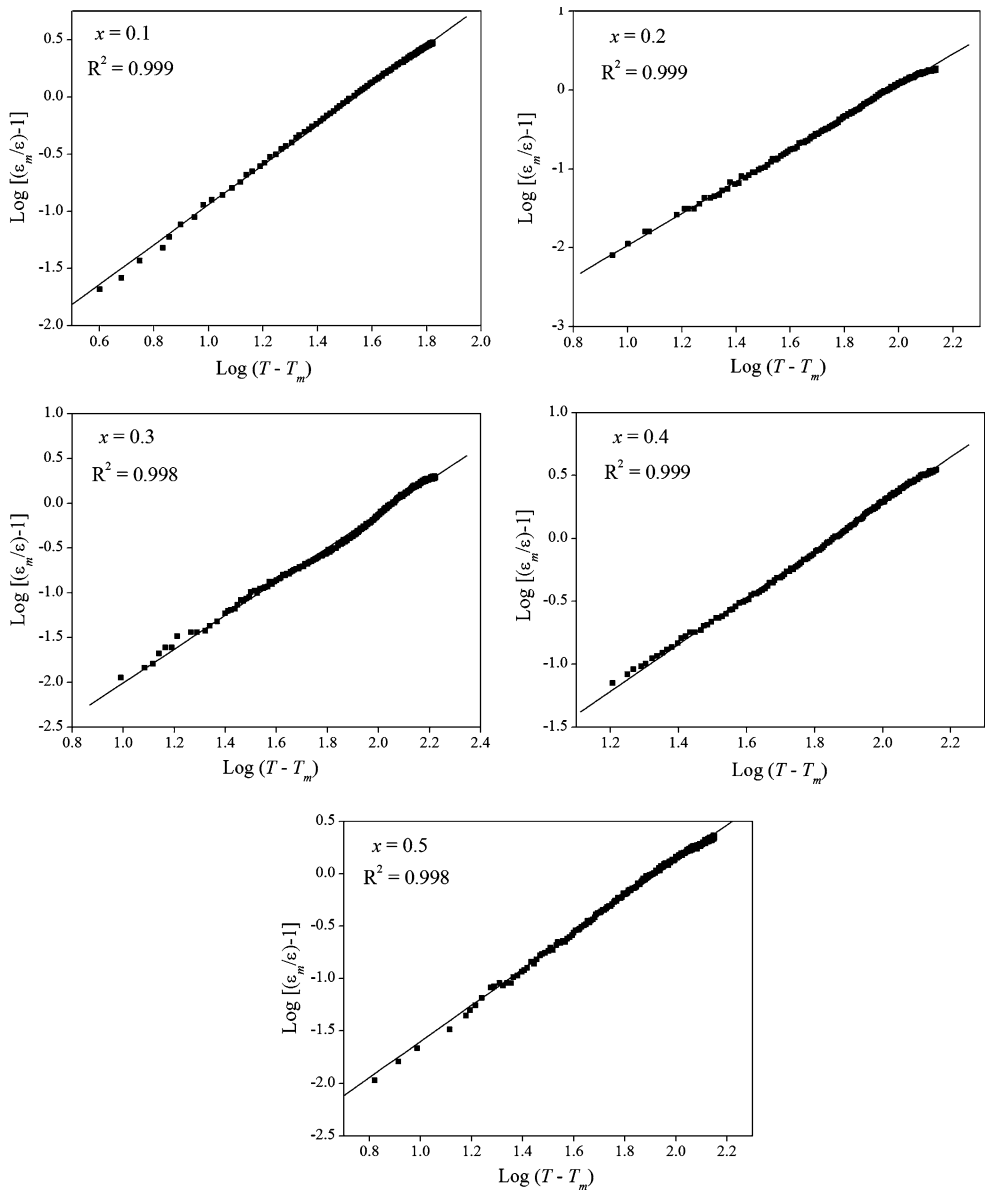

Fig. 6 Plots of $\log[(\varepsilon_{\mathrm{m}}/\varepsilon) - 1)]$ vs. $\log(T - T_{\mathrm{m}})$ for $(1 - x)$ PZT $- x$PZnTa ceramics. The solid lines are fits to Eq. 5. γ, δ and R^2 indicate fitting parameters (γ and δ) and correlation of the fit (R^2)

parameter ε'_m is the maximum value of the relative permitivity at $T = T_m$ (f) and $\varepsilon'(f, T)$ is the relative permittivity of the sample. If $\log[\varepsilon'_m/\varepsilon'(f, T) - 1]$ is plotted versus $\log[T - T_m(f)]$, the values of γ and δ_γ can be determined as seen in Fig. 6. The parameter γ was determined to be in the range of 1.72–1.98 and the diffuseness parameter δ_γ was measured to be 11.87–22.36, which confirms the diffuse phase transitions in PZT–PZnTa due to a high degree of disorder. The calculations suggest that the addition of PZnTa into PZT leads to lower degree of disorder but can be attributed to the pyrochlore phase present in high PZnTa-content compositions.

Conclusions

Ceramic solid solutions based on $(1 - x)$ $Pb(Zr_{1/2}Ti_{1/2})O_3 - (x)Pb(Zn_{1/3}Ta_{2/3})O_3$ (where $x = 0.1$, 0.2, 0.3, 0.4, and 0.5) were prepared via a columbite–wolframite method. The PZT–PZnTa solid solutions exhibit a single-phase perovskite structure for $x \leq 0.2$. As the content of PZnTa increases (i.e., $x \geq 0.3$), a secondary pyrochlore phase $Pb_{1.83}(Zn_{0.29}Ta_{1.71})O_{6.39}$ was formed. The results indicate that it is more difficult to obtain pure perovskite in tantalate solid solutions than it is in niobates solid solutions. The dielectric response of 0.9PZT–0.1PZnTa is closer to normal ferroelectric behavior, while the other compositions exhibit a diffuse phase transition. Investigations of the structure and properties of the PZT–PZnTa system over the range $x = 0.1$–0.5 have revealed an MPB at $x = 0.1$, separating a tetragonal phase from a pseudo-cubic phase. Examination of the dielectric spectra indicates that PZT–PZnTa exhibits a high relative permittivity at the MPB composition. The permittivity shows a ferroelectric to paraelectric phase transition at 330 °C with a maximum value of 19,600 at 100 Hz at the MPB composition.

Acknowledgements This work was supported by the Thailand Research Fund (TRF), the Commission on Higher Education (CHE), the National Research Council of Thailand (NRCT), and the King Mongkut's Institute of Technology Ladkrabang (KMITL).

References

1. Uchino K (2000) Ferroelectric devices. Marcel Dekker, Inc., New York
2. Bhalla AS, Guo R, Roy R (2000) Mat Res Innovat 4:3. doi: 10.1007/s100190000062
3. Jaffe B, Cook WR (1971) Piezoelectric ceramic. R.A.N. Publishers
4. George A Rossetti J, Zhang W, Khachaturyan AG (2006) Appl Phys Lett 88:072912. doi:10.1063/1.2173721
5. Haertling GH (1999) J Am Ceram Soc 82:797
6. Xu Y (1991) Ferroelectric materials and their application. Elsevier Science Publishers B.V
7. Seung-Eek P, Shrout TR (1997) IEEE Trans Ultrason Ferroelectr Freq Control 44:1140
8. Takenaka T, Muramata K, Fujii T (1992) Ferroelectrics 134:133. doi:10.1080/00150199208015577
9. Vittayakorn N, Puchmark C, Rujijanagul G, Tan X, Cann DP (2006) Curr Appl Phys 6:303
10. Bing Y-H, Ye Z-G (2006) J Cryst Growth 287:326. The 16th American Conference on Crystal Growth and Epitaxy – ACCGE 16
11. Cornejo IA, Jadidian B, Akdogan EK, Safari A (1998) Dielectric and Electromechanical properties of PNN–PT–PZ system: a processing-property study. In: Proc IEEE ISAF'98
12. Kuwata J, Uchino K, Nomura S (1982) Jpn J Appl Phys 21:1298
13. Shrout TR, Halliyal A (1987) Am Ceram Soc Bull 66:704
14. Vittayakorn N, Wirunchit S (2007) Smart Mater Struct 16:851
15. Vittayakorn N, Rujijanagul G, Tunkasiri T, Tan X, Cann DP (2003) J Mater Res 18:2882
16. Vittayakorn N, Rujijanagul G, Tunkasiri T, Tan X, Cann DP (2004) Mater Sci Eng B 108:258
17. Ahn B-Y, Kim N-K (2002) J Mater Sci 37:4697
18. Kim J-S, Kim N-K (2003) J Am Ceram Soc 86:929
19. Vittayakorn N, Rujijanagul G, Tan X, He H, Marquardt MA, Cann DP (2006) J Electroceram 16:141
20. Vittayakorn N, Rujijanagul G, Tan X, Marquardt MA, Cann DP (2004) J Appl Phys 96:5103
21. Vittayakorn N, Tunkasiri T (2007) Phys Scr T129:199
22. Koval V, Alemany C, Brianin J, Brunckovа H (2004) J Electroceram 10:19
23. Yimnirun R, Ananta S, Laoratanakul P (2005) J Eur Ceram Soc 25:3235
24. Randall CA, Bhalla AS, Shrout TR, Cross LE (1990) Ferroelectrics 11:103

J. Phys. D: Appl. Phys. **41** (2008) 125406 (7pp) doi:10.1088/0022-3727/41/12/125406

Physical properties and phase transitions in perovskite $Pb[Zr_{1-x}(Ni_{1/3}Nb_{2/3})_x]O_3$ ($0.0 \leqslant x \leqslant 0.5$) ceramics

Supamas Wirunchit[1], **Pitak Laoratanakul**[2] **and Naratip Vittayakorn**[1,3]

[1] Material Science Research Unit, Department of Chemistry, Faculty of Science, King Mongkut's Institute of Technology Ladkrabang, Bangkok 10520, Thailand
[2] National Metal and Materials Technology Center (MTEC), Pathumthani 12120, Thailand

E-mail: naratipcmu@yahoo.com

Received 5 February 2008, in final form 30 March 2008
Published 23 May 2008
Online at stacks.iop.org/JPhysD/41/125406

Abstract
A solid solution of lead zirconate–lead nickel niobate ceramics, $Pb[Zr_{1-x}(Ni_{1/3}Nb_{2/3})_x]O_3$ (PZNN) with $x = 0.0$–0.5, was synthesized via the columbite precursor method. The crystal structures as well as the thermal and dielectric properties were investigated in terms of the lead nickel niobate (PNN) concentration. X-ray diffraction indicated that all samples exhibited a single-phase perovskite structure. At room temperature, $Pb[Zr_{1-x}(Ni_{1/3}Nb_{2/3})_x]O_3$ is orthorhombic for a composition where $x = 0$, rhombohedral for the compositions where $x = 0.1$, 0.2 and 0.3 and pseudo-cubic for compositions where $x = 0.4$ and 0.5. The results of the addition of lead nickel niobate to the lead zirconate ceramic showed enhancement of the room-temperature dielectric permittivity. Lead nickel niobate substitution also led to lower transition temperatures. Furthermore, this transition from normal to relaxor FE ceramics was typified by a quasi-linear relationship between the diffuseness parameter δ_γ and the PNN mole fraction x.

(Some figures in this article are in colour only in the electronic version)

1. Introduction

Since the discovery of antiferroelectricity in the perovskite structure in the 1950s, lead zirconate oxide ($PbZrO_3$ or PZ) has been the focus of extensive experimental and theoretical studies [1]. $PbZrO_3$ has a phase transition which occurs at ca 230 °C, but the transition from the orthorhombic antiferroelectric (AFE) structure to the rhombohedral ferroelectric (FE) structure a few degrees below the paraelectric (PE) transition temperature has been reported by several authors [2, 3]. Both AFE-to-FE and FE-to-PC phase transitions are first order and show a thermal hysteresis of around 10 °C [3, 4]. The structure of the $PbZrO_3$ is orthorhombic with $a = 5.87$ Å, $b = 11.74$ Å and $c = 8.20$ Å. Antiparallel shifts of Pb^{2+} ions in the $PbZrO_3$ are responsible for the quadrupling of the pseudo-cubic cell and the AFE behaviour [5, 6]. The characteristic double hysteresis loop resulting from forward phase switching with zero remanent polarization makes AFE material compositions suitable for high charge storage applications [7, 8]. The most intensively studied AFE $PbZrO_3$ is chemically modified by adding Sn, Ti, Nb and Ba or La to adjust the critical field for the phase transition and to optimize properties for processing and applications [3, 4]. $PbZrO_3$ was also studied for its microwave dielectric properties, but it shows a dielectric relaxation near microwave frequencies [9]. The FE relaxor PNN exhibits a broad maximum in the dielectric constant and a diffuse phase transition. Its Curie temperature is about −120 °C, and the maximum dielectric constant is about 3500 at 1 kHz [10].

Recently, many piezoelectric ceramic materials have been developed from binary systems containing combination types of piezoelectric materials which have high piezoelectric and dielectric properties [7, 8]. Much research has been done on solid solutions containing PZ, such as $Pb_{1-x}Ba_xZrO_3$ (PBZ) [4], $Pb(Zr_{1-x},Ti_x)O_3$

[3] Author to whom any correspondence should be addressed.

(PZT) [1], $PbZrO_3$–$PbTiO_3$–$Pb(Mg_{1/3}Nb_{2/3})O_3$ (PZ–PT–PMN) [11, 12], $PbZrO_3$–$PbTiO_3$–$Pb(Zn_{1/3}Nb_{2/3})O_3$ (PZ–PT–PZN) [13–15] and $Pb(Zn_{1/3}Nb_{2/3})O_3$–$PbZrO_3$ (PZN–PZ) [16]. New piezoelectric ceramics for high-frequency ultrasonic transducer applications using modified $PbZrO_3$ ceramic compositions in a $(1-x-y)PbZrO_3 + xPb(Mn_{1/3}Nb_{2/3})O_3 + yPbTiO_3$ system with an FE rhombohedral phase near the AFE orthorhombic phase ($0.0 < x \leqslant 0.1$ and $0.0 < y \leqslant 0.2$) have been reported by Takeuchi *et al* [17]. Changes in the electromechanical properties of ceramics with compositions at the morphotropic phase boundary (MPB) in the rhombohedral phase ($y = 0.05$ and $x = 0.05$ and $y = 0.025$ and $x = 0.1$) were rather sharp, although no noticeable changes could be observed in the lattice parameters. The anisotropy of electromechanical coupling factors (k_t/k_p ratio) was 24 for $x = 0.05$ and $y = 0.00$, which is a boundary composition between the AFE orthorhombic phase and the FE rhombohedral phase. One of the most famous systems is the solid solution of the $PbNi_{1/3}Nb_{2/3}O_3$–$PbTiO_3$–$PbZrO_3$ (PNN–PT–PZ) system which has a MPB at a lead zirconate (PZ) concentration around 0.20–0.45 [18, 19]. At these PZ concentrations the longitudinal electromechanical coupling coefficient (k_{33}) in the compound reaches 0.8 [18]. As a part of a series of investigations on the solid solution with $PbZrO_3$, this study deals with the PZ–PNN binary compound because no detailed report on the structural and dielectric properties of this entire system exists.

In this work, the effect of PNN substitution on the phase transformation behaviour of PZ was investigated. The phase structure, phase transitions and related properties are studied by a differential scanning calorimeter and dielectric measurement. Furthermore, the influence of the PNN content in the system that was studied on the diffuseness of the dielectric peaks is discussed.

2. Experimental

Ceramic powders with a composition of $Pb[Zr_{1-x}(Ni_{1/3}Nb_{2/3})_x]O_3$ with $x = 0.0$–0.5 (hereinafter abbreviated as PZNN) were synthesized using the columbite precursor method in order to avoid the formation of a pyrochlore phase. Commercial oxide powders of PbO, NiO and Nb_2O_5 (99.9% purity, Aldrich Chemicals, USA) and ZrO_2 (99% purity, Aldrich Chemicals, USA) were used as the starting materials. The columbite precursor $NiNb_2O_6$ was prepared from the reaction between NiO and Nb_2O_5 at 1100 °C for 4 h and then the precursor was mixed with PbO and ZrO_2. Each mixture of the starting powders was milled and mixed in a ball mill as well as wet-homogenized with ethanol using nylon-coated YTZ zirconia milling as media for 18 h. The mixture was dried and reacted at 650–900 °C; dwell times of 4 h and heating/cooling rates of 20 °C min^{-1} in a closed alumina crucible were utilized. Calcined powders were subsequently examined by room-temperature x-ray diffraction (XRD; Philips PW 1729 diffractometer) using Ni-filtered Cu K_α radiation to identify the phases formed and the optimum calcination conditions for the formation of PZNN powders. The calcined powders were milled for 3 h to reduce the particle size. After grinding and sieving, the calcined powder was mixed with a 5 wt% polyvinyl alcohol binder and uniaxially pressed into a pellet. Binder burnout occurred by slowly heating the pellets to 500 °C and holding them at that temperature for 2 h. Sintering occurred between 1100 and 1250 °C with a dwell time of 4 h depending on the composition. To mitigate the effects of lead loss during sintering, the pellets were sintered in a closed alumina crucible containing $PbZrO_3$ powder. The density of the sintered PZNN pellets was measured by the Archimedes water immersion method. The relative density of all the sintered pellets was approximately 94–96% of the theoretical density. Lattice parameters of the perovskite phases were determined by Cohen's method in conjunction with the least squares method [20]. Ceramic morphologies were directly imaged using scanning electron microscopy ((SEM) JEOL JSM-840A). To determine the dielectric and FE properties, the maximum density of each composition sample was mapped on their major faces, and silver electrodes were made from a low-temperature silver paste by firing at 500 °C for 30 min to enable electrical measurements to be taken. The relative permittivity (ε_r) and dissipation factor ($\tan\delta$) of stress-free samples were measured using an HP-4284A LCR meter. The capacitance and dissipation factors of the samples were measured at 100 Hz–1 MHz; the temperature varied between 25 and 300 °C, and a heating rate of 2 °C min^{-1} was used during the measurements. The phase transitions were also measured by a differential scanning calorimeter (DSC 2920, TA Instrument) between ambient and 350 °C at a rate of 10 °C min^{-1}.

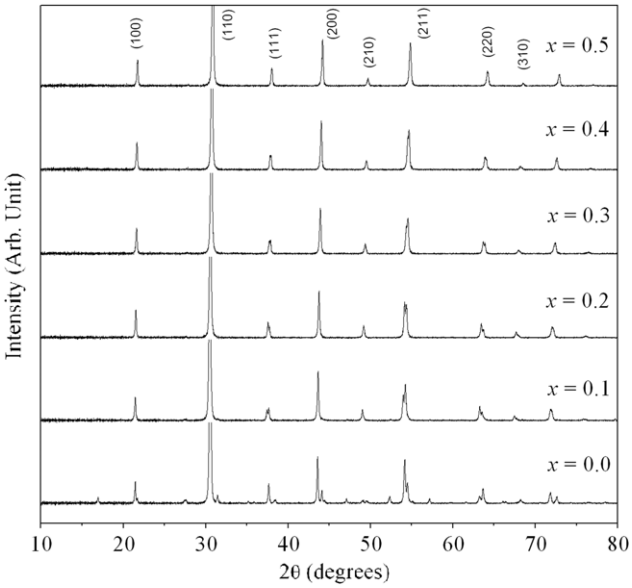

Figure 1. XRD profiles of $Pb[Zr_{1-x}(Ni_{1/3}Nb_{2/3})_x]O_3$; $x = 0.0$–0.5 ceramics at optimum sintering conditions.

3. Results and discussion

3.1. Crystal structure

X-ray diffraction (XRD) was performed on the sintered samples with the composition in the range $x = 0.0$–0.5. As shown in figure 1, all samples exhibited the characteristics

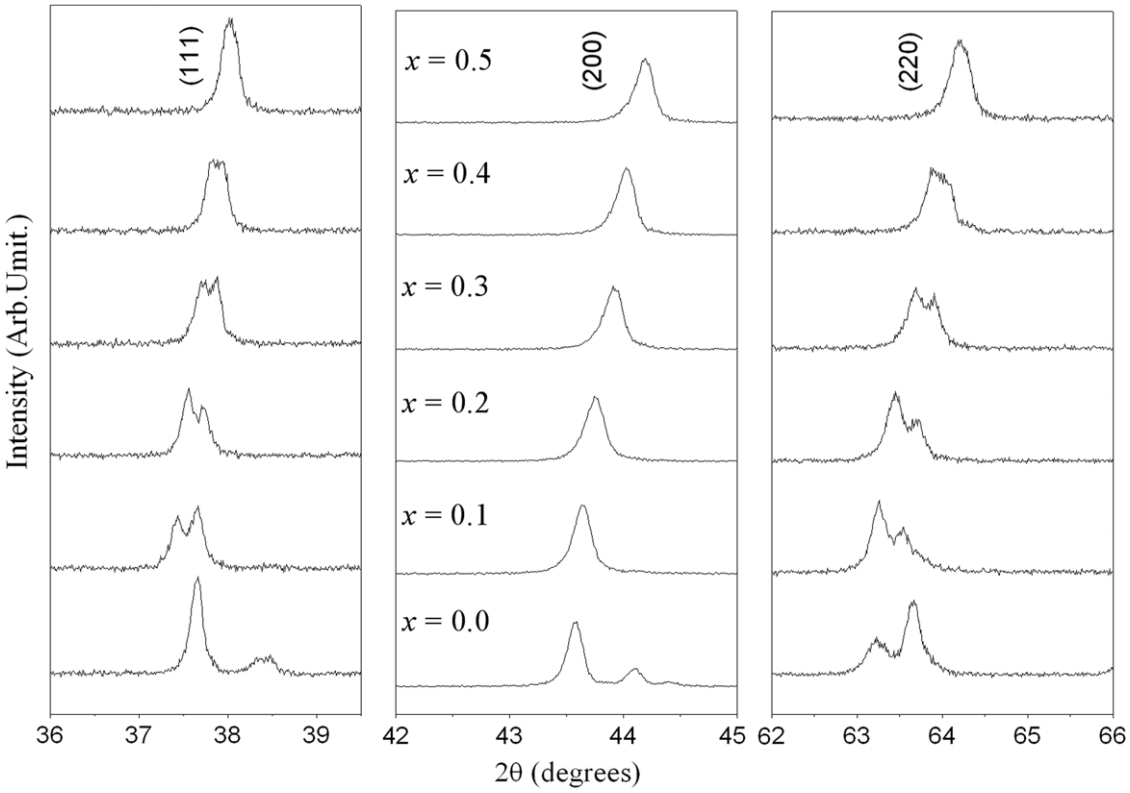

Figure 2. X-ray pattern of the (1 1 1), (2 0 0) and (2 2 0) peaks of $Pb[Zr_{1-x}(Ni_{1/3}Nb_{2/3})_x]O_3$; $x = 0.1$–0.5 ceramics.

of a single-phase perovskite structure. The XRD patterns of the PZNN compositions show a combination of PZ and PNN patterns with the symmetry varying between orthorhombic and pseudo-cubic types. The PNN composition at room temperature was determined to be cubic with the lattice parameter $a = 4.031$ Å, space group $Pm3m$. Superstructure lines along with strong peaks are clearly observed in the composition $x = 0.0$, indicating that this composition belongs to the AFE phase. At room temperature, pure PZ has an orthorhombic perovskite-type structure with lattice parameters $a = 8.231$ Å, $b = 11.77$ Å and $c = 5.881$ Å, space group $P2cb$ (no. 32) [21, 22]. For the composition $x = 0.0$, the 0 0 4, 2 4 0, 1 3 0, 1 1 2 and 1 1 0 peaks are observed, indicating that the major phase in this composition had an orthorhombic symmetry which could be matched with ICDD file no. 75–1607 [23]. However, for $x = 0.1$, 0.2 and 0.3, the enlarged profiles of the diffraction lines 1 1 1, 2 0 0 and 2 2 0 are shown in figure 2. Although a single peak is indicated for 2 0 0, splitting was clearly observed for 1 1 1 and 2 2 0, and therefore the crystal structure is rhombohedral. These results indicate that the phase transition from the orthorhombic to the rhombohedral phase should be located between the composition $x = 0.0$–0.1. The substitution of larger $(Ni_{1/3}Nb_{2/3})^{4+}$ ions with Zr^{4+} sites, implying the transition of the $Pb[Zr_{1-x}(Ni_{1/3}Nb_{2/3})_x]O_3$ structure from orthorhombic to rhombohedral as shown in figure 2, may facilitate parallel displacement along the [1 1 1] direction and the associated displacements of three oxygen ions in the $Pb[Zr_{1-x}(Ni_{1/3}Nb_{2/3})_x]O_3$ structure, resulting in an improvement in the ferroelectricity. The presence of a polar axis in the [1 1 1] direction has been reported for the FE rhombohedral structure [24]. For the composition $x = 0.4$ and 0.5, the XRD data show that splitting of the 2 0 0 and 1 1 1 peaks is not observed. Only a single 2 2 0 peak is visible, indicating that the major phase in these compositions has pseudo-cubic symmetry, reflecting the phenomenon that these compositions have a transition temperature higher than room temperature as shown in the dielectric section. With the peaks properly indexed, a lattice parameter was determined using UnitCell, a linear least squares refinement program. The calculated lattice parameters of the perovskite structures are presented in table 1. In the PZ–PNN system, the A site is occupied by Pb^{2+} (0.1630 nm) ions, and the Ni^{2+}, Nb^{5+} and Zr^{4+} ions occupy the B site of the ABO_3 perovskite crystal structure. The average ionic radius of B site ions in the composition $Pb[Zr_{1-x}(Ni_{1/3}Nb_{2/3})_x]O_3$ can be calculated from the following equation:

$$r_{\text{B site}} = (1-x)[r_{Zr^{4+}}] + x[\tfrac{1}{3}r_{Ni^{2+}} + \tfrac{2}{3}r_{Nb^{5+}}], \qquad (1)$$

where the ionic radii of Ni^{2+}, Nb^{5+} and Zr^{4+} are 0.0830 nm, 0.0780 nm and 0.0860 nm, respectively [25]. In general, the lattice parameters of the perovskite structure also gradually decrease as x increases, undoubtedly because of the introduction of the smaller nickel/niobium ion ($r = 0.79$ Å) into the zirconium site ($r = 0.86$ Å), resulting in a decrease in the unit cell according to the Vegard rule [26]. The influence of the addition of Ni^{2+}/Nb^{5+} ions on the lattice constant of the $Pb[Zr_{1-x}(Ni_{1/3}Nb_{2/3})_x]O_3$ system is similar to that of the $PbZrO_3$–$Pb(Cd_{1/2}W_{1/2})O_3$ and the $PbZrO_3$–$Pb(Mn_{1/2}W_{1/2})O_3$ systems [27].

Table 1. Characteristics of $Pb[Zr_{1-x}(Ni_{1/3}Nb_{2/3})_x]O_3$ ceramics with optimized processing conditions (R, rhombohedral; PC, pseudo-cubic).

x	Crystal structure	Lattice parameter (Å)	T_m (°C) at 100 Hz	Relative permittivity at 25 °C	Relative permittivity at T_{max}	γ	δ_γ
$x = 0.1$	R	4.149 ± 0.0061	200	325	13 000	1.06	7.9
$x = 0.2$	R	4.134 ± 0.0032	175	580	19 400	1.20	14.1
$x = 0.3$	R	4.126 ± 0.0025	155	960	17 200	1.39	16.3
$x = 0.4$	PC	4.110 ± 0.0040	123	1415	16 500	1.57	22.0
$x = 0.5$	PC	4.099 ± 0.0027	80	2635	12 000	1.70	30.3

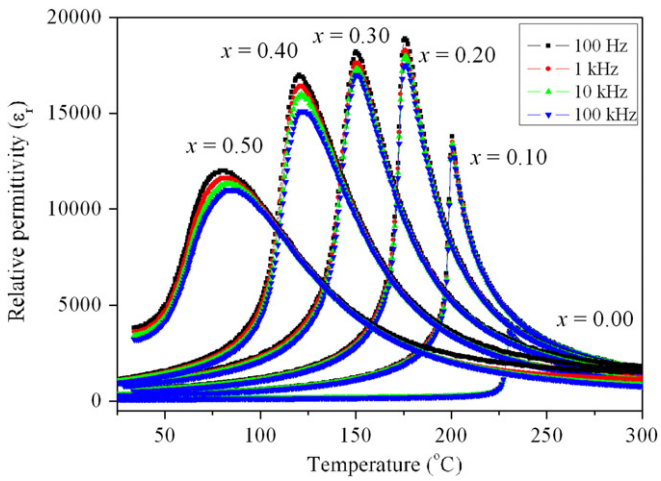

Figure 3. Temperature dependence of the relative permittivity ε_r for $Pb[Zr_{1-x}(Ni_{1/3}Nb_{2/3})_x]O_3$; $x = 0.0$–0.5 ceramics.

3.2. Dielectric and thermal properties

The compositional dependence of the dielectric response characteristics for PZNN ceramics where the normal and relaxor FE behaviour cross over is shown in figure 3 for the compositions $x = 0.0$–0.5 taken at measurement frequencies of 0.1, 1, 10 and 100 kHz. For composition $x = 0.0$, the relative permittivity increased slowly until the temperature approached 230 °C. At 235 °C the relative permittivity increased considerably, passing through a maximum at about 236 °C. With further heating, the relative permittivity decreased in accordance with the Curie–Weiss law, $\varepsilon_r = C/(T - T_o)$, where ε_r is the relative permittivity of a stress-free sample, T is the temperature and C and T_o are constants which, in this study, were 1.04×10^5 and 460.7 K, respectively. With an increase in the PNN concentration to $x = 0.3$, the first-order dielectric features of the spontaneous transformation became increasingly less distinct, whereas the relaxor-like dielectric dispersion became increasingly more pronounced, existing over a broader temperature range near T_{max}. These results clearly show that dielectric response crossovers between the relaxor and the normal states exist over a relatively wide PNN content range between $x = 0.3$ and 0.4. Upon increasing the PNN concentration to $x = 0.5$, the ceramic exhibits a broad maximum of relative permittivity with a strong frequency dispersion which is reminiscent of the relaxor FE behaviour of a PNN crystal. The maximum value of the relative permittivity decreases with increased frequency. The dielectric dispersion below the transition temperature reflects typical relaxor FE behaviour arising from the responses of polar micro-domains with the spectrum of relaxation time [28, 29].

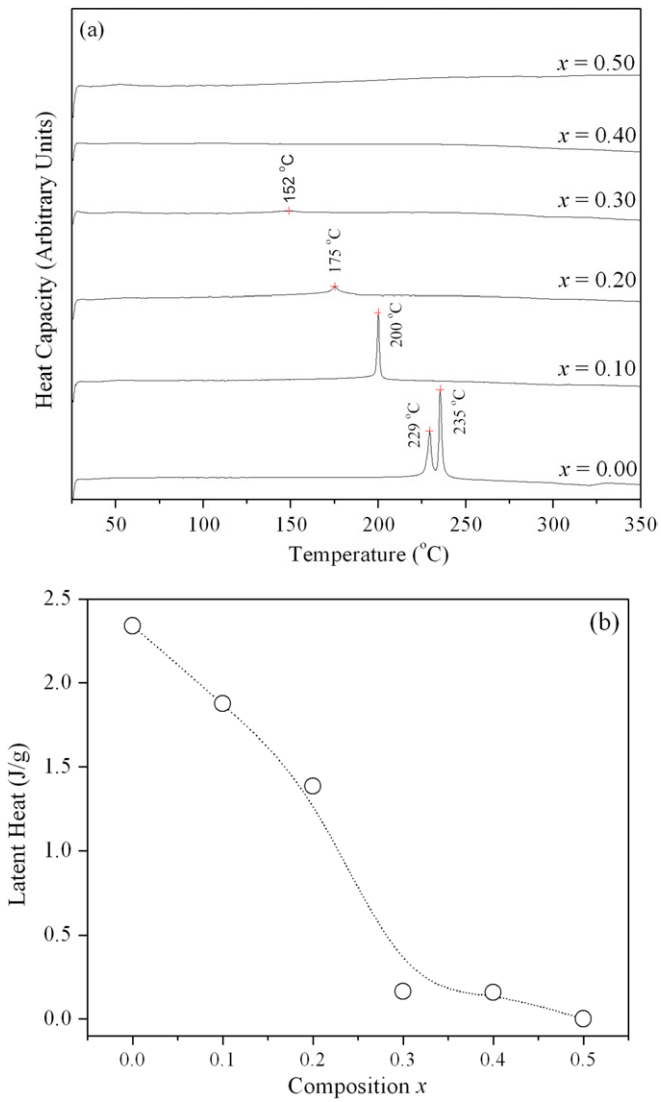

Figure 4. (*a*) Typical DSC curves for $Pb[Zr_{1-x}(Ni_{1/3}Nb_{2/3})_x]O_3$; $x = 0.0$–0.5 ceramics. (*b*) Nonlinear decrease in latent heat with increasing PNN concentration.

From dielectric permittivity–temperature measurements and also differential scanning calorimetry (DSC), we investigated the nature of the FE–PE phase transitions in the PZNN system. The transition temperature was determined from both the latent heat anomaly in the DSC data and the peak of the permittivity–temperature plots. Figures 4(*a*)

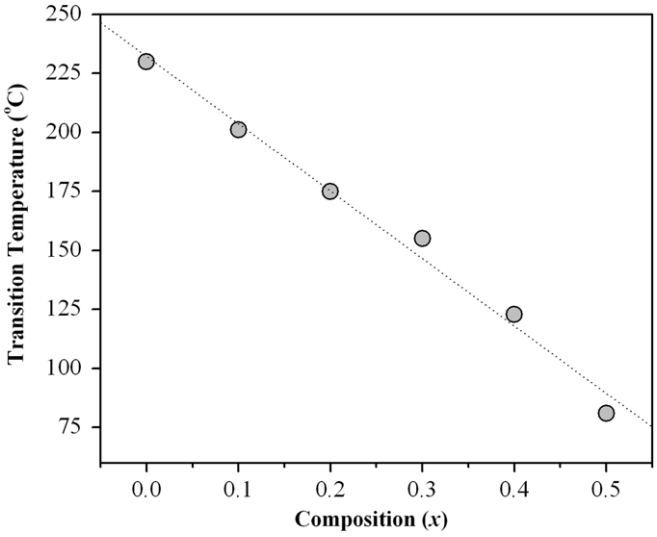

Figure 5. Transition temperatures (T_{max}) as a function of the composition x.

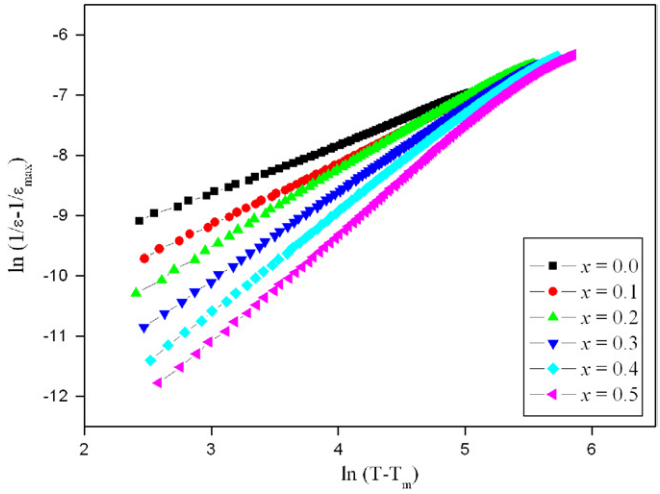

Figure 6. Double logarithmic plot of $\ln(1/\varepsilon - 1/\varepsilon_{max})$ versus $\ln(T - T_m)$ for evaluating the diffusivity exponent γ for the $(Pb[Zr_{1-x}(Ni_{1/3}Nb_{2/3})_x]O_3$ceramic.

and (b) show the results of the DSC for the PZNN system. As shown in figure 4(a), two anomalies at about 229 and 235 °C have been observed for pure $PbZrO_3$. The lower temperature corresponds to the transition temperature of the AFE → FE phase transition, while the higher temperature corresponds to the FE → PE phase transition. The trend of latent heat for the FE phase transition was found to lessen with a progressive increase in the PNN content as shown in figure 4(b). The tricritical point, the composition at which a first-order transition becomes a second-order transition, is close to the composition $x = 0.3$ which has a tolerance factor of $t \sim 1.0$ using the ionic radii of Shannon [25]. Choi *et al* [30] reported that in $Bi(Ni_{1/2}Ti_{1/2})O_3$–$PbTiO_3$ (BNiT–PT) the tricritical point in the solid solution also corresponded closely to $t \sim 1.0$. Similar behaviour was also observed in the $Bi(Mg_{3/4}W_{1/4})O_3$–$PbTiO_3$ (BMW-PT) system by Stringer *et al* [31] and in the PZT system by Rossetti and Navrotsky [32].

A clear transition in T_{max} (defined as the temperature at which ε_r is maximum at 100 Hz) is observed with T_{max} decreasing with x. The transition temperature (T_{max}) as a function of the mole fraction of PNN (x) is represented in figure 5. A good linear relationship between T_{max} and x indicates that this system is a well-behaved and complete solid solution, suggesting that the transition temperature of the PZNN system can be varied over a wide range from −120 to 236 °C by controlling the amount of PNN in the system. The results show that PNN substitution produces a linear reduction in the transition temperature $(T_m) = 232.19 - 285x$ °C with the concentration (x). The PNN shifts the transition temperature of this system at a rate of 28.5 °C mol^{-1}, agreeing quantitatively with other lead-based perovskite systems [14, 19, 33].

The relative permittivity of normal FE materials above the maximum relative permittivity temperatures can be expressed by the Curie–Weiss law. However, the broad relative permittivity of the relaxor FE composition more appropriately follows the quadratic law. The relative permittivity can be derived via the following expression [34, 35]:

$$\frac{\varepsilon'_m}{\varepsilon'(f,T)} = 1 + \frac{(T - T_m(f))^\gamma}{2\delta_\gamma^2} \qquad (1 \leqslant \gamma \leqslant 2), \qquad (2)$$

where ε'_m is the maximum value of the permittivity at $T = T_m(f)$, γ is the diffusivity and δ is the diffuseness parameter. The value of γ is the expression of the degree of dielectric relaxation while the parameter δ_γ is used to measure the degree of diffuseness of the phase transition. The limiting values $\gamma = 1$ and $\gamma = 2$ reduce expression (2) to the Curie–Weiss law valid for the case of a normal FE and the quadratic dependence valid for an ideal relaxor, respectively. The quadratic dependence of $1/\varepsilon_r$ on temperature has been claimed to be obeyed by several materials with diffuse phase transition behaviour.

By plotting $\ln(1/\varepsilon - 1/\varepsilon_{max})$ versus $\ln(T - T_m)$, γ can be determined directly from the gradient. Figure 6 gives these results; the plotted lines for all specimens show remarkably good linearity within the measured temperature range. Using the intercept and slope of the lines in figure 6, δ_γ and γ for each specimen are calculated and shown in figure 7. The values of γ and δ illustrated in figure 7 vary between 1.06 and 1.70, confirming that a diffuse phase transition occurs in the PZNN system. Both diffuseness parameters δ_γ and γ increased with an increase in the mole fraction of PNN. As illustrated in figure 7, a near-linear relationship was observed over the wide compositional range which is consistent with a perfect solid solution. The diffuseness of the phase transition in the $x = 0.5$ composition can be attributed to the relaxor nature of PNN.

The dielectric behaviour of Pb containing the relaxor ferroelectrics is generally explained in the literature in terms of small regions of local spontaneous polarization (so-called polar regions) with a nanometre scale size [28, 36]. In a mixed-perovskite system, where the same site is occupied by two differently charged ions (e.g. Ni^{2+} and Nb^{5+} in the case of the PNN), a self-limiting mechanism operates for the

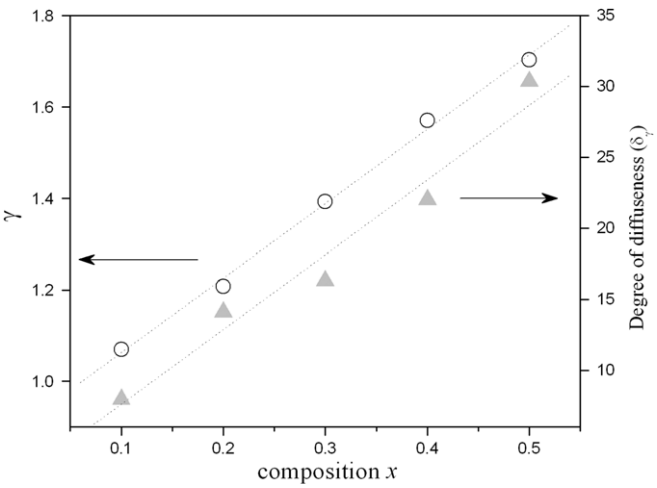

Figure 7. Dependence of γ and the degree of diffuseness (δ_γ) for $Pb[Zr_{1-x}(Ni_{1/3}Nb_{2/3})_x]O_3$, $x = 0.1$–0.5 ceramics.

average size of the ordered regions. Although the global value of the Ni : Nb ratio in PNN is 1 : 2, the local value in the unit cell is 1 : 1, resulting in a net charge for the unit cell, a situation that cannot exist over too many unit cells. Small ordered (polar) regions are therefore surrounded by disordered regions to compensate for the charge imbalance. These ordered polar regions exhibit relaxational behaviour as observed in the dielectric measurements. There are several theories which attempt to explain these properties. Such materials have some features analogous to magnetic spin glasses [37]. As the PNN content increases, the relaxor characteristic of PZNN is observed to increase because the substitution of $(Ni_{1/3}Nb_{2/3})^{4+}$ for the B site ions Zr^{4+} increases the number of polar regions as well as their size. The distribution of the relaxation times depends on the distribution of the size and the polarization strength of the polar regions. It is very possible that the region size is diverse, leading to the broadening of the relaxation time and an increase in the degree of frequency dispersion. A similar tendency has also been observed in several prior investigations [11, 14, 19, 38].

3.3. Microstructure characterization

Figures 8(*a*) and 8(*b*) show SEM images of the surfaces of $Pb[Zr_{1-x}(Ni_{1/3}Nb_{2/3})_x]O_3$ ceramics at $x = 0.2$ and 0.5, respectively. No plate-like grains were observed in either sample, indicating the absence of pyrochlore formation. Other compositions of the system also exhibited a high density and an irregular grain size and shape. By applying the linear intercept methods to these SEM micrographs, the average grain size was calculated to be between 2.6 and 3.8 μm for all the samples. There was no systematic variation in the grain size as a function of the composition according to the different sintering schedules used.

4. Conclusions

For the first time, we have demonstrated the effect of PNN in stabilizing the rhombohedral phase relative to the orthorhombic phase in PZ powders and ceramics. Relaxor FE PNN has been found to strongly influence the phase development and dielectric responses of PZ ceramics. The crystal structure data obtained from XRD indicate that the solid solution $Pb[Zr_{1-x}(Ni_{1/3}Nb_{2/3})_x]O_3$, where $x = 0.0$–0.5, successively transforms from orthorhombic to rhombohedral to pseudo-cubic symmetry with an increase in the PNN concentration. The dielectric constant of $Pb[Zr_{1-x}(Ni_{1/3}Nb_{2/3})_x]O_3$ was found to increase with increased PNN concentration. The PNN shows a clear trend of a reduced temperature (T_m) of maximum permittivity (ε_m), while slightly increasing the diffuse nature of the FE-to-PE phase transition. Furthermore, the transition from the normal FE to the relaxor FE state was clearly observed as the mole fraction of the PNN increased. Furthermore, this transition from the normal to the relaxor FE state was typified by a quasi-linear relationship between the diffuseness parameter δ_γ and the PNN mole fraction x. Optimum dielectric properties were observed for the $x = 0.4$ composition with a permittivity of 16 000.

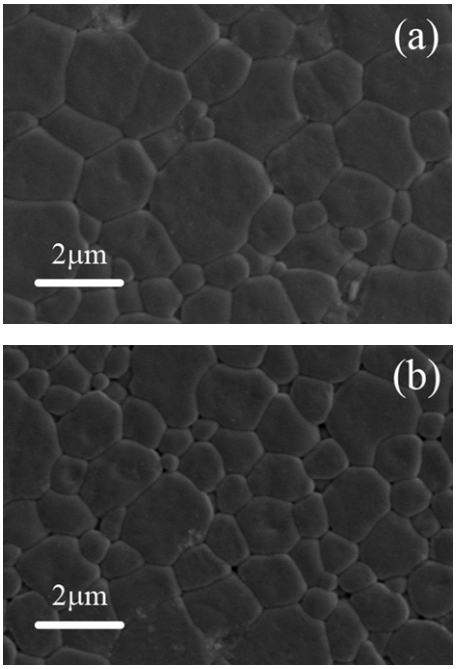

Figure 8. SEM micrographs of thermally etched surfaces of $Pb[Zr_{1-x}(Ni_{1/3}Nb_{2/3})_x]O_3$ ceramics; (*a*) $x = 0.2$, (*b*) $x = 0.5$.

Acknowledgments

This work was supported by the Thailand Research Fund (TRF), the Commission on Higher Education (CHE), Thailand Graduate Institute of Science and Technology (TGIST) and King Mongkut's Institute of Technology Ladkrabang (KMITL).

References

[1] Jaffe B, Cook W R Jr and Jaffe H 1971 *Piezoelectric Ceramic* (London: Academic)

[2] Balyunis L E, Topolov V Y, Bah I S and Turik A V 1993 *J. Phys.: Condens. Matter* **5** 1419–26
[3] Pokharel B P and Pandey D 2002 *Phys. Rev.* B **65** 214108
[4] Pokharel B P and Pandey D 1999 *J. Appl. Phys.* **86** 3327–32
[5] Shatalova G E, Filip'ev V S, Kantsel L M and Fesenko E G 1974 *Sov. Phys. Crystallogr.* **19** 257
[6] Fujishita H, Shiozaki Y and Sawaguchi E 1979 *J. Phys. Soc. Japan* **16** 1391
[7] Uchino K 2000 *Ferroelectric Devices* (New York: Dekker)
[8] Haertling G H 1999 *J. Am. Ceram. Soc.* **82** 797–818
[9] Lanagan M T, Kim J H, Jang S and Newnham R E 1988 *J. Am. Ceram. Soc.* **71** 311
[10] Sharma S, Sati R and Choudhary R N P 1993 *Can. J. Phys.* **71** 322
[11] Yimnirun R, Ananta S and Laoratanakul P 2005 *J. Eur. Ceram. Soc.* **25** 3235–42
[12] Yimnirun R, Ananta S and Laoratanakul P 2005 *J. Eur. Ceram. Soc.* **25** 3235–42
[13] Vittayakorn N, Puchmark C, Rujijanagul G, Tan X and Cann D P 2006 *Curr. Appl. Phys.* **6** 303–6
[14] Vittayakorn N, Rujijanagul G, Tan X, He H and Marquardt M A and Cann D P 2006 *J. Electroceram.* **16** 141–9
[15] Vittayakorn N, Rujijanagul G, Tunkasiri T, Tan X and Cann D P 2004 *Mater. Sci. Eng.* B **108** 258
[16] Xu Y 1991 *Ferroelectric Materials and Their Application* (Amsterdam: Elsevier)
[17] Takeuchi H, Jyomura S and Nakaya C 1985 *Japan. J. Appl. Phys.* **24** 36–40
[18] Alberta E F and Bhalla A S 2001 *Int. J. Inorg. Mater.* **3** 987
[19] Vittayakorn N, Rujijanagul G, Tan X, Marquardt M A and Cann D P 2004 *J. Appl. Phys.* **96** 5103
[20] Cullity B D and Stock S R 2001 *Elements of x-ray Diffraction* (Englewood Cliffs, NJ: Prentice Hall)
[21] 2000 Powder Diffraction File No. 87-0570, International Centre for Diffraction Data, Newton Square, PA
[22] Jona F, Shirane G, Mazzi F and Pepinsky R 1957 *Phys. Rev.* **105** 849–56
[23] 2000 Powder Diffraction File no. 75-1607. International Centre for Diffraction Data, Newtown Square, PA
[24] Shirane G and Hoshino S 1954 *Acta Crystallogr.* **7** 203
[25] Shannon R D 1976 *Acta. Crysallogr.* A **32** 751
[26] Kingary W D, Bowen H K and Uhlmann D R 1976 *Introduction to Ceramics* (New York: Wiley)
[27] Yokosuka M 1998 *Japan. J. Appl. Phys.* **37** 5257
[28] Cross L E 1987 *Ferroelectrics* **76** 241
[29] Cross L E 1994 *Ferroelectrics* **151** 305
[30] Choi S M, Stringer C J, Shrout T R and Randall C A 2005 *J. Appl. Phys.* **98** 034108
[31] Stringer C J, Eitel R E, Shrout T R, Randall C A and Reaney I M 2005 *J. Appl. Phys.* **97** 024101
[32] Rossetti G A and Navrotsky A 1999 *J. Solid State Chem.* **144** 188
[33] Vittayakorn N, Rujijanagul G, Tunkasiri T, Tan X and Cann D P 2003 *J. Mater. Res.* **18** 2882–9
[34] Martirena H T and Burfoot J C 1974 *Ferroelectrics* **7** 151
[35] Uchino K and Nomura S 1982 *Ferroelectr. Lett. Sect.* **44** 55
[36] Uchino K 1994 *Ferroelectrics* **151** 321
[37] Viehland D, Jang S J and Cross L E 1990 *J. Appl. Phys.* **68** 2916–21
[38] Vittayakorn N, Uttiya S, Rujijanagul G and Cann D P 2005 *J. Phys. D: Appl. Phys.* **38** 2942–6

Structural transformation in antiferroelectric $PbZrO_3$-relaxor ferroelectric $Pb(Ni_{1/3}Nb_{2/3})O_3$ solid solution system

S. Wirunchit and N. Vittayakorn[a)]
Faculty of Science, Materials Science Research Unit, Department of Chemistry, King Mongkut's Institute of Technology Ladkrabang, Bangkok 10520, Thailand

(Received 8 March 2008; accepted 10 May 2008; published online 18 July 2008)

The solid solution between the antiferroelectric (AFE) $PbZrO_3$ (PZ) and the relaxor ferroelectric (FE) $Pb(Ni_{1/3}Nb_{2/3})O_3$ (PNN) was synthesized by the columbite precursor method. The crystal structure, phase transformations, and dielectric and thermal properties of $(1-x)$PZ-xPNN where $x=0.00-0.30$ were investigated. With these data, the FE phase diagram between PZ and PNN has been established. The crystal structure data obtained from X-ray diffraction indicate that the solid solution PZ-PNN, where $x=0.00-0.30$, successively transforms from orthorhombic to rhombohedral symmetry with an increase in the PNN concentration. The AFE phase→FE phase transition occurs in compositions of $0.00 \leqslant x \leqslant 0.08$. The AFE→FE phase transition shifts to lower temperatures with higher compositions of x. The FE phase temperature range width increases with increased PNN. Apparently the replacement of the Zr^{4+} ion by Ni^{2+}/Nb^{5+} ions decreases the driving force for an antiparallel shift of Pb^{2+} ions because they interrupt the translational symmetry and facilitates the appearance of a rhombohedral FE phase when the amount of PNN is higher than 8 mol %. © *2008 American Institute of Physics*. [DOI: 10.1063/1.2956598]

INTRODUCTION

Since the 1990s, many studies on the phase transition between the antiferroelectric (AFE) and the ferroelectric (FE) phase in pure and compositionally modified lead zirconate [$PbZrO_3$ (PZ)] ceramics have been completed.[1–4] AFE PZ-based ceramics can undergo transformation from AFE to FE with a large volume change under an external ac bias, temperature, or hydrostatic pressure.[5,6] The maximal longitudinal strain reached 0.87%.[7] These high-strain phenomena have been investigated for applications including charge-storage capacitors, large displacement actuators, and shape memory devices.[3,8] The relative stability of the AFE and FE phases can be altered through chemical substitutions such as Ba^{2+}, Sr^{2+}, and Ca^{2+} at the Pb^{2+} site[9] and Ti^{4+} at the Zr^{4+} site. The substitution of Ba^{2+} for Pb^{2+} in PZ is of considerable interest for transducer applications since the volume change associated with the field forced AFE to FE transition increases with Ba^{2+} substitution.[10] Also the switching field for the AFE to FE transition decreases as a result of Ba^{2+} substitution.[11]

Lead nickel niobate [$Pb(Ni_{1/3}Nb_{2/3})O_3$ (PNN)] is a relaxor FE having a Ni^{2+} and Nb^{5+} complex on the B-site of $Pb(B'B'')O_3$ perovskite with a cubic symmetry at room temperature,[12] PNN-based ceramics are considered to possess low sintering temperatures and high permittivity, high electrical resistivity, and diffuse phase transition characteristics. Therefore, these materials can be used to fabricate multilayer capacitors with low-temperature melting inner electrodes.[13,14] When PNN forms solid solutions with $Pb(Zr_{1-x}Ti_x)O_3$, the system exhibits excellent piezoelectricity and becomes a potential candidate for use in actuators.[15–17] Since PNN is a relaxor FE with a broad dielectric peak near $T_C \approx -120\,^{\circ}C$[18] and PZ is AFE with a sharp maximum permittivity at $T_C \sim 230\,^{\circ}C$, the Curie temperature in a PZ-PNN system can be engineered over a wide range of temperatures by controlling the amount of PNN in the system. Although PZ ceramics have better dielectric breakdown strength than PNN, the sintering temperature is also higher.[9,13] Thus, mixing PNN with PZ is expected to decrease the sintering temperature of PZ ceramics, a desirable move toward lower-cost electrodes.[19] Moreover, since PZ-PNN is not a pure-relaxor FE system, it is easier to prepare single phase ceramics with a smaller amount of undesirable pyrochlore phases.[14] Furthermore, no work has been done on the metastable FE phase induced by the B-site substitution in perovskite PZ. With their complimentary characteristics, it is expected that excellent properties can be obtained from ceramics in a PZ-PNN system.

In this study, a metastable FE phase induced by a B-site substitution was studied as a function of composition. The columbite precursor method was used to synthesize the $(1-x)PbZrO_3-xPb(Ni_{1/3}Nb_{2/3})O_3$ (PZ-PNN) with $x=0.00-0.30$. The structural phase and the dielectric and thermal properties of PZ-PNN ceramics were investigated as a function of composition x. Differential scanning calorimeter (DSC) measurements were also used to study the details of AFE to FE and FE to PE phase transformations accompanied by an evaluation of the thermal behaviors of the PZ-PNN samples. The results are discussed.

EXPERIMENTAL PROCEDURE

Perovskite-phase powders were synthesized using a columbite precursor method to avoid the formation of a pyrochlore phase. Commercial oxide powders of PbO, NiO, Nb_2O_5 (99.9% purity, Aldrich Chemicals, Milwaukee, WI),

[a)]Author to whom correspondence should be addressed. Tel.: 66-89-7002136. FAX: 66-2-3264415. Electronic mail: naratipcmu@yahoo.com.

and ZrO_2 (99% purity, Aldrich Chemicals, Milwaukee, WI) were used as starting materials. $NiNb_2O_6$ was first formed at 1100 °C for 4 h, and then $NiNb_2O_6$ and ZrO_2 were mixed with PbO, according to the composition of $(1-x)PbZrO_3-xPb(Ni_{1/3}Nb_{2/3})O_3$, $0.00 \leqslant x \leqslant 0.30$, with an excessive content of 2 mol % PbO.

Each mixture of the starting powders was milled and mixed in a ball mill, as well as wet homogenized with isopropyl alcohol for 18 h using nylon-coated YTZ zirconia milling as media. The mixtures were dried in an oven and calcined at 900–950 °C for 4 h in a double crucible configuration with a heating rate of 20 °C/min. After remilling, drying, and sieving, the various powders were cold pressed into disks 15 mm in diameter and then sintered at temperatures ranging from 950 to 1250 °C using a heating rate of 5 °C/min and a dwell time of 2 h in sealed alumina crucibles. To limit the loss of PbO, the disks were covered with $PbZrO_3$ powder. X-ray diffraction (XRD) patterns of the sintered pellets were measured using an x-ray diffractometer (PW1729, Philips, Netherlands). Cu$K\alpha$ radiation with step scanning was used with a step size of 0.02° and a scan rate of 2 s per step. The density of the sintered PZ-PNN pellets was measured by water immersion (Archimedes method). The relative density of all the sintered pellets was approximately 95%–97% of the theoretical density. To determine dielectric properties, the maximum density of each composition sample was lapped on its major face. Silver electrodes were made from a low-temperature silver paste by firing at 500 °C for 30 min to enable electrical measurements to be taken. Relative permittivity measurements were made using an automated measurement system consisting of an *LCR* meter (HP-4284, Hewlett-Packard Inc.). The relative permittivity was then calculated from $\varepsilon_r = Cd/\varepsilon_0 A$, where C is the capacitance of the sample, d and A are the thickness of the sample and the area of the electrode, respectively, and ε_0 is the dielectric permittivity of the vacuum (8.854×10^{-12} F/m). The phase transition temperatures and enthalpy (ΔH) of the phase transitions were determined by DSC at room temperature to 350 °C with a heating rate of 10 °C/min.

RESULTS AND DISCUSSION

Crystal structure

The XRD patterns of $(1-x)$PZ-xPNN ceramics with various x values are shown in Fig. 1. A complete crystalline solution of perovskite structure is formed throughout the composition range without the presence of pyrochlore or unwanted phases. Ceramics with $0.02 \leqslant x \leqslant 0.08$ have the same crystal structure with pure PZ ($x=0.00$), i.e., an orthorhombic unit cell at room temperature. Furthermore, the XRD patterns indicate that the replacement of Zr^{4+} by Ni^{2+}/Nb^{5+} ions apparently influenced the orthorhombic $PbZrO_3$ structure. If the XRD pattern of PZ is indexed on the basis of the pseudocubic cell, then $\frac{1}{4}$ $(h\ k\ l)$-type superlattice reflections representing the antiparallel shifts of Pb^{2+} ions will appear.[20]

In Fig. 1, all the indices were based on the pseudocubic cell and the XRD patterns of the samples with $0.02 \leqslant x \leqslant 0.08$ showed the presence of $\frac{1}{4}$ $(h\ k\ l)$-type superlattice reflections. The intensity ratio of 004/240 peaks and the relative intensity of $\frac{1}{4}$ $(h\ k\ l)$-type superlattice reflections (namely, 130/112) decreased with increased Ni^{2+}/Nb^{5+} content, as shown in Fig. 2. According to Glaze,[20] these types of reflections represent antiphase tilting of the oxygen octahedra without distortion. Furthermore, the PZ-PNN samples with $0.1 \leqslant x \leqslant 0.3$ showed only the fundamental reflections of the pseudocubic perovskite cell. The relative intensity of superlattice reflections decreased with increased PNN content, as shown in Fig. 2, demonstrating that the superlattice disappeared with the addition of 10 mol % PNN. Figure 2 also shows the results for $\frac{1}{4}$ $(h\ k\ l)$-type superlattice (1 1 1), (2 0 0), and (2 2 0) reflections. The samples with $x=0.1$, 0.2, and 0.3 had a split (1 1 1) and (2 2 0) reflection and a single (2 0 0) reflection, confirming that the crystal structure of the samples with $x=0.1$, 0.2, and 0.3 is primitive rhombohedral perovskite. For a pure rhombohedral structure, the 2 0 0 group of reflections should be a singlet.

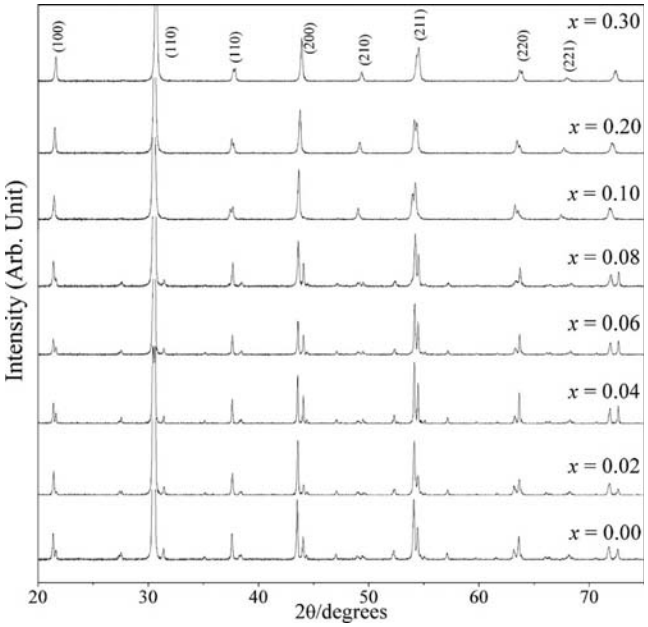

FIG. 1. XRD patterns of $(1-x)$PZ-xPNN; $x=0.0-0.3$ ceramics at the optimum sintering conditions.

Furthermore, the specimens displayed a progressive peak shift toward higher diffraction angle directions with increased PNN. This phenomenon can be qualitatively explained with respect to the unit cell volume caused by the Ni^{2+}/Nb^{5+} incorporation. According to Shannon's effective ionic radii with a coordination number of 6, the average ionic radius of B-site ions $(Ni_{1/3}Nb_{2/3})^{4+}$ has a radius of 0.79 Å, which is close to a radius of Zr^{4+} (0.86 Å).[21] Therefore, $(Ni_{1/3}Nb_{2/3})^{4+}$ can enter into the sixfold coordinated B-site of the perovskite structure to substitute for Zr^{4+} due to radius matching. The structure of ABO_3 type perovskites can be viewed as a network of $[BO_6]$ oxygen octahedra. The substitution of the relatively smaller $(Ni_{1/3}Nb_{2/3})^{4+}$ for the relatively larger Zr^{4+} led to a decrease in the unit cell volume. This radius effect is presumably responsible for the steady shift of the XRD peak positions to higher diffraction angle directions with increased PNN. The influence of the addition of $(Ni_{1/3}Nb_{2/3})^{4+}$ on the phase structure of the

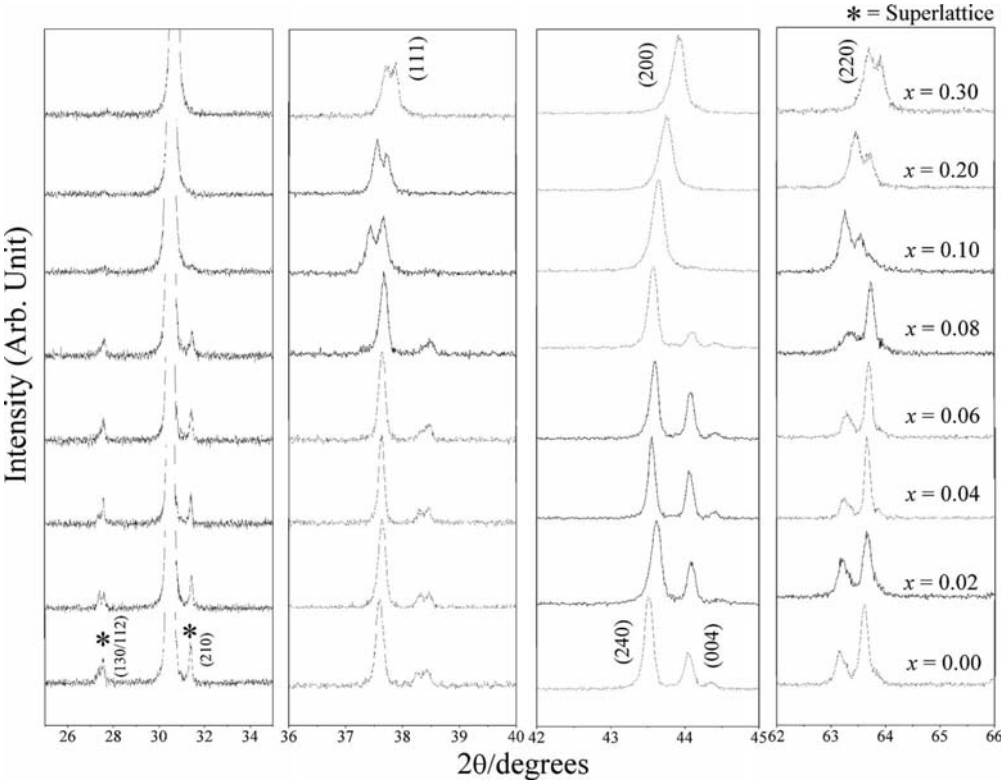

FIG. 2. XRD patterns of the $\frac{1}{4}$ $(h\ k\ l)$-type superlattice reflections, (111), (200), and (220) peaks of $(1-x)$PZ-xPNN; $x=0.0-0.3$ ceramics.

$PbZrO_3-Pb(Ni_{1/3}Nb_{2/3})O_3$ system is similar to the influence of $(Pb_{1-x}Ba_x)ZrO_3$.[5] The substitution of smaller $(Ni_{1/3}Nb_{2/3})^{4+}$ ions with Zr^{4+} sites (which implies the transition of the PZ-PNN structure from orthorhombic to rhombohedral, as shown in Fig. 2) may facilitate the parallel displacement along a [1 1 1] direction and the associated displacements of three oxygen ions in the PZ-PNN structure, resulting in an improvement of ferroelectricity. The presence of a polar axis in the [1 1 1] direction has been reported for a FE rhombohedral structure.[22]

Phase transition and dielectric properties

The permittivity temperature dependences of $(1-x)PbZrO_3-xPb(Ni_{1/3}Nb_{2/3})O_3$ ceramics were measured at several frequencies from 25 to 350 °C. Figures 3(a)–3(h) show the relative permittivity versus temperature of $(1-x)PbZrO_3-xPb(Ni_{1/3}Nb_{2/3})O_3$ ceramics for compositions $x=0.00$, 0.02, 0.04, 0.06, 0.08, 0.10, 0.20, and 0.30, respectively, at frequencies of 100 Hz, 1 kHz, 10 kHz, 100 kHz, and 500 kHz. For composition $x=0.0$, the relative permittivity increased slowly until the temperature approached 225 °C. Near 230 °C the relative permittivity increased greatly, passing through a maximum at about 231 °C. With further heating, the relative permittivity decreased in accordance with the Curie–Weiss law, $\varepsilon_r=C/(T-T_0)$, where ε_r is the relative permittivity, T is the temperature, and C and T_0 are constants which, in this study, were 1.04×10^5 and 460.7 K, respectively.

The substitution of PNN lowers the AFE to FE phase transition temperature. The AFE to FE phase transition occurs at 200, 150, and 105 °C for 0.02, 0.04, and 0.06, respectively [see Figs. 3(b)–3(d)]. The jumps in the relative permittivity at the transition temperature are found to be nearly 2250, 1240, and 650 for $x=0.02$, 0.04, and 0.06, respectively. Furthermore, for $x\geqslant0.08$, no dielectric anomaly corresponding to the AFE-FE transition is observed [Fig. 3(e)].

Since the AFE to FE transition decreases nearly linearly at the rate of 22.5 °C/mol % of PNN with respect to its value for pure PZ, the expected AFE to FE transition temperature for the composition $x=0.08$ is around 64 °C. No anomaly corresponding to AFE-FE transition in the composition $x\geqslant0.08$ was found. From these results, we can conclude that the AFE phase of pure PZ persists in the PZ-PNN system for $x<0.08$ only. At the composition $x\geqslant0.10$, the relative permittivity peak values became gradually higher in parallel with the decrease in the transition temperature (T_m). The $x=0.2$ and 0.3 compositions showed a broadening of the permittivity maxima, and the T_m increased with an increased measurement frequency [Figs. 3(c) and 3(h)], indicating that this composition shows a diffuse phase transition with a strong frequency dispersion which is characteristic of relaxor ferroelectricity.

The DSC technique was also used as the primary tool to confirm the AFE-FE phase transition in the PZ-PNN system. AFE-FE phase transition temperatures, enthalpy, and paraelectric (PE) transitions are summarized in Table I. Figure 4 shows the results of the DSC analysis of the PZ-PNN samples. As shown in Fig. 4, two distinct endothermic peaks were observed for PZ-PNN samples with $0.0\leqslant x<0.08$. The lower temperature corresponds to the transition temperature

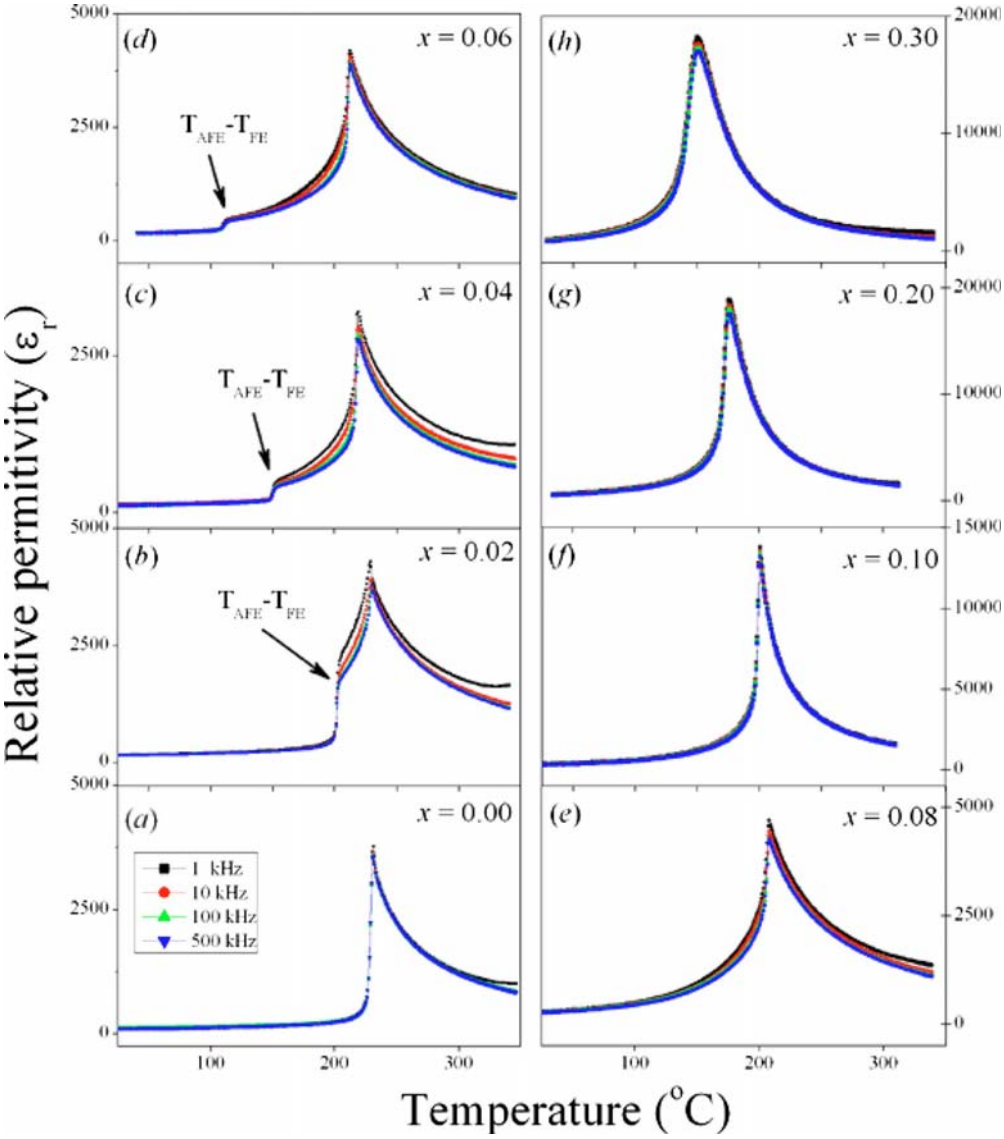

FIG. 3. (Color online) Dielectric properties as a function of temperature on heating at a frequency of 1–500 kHz varies PNN concentration.

of the AFE→FE phase transition, while the higher temperature corresponds to the FE→PE phase transition. It is well known that good quality ceramics as well as single crystal samples of PZ show two distinct endothermic peaks around 230 and 215 °C corresponding to the PE to FE and FE to AFE transitions, respectively, on heating and cooling.[23,24] The AFE→FE phase transition was found in compositions of $0.0 \leqslant x < 0.08$. The peaks shift to lower temperatures with

TABLE I. Characteristics of $(1-x)$PZ-xPNN ceramics with optimized processing conditions (R, rhombohedral; O, orthorhombic).

Composition (x)	Crystal structure	$\varepsilon_{r\ \mathrm{room}}$	$\varepsilon_{r\ \mathrm{max}}$	Phase transition temperature (°C)		Enthalpy (J/g)	
				AFE→FE	FE→PE	AFE→FE	FE→PE
0.00	O	120	3 370	229.5	235.5	1.53	2.34
0.02	O	166	4 300	200.7	227.0	1.56	2.95
0.04	O	127	3 200	150.2	220.8	1.33	2.89
0.06	O	177	4 200	105.7	213.3	1.10	2.70
0.08	O	319	4 700	⋯	205.5	⋯	2.44
0.10	R	375	13 800	⋯	200.2	⋯	1.88
0.20	R	602	18 900	⋯	175.3	⋯	1.39
0.30	R	1120	18 200	⋯	149.0	⋯	0.16

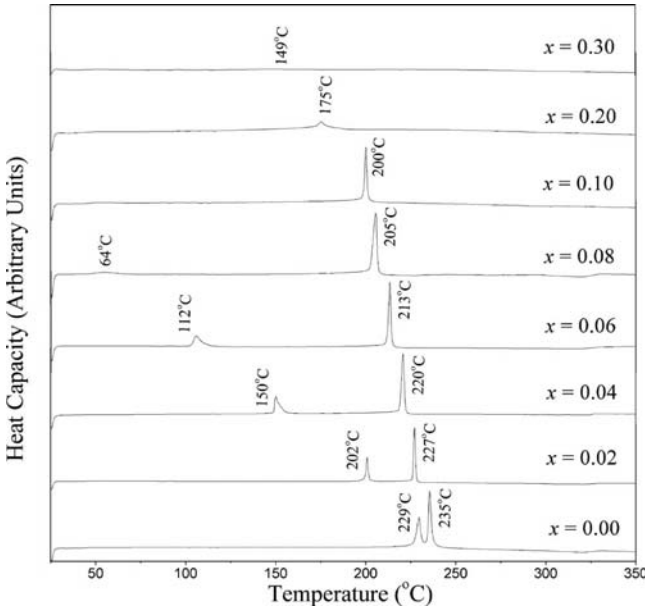

FIG. 4. Typical DSC curves for $(1-x)$PZ-xPNN; $x=0.0-0.3$ ceramics.

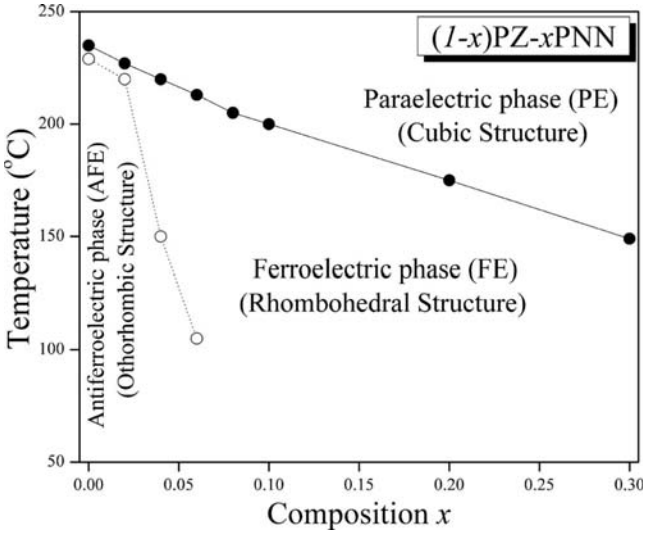

FIG. 5. Phase diagram of $(1-x)$PZ-xPNN, $x=0.0-0.3$ binary system determined from room temperature XRD, DSC as a function of temperature. The symbols refer to ○=the transition temperature from AFE state to FE state; ●=the transition temperature from FE state to PE state.

higher compositions of x. From Table I, the temperature range width of the FE phase continuously increases progressively with the PNN content. The temperature range widths of the FE phase are around 6, 25, 70, and 101 °C for compositions $x=0.00$, 0.02, 0.04, and 0.06, respectively. Furthermore, the areas under two endothermic peaks in Fig. 4 decreased with increased PNN. Since those areas represent a free-energy difference between the two phases, this result indicates that the addition of PNN decreases the stability of orthorhombic phase. Apparently the replacement of the Zr^{4+} ion by $(Ni_{1/3}Nb_{2/3})^{4+}$ ions decreases the driving force for an antiparallel shift of Pb^{2+} ions because they interrupt the translational symmetry.[20] This interruption caused the appearance of a rhombohedral FE phase when the amount of PNN was more than 8 mol %. Gotor *et al.*[25] studied relationships between the structure change of $BaTiO_3$ and its enthalpy by using DSC. They found that the tetragonality (c/a) of $BaTiO_3$ is reduced along with the reduction in enthalpy. However, in the present work, the decrease in ΔH is proportional to the fraction ratio of the FE and PE phases in the PZ-PNN. The tricritical point (the composition at which a first-order transition becomes a second-order transition) is close to the composition $x=0.3$, which has a tolerance factor, $t\sim 1.0$, using the ionic radii of Shannon.[21] Choi *et al.*[26] reported that in the $Bi(Ni_{1/2}Ti_{1/2})O_3-PbTiO_3$, the tricritical point in the solid solution also corresponded closely to $t\sim 1.0$. Similar behavior was also observed in the $Bi(Mg_{3/4}W_{1/4})O_3-PbTiO_3$ system by Stringer *et al.*[27] and PZT by Rossetti and Navrotsky.[28]

Based on the results of XRD, dielectric properties, and DSC data, the FE phase diagram for the $(1-x)$PZ-xPNN binary system has been established (see Fig. 5). The transition temperature decreases approximately linearly with x, from $T_C=235$ °C for $x=0.0$ to 149 °C for $x=0.3$. The phase diagram consists of three distinct crystallographic phases in this system: high-temperature PE cubic $(Pm3m)$, rhombohedral $(R3m)$, and FE orthorhombic $[P2cb$ (No. 32)]. At low concentrations of PNN $x\leqslant 0.08$, the symmetry can be defined as orthorhombic. The orthorhombic symmetry transforms into rhombohedral at the composition near $x=0.08$.

CONCLUSIONS

Relaxor FE PNN has been found to strongly influence crystal structure dielectric responses and thermal properties of PZ ceramics. The crystal structure data obtained from XRD indicate that the solid solution $(1-x)$PZ-xPNN, where $x=0.0-0.3$, successively transforms from orthorhombic to rhombohedral symmetry with increased PNN concentration. The AFE→FE phase transition is found in compositions of $0.0\leqslant x\leqslant 0.08$. The AFE→FE phase transition shifts to lower temperatures with higher compositions of x. The temperature range width of the FE phase increases with increased PNN. It is apparent that the replacement of the Zr^{4+} ion by Ni^{2+}/Nb^{5+} ions would decrease the driving force for an antiparallel shift of Pb^{2+} ions because they interrupt the translational symmetry. The dielectric properties of $(1-x)$PZ-xPNN was found to increase with increased PNN concentration. PNN shows a clear trend toward reducing the temperature (T_m) of maximum permittivity (ε_m), while slightly increasing the diffuse nature of the FE to PE phase transition. Furthermore the transition from the normal FE to the relaxor FE state was clearly observed as the mole fraction of PNN increased.

ACKNOWLEDGMENTS

This work was supported by the Thailand Research Fund (TRF), the Commission on Higher Education (CHE), Thailand Graduate Institute of Science and Technology (TGIST), and King Mongkut's Institute of Technology Ladkrabang (KMITL)

[1]W.-H. Chan, Z. Xu, T. F. Hung, and H. Chen, J. Appl. Phys. **96**, 6606 (2004).

[2]J. Zhai and H. Chen, J. Appl. Phys. **94**, 589 (2003).
[3]K. Uchino, *Ferroelectric Devices* (Dekker, New York, 2000).
[4]E. Sawaguchi, H. Maniwa, and S. Hoshino, Phys. Rev. **83**, 1078 (1951).
[5]B. P. Pokharel and D. Pandey, J. Appl. Phys. **86**, 3327 (1999).
[6]B. P. Pokharel and D. Pandey, Phys. Rev. B **65**, 214108 (2002).
[7]W. Y. Pan, C. Q. Dam, Q. M. Zhang, and L. E. Cross, J. Appl. Phys. **66**, 6014 (1989).
[8]K. Uchino, *Piezoelectric Actuators and Ultrasonic Motors* (Kluwer Academic, Boston, 1996).
[9]B. Jaffe and W. R. Cook, *Piezoelectric Ceramic* (Academic Press, New York, 1971).
[10]G. Rujijanagul and T. Bongkarn, Phase Transitions **80**, 209 (2007).
[11]N. Vittayakorn, T. Bongkarn, and G. Rujijanagul, Physica B **387**, 415 (2007).
[12]L. E. Cross, Ferroelectrics **151**, 305 (1994).
[13]G. H. Haertling, J. Am. Ceram. Soc. **82**, 797 (1999).
[14]T. R. Shrout and A. Halliyal, Am. Ceram. Soc. Bull. **66**, 704 (1987).
[15]N. Vittayakorn, G. Rujijanagul, X. Tan, M. A. Marquardt, and D. P. Cann, J. Appl. Phys. **96**, 5103 (2004).
[16]E. F. Alberta and A. S. Bhalla, Int. J. Inorg. Mater. **3**, 987 (2001).
[17]G. Robert, M. Demartin, and D. Damjanovic, J. Am. Ceram. Soc. **81**, 749 (1998).
[18]S. Sharma, R. Sati, and R. N. P. Choudhary, Can. J. Phys. **71**, 322 (1993).
[19]Y. Xu, *Ferroelectric Materials and Their Application* (Elsevier Science, Amsterdam, 1991).
[20]A. M. Glazer, Acta Crystallogr., Sect. A: Cryst. Phys., Diffr., Theor. Gen. Crystallogr. **A31**, 756 (1975).
[21]R. D. Shannon, Acta Crystallogr., Sect. A: Cryst. Phys., Diffr., Theor. Gen. Crystallogr. **A32**, 751 (1976).
[22]G. Shirane and S. Hoshino, Acta Crystallogr. **7**, 203 (1954).
[23]G. Shirane, E. Sawaguchi, and Y. Takagi, Phys. Rev. **84**, 476 (1951).
[24]R. W. Whatmore and A. M. Glazer, J. Phys. C **12**, 1505 (1979).
[25]F. J. Gotor, C. Real, M. J. Dianez, and J. M. Criado, J. Solid State Chem. **123**, 301 (1996).
[26]S. M. Choi, C. J. Stringer, T. R. Shrout, and C. A. Randall, J. Appl. Phys. **98**, 034108 (2005).
[27]C. J. Stringer, R. E. Eitel, T. R. Shrout, C. A. Randall, and I. M. Reaney, J. Appl. Phys. **97**, 024101 (2005).
[28]G. A. Rossetti and A. Navrotsky, J. Solid State Chem. **144**, 188 (1999).

Journal of Ceramic Processing Research. Vol. 9, No. 4, pp. 381~384 (2008)

JOURNAL OF
Ceramic Processing Research

Effect of calcination conditions on phase formation of microwave dielectric cobalt niobate ($CoNb_2O_6$) powders via a mixed oxide synthesis route

Nopsiri Chaiyo and Naratip Vittayakorn*

King Mongkut's Institute of Technology Ladkrabang Nanotechnology Research Center (NRC), King Mongkut's Institute of Technology Ladkrabang, Bangkok, Thailand 10520

Cobalt niobate ($CoNb_2O_6$) powders have been prepared using a mixed oxide synthesis route. The formation of the $CoNb_2O_6$ phase in the calcined powders has been investigated as a function of calcination conditions by differential thermal analysis (DTA) and X-ray diffraction (XRD) techniques. The morphological evolution was determined by scanning electron microscopy (SEM). It has been found that the minor phases of unreacted Co_3O_4 and the orthorhombic-Nb_2O_5 and monoclinic-β-Nb_2O_5 phase tend to form together with the columbite $CoNb_2O_6$ phase, depending on calcination conditions. It is seen that optimization of calcination conditions can lead to a single-phase orthorhombic $CoNb_2O_6$. The calcination temperature and dwell time have been found to have a pronounced effect on the phase formation of the calcined cobalt niobate ($CoNb_2O_6$) powders. Optimization of calcination conditions can lead to a single-phase $CoNb_2O_6$ in a columbite phase.

Key words: $CoNb_2O_6$, Calcination, Powder synthesis.

Introduction

Advances in wireless communication systems are very dependent upon improvements in microwave dielectric materials. In particular, centimetre and millimetre wave wireless applications require high-*Q* materials that would be less expensive than the known high-*Q* perovskite-structure, barium-tantalate-based microwave dielectrics and would not need high sintering temperatures [1]. Cobalt niobate $CoNb_2O_6$ is a potential candidate for mechanical filter coatings and electrical applications such as for resonators and capacitors which has a columbite structure having the general formula AB_2O_6, with a *Pcan (no.60)* space group and can be used for capacitors or dielectric resonators for microwave applications due to its low tangent loss (tan δ) and high dielectric constant (ε_r) [1, 2]. Figure 1 shows the columbite structure of $CoNb_2O_6$. Regarding the structure, [M-O_6] (M = Co or Nb) octahedra share edges forming chains along the *c*-axis. Parallel Co-O_6 and Nb-O_6 chains alternate along the *b*-axis. $CoNb_2O_6$ is well known as the key precursor for the successful preparation of single-phase perovskite $Pb(Co_{1/3}Nb_{2/3})O_3$ (PCoN), which is becoming increasingly important for multilayer ceramic capacitor, transducer, electrostrictor and actuator applications [3, 4]. The objective of this investigation was to study the reaction between the starting cobalt oxide and niobium oxide precursors, phase formation, microstructure and microwave dielectric properties of columbite-structure cobalt niobate ceramics.

*Corresponding author:
Tel : +66-9-700-2136
Fax: +66-2-3264415
E-mail: naratipcmu@yahoo.com

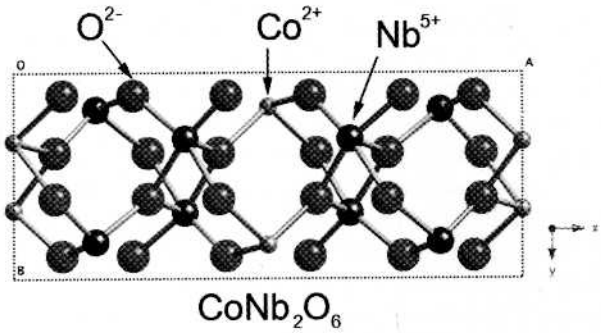

Fig. 1. Crystal structure of $CoNb_2O_6$ compound.

Experimental

Ceramics with the composition $CoNb_2O_6$ were produced by the conventional mixed-oxide route. All samples in this study were prepared from reagent-grade oxides: Co_3O_4 (99.99%, Aldrich, U.S.A.) and Nb_2O_5 (99.9%, Aldrich, U.S.A.). Co_3O_4 and Nb_2O_5 powders were weighed and mixed by ball-milling in a polyethylene bottle together with methyl alcohol and partially stabilized zirconia media. Methyl alcohol was removed by heating at 80 °C for appropriate durations. After drying, the reaction of the uncalcined powders taking place during heat treatment was investigated by differential thermal analysis (DTA; Perkin-Elmer 7 series) using a heating rate of 10 Kminute^{-1} in air from room temperature up to 1350 °C. Based on the DTA results, various calcinations conditions, i.e. temperature ranging from 700-1100 °C and dwell time ranging from 15 to 240 minutes, were applied with a heating/cooling rate of 5 Kminute^{-1}, in order to investigate the formation of $CoNb_2O_6$.

All powders were subsequently examined by room temperature X-ray diffraction (XRD; Bruker D8 Advance) using Ni-filtered CuK_α radiation to identify the phases formed and optimum calcination conditions for the formation of $CoNb_2O_6$ powders. The relative proportions of $CoNb_2O_6$, Co_3O_4, orthorhombic-Nb_2O_5 and monoclinic-β-Nb_2O_5 have been calculated according to the following approximate relationship, by analogy with our treatment of the yield of $CoNb_2O_6$ in a related synthesis [5, 6]:

Wt% columbite phase

$$= \left(\frac{I_{col}}{I_{col} + I_{Co_3O_4} + I_{Otho-Nb_2O_5} + I_{\beta-Nb_2O_5}} \right) \times 100 \qquad (1)$$

here I_{col}, $I_{Co_3O_4}$ $I_{Otho-Nb_2O_5}$ and $I_{\beta-Nb_2O_5}$ refer to the intensities of the (311) columbite peak, (311) cubic-Co_3O_4 peak, (180) orthorhombic-Nb_2O_5 and (400) monoclinic-β-Nb_2O_5 peak respectively, these being the strongest reflections in all cases. Microstructural analysis of the ceramic samples was performed by means of scanning electron microscopy (LEO 1455VP, Cambridge, England).

Results and Discussions

Figure 2 shows the DTA curves for the mixture of Co_3O_4 and Nb_2O_5 with a molar ratio of 1 : 3. From Fig. 2, three endothermic peaks centered at 100.6, 357 and 810 °C are observed. The first endothermic peak at 100.6 °C is attributed to the evaporation of water molecules [7]. The second endothermic peak occurring at 357 °C should correspond to the decomposition of the organic species from the milling process [8]. The different temperature, intensities, and shapes of the thermal peaks are probably related to the different nature of the organic species and consequently, caused by the removal of species bounded differently in the network [7, 8]. The third endothermic peak at 810 °C is assigned to the formation of $CoNb_2O_6$ by combination reactions of Co_3O_4 and Nb_2O_5. According

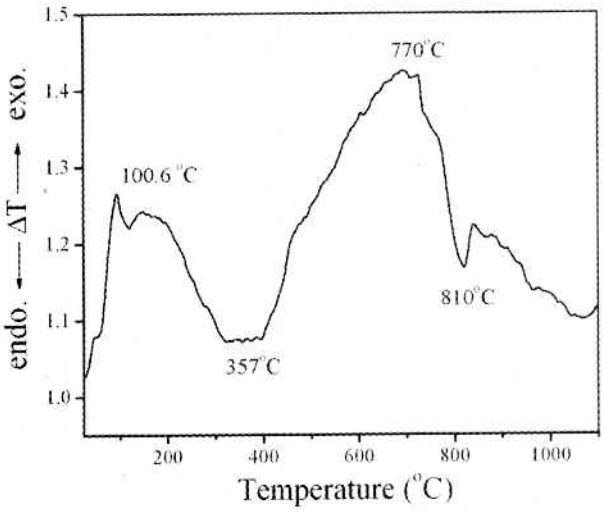

Fig. 2. DTA curve for the mixture of Co_3O_4-Nb_2O_5 powders.

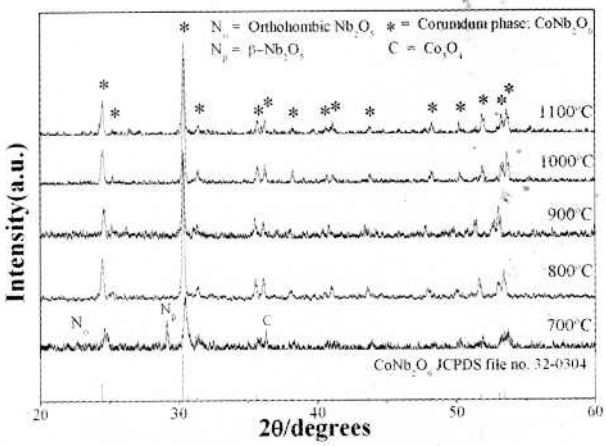

Fig. 3. XRD patterns of $CoNb_2O_6$ powder calcined at various temperatures for 4 h with heating/cooling rates of 20 Kminute^{-1}.

to the DTA measurements, these data were used to define the range of calcination temperature for XRD investigation between 700 °C and 1100 °C.

XRD paterns of all calcined powders are given in Fig. 3. It is seen that $CoNb_2O_6$ crystallites were already developed in the powder at a calcination temperature as low as 700 °C, accompanied with cubic-Co_3O_4 (JCPDS files No 78-1969), orthorhombic-Nb_2O_5 (JCPDS files No 27-1003), monoclinic-β-Nb_2O_5 (JCPDS files No 26-0885). No evidence of a cubic phase of CoO was found. The strongest reflection from Co_3O_4, (200), was located at 2θ = 36.8 whereas the observed temperature variation of Nb_2O_5 in terms of the intensity and position of the peaks attested to a number of phase changes. In niobium oxide synthesis through precipitation from solution, the calcination temperature has a significant effect on the crystal structure of the resulting oxide. The XRD patterns show that the transformation from the orthorhombic-Nb_2O_5 to monoclinic-β-Nb_2O_5 takes place as the calcination temperature increases, which was reported earlier by Belous et al. [9]. As the temperature increased to 800 °C, the intensity of the columbite $CoNb_2O_6$ peaks was further enhanced and it became the only phase. Upon calcination at 900, 1000 and 1100 °C, an essentially single of $CoNb_2O_6$ phase was obtained. This $CoNb_2O_6$ phase was able to be indexed according to an orthorhombic columbite-type structure with lattice parameters a = 571 pm, b = 1414 pm and c = 504 pm, space group *Pcan (no. 60)*, consistent with JCPDS file number 32-0304. Having established the optimum calcination temperature, dewll times ranging from 15 minute to 120 minute with constant heating/cooling rate of 5 Kminute^{-1} were applied at 800 °C, as shown in Fig. 4. It can be seen that a single-phase of $CoNb_2O_6$ powders was also successfully obtained with a calcinations temperature of 800 °C and a dwell time of 120 minutes or more applied. This was apparently a consequence of the enhancement in crystallinity of the $CoNb_2O_6$ phase with increasing dwell time. The disappearance of monoclinic-β-Nb_2O_5 and orthorhombic-Nb_2O_5 phase indicated that full crystallization has occurred at relative shorter calcinations

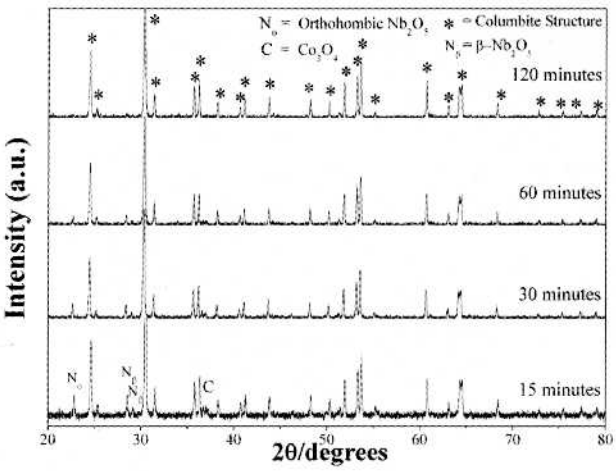

Fig. 4. XRD patterns of $CoNb_2O_6$ powder calcined with heating/cooling rates of 20 Kminute^{-1} at 800 °C for 15-240 minutes.

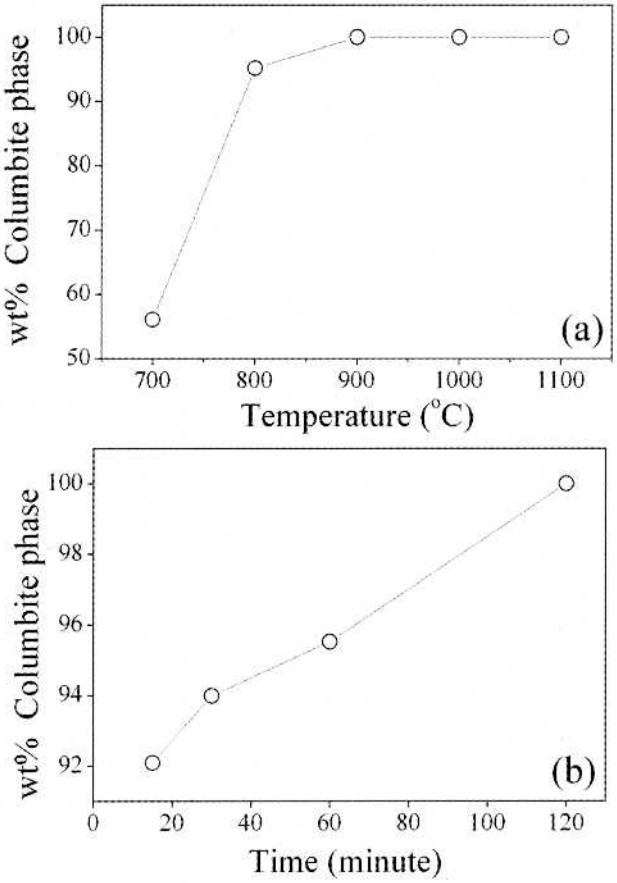

Fig. 5. Fraction of the columbite phase formed in $CoNb_2O_6$ specimens (a) as a function of calcination temperature (calcined for 4 hours) (b) as a function of calcination time (calcined at 800 °C).

times. The observation that the dwell time may also play an important role in obtaining a single phase product is also consistent with other systems [10, 11]. The columbite phase formation at various calcination temperatures and time is shown in Fig. 5(a) and (b). By increasing the calcination temperature from 700 to 1100 °C, the yield of the columbite phase increased significantly until at 800 °C, a single phase of $CoNb_2O_6$ was formed. However, form the present study, there are no significant differences between the powders calcined at temperatures ranging from 800 to 1100 °C. This observation agrees well with those derived from the DTA results. Apart from the calcination temperature, the effect of dwell time was also found to be quite significant (Fig. 4). It is seen that the single phase of $CoNb_2O_6$ (yield 100% within the limitations of the XRD technique) was found to be in powders, calcined at 800 °C with a dwell time of 120 minutes or more. The average grain sizes were determined from XRD patterns according to the Scherrer's equation:

$$D = \frac{k\lambda}{\beta \cos \theta_B} \tag{2}$$

where D is the average grain size, k is a constant equal to 0.89, θ_B is the (311) peak angle, λ is the X-ray wavelength equal to 1.5406 Å and β is the half peak width. The average grain size of $CoNb_2O_6$ powders at 800 °C with a dwell time of 120 minutes was about 280 nm.

Because the raw materials used were multiphase, the formation reaction of the columbite phase belongs to a heterogeneous system. A model used to treat multiphase reaction kinetics was derived by Johnson and Mehl and the equation for this reaction is:

$$\ln[1/(1-y)] = (kt)^n \tag{3}$$

where y is the constant of the columbite phase formed, k the reaction rate constant, t the calcination time and n is the reaction order [12, 13]. The relation of ln [ln $1/(1-y)$] versus ln t is plotted in Fig. 6. From this graph, it was found that the phase transformation of the columbite phase obeys this theory of phase transformations [14]. This phenomenological model is based on the theory of nucleation and growth and is accurate for a large number of systems. The fact that the data in Fig. 6 closely follow Eq. (3) indicates that the columbite phase grows at a constant rate from a random distribution of point nuclei [14]. SEM micrographs of the calcined $CoNb_2O_6$ powders are given in Fig. 7(a) and 7(b). In general, the particles are agglomerated

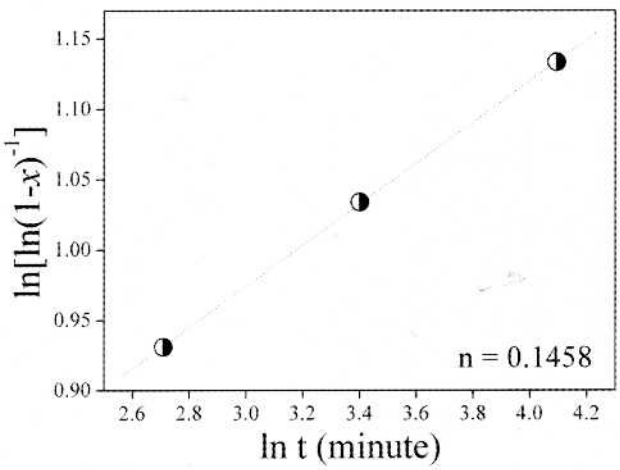

Fig. 6. Johnson-Mehl-Avrami-type for the formation of columbite phase in $CoNb_2O_6$ specimens isothermally heat treated at 800 °C.

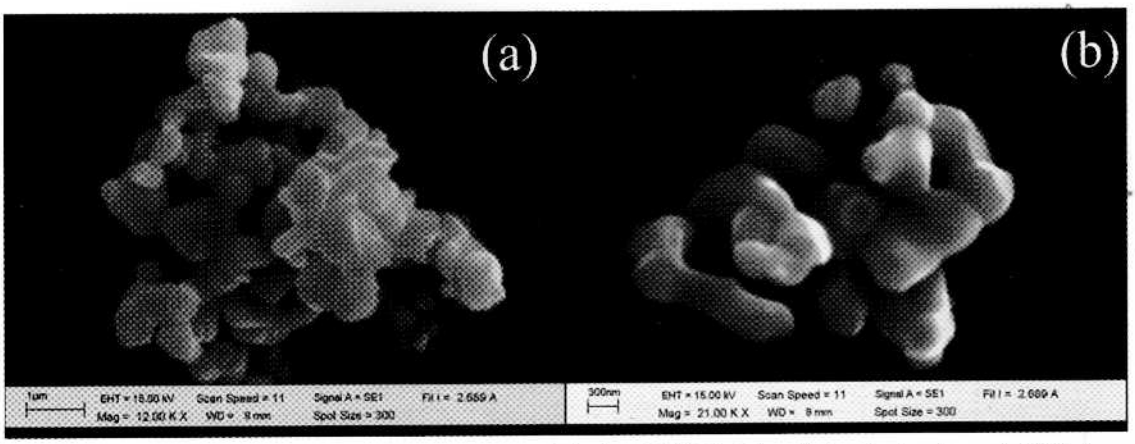

Fig. 7. Scanning electron micrographs of the $CoNb_2O_6$ powders calcined at 800 °C for 2 h, with heating/cooling rate 5 °C/min.

and basically irregular in shape, with a substantial variation in particle size and morphology. The particle size can be estimated from SEM micrographs to be in the range of 70-300 nm. A detailed study at higher magnification (Fig. 7(b)) showed that the particles had spherical secondary particles, composed of nano-sized primary particulates.

Conclusions

Polycrystalline powder of $CoNb_2O_6$ was synthesized using solid state synthesis using oxides as starting materials. Evidence has been obtained for a 100% yield of $CoNb_2O_6$ at a calcination temperature of 800 °C for 120 minutes with heating/cooling rates of 5 Kminute^{-1}. XRD showed the compound to have the columbite structure, having orthorhombic lattice parameters of a = 5.06880(± 0.0014)Å, b = 14.1348 (± 0.0046)Å and c = 5.2230 (± 0.0072)Å.

Acknowlegements

This work was supported by the Thailand Research Fund (TRF), the Commission on Higher Education (CHE), Thailand Graduate Institute of Science and Technology (TGIST), National Research Council of Thailand (NRCT) and King Mongkut's Institute of Technology Ladkrabang.

References

1. A.J. Moulson and J.M. Herbert, Electroceramics: Materials, Properties, Appications, Chapman and Hall, New York (1990).
2. A.S. Bhalla, R. Guo and R. Roy, Mat. Res. Innovat. 1 (2000) 3-26.
3. N. Vittayakorn and T. Tunkasiri, Phys. Scr. T129 (2007) 199-204.
4. T.R. Shrout and A. Halliyal, Am. Ceram. Soc. Bull. 66[4] (1987) 704-711.
5. S.L. Swartz and T.R. Shrout, Mater. Res. Bull. 17 (1982) 1245-1250.
6. N. Vittayakorn, J. Ceram. Process. Res. 7 (2006) 288-291.
7. N. Vittayakorn and S. Wirunchit, Smart Mater. Struct. 16 (2007) 851-857.
8. A. Ngamjarurojana, O. Khamman, R. Yimnirun and S. Ananta, Materials Letters 60 (2006) 2867-2872.
9. A.G. Belous, O.V. Ovchar, D.O. Mishchuk, A.V. Kramarenko, B. Jancar, J. Bezjak and D. Suvorov, Inorg. Mater. 43 (2007) 412-417.
10. R. Wongmaneerung, R. Yimnirun and S. Ananta, Materials Letters 60 (2006) 2666-2671.
11. R. Wongmaneerung, T. Sarakonsri, R. Yimnirun and S. Ananta, Mat. Sci. Eng. B-Solid. 132 (2006) 292-299.
12. M.J. Avrami, J. Chem. Phys. 8 (1940) 212-224.
13. M.J. Avrami, J. Chem. Phys. 9 (1941) 177-184.
14. J.W. Christian, The Theory of Transformations in Metals and Alloys: Part I., Pergamon Press, Oxford (2002).

Appl Phys A (2008) 93: 565–569
DOI 10.1007/s00339-008-4677-x

Applied Physics A
Materials Science & Processing

Ferroelectric phase stabilization, phase transformations and thermal properties in $(1-x)PbZrO_3$–$xPb(Co_{1/3}Nb_{2/3})O_3$ solid solution

Wanwimon Banlue · Naratip Vittayakorn

Received: 12 February 2008 / Accepted: 15 May 2008 / Published online: 6 June 2008

Abstract The solid solution between the antiferroelectric $PbZrO_3$ (PZ) and relaxor ferroelectric $Pb(Co_{1/3}Nb_{2/3})O_3$ (PCoN) was synthesized by the columbite method. The phase structure and thermal properties of $(1-x)$PZ–xPCoN, where $x = 0.0$–0.3, were investigated. With these data, the ferroelectric phase diagram between PZ and PCoN has been established. The crystal structure data obtained from XRD indicates that the solid solution PZ–PCoN, where $x = 0.0$–0.3, successively transforms from orthorhombic to rhombohedral symmetry with an increase in PCoN concentration. The AFE → FE phase transition was found in the compositions of $0.0 \leq x \leq 0.10$. The AFE → FE phase transition shift to lower temperatures with higher compositions of x. The width of the temperature range of FE phase was increased with increasing amount of PCoN. It is apparent that the replacement of the Zr^{4+} ion by $(Co_{1/3}Nb_{2/3})^{4+}$ ions would decrease the driving force for antiparallel shift of Pb^{2+} ions, because they interrupt the translational symmetry. This interruption caused the appearance of a rhombohedral ferroelectric phase when the amount of PCoN was more than 10 mol%.

PACS 61.05.cp · 77.80.Bh · 65.40.-b · 77.22.-d · 77.80.-e · 77.84.Dy

W. Banlue · N. Vittayakorn (✉)
Materials Science Research Unit, Department of Chemistry, Faculty of Science, King Mongkut's Institute of Technology Ladkrabang, Bangkok 10520, Thailand
e-mail: naratipcmu@yahoo.com

1 Introduction

A lot of attention has been given to the lead zirconate, ($PbZrO_3$; PZ) and modified-PZ in several recent years as regards theoretical, experimental and industrial applications [1–3]. At room temperature PZ has an antiferroelectric phase (AFE) which has an orthorhombic structure. It undergoes the AFE to a paraelectric phase (PE) and transforms from an orthorhombic structure to a cubic structure at 236 °C [1]. It is reported that there exists a ferroelectric phase (FE) over a very narrow temperature range (230–233 °C). The FE intermediate phase can also be introduced by partial replacement of Pb^{2+} ions with A-site ions such as Ba^{2+} ions [4] or La^{3+} ions [5]. Due to the differences of AFE and FE phases in the unit cell parameters, this phase transition is accompanied by a nonlinear change in physical properties, such as an abrupt jump in polarization and strain, or a large charge release [4]. Lead cobalt niobate $Pb(Co_{1/3}Nb_{2/3})O_3$ (PCoN) is one of the first known relaxor ferroelectrics (RFE). The sub-micro-scale heterogeneous distribution of the B-cations is believed to be the origin of their relaxor nature, typically having a diffuse and frequency-dependent maximum in the variation of the relative permittivity with temperature [6]. PCoN was first reported by Smolenskii and Agranovskaya in 1958 [6, 7] that PCoN displays typical RFE behavior with a maximum dielectric constant occurring near −90 °C, and at 1 kHz [6].

Since PCoN is a relaxor ferroelectric with a broad dielectric peak near $T_c \approx -90$ °C and PZ is an antiferroelectric with a sharp maximum in the permittivity at $T_c \sim 230$ °C, the Curie temperature in the PZ–PCoN system can be engineered over a wide range of temperature by controlling the amount of PCoN in the system. Although the PZ ceramic has a better dielectric breakdown strength than PCoN, the sintering temperature is also higher [3, 8]. Thus, mixing

PCoN with PZ is expected to decrease the sintering temperature of PZ-based ceramics, a desirable move towards an electrode of lower cost [5]. Moreover, since PZ–PCoN is not a pure-relaxor ferroelectric system, it is easier to prepare single phase ceramics with a lower amount of undesirable pyrochlore phases [9]. Furthermore, no work has been done on the metastable FE phase induced by b-site substitution in perovskite PZ. With their complementary characteristics, it is expected that excellent properties can be obtained from ceramics in the PZ–PCoN system.

In this study, a metastable FE phase induced by b-site substitution was studied as a function of composition and temperature. The columbite precursor method was used to synthesize the $(1-x)PbZrO_3$–$xPb(Co_{1/3}Nb_{2/3})O_3$ (PZ–PCoN), with $x = 0.00$–0.30. The structural phase, microstructure and thermal properties of the PZ–PCoN ceramics were investigated as a function of composition x. DSC measurements were also used to study the details of AFE to FE and FE to PE phase transformations accompanied with an evaluation of the thermal behavior of the PZ–PCoN samples. The results were discussed.

2 Experimental procedure

The $(1-x)PbZrO_3$–$xPb(Co_{1/3}Nb_{2/3})O_3$ (PZ–PCoN), $0.00 \le x \le 0.30$, ceramics were prepared using a columbite precursor method in order to avoid the formation of a pyrochlore phase. The columbite phase $CoNb_2O_6$ was formed by reacting CoO (99.9%) with Nb_2O_5 (99.9%) at 1100 °C for 4 hours. The raw materials of PbO, ZrO_2 and $CoNb_2O_6$ were weighed and mixed. Each mixture of the starting powders was milled and mixed in a ball mill, as well as wet-homogenized with ethanol for 18 h using YTZ zirconia grinding media. The suspensions were dried and the powders were ground using an agate mortar and sieved into fine powder. All obtained powders were calcined at 850 °C for 2 h. The calcined powders were milled for 3 hours for reduced particle size. After grinding and sieving, the calcined powder was mixed with 5 wt% poly (vinyl alcohol) binder and uniaxially pressed into a pellet. Binder burnout occurred by slowly heating to 500 °C and holding for 2 hours. Sintering occurred between 1100–1250 °C with a dwell time of 4 hours depending on the composition. To mitigate the effects of lead loss during sintering, the pellets were sintered in a closed alumina crucible containing $PbZrO_3$ powder. The density of the sintered PZ–PCoN pellets was measured by the water immersion method (Archimedes method). The relative density of all the sintered pellets was approximately 94–96% of the theoretical density. The phase transition temperatures and enthalpy (ΔH) of the phase transitions were determined by DSC. This was operated from room temperature to 250 °C with a heating rate of 10 °C/min.

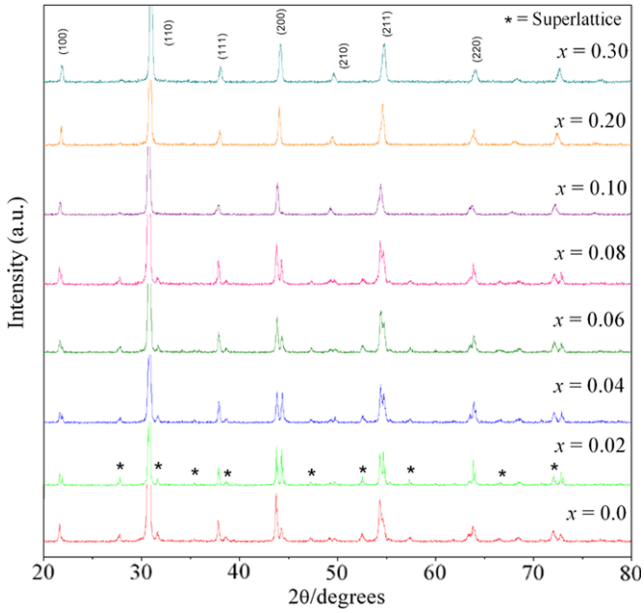

Fig. 1 XRD patterns of $(1-x)$PZ–xPCoN ceramics with $x = 0.0$–0.3 at the optimum sintering conditions

3 Results and discussion

Figure 1 shows XRD patterns of ceramics in the PZ–PCoN system with a well crystallized perovskite structure for all compositions. The pyrochlore phase was not observed in this system at all. Ceramics with $0.02 \le x < 0.1$ had the same crystal structure with PZ, i.e., an orthorhombic unit cell at room temperature. If the XRD pattern of PZ is indexed on the basic of the pseudo-cubic cell, then $1/4(h\ k\ l)$-type superlattice reflections representing the antiparallel shifts of Pb^{2+} ions will appear. In Fig. 1, all the indices were based on the pseudo-cubic cell, and the XRD patterns of the samples with $0.02 \le x < 0.1$ showed the presence of $1/4(h\ k\ l)$-type superlattice reflections. According to Glazer [10], these types of reflections represent antiphase tilting of the oxygen octrahedra without distortion. In Fig. 1, PZ–PCoN samples with $0.1 \le x \le 0.3$ showed only the fundamental reflections of the pseudo-cubic perovskite cell. The relative intensity of superlattice reflections decreased with increasing PCoN content as shown in Fig. 2. This result demonstrates that the superlattice disappeared with the addition of 10 mol% PCoN. Figure 2 shows the results for $1/4(h\ k\ l)$-type superlattice reflections, (1 1 1), (2 0 0) and (2 2 0) reflections. The samples with $x = 0.1$, 0.2 and 0.3 had a split (1 1 1) and (2 2 0) reflection and a single (2 0 0) reflection. This results confirms that the crystal structure of the samples with $x = 0.1$, 0.2 and 0.3 is primitive rhombohedral perovskite. For the pure rhombohedral structure, the 2 0 0 group of reflections should be a singlet. In the PZ–PCoN system, the A-site is occupied by Pb^{2+} (0.1630 nm) ions, and the Co^{2+}, Nb^{5+} and Zr^{4+} ions occupy the B site of

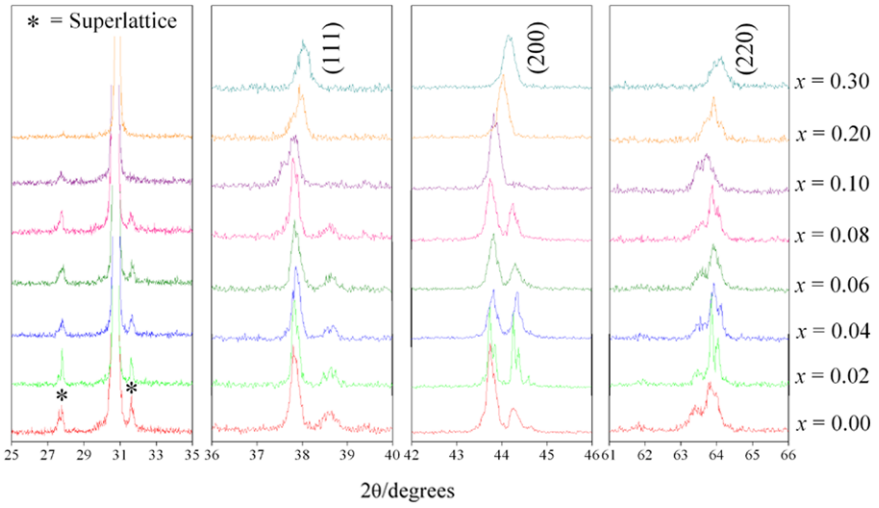

Fig. 2 XRD patterns of the 1/4(h k l)-type superlattice reflections, and the (1 1 1), (2 0 0) and (2 2 0) peaks of $(1-x)$PZ–xPCoN ceramics with $x = 0.0$–0.3

the ABO_3 perovskite crystal structure. The average ionic radius of B-site ions in the composition $(1-x)PbZrO_3$–$xPb(Co_{1/3}Nb_{2/3})O_3$ can be calculated from the following equation:

$$r_{\text{B-site}} = (1-x)\lfloor r_{Zr^{4+}}\rfloor + x\lfloor 1/3 r_{Co^{2+}} + 2/3 r_{Nb^{5+}}\rfloor, \quad (1)$$

where the ionic radii of Co^{2+}, Nb^{5+} and Zr^{4+} are 0.0790, 0.0780 and 0.0860 nm, respectively [11]. In general, the lattice parameters of the perovskite structure also decreased gradually as x increased, undoubtedly because of the introduction of the smaller cobalt niobium ion ($r = 0.783$ Å) into the zirconium site ($r = 0.86$ Å), resulting in a decreasing of the unit cell according to the Vegard rule. The effective size of the B-site ion increased with increasing mole fraction of PCoN primarily due to the smaller ionic radii of $(Co_{1/3}Nb_{2/3})^{4+}$. This shift in the B-site ionic radius is shown in the XRD data in Fig. 2 as the diffraction peaks are shifted toward higher angles. The influence of the addition of $Pb(Co_{1/3}Nb_{2/3})O_3$ on the phase structure of the $PbZrO_3$–$Pb(Co_{1/3}Nb_{2/3})O_3$ system is similar to that of $(Pb_{1-x}Ba_x)ZrO_3$ [12]. The substitution of smaller $(Co_{1/3}Nb_{2/3})^{4+}$ ions with Zr^{4+} sites, which implies the transition of the PZ–PCoN structure from orthorhombic to rhombohedral as shown in Fig. 2, may facilitate the parallel displacement along the [1 1 1] direction and the associated displacements of three oxygen ions in the PZ–PCoN structure, resulting in an improvement of ferroelectricity. The presence of a polar axis in the [1 1 1] direction has been reported for the ferroelectric rhombohedral structure [13].

The DSC technique was used as the primary tool to investigate the influence of the addition of $Pb(Co_{1/3}Nb_{2/3})O_3$ on phase transitions. Transition temperatures, including paraelectric (PE) transitions, are summarized in Table 1. Figure 3 shows the results of a differential scanning calorimeter (DSC) analysis of the PZ–PCoN samples. As shown in Fig. 3, two distinct endothermic peaks were observed for

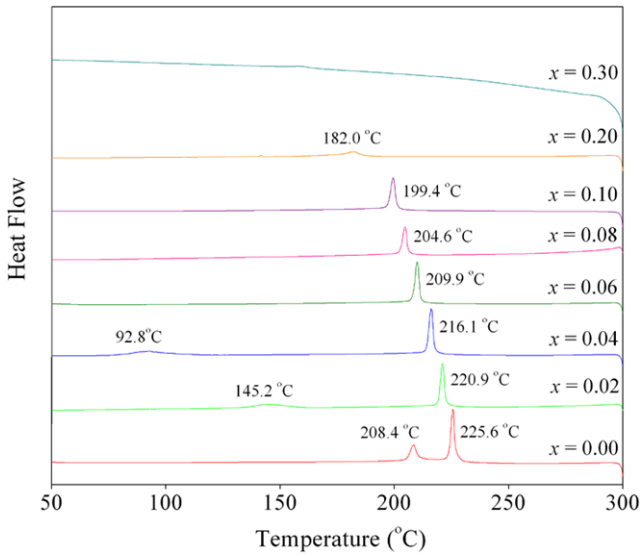

Fig. 3 Typical differential scanning calorimetry (DSC) curves for $(1-x)$PZ–xPCoN ceramics with $x = 0.0$–0.3

PZ–PCoN samples with $0.0 \le x \le 0.10$. The lower temperature corresponds to the transition temperature of the AFE → FE phase transition, while the higher temperature corresponds to the FE → PE phase transition. It is well known that the good quality ceramic as well as single crystal samples of PZ show two distinct endothermic peaks around 230 °C and 215 °C corresponding to the PE to FE and FE to AFE transitions, respectively, on cooling [14, 15]. The AFE → FE phase transition was found in the compositions of $0.0 \le x \le 0.10$. The peaks shift to lower temperatures with higher compositions of x. From Table 1, the width of the temperature range of FE phase continuously increases with PCoN content. The width of the temperature range of FE phase is around 17.2, 75.7, 123.3 and 176.9 °C for composition $x = 0.00$, 0.02, 0.04 and 0.06, respectively.

Table 1 Characteristics of $(1-x)$PZ–xPCoN ceramics with optimized processing conditions (R, Rhombohedral; O, Orthorhombic)

Composition (x)	Crystal structure	Lattice parameter (Å)			Phase transition temperature (°C)		Enthalpy (J/g)	
		a	b	c	AFE → FE	FE → PE	AFE → FE	FE → PE
0.00	O	7.27	9.92	8.21	208.4	225.6	1.19	2.63
0.02	O	7.25	9.92	8.21	145.2	220.9	1.60	3.44
0.04	O	7.23	9.91	8.21	92.8	216.1	1.71	3.47
0.06	O	7.27	9.92	8.2	33.3	209.9	1.03	2.83
0.08	O	7.25	9.93	8.22	–	204.6	–	2.78
0.10	R		4.11		–	199.4	–	2.40
0.20	R		4.10		–	182.0	–	1.20
0.30	R		4.09		–	158.2	–	0.44

It is of interest to note that the areas under two endothermic peaks in Fig. 3 decreased with increasing amount of PCoN. Since those areas represent the free-energy difference between the two phases, this result indicates that the addition of PCoN decreases the stability of the orthorhombic phase. It is apparent that the replacement of the Zr^{4+} ion by $(Co_{1/3}Nb_{2/3})^{4+}$ ions would decrease the driving force for antiparallel shift of Pb^{2+} ions, because they interrupt the translational symmetry. This interruption caused the appearance of a rhombohedral ferroelectric phase when the amount of PCoN was more than 10 mol%. Gotor et al. [16] studied the relationships between the structure change of $BaTiO_3$ and its enthalpy by using DSC. They found that the reduction of the tetragonality (c/a) of $BaTiO_3$ is accompanied by a reduction of the enthalpy. However, in the present work, the decreasing of ΔH is proportional to the fraction ratio of FE and PE phase in PZ–PCoN. Based on the results of x-ray diffraction and DSC data, the phase diagram for the $(1-x)$PZ–xPCoN binary system has been established, as shown in Fig. 4. The transition temperature decreases approximately linearly with x, from $T_c = 225.6\,°C$ for $x = 0.0$ to $158.2\,°C$ for $x = 0.3$. The phase diagram consists of three distinct crystallographic phases in this system; high temperature paraelectric cubic (*Pm3m*), rhombohedral (*R3m*), and ferroelectric orthorhombic (*P2cb* (no. 32)). At the low concentrations of PCoN with $x < 0.1$ the symmetry can be defined as orthorhombic. The orthorhombic symmetry transforms into rhombohedral at a composition near $x = 0.1$.

Figure 5(a) and (b) show scanning electron microscopy (SEM) images of the fracture surfaces of the PZ–PCoN ceramics at $x = 0.02$ and 0.2, respectively. No plate-like grains were observed in both samples, indicating the absence of pyrochlore formation. Other compositions of the system also exhibited a high density and an irregular grain size and shape. By applying the linear intercept methods to these SEM micrographs, the average grain size was calculated to be between 0.57 and 0.59 µm for all of the samples. There was no systematic variation in grain size as a function of composition according to the different sintering schedules used.

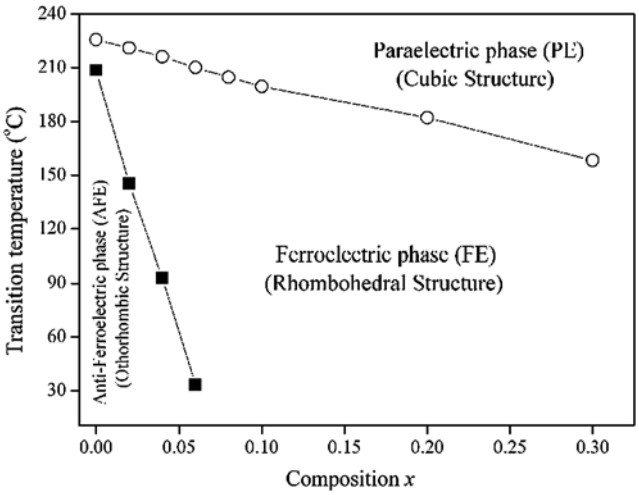

Fig. 4 Phase diagram of the $(1-x)$PZ–xPCoN binary system with $x = 0.0$–0.3 determined from room temperature XRD and DSC as a function of temperature. The symbols refer to quantities as follows: ■ = the transition temperature from the antiferroelectric state (AFE) to the ferroelectric state (FE); ○ = the transition temperature from the ferroelectric state (FE) to the paraelectric state (PE)

4 Conclusions

We have been the first to demonstrate the effect of PCoN in stabilizing the rhombohedral phase relative to the orthorhombic phase in PZ ceramics. The crystal structure data obtained from XRD indicates that the solid solution PZ–PCoN, where $x = 0.0$–0.3, successively transforms from orthorhombic to rhombohedral symmetry with an increase in PCoN concentration. The AFE → FE phase transition was found in the compositions of $0.0 \le x \le 0.10$. The AFE → FE phase transition shifts to lower temperatures with higher compositions of x. The width of the temperature range of the FE phase increases with increasing amount

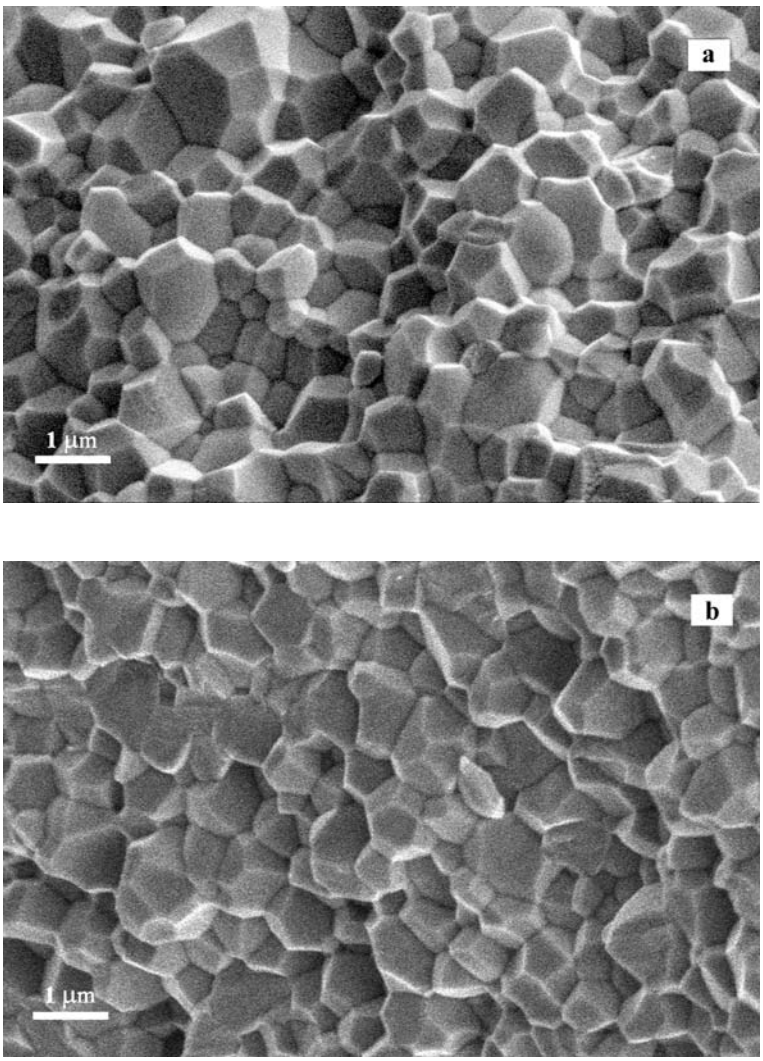

Fig. 5 Fracture surfaces of $(1-x)$PZ–xPCoN ceramics with (**a**) $x = 0.02$ and (**b**) $x = 0.2$

of PCoN. It is apparent that the replacement of the Zr^{4+} ion by $(Co_{1/3}Nb_{2/3})^{4+}$ ions would decrease the driving force for an antiparallel shift of Pb^{2+} ions because they interrupt the translational symmetry. This interruption caused the appearance of a rhombohedral ferroelectric phase when the amount of PCoN was more than 10 mol%.

Acknowledgements This work was supported by the Thailand Research Fund (TRF), National Research Council of Thailand (NRCT) and King Mongkut's Institute of Technology Ladkrabang (KMITL).

References

1. E. Sawaguchi, G. Shirane, S. Hoshino, Phys. Rev. **83**, 1078 (1951)
2. K. Uchino, *Ferroelectric Devices* (Dekker, New York, 2000)
3. G.H. Haertling, J. Am. Ceram. Soc. **82**, 797–818 (1999)
4. B.P. Pokharel, D. Pandey, Phys. Rev. B **65**, 214108 (2002)
5. Y. Xu, *Ferroelectric Materials and Their Application* (Elsevier, Amsterdam, 1991)
6. G.A. Smolenskii, A.L. Agranovskaya, Sov. Phys. Tech. Phys. 1380 (1958)
7. V.A. Isupov, Sov. Phys. Solid State **5**, 136 (1958)
8. B. Jaffe, W.R. Cook, *Piezoelectric Ceramic* (R.A.N. Publishers, 1971)
9. T.R. Shrout, A. Halliyal, Am. Ceram. Soc. Bull. **66**, 704 (1987)
10. A.M. Glazer, Acta Crystallogr. A **31**, 756 (1975)
11. R.D. Shannon, Acta Crystallogr. A **32**, 751 (1976)
12. B.P. Pokharel, D. Pandey, J. Appl. Phys. **86**, 3327–3332 (1999)
13. G. Shirane, S. Hoshino, Acta Crystallogr. **7**, 203 (1954)
14. G. Shirane, E. Sawaguchi, Y. Takagi, Phys. Rev. **84**, 476 (1951)
15. R.W. Whatmore, A.M. Glazer, J. Phys. C **12**, 1505 (1979)
16. F.J. Gotor, C. Real, M.J. Dianez, J.M. Criado, J. Solid State Chem. **123**, 301 (1996)

Japanese Journal of Applied Physics
Vol. 47, No. 2, 2008, pp. 998–1002

Synthesis and Dielectric and Ferroelectric Properties of Ceramics in $(1-x)Pb(Zr_{1/2}Ti_{1/2})O_3$–$(x)Pb(Co_{1/3}Nb_{2/3})O_3$ System

Anurak PRASATKHETRAGARN*, Naratip VITTAYAKORN[1], Supon ANANTA, Rattikorn YIMNIRUN, and David P. CANN[2]

Department of Physics, Faculty of Science, Chiang Mai University, Chiang Mai 50200, Thailand
[1]*Department of Chemistry, Faculty of Science, King Mongkut's Institute of Technology Ladkrabang, Bangkok 10520, Thailand*
[2]*Materials Science, Department of Mechanical Engineering, Oregon State University, Corvallis, OR 97331, U.S.A.*

(Received August 16, 2007; revised September 28, 2007; accepted October 26, 2007; published online February 15, 2008)

Ceramics in a PZT–PCN system with the formula $(1-x)Pb(Zr_{1/2}Ti_{1/2})O_3$–$(x)Pb(Co_{1/3}Nb_{2/3})O_3$, where $x = 0.1$–0.5, were prepared using a solid-state mixed-oxide technique (the columbite-wolframite precursor method). The phase formation behavior and microstructure were studied using X-ray diffraction (XRD) analysis and scanning electron microscopy (SEM), respectively. The dielectric and ferroelectric properties of the compounds were studied and discussed. Phase-pure perovskites of PZT–PCN ceramics were obtained over a wide compositional range. In addition, the XRD, dielectric, and ferroelectric properties confirmed that the morphotropic phase boundary (MPB) composition between the tetragonal and pseudo cubic phases of this system lied between $0.2 \leq x \leq 0.3$. [DOI: 10.1143/JJAP.47.998]

KEYWORDS: ferroelectric properties, perovskites, MPB, phase transition

1. Introduction

Lead-based perovskite-type solid solutions consisting of ferroelectric and relaxor materials have attracted more and more fundamental and practical attention because of their excellent dielectric, piezoelectric, and electrostrictive properties, which are useful in actuating and sensing applications.[1] Recently, many piezoelectric ceramic materials have been developed from binary systems containing a combination of relaxor and normal ferroelectric materials[2] that yield high dielectric permittivities [e.g., $Pb(Zn_{1/3}Nb_{2/3})O_3$–$PbTiO_3$ (PZN–PT)[3,4] and $Pb(Zr_{1/2}Ti_{1/2})O_3$–$Pb(Ni_{1/3}Nb_{2/3})O_3$ (PZT–PNN)[5]], excellent piezoelectric coefficients [e.g., $Pb(Zn_{1/3}Nb_{2/3})O_3$–$PbTiO_3$ (PZN–PT),[3,4] $Pb(Zr_{1/2}Ti_{1/2})O_3$–$Pb(Zn_{1/3}Nb_{2/3})O_3$ (PZN–PZT),[6] and $Pb(Sc_{1/3}Nb_{2/3})O_3$–$PbTiO_3$ (PSN–PT)[7,8]], and high pyroelectric coefficients [e.g., $Pb(Ni_{1/3}Nb_{2/3})O_3$–$PbTiO_3$–$PbZrO_3$ (PNN–PT–PZ)[9]]. Of the lead-based complex perovskites, lead zirconate titanate [$Pb(Zr_{1/2}Ti_{1/2})O_3$ or PZT] ceramics have been investigated from both fundamental and applied viewpoints.[10] A solid solution of $Pb(Zr_{1-x}Ti_x)O_3$ (PZT) was found to host exceptionally high value for dielectric and piezoelectric properties for compositions close to the morphotropic phase boundary (MPB). This MPB is located at a $PbTiO_3$:$PbZrO_3$ of $\sim 1:1$ and separates the Ti-rich tetragonal phase from the Zr-rich rhombohedral phase.[10] Furthermore, it has a high T_C of 390 °C, which allows piezoelectric devices to be operated at relatively high temperatures. Most commercial PZT ceramics are designed in the vicinity of the MPB with various doping methods in order to achieve high properties.

Lead cobalt niobate (PCN) is a perovskite relaxor ferroelectric with a broad diffuse phase transition near −70 °C.[11] The structure is cubic at room temperature (RT). In this compound, the octahedral sites of the crystal are randomly occupied by Co^{2+} and Nb^{5+} ions.[12] Malkov and Venevtsev have indicated that there are large deviations in the temperatures at which the permittivity is maximum (T_m) for single-crystal and ceramic samples.[13] The effects of the DC bias on the dielectric properties have been reported as a function of temperature for single-crystal $Pb(Co_{1/3}Nb_{2/3})O_3$ with a diffuse phase transition.[14] Although the paraelectric–ferroelectric transition temperature of PCN is below RT, it can be easily shifted upward with the addition of $PbTiO_3$ (PT), which is a normal ferroelectric compound with a phase transition at 490 °C.[15] In addition, it is well known that the addition of PZT enhances the piezoelectric, dielectric, and ferroelectric properties in a solid solution with a relaxor ferroelectric such as PZT–PZN,[16,17] PZT–PNN,[5] and PZT–PMN.[18] On the basis of this approach, solid solutions of PZT and PCN are expected to synergistically combine the properties of both the normal ferroelectric PZT and relaxor ferroelectric PCN, which could exhibit piezoelectric and dielectric properties that are better than those of the single-phase PZT and PCN.[12,19] There have been no systematic studies on the electrical properties of ceramics within a wide composition range between PZT and PCN.

The overall purpose of this study is to determine the phase transition, grain size, and composition dependence of the dielectric properties and ferroelectric behavior of ceramics in a $(1-x)Pb(Zr_{1/2}Ti_{1/2})O_3$–$(x)Pb(Co_{1/3}Nb_{2/3})O_3$ (where $x = 0.1$–0.5) binary system prepared using the columbite-wolframite precursor method.

2. Experimental Procedure

Reagent-grade oxides of PbO, CoO, Nb_2O_5, ZrO_2, and TiO_2 (anatase-structure) were used as raw materials. The columbite $CoNb_2O_6$ and wolframite $ZrTiO_4$ precursors were weighed and introduced into the batch calculations. $CoNb_2O_6$ and $ZrTiO_4$ powders were prepared at calcination temperatures of 1100 and 1450 °C for 2 h, respectively. In the present work, $(1-x)Pb(Zr_{1/2}Ti_{1/2})O_3$–$(x)Pb(Co_{1/3}Nb_{2/3})O_3$ samples with compositions of $x = 0.1$–0.5 were prepared from $ZrTiO_4$, $CoNb_2O_6$, and PbO powders. PZT–PCN powders were synthesized using the solid-state reaction of these raw materials and mixed by a vibro-milling technique in ethanol for 1 h. PbO excess of 2.0 mol % was constantly added to compensate for lead losses during calcination and sintering.[17] After drying, the product was calcined in an alumina crucible at a temperature of 950 °C.

*E-mail address: Prasatkhetragarn@yahoo.com

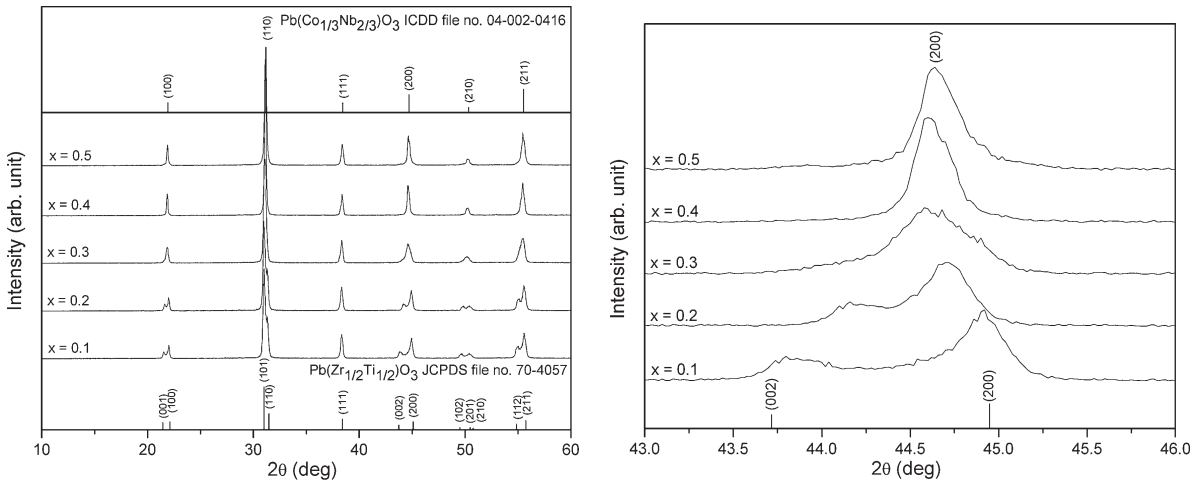

Fig. 1. XRD patterns of $(1-x)$PZT–(x)PCN ceramics, where $x = 0.1$–0.5.

The calcined powders were pressed hydraulically to form disc-shaped pellets with a diameter of 10 mm and a thickness of 1 mm, with 1 wt % poly(vinyl alcohol) (PVA) added as a binder. The pellets were sintered at 1200 °C for 2 h at a heating/cooling rate of 5 °C/min. The phase structure of the powders was analyzed via X-ray diffraction (XRD; Siemens-D500 diffractometer) analysis using Cu Kα radiation. The microstructures of the sintered samples were examined using scanning electron microscopy (SEM; JEOL JSM-840A). The dielectric properties of the samples were measured using an automated measurement system. This system consisted of an LCR meter (Hewlett-Packard HP-4284A) in connection with a Delta Design 9023 temperature chamber and a sample holder (Norwegian Electroceramics) capable of high-temperature measurement. The ferroelectric properties were examined using a simple Sawyer–Tower circuit.[18]

3. Results and Discussion

The XRD patterns of $(1-x)$PZT–(x)PCN ceramics with various x values are shown in Fig. 1. It can be seen that a complete crystalline solution of the perovskite structure is formed throughout the entire compositional range without the presence of pyrochlore or unwanted phases. From the XRD data, the $Pb(Zr_{1/2}Ti_{1/2})O_3$ ceramic is identified as a single-phase material with a perovskite structure having tetragonal symmetry, which was matched with JCPDS file no. 70-4057. The XRD patterns of the PZT–PCN compositions show a range in symmetry between the tetragonal and pseudo cubic perovskite types.[20] For a better comparison, ICDD file no. 04-002-0416 for $Pb(Co_{1/3}Nb_{2/3})O_3$ with pseudo cubic structural symmetry is also displayed in Fig. 1. It is clear that the crystal symmetry should change owing to the effects of increasing the PCN fraction and a corresponding decrease in T_C. It is well known that in the pseudo cubic phase, the (200) profile will show a single narrow peak, while in the tetragonal phase, the (200) profile should be split into two peaks. More interestingly, the composition at $x = 0.3$ exhibited peak broadening at a 2θ of $\sim$44–45°, indicating the structural transformation from the tetragonal phase, characterized by the shifting of the (002)/(200) peaks to the pseudo cubic phase. This observation is obviously associated with the composition showing the coexistence of two symmetries, which in this case are the tetragonal and pseudo cubic phases. To a first approximation, it could be said that the composition with $x = 0.3$ is close to the MPB of the $(1-x)$PZT–(x)PCN system, where the structure of the PZT–PCN compositions gradually changes from tetragonal to pseudo cubic. The electrical data described later on will further support this assumption.

The SEM images in Fig. 2 reveal that the addition of PCN resulted in significant changes in the microstructure of the ceramics. Some grains are observed to have irregular shapes with both open and close pores as a result of the high rate of the evaporation of PbO during the sintering.[17] The images also show that the grain size of the ceramics varied considerably from 0.43 to 19.56 µm (Table I). However, the average grain size significantly decreased with an increase in the content of PCN. It can also be seen that the maximum density is obtained in the 0.7PZT–0.3PCN ceramics, while the minimum density is observed in the 0.5PZT–0.5PCN ceramics. Interestingly, the density results can be correlated to the microstructure because high-density 0.7PZT–0.3PCN ceramics show high degrees of grain close packing, whereas low-density 0.5PZT–0.5PCN ceramics contain many closed pores.

The dielectric properties of $(1-x)$PZT–(x)PCN, where $x = 0.1$–0.5, are illustrated in Fig. 3. At RT, with an increase in the concentration of PCN, the dielectric constant tends to increase because the transition temperature of the PZT–PCN ceramics shift across RT; hence, the value of the dielectric properties measured at RT increased, as shown in Table II. Other authors have reported a similar behavior.[5] The temperature dependence of the dielectric constant for the compositions of the $(1-x)$PZT–(x)PCN system show broad dielectric peaks with an increase in the concentration of PCN, which indicate a diffuse phase transition. The diffuse phase transition may have been caused by a decrease in grain size; the observed difference in the degree of diffuseness could be a result of the grain size variation, as shown in Table II,[21] and chemical inhomogenieties within the $(1-x)$PZT–(x)PCN solid solution.[20]

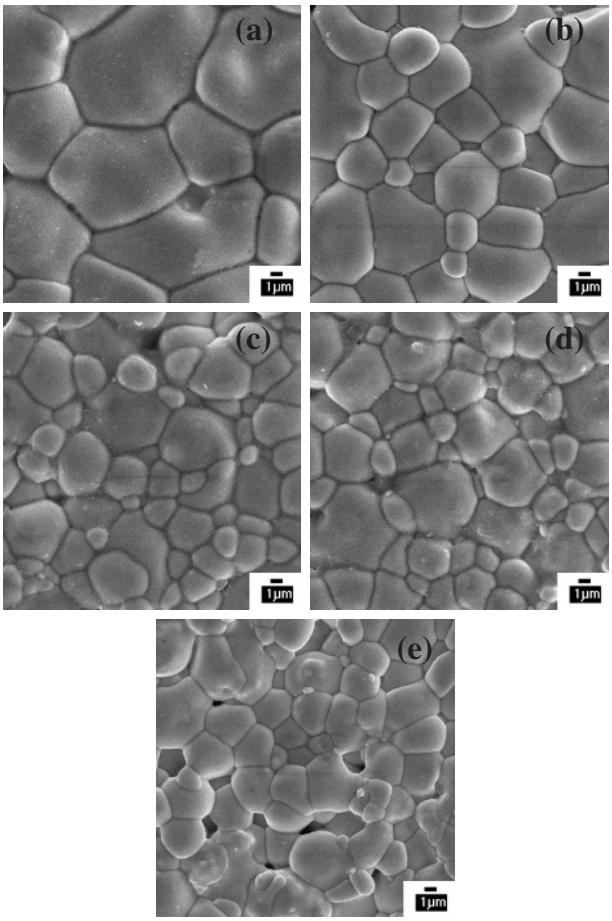

Fig. 2. SEM images of $(1-x)$PZT–(x)PCN ceramics with various compositions: $x =$ (a) 0.1, (b) 0.2, (c) 0.3, (d) 0.4, and (e) 0.5.

It should be noted that the formation of MPB could be clearly seen by the crystal structure analysis as described earlier. As is well known, the value of the dielectric and ferroelectric properties of a solid solution with MPB usually maximize approximately at the MPB. An anomaly at the MPB has been observed by our group in solid solution (x)PZT–$(1-x)$PNN.[5] However, no anomalies approximately at the MPB in the dielectric properties (Table II) could be found in the present work. In addition, the ferroelectric properties at approximately $x = 0.3$ are only slightly different from those of other compositions ($x = 0.2$, 0.4), rather than being "anomalously high". This could possibly be caused by a substitution of Ni^{2+} by Co^{2+} in the B-site, which shifts the MPB composition from $x = 0.2$ in the PZT–PNN system to $0.2 \leq x \leq 0.3$ in PZT–PCN. Since in this current work, we only started with compositions at 0.1 intervals, the exact MPB composition could not be clearly identified. However, as seen in Table II, the argument that the MPB composition should fall between $0.2 \leq x \leq 0.3$ in PZT–PCN is supported by all the XRD and electrical data, which show drastic decreases in the value of the electrical properties in compositions with $x > 0.3$.

The temperature dependence of the dielectric constant (ε_r) measured at 100 kHz for the $(1-x)$PZT–(x)PCN samples with $x = 0.1$–0.5 is shown in Fig. 3. In an ideal solid solution of PZT and PCN, the transition temperature is expected to vary linearly between 341 and 167 °C. As shown in Table II, the Curie temperature decreased as expected with an increase in PCN content. However, the ε_r peaks became broader with increasing PCN content at $x \geq 0.3$. It was confirmed that the composition with $0.2 \leq x \leq 0.3$ is close to the morphotropic phase boundary (MPB) of the $(1-x)Pb(Zr_{1/2}Ti_{1/2})O_3$–$(x)Pb(Co_{1/3}Nb_{2/3})O_3$ system.

Table I. Physical characteristics of $(1-x)$PZT–(x)PCN ceramics, where $x = 0.1$–0.5.

Ceramics ($x = 0.1$–0.5)	Density (g/cm^3)	Grain size range (μm)	Average grain size (μm)
0.9PZT–0.1PCN	7.39 ± 0.05	4.54–19.56	7.45 ± 0.05
0.8PZT–0.2PCN	7.46 ± 0.05	2.60–12.35	4.13 ± 0.05
0.7PZT–0.3PCN	7.62 ± 0.05	0.43–9.48	2.82 ± 0.05
0.6PZT–0.4PCN	7.42 ± 0.05	0.60–10.75	2.77 ± 0.05
0.5PZT–0.5PCN	7.31 ± 0.05	0.47–9.53	2.61 ± 0.05

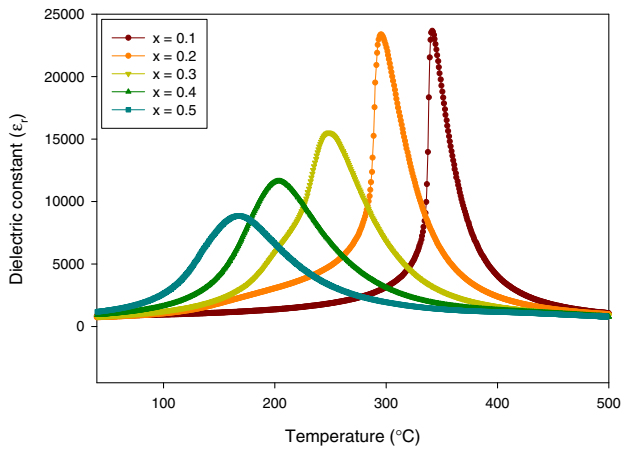

Fig. 3. (Color online) Dielectric constant (ε_r) of $(1-x)$PZT–(x)PCN ceramics at 100 kHz.

Table II. Dielectric and ferroelectric properties of $(1-x)$PZT–(x)PCN ceramics, where $x = 0.1$–0.5.

Ceramics ($x = 0.1$–0.5)	T_C (°C)	Dielectric properties				Ferroelectric properties (at 25 °C)			Loop squareness (R_{sq})
		ε_{max}	ε_{RT}	γ	δ	P_r (μC/cm^2)	P_s (μC/cm^2)	E_c (kV/cm)	
0.9PZT–0.1PCN	341.40	23700	740	1.52	14.72	2.9	4.1	8.45	1.52
0.8PZT–0.2PCN	295.50	23400	800	1.68	15.73	20.1	21.6	6.84	1.91
0.7PZT–0.3PCN	248.40	15500	840	1.81	16.55	20.9	22.6	6.92	1.94
0.6PZT–0.4PCN	203.50	11600	910	1.82	16.68	18.6	20.3	6.30	1.93
0.5PZT–0.5PCN	167.50	8900	1180	1.97	16.92	14.5	15.2	6.10	1.92

To further understand the dielectric behavior of the PZT–PCN system, the ferroelectric transition can analyzed through the Curie–Weiss relationship. For normal ferroelectrics such as PZT and PCN, above the Curie temperature, the dielectric constant follows the following equation:

$$\varepsilon = \frac{c}{T - T_0}, \tag{1}$$

where c is the Curie constant and T_0 is the Curie–Weiss temperature.[10,21,23] For a ferroelectric with a diffuse phase transition such as the PZT–PCN solid solutions, the following equation applies:

$$\frac{1}{\varepsilon} \approx (T - T_m)^2, \tag{2}$$

The above equation has been shown to be valid over a wide temperature range compared with the normal Curie–Weiss law [eq. (1)].[24,25] In eq. (2), T_m is the temperature at which the dielectric constant is maximum. If the local Curie temperature distribution is Gaussian, the reciprocal permittivity can be written in the form:[5,24]

$$\frac{1}{\varepsilon} = \frac{1}{\varepsilon_m} + \frac{(T - T_m)^\gamma}{2\varepsilon_m \delta^2}, \tag{3}$$

where ε_m is the maximum permittivity, γ is the diffusivity, and δ is the diffuseness parameter. For $(1-x)$PZT–(x)PCN compositions, the diffusivity (γ) and diffuseness parameter (δ) can be estimated from the slope and intercept of the dielectric data shown in Fig. 4, and tabulated in Table II.

γ and δ are both material constants depending on the composition and structure of the material.[5] γ is the expression of the degree of dielectric relaxation, while δ is used to measure the degree of diffuseness of the phase transition. In a material with a "pure" diffuse phase transition described by the Smolenskii–Isutov relation [eq. (2)], γ is expected to be 2.[26] The mean value of the diffusivity (γ) is extracted from these plots by fitting a linear equation. The values of γ vary between 1.52 and 1.97, which confirms that diffuse phase transition occurs in the PZT–PCN system. It is important to note that in perovskite ferroelectrics, it has been established that γ and δ can be affected by microstructure features, density, and grain size.[18] For PZT-rich ceramics, γ and δ increase with an increase in PCN content, confirming the diffuse phase transitions in PZT–PCN solid solutions. It is clear that the addition of PCN increases the degree of disorder in $(1-x)$PZT–(x)PCN over the compositional range $0.1 \leq x \leq 0.5$ with the highest degree of diffuseness exhibited in the 0.5PZT–0.5PCN composition. It should also be mentioned here that different dielectric behaviors could also be caused by grain size variation,[21] as noted in Table I.

The polarization–field (P–E) hysteresis loops of $(1-x)$PZT–(x)PCN ceramics measured at 15 kV/cm are shown in Fig. 5. A series of well-developed and mostly symmetric hysteresis loops are observed for all compositions. It is seen that the remanent polarization (P_r) varies significantly across the compositional range. However, the coercive field E_c is relatively constant, as shown in Table II. The ferroelectric parameters obtained from the P–E loops are plotted in Fig. 6. The remnant polarization (P_r) and saturated polarization (P_s) increased from $P_r = 2.9\,\mu C/cm^2$ and $P_s = 4.1\,\mu C/cm^2$ in 0.9PZT–0.1PCN to reach maximum values of $P_r = 20.9\,\mu C/cm^2$ and $P_s = 22.6\,\mu C/cm^2$ in 0.7PZT–0.3PCN. At higher PCN contents, they then drop to $P_r = 14.5\,\mu C/cm^2$ and $P_s = 15.2\,\mu C/cm^2$ in 0.5PZT–0.5PCN. However, it should be noted that the P_r ($2.9\,\mu C/cm^2$) for the composition $x = 0.1$ in the present work is

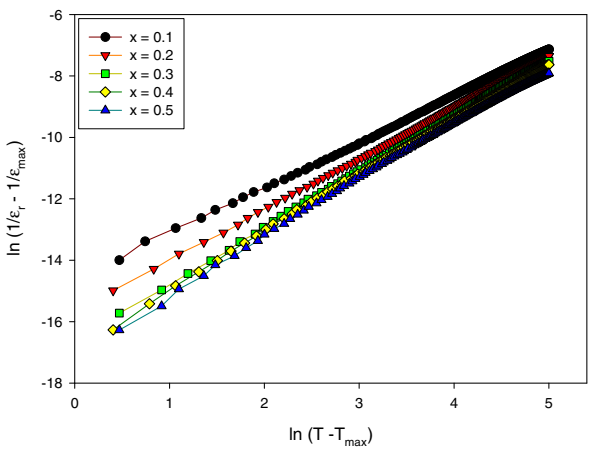

Fig. 4. (Color online) Variation of $\ln(1/\varepsilon_r - 1/\varepsilon_{max})$ vs $\ln(T - T_{max})$ of $(1-x)$PZT–(x)PCN ceramics.

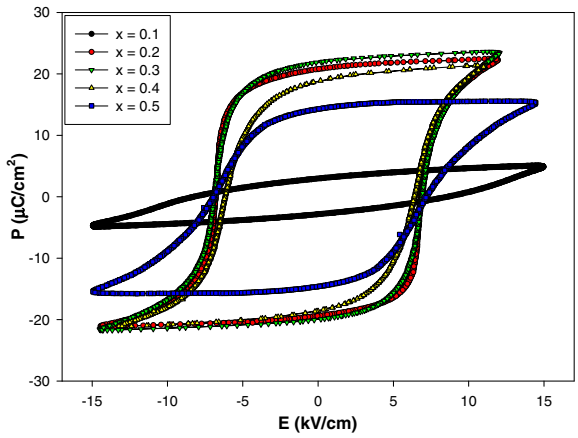

Fig. 5. (Color online) Effect of composition (x) on P–E hysteresis loops for $(1-x)$PZT–(x)PCN ceramics with $x = 0.1$–0.5.

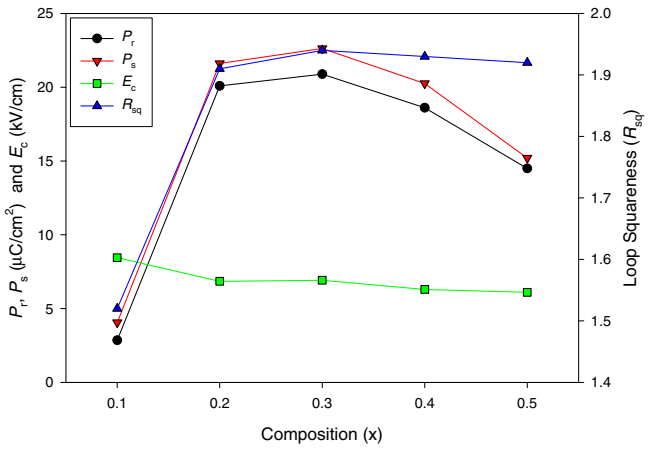

Fig. 6. (Color online) Remnant polarization (P_r), saturation polarization (P_s), coercive field (E_c), and loop squareness (R_{sq}) of $(1-x)$PZT–(x)PCN ceramics.

lower than the P_r ($\sim 15\,\mu C/cm^2$) in a previous study,[20] probably due to the fact that the solid-state conventional mixed oxide method used in the previous study[20] yielded two MPB compositions at $x = 0.1$ and 0.5, which is different from the columbite–wolframite method used in this study, which showed only one MPB composition at approximately $0.2 \leq x \leq 0.3$. It is well known that ferroelectric values, such as P_r, P_s, and E_c, show maximum values approximately at the MPB composition.

An empirical relationship between remnant polarization (P_r), saturation polarization (P_s) and polarization at the fields above the coercive field was derived by Haertling and Zimmer.[27] This permits the quantification of changes in the hysteresis behavior for the $(1-x)$PZT–(x)PCN samples through the following equation:

$$R_{sq} = \frac{P_r}{P_s} + \frac{P_{1.1E_c}}{P_s}, \tag{4}$$

where R_{sq} is the squareness of the hysteresis loop and $P_{1.1E_c}$ is the polarization at an electric field equal to 1.1 times the coercive field (E_c). For an ideal hysteresis loop, R_{sq} is equal to 2.0. As listed in Table II, the loop squareness parameter R_{sq} increased from 1.52 in 0.9PZT–0.1PCN to reach the maximum value of 1.94 in 0.7PZT–0.3PCN before decreasing to 1.92 in the 0.5PZT–0.5PCN composition. This observation is in good agreement with the *P–E* hysteresis loops, as depicted in Fig. 5. The results imply that the addition of 30 mol % PCN into PZT results in an optimized square *P–E* loop.

4. Conclusion

In this study, ceramics within the $(1-x)Pb(Zr_{1/2}Ti_{1/2})O_3$–$(x)Pb(Co_{1/3}Nb_{2/3})O_3$ solid solution system (where $x = 0.1$–0.5) were successfully prepared using a solid-state mixed-oxide technique. The PZT ceramic was identified by XRD analysis as a single-phase tetragonal perovskite, while the addition of PCN resulted in a gradual shift from tetragonal symmetry to pseudo cubic symmetry, with a possible MPB between the two phases located near the 0.7PZT–0.3PCN composition. However, the dielectric and ferroelectric properties did not show anomalously high value for the dielectric and ferroelectric properties at the 0.7PZT–0.3PCN composition, indicating that the MPB composition shifted to $0.2 \leq x \leq 0.3$ in the PZT–PCN system.

Acknowledgements

This work was supported by the Commission on Higher Education (CHE), the Thailand Research Fund (TRF), the Faculty of Science, and the Graduate School of Chiang Mai University.

1) A. J. Moulson and J. M. Herbert: *Electroceramics: Materials, Properties, Applications* (Wiley, Chichester, U.K., 2003).
2) S.-E. Park and T. R. Shrout: IEEE Trans. Ultrason. Ferroelectr. Freq. Control **44** (1997) 1140.
3) J. Kuwata, K. Uchino, and S. Nomura: Ferroelectrics **37** (1981) 579.
4) M. L. Mulvihill, L. E. Cross, W. Cao, and K. Uchino: J. Am. Ceram. Soc. **80** (1997) 1462.
5) N. Vittayakorn, G. Rujijanagul, X. Tan, M. A. Marquardt, and D. P. Cann: J. Appl. Phys. **96** (2004) 5103.
6) H. Fan, G.-T. Park, J.-J. Choi, J. Ryu, and H.-E. Kim: J. Mater. Res. **17** (2002) 180.
7) O. Furukawa, Y. Yamashita, M. Harata, T. Takahashi, and K. Inagaki: *5th Meet. Ferroelectric Materials and Their Applications, Kyoto, 1985*, Jpn. J. Appl. Phys. **24** (1985) Suppl. 24-3, p. 96.
8) V. J. Tennery, K. W. Hang, and R. E. Novak: J. Am. Ceram. Soc. **51** (1968) 671.
9) D. Luff, R. Lane, K. R. Brown, and H. J. Marshallsay: Trans. J. Br. Ceram. Soc. **73** (1974) 251.
10) L. E. Cross: Mater. Chem. Phys. **43** (1996) 108.
11) G. A. Smolenskii and A. L. Agranovskaya: Sov. Phys. Tech. Phys. **3** (1958) 1380.
12) T. Kudo, T. Yazaki, F. Naito, and S. Sugaya: J. Am. Ceram. Soc. **53** (1970) 326.
13) B. A. Malkov and Y. N. Venevtsev: Izv. Akad. Nauk Neorg. Mater. **13** (1977) 1468 [in Russian].
14) V. D. Saĺniov, Y. S. Kuźminov, and Y. N. Venevtsev: Izv. Akad. Nauk Neorg. Mater. **7** (1971) 1277 [in Russian].
15) C. Xu, Z. Duan, X. Wang, D. Yang, and K. Chen: J. Cryst. Growth **281** (2005) 543.
16) N. Vittayakorn, C. Puchmark, G. Rujijanagul, X. Tan, and D. P. Cann: Curr. Appl. Phys. **6** (2006) 303.
17) N. Vittayakorn, G. Rujijanagul, T. Tankasiri, X. Tan, and D. P. Cann: Mater. Sci. Eng. B **108** (2004) 258.
18) R. Yimnirun, S. Ananta, and P. Laoratanakul: J. Eur. Ceram. Soc. **25** (2005) 3235.
19) T. Hachiga, S. Fujimoto, and N. Yasuda: J. Phys. D **20** (1987) 1291.
20) N. Vittayakorn, S. Wirunchit, S. Traisak, R. Yimnirun, and G. Rujijanagul: Curr. Appl. Phys. **8** (2008) 128.
21) R. Yimnirun, S. Ananta, and P. Laoratanakul: Mater. Sci. Eng. B **112** (2004) 79.
22) I. W. Chen, P. Li, and Y. Wang: J. Phys. Chem. Solids **57** (1996) 1525.
23) G. H. Haertling: J. Am. Ceram. Soc. **82** (1999) 797.
24) A. Halliyal, U. Kumar, R. E. Newnham, and L. E. Cross: Am. Ceram. Soc. Bull. **66** (1987) 671.
25) R. D. Shannon and C. T. Prewitt: Acta Crystallogr., Sect. B **25** (1969) 925.
26) Y.-M. Chiang, D. P. Birnie, and W. D. Kingery: *Physical Ceramics* (Wiley, Chichester, U.K., 1997) p. 522.
27) G. H. Haertling and W. J. Zimmer: Am. Ceram. Soc. Bull. **45** (1966) 1084.

Phase Transitions and Dielectric Properties in $Bi(Zn_{1/2}Ti_{1/2})O_3$–$(Na_{1-y}Li_y)NbO_3$ Perovskite Solid Solutions

Chien-Chih Huang, Naratip Vittayakorn[1], Anurak Prasatkhetragarn[2], Brady J. Gibbons, and David P. Cann

Department of Mechanical Engineering, Oregon State University, Corvallis, OR 97331-6001, U.S.A.
[1] *Department of Chemistry, King Mongkut's Institute of Technology Ladkrabang, Bangkok 10520, Thailand*
[2] *Department of Physics, Chiang Mai University, Chiang Mai 50200, Thailand*

Received June 11, 2008; accepted November 24, 2008; published online March 23, 2009

Perovskite solid solutions based on the system $Bi(Zn_{1/2}Ti_{1/2})O_3$–$NaNbO_3$ were obtained via solid-state processing techniques. The crystal structure and ferroelectric phase transitions were studied by means of X-ray diffraction and dielectric measurements. A stable perovskite phase was obtained for $Bi(Zn_{1/2}Ti_{1/2})O_3$ substitutions up to 10 mol %. The dielectric characterization revealed that as the $Bi(Zn_{1/2}Ti_{1/2})O_3$ content increased, the transition temperature decreased and the transition peak became very diffuse. The polarization hysteresis loop and strain measurements presented evidence of an induced ferroelectric phase with 1 mol % $Bi(Zn_{1/2}Ti_{1/2})O_3$ substitutions. The planar coupling factor (k_p) for $0.01Bi(Zn_{1/2}Ti_{1/2})O_3$–$0.99NaNbO_3$ was measured to be 0.28. In addition, with the substitution of Li for Na in the $Bi(Zn_{1/2}Ti_{1/2})O_3$–$(Na_{1-y}Li_y)NbO_3$ system, the diffuseness of the transition peak decreased and the transition temperature increased.

DOI: 10.1143/JJAP.48.031401

1. Introduction

Sodium niobate, $NaNbO_3$, is a well-known perovskite material which possesses attractive dielectric properties and a complex series of phase transitions.[1–3] At room temperature, $NaNbO_3$ exhibits anti-ferroelectric behavior. However, by replacing Na with a small amount of dopant (e.g., Li or K), a ferroelectric phase can be induced.[4–6] Since $NaNbO_3$ is known to exhibit a wide range of solid solutions with other ABO_3 perovskites, it is a promising candidate for the development of lead-free piezoelectric materials.

In studying past literature reports, solid solutions between $NaNbO_3$ and other ABO_3 compounds can be divided into two groups.[7,8] In the first group, solid solutions with a small amount of a second component ABO_3 (e.g., $LiNbO_3$)[4] resulted in an intermediate pseudo-tetragonal ferroelectric phase and the compositional dependence of the transition temperature is rather smooth. In the second group, a ferroelectric orthorhombic phase replaces the anti-ferroelectric phase at a critical mole fraction of the second component (e.g., $NaTaO_3$).[9] More importantly, there is an abrupt change in the transition temperature as a function of composition.

There have been many efforts aimed at developing new materials without lead for piezoelectric applications. Perovskite compounds with Bi are excellent candidates for the substitution of Pb since Bi has a similar electronic structure to Pb. In addition, there are numerous Bi-based perovskite compounds that can be used in designing solid solutions to optimize properties.[10–12] Recently, Suchomel *et al.* reported a new piezoelectric material based on $Bi(Zn_{1/2}Ti_{1/2})O_3$–$PbTiO_3$. Their research revealed that $Bi(Zn_{1/2}Ti_{1/2})O_3$ acts to increase the transition temperature and enhances the tetragonality of $PbTiO_3$.[12] However, due to the smaller size of Bi^{3+} compared to Pb^{2+}, $Bi(Zn_{1/2}Ti_{1/2})O_3$ is unstable in its pure perovskite form.

In previous work, solid solutions within the ternary perovskite system $Bi(Zn_{1/2}Ti_{1/2})O_3$–$BiScO_3$–$BaTiO_3$ were explored. A stable perovskite phase was obtained for all compositions with a $BaTiO_3$ content greater than 50 mol %.

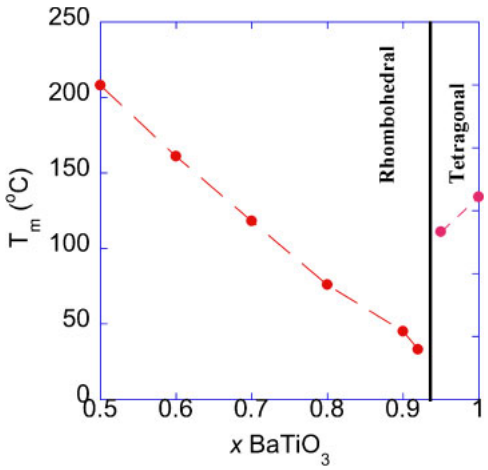

Fig. 1. (Color online) $(1-x)[Bi(Zn_{1/2}Ti_{1/2})O_3$–$BiScO_3]$–$xBaTiO_3$ system.[13]

Furthermore, a change in symmetry from pseudo-cubic to tetragonal was observed as the mole fraction of $BaTiO_3$ increased (Fig. 1).[13] Dielectric measurements showed a dielectric anomaly associated with a phase transformation over the temperature range of 30 to 210 °C for all compositions. Examination of the polarization hysteresis behavior revealed weakly non-linear hysteresis loops. With these data, ferroelectric phase diagrams were derived showing the transition between the pseudo-cubic relaxor behavior to the tetragonal normal ferroelectric behavior. This transition was also correlated to changes in the diffuseness parameter.

In order to develop lead-free piezoelectric materials, $NaNbO_3$ (NN) was used for this research due to its stable perovskite phase and highly solubility with other perovskite end members. In this paper, the phase equilibria and dielectric properties of the binary solid solution $Bi(Zn_{1/2}Ti_{1/2})O_3$–$NaNbO_3$ (BZT–NN) was examined. The doping effect was also studied to examine the effects of substituting Li for Na in the BZT–NN solid solutions. The purpose of this research is to focus on the influence of BZT on the

perovskite end member $NaNbO_3$ in terms of the transition temperature and its ferroelectric and dielectric properties.

2. Experimental Procedure

The synthesis of xBi($Zn_{1/2}Ti_{1/2}$)O_3–$(1-x)Na_{1-y}Li_yNbO_3$ ceramics followed conventional ceramic processing procedures. Reagent grade oxide powders of Bi_2O_3 (≥99.9%), ZnO (≥99%), TiO_2 (≥99.9%), Na_2CO_3 (≥99.5%), Nb_2O_5 (≥99.9%), and Li_2CO_3 (≥99%) were batched in stoichiometric amounts and ball-milled with ethanol and yttrium-stabilized zirconia media for 6 h. The dried powders were calcined in open crucibles at 920 °C for 6 h followed by an additional milling and drying step. The calcined powders were mixed with 3 wt % poly(vinyl butyral) (PVB) and then uniaxially cold-pressed at 150 MPa into 12.7 mm diameter pellets. Following binder burnout at 400 °C, the pellets were sintered in sealed crucibles between 1110–1150 °C for 2 h. For phase determination, X-ray diffraction (XRD; Bruker-AXS D8) was utilized in the 2θ scan range of 10–80° using sintered pellets.

Prior to the electrical measurements, the pellets were polished to obtain smooth and parallel surfaces. After polishing, a silver electrode paste (Heraeus C1000) was applied and then fired at 650 °C. An Agilent 4284A LCR meter was used to measure the dielectric properties over a wide temperature range using a NorECS ProboStat high temperature measurement cell. Polarization hysteresis measurements (P–E) were determined at a frequency of 4 Hz using a ferroelectrics test system (Radiant). The strain as a function of applied electric field was obtained by using an optical displacement sensor (MTI-2100). Before the measurement of piezoelectric properties, the samples were sputtered with gold and poled under an electric field of 6–7 kV/mm in silicon oil at room temperature for 10 min. At 24 h after the samples were poled, the planar coupling factors (k_p) were determined by the resonance–antiresonance[13] method which was measured by using Solartron impedance analyzer (SI-1260). The piezoelectric coefficient, d_{33}, was measured by using a d_{33} meter (Sinocera YE2730A).

3. Results and Discussion

3.1 Crystal structure of Bi($Zn_{1/2}Ti_{1/2}$)O_3–$NaNbO_3$ (BZT–NN) solid solutions

The XRD patterns of sintered xBZT–$(1-x)$NN ceramics shown in Fig. 2 revealed that the perovskite phase was retained with a maximum of 10 mol % BZT added. Higher concentrations of BZT resulted in the formation of numerous secondary phases. Initially, compositions rich in $NaNbO_3$ exhibited peak splitting consistent with orthorhombic symmetry as expected. However, with increasing BZT content the separation between diffraction peaks corresponding to orthorhombic symmetry became narrower and eventually merged into a single broad peak at about $x = 0.05$. The merging of peaks indicates a decrease in the tilt angle within the monoclinic system.

Figure 3 highlights the diffraction peaks that illustrate the evolution of the crystal structure and symmetry as a function of composition. The data clearly shows that the orthorhombic structure is maintained, though the decrease in peak intensity suggests that the orthorhombic distortion becomes vanishingly small. The following section presents data on the phase transition via dielectric measurements, and it is clear that as the BZT content increases the phase transition approaches room temperature and becomes diffuse. For these reasons, it is not unexpected that the diffraction data is somewhat ambiguous.

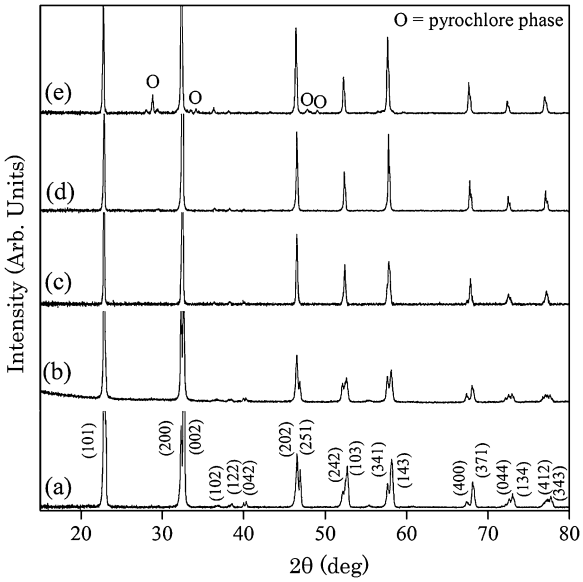

Fig. 2. XRD data for xBi($Zn_{1/2}Ti_{1/2}$)O_3–$(1-x)NaNbO_3$: (a) x = 0.01, (b) x = 0.05, (c) x = 0.075, (d) x = 0.1, and (e) x = 0.15.

Table I. Physical properties of xBZT–$(1-x)$NN perovskite ceramics.

	x BZT				
	0	0.01	0.05	0.075	0.1
$\rho_{theoretical}$ (g/cm^3)	4.575	4.613	4.774	4.877	4.955
ρ (%)	95	92.4	93.2	92.5	93.1

3.2 Dielectric properties of BZT–NN solid solutions

Table I shows the densities of the ceramics as a function of BZT content. The measured density decreased slightly when a small amount of BZT was added into the solid solution. The dielectric constant plotted against temperature for xBi($Zn_{1/2}Ti_{1/2}$)O_3–$(1-x)NaNbO_3$ from $x = 0.01$ to 0.1 is presented in Fig. 4. It is shown that the maximum permittivity, ε_m, retained similar values for all compositions. However, a diffuse phase transition was observed for compositions where $x > 0.05$ and the transition became more diffuse with increasing BZT content. The dielectric anomaly at around 50 °C for the $x = 0.01$ composition shown in Fig. 4(b) may be related to the phase transition that occurs at a similar temperature in pure $NaNbO_3$.[3]

The temperature at which the maximum dielectric constant appeared, defined as T_m, is plotted as a function of composition in Fig. 5. It is clear that for small amounts of BZT in the solid solution, a decrease in T_m was observed with increasing BZT content. At BZT concentrations greater than $x = 0.05$, T_m dramatically decreased. The trend of the transition temperature as a function of composition matches the description of the second group of $NaNbO_3$–ABO_3 solid solutions in which the antiferroelectric phase transitions to a

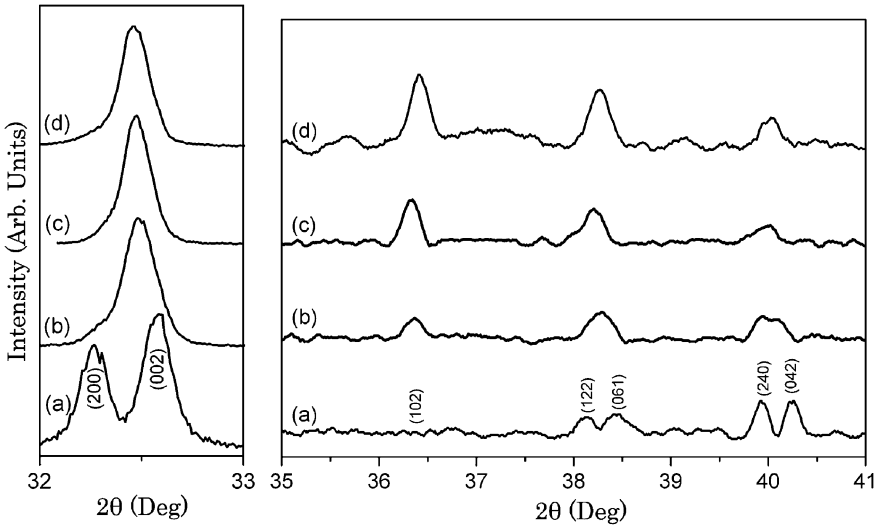

Fig. 3. XRD data for xBi($Zn_{1/2}Ti_{1/2}$)O_3–(1 − x)$NaNbO_3$: (a) x = 0.01, (b) x = 0.05, (c) x = 0.075, and (d) x = 0.1.

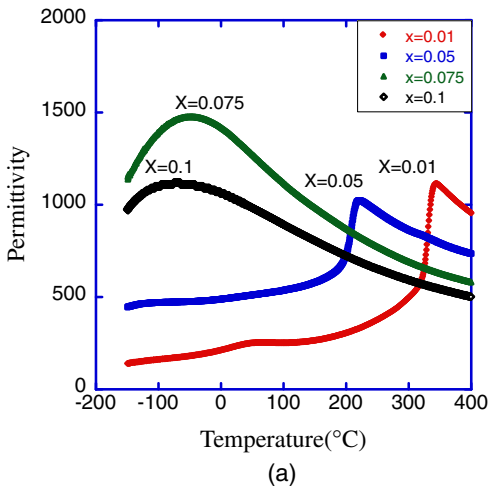

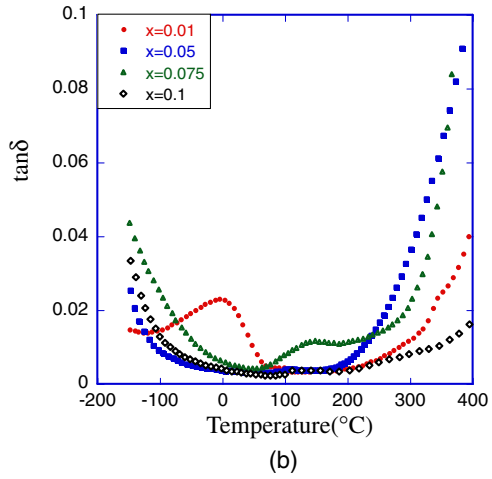

Fig. 4. (Color online) Permittivity and tan δ as a function of temperature for xBi($Zn_{1/2}Ti_{1/2}$)O_3–(1 − x)$NaNbO_3$ at a measuring frequency of 10 kHz.

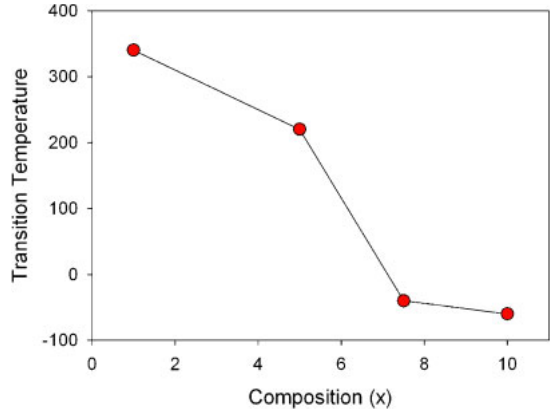

Fig. 5. (Color online) Compositional dependence of the transition temperature for xBi($Zn_{1/2}Ti_{1/2}$)O_3–(1 − x)$NaNbO_3$.

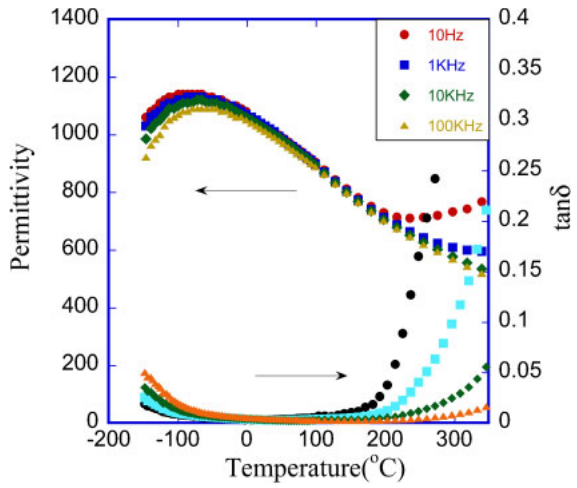

Fig. 6. (Color online) Permittivity and tan δ as a function of frequency for 0.1Bi($Zn_{1/2}Ti_{1/2}$)O_3–0.9$NaNbO_3$.

ferroelectric phase with the addition of second component.[6] This general trend is also similar to that observed in the ternary Bi($Zn_{1/2}Ti_{1/2}$)O_3–$BiScO_3$–$BaTiO_3$ system. Based on these reports, ferroelectric properties can be expected within the Bi($Zn_{1/2}Ti_{1/2}$)O_3–$NaNbO_3$ solid solution.

The dielectric properties as a function of frequency for the 0.1Bi($Zn_{1/2}Ti_{1/2}$)O_3–0.9$NaNbO_3$ composition is shown in Fig. 6. With only 10 mol % BZT introduced into the solid solution the maximum dielectric constant is shifted to below room temperature indicating a significant destabilization of

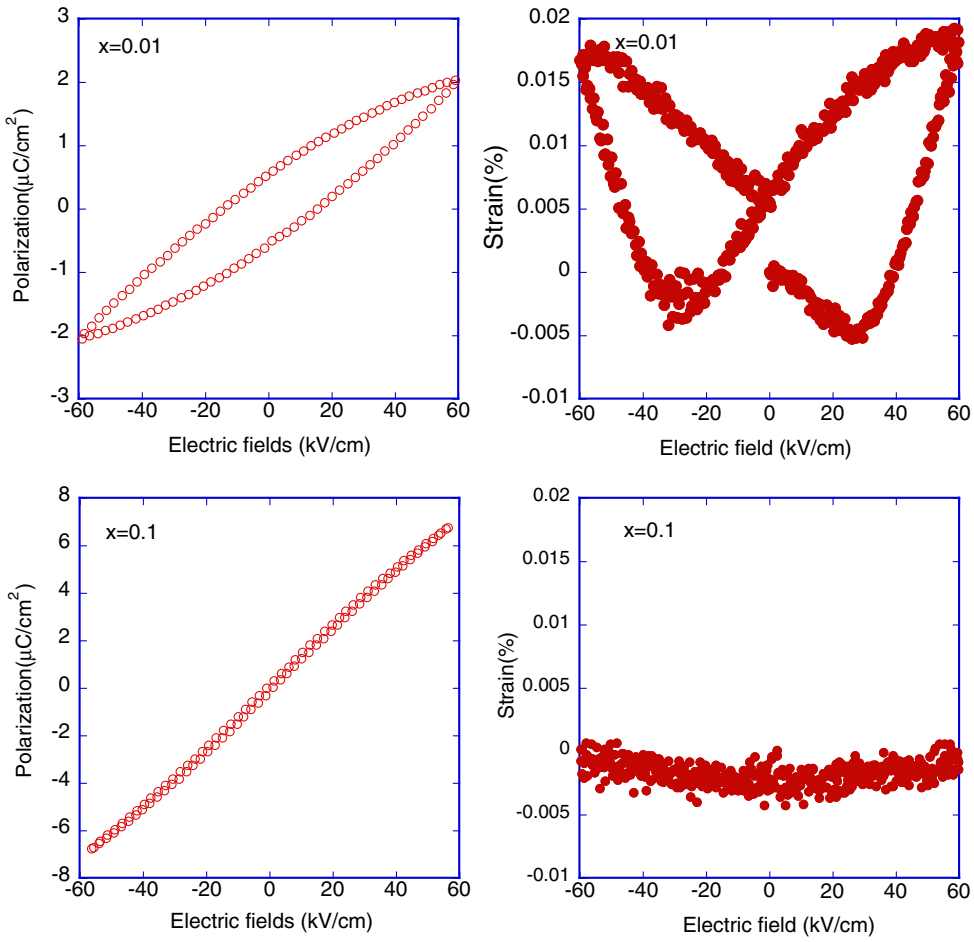

Fig. 7. (Color online) Polarization and strain vs electric field for xBi($Zn_{1/2}Ti_{1/2}$)O_3–(1 – x)$NaNbO_3$ at 4 Hz at room temperature.

the ferroelectric phase. This is confirmed in the XRD data where room temperature measurements indicated very weak orthorhombic distortions.

At higher temperatures, the increase in permittivity and dielectric loss is most likely not due to a phase transition but rather due to the onset of conduction losses presumably tied to non-stoichiometry. At lower temperatures, a strong frequency dependence characteristic of relaxor ferroelectric behavior was observed in the vicinity of the dielectric maximum.

The polarization and strain as a function of applied electric field was measured at room temperature for a number of BZT–NN solid solutions (Fig. 7). The broad hysteresis loop observed for the 1 mol % BZT composition indicates that ferroelectric behavior was induced with the substitution of BZT. The strain data confirmed the existence of ferroelectric behavior. However at higher BZT concentrations, the *P–E* data exhibited linear behavior. The loss of hysteresis can be explained by the decrease of the transition temperature due to the increase in cation disorder at higher BZT concentrations.

The planar coupling factor (k_p) for 0.01Bi($Zn_{1/2}Ti_{1/2}$)O_3–0.99$NaNbO_3$ was measured to be 0.28 based on the resonance–antiresonance method. The measurement was conducted 24 h after the sample was poled. The piezoelectric coefficient, d_{33}, was measured at 38 pC/N. The depolarization temperature (T_d) was measured to be 280 °C which is lower than the transition temperature $T_C \approx 340$ °C shown in Fig. 4(a). Combining all the data from the polarization hysteresis, strain, and piezoelectric measurements, the existence of the ferroelectric state can be confirmed with only $x = 0.01$ mole fraction of BZT added. This behavior is very similar to the effects of small amounts of Li substituted into $NaNbO_3$.[15]

3.3 Doping effects in BZT–NN

In order to investigate the effect of doping within $NaNbO_3$–ABO_3 solid solutions, $LiNbO_3$ was substituted for $NaNbO_3$. The Li ion is approximately 20% smaller than Na and has been found to introduce an instability into the crystal structure. The effects of replacing Li^+ for Na^+ in the composition 0.1Bi($Zn_{1/2}Ti_{1/2}$)O_3–0.9$Na_{1-y}Li_yNbO_3$ is shown in Figs. 8 and 9. The perovskite structure remained stable with up to 10 mol % Li added. At higher concentrations secondary phases appeared in the diffraction data. As can be seen in the dielectric and *P–E* hysteresis data, the addition of Li had two effects. First, it increased T_m from below room temperature to nearly 100 °C for 10 mol % Li added. This indicates that the stability of the ferroelectric phase was enhanced with the addition of Li which is confirmed by the broadening of the ferroelectric hysteresis loops as shown in Fig. 9. In addition, the phase transition sharpened with the addition of Li as the system shifted from relaxor to normal ferroelectric behavior. Room temperature XRD measurements are mostly inconclusive because the phase transition is in the vicinity of room temperature.

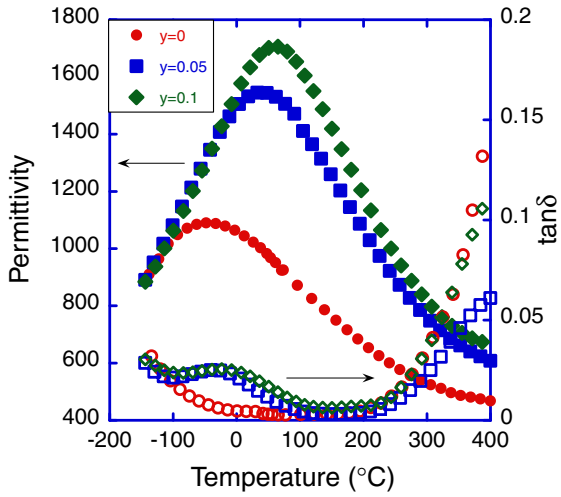

Fig. 8. (Color online) Permittivity and tan δ as a function of temperature for $0.1Bi(Zn_{1/2}Ti_{1/2})O_3$–$0.9Na_{1-y}Li_yNbO_3$.

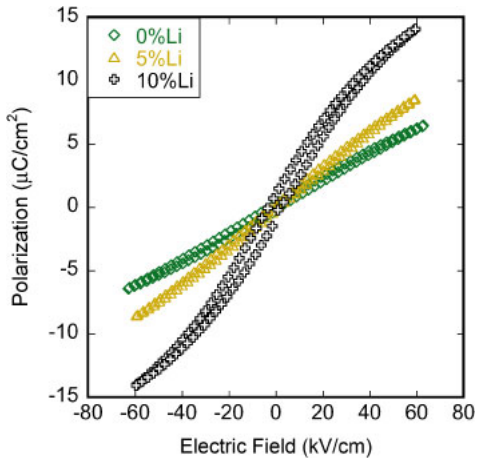

Fig. 9. (Color online) Polarization vs electric field for $0.1Bi(Zn_{1/2}Ti_{1/2})O_3$–$0.9Na_{1-y}Li_yNbO_3$ at 4 Hz at room temperature.

Temperature dependent diffraction measurements are currently underway to track the change in symmetry as a function of temperature. These results are very different than observations in the $NaNbO_3$–$LiNbO_3$ and $NaNbO_3$–$KNbO_3$ binary system,[4,6] where a pseudo-tetragonal phase transition was not observed in XRD and dielectric data.

4. Conclusions

In this work, the phase equilibria and dielectric properties of the binary solid solution $Bi(Zn_{1/2}Ti_{1/2})O_3$–$NaNbO_3$ (BZT–NN) were examined. A combination of XRD and dielectric data indicated that a stable perovskite phase with orthorhombic symmetry was observed for compositions rich in $NaNbO_3$. As the BZT concentration increased the transition temperature dropped below room temperature and correspondingly the orthorhombic distortion weakened. The abrupt decrease of the transition temperature indicates the formation of a ferroelectric phase which was confirmed by *P*–*E* loop and strain measurements. The planar coupling factor (k_p) for $0.01Bi(Zn_{1/2}Ti_{1/2})O_3$–$0.99NaNbO_3$ was measured at 0.28. Through substitution of Li for Na in the NN–BZT solution, the diffuseness of the transition peak decreased and transition temperature increased.

1) H. D. Megaw: Ferroelectrics **7** (1974) 87.
2) C. N. W. Darlington and K. S. Knight: Acta Crystallogr., Sect. B **55** (1999) 24.
3) S. Lanfredi, M. H. Lente, and J. A. Eiras: Appl. Phys. Lett. **80** (2002) 2731.
4) T. Nitta: J. Am. Ceram. Soc. **51** (1968) 623.
5) M. A. L. Nobre and S. Lanfredi: J. Appl. Phys. **93** (2003) 5557.
6) G. Shirane, R. Newnham, and R. Pepinsky: Phys. Rev. **96** (1954) 581.
7) G. A. Smolenskii, V. A. Bokov, V. A. Isupov, N. N. Krainik, R. E. Pasynkov, and A. I. Sokolov: *Ferroelectrics and Related Materials* (Gordon & Breach, New York, 1984) p. 634.
8) I. P. Raevski and A. A. Prosandeev: J. Phys. Chem. Solids **63** (2002) 1939.
9) H. Iwasaki and T. Ikeda: J. Phys. Soc. Jpn. **18** (1963) 157.
10) R. E. Cohen: Nature **358** (1992) 136.
11) M. R. Suchomel and P. K. Davies: J. Appl. Phys. **96** (2004) 4405.
12) M. R. Suchomel and P. K. Davies: Appl. Phys. Lett. **86** (2005) 262905.
13) C.-C. Huang, D. P. Cann, X. Tan, and N. Vittayakorn: J. Appl. Phys. **102** (2007) 044103.
14) M. Onoe and H. Jumonji: J. Acoust. Soc. Am. **41** (1967) 974.
15) R. R. Zeyfang, R. M. Henso, and W. J. Maier: J. Appl. Phys. **48** (1977) 3014.

High temperature phases in the $0.98PbZrO_3-0.02Pb(Ni_{1/3}Nb_{2/3})O_3$ ceramic

W. Qu,[1] X. Tan,[1,a)] N. Vittayakorn,[2] S. Wirunchit,[2] and M. F. Besser[3]
[1]*Department of Materials Science and Engineering, Iowa State University, Ames, Iowa 50011, USA*
[2]*Department of Chemistry, King Mongkut's Institute of Technology, Ladkrabang, Bangkok 10502, Thailand*
[3]*Materials and Engineering Physics Program, Ames Laboratory, U.S.-DOE, Ames, Iowa 50011, USA*

(Received 28 September 2008; accepted 22 November 2008; published online 13 January 2009)

The phase evolution with temperature in the $0.98PbZrO_3-0.02Pb(Ni_{1/3}Nb_{2/3})O_3$ ceramic was investigated with dielectric permittivity and polarization measurements, hot stage transmission electron microscopy, and high temperature x-ray diffraction. Below 190 °C, the ceramic is in the antiferroelectric phase with characteristic $\frac{1}{4}\{110\}_c$ superlattice diffractions. In this stage, typical antiferroelectric 180° domains were observed. Between 190 and 220 °C, an intermediate phase, which is characterized by $\frac{1}{2}\{110\}_c$-type superlattice diffractions, was detected. Evidences are found to suggest that this intermediate phase is ferroelectric. The $\frac{1}{2}\{110\}_c$-type superlattice diffraction persists even into the paraelectric phase above 220 °C. In addition, there exists an incommensurate phase between the low temperature antiferroelectric phase and the intermediate ferroelectric phase.
 [DOI: 10.1063/1.3065087]

I. INTRODUCTION

The classic antiferroelectric (AFE) compound lead zirconate ($PbZrO_3$ or PZ) has been extensively studied since 1950s.[1] At temperatures below 220 °C, $PbZrO_3$ displays an orthorhombic perovskite structure with antiparallel shifts of Pb^{2+} ions along the pseudocubic ⟨110⟩ direction, which leads to the AFE behavior.[1,2] The space group for the low temperature AFE phase was determined to be *Pbam*.[3–5] At temperatures above 230 °C, $PbZrO_3$ is in the paraelectric phase with the cubic $m3m$ symmetry.[2] In between the AFE and the paraelectric phase within a narrow temperature range, there is an intermediate phase, which is characterized by $\frac{1}{2}\{110\}_c$-type superlattice diffractions.[2,5–8] However, the nature of this intermediate phase is still open for debate. Experimental evidence have been found to support either a ferroelectric[2,6,7] or an AFE[5,8] phase.

In our previous study, it has been found that by introducing minor amounts (2–6 mol %) of relaxor ferroelectric $Pb(Ni_{1/3}Nb_{2/3})O_3$ (PNN) into PZ, the temperature range is expanded for an intermediate phase, which is characterized by an evident frequency dispersion in dielectric permittivity. As a consequence, a series of striking phase transitions was revealed by the dielectric measurement.[9] In the present work, the $0.98PbZrO_3-0.02Pb(Ni_{1/3}Nb_{2/3})O_3$ (PZ98-PNN2) ceramic was selected to further investigate the phase evolution sequence during heating up to 300 °C with hot stage transmission electron microscopy (TEM) and high temperature x-ray diffraction (XRD).

II. EXPERIMENTAL PROCEDURE

The phase pure PZ98-PNN2 ceramic was prepared using the columbite precursor method in order to avoid the pyrochlore phase formation. Detailed preparation procedures have been reported in our previous publications.[9–11] The relative density of the as-sintered ceramic was measured using the Archimedes method to be 98%. The grain size was examined by scanning electron microscopy (SEM) (JEOL JSM-606LV). As shown in Fig. 1, the freshly fractured cross section of the PZ98-PNN2 ceramic is almost free of pores and the grain size is in the range of 2–5 μm.

The surface layers of the sintered pellets were removed by mechanical grinding. XRD analysis was performed with Cu $K\alpha$ radiation at a series of temperatures up to 300 °C on a PANalytical X-Pert Pro diffraction system to investigate the structural evolution. Dielectric properties were measured with an *LCR* meter (HP-4284A, Hewlett-Packard) on a Au-electroded specimen during heating from room temperature to 300 °C at a rate of 2 °C/min. The electrical polarization versus field hysteresis loops were recorded at a series of temperature with a standardized ferroelectric test system (RT-66A, Radiant Technologies). The peak field was maintained at 20 kV/cm during measurement.

Thin disks with a diameter of 3 mm were cut from the as-sintered ceramic pellet, ground, and polished to a thickness of 0.15 mm for TEM specimen preparation. The central portion of the disks was further thinned and polished by mechanical dimpling. Argon ion mill was then used to per-

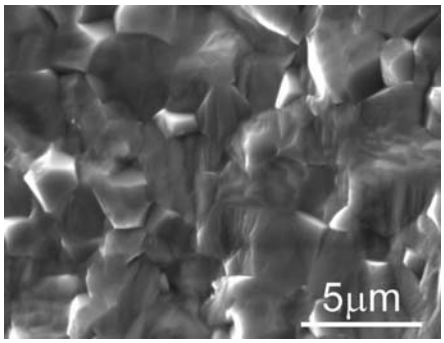

FIG. 1. SEM micrograph of the freshly fractured cross section of the PZ98-PNN2 ceramic.

a)Electronic mail: xtan@iastate.edu.

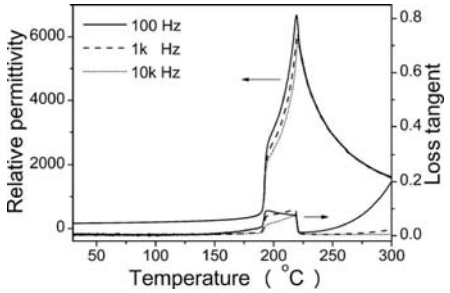

FIG. 2. Dielectric properties during heating at 100 Hz, 1 kHz, and 10 kHz in a bulk PZ98-PNN2 ceramic.

forate the disk at the center. Hot-stage TEM observations were performed with a heating rate less than 2 °C/min on a Philips CM30 instrument operating at 300 kV. Bright field images and selected area electron diffraction (SAED) patterns were recorded 10 min after the temperature was stabilized.

III. RESULTS AND DISCUSSION

A. Electrical properties

The temperature dependence of relative dielectric permittivity and loss tangent was measured at frequencies of 100 Hz, 1 kHz, and 10 kHz during heating from 30 to 300 °C and the results are displayed in Fig. 2. Clearly, there are two abrupt changes in both relative permittivity and loss tangent in the PZ98-PNN2 ceramic. The first one occurred at around 190 °C where both relative permittivity and loss tangent increased by one order of magnitude. The second abrupt change took place at the Curie temperature of 220 °C where significant suppression of loss tangent is seen. Therefore, the dielectric response in the PZ98-PNN2 ceramic can be divided into three stages. At temperatures below 190 °C, the relative permittivity and the loss tangent both have low values and show negligible increases with increasing temperatures. At temperatures above 220 °C, the relative permittivity starts to decrease following the Curie–Weiss law, $\varepsilon_r = C/(T-T_0)$, where ε_r is the relative permittivity, T is the temperature, and C and T_0 are Curie constant and Curie point, respectively. By fitting the data between 220 and 300 °C in Fig. 2, C and T_0 were determined to be 1.89×10^5 and 185.8 °C, respectively. In the intermediate temperature range (190–220 °C), the relative permittivity increases dramatically, while the loss tangent remains high around 0.1. The most remarkable feature of the dielectric behavior in this temperature range is the evident frequency dispersion of both relative permittivity and loss tangent, resembling that in relaxor ferroelectric ceramics. T_{max}, the temperature at which the maximum dielectric permittivity is achieved, was measured to be 219.4 °C at 100 Hz, 220.1 °C at 1 kHz, and 220.4 °C at 10 kHz, respectively, shifting slightly toward higher temperatures with increasing frequency.

To further clarify the dielectric behavior of the different phases in the PZ98-PNN2 ceramic, electrical polarization hysteresis loop measurements were performed under a peak field of 20 kV/cm at a series of temperatures. During heating,

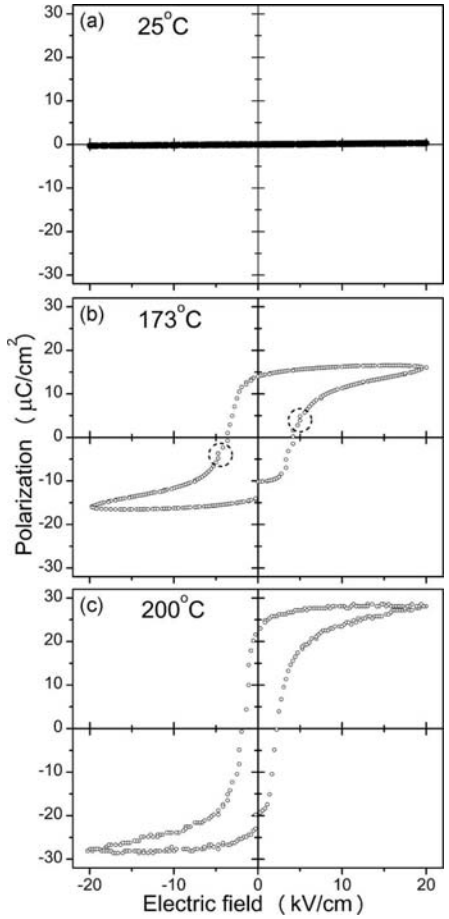

FIG. 3. Polarization hysteresis loops recorded from a bulk PZ98-PNN2 ceramic at 4 Hz during heating at (a) 25 °C, (b) 173 °C, and (c) 200 °C.

the two electrodes were shortened. The loop was recorded after the temperature was stabilized for at least 5 min. As shown in Fig. 3(a), very small polarizations can be induced by the applied electric field in the ceramic at room temperature. This is typical for an AFE ceramic subjected to electric fields that are not sufficient to induce the AFE to ferroelectric phase transition. Such a linear behavior with minimum polarization remains at temperatures up to 170 °C.

When the temperature further increases, a hysteretic behavior starts to develop. As shown in Fig. 3(b), a regular hysteresis loop with a coercive field E_c of 3.9 kV/cm was recorded at 173 °C. However, the observed hysteresis loop does not indicate the presence of a ferroelectric phase. Close examination of the loop in Fig. 3(b) reveals that slight distortions occurred at ~5 kV/cm, marked with the two dashed circles on the hysteresis loop. Similar distortions on hysteresis loops were found in $Pb_{0.99}Nb_{0.02}[(Zr_{0.57}Sn_{0.43})_{1-y}Ti_y]_{0.98}O_3$ ceramics and have been attributed to the onset of the electric field-induced AFE to ferroelectric phase transition.[12] Therefore, the PZ98-PNN2 ceramic at this temperature is still in the AFE phase. It should be noted that the distortions marked in Fig. 3(b) indicate the AFE-to-ferroelectric phase transition. The distortion associated with the backward ferroelectric-to-AFE transition was not seen because it may overlap with the coercive field of the induced ferroelectric phase. The observed large

polarization is due to the induced ferroelectric phase by the applied field of 20 kV/cm, which is much higher than the critical electric field E_F of ~5 kV/cm.

Further increase in temperature leads to the decrease in the critical field E_F and the increase in both the saturation polarization P_s and the remanent polarization P_r. P_r saturates at 25 μC/cm^2 when the temperature reaches 177 °C and stays unchanged up to 186 °C. It should be noted that the coercive field E_c (not the critical field E_F) remains the same at 3.9 kV/cm in the temperature range of 172–186 °C. The results suggest that the volume fraction of the ferroelectric phase induced by a field of 20 kV/cm in the ceramic increases with increasing temperatures between 172 and 177 °C. In the temperature range of 177–186 °C, the whole piece of sample was forced into a ferroelectric phase by the external electric field of 20 kV/cm. Therefore, the P_r saturates in this temperature range.

Dramatic change in the coercive field E_c was observed at 186 °C. At this temperature, although a well defined hysteresis loop was still observed, E_c abruptly reduced to 2.4 kV/cm, indicating the appearance of a new phase. Up to 200 °C, the hysteresis loop remains largely unchanged, with the one at 200 °C shown in Fig. 3(c).

Combined with the results presented in Fig. 2, we believe that the abrupt change in E_c at 186 °C marks the phase transition at 190 °C revealed by the dielectric measurement. The discrepancy in temperature is due to the different test conditions. In the dielectric measurement, the ceramic sample was subjected to continuous heating at a rate of 2 °C/min, while in the polarization measurement, the hysteresis loops were recorded after at least 5 min the temperature is stabilized. In summary, the macroscopic property measurements reveal that at temperatures below 190 °C, the PZ98-PNN2 ceramic is AFE with stable and low dielectric permittivity and loss tangent. Under applied electric fields, the AFE phase can be transformed into a ferroelectric phase at temperatures slightly below the transition temperature. An intermediate phase exists between 190 and 220 °C. The increased loss tangent and the well defined hysteresis loops with reduced coercive fields E_c seem to suggest that this phase is ferroelectric.[2] Further supporting evidence is found in our previous study where the intermediate phase is stabilized down below room temperature in the PZ90-PNN10 ceramic and an undistorted hysteresis loop was observed in this ceramic at room temperature.[10] However, this intermediate phase is a unique ferroelectric phase with evident frequency dispersion in its dielectric behavior.

B. Hot stage TEM

The temperature induced phase transitions were visualized by hot stage TEM during heating. One grain about 3 μm in size was tilted so that its ⟨001⟩-zone axis was aligned with the electron beam direction. The evolution of the SAED pattern with temperature is exemplified in Fig. 4. At room temperature, the primary feature is the presence of the $\frac{1}{4}\{110\}_c$-type superlattice diffraction spots [Fig. 4(a)], where the subscript c indicates that the indices are based on the parent cubic perovskite unit cell. The superlattice structure is identical to that of $PbZrO_3$ at room temperature.[2,6,7] Therefore, adding 2 mol % of PNN does not change the crystal structure of $PbZrO_3$. The SAED pattern with the $\frac{1}{4}\{110\}_c$ superlattice spots does not change with increasing temperature up to 179 °C.

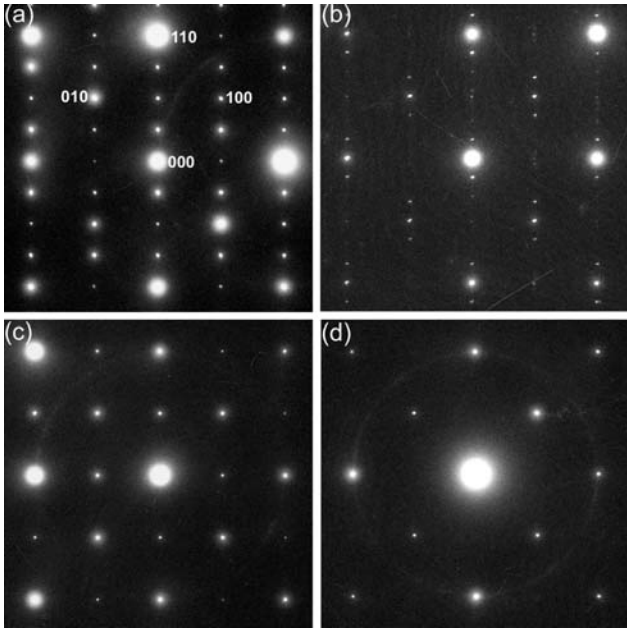

FIG. 4. Hot stage *in situ* TEM experiment on a thin foil specimen of the PZ98-PNN2 ceramic. The $\langle 001\rangle_c$-zone axis SAED patterns observed during heating at (a) 25 °C, (b) 179 °C, (c) 194 °C, and (d) 240 °C.

At 179 °C, the $\frac{1}{4}\{110\}_c$ superlattice spots disappeared, as shown in Fig. 4(b). Instead, incommensurate superlattice diffraction spots emerged. These extra diffraction spots are of the $\frac{1}{n}\{110\}_c$-type, where n is not an integer. The value of n is determined to be 6.48 for the PZ98-PNN2 ceramic from Fig. 4(b). The incommensurate superlattice diffraction spots only existed over a narrow temperature range of ~3 °C and completely disappeared at 181 °C. This type of incommensurate superlattice diffraction has been previously observed in $PbZrO_3$ and was attributed to the competition between the low temperature AFE phase and the intermediate ferroelectric phase.[6]

In the temperature range of 181–212 °C, the primary feature in SAED patterns is the presence of $\frac{1}{2}\{110\}_c$-type superlattice diffraction, as exemplified by the diffraction pattern recorded at 194 °C shown in Fig. 4(c). The $\frac{1}{2}\{110\}_c$ superlattice diffraction was reported previously and has been considered as the signature of the intermediate phase in PbZrO3.[2,5–8] However, considerable controversy remains concerning the symmetry and the nature of the intermediate phase. It was reported to be either rhombohedral[6] or orthorhombic,[5,7] either ferroelectric[2,6,7] or AFE.[5,8]

The $\frac{1}{2}\{110\}_c$ superlattice diffraction started to become weaker and diffuse at 212 °C and finally vanished at 240 °C. Further increase in temperature up to 300 °C did not lead to any change in the diffraction pattern. The SAED pattern at 240 °C is shown in Fig. 4(d) and can be indexed with the parent cubic perovskite structure.

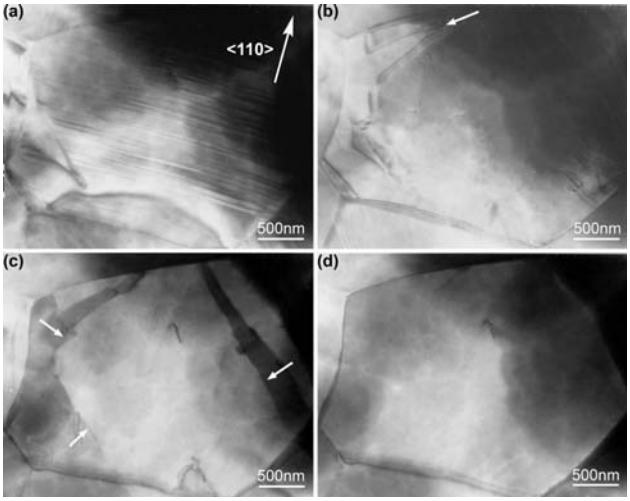

FIG. 5. The bright field micrographs under the $\langle 001\rangle_c$-zone axis of the grain used for the electric diffraction study in Fig. 4 at (a) 148 °C, (b) 179 °C, (c) 186 °C, and (d) 300 °C.

Corresponding changes in the bright field image of the same grain were observed as well, as shown in Fig. 5. From room temperature to 179 °C, one set of lamellar 180° AFE domains was observed in the grain [Fig. 5(a)], consistent with the one set of $\frac{1}{4}\{110\}_c$ superlattice spots in the diffraction pattern. These lamellar domains became thinner as temperature was increased. At 179 °C, corresponding to the appearance of the $1/n\{110\}_c$ incommensurate and the disappearance of the $\frac{1}{4}\{110\}_c$ superlattice diffraction, the 180° AFE domains in the whole grain were replaced by wedge-shaped domains near grain boundaries. The tip of one wedge-shaped domain is marked by an arrow in Fig. 5(b). In the temperature range of 181–212 °C, corresponding to the $\frac{1}{2}\{110\}_c$-type superlattice diffraction in SAED patterns, the grain displays a checkerboard-like domain morphology with domain walls primarily on the $\{100\}_c$ planes. The domain walls of the large domain with bright contrast are indicated by arrows in Fig. 5(c). Such domain morphology is a reminiscence of the AFE domains in lead zirconate stannate titanate ceramics.[13] The walls of these checkerboard-like domains started to move and disappear at 212 °C and completely vanished at 224 °C. This grain remains contrast free during the further heating up to 300 °C, as shown in Fig. 5(d).

Compared with the results from dielectric measurement in bulk samples, the *in situ* TEM heating experiment reveals almost the same phase transition sequence. Below 179 °C, the PZ98-PNN2 ceramic is in the AFE phase that is isostructural to $PbZrO_3$. Between 181 and 212 °C, the ceramic is in the intermediate ferroelectric phase characterized by the $\frac{1}{2}\{110\}_c$-type superlattice diffraction and the checkerboard-like domains. Above 212 °C, the ceramic is in the paraelectric phase. However, the $\frac{1}{2}\{110\}_c$-type superlattice diffraction and the checkerboard domain morphology persists up to 224 °C in the paraelectric phase. The persistence of the $\frac{1}{2}\{110\}_c$ superlattice into paraelectric phase was noticed before in $PbZrO_3$.[2,6] The difference in the transition temperatures between the TEM experiment and the dielectric measurement is due primarily to the different sample geometries. The advantage of the *in situ* TEM study over the dielectric measurement is manifested in the revealing of the transient incommensurate phase around 179 °C between the low temperature AFE phase and the intermediate phase.

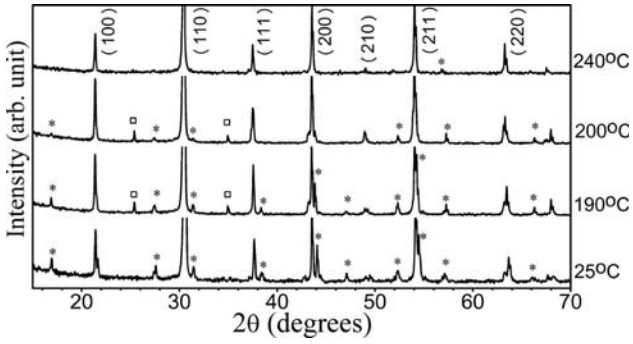

FIG. 6. XRD patterns of a bulk PZ98-PNN2 ceramic during heating at 25, 190, 200, and 240 °C.

C. High temperature XRD

The crystal structure of the PZ98-PNN2 ceramic was further analyzed with XRD at a series of temperatures during the heating process. Four temperatures were selected to record the diffraction pattern: 25 °C where the AFE phase isostructural to $PbZrO_3$ is expected, 190 °C where the incommensurate phase is expected in the bulk sample, 200 °C where the intermediate phase is expected, and 240 °C where the paraelectric phase should be dominant. All the patterns were recorded after the temperature was stabilized at the desired temperature for at least 10 min. The results are shown in Fig. 6, where the major peaks are indexed based on a cubic unit cell.

At 25 °C, the diffraction pattern fits the space group *Pbam*, the same as $PbZrO_3$ at room temperature.[3–5] The peaks marked by the asterisks indicate the peaks that belong to this symmetry but are forbidden in the cubic structure. All these peaks can be indexed as $\frac{1}{4}\{110\}_c$-type superlattice diffractions. When the temperature increased to 190 °C, orthorhombic *Pbam* symmetry remained, as indicated by the asterisks. However, two additional peaks, one on each side of the $\{110\}_c$ peak, emerged at 25.4° and 35.0°, respectively. They are marked with squares in Fig. 6. These additional peaks cannot be indexed with either cubic or orthorhombic symmetry. Considering the observed incommensurate phase observed in TEM, these two peaks may be the satellite diffraction peaks of the strongest $\{110\}_c$ peak. This is indeed the case. They can be indexed as $\{110\}_c - 1/n\{110\}_c$ and $\{110\}_c + 1/n\{110\}_c$, respectively, with $n=6.48$. This value of n is exactly the same as determined by the TEM result. The observation of the incommensurate modulation with XRD is significant because so far it has been only revealed by electron diffraction in TEM in $PbZrO_3$-based ceramics.[14]

On further heating to 200 °C, the $\frac{1}{4}\{110\}_c$-type superlattice peaks became weaker and some of them even disappeared. While an orthorhombic symmetry was reserved, the overall pattern fits better with the space group *P2cb*. To our surprise, the incommensurate superlattice peaks can still be

clearly observed. This appears to disagree with the TEM result shown in Fig. 4, where the incommensurate satellite spots existed over a very narrow temperature range of less than 3 °C. This discrepancy can be explained by considering the difference in the experimental conditions. In the TEM experiment, observations were made in a single grain, while in XRD, hundreds of thousands of grains were exposed to the x-ray beam. The unsynergized phase transition of each individual grain leads to a much wider temperature range for the incommensurate phase.

At 240 °C where the PZ98-PNN2 ceramic is supposed to be in the high temperature paraelectric phase, the major peaks can be indexed with a cubic symmetry. However, close examination revealed the presence of trace amount of the orthorhombic phase.

IV. CONCLUSIONS

By introducing 2 mol % $Pb(Ni_{1/3}Nb_{2/3})O_3$ into $PbZrO_3$, a series of phase transitions occurred above room temperature. The high temperature phases show distinct crystal structures and domain morphologies, as well as distinct dielectric and ferroelectric properties. Below 190 °C, the ceramic is in the *Pbam* symmetry with AFE 180° domains. Both the dielectric permittivity and the loss tangent are low and stable against temperature change. Around 190 °C, one order of magnitude increase in dielectric permittivity and loss tangent occurs within a narrow temperature range. Corresponding to the dramatic change in dielectric property is the presence of an incommensurate phase with $\frac{1}{6.48}\{110\}_c$ satellite diffractions. In the temperature range of 190–220 °C, the ceramic is in an intermediate phase, which is believed to be ferroelectric. This phase is characterized by the fast increasing dielectric permittivity, stable and high loss tangent, well defined polarization hysteresis loops, and the $\frac{1}{2}\{110\}_c$ superlattice diffraction. This ferroelectric intermediate phase is unique because of the frequency dispersion in its dielectric properties, the checkerboard-like morphology of its domain structure, and the orthorhombic space group of *P*2*cb*. Above 220 °C, the ceramic is in the cubic paraelectric phase with the relative permittivity following the Curie–Weiss law. However, the structural change at the Curie point is by no means abrupt. Some residual orthorhombic phase persists even at temperatures several tens of degrees above 220 °C.

ACKNOWLEDGMENTS

This work was supported by the National Science Foundation through the CAREER Grant No. DMR-0346819 and the U.S.-Israel Binational Science Foundation through Grant No. 2006235. The *in situ* TEM and high temperature XRD experiments were carried out at the Materials & Engineering Physics Program, Ames Laboratory, which is supported by the United States Department of Energy–Basic Energy Sciences under Contract No. DE-AC02-07CH11358.

[1]E. Sawaguchi, H. Maniwa, and S. Hoshino, Phys. Rev. **83**, 1078 (1951).
[2]D. Viehland, Phys. Rev. B **52**, 778 (1995).
[3]D. L. Corker, A. M. Glazer, J. Dec, K. Roleder, and R. W. Whatmore, Acta Crystallogr., Sect. B: Struct. Sci. **53**, 135 (1997).
[4]K. Yamasaki, Y. Soejima, and K. F. Fischer, Acta Crystallogr., Sect. B: Struct. Sci. **54**, 524 (1998).
[5]S. Teslic and T. Egami, Acta Crystallogr., Sect. B: Struct. Sci. **54**, 750 (1998).
[6]Z. Xu, X. Dai, D. Viehland, and D. A. Payne, J. Am. Ceram. Soc. **78**, 2220 (1995).
[7]M. Tanaka, R. Saito, and K. Tsuzuki, Jpn. J. Appl. Phys., Part 1 **21**, 291 (1982).
[8]H. Fujishita and S. Hoshino, J. Phys. Soc. Jpn. **53**, 226 (1984).
[9]S. Wirunchit and N. Vittayakorn, J. Appl. Phys. **104**, 024103 (2008).
[10]N. Vittayakorn and S. Wirunchit, Smart Mater. Struct. **16**, 851 (2007).
[11]S. Wirunchit, P. Laoratanakul, and N. Vittayakorn, J. Phys. D **41**, 125406 (2008).
[12]H. He and X. Tan, J. Phys.: Condens. Matter **19**, 136003 (2007).
[13]H. He and X. Tan, Phys. Rev. B **72**, 024102 (2005).
[14]J. Ricote, D. L. Corker, R. W. Whatmore, S. A. Impey, A. M. Glazer, J. Dec, and K. Roleder, J. Phys.: Condens. Matter **10**, 1767 (1998).

Journal of Alloys and Compounds 479 (2009) 462–466

Contents lists available at ScienceDirect

Journal of Alloys and Compounds

journal homepage: www.elsevier.com/locate/jallcom

Phase transitional behavior and dielectric properties of lead free $(1-x)(K_{0.5}Na_{0.5})NbO_3-xBi(Zn_{0.5}Ti_{0.5})O_3$ ceramics

Manoon Sutapun [a], Chien-Chih Huang [b], David P. Cann [b], Naratip Vittayakorn [a,c,*]

[a] Materials Science Research Unit, Department of Chemistry, Faculty of Science, King Mongkut's Institute of Technology Ladkrabang, Bangkok 10520, Thailand
[b] Materials Science, Mechanical, Industrial, & Manufacturing Engineering, Oregon State University, Corvallis, OR 97331, USA
[c] Collage of KMITL Nanotechnology King Mongkut's Institute of Technology Ladkrabang, Bangkok 10520, Thailand

ARTICLE INFO

Article history:
Received 25 November 2008
Received in revised form 21 December 2008
Accepted 23 December 2008
Available online 4 January 2009

Keywords:
Lead-free piezoelectric ceramics
Dielectric properties
Perovskites structure
$(K_{0.5}Na_{0.5})NbO_3$
$Bi(Zn_{0.5}Ti_{0.5})O_3$

ABSTRACT

Lead-free ceramics based on potassium sodium niobate [$(K_{0.5}Na_{0.5})NbO_3$; KNN]–bismuth zinc titanate [$Bi(Zn_{0.5}Ti_{0.5})O_3$; BZT] were prepared by the modified-conventional mixed oxide route with normal sintering. The crystal structure and ferroelectric phase transitions were studied by means of X-ray diffraction, thermal and dielectric measurements. The ceramics with perovskite structure were in orthorhombic phase at $x \leq 0.010$. When reaching $0.01 < x \leq 0.03$, they became a rhombohedral perovskite structure; and with increasing BZT content, cubic within the studied composition range. The phase $Bi_2Ti_2O_7$ with cubic structure began to appear at $x > 0.25$ and became dominant while increasing the content of BZT. Furthermore, the phase transition temperature of orthorhombic–tetragonal (T_{O-T}) and tetragonal–cubic (T_C) decreased when a small amount of BZT was added. As the amount of BZT concentration increased, the structure became denser, and well developed grain morphology with almost no porosity was finally obtained.

1. Introduction

Lead-based piezoelectric ceramics have been a subject of fundamental researches and practical interest for many years [1]. They exhibit a great variety of physical behavior and, due to their excellent properties, are widely used as sensors, transducers, actuators and multilayer capacitors [1,2]. However, because of the toxicity of lead oxide and its high vapor pressure during processing and the requirement of environmental protection, lead-free piezoelectric ceramics have received much attention over the past decade [3,4].

In recent years, $(K_{0.5}Na_{0.5})NbO_3$ (KNN) has been considered a promising candidate for lead-free piezoelectric ceramics because of its high Curie temperature (above 420 °C), good ferroelectric properties ($P_r = 33\ \mu C/cm^2$), large piezoelectric longitudinal response ($d_{33} \sim 160$ pC/N), and high planar coupling coefficient ($k_p \sim 46\%$) [5,6]. However, it is very difficult to obtain dense KNN ceramics due to the high volatility of alkaline elements at high temperatures. To improve densification and piezoelectric properties of KNN ceramics, various additions are added into KNN to form new KNN-based ceramics, such as KNN-$BaTiO_3$ [7], KNN-$SrTiO_3$ [8], KNN-$LiNbO_3$ [9], KNN-$LiSbO_3$ [10–12], KNN-$LiTaO_3$ [13], KNN-$(Bi_{0.5}Na_{0.5})TiO_3$ [14] and KNN-$LiTaO_3$-$LiSbO_3$ [15].

Bismuth zinc titanate [$Bi(Zn_{0.5}Ti_{0.5})O_3$; BZT] is a new lead-free polar compound with a calculated ionic polarization of over 150 $\mu C/cm^2$, the largest calculated point-charge polarization of any previously reported Pb or Bi-based perovskite [16]. The tetragonal distortion of BZT, quantified by a c/a ratio of 1.211, is the highest reported for any lead based perovskite or Bi based compound [16]. However, BZT is unstable in its pure form and can only be stabilized under high pressures or in solid solutions with other perovskite end members [17,18]. Recently, it was shown that the addition of BZT is effective in enhancing the tetragonality and increasing the transition temperature of $PbTiO_3$ ceramics [19]. However, there were no systematic investigations on the solid solution of KNN–BZT ceramics. In this study, a small amount of BZT was used to partially substitute KNN. The influence of BZT addition on the sinterability, phase transitions, and electrical properties of KNN ceramics was investigated. This article may provide an alternative approach for the development of lead-free piezoelectric materials.

2. Experimental procedure

$(1-x)$KNN–xBZT ceramics ($x = 0.0$–0.3) were synthesized by means of a modified-conventional mixed oxide route. High-purity oxides and carbonates, K_2CO_3 (99.0%), Na_2CO_3 (99.5%), Nb_2O_5 (99.9%), Bi_2O_3 (99.97%), ZnO (99.9%) and TiO_2 (99.9%) were used as starting materials, which had been treated carefully by a special drying process before use, particularly for sodium/potassium carbonates. These

* Corresponding author at: Materials Science Research Unit, Department of Chemistry, Faculty of Science, King Mongkut's Institute of Technology Ladkrabang, Bangkok 10520, Thailand.
E-mail address: naratipcmu@yahoo.com (N. Vittayakorn).

0925-8388/$ – see front matter © 2008 Elsevier B.V. All rights reserved.
doi:10.1016/j.jallcom.2008.12.096

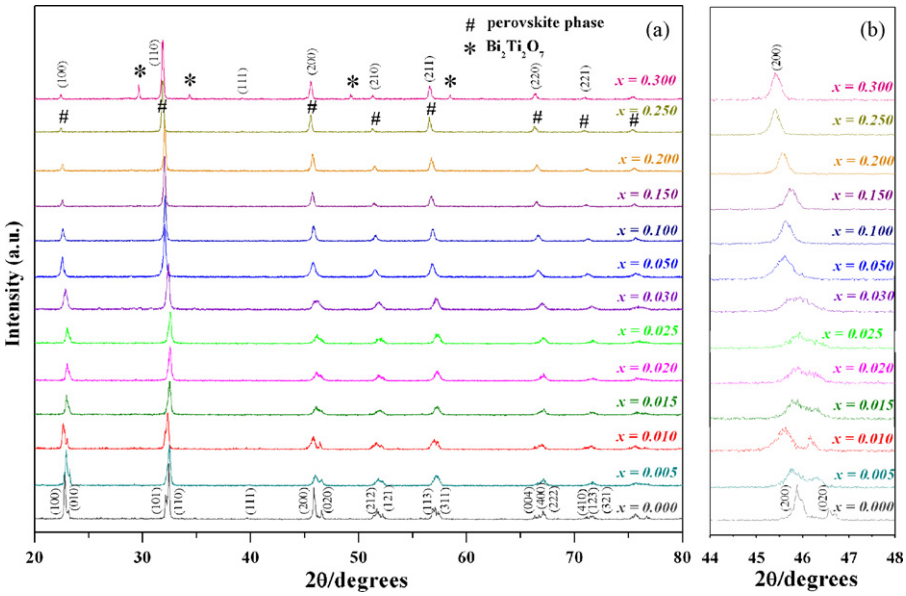

Fig. 1. XRD patterns of the ceramics with different BZT contents.

powders were placed in an oven at 240 °C for 2 days and then stored in a moisture-free vessel. In the first stage, K_2CO_3, Na_2CO_3 and Nb_2O_5 were thoroughly mixed in the stoichiometric ratio, and then calcined at 900 °C for 2 h to form $(K_{0.5}Na_{0.5})NbO_3$; KNN. In the second stage, the precursor (KNN) was mixed in the stoichiometric ratio with other starting materials. An excess of 2 mol% K_2CO_3 and Na_2CO_3 were added to all compositions. After drying, the calcination was carried out at temperatures ranging from 850 to 900 °C for 4 h according to the compositions in a covered alumina crucible. The calcined powders were mixed with 3 wt% poly(vinyl alcohol) (PVA) and then uniaxially cold-pressed at 150 MPa into 15 mm diameter pellets. Following binder burnout at 550 °C, the pellets were sintered in sealed crucibles at between 1000 and 1100 °C for 2 h. For phase determination, X-ray diffraction (Bruker-D8 Advance) was utilized in the 2θ scan range of 20–80° using sintered pellets.Prior to the electrical measurements, the pellets were polished to obtain smooth and parallel surfaces. After polishing, a silver electrode paste (Heraeus C1000) was applied and then fired at 650 °C. An Agilent 4284A LCR meter was used to measure the dielectric properties. The capacitance and dissipation factors of the samples were measured at 100 kHz; the temperature varied between 25 and 500 °C, and a heating rate of 2 °C/min was used during the measurements.

3. Results and discussion

Fig. 1(a) shows the XRD patterns of the $(1-x)$KNN–xBZT ceramics. It was clearly found that the phase structure in $x \leq 0.20$ was a perovskite phase, with no any secondary impurity being detected, and a small amount of secondary phase $Bi_2Ti_2O_7$ could be observed when the content of BZT increased to more than 0.20. The characteristic peaks for $Bi_2Ti_2O_7$ were identified by comparison with the Powder Diffraction File No. 23–0118.

Based on these results, it can be concluded that the BZT completely diffused into the KNN lattice to form a solid solution when the content of BZT was ≤0.20. At $0.0 \leq x \leq 0.01$, the ceramics showed peak splitting consistent with orthorhombic symmetry. However, with increasing BZT content the separation between diffraction peaks corresponding to the orthorhombic phase became narrower and eventually merged into singlet peaks at about $x = 0.015$. The observed symmetry transition was diffused and there was no boundary composition seen separating the orthorhombic and rhombohedral phase. No morphotropic phase boundary was found between these phases. Fig. 1(b) shows a close up of the diffraction peaks illustrating the evolution of the structure as a function of composition. The $(1-x)$KNN–xBZT solid solution ceramics begin to exhibit rhombohedral structures approximately at $x < 0.01$. However, the rhombohedral symmetry remains in a limited composition range. The cubic structure starts to appear when x is greater than 0.03 until $x = 0.25$ approximately. This is because the addition of BZT

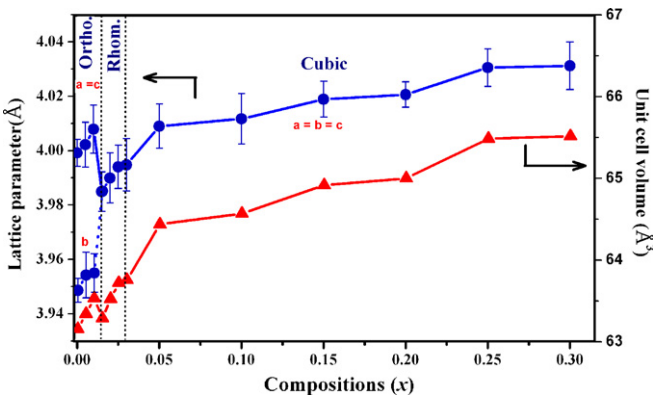

Fig. 2. Lattice parameters and unit cell volume of the ceramics with different BZT contents.

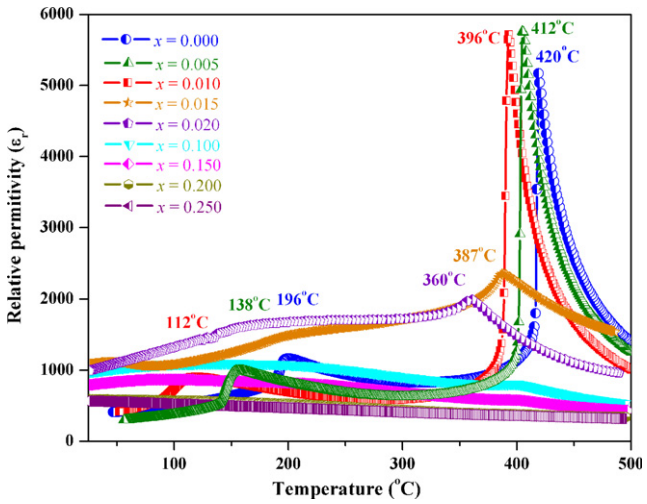

Fig. 3. Relative permittivity as a function of temperature of ceramics with different BZT contents.

Table 1
Physical properties and dielectric data of $(1-x)$KNN–xBZT; $x = 0.0$–0.3 ceramics.

Composition (x)	Crystal structure	Density (g/cm^3)	%T.D.	Relative permittivity (ε_r)			Transition temperature (°C)	
				Room temperature	O–T	T–C	O–T	T–C
$x = 0.000$	O	4.21 ± 0.08	93.42	500	1250	5300	196	420
$x = 0.005$	O	4.25 ± 0.05	93.83	420	1100	5900	118	412
$x = 0.010$	O	4.28 ± 0.03	94.23	570	1050	5800	112	396
$x = 0.015$	R	4.29 ± 0.09	94.05	1200	–	2400	–	387[a]
$x = 0.020$	R	4.32 ± 0.08	94.37	1150	–	2100	–	360[a]
$x = 0.025$	R	4.35 ± 0.09	94.77	1120	–	–	–	–
$x = 0.030$	R	4.45 ± 0.04	96.61	1070	–	–	–	–
$x = 0.050$	C	4.49 ± 0.07	96.07	1020	–	–	–	–
$x = 0.100$	C	4.70 ± 0.03	97.24	960	–	–	–	–
$x = 0.150$	C	4.85 ± 0.06	97.26	800	–	–	–	–
$x = 0.200$	C	4.93 ± 0.11	95.66	530	–	–	–	–
$x = 0.250$	C	5.07 ± 0.08	95.48	520	–	–	–	–

%T.D. = percentage of theoretical density; O = orthorhombic; R = rhombohedral; C = cubic; O–T = orthorhombic to tetragonal; T–C = tetragonal to cubic.
[a] Rhombohedral to cubic.

shifts the Curie point of KNN ceramics below room temperature. Dielectric data described later further supports this assumption.

Furthermore, a slight shift to lower angles in the diffraction peaks indicates a change in the unit-cell parameters, and this can be seen in a detailed scan such as that shown in Fig. 1(b). This indicated that the unit cell volume increased with more BZT content. Although Bi^{3+} is slightly smaller than $(K_{0.5}Na_{0.5})^{2+}$ based on 12-fold coordination, the unit cell volume increased with increasing BZT content due to the substitution of larger average size of B-site cations Zn^{2+}(0.88 Å) and Ti^{4+}(0.745 Å) for Nb^{5+}(0.78 Å). The difference in the unit cell volume between BZT ($V = 67.601$ Å^3)[16] and KNN ($V = 63.156$ Å^3) is 4.445 Å^3. With the peaks properly indexed, a lattice parameter was determined using UnitCell: a linear least squares refinement program. The calculated lattice parameters of the perovskite structures and the unit-cell volume are presented in Fig. 2. By combining Figs. 1(b) and 2, it can be seen that the ceramics have orthorhombic symmetry at $x \leq 0.01$. The structure changes from orthorhombic to rhombohedral when increasing x to 0.03, and to the cubic phase when increasing x to 0.3. The same phenomenon has also been observed by Zuo et al. [20] By adding $BiFeO_3$ to $K_{0.5}Na_{0.5}NbO_3$, the phase structure firstly changes firstly from orthorhombic to rhombohedral symmetry, and then to cubic symmetry.

The relative permittivity at the frequency of 100 kHz as a function of temperature for ceramics $(1-x)$KNN–xBZT is shown in Fig. 3. It is very clear from the data that, while pure KNN exhibited a strong first-order phase transition, the addition of BZT caused a shift toward diffuse phase transition behavior. For pure KNN, phase transitions were observed at 420 and 196 °C, corresponding to the phase transitions of paraelectric cubic–ferroelectric tetragonal (T_C) and ferroelectric tetragonal–ferroelectric orthorhombic (T_{T-O}), respectively. In the ceramics with $x = 0.005$ and 0.010, similar to that of pure KNN, the two phase transitions were observed, however, both of these phase transitions are shifted to lower temperatures. The dielectric data, phase transition and other physical properties are listed in Table 1. When $x = 0.015$, the orthorhombic–tetragonal phase transition disappears and the ceramic becomes a solely rhombohedral structure with a Curie temperature of ~387 °C. This result confirms that the compositions of $0.01 < x \leq 0.03$ are rhombohedral ferroelectrics, not cubic paraelectrics. For samples with $x > 0.15$, no peaks in dielectric constant versus temperature curves can be observed, probably because the peaks shifted below room temperature. These results are consistent with XRD analysis. Moreover, it is noticeable that the rhombohedral ferroelectric compositions show much lower peak dielectric constants and broad phase transitions, compared to orthorhombic ferroelectric com-

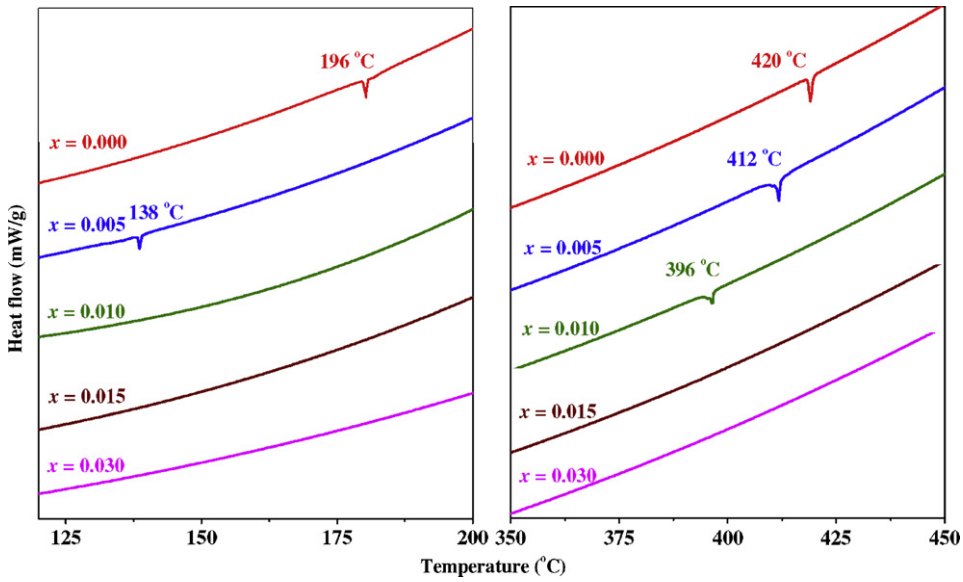

Fig. 4. DSC curves of the ceramics with difference BZT contents.

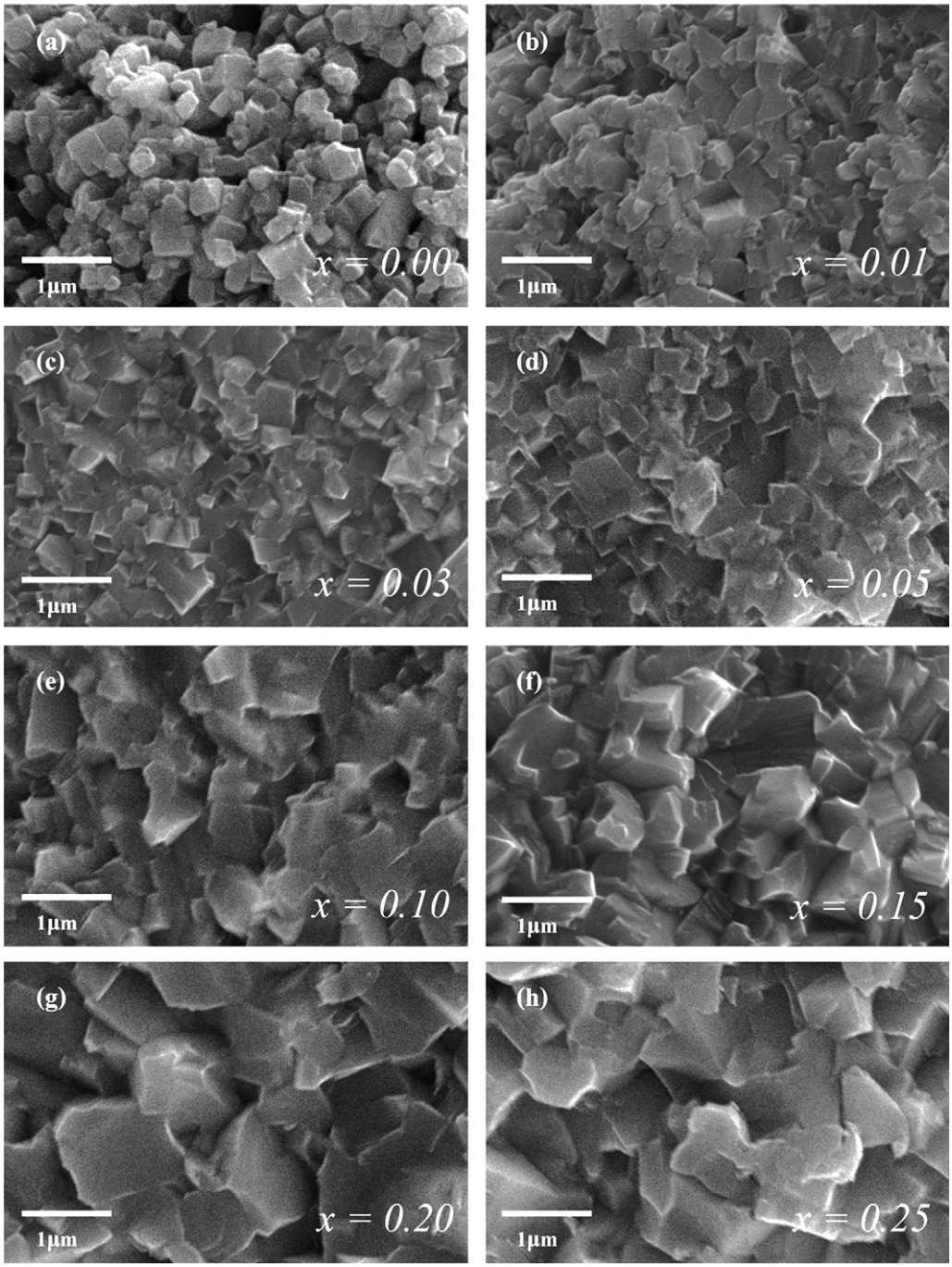

Fig. 5. SEM micrographs of the fractured surfaces of the ceramics with different BZT contents, (a) $x = 0.0$, (b) $x = 0.01$, (c) $x = 0.03$, (d) $x = 0.05$, (e) $x = 0.10$, (f) $x = 0.15$, (g) $x = 0.20$ and (h) $x = 0.25$.

positions. This behavior can originate from the more complex occupation of the A and B sites in an ABO_3 perovskite structure and heterogeneous compositions. This composition heterogeneity also gives rise to random fields, which tend to make the phase transition "diffuse" instead of sharp as in a normal ferroelectric. The general trend is also similar to that observed in the ternary $Bi(Zn_{1/2}Ti_{1/2})O_3$–$BiScO_3$–$BaTiO_3$ system [18].

From dielectric permittivity-temperature measurements and also differential scanning calorimetry (DSC), we investigated the nature of phase transitions in the KNN–BZT system. The transition temperature was determined from both the anomaly peaks in the DSC data and the peaks of the permittivity-temperature plots. Fig. 4 shows the results of the DSC for the KNN–BZT system. It was clear that pure KNN and the compositions, $x = 0.005$ and 0.01, showed two peaks, indicating existence of two first order phase transitions. The lower temperature corresponds to the transition temperature of the orthorhombic → tetragonal phase transition, while the higher temperature corresponds to the tetragonal → cubic phase transition. There is a sharp decrease in phase transition energy with increasing BZT contents. The tricritical point, the composition at which a first-order transition becomes a second-order transition, is close to the composition, $x = 0.015$, which has a tolerance factor of $t \sim 1.0$ using the ionic radii of Shannon and Prewitt [21]. Choi et al. [22] reported that in the $Bi(Ni_{1/2}Ti_{1/2})O_3$–$PbTiO_3$ (BNiT–PT), the tricritical point in the solid solution also corresponded closely to $t \sim 1.0$. Similar phenomena have been observed in the $Bi(Mg_{3/4}W_{1/4})O_3$–$PbTiO_3$

(BMW–PT) system by Stringer et al. [23] and our previous work on $PbZrO_3$ related materials [24,25].

The SEM micrographs of fractured surface KNN–BZT ceramics were obtained in Fig. 5. No abnormal or plate-like grains were observed in the samples, indicating an absence of pyrochlore formation. It was clearly seen that pure KNN could not be sintered to sufficient densities and the theoretical densities of ceramics in this range were about 92.0–93.4%. It is possible that volatilization of potassium and sodium during firing is the main reason for the failure in preparing dense ceramics in this composition. As the amount of BZT concentration increased, the structure became denser, and well developed grain morphology with almost no porosity was finally obtained. Average values of grain size, as measured by the linear intercept method, increased from ~0.4 μm for the pure KNN to ~1.4 μm for the sample composition, $x = 0.25$ sample. Table 1 also shows the density of sample with difference BZT contents. The density of the pure KNN without BZT added is lower. When BZT is added, the density increases markedly. It can be illustrated by the fact that Bi^{3+} and Zn^{2+}/Ti^{4+} ions are considered to enter the A and B-sites of the ceramics, respectively, and a large amount of oxygen vacancies could be found in the samples, which expedites lattice diffusion, and leads to the enhancement of the bulk density of the ceramics [26]. As the concentration x up to 0.20, excess BZT beyond the solubility limit will be segregated at the grain boundary and make the density of ceramics decreases slightly.

4. Conclusions

Lead free piezoelectric ceramics KNN–BZT have been prepared the modified-conventional mixed oxide route with normal sintering. At room temperature, the ceramics with a perovskite structure are in the orthorhombic phase at $x \leq 0.01$. At $0.01 < x \leq 0.03$, they become a rhombohedral perovskite structure; and with increasing BZT content, cubic within the studied composition range. The phase $Bi_2Ti_2O_7$ with cubic structure begins to appear at $x > 0.25$ and becomes dominant while increasing the content of BZT. Furthermore, the phase transition temperature of orthorhombic–tetragonal (T_{O-T}) and tetragonal–cubic (T_C) decreases when a small amount of BZT is added. SEM micrographs of the pure KNN ceramics showed a rather porous structure. As the amount of BZT concentration increased, the structure became denser, and well developed grain morphology with almost no porosity was finally obtained. The results show that KNN–BZT ceramics possess good dielectric properties and sintering characteristics, which indicate their promise as lead free piezoelectric ceramics.

Acknowledgments

This work has partially been supported by the Thailand Research Fund (TRF) and the National Nanotechnology Center (NANOTEC) NSTDA, Ministry of Science and Technology, Thailand through its program of Center of Excellence Network.

References

[1] G.H. Haertling, J. Am. Ceram. Soc. 82 (1999) 797–818.
[2] K. Uchino, Ferroelectric Devices, Marcel Dekker, Inc., New York, 2000.
[3] T. Takenaka, H. Nagata, J. Eur. Ceram. Soc. 25 (2005) 2693–2700.
[4] E. Ringgaard, T. Wurlitzer, J. Eur. Ceram. Soc. 25 (2005) 2701–2706.
[5] R.E. Jaeger, L. Egerton, J. Am. Ceram. Soc. 45 (1962) 209–213.
[6] K.-I. Kakimoto, I. Masuda, H. Ohsato, J. Eur. Ceram. Soc. 25 (2005) 2719–2722.
[7] C.-H. Choi, C.-W. Ahn, S. Nahma, Appl. Phys. Lett. 90 (2007) 132905.
[8] R. Wang, R. Xie, K. Hanada, K. Matsusaki, H. Bando, M. Itoh, J. Appl. Phys. Res. 202 (2005) R57–R59.
[9] Y. Guo, K. Kakimoto, H. Ohsato, Appl. Phys. Lett. 85 (2004) 4121–4123.
[10] S. Zhang, R. Xia, T.R. Shrout, G. Zang, J. Wang, Solid State Commun. 141 (2007) 675–679.
[11] Z. Yang, Y. Chang, B. Liu, L. Wei, Mater. Sci. Eng. A 432 (2006) 292–298.
[12] S. Zhang, R. Xia, T.R. Shrout, G. Zang, J. Wang, J. Appl. Phys. 100 (2006) 104108.
[13] Y. Dai, X. Zhang, G. Zhou, Appl. Phys. Lett. 90 (2007) 262903.
[14] R. Zuo, X. Fang, C. Ye, Appl. Phys. Lett. 90 (2007) 9290–9294.
[15] G.-Z. Zang, J.-F. Wang, H.-C. Chen, W.-B. Su, C.-M. Wang, P. Qi, B.-Q. Ming, J. Du, L.-M. Zheng, Appl. Phys. Lett. 88 (2006) 212908.
[16] M.R. Suchomel, A.M. Fogg, M. Allix, H. Niu, J.B. Claridge, M.J. Rosseinsky, Chem. Mater. 18 (2006) 4987–4989.
[17] M.R. Suchomel, P.K. Davids, Appl. Phys. Lett. 86 (2005) 262905.
[18] C.-C. Huang, D.P. Cann, X. Tan, N. Vittayakorn, J. Appl. Phys. 102 (2007) 044103.
[19] T.R. Shrout, R. Eitel, C.A. Randall, IEEE Tr. UFFC. 44 (2002) 1140.
[20] R. Zuo, C. Ye, X. Fang, J. Phys. Chem. Solids 69 (2008) 230–235.
[21] R.D. Shannon, Acta Cryst. A32 (1976) 751.
[22] S.M. Choi, C.J. Stringer, T.R. Shrout, C.A. Randall, J. Appl. Phys. 98 (2005) 034108.
[23] C.J. Stringer, R.E. Eitel, T.R. Shrout, C.A. Randall, I.M. Reaney, J. Appl. Phys. 97 (2005) 024101.
[24] S. Wirunchit, P. Laoratanakul, N. Vittayakorn, J. Phys. D: Appl. Phys. 41 (2008) 125406.
[25] S. Wirunchit, N. Vittayakorn, J. Appl. Phys. 104 (2008) 024103-6.
[26] C.-W. Ahn, S.-Y. Noh, S. Nahm, J. Ryu, K. Uchino, S.-J. Yoon, J.-S. Song, Jpn. J. Appl. Phys. 42 (2003) 5676–5680.

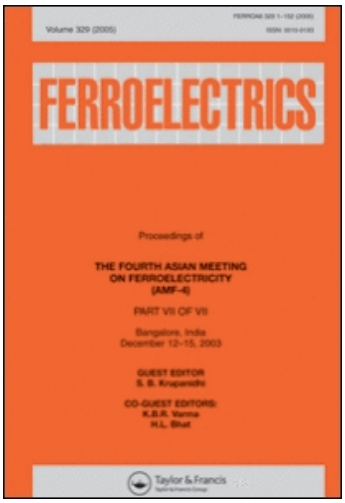

Ferroelectrics
Publication details, including instructions for authors and subscription information:
http://www.informaworld.com/smpp/title~content=t713617887

Synthesis and Morphology Evolution of Lead-Free Piezoelectric $K_{1/2}Na_{1/2}NbO_3$ Powder at Low Temperature

Nopsiri Chaiyo [a]; Anucha Ruangphanit [b]; Rangson Muanghlua [c]; Surasak Niemcharoen [c]; Atchara Sangseub [d]; Saowanee Taopen [d]; Sunanta Leelapattana [d]; Wanwilai C. Vittayakorn [e]; Naratip Vittayakorn [ad]
[a] Collage of KMITL Nanotechnology King Mongkut's Institute of Technology, Ladkrabang, King Mongkut's Institute of Technology, Ladkrabang, Bangkok, Thailand [b] Ministry of Science and Technology, Thai Microelectronics Center (TMEC), National Electronics and Computer Technology Center, Nation Science and Technology Development Agency, Chachoengsao, Thailand [c] Department of Electronics, Faculty of Engineering, King Mongkut's Institute of Technology, Ladkrabang, Bangkok, Thailand [d] Materials Science Research Units, Department of Chemistry, Faculty of Science, King Mongkut's Institute of Technology, Ladkrabang, Bangkok, Thailand [e] Department of Physics and Materials Science, Faculty of Science, Chiang Mai University, Chiang Mai, Thailand

Online Publication Date: 01 January 2009

To cite this Article Chaiyo, Nopsiri, Ruangphanit, Anucha, Muanghlua, Rangson, Niemcharoen, Surasak, Sangseub, Atchara, Taopen, Saowanee, Leelapattana, Sunanta, Vittayakorn, Wanwilai C. and Vittayakorn, Naratip(2009)'Synthesis and Morphology Evolution of Lead-Free Piezoelectric $K_{1/2}Na_{1/2}NbO_3$ Powder at Low Temperature',Ferroelectrics,383:1,8 — 14
To link to this Article: DOI: 10.1080/00150190902873311
URL: http://dx.doi.org/10.1080/00150190902873311

Ferroelectrics, 383:8–14, 2009

ISSN: 0015-0193 print / 1563-5112 online
DOI: 10.1080/00150190902873311

Synthesis and Morphology Evolution of Lead-Free Piezoelectric $K_{1/2}Na_{1/2}NbO_3$ Powder at Low Temperature

NOPSIRI CHAIYO,[1] ANUCHA RUANGPHANIT,[2] RANGSON MUANGHLUA,[3] SURASAK NIEMCHAROEN,[3] ATCHARA SANGSEUB,[4] SAOWANEE TAOPEN,[4] SUNANTA LEELAPATTANA,[4] WANWILAI C. VITTAYAKORN,[5] AND NARATIP VITTAYAKORN[1,4,*]

[1]College of KMITL Nanotechnology King Mongkut's Institute of Technology, Ladkrabang, King Mongkut's Institute of Technology, Ladkrabang, Bangkok 10520, Thailand
[2]Thai Microelectronics Center (TMEC), National Electronics and Computer Technology Center, Nation Science and Technology Development Agency, Ministry of Science and Technology, Chachoengsao 24000, Thailand
[3]Department of Electronics, Faculty of Engineering, King Mongkut's Institute of Technology, Ladkrabang, Bangkok, Thailand 10520
[4] Materials Science Research Units, Department of Chemistry, Faculty of Science, King Mongkut's Institute of Technology, Ladkrabang, Bangkok 10520, Thailand
[5]Department of Physics and Materials Science, Faculty of Science, Chiang Mai University, Chiang Mai 50200, Thailand

A synthetic route for modified solid state reaction has been developed for the synthesis of the perovskite phase of potassium sodium niobate, $K_{1/2}Na_{1/2}NbO_3$ (KNN). Potassium oxalate monohydrate ($K_2C_2O_4.H_2O$) and sodium oxalate ($Na_2C_2O_4$) were employed as a source of potassium and sodium, respectively. The formation of the $K_{1/2}Na_{1/2}NbO_3$ phase was investigated as a function of calcination conditions by TG-DTA and XRD techniques. Morphology and particle size were determined via an SEM technique. It was found that the minor phases of Na_2CO_3 and K_2CO_3 tend to form together with $K_{1/2}Na_{1/2}NbO_3$, depending on calcination conditions. The perovskite phase was successfully synthesized at a low temperature of 400°C. As calcination temperatures increased from 600° to 850°C, the KNN solid solution became more homogeneous, XRD peaks became narrower, and a pattern similar to that expected for orthorhombic $K_{1/2}Na_{1/2}NbO_3$ was achieved after 600°C, as indicated by the separate peaks of 0 2 2 and 2 0 0.

Keywords Materials preparation; piezoceramics; potassium compounds and sodium compounds

PACS: 64.70.K-; 77.22.Ch, 81.05.Je; 85.80.-n; 77.84.Dy

Received August 3, 2008; in final form December 31, 2008.
*Corresponding author. E-mail: naratipcmu@yahoo.com

Introduction

For almost half a century, lead zirconate titanate (PZT) and PZT-based ceramics have been widely investigated and used as actuators, sensors, transducers, resonators, surface acoustic wave (SAW) filters and other piezoelectric devices, due to their excellent dielectric, piezoelectric and electromechanical properties [1–5]. Lead-based PZT materials contain more than 60 wt% of lead oxide, which cause various environmental problems and numerous medical symptoms, i.e. headaches, constipation, nausea, anemia and reduced fertility [6]. In terms of legislation at the EU level, two recent directives have put severe restrictions on the use of hazardous substances in electronic equipment. According to these, lead and other heavy metals should have been phased out by 1st July, 2006 [7]. Therefore, lead-free and/or low-lead-content piezoelectric compositions have been studied and developed for replacing the lead-based compositions in commercial application [1, 5]. Alkali niobates of the general form, $ANbO_3$ (A: alkali metal), were proposed as alternative piezoelectric materials [7]. Among various candidates, potassium sodium niobate [$(K,Na)NbO_3$; KNN] is the most promising one, because of its outstanding piezoelectric and ferroelectric properties. Although KNN has been studied since the 1950s, research on it has not been intensive. A recent article in *Nature* by Saito et al. attracted more attention on this lead-free piezoelectric ceramic [8]. KNN powders have been prepared by a conventional solid-state reaction method using oxide or carbonate compound as raw materials [9]. This reaction creates several problems, which are caused by moisture-sensitive compound [7]. Moreover, high calcination temperature can lead to the evaporation of volatile compound. It was found that potassium niobate ($KNbO_3$) powder has been successfully synthesized at a temperature as low as 500°C through a modified solid state reaction [10] and other compositions such as $NaTaO_3$ powder, which also was synthesized by using this method [11].

Thus, the purpose of this study was to explore a modified solid state reaction method for the production of $K_{1/2}Na_{1/2}NbO_3$ powder at a low calcination temperature. The phase evolution, morphology and particle size of the powder calcined at various temperatures were investigated and discussed.

Experimental Procedure

Potassium sodium niobate ($K_{1/2}Na_{1/2}NbO_3$) powders were prepared by the modified solid state reaction method. Reagent grade potassium oxalate monohydrate ($K_2C_2O_4.H_2O$, 99.9%), sodium oxalate ($Na_2C_2O_4$, 99.9%) and niobium oxide (Nb_2O_5, 99.9%), in required stoichiometric ratio related to reaction bellow, were mixed by the ball-milling method in isopropanol for 18 h.

$$\begin{aligned} &0.5K_2C_2O_4.H_2O_{(s)} + 0.5Na_2C_2O_{4(s)} + Nb_2O_{5(s)} + O_{2(g)} \\ &\rightarrow 2K_{0.5}Na_{0.5}NbO_{3(s)} + 2CO_{2(g)} + 0.5O_{2(g)} + 0.5H_2O_{(g)} \end{aligned} \quad (1)$$

The mixture was dried at 80°C for an approximate length of time. After drying, the reaction of the uncalcined powders taking place during heat treatment was determined by thermo gravimetric and differential thermal analysis (TG-DTA, Perkin Elmer). Based on the TG-DTA results, the mixture was calcined in air at various temperatures ranging from 300°C to 850°C in a closed alumina crucible in order to investigate the formation of KNN.

All powders were subsequently inspected by room temperature X-ray diffraction (XRD, Advance D8) using Ni-filtered CuK_α radiation to examine the phases formed and the optimum calcination condition for the formation of KNN powder. Powder morphologies and

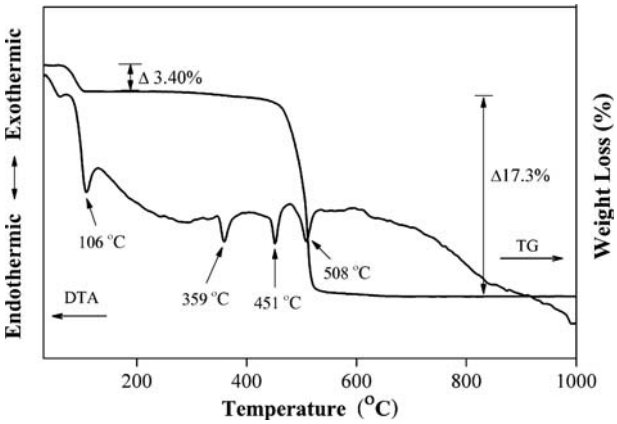

Figure 1. TG-DTA result of an uncalcined powder mixed in the stoichiometric proportion of $K_{1/2}Na_{1/2}NbO_3$.

particle size were directly imaged using a scanning electron microscope (SEM, LEO1455 VP).

Results and Discussion

The TG-DTA simultaneous analysis of a powder mixed in the stoichiometric proportions of $K_{1/2}Na_{1/2}NbO_3$ is illustrated in Fig.1. From Fig. 1, four endothermic peaks centered at 106, 359, 451 and 508°C are observed. The first endothermic peak is attributed to the dehydration of potassium oxalate monohydrate with mass loss of 3.4% on the TG curve [12]. The second endothermic peak can be ascribed to the formation of potassium carbonate through potassium oxalate decomposition [12]. The third endothermic peak also results from the formation of sodium carbonate through sodium oxalate decomposition [13]. The fourth endothermic peak is assigned to the formation of $K_{1/2}Na_{1/2}NbO_3$ by combination reactions of Na_2O, K_2O and Nb_2O_5. In addition, there is an obvious mass loss of 17.3% during the temperature rise from 460 to 530°C on the TG curve, which indicates the decarbonation of K_2CO_3 and Na_2CO_3. These data were used to define the range of calcination temperatures for XRD investigation between 300°C to 850°C.

Therefore, to investigate the effect of calcination temperature on the phase development, the mixed powders were calcined for 2 h in air at various temperatures up to 850°C, followed by phase analysis using XRD. Figure 2 shows the XRD pattern of the KNN powders calcined at different temperatures for 2 h. It can be seen that fine KNN crystallites were developed in the powder at a calcination temperature as low as 350°C, accompanied by Nb_2O_5, K_2CO_3 and Na_2CO_3. Upon calcinations at 400°C, an essentially monophasic of perovskite phase (yield of 100% within the limitations of the XRD technique) was observed. This phase was indexed based on a simple orthorhombic perovskite cell, as proposed by Stannek [14]. However, for the composition, $K_{1/2}Na_{1/2}NbO_3$, a JCPDS-ICDD powder diffraction card did not exist. The material was orthorhombic and isostructural with orthorhombic $KNbO_3$, with a unit cell derived from the simple perovskite cell by rotating two axes by 45°[15, 16]. We successfully synthesized the single perovskite phase by firing at a low temperature of 400°C. The results of the X-ray diffraction measurement

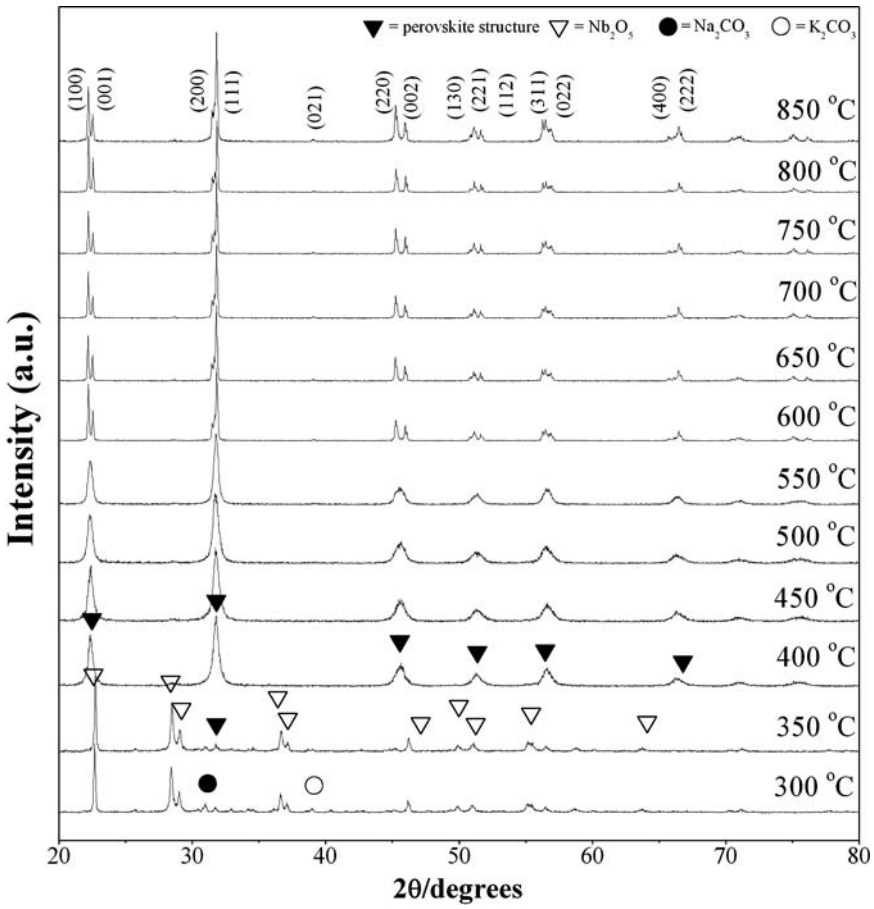

Figure 2. XRD patterns of $K_{1/2}Na_{1/2}NbO_3$ powder calcined at various temperatures for 2 h with heating/cooling rates of 20°C /min.

support the DTA observation (Fig. 1) that the perovskite phase is formed at a temperature of ∼400−500°C. This temperature was more than 350°C lower than the ordinary synthesis temperature of solid state reaction.

Although the pure perovskite phase was obtained at a low temperature of 400°C, broadening of the XRD peaks was observed at temperatures between 400–550°C. This indicated that the KNN powder at 400–550°C was not a good homogeneous solid solution phase. Any spatial variations in the Na and K ratios, due to imperfect mixing and incomplete reaction, would produce a series of $K_{(1-x)}Na_xNbO_3$ solid solution compositions with differing values of x, in different regions of the sample. Because of the small shifts in d-spacings with changing composition reported for intermediate values of x, an overlap of XRD peaks from compositionally inhomogeneous regions would occur, and result in single broad peaks for temperatures $\leq$ 550°C, as shown in Fig. 2. As calcination temperatures increased from 600° to 850°C, the KNN solid solution became more homogeneous, XRD peaks became narrower, and a pattern similar to that expected for orthorhombic $K_{1/2}Na_{1/2}NbO_3$ was achieved after 600°C, as indicated by the separate peaks of 0 2 2 and 2 0 0 in Fig. 3. Estimated lattice parameters were a = 5.56 Å, b =15.70 Å, and c = 5.62 Å for powder

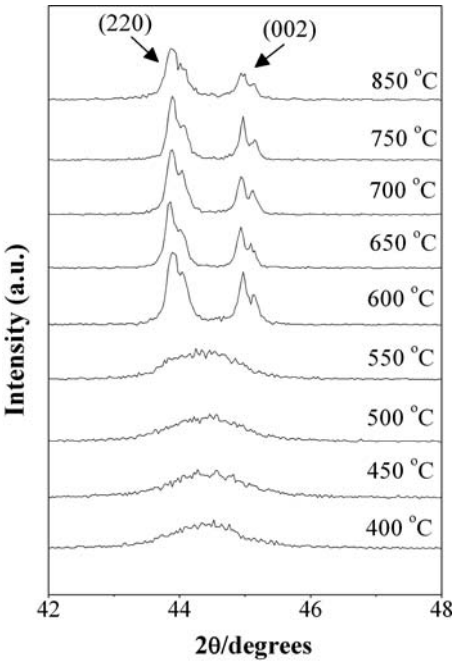

Figure 3. XRD pattern of the $K_{1/2}Na_{1/2}NbO_3$ powder, showing doublets (2 2 0) and (0 0 2).

that was calcined at 600°C; which is close to the values reported in the literature [17]. This study also shows that crystalline orthorhombic KNN is the only detectable phase in the powder, after calcinations in the range of 600–850°C. The experimental work carried out here suggests that the optimal calcination conditions for the single orthorhombic phase, $K_{1/2}Na_{1/2}NbO_3$ (with impurities undetected by the XRD technique), is 600°C for 2, with heating/cooling rates of 20°C/min. Moreover, the formation temperature and dwell time for the production of $K_{1/2}Na_{1/2}NbO_3$ powders observed in this work are also lower than those reported by Ichiki et al. [18] (950°C for 5 h) and Singh et al. [19] (900°C for 1 h). The morphology evolution and particle sizes can be directly investigated using scanning electron microscopy (SEM). Micrograph of KNN powders calcined at 400°C for 2 h, with a heating/cooling rate of 20°C/min. is displayed in Fig.4(a) and 4(b). In general, the particles are conglomerated and irregular in shape and the morphology of the calcined powders are

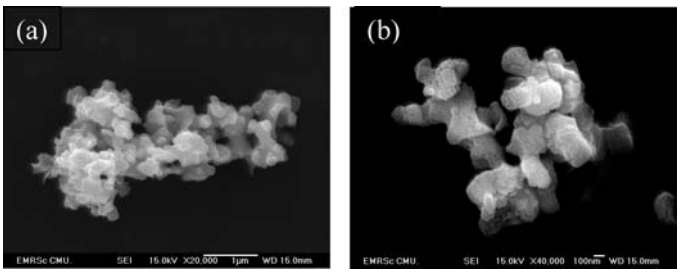

Figure 4. Scanning electron micrograph of the $K_{1/2}Na_{1/2}NbO_3$ powders calcined at 400°C for 2 h, with a heating/cooling rate of 20°C/min. (a) low magnification and (b) higher magnification.

about the same. The range of particle size was found to be about 70 to 300 nm. No evidence of secondary phase was found. This observation was in good agreement with the evidence suggested from the XRD technique. A detailed study at higher magnification [Fig. 4(b)] showed that the smallest particle size estimated from SEM micrographs was ∼40 nm.

Conclusions

In summary, we have exploited a simple method to synthesize perovskite-type $K_{1/2}Na_{1/2}NbO_3$ powder, with high crystallinity at a lower temperature. A pyrochlore-free perovskite $K_{1/2}Na_{1/2}NbO_3$ phase was obtained in this study by using potassium oxalate monohydrate and sodium oxalate as a source of potassium and sodium, respectively, together with a careful calcination treatment. The perovskite phase was successfully synthesized at the low temperature of 400°C**.** As calcination temperatures increased from 600° to 850°C, the KNN solid solution became more homogeneous, XRD peaks became narrower, and a pattern similar to that expected for orthorhombic $K_{1/2}Na_{1/2}NbO_3$ was achieved after 600 °C, as indicated by the separate peaks of 0 2 2 and 2 0 0. The resulting KNN powders consisted of agglomerated particles of 70 to 300 nm in size. As a final remark, the present method could also be applicable to the preparation of other materials such as $KNbO_3$, $NaNbO_3$ etc.

Acknowledgments

This work was supported by the Thailand Research Fund (TRF), the Commission on Higher Education (CHE), Thailand Graduate Institute of Science and Technology (TGIST), National Research Council of Thailand (NRCT), and the National Nanotechnology Center (NANOTEC) NSTDA, Ministry of Science and Technology, Thailand through its program of Center of Excellence Network.

References

1. Z. X. Ruzhong Zuoa and L. Li, Dielectric and piezoelectric properties of Fe_2O_3-doped $(Na_{0.5}K_{0.5})_{0.96}Li_{0.04}Nb_{0.86}Ta_{0.1}Sb_{0.04}O_3$ lead-free ceramics. *J. Phys. Chem. Sol.* **69**, 1728–1732 (2008).
2. Y. G. Lv, C. L. Wang, J. L. Zhang, M. L. Zhao, M. K. Li, and H. C. Wang, Modified $(K_{0.5}Na_{0.5})(Nb_{0.9}Ta_{0.1})O_3$ ceramics with high Qm. *Mater. Lett.* **62**, 3425–3427 (2008).
3. Y. Wang, J. Wu, D. Xiao, J. Zhu, P. Yu, L. Wu, and X. Li, Piezoelectric properties of (Li, Ag) modified $(Na_{0.50}K_{0.50})NbO_3$ lead-free ceramics with high Curie temperature. *J. Alloys Compd.* **459**, 414–417 (2008).
4. S. J. Park, H. Y. Park, K. H. Cho, S. Nahm, H. G. Lee, D. H. Kim, and B. H. Choi, Effect of CuO on the sintering temperature and piezoelectric properties of lead-free $0.95(Na_{0.5}K_{0.5})NbO_3$-$0.05CaTiO_3$ ceramics. *Mater. Res. Bull.*, vol. In Press, Corrected Proof.
5. R. C. Chang, S. Y. Chu, Y. P. Wong, C. S. Hong, and H. H. Huang, The effects of sintering temperature on the properties of lead-free $(Na_{0.5}K_{0.5})NbO_3$-$SrTiO_3$ ceramics. *J. Alloys Compd.* **456**, 308–312 (2008).
6. T. Takenaka and H. Nagata, Current status and prospects of lead-free piezoelectric ceramics. *J. Eur. Ceram. Soc.* 25, 2693–2700 (2005).
7. [7] E. Ringgaard and T. Wurlitzer, Lead-free piezoceramics based on alkali niobates. *J. Eur. Ceram. Soc.* 25, 2701–2706 (2005).
8. Y. Saito, H. Takao, T. Tani, T. Nonoyama, K. Takatori, T. Homma, T. Nagaya, and M. Nakamura, Lead-free piezoceramics. *Nature* **432**, 84–87 (2004).

9. K. Singh, V. Lingwal, S. C. Bhatt, N. S. Panwar, and B. S. Semwal, Dielectric properties of potassium sodium niobate mixed system. *Mater. Res. Bull.* **36**, 2365–2374 (2001).
10. A. S. T. Wada and T. Saito, Fabrication of lead-free piezoelectric $KNbO_3$ ceramics by modified solid state reaction method. *Jpn. Soc. Appl. Phys.* **45**, 7431–7434 (2006).
11. J. Xu, D. D. Xue, and C. Yan, Chemical synthesis of $NaTaO_3$ powder at low-temperature. *Mater. Lett.* **59**, 2920–2922 (2005).
12. M. A. Mohamed, A. K. Galwey, and S. A. Halawy, The activities of some metal oxides in promoting the thermal decomposition of potassium oxalate. *Thermochim. Acta.* **387**, 63–74 (2002).
13. L. H. McAlexander, C. M. Beck, J. J. Burdeniuc, and R. H. Crabtree, Fluoroalkane aromatization over hot sodium oxalate. *J. Fluor. Chem.* **99**, 67–72 (1999).
14. W. Stanek, Characterization of sintering phenomena of $K_{0.5}Na_{0.5}NbO_3$. vol. M. Sc. Berkeley: University of Californa, 1970.
15. B. Jaffe and W. R. Cook, Piezoelectric ceramic: R.A.N. Publishers, 1971.
16. L. Katz and H. D. Megaw, The structure of potassium niobate at room temperature: the solution of pseudosymmetric structure by fourier mathods. *Acta Crystallogr.* **22**, 639–684 (1967).
17. V. Lingwal, B. S. Semwal, and N. S. Panwar, Dielectric properties of $Na_{1-x}K_xNbO_3$ in orthorhombic *Phase. Bull. Mater. Sci.* **26**, 619–625 (2003).
18. M. Ichiki, L. Zhang, M. Tanaka, and R. Maeda, Electrical properties of piezoelectric sodium-potassium niobate. *J. Eur. Ceram. Soc.* **24**, 1693–1697 (2004).
19. K. Singh, V. Lingwal, S. C. Bhatt, N. S. Panwar, and B. S. Semwal, Dielectric properties of potassium sodium niobate mixed system. *Mater. Res. Bull.* **36**, 2365–2374 (2001).
20. J. H. Lv, M. Zhang, M. Guo, and W. C. Li, Hydrothermal synthesis and characterization of $K_xNa_{(1-x)}NbO_3$ powders. *Int. J. Appl. Ceram. Technol.* **4**, 571–577 (2007).

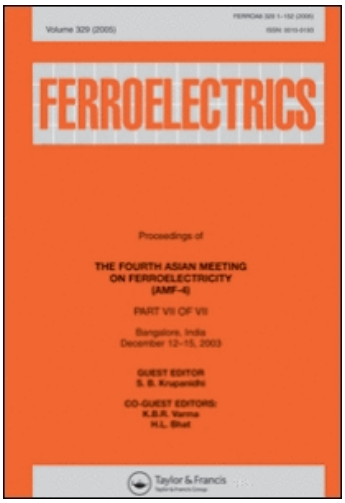

Ferroelectrics
Publication details, including instructions for authors and subscription information:
http://www.informaworld.com/smpp/title~content=t713617887

Preparation and Properties of Lead Free Bismuth Sodium Titanate-Bismuth Zinc Titanate Ceramics

Rangson Muanghlua [a]; Surasak Niemcharoen [a]; Wanwilai C. Vittayakorn [b]; Nattapong Tungsitvisetkul [c]; Pimjan Chinwaro [c]; Anucha Ruangphanit [d]; Nopsiri Chaiyo [e]; Naratip Vittayakorn [ce]
[a] Department of Electronics, Faculty of Engineering, King Mongkut's Institute of Technology, Ladkrabang, Bangkok, Thailand [b] Department of Physics and Materials Science, Faculty of Science, Chiang Mai University, Chiang Mai, Thailand [c] Materials Science Research Units, Department of Chemistry, Faculty of Science, King Mongkut's Institute of Technology, Ladkrabang, Bangkok, Thailand [d] Ministry of Science and Technology, Thai Microelectronics Center (TMEC), National Electronics and Computer Technology Center, Nation Science and Technology Development Agency, Chachoengsao, Thailand [e] Collage of KMITL Nanotechnology King Mongkut's Institute of Technology, Ladkrabang, King Mongkut's Institute of Technology, Ladkrabang, Bangkok, Thailand

Online Publication Date: 01 January 2009

To cite this Article Muanghlua, Rangson, Niemcharoen, Surasak, Vittayakorn, Wanwilai C., Tungsitvisetkul, Nattapong, Chinwaro, Pimjan, Ruangphanit, Anucha, Chaiyo, Nopsiri and Vittayakorn, Naratip(2009)'Preparation and Properties of Lead Free Bismuth Sodium Titanate-Bismuth Zinc Titanate Ceramics',Ferroelectrics,383:1,1 — 7
To link to this Article: DOI: 10.1080/00150190902873303
URL: http://dx.doi.org/10.1080/00150190902873303

Ferroelectrics, 383:1–7, 2009

ISSN: 0015-0193 print / 1563-5112 online
DOI: 10.1080/00150190902873303

Preparation and Properties of Lead Free Bismuth Sodium Titanate–Bismuth Zinc Titanate Ceramics

RANGSON MUANGHLUA,[1] SURASAK NIEMCHAROEN,[1] WANWILAI C. VITTAYAKORN,[2] NATTAPONG TUNGSITVISETKUL,[3] PIMJAN CHINWARO,[3] ANUCHA RUANGPHANIT,[4] NOPSIRI CHAIYO,[5] AND NARATIP VITTAYAKORN[3,5,*]

[1]Department of Electronics, Faculty of Engineering, King Mongkut's Institute of Technology, Ladkrabang, Bangkok, Thailand 10520
[2]Department of Physics and Materials Science, Faculty of Science, Chiang Mai University, Chiang Mai 50200, Thailand
[3]Materials Science Research Units, Department of Chemistry, Faculty of Science, King Mongkut's Institute of Technology, Ladkrabang, Bangkok 10520, Thailand
[4]Thai Microelectronics Center (TMEC), National Electronics and Computer Technology Center, Nation Science and Technology Development Agency, Ministry of Science and Technology, Chachoengsao 24000, Thailand
[5]Collage of KMITL Nanotechnology King Mongkut's Institute of Technology, Ladkrabang, King Mongkut's Institute of Technology, Ladkrabang, Bangkok 10520, Thailand

Lead-free piezoelectric ceramics based on $(1-x)Bi_{1/2}Na_{1/2}TiO_3 - x\ Bi(Zn_{1/2}Ti_{1/2})O_3$ *(x = 0.0, 0.02, 0.04, 0.06, 0.08, 0.10, 0.20, 0.30, 0.40, and 0.5) were obtained via solid-state processing techniques. The influence of BZT addition on BNT characteristics, sintering, microstructure and properties was investigated. A single perovskite phase with rhombohedral symmetry was obtained for* $Bi(Zn_{1/2}Ti_{1/2})O_3$ *substitutions of up to 10 mole%. A small amount of BZT was effective for improving both sintering behavior and dielectric properties of BNT ceramics. Optimized dielectric properties were obtained for samples with a maximum density of* $\rho = 98.3\%$ *for the composition,* $x = 0.1$.

Keywords Lead-free piezoelectric ceramics; dielectric properties; perovskite structure; $(Bi_{0.5}Na_{0.5})TiO_3$; $Bi(Zn_{0.5}Ti_{0.5})O_3$

PACS: 64.70.K-, 77.22.Ch, 81.05.Je, 85.80.-n and 77.84.Dy

Introduction

The effects of toxic lead oxide, a major constituent of the most widely used piezoelectric materials $PbZrO_3$-$PbTiO_3$ (PZT), are considered a danger to nature. For protection of the

Received August 3, 2008; in final form December 31, 2008.
*Corresponding author. E-mail: naratipcmu@yahoo.com

environment, Restriction of Hazardous Substances (RoHS) regulations, European Union's Waste Electrical and Electronics Equipment (WEEE) and other requirements have been established [1, 2]. As of July 1st, 2006, all new electrical and electronic products put on the European Market and falling under the scope of the European Union directive, RoHS, have to comply with stated requirements. Every homogeneous material within covered products is restricted to a maximum concentration of 0.1% by weight of lead, mercury, hexavalent chromium, PBB and PBDE, and a maximum of 0.01% by weight of cadmium. According to supporting requirements, there was an increase in the attentiveness of lead-free materials. As many researches have reported, $Bi_{0.5}Na_{0.5}TiO_3$; BNT (which was discovered by Smolensky et al. in 1960 [3]) is one of the most important lead-free piezoelectric materials with a perovskite structure. BNT possesses strong ferroelectric properties at a relatively high Curie temperature ($T_c = 320°C$) and phase transition point from ferroelectric to antiferroelectric ($T_p = 200°C$), with a relatively large remanent polarization ($P_r = 38\ \mu C/cm^2$) and coercive field ($E_c = 73$ kV/cm) at room temperature [3–8]. Apart from its strong ferroelectric, when compared with PZT, BNT-based materials possess high anisotropic electromechanical coupling properties ($k_t \geq 0.48$, $k_p \approx 0.165$–0.255), high frequency constant ($N_t \geq 2550$ Hz · m) and lower dielectric constant ($\varepsilon_{33}^T \approx 290$–$524$) [6]. Nevertheless, it is hard to pole pure BNT for its large coercive field and relatively large conductivity. To improve some poor properties of BNT, numerous modifications of BNT-based ceramics have been developed. Many researches have suggested that the improvement of piezoelectric properties can be achieved by forming solid solution with other perovskite oxides. Several solid solutions of BNT, with $SrTiO_3$, $La_2(TiO_3)_3$, $NaNbO_3$, and $BaTiO_3$, have been investigated [4].

$Bi(Zn_{1/2}Ti_{1/2})O_3$ (BZT) is a ferroelectric material, which has a Zn^{2+} and Ti^{4+} complex on the B-site of the ABO_3 perovskite structure, with a tetragonal symmetry [9]. The solid solution of $(x)PbTiO_3$–$(1–x)Bi(Zn_{1/2}Ti_{1/2})O_3$ has been studied by Suchomel et al.[10]. The $(x)PbTiO_3$ – $(1–x)Bi(Zn_{1/2}Ti_{1/2})O_3$ system exhibits a high c/a ratio of 1.11 for $x = 0.60$. However, there have been no systematic investigations on the solid solution of BNT-BZT ceramics. In this paper, the preparation of bismuth zinc titanate (BZT) —modified bismuth sodium titanate (BNT) ceramics, with compositions $(1 - x)Bi_{1/2}Na_{1/2}TiO_3 - x$ $Bi(Zn_{1/2}Ti_{1/2})O_3$ ($x = 0.0$, 0.2, 0.4, 0.6, 0.8, 0.10, 0.20, 0.30, 0.40, and 0.5) ceramics through the solid-state processing techniques, was investigated. The influence of BZT addition on the powder, crystal structure, microstructure and dielectric properties was examined.

Experimental Procedure

Bismuth zinc titanate (BZT) — modified bismuth sodium titanate (BNT) ceramics with compositions $(1\text{-}x)Bi_{1/2}Na_{1/2}TiO_3 - x$ $Bi(Zn_{1/2}Ti_{1/2})O_3$ ($x = 0.0$, 0.2, 0.4, 0.6, 0.8, 0.10, 0.20, 0.30, 0.40, and 0.5) were prepared by the solid-state processing techniques. High-purity oxides and carbonates; Na_2CO_3 (99.5%), Bi_2O_3 (99.97%), ZnO (99.9%) and TiO_2 (99.9%) were used as starting materials, which had been treated carefully by a special drying process before use, particularly for sodium carbonates. In the first stage, Bi_2O_3, Na_2CO_3 and TiO_2 were thoroughly mixed in the stoichiometric ratio, and then calcined at 900°C for 24 h to form $(Bi_{0.5}Na_{0.5})TiO_3$; BNT. In the second stage, the precursor (BNT) was mixed in the stoichiometric ratio with other starting materials. After drying at 80°C for 16 h, powders were calcined in a closed alumina crucible at 900°C for 4 h, with a heating/cooling rate of 20°C/min. The calcined powders were then mixed with 5 wt% polyvinyl alcohol (PVA) and pressed into discs, 1.5 cm in diameter. The green discs were sintered at 1,150°C for 6

h, with a heating/cooling rate of 5°C/min and covered with calcined powders in order to protect from the loss of bismuth. Formation of the perovskite phase and crystal structure of BNT-BZT was examined by room temperature X-ray diffraction (XRD, Advance D8) using Ni-filtered CuK_α radiation. Morphologies and grain size were imaged directly using a scanning electron microscope (SEM, LEO1455 VP). Dielectric measurements were carried out at room temperature by an LCR meter (Hewlett-Packard, 4284A).

Results and Discussion

Figure 1 illustrates the X-ray diffraction patterns of $(1-x)$BNT-xBZT; $x = 0.0$–0.5 powders calcined at 900°C for 4 h, with a heating/cooling rate of 20°C/min. At a BZT ratio of up to 0.10, X-ray diffraction patterns showed that a pure perovskite structure was obtained with no impurity phases, and/or no individual phases from the precursors were presented. As the fraction of BZT in the solid solution was increased to above 0.10, the pyrochlore phase began to develop and increase in intensity with increasing BZT concentration. These results indicate that the presence of BZT in the solid solution decreases the structural stability of the BNT perovskite phase. In other words, this result indicates that BZT has limited solubility in BNT ceramics, which tends to be solved at a concentration of 0.1mol. In addition, the X-ray diffraction patterns revealed that the crystal structure was influenced by BZT addition. Without BZT doping, the pure BNT possesses a rhombohedral phase, with a (110) peak detectable at 32.48° (2θ), which could be matched with $Bi_{1/2}Na_{1/2}TiO_3$ JCPDS file no. 36-0340. As the BZT content in the compounds is increased, the diffraction angle of (1 1 1) peaks in the BNT-BZT powders and shifts downwards to lower 2θ angles, as illustrated in Fig. 2(a). This phenomenon indicated that a consecutive increase in lattice constant is a function of BZT fraction. As we know, the ionic radius of Zn^{2+} ($r_{Zn^{2+}} =$ 88 pm) is larger than that of Ti^{4+} ($r_{Ti^{4+}} = 74.5$ pm), which results in lattice distortion and an increased lattice constant of the ceramic. The X-ray diffraction patterns of these

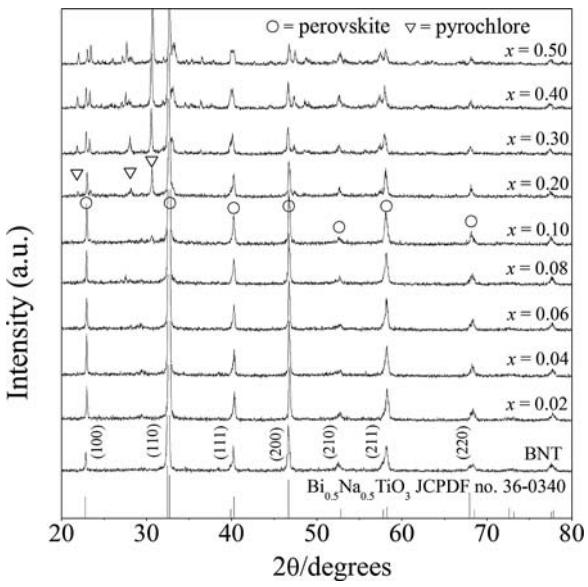

Figure 1. X-ray diffraction patterns of (1-x)BNT-xBZT; $x = 0.0$–0.5 powders calcined at 900°C for 4 h, with a heating/cooling rate of 20°C/min.

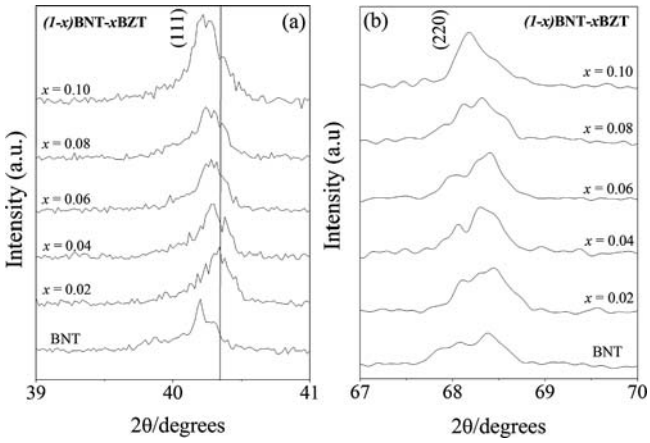

Figure 2. X-ray diffraction patterns of (1-x)BNT-xBZT; $x = 0.0$-0.1 powders calcined at 900°C for 4 h, with a heating/cooling rate of 20°C/min.

powders also indicate a phase transition from rhombohedral to cubic, with increasing BZT concentration. The rhombohedral symmetry of BNT ceramics can be characterized at room temperature by a (2 2 0)/(1 4 0) peak split between 66° and 69°, and a single peak of (2 0 0) between 45° and 48° [5]. The rhombohedral (2 2 0)/(1 4 0) peak split remains until $x = 0.08$ and then combines into a slightly asymmetric peak at $x = 0.1$[Fig. 2(b)]. The microstructure of the $(1-x)$BNT$-x$BZT ceramics sintered at 1,150°C for 6 h, with a heating/cooling rate of 5°C/min, is presented in Fig. 3. The SEM observation confirms that the BNT-BZT ceramics are densely sintered. Furthermore, all BNT-BZT samples have a high density of around 92.5–98.3% of the theoretical density, as reported in Table 1. The theoretical densities of each composition were calculated based on the rule of BNT mixture and the theoretical densities of BZT. The microstructure of the ceramics clearly showed the apparent increase in density, as shown in Fig. 3. The density increased to the maximum value of 98.3% compared to the theoretical density of 10 mol% BZT. Beyond 10 mol% BZT, a decrease in density resulted. The fracture mode of pure BNT ceramics was preferentially intergranular, but it became a more transgranular oriented fracture with

Table 1
Physical and dielectric properties of (1-x)BNT-xBZT; $x = 0.0 - 0.2$ ceramics sintered at 1,150°C for 6 h (P = perovskite, P_y = pyroclore, R = rhombohedrol, C = cubic)

x	Phase	Crystal structure	Grain size (μm)	Density (%)	Dielectric constant	tan δ
0.00	P	R	2.02 ± 0.37	92.5	420	0.73
0.02	P	R	1.78 ± 0.26	95.6	750	0.35
0.04	P	R	2.35 ± 0.40	96.1	760	0.42
0.06	P	R	1.97 ± 0.32	96.5	710	0.22
0.08	P	R	1.83 ± 0.24	96.6	770	0.17
0.10	P	C	2.24 ± 0.57	98.3	840	0.04
0.20	P+P_y	C	2.08 ± 0.35	97.6	950	0.28

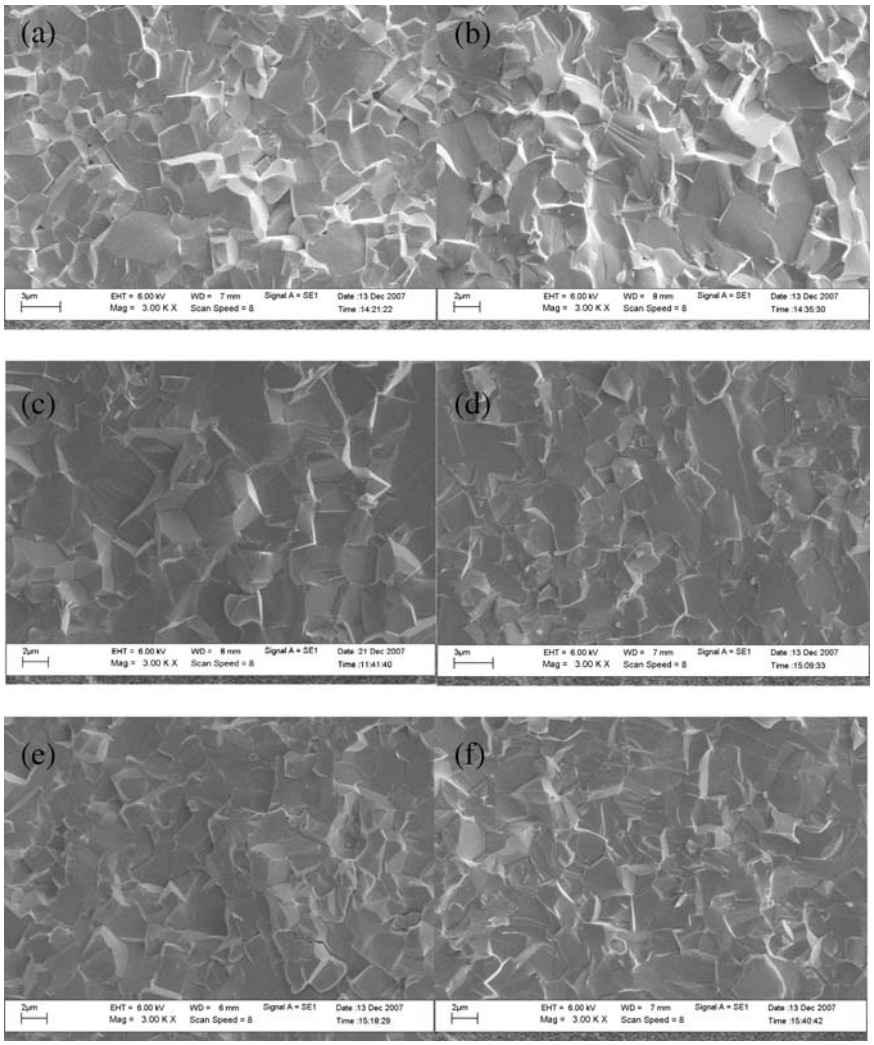

Figure 3. SEM micrograph of (1-x)BNT-xBZT; (a) $x = 0.0$, (b) $x = 0.02$, (c) $x = 0.04$, (d) $x = 0.06$, (e) $x = 0.08$, and (f) $x = 0.1$ ceramics sintered at 1,150°C for 6 h, with a heating/cooling rate of 5°C/min.

increasing amounts of added BZT. Figure 4 shows the relative permittivity (ε_r) and loss tangent (tan δ) at room temperature of $(1-x)$BNT-xBZT; $x = 0.0$-0.2 ceramics as a function of the BZT fraction. The ε_r of pure BNT was only about 420, but it increased significantly with increasing BZT content to about 750, 760 and 840 for 0.02, 0.04 and 0.10 mol BZT-doped BNT ceramics, respectively. Moreover, dielectric loss was decreased. The decrement in dielectric loss is believed to be proportional to the sintered density. However, higher dielectric loss observed at composition $x = 0.2$ is due to the formation of the pyrochlore phase. This was related to the result from the X-ray diffraction technique, which indicated that pyroclore phases were found in ceramics of BZT mole fractions above 0.10. In addition, the lower transition temperature of BNT-BZT ceramics may have increased the relative permittivity.

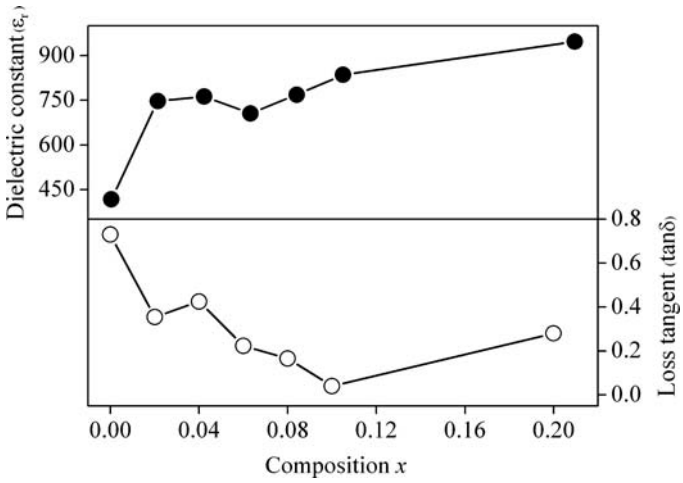

Figure 4. Dielectric constant (ε_r) and loss tangent (tan δ) at room temperature of (1-x)BNT-xBZT; $x = 0.0$-0.2 ceramics sintered at 1,150°C for 6 h, with a heating/cooling rate of 5°C/min in a bismuth atmosphere.

Conclusion

The microstructure, crystal structure and dielectric properties of $(1-x)Bi_{1/2}Na_{1/2}TiO_3 - x$ $Bi(Zn_{1/2}Ti_{1/2})O_3$ piezoelectric ceramics were investigated with different contents of $Bi(Zn_{1/2}Ti_{1/2})O_3$. A single perovskite phase with rhombohedral symmetry was obtained for $Bi(Zn_{1/2}Ti_{1/2})O_3$ substitutions of up to 10 mole%. A small amount of BZT was effective for improving both sintering behavior and dielectric properties of BNT ceramics. The density of BNT ceramics was increased with BZT addition to a relative density of approximately 98.3% for 10 mol% of BZT added.

Acknowledgments

This work was supported by the Thailand Research Fund (TRF), the Commission on Higher Education (CHE), Thailand Graduate Institute of Science and Technology (TGIST), National Research Council of Thailand (NRCT), and the National Nanotechnology Center (NANOTEC) NSTDA, Ministry of Science and Technology, Thailand through its program of Center of Excellence Network.

References

1. RoHS and WEEE compliant flame retardants developed for electrical connectors. *Reinforced Plastics* **51**(8), 12–12 (2007).
2. Endwave transceivers comply with upcoming ROHS deadline. *III-Vs Review* **19**(2), 11–11 (2006).
3. C. Peng, J. F. Li, and W. Gong, Preparation and properties of $(Bi_{1/2}Na_{1/2})TiO_3$-$Ba(Ti,Zr)O_3$ lead-free piezoelectric ceramics. *Mater. Lett.* **59**(12), 1576–1580 (2005).
4. L. Gao, Y. Huang, Y. Hu, and H. Du, Dielectric and ferroelectric properties of (1 - x)$BaTiO_3$-x$Bi_{0.5}Na_{0.5}TiO_3$ ceramics. *Ceramics International* **33**(6), 1041–1046 (2007).
5. H. Y. Tian, D. Y. Wang, D. M. Lin, J. T. Zeng, K. W. Kwok, H. L. W. Chan, Diffusion phase transition and dielectric characteristics of $Bi_{0.5}Na_{0.5}TiO_3$-$Ba(Hf,Ti)O_3$ lead-free ceramics. *Solid State Commu.* **142**(1–2), 10–14 (2007).

6. X. Jing, Y. Li, and Q. Yin, Hydrothermal synthesis of $Na_{0.5}Bi_{0.5}TiO_3$ fine powders. *Mater. Sci. Eng. B* **99**(1–3), 506–510 (2003).
7. T. Motohashi and T. Kimura, Development of texture in $Bi_{0.5}Na_{0.5}TiO_3$ prepared by reactive-templated grain growth process. *J. Eur. Ceram. Soc.* **27**(13–15), 3633–3636 (2007).
8. H. Nagata and T. Takenaka, Additive effects on electrical properties of $(Bi_{1/2}Na_{1/2})TiO_3$ ferroelectric ceramics. *J. Eur. Ceram. Soc.* **21**(10–11), 1299–1302 (2001).

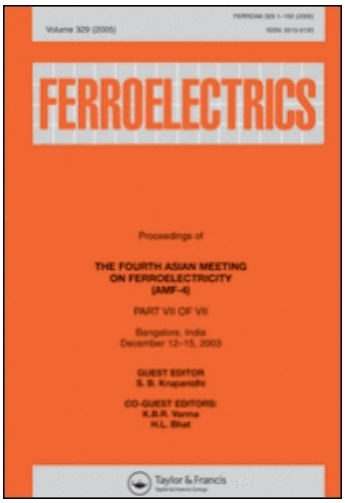

Ferroelectrics
Publication details, including instructions for authors and subscription information:
http://www.informaworld.com/smpp/title~content=t713617887

Effect of Firing Temperatures on Phase Formation and Microstructure of $Ba(Zr_{0.3}Ti_{0.7})O_3$ Ceramics Prepared via Mixed Oxide Method

Theerachai Bongkarn [a]; Nalinee Phungjitt [b]; Naratip Vittayakorn [c]
[a] Department of Physics, Faculty of Science, Naresuan University, Phitsanulok, Thailand [b] Department of Physics, Faculty of Science, Uttaradit Rajabhat University, Uttaradit, Thailand [c] Department of Chemistry, Faculty of Science, King Mongkut's Institute of Technology Ladkrabang, Bangkok, Thailand

Online Publication Date: 01 January 2009

To cite this Article Bongkarn, Theerachai, Phungjitt, Nalinee and Vittayakorn, Naratip(2009)'Effect of Firing Temperatures on Phase Formation and Microstructure of $Ba(Zr_{0.3}Ti_{0.7})O_3$ Ceramics Prepared via Mixed Oxide Method',Ferroelectrics,383:1,65 — 72
To link to this Article: DOI: 10.1080/00150190902876280
URL: http://dx.doi.org/10.1080/00150190902876280

Ferroelectrics, 383:65–72, 2009

ISSN: 0015-0193 print / 1563-5112 online
DOI: 10.1080/00150190902876280

Effect of Firing Temperatures on Phase Formation and Microstructure of $Ba(Zr_{0.3}Ti_{0.7})O_3$ Ceramics Prepared via Mixed Oxide Method

THEERACHAI BONGKARN,[1,*] NALINEE PHUNGJITT,[2] AND NARATIP VITTAYAKORN[3]

[1]Department of Physics, Faculty of Science, Naresuan University, Phitsanulok, Thailand
[2]Department of Physics, Faculty of Science, Uttaradit Rajabhat University, Uttaradit, Thailand
[3]Department of Chemistry, Faculty of Science, King Mongkut's Institute of Technology Ladkrabang, Bangkok, Thailand

$Ba(Zr_{0.3}Ti_{0.7})O_3$ (BZT) ceramics were fabricated by a mixed oxide synthetic route. The effect of calcination and sintering temperatures on phase formation and the microstructure of the ceramics were investigated. The pure perovskite phase of BZT powders was obtained with a calcination condition of 1300°C for 4 h. The sintered pellets showed a pure peroverskite cubic phase in all samples. The microstructure of the powders exhibited an almost-spherical morphology and had a porous agglomerated form. The average particle sizes and the average grain sizes were increased from 0.2 to 1.1 μm and 3.9 to 25.1 μm with increasing calcination and sintering temperatures, respectively. The densest and the highest maximum dielectric constant was found in the BZT ceramic sintered at 1550°C.

Keywords Barium zirconate titanate; microstructure; phase formation; mixed oxide

Introduction

Barium titanate ($BaTiO_3$, BT) is well known as a fundamental ferroelectric perovskite oxide [1] and is often used in multilayer ceramic capacitors (MLCs) due to its' high dielectric constant [2]. $BaTiO_3$ displays dielectric anomalies at 130, 0, and −90°C with respective transformations in symmetry from cubic to tetragonal, from tetragonal to orthorhombic, and from orthorhombic to rhombohedral, respectively. Those anomalies are accompanied by a high dielectric constant near the phase transition [3]. The nature and phase transition temperature of BT can be modified via the partial substitution of either Ba ions (A-site doping) or Ti ions (B-site doping). A-site doping with cations of the same valence as Ba causes the Curie temperature (T_c) (∼130°C) to either decrease (Sr substitution) or increase (Pb substitution) without any significant broadening of the transition [4]. With B-site doping, the ferroelectric domains, which are associated with a cooperative

Received August 3, 2008; in final form December 31, 2008.
*Corresponding author. E-mail: researchcmu@yahoo.com

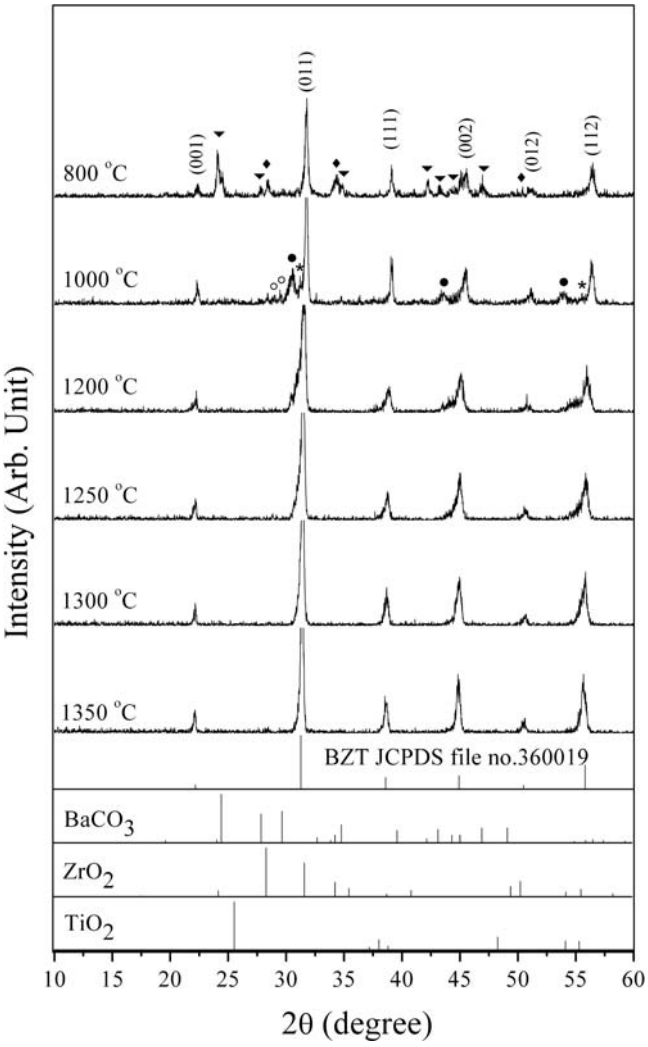

Figure 1. XRD patterns of $Ba(Zr_{0.3}Ti_{0.7})O_3$ powders: (▼) $BaCO_3$; (♦) ZrO_2; (●)$BaZrO_3$;(○)Ba_2ZrO_4; (*) $BaTiO_3$.

off-center displacement of Ti^{4+} ions in their TiO_6 octahedra, are disrupted, which often leads to a broadening of the transition at T_c. Partial replacement of titanium by tin or hafnium generally leads to a reduction in T_c and an increase in the permittivity maximum with dopant content [5].

Barium zirconate titanate ($Ba(Zr_xTi_{1-x})O_3$) is obtained by substituting ions at the B site of $BaTiO_3$ with Zr ions. This substitution results in a decrease in the temperature and a broadening of the permittivity maximum [6]. Brajer and Kulscar showed that, as the zirconium content increases, the orthorhombic-tetragonal phase transition temperature increases and the tetragonal-cubic phase transition temperature decreases [7, 8]. At a Zr/Ti ratio greater than 0.10, the three dielectric constant peaks coalesce into a single broad maximum [9]. $Ba(Zr_xTi_{1-x})O_3$ with $0.20 \leq x \leq 0.35$ ceramics were prepared by a sol-gel process [10]. The dielectric study of the ceramics showed a normal ferroelectric with weak

Table 1
The percent perovskite phase, average particle size, average grain size, T_c and density of BZT.

Calcined powders			Sintered ceramics			
Calcination temperatures (°C)	% perovskite phase (%)	Average particle size (μm)	Sintering temperatures (°C)	Average grain size (μm)	T_c (°C)	Density (g/cm^3)
800	68	0.26	1400	3.1	–64	5.70
1000	80	0.31	1450	7.2	–64	5.74
1200	83	0.79	1500	11.5	–63	5.78
1250	91	0.87	1550	12.2	–63	5.80
1300	100	0.91	1600	20.8	–92	5.69
1350	100	1.37				

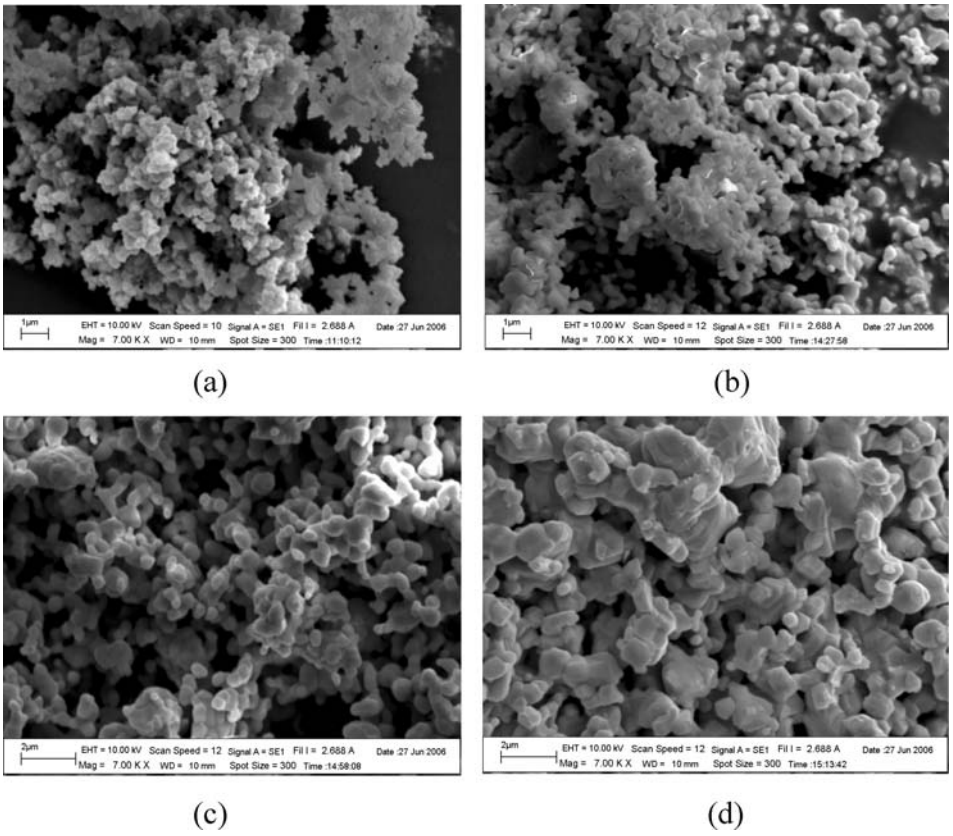

Figure 2. SEM photographs of BZT powders calcined at (a) 800°C, (b) 1200°C, (c) 1250°C and (d) 1350°C.

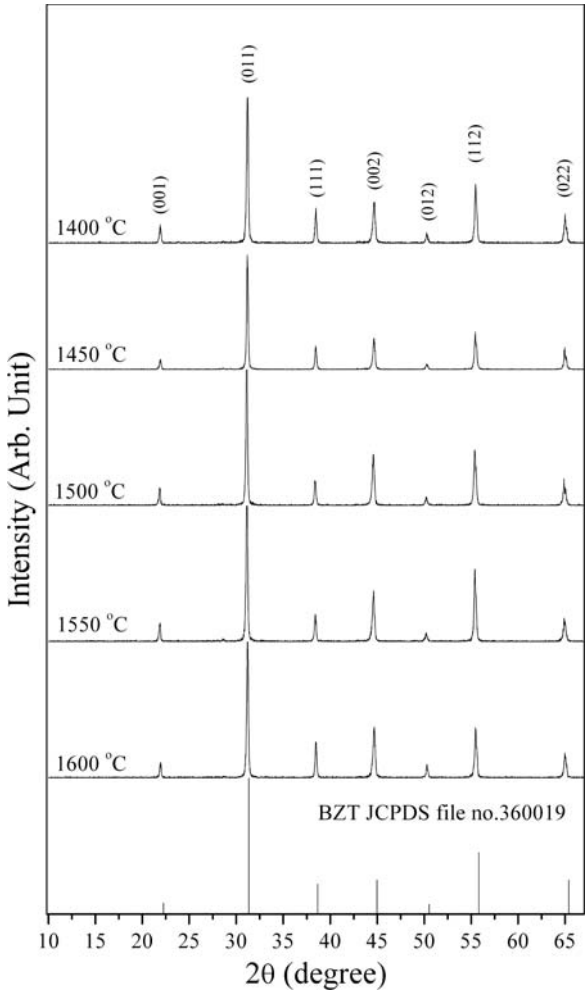

Figure 3. XRD patterns of $Ba(Zr_{0.3}Ti_{0.7})O_3$ ceramics.

diffuse phase transition behaviors for the ceramics with $x = 0.20$ and 0.25 [10]. The diffuse phase transition and a relaxor-like behavior were found at high Zr contents ($x = 0.30$ and 0.35). The tunability and dielectric loss of $Ba(Zr_{0.3}Ti_{0.7})O_3$ (BZT) ceramic measured at room temperature under the biasing field 40 kV/cm are 45% and 0.002, respectively [11]. This make the $Ba(Zr_{0.3}Ti_{0.7})O_3$; BZT ceramic promising material for tunable materials applications. However, to the author's best knowledge, the effect of firing temperature on crystal structure and morphology of $Ba(Zr_{0.3}Ti_{0.7})O_3$ powders and ceramics prepared by mixed oxide method have not been reported yet. Therefore, in the present work, the effect of calcination and sintering temperatures on microstructure and the phase formation of $Ba(Zr_{0.3}Ti_{0.7})O_3$ (BZT) ceramics prepared via a solid state reaction method was chosen. This would extend an understanding on the processing-properties relationships in the BZT ceramics.

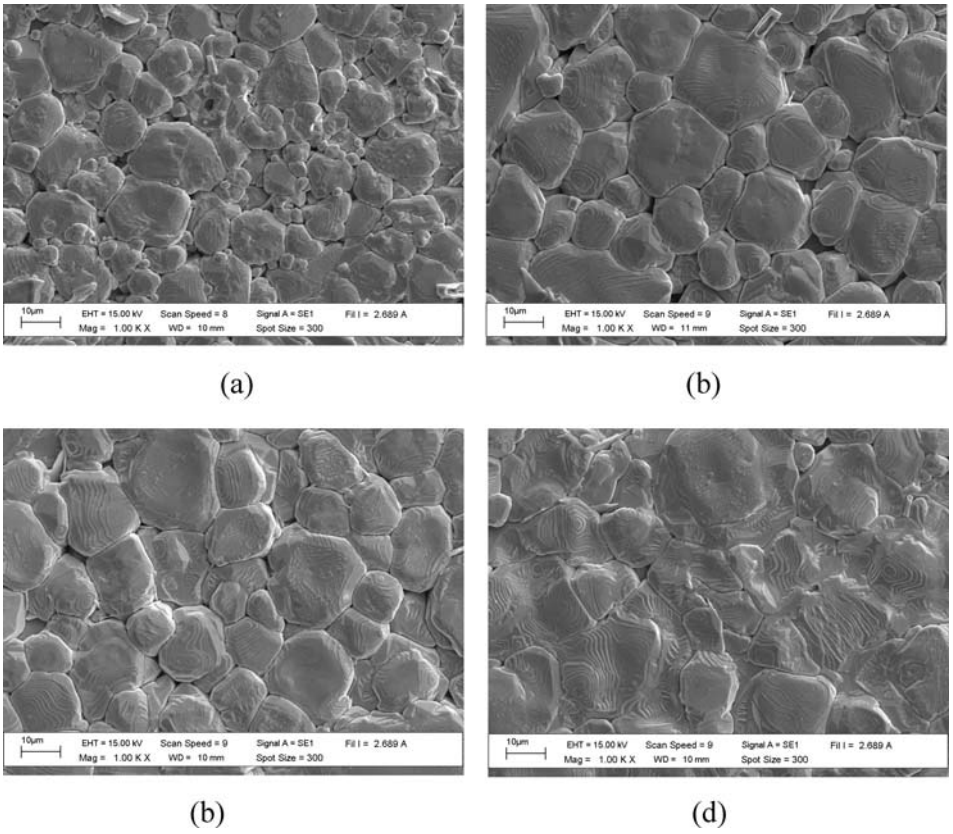

Figure 4. SEM photomicrograph of BZT ceramics sintered at (a) 1450°C, (b) 1500°C, (c) 1550°C and, (d) 1600°C.

Experimental

The starting materials were commercially available barium carbonate, $BaCO_3$ (99%) titanium (IV) oxide, TiO_2 (99%) and zirconium (IV) oxide, ZrO_2 (99%). Barium zirconate titanate ($Ba(Zr_{0.3}Ti_{0.7})O_3$, BZT) powder was synthesized by the solid state reaction of thoroughly ground mixtures of $BaCO_3$, TiO_2 and ZrO_2 powders by a ball milling procedure (zirconia milling media under ethanol for 24 h). Drying was carried out at 120°C for 4 h. After sieving, the mixture was calcined at various calcination temperatures, ranging from 800 to 1350°C, with a dwell time of 4 h and heating/cooling rate of 5°C/min. The calcined powders were then pressed into disks with a diameter of 15 mm at a pressure of 40 MPa. The pellets were sintered from 1400 to 1600°C for 2 h and cooled in a furnace. For electrical measurements, silver paste was fired on both sides of the polished samples at 500°C for 30 min and used as electrodes.

X-ray diffraction (XRD; Philip PW3040/60 X' Pert Pro) was employed to identify the phase formed and optimum temperature of BZT powders and ceramics. Calcined powders and sintered ceramics morphologies were imaged using scanning electron microscopy (SEM; LEO 1455 VP). Densities of sintered ceramics were measured by Archimedes method and the average grain size was determined by using a mean linear intercept method. The capacitance was measured with a LCR meter (Agilent 4263B) ranging from −170 to

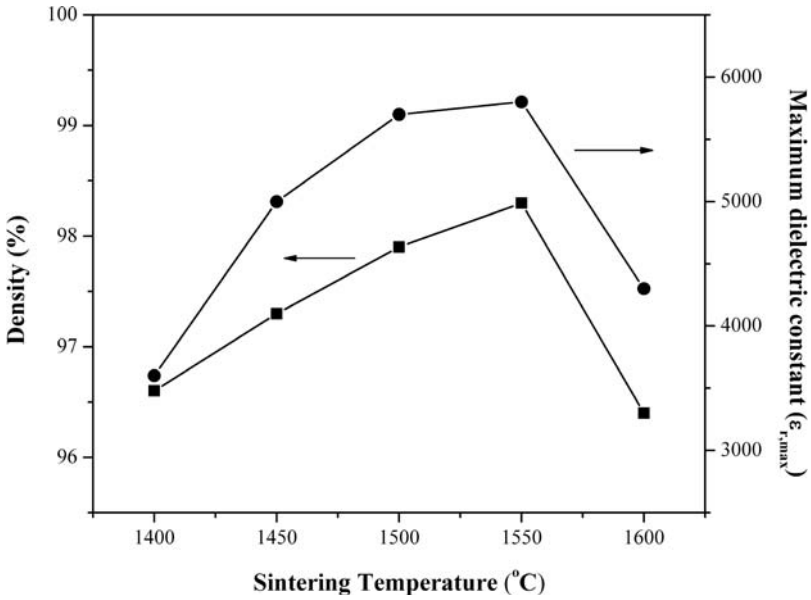

Figure 5. Variation of maximum dielectric constant and density of BZT ceramics as function of sintering temperatures.

25°C. The dielectric constant (ε_r) was calculated using the geometric area and thickness of the discs.

Results and Discussion

XRD patterns of BZT powders calcined at various temperatures are plotted in Fig. 1. After calcination at 800°C, the crystalline phase of BZT was accompanied with $BaCO_3$ and ZrO_2 as separate phases, whose X-ray peak matches the JCPDS file number 41-0373 [12] and 24-1165 [13]. As the temperature increased to 1000°C, the peaks corresponding to the raw materials disappeared, while the intensities of the $BaTiO_3$, $BaZrO_3$ and Ba_2ZrO_4 peaks became minor phases, which can correlate with JCPDS file number 03-0726 [14], 06-0399 [15] and 24-0130 [16] respectively. After calcination at 1250°C, the peaks corresponding to $BaTiO_3$, $BaZrO_3$ and Ba_2ZrO_4 were not detectable. Evidently, a single phase of BZT is formed by calcination at 1300°C. The strongest reflections in the majority of the XRD patterns can be identified as the perovskite phase of the composition $Ba(Zr_{0.3}Ti_{0.7})O_3$, which can be matched with the JCPDS file number 36-0019 [17]. To a first approximation, this phase is a cubic perovskite type structure.

The percentage of the perovskite phase of BZT powders as a function of calcination temperatures was calculated. The perovskite phase of 800 to 1250°C calcined samples did not reach a hundred percent. The single phase of perovskite of the calcined samples at a temperature higher than 1300°C was formed. The percentage of the BZT perovskite phase was increased with increasing of calcination temperatures listed in Table 1.

SEM photographs of BZT powders calcined between 800 and 1350°C are shown in Fig. 2. These powders exhibit an almost spherical morphology and have a porous agglomerated form. As the temperature increased, more agglomerate particles could be observed.

The average particle size tended to increase as calcination temperatures increased as shown in Table 1.

The BZT powders, calcined at 1300°C, were pressed into pellets and sintered at various temperatures. The XRD patterns of sintered ceramics are plotted in Fig. 3. It confirms that all samples were free of minor phase peaks. BZT ceramics are identified as a single phase with a perovskite structure which has a cubic symmetry, as reported in previous investigations [18].

Microstructure developments of sintered pellets were investigated by SEM. The surface of BZT ceramics at various sintering temperatures from 1450 to 1600°C are shown in Fig. 4. The average grain sizes increased from 3.9 to 25.1 μm (Table 1) with increasing of sintering temperature from 1400°C to 1600°C and the results also show a nonuniform distribution of grain size. These results agreed with previous work [11].

The maximum of dielectric constant ($\varepsilon_{r,\max}$) increased from 3600 to 5800 as the sintering temperature increased from 1400 to 1550°C. A further increase in the sintering temperature to 1600°C results in a drop in the values of $\varepsilon_{r,\max}$ to 4300 as show in Fig. 5. In the sintering temperature range of 1400 to 1550°C, the density increases with increasing sintering temperature. Further increase in the temperature to 1600°C leads to the decrease of the density (Figure 5). This feature creates a maximum density value of 98.3 % of theoretical density which is comparable to the value of JCPDS file No. 36-0019. The maximum dielectric constant corresponded with the density. The Curie temperature (T_c) of BZT ceramics are shown in Table 1. The T_c of BZT ceramics sintered between 1400 and 1550°C were about −63°C. While, the T_c of BZT ceramics sintered at 1600°C dropped to −92°C. These results suggested that the optimum sintering temperature of BZT ceramics is 1550°C. The decrease in $\varepsilon_{r,\max,}$ density and T_c of 1600°C sintered ceramic indicated that the composition of BZT was changed with a high sintering temperature.

Conclusion

$Ba(Zr_{0.3}Ti_{0.7})O_3$ powders can be formed through the reaction of barium carbonate, titanium (IV) oxide and zirconium (IV) oxide via calcined temperature at 1300°C. The resulting BZT powders were more agglomerated as the calcination temperature increased. BZT ceramic was identified by XRD as a single phase with the perovskite structure having cubic symmetry and the effect of sintering temperature on the densification, average grain size and dielectric properties was investigated. High density and dielectric constant of BZT ceramics were obtained for the sintering temperature about 1550°C.

Acknowledgment

This work was financially supported by the Thailand Research Fund (TRF), Commission on Higher Education (CHE), Faculty of Science, Naresuan University, Uttaradit Rajabhat University and King Mongkut's Institute of technology, Ladkrabang (KMITL). Thanks also to Mr. Don Hindle for his help in editing the manuscript.

References

1. W. S. Clabaugh, R. Swiggard, and R. Gilchrist, Preparation of barium titanyl oxalate tetrahydrate for conversion to barium titanate of high purity. *J. Res. Nat. Bur. Stand.* **56**, 289 (1956).
2. Y. Sakabe, K. Minai, and K. Wakino, Ferroelectric materials and their applications. *Jpn. J. Appl. Phys.* **20**, 147 (1981).

3. B. Jaffe, J. Cook, and H. Jaffe, Piezoelectric Ceramics. U.K.: London Acadamic Press. 1997.
4. H. Nemoto, and I. Oda, Direct examinations of PTC action of single grain boundaries in semi-conducting BaTiO3 ceramics. *J. Am. Ceram. Soc.* **63**, 398 (1980).
5. M. Kuwabara, K. Morimo, and T. Matsunaga, Single-grain boundaries in PTC resistors. *J. Am. Ceram. Soc.* **79**, 997 (1996).
6. W. Ulrich, G. Georg, B. Ulrich, W. Sophie, H. Detlev, and W. Rainer, Dielectric properties of Ba(Zr,Ti)O3-based ferroelectrics for capacitor applications. *J. Am. Ceram. Soc.* **84**, 759 (2001).
7. E. J. Brajer, U.S. Patent 2. **708**, 243 (1955).
8. F. Kulscar, U.S. Patent 2. **735**, 024 (1956).
9. D. Hennings, A. Schnell, and G. Simon, Diffuse ferroelectric phase transitions in Ba(Ti1-yZry)O3 ceramics. *J. Am. Ceram. Soc.* **65**, 539 (1982).
10. X. G. Tang, K. H. Chew, and H. L. W. Chan, Diffuse phase transition and dielectric tunability of Ba(ZryTi1-y)O_3 relaxor ferroelectric ceramics. *Act. Mater.* **52**, 5177 (2004).
11. Z. Yu, C. Ang, R. Guo, and A. S. Bhalla, Dielectric properties of sol–gel-derived MgO:$Ba_{0.5}Sr_{0.5}TiO_3$ thin-film composites. *Appl. Phys. Lett.* **81**, 1285 (2002).
12. Powder Diffraction File No. 41-0373. International Center for Diffraction Data, Newton Square, PA. (2003).
13. Powder Diffraction File No. 24-1165. International Center for Diffraction Data, Newton Square, PA. (2003).
14. Powder Diffraction File No. 03-0726. International Center for Diffraction Data, Newton Square, PA. (2003).
15. Powder Diffraction File No. 06-0399. International Center for Diffraction Data, Newton Square, PA. (2003).
16. Powder Diffraction File No. 24-0130. International Center for Diffraction Data, Newton Square, PA. (2003).
17. Powder Diffraction File No. 36-0019. International Center for Diffraction Data, Newton Square, PA. (2003).
18. T. N. Verbitskaia, G. S. Zndanov, I. N. Venevtsev, and S. P. Solviev, Soviet Phys-Crystallogr. 1958; 3, 182.

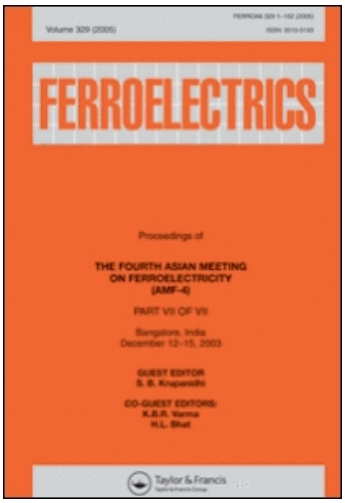

Ferroelectrics
Publication details, including instructions for authors and subscription information:
http://www.informaworld.com/smpp/title~content=t713617887

Hysteresis Response of Lead Zirconate—Lead Nickel Niobate Ferroelectric Ceramic Under Compressive Stress

W. C. Vittayakorn [a]; N. Vittayakorn [bc]
[a] Department of Physics, Faculty of Science, Chiang Mai University, Chiang Mai, Thailand [b] Materials Science Research Unit, Department of Chemistry, Faculty of Science, King Mongkut Institute of Technology Ladkrabang, Bangkok, Thailand [c] College of KMITL Nanotechnology, King Mongkut's Institute of Technology Ladkrabang, Bangkok, Thailand

Online Publication Date: 01 January 2009

To cite this Article Vittayakorn, W. C. and Vittayakorn, N.(2009)'Hysteresis Response of Lead Zirconate—Lead Nickel Niobate Ferroelectric Ceramic Under Compressive Stress',Ferroelectrics,382:1,1 — 6
To link to this Article: DOI: 10.1080/00150190902877569
URL: http://dx.doi.org/10.1080/00150190902877569

Ferroelectrics, 382:1–6, 2009

ISSN: 0015-0193 print / 1563-5112 online
DOI: 10.1080/00150190902877569

Hysteresis Response of Lead Zirconate—Lead Nickel Niobate Ferroelectric Ceramic Under Compressive Stress

W. C. VITTAYAKORN[1,*] AND N. VITTAYAKORN[2,3]

[1]Department of Physics, Faculty of Science, Chiang Mai University, Chiang Mai, Thailand
[2]Materials Science Research Unit, Department of Chemistry, Faculty of Science, King Mongkut Institute of Technology Ladkrabang, Bangkok, Thailand
[3]College of KMITL Nanotechnology, King Mongkut's Institute of Technology, Ladkrabang, Bangkok 10520, Thailand

In this work, PZ–PNN ceramic was prepared by a columbite method and sintered at optimum temperature. The effect of uniaxial compressive stress on the hysteresis properties of PZ–PNN ceramics is investigated. The hysteresis loop and ferroelectric properties under the compressive stress of the ceramics are observed at stress up to 100 MPa using a compressometer in conjunction with a modified Sawyer–Tower circuit. The results show that the applied stress has a significant influence on the hysteresis of PZ–PNN ceramics. The ferroelectric characteristics, i.e. the area of loops, P_s and P_r decrease with increasing compressive stress.

Keywords Lead zirconate; lead nickel niobate; hysteresis loop; ferroelectric property; compressive stress

Introduction

Lead zirconate (PZ) is an antiferroelectric ceramic with T_C of 230°C. It is reported that the antiferroelectric to ferroelectric transition leads to significant energy storage for DC field, which made PZ ceramic is the potential candidate for this application [1]. Moreover, the double hysteresis behavior of PZ ceramic is attracted to special electronic applications such as nonvolatile memories, micro-actuator and electro-optic devices. Although, PZ ceramic exhibits the great electrical characteristics and high dielectric breakdown strength, but the sintering temperature of this ceramic is also high. Therefore, the attempt to decrease the sintering temperature of PZ ceramics is necessary. Lead nickel niobate (PNN) is a relaxor ferroelectric with a broad dielectric peak near $T_C \sim -120$°C. It is reported that high densification PNN ceramic can be fabricated with the low sintering temperature. Thus, mixing PZ with PNN is a very interested system and expected to decrease the sintering temperature of this system. Moreover, with their complementary characteristics, it is expected that excellent properties can be obtained from ceramics in the PZ–PNN system. Because of these distinguish properties, PZ–PNN ceramics are attractive for various electronic applications,

Received August 3, 2008; in final form December 31, 2008.
*Corresponding author. E-mail: wanwilai_chaisan@yahoo.com

such as medical ultrasonic transducers, multilayer high frequency piezoelectric actuators and electro-mechanical actuators [2, 3]. In many of these applications, PZ–PNN ceramics are often subjected to mechanical loading, either deliberately in the design of the device itself or the device is used under environmental stresses. Despite in fact, material constants used in any design calculations are often obtained from a stress-free measuring condition, which in turn may lead to incorrect or inappropriate actuator and transducer designs. It is therefore important to determine the electrical properties of these ceramics as a function of applied stress. Previous investigates on stress–dependence of electrical properties of many ferroelectric ceramics, such as PZT, PMN, PMN–PT and BT [4, 5], have clearly emphasized the importance of this subject. Zhou et al. [6] and Yimnirun et al. [4] investigated the effect of external stress on the ferroelectric properties of soft PZT ceramics. Their results showed that the ferroelectric characteristics decrease with increasing compressive stress. Moreover, Chaisan et al. [7] have been studied the effect of compressive stress on the hysteresis properties of barium titanate ceramic. Their work found out that applied stress had a significant influence on the ferroelectric properties of BT ceramic.

Thus far, even though there have been many works about electrical properties of PZ [8] and PNN [9], but there are no previous reports about the ferroelectric hysteresis loops under various environmental stresses of PZ–PNN ceramic. Therefore, in this work, 0.5PZ–0.5PNN ceramic was prepared by a columbite precursor method and sintered at optimum temperature. The effect of compressive stress on the hysteresis properties of PZ–PNN ceramics is investigated. The ferroelectric data, i.e. the saturation polarization (P_s), the remanent polarization (P_r) and the coercive field (E_c), of 0.5PZ–0.5PNN ceramic under compressive stress will be reported.

Experimental Procedure

Investigations were performed on $0.5PbZrO_3$–$0.5Pb(Ni_{1/3}Nb_{2/3})O_3$ (0.5PZ–0.5PNN) ceramics produced by columbite precursor method and sintered at 1150°C for 4 h with heating/cooling rates of 5°C/min. The XRD measurement at room temperature showed that 0.5PZ–0.5PNN ceramic have a single perovskite phase with combination of orthorhombic and psudo-cubic symmetry as exhibited in Fig. 1, with unit cell parameters of 4.099 Å and unit cell volume of 68.87 $Å^3$ [1]. The disk samples with a diameter of 12.5 mm and a thickness of 0.8 mm were chosen for the electrical measurements and the samples were electroded by silver painting. The P–E hysteresis loops were characterized by using a computer controlled modified Sawyer-Tower circuit. The electric field was applied to a sample by a high voltage *ac* amplifier (Trek, model 610D) with the input sinusoidal signal with a frequency of 50 Hz from a signal generator (Goodwill, model GAG-809). To study the effect of the compressive stress on the hysteresis properties, the uniaxial compressometer was constructed. The detailed descriptions of this system are explained elsewhere [4, 10]. During the measurements, the specimen was immersed in silicone oil to prevent high voltage arcing during electric loading. Measurements were performed as a function of mechanical stress applied discretely between 0 and 100 MPa. During the measurements, a desired stress was first applied to the sample and then the electric field was applied. The P–E hysteresis loops were recorded at room temperature. The parameters obtained from the loops were the saturation polarization (P_s), the remanent polarization (P_r) and the coercive field (E_c), which are defined as the points where the loops reach the maximum polarization, cross the zero field and cross the zero polarization, respectively.

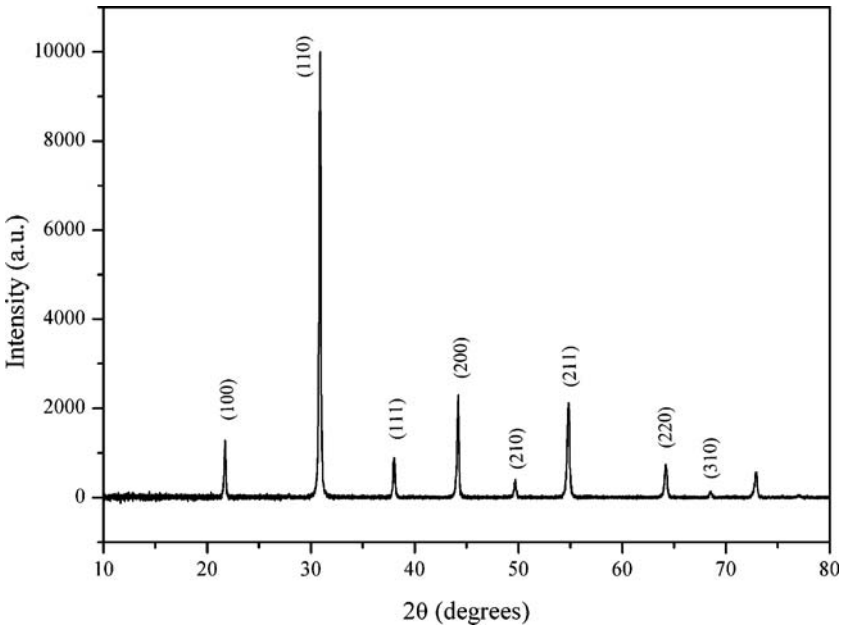

Figure 1. XRD pattern of 0.5PZ–0.5PNN ceramic sintered at 1150°C for 4 h with heating/cooling rates of 5°C/min.

Results and Discussion

The P–E hysteresis loops of the 0.5PZ–0.5PNN ceramic under various compressive stresses are shown in Fig. 2. For the first approximation, it can be noticed that the area of these P-E loops decrease with increasing stress. The P–E loop which represents the unit-volume polarization dissipation energy of a ferroelectric ceramics subject to one full cycle of electric field loading [11] is plotted in Fig. 3 as a function of compressive stress. The graph showed that the dissipation energy tends to decrease with stress rising. The dissipation energy is also represented the loss of energy which being consumed for self-heating of the ceramics and related directly to the amount of domains participating in the switching process during electrical loading [6]. From the P-E loop area results, it can be assumed that the amount of domains contributing to polarization reversal decreases with increasing compressive stress. Moreover, the ferroelectric parameters under various compressive stresses are obtained from these loops which are the saturation polarization (P_s), defined as the points where the loops reach the maximum polarization, the remanent polarization (P_r), defined as the points where the loops cross the zero field, and the coercive field (E_c), defined as the points where the loops cross the zero polarization. The variations of the P_s, P_r and E_c with the compressive stress are plotted in Figs. 4 and 5, respectively. Similar trend with the dissipation energy, both P_s and P_r values decrease as the compressive stress increases, which implied that a significant stress induced decrease in the switchable part of the spontaneous polarization of the PZ–PNN ceramic. For the coercive field (E_c), although the compressive stress increases but the E_c value still fluctuates in the same range (4.5–4.6 kV/cm), as showed in Fig. 5, which indicated that the PZ–PNN ceramic is not suitable for any applications under high compressive stress.

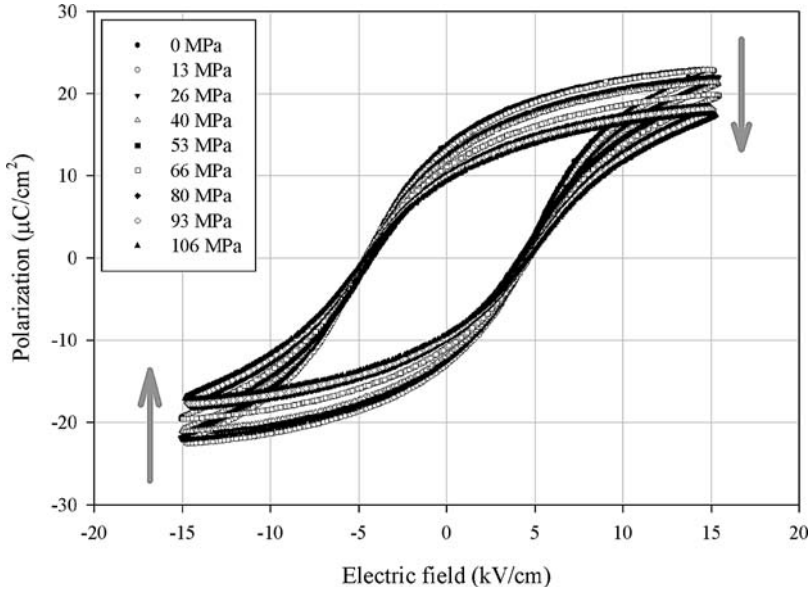

Figure 2. $P - E$ hysteresis loops as a function of compressive stress for 0.5PZ–0.5PNN ceramic.

For better understanding of the hysteresis results on the PZ–PNN ceramic, it can be explained the changes of the P_s, P_r and E_c values in term of domain reorientation processes. When the compressive stress is applied in the direction parallel to the poling direction, the applied stress tends to keep the ferroelectric domains aligned with their polar axes away from the stress direction through the non -180° domain switching processes. Thus, it is harder than usual applied electric field to reorient the domain along the stress direction,

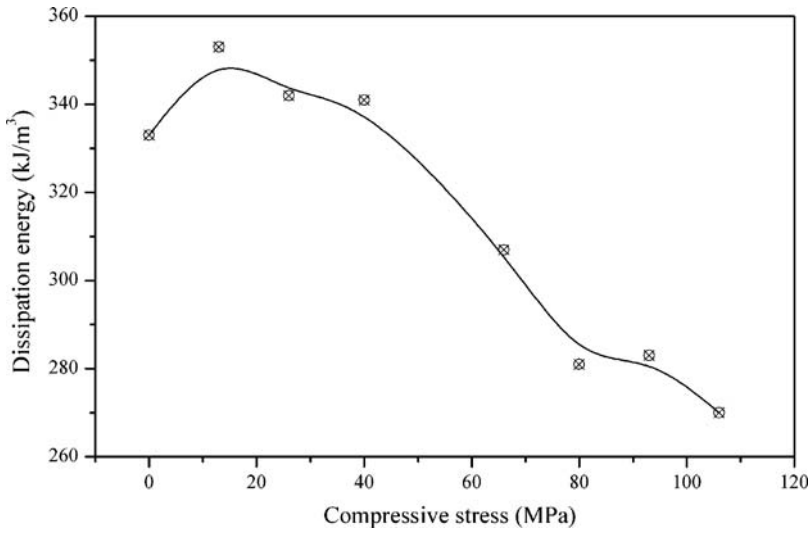

Figure 3. Variation of hysteresis loop area (dissipation energy) with compressive stress for 0.5PZ–0.5PNN ceramic.

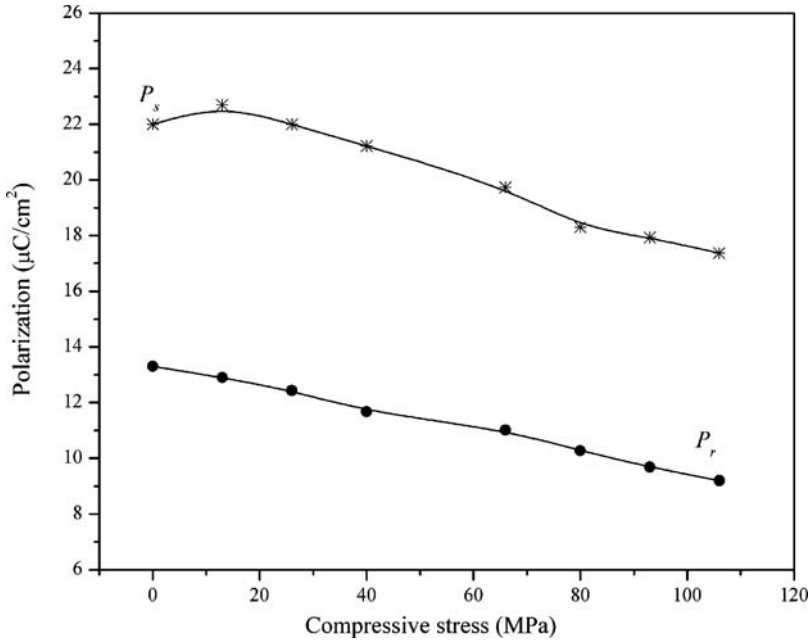

Figure 4. Variation of saturated polarization (P_s) and remanent polarization (P_r) with compressive stress for 0.5PZ–0.5PNN ceramic.

which resulting in lower value of the saturation polarization. Likewise for resulting in lower remanent polarization than usual, when the electric field is reduced to zero the domain tend to rotate back away from the stress direction. Furthermore, the decrease in the dissipation energy with increasing compressive stress indicates that more and more ferroelectric domains are constrained by the stress and cannot be reoriented by the electric field so as participate in the polarization reversal. It should be noted here that the previous works on many ferroelectric systems [4, 6, 12] show similar tendency with this work which reported that ferroelectric characteristics can be influenced by compressive stress.

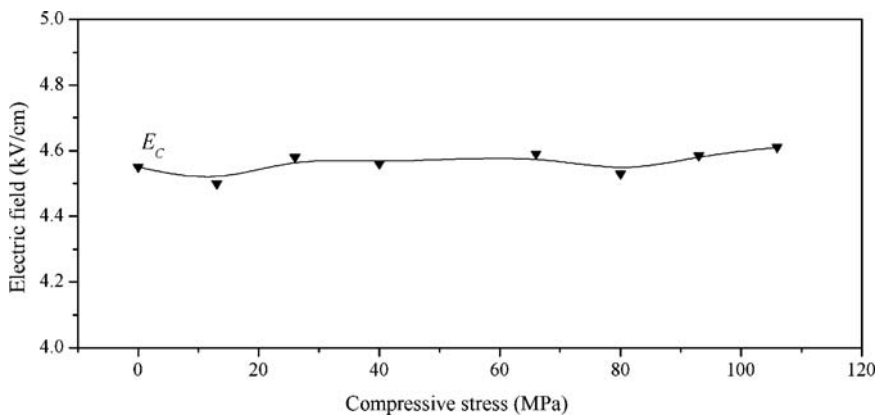

Figure 5. Variation of coercive field (E_c) with compressive stress for 0.5PZ–0.5PNN ceramic.

Conclusions

The effect of compressive stress on the hysteresis properties of the 0.5PZ–0.5PNN ceramic was investigated in this study. The P–E loop under compressive stress of all samples were observed up to 100 MPa using compressometer in conjunction with a modified Sawer-Tower circuit. The results show that the area of hysteresis loops, which corresponds to the dissipation energy, the saturation polarization (P_s) and the remanent polarization (P_r) decrease with increasing stress. The changes of these values explain by suppression of ferroelectric domain switching and stress–induced domain wall. Moreover, these values (P_s, P_r, and E_c) confirmed that the ferroelectric characteristics of 0.5PZ–0.5PNN ceramic decrease considerably under application of the compressive stress.

Acknowledgments

This work is supported by the Thailand Research Fund (TRF), the Commission on Higher Education (CHE) and the Faculty of Science, Chiang Mai University.

References

1. N. Vittayakorn, and S. Wirunchit, Perovskite formation, dielectric and ferroelectric properties of $PbZrO_3$–$Pb(Ni_{1/3}Nb_{2/3})O_3$ ceramics via a columbite precursor synthetic route. *Smart Mater. Struct.* **16**, 851–857 (2007).
2. D. M. Mills and S. W. Smith, Multi-layer composite hybrid transducer for medical ultrasound. *Proc. 2000 IEEE Ultrason. Symp.* 1153–1156 (2000).
3. S. E. Park and T. R. Shrout, Relaxor based ferroelectric single crystals for electro-mechanical actuators. *Mat. Res. Innov.* **1**, 20–25 (1997).
4. R. Yimnirun, Y. Laosiritaworn, and S. Wongsaenmai, Effect of uniaxial compressive pre-stress on ferroelectric properties of soft PZT ceramics. *J. Phys. D: Appl. Phys.* **39**, 759–764 (2006).
5. O. Steiner, A. K. Tagantsev, E. L. Colla, and N. Setter, Uniaxial stress dependence of the permittivity of electroceramics. *J. Eur. Ceram. Soc.* **19**, 1243–1246 (1999).
6. D. Zhou, M. Kamlah, and D. Munz, Effects of uniaxial prestress on the ferroelectric hysteretic response of soft PZT. *J. Eur. Ceram. Soc.* **25**, 425–432 (2005).
7. W. Chaisan, R. Yimnirun, and S. Ananta, Changes in ferroelectric properties of barium titanate ceramic with compressive Stress. *Phys. Scr.* **T129**, 205–208 (2007).
8. L. B. Kong, J. Ma, W. Zhu, and O. K. Tan, Preparation and characterization of lead zirconate ceramics from high-energy ball milled powder. *Materials Letters.* **49**, 96–101 (2001).
9. E. F. Alberta and A. S. Bhalla, Low-temperature properties of lead nickel-niobate ceramics. *Materials Letters.* **54**, 47–54 (2002).
10. S. E. Park and T. R. Shrout, Ultrahigh strain and piezoelectric behavior in relaxor based ferroelectric single crystals. *J. Appl. Phys.* **82**, 1804–1811 (1997).
11. M. E. Lines and A. M. Glass, *Principles and applications of ferroelectrics and related materials*, Clarendon Press, Oxford, p. 541 (1977).
12. R. Yimnirun, S. Ananta, A. Ngamjarurojana, and S. Wongsaenmai, Uniaxial sress Dependence of ferroelectric properties of xPMN-(1–x)PZT ceramic systems. *Appl. Phys. A: Mat. Sci. Proc.* **81**, 1227–1231 (2005).

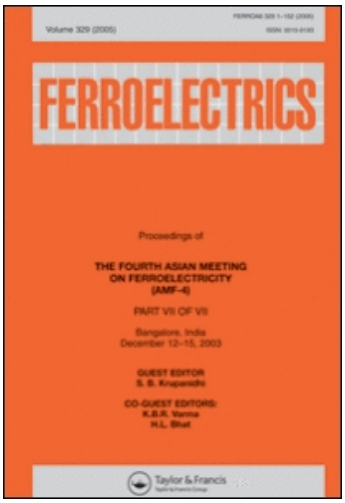

Ferroelectrics
Publication details, including instructions for authors and subscription information:
http://www.informaworld.com/smpp/title~content=t713617887

Synthesis, Ferroelectric Phase Stabilization, Phase Transition and Thermal Properties in (1-x)$PbZrO_3$-x$Pb(Zn_{1/3}Nb_{2/3})O_3$ Solid Solution

Naratip Vittayakorn [ab]; Wanwimon Banlue [a]
[a] Materials Science Research Unit, Department of Chemistry, Faculty of Science, King Mongkut's Institute of Technology Ladkrabang, Bangkok, Thailand [b] College of KMITL Nanotechnology, King Mongkut's Institute of Technology Ladkrabang, Bangkok, Thailand

Online Publication Date: 01 January 2009

To cite this Article Vittayakorn, Naratip and Banlue, Wanwimon(2009)'Synthesis, Ferroelectric Phase Stabilization, Phase Transition and Thermal Properties in (1-x)$PbZrO_3$-x$Pb(Zn_{1/3}Nb_{2/3})O_3$ Solid Solution',Ferroelectrics,382:1,110 — 114
To link to this Article: DOI: 10.1080/00150190902869988
URL: http://dx.doi.org/10.1080/00150190902869988

Ferroelectrics, 382:110–114, 2009

ISSN: 0015-0193 print / 1563-5112 online
DOI: 10.1080/00150190902869988

Synthesis, Ferroelectric Phase Stabilization, Phase Transition and Thermal Properties in $(1-x)PbZrO_3$-$xPb(Zn_{1/3}Nb_{2/3})O_3$ Solid Solution

NARATIP VITTAYAKORN[1,2,*] AND WANWIMON BANLUE[1]

[1]Materials Science Research Unit, Department of Chemistry, Faculty of Science, King Mongkut's Institute of Technology Ladkrabang, Bangkok 10520, Thailand
[2]College of KMITL Nanotechnology, King Mongkut's Institute of Technology, Ladkrabang, Bangkok 10520, Thailand

The solid solution between the antiferroelectric $PbZrO_3$ (PZ) and relaxor ferroelectric $Pb(Zn_{1/3}Nb_{2/3})O_3$ (PZN) was synthesized by the columbie method. The phase structure and thermal properties of (1-x)PZ-xPZN, where x = 0.00–0.30, were investigated. The crystal structure of the sintered ceramics was investigated as function of composition via x-ray diffraction (XRD) and Differential scanning calorimetry (DSC). The results indicated that the solid solution, PZ-PZN, successively transforms from orthorhombic to rhombohedral symmetry with an increase in PZN concentration. The AFE→FE phase transition was found in the compositions of $0.00 \leq x \leq 0.20$, and its temperatures were decreased by increasing the concentration of PZN. Furthermore, the temperature range width of the FE phase was increased by increasing the amount of PZN. This interruption caused the appearance of a rhombohedral ferroelectric phase when the amount of PZN was more than 20 mol%.

Keywords Materials preparation; Piezoceramics; Lead Zirconate and Lead Zinc Niobate

PACS: 64.70.K-, 77.22.Ch, 81.05.Je, 85.80.-n and 77.84.Dy

Introduction

Lead zirconate [$PbZrO_3$, abbreviated as PZ] is an antiferroelectric ceramic with a Curie temperature of 230°C [1, 2]. At room temperature, PZ has an antiferroelectric phase (AFE) with an orthorhombic structure [1]. PZ is a parent compound of $PbZr_{1-x}Ti_xO_3$ (PZT) solid solutions, which are of high scientific and technological interest for their ferroelectricity and piezoelectricity observed over a wide range of compositions [3]. The ferroelectric (FE) intermediate phase can also be introduced by partial replacement of Pb^{2+} ions with A-site ions such as Ba^{2+} ions [4] or La^{3+} ions [5]. Due to the differences of AFE and FE phases in the unit cell parameters, this phase transition is accompanied by a nonlinear change in physical properties, such as an abrupt jump in polarization and strain, or large charge release [4]. This feature of $PbZrO_3$ makes it a candidate material for energy storage

Received August 3, 2008; in final form December 31, 2008.
*Corresponding author: E-mail: naratipcmu@yahoo.com

applications [3]. There have been many studies concerning the solid solution of PZ and other perovskite materials such as $PbTiO_3$ [6], $BaZrO_3$ [4, 7], $PbSnO_3$ [5], $SrZrO_3$ [6] and $PbNi_{1/3}Nb_{2/3}O_3$ [8–10]. Lead zinc niobate [$Pb(Zn_{1/3}Nb_{2/3})O_3$ abbreviated as PZN] is an important relaxor ferroelectric material with the rhombohedral structure at room temperature. A diffuse phase transition from the paraelectric state to a ferroelectric polar state occurs at 140°C [11]. Extensive research has been carried on PZN single crystals because of their excellent dielectric, electrostrictive and optical properties [11]. However, to the best of the authors' knowledge, no work has been done on the solid solution between PZ and PZN. Therefore, the objective of our present study is to investigate phase transition of $(1–x)PbZrO_3– xPb(Zn_{1/3}Nb_{2/3})O_3$ (PZ – PZN) with $x = 0.00 – 0.30$ as a function of composition and temperature.

Experimental Procedure

The $(1-x)PbZrO_3 – xPb(Zn_{1/3}Nb_{2/3})O_3$ ceramics, where $x = 0.00$, 0.02, 0.04, 0.06, 0.08, 0.10, 0.20 and 0.30, were prepared by a columbite precursor. First, a columbite ($ZnNb_2O_6$) precursor was prepared using reagent-grade ZnO and Nb_2O_5 in stoichiometric proportions. The powders were thoroughly mixed in a ball mill for 18 h, using ethanol as a grinding medium, and the mixed powder was calcined at 1,050°C for 4 h to obtain the columbite precursor. Single-phase formation of the precursor was confirmed by X-ray diffraction (XRD). The columbite precursor was mixed with PbO (99% purity), and ZrO_2 (99% purity) in different proportions for making different compositions, and each mix was calcined at 900°C for 4 h to acquire the desired composition of $(1-x)PZ-xPZN$. Two mol percent of excess PbO was added to all the compositions to compensate for the lead loss during sintering. Single-phase formation was verified by powder XRD. Powders were compacted in disk form with a diameter of 15 mm and thickness of 2–3 mm. These disks were sintered in PbO-rich atmosphere at 1,250°C for 4 h. The densities of the sintered samples were measured to ∼95% of the theoretical values. The crystal structure of the sintered pellets was determined by XRD. The differential scanning calorimetry (DSC) has been used to determine the phase transition temperatureand the associated transition enthalpy. DSC is a useful tool for determining temperatures and enthalpies of phase transitions; it can give valuable information for the phase structure. This was operated from room temperature to 250°C with a heating rate of 10°C/min.

Results and Discussion

Figure 1 illustrates the XRD patterns of $(1 - x)PZ$-$xPZN$ sintered pellets for $0.00 \leq x \leq 0.30$. It can be seen that the sintered pellets are single-phase: all the lines in each XRD pattern could be indexed with a perovskite cell. The diffraction peaks move gradually towards higher angles with increasing PZN contents, indicating smaller cell parameters.

For the composition $0.00 \leq x \leq 0.20$, superstructure lines along with strong peaks are clearly observed, indicating that this composition belongs to the AFE orthorhombic phase. Furthermore, the samples with $x = 0.30$ had a split (1 1 1) and (2 2 0) reflection and single (2 0 0) reflection, confirming that the crystal structure of the samples with $x = 0.30$ is a rhombohedral perovskite. The DSC technique is a technique for measuring the energy necessary to establish a nearly zero temperature difference between a sample and an inert reference material. The DSC technique was used to investigate the phase transition of PZ-PZN ceramics, with increasing PZN concentration. A typical result of the DSC of PZ-PZN for the composition $x = 0.00$, 0.04 and 0.10 is presented in Figure 2(a)–(c). Two

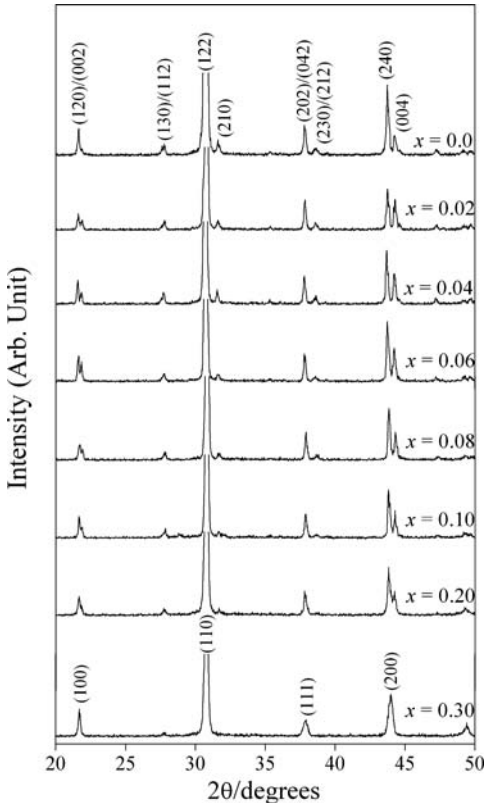

Figure 1. XRD patterns of $(1-x)PbZrO_3$–$xPb(Zn_{1/3}Nb_{2/3})O_3$ sintered pellets.

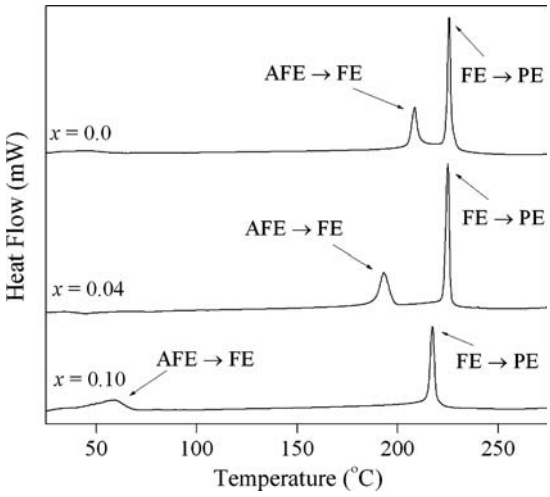

Figure 2. DSC thermographs of PZ-PZN ceramics for: (a) $x = 0.00$, (b) $x = 0.04$ and (c) $x = 0.10$.

Table 1
Phase transition temperatures of $(1 - x)$PZ-xPZN ceramics

	Phase transition temperature (°C)	
Composition x	AFE→FE	FE→PE
0.00	208.4	225.6
0.02	193.1	224.9
0.04	184.7	223.2
0.06	137.4	222.1
0.08	94.7	219.5
0.10	59.0	217.3
0.20	—	211.2
0.30	—	209.4

distinct endothermic peaks were observed for PZ at about 208.4 and 225.6°C as shown in Fig. 2(a). The lower temperature corresponds to the transition temperature of the AFE→FE phase transition, while the higher temperature corresponds to the FE→PE phase transition. In Fig. 2(b), two endothermic peaks are shown at 184.7 and 223.2°C for the composition, $x = 0.04$. In Fig. 2(c), two endothermic peaks are shown at 59.036 and 217.3°C for the composition, $x = 0.10$. The AFE→FE phase transition was found in the compositions of $0.00 \leq x \leq 0.20$. The peaks shift to lower temperatures, with a higher composition of x. This result corresponds to a decreasing AFE phase, with increasing amounts of PZN content. Table 1 gives the transition temperature, including AFE→FE and FE→PE transitions of different PZ-PZN compositions observed from DSC. The temperature range width of the FE phase increases progressively with PZN content. After accumulating all these data, the ferroelectric phase diagram of $(1 - x)$PZ–xPZN has been finally established as a function of temperature and composition, as shown in Fig. 3.

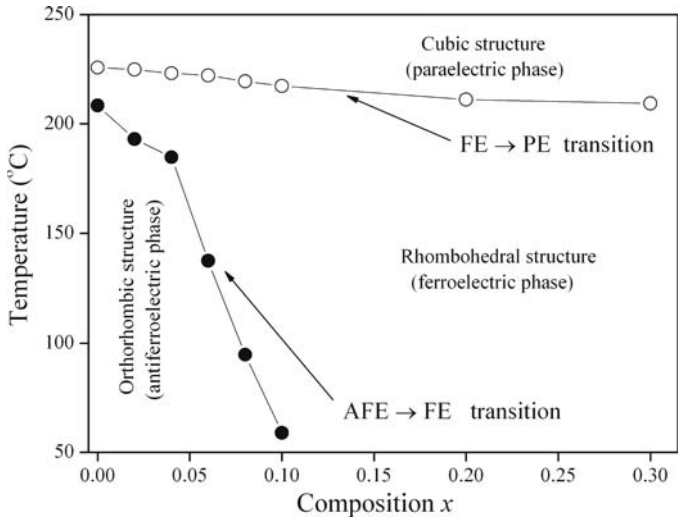

Figure 3. Ferroelectric phase diagram of the $(1 - x)$PZ-xPZN, $x = 0.00$–0.30 binary system determined from room temperature XRD, DSC as a function of temperature.

The transition temperature decreases linearly with x, from approximately $T_c = 225.6°C$ for $x = 0.0$ to 209.4°C for $x = 0.30$. At room temperature, the phase boundary between the orthorhombic antiferroelectric and rhombohedral ferroelectric phases was observed near $x = 0.10$. The phase diagram consists of three distinct crystallographic phases in this system; high temperature paraelectric cubic, rhombohedral, and ferroelectric orthorhombic.

Summary

Relaxor ferroelectric PZN has been found to strongly influence crystal structure and thermal properties of PZ ceramics. The crystal structure data obtained from XRD indicate that the solid solution $(1 - x)$PZ - xPZN, where $x = 0.00$–0.30, successively transforms from orthorhombic to rhombohedral symmetry with increased PZN concentration. The AFE→FE phase transition is found in compositions of $0.00 \leq x \leq 0.10$. The AFE→FE phase transition shifts to lower temperatures with higher compositions of x. The temperature range width of the FE phase increases with increased PZN.

Acknowledgment

This work was supported by the Thailand Research Fund (TRF) King Mongkut's Institute of Technology Ladkrabang (KMITL), and the National Nanotechnology Center (NANOTEC) NSTDA, Ministry of Science and Technology, Thailand, through its program of Center of Excellence Network.

References

1. E. Sawaguchi, G. Shirane, and S. Hoshino, Antiferroelectric structure of lead zirconate. *Phys. Rev.* **83**, 1078 (1951).
2. F. Jona, G. Shirane, F. Mazzi, and R. Pepinsky, X-ray and neutron diffraction study of antiferroelectric lead zirconate, $PbZrO_3$. *Phys. Rev.* **105**, 849–856 (1957).
3. G. H. Haertling, Ferroelectric ceramics: history and technology. *J. Am. Ceram. Soc.* **82**, 797–818 (1999).
4. B. P. Pokharel and D. Pandey, Effect of Ba^{2+} substitution on the stability of the antiferroelectric and ferroelectric phases in $(Pb_{1-x}Ba_x)ZrO_3$: Phenomenological theory considerations. *Phys. Rev. B* **65**, 214108 (2002).
5. Y. Xu, Ferroelectric materials and their application: Elsevier Science Publishers B.V. 1991.
6. B. Jaffe and W. R. Cook, Piezoelectric ceramic: R.A.N. publishers, 1971.
7. B. P. Pokharel and D. Pandey, Irreversibility of the antiferroelectric to ferroelectric phase transition in $(Pb_{0.90}Ba_{0.10})ZrO_3$ ceramics. *J. Appl. Phys.* **86**, 3327–3332 (1999).
8. S. Wirunchit, P. Laoratanakul, and N. Vittayakorn, Physical properties and phase transitions in perovskite $Pb[Zr_{1-x}(Ni_{1/3}Nb_{2/3})_x]O_3$ $(0.0 \leq x \leq 0.5)$ ceramics. *J. Phys. D: Appl. Phys.* **41**, 125406 (2008).
9. S. Wirunchit and N. Vittayakorn, Structural transformation in antiferroelectric $PbZrO_3$-relaxor ferroelectric $Pb(Ni_{1/3}Nb_{2/3})O_3$ solid solution system. *J. Appl. Phys.* **104**, 024103–6 (2008).
10. N. Vittayakorn and S. Wirunchit, Perovskite formation, dielectric and ferroelectric properties of $PbZrO_3$–$Pb(Ni_{1/3}Nb_{2/3})O_3$ ceramics via a columbite precursor synthetic route. *Smart Mater. Struct.* **16**, 851–857 (2007).
11. T. Takenaka, K. Muramata, and T. Fujii, Piezoelectric properties of PZN-PT prepared by HIP. *Ferroelectrics* **134**, 133 (1992).

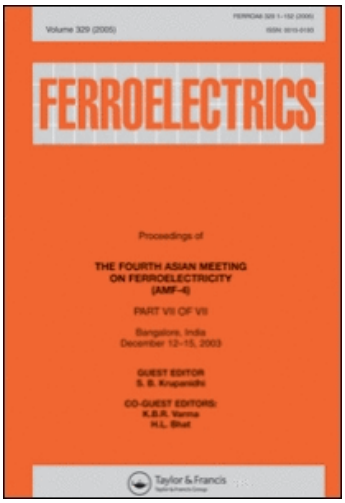

Ferroelectrics
Publication details, including instructions for authors and subscription information:
http://www.informaworld.com/smpp/title~content=t713617887

Phase Transition and Dielectric Properties of Lead Free $(K_{0.5}Na_{0.5})NbO_3$-$Bi(Zn_{0.5}Ti_{0.5})O_3$ Piezoelectric Ceramics

Manoon Sutapun [a]; Naratip Vittayakorn [ab]
[a] Materials Science Research Unit, Department of Chemistry, Faculty of Science, King Mongkut's Institute of Technology Ladkrabang, Bangkok, Thailand [b] College of KMITL Nanotechnology, King Mongkut's Institute of Technology Ladkrabang, Bangkok, Thailand

Online Publication Date: 01 January 2009

To cite this Article Sutapun, Manoon and Vittayakorn, Naratip(2009)'Phase Transition and Dielectric Properties of Lead Free $(K_{0.5}Na_{0.5})NbO_3$- $Bi(Zn_{0.5}Ti_{0.5})O_3$ Piezoelectric Ceramics',Ferroelectrics,382:1,115 — 121
To link to this Article: DOI: 10.1080/00150190902870002
URL: http://dx.doi.org/10.1080/00150190902870002

Ferroelectrics, 382:115–121, 2009

ISSN: 0015-0193 print / 1563-5112 online
DOI: 10.1080/00150190902870002

Phase Transition and Dielectric Properties of Lead Free $(K_{0.5}Na_{0.5})NbO_3$- $Bi(Zn_{0.5}Ti_{0.5})O_3$ Piezoelectric Ceramics

MANOON SUTAPUN[1] AND NARATIP VITTAYAKORN[1,2,*]

[1]Materials Science Research Unit, Department of Chemistry, Faculty of Science, King Mongkut's Institute of Technology Ladkrabang, Bangkok 10520, Thailand
[2]College of KMITL Nanotechnology King Mongkut's Institute of Technology Ladkrabang, King Mongkut's Institute of Technology Ladkrabang Bangkok 10520, Thailand

Lead-free piezoelectric ceramics of $(1\text{-}x)(K_{0.5}Na_{0.5})NbO_3 - x(Bi(Zn_{0.5}Ti_{0.5})O_3$; $x = 0.00$–0.30 were prepared via the two−stage mixed oxide fabrication technique. The crystal structure and ferroelectric phase transitions were studied by means of x-ray diffraction and thermal measurements. XRD results showed that a single-phase perovskite structurewas formed in the ceramics with $x \leq 0.25$. For the ceramics with $x = 0.30$, a small amount of secondary phase $Bi_2Ti_2O_7$ with a cubic structure was formed. The ceramics with a perovskite structure showed an orthorhombic phase at $0.00 \leq x \leq 0.010$ and became rhombohedral at $0.010 < x \leq 0.015$ before transforming to a cubic phase at $0.015 < x \leq 0.25$. In addition, DSC results showed that the phase transition temperature of orthorhombic–tetragonal (T_O–T) and tetragonal–cubic (T_C) decreased when a small amount of BZT was added. The trend of enthalpy for orthorhombic → tetragonal phase transition and tetragonal → cubic phase were found to reduce with progressive increases in small amounts of BZT content. This behavior could originate from the more complex occupation of the A and B sites in an ABO_3 perovskite structure.

Keywords Lead-free piezoelectric ceramics; Dielectric properties; perovskites structure; $(K_{0.5}Na_{0.5})NbO_3$; $Bi(Zn_{0.5}Ti_{0.5})O_3$

PACS: 64.70.K-, 77.22.Ch, 81.05.Je, 85.80.-n and 77.84.Dy

Introduction

Lead zirconate titanate($Pb(Zr_{1-x}Ti_x)O_3$; PZT) and lead-based perovskite ceramics havebeen widely usedfor various applications such as buzzers, transducers, and piezoelectric transformers,due to their outstanding piezoelectric properties [1]. However, from an environmental viewpoint, lead-free piezoelectric materials have been desirable over the last few years because of draft directives on waste from electrical and electronic equipment (WEEE), and restriction of hazardous substances (RoHS) [2, 3]. A number of lead-free piezoelectric ceramics, such as alkaline niobate-based systems, $(Bi_{0.5}Na_{0.5})TiO_3$ based systems, Bi-layer structure systems, $BaTiO_3$-based systems and tungsten bronze structure

Received August 3, 2008; in final form December 31, 2008.
*Corresponding author. E-mail: naratipcmu@yahoo.com

systems, have been investigated [2, 3]. Among them, much attention has been paid to $K_{0.5}Na_{0.5}NbO_3$ (KNN)-based ceramics, since Saito et al. [4] had developed KNN-based textured ceramics with properties comparable to those of basic, unmodified PZT ceramics. However, it is very difficult to obtain dense KNNceramics because of the high volatility of alkaline elements athigh temperatures. To improve densification and piezoelectric properties of KNNceramics, different additions are added into KNN to formnew KNN-based ceramics, such as KNN-$BaTiO_3$ [5], KNN-$SrTiO_3$ [5], KNN-$LiNbO_3$ [6], KNN-$LiSbO_3$ [7] and KNN-$LiTaO_3$ [8].

$Bi(Zn_{1/2}Ti_{1/2})O_3$ (BZT) is a ferroelectric material, which has a Zn^{2+} and Ti^{4+} complex on the B-site of ABO_3 perovskite structure, with a tetragonal symmetry [9]. The solid solution of $(x)PbTiO_3$–$(1–x)Bi(Zn_{1/2}Ti_{1/2})O_3$ has been studied by Suchomel et al. [10]. The $(x)PbTiO_3$ – $(1–x)Bi(Zn_{1/2}Ti_{1/2})O_3$ system exhibits a high c/a ratio of 1.11 for $x = 0.60$. Accordingly, the Curie temperature (T_C) also increases to over 700°C at the same composition [10]. However, there have been no systematic investigations on the solid solution of KNN-BZT ceramics. The purpose of our research was to investigate the effect of BZT in perovskite KNN materials on the phase formation and thermal and dielectric properties in order to elaborate on new lead-free ceramics and ceramics with interesting properties for applications.

Experimental Procedure

The new polycrystalline ceramic samples of $(1 - x)K_{0.5}Na_{0.5}NbO_3 - xBi(Zn_{1/2}Ti_{1/2})O_3$ with $x = 0.00$–0.30 were prepared by a two-stage technique. High-purity oxides and carbonates; K_2CO_3 (99.0%), Na_2CO_3 (99.5%), Nb_2O_5 (99.9%), Bi_2O_3 (99.97%), ZnO (99.9%) and TiO_2(99.9%) were used as starting materials, which had been treated carefully by a special drying process before use, particularly for sodium/potassium carbonates. These powders were placed in an oven at 240°C for 2 days and then stored in a moisture-free vessel. In the first stage, K_2CO_3, Na_2CO_3 and Nb_2O_5 were thoroughly mixed in the stoichiometric ratio, and then calcined at 900°C for 2 h to form $(K_{0.5}Na_{0.5})NbO_3$; KNN. In the second stage, the precursor (KNN) was mixed in the stoichiometric ratio with other starting materials. After drying at 120°C for 2 h, the reaction of the uncalcined powders, taking place during heat treatment, was investigated by differential thermal analysis (DTA; Shimadzu) and thermogravimetry analysis (TGA; Shimadzu), using a heating rate of 10°C/min in air from room temperature up to 1,400°C. In order to investigate the perovskite phase formation based on the TG–DTA results, the mixture was calcined at various temperatures ranging from 650 to 850°C, with a dwell time of 4 h and heating/cooling rates ranging from 20°C/min [11] in a closed alumina crucible. The calcined powders were mixed with 3 wt% poly (vinyl alcohol) (PVA) and then uniaxially cold-pressed at 150 MPa into 15 mm diameter pellets. Following binder burnout at 550°C, the pellets were sintered in sealed crucibles at between 1,000-1,100°C for 2h. For phase determination, x-ray diffraction (Bruker-D8 Advance) was utilized in the 2θ scan range of 20°–80° using sintered pellets.

For measuring the dielectric characteristics, the specimens were polished to a 1 mm thickness. After ultrasonic cleaning in an ethanol bath, silver-paste was coated on both sides of the polished samples by the screen printing method, and subsequently fired at 650°C for 30 min. For the dielectric property measurement, capacitance was measured at 1 kHz using an automated measurement system consisting of an LCR meter (HP-4284, Hewlett–Packard Inc.). The dielectric constant was then calculated from $\varepsilon_r = Cd/\varepsilon_0 A$, where C was the capacitance of the sample, and d and A were the thickness and area of the electrode, respectively, and ε_0 was the dielectric permittivity of vacuum (8.854×10^{-12} F/m).

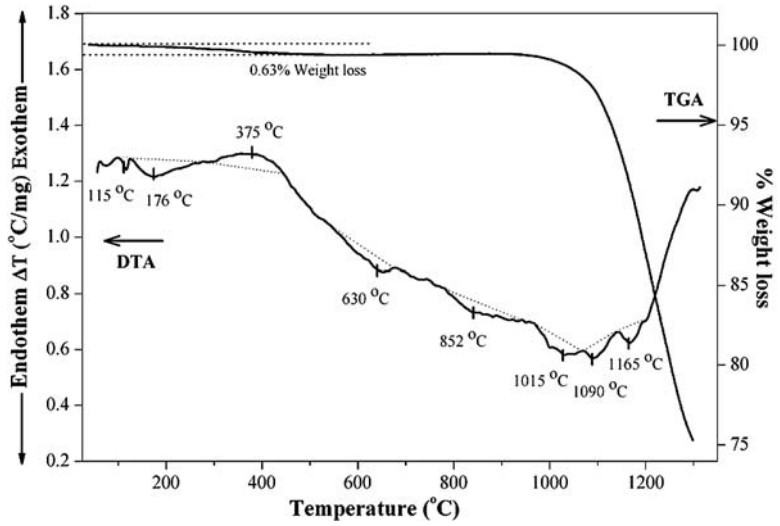

Figure 1. TG-DTA curves for the powder mixture of the starting reagent for the two−stage mixed oxide method.

Results and Discussion

The simultaneous TG–DTA analysis of a powder mixed in the stoichiometric proportions of KNN-BZT is illustrated in Fig. 1. The TGA curve, showing overall weight loss, was equal to 24.5% in this fabrication technique. The DTA curve showed an endothermic peak

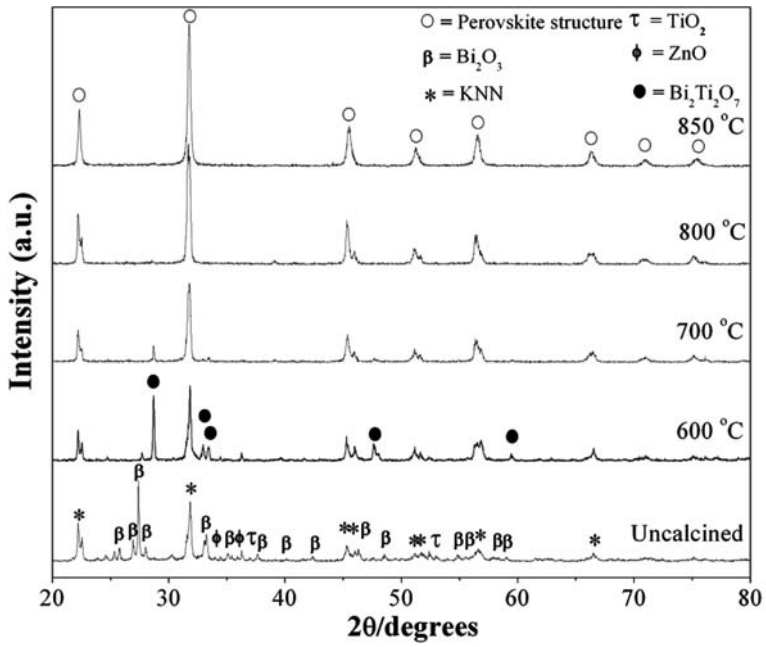

Figure 2. XRD patterns of $(1-x)$KNN–xBZT ceramics with $x = 0.01$ powder calcined at various temperatures for 4 h.

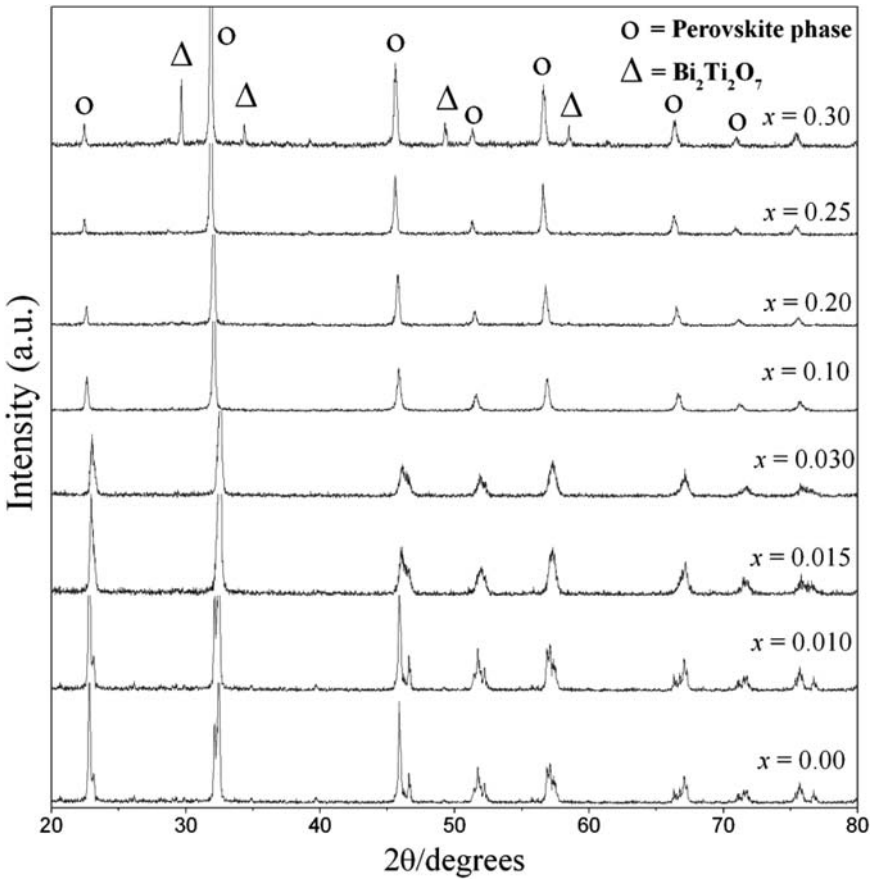

Figure 3. XRD patterns of $(1-x)$KNN–xBZT; x = 0.00-0.30 ceramics.

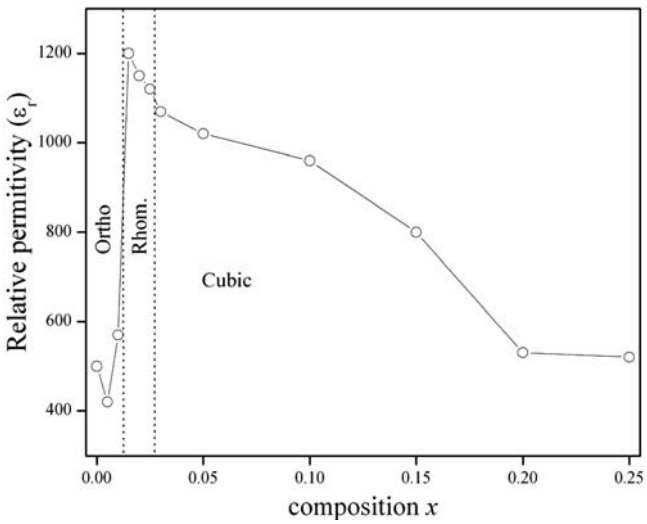

Figure 4. Relative permittivity of $(1-x)$KNN–xBZT as a function of compositions.

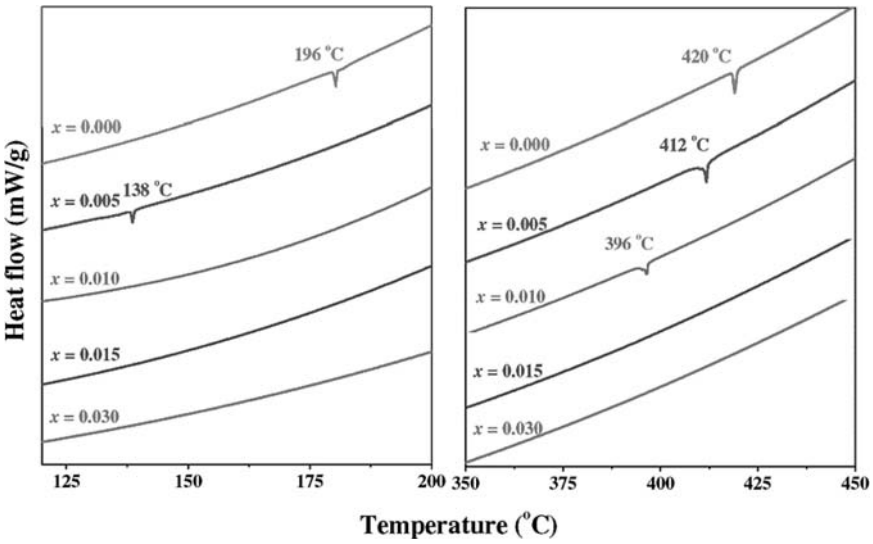

Figure 5. DSC curves of the ceramics with difference BZT contents. (See Color Plate XXXIV)

positioned at around 115−179°C, which associated with the decomposition of water molecules [12, 13]. Because the two-stage method used $K_{1/2}Na_{1/2}NbO_3$ as a starting material, the decarbonation of K_2CO_3 and Na_2CO_3 were not observed at all in temperatures between 400°C to 600°C, as expected [14]. Furthermore, weight loss was not observed at all at the same temperature. The endothermic peaks at 850°C should have correlated to the formation of perovskite structure because there was no weight loss on the TGA curves. These data were used to define the range of temperatures (600–850°C) for XRD investigation. To study the phase development with increasing calcination temperature, all compositions were calcined at various temperatures for 4 h in air, with constant heating/cooling rates of 20°C/min, followed by phase analysis using the XRD technique. Figure 2 shows the XRDpatterns of the $(1-x)$KNN–xBZT with $x = 0.1$ ceramics. As shown in Fig. 2, in uncalcined powders, only the x-ray peaks of precursors Bi_2O_3 (β), TiO_2 (τ) and ZnO (Φ) could be matched with JCPDS file numbers 76–1730, 84–1284 and 80–0075, respectively, from the International Centre for Diffraction Data, Newton Square, PA (2000). This indicated that at the time, no reaction had yet been triggered during the milling processes. As the temperature increased to 600°C, it was found that the intensity of the precursor phases of TiO_2 and ZnO completely disappeared, and crystalline KNN-BZT (O) started to materialize, accompanied by Bi_2O_3 and $Bi_2Ti_2O_7$ as separated phases in the powder. Consistent with JCPDS file numbers 32–0118, this $Bi_2Ti_2O_7$ phase was indexable according to a cubic pyrochlore structure with lattice parameters $a = 20.68$ pm and space group *Fd3m* (no. 227). Upon calcination at 800°C, the desired KNN-BZT phase became the predominant phase, only detectable in the powders after calcination at 850°C, which was consistent with the TG-DTA results. Figure 3 shows the XRD patterns of the $(1-x)$KNN–xBZT ceramics with $0.0 \leq x \leq 0.3$. Single-phase perovskite structure could be seen to form in the ceramics with $x \leq 0.25$. For the ceramics with $x = 0.30$, a smallamount of secondary phase $Bi_2Ti_2O_7$ with the cubic structure was formed. These results indicated that the presence of BZT in the solid solution decreases the structural stability of KNN perovskite phase by its tolerance factor and electronegativity [15–17].

At $x \leq 0.010$, ceramics could be seen to have an orthorhombicperovskite structure. As x increases,a rhombohedral phase appears and increases continuously until $x \leq 0.015$. With $x > 0.015$, theceramic becomes a cubic perovskite phase. This suggests that the (perovskite) orthorhombic and rhombohedral phases coexist in the $(1-x)$KNN–xBZT ceramicswith $0.010 < x < 0.020$. Figure 4 shows the relative permittivity at room temperature as a function of composition x. The maximum value of relative permittivity at room temperature was observed in the composition, $x = 0.015$. Combined with the XRD examination described above, the anomaly in dielectric properties clearly indicates a phase transformation over that compositional range. Therefore, a phase separating the orthrohombic phase from the rhombohedral exists at the composition, $x \sim 0.015$. To investigate the role of BZT content on ferroelectric phase transition of KNN ceramics, the Differential scanning calorimetry (DSC) was performed. The DSC technique is a technique for measuring the energy necessary to establish a nearly zero temperature difference between a sample and an inert reference material. A typical result of the DSC of KNN–BZT for composition $x = 0.0$–0.03 is presented in Fig. 5. It was clearly seen that pure KNN and the composition, $x = 0.005$, showed two peaks, indicating existence of two first order phase transitions. The lower temperature corresponds to the transition temperature of the orthorhombic → tetragonal phase transition, while the higher temperature corresponds to the tetragonal → cubic phase transition [5]. There is a sharp decrease in phase transition energy with increasing BZT contents. The peaks shift to lower temperatures with the higher compositions of x. The trend of enthalpy for orthorhombic → tetragonal phase transition and tetragonal → cubic phase were found to reduce with the progressive increase of BZT content, as seen in Fig. 5. This behavior can originate from the more complex occupation of the A and B sites in an ABO_3 perovskite structure and heterogeneous compositions. This composition of heterogeneity also gives rise to random fields, which tend to make the phase transition "diffuse" instead of sharp, as in a first-order phase transition.

Conclusions

In this work, the phase structure and thermal properties of the binary solid solution, $K_{1/2}Na_{1/2}NbO_3-$ $Bi(Zn_{1/2}Ti_{1/2})O_3$ (KNN − BZT), were examined. A combination of XRD and thermal data indicated that a stable perovskite phase with orthorhombic symmetry was observed for compositions rich in KNN. Addition of the BZT phase in KNN ceramics caused a systematic change in the crystal structure from distorted orthorhombic KNN-rich solid solution phase to distorted rhombohedral solid solution phase, and then to cubic solid solution phase. Furthermore, DSC results showed that orthorhombic → tetragonal phase transition temperature and tetragonal → cubic phase transition temperature progressively decreased with a continuous increase of BZT concentration in the composition $0.00 \leq x \leq 0.01$. The peaks shifted to lower temperatures with higher compositions of x. The trend of enthalpy for orthorhombic → tetragonal phase transition and tetragonal → cubic phase were found to reduce with a progressive increase of BZT content. This behavior can originate from the more complex occupation of the A and B sites in an ABO_3 perovskite structure and heterogeneous compositions.

Acknowledgments

This work was supported by the Thailand Research Fund (TRF), and the National Nanotechnology Center (NANOTEC) NSTDA, Ministry of Science and Technology, Thailand through its program of Center of Excellence Network.

References

1. G. H. Haertling, Ferroelectric ceramics: History and technology. *J. Am. Ceram. Soc.* **82**, 797–818 (1999).
2. E. Ringgaard and T. Wurlitzer, Lead-free piezoceramics based on alkali niobates. *J. Eur. Ceram. Soc.* **25**, 2701–2706 (2005).
3. T. Takenaka and H. Nagata, Current status and prospects of lead-free piezoelectric ceramics. *J. Eur. Ceram. Soc.* **25**, 2693–2700 (2005).
4. Y. Saito, H. Takao, T. Tani, T. Nonoyama, K. Takatori, T. Homma, T. Nagaya, and M. Nakamura, Lead-free piezoceramics. *Nature* **432**, 84–87 (2004).
5. B. Malic, J. Bernard, J. Holc, D. Jenko, and M. Kosec M, Alkaline-earth doping in (K,Na)NbO_3 based piezoceramics. *J. Eur. Ceram. Soc.* **25**, 2707–2711 (2005).
6. Y. Guo, K. Kakimoto, and H. Ohsato, Phase transitional behavior and piezoelectric properties of $(Na_{0.5}K_{0.5})O_3$-$LiNbO_3$ ceramics. *Appl. Phys. Lett.* **85**, 4121–4123 (2004).
7. S. Zhang, R. Xia, T. R. Shrout, G. Zang, and J. Wang J, Characterization of lead free $(K_{0.5}Na_{0.5})NbO_3$-$LiSbO_3$ piezoceramic. *Solid State Commun.* **141**, 675-679 (2007).
8. Y. Dai, X. Zhang, and G. Zhou, Phase transitional behavior in $K_{0.5}Na_{0.5}NbO_3$–$LiTaO_3$ ceramics. *Appl. Phys. Lett.* **90**, 262903 (2007).
9. M. R. Suchomel, A. M. Fogg, M. Allix, H. Niu, J. B. Claridge, and M. J. Rosseinsky, Bi_2ZnTiO_6: A Lead-free closed-shell polar perovskite with a Calculated Ionic polarization of 150 μC cm^{-2}. *Chem. Mater.* **18**, 4987–4989 (2008).
10. M. R. Suchomel and P. K. Davids, Enhanced tetragonality in PT-BZT and related solid solution systems. *Appl. Phys. Lett.* **86**, 262905 (2005).
11. S. Wirunchit, P. Laoratanakul, and N. Vittayakorn, Physical properties and phase transitions in perovskite $Pb[Zr_{1-x}(Ni_{1/3}Nb_{2/3})_x]O_3$ $(0.0 \leq x \leq 0.5)$ ceramics. *J. Phys. D: Appl. Phys.* **41**, 125406 (2008).
12. N. Vittayakorn, S. Wirunchit, S. Traisak, R. Yimnirun, and G. Rujijanagul, Development of perovskite and phase transition in lead cobalt niobate modified lead zirconate titanate system. *Curr. Appl. Phys.* **8**, 128–133 (2008).
13. N. Vittayakorn and S. Wirunchit, Perovskite formation, dielectric and ferroelectric properties of $PbZrO_3$–$Pb(Ni_{1/3}Nb_{2/3})O_3$ ceramics via a columbite precursor synthetic route. *Smart Mater. Struct.* **16**, 851-857 (2007).
14. K. Singh, V. Lingwal, S. C. Bhatt, N. S. Panwar, and B. S. Semwal, Dielectric properties of potassium sodium niobate mixed system. *Mat. Res. Bull.* **36**, 2365–2374 (2001).
15. T. R. Shrout and A. Halliyal, Proparation of lead-based ferroelectric relaxors for capacitors. *Am. Ceram. Soc. Bull.* **66**, 704 (1987).
16. A. S. Bhalla, R. Guo, and R. Roy, The perovskite structure-a review of its role in ceramic science and technology. *Mat. Res. Innovat.* **4**, 3 (2000).
17. X. H. Zhao, W. G. Qu, H. He, N. Vittayakorn, and X. L. Tan, Influence of cation order on the electric field-induced phase transition in $Pb(Mg_{1/3}Nb_{2/3})O_3$-based relaxor ferroelectrics. *Journal of the American Ceramic Society.* **89**, 202-209 (2006).

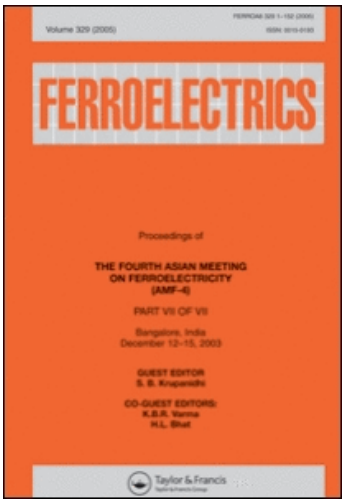

Ferroelectrics
Publication details, including instructions for authors and subscription information:
http://www.informaworld.com/smpp/title~content=t713617887

Effect of $Pb(Zn_{1/3}Nb_{2/3})O_3$ Additions on Phase Structure, Ferroelectric and Dielectric Properties of $PbZrO_3$ Ceramics

Wanwimon Banlue [a]; Naratip Vittayakorn [ab]
[a] Materials Science Research Units, Department of Chemistry, Faculty of Science, King Mongkut's Institute of Technology Ladkrabang, Bangkok, Thailand [b] College of KMITL Nanotechnology, King Mongkut's Institute of Technology Ladkrabang, Bangkok, Thailand

Online Publication Date: 01 January 2009

To cite this Article Banlue, Wanwimon and Vittayakorn, Naratip(2009)'Effect of $Pb(Zn_{1/3}Nb_{2/3})O_3$ Additions on Phase Structure, Ferroelectric and Dielectric Properties of $PbZrO_3$ Ceramics',Ferroelectrics,382:1,122 — 126
To link to this Article: DOI: 10.1080/00150190902870028
URL: http://dx.doi.org/10.1080/00150190902870028

Ferroelectrics, 382:122–126, 2009

ISSN: 0015-0193 print / 1563-5112 online
DOI: 10.1080/00150190902870028

Effect of $Pb(Zn_{1/3}Nb_{2/3})O_3$ Additions on Phase Structure, Ferroelectric and Dielectric Properties of $PbZrO_3$ Ceramics

WANWIMON BANLUE[1] AND NARATIP VITTAYAKORN[1,2,*]

[1]Materials Science Research Units, Department of Chemistry, Faculty of Science, King Mongkut's Institute of Technology Ladkrabang, Bangkok 10520, Thailand
[2]College of KMITL Nanotechnology King Mongkut's Institute of Technology Ladkrabang, King Mongkut's Institute of Technology Ladkrabang Bangkok 10520, Thailand

Polycrystalline samples of (1-x)$PbZrO_3 - xPb(Zn_{1/3}Nb_{2/3})O_3$, where $x = 0.0$–0.3, were prepared by the columbite method. Sintering was performed at 1,250°C for 2–4 h in PbO atmosphere. The X-ray diffraction (XRD) was used to investigate pure phase perovskite in sintered ceramics. Moreover, dielectric and ferroelectric properties have been determined via dielectric spectroscopy and hysteresis loop measurement, respectively. Complete solid solutions of the perovskite phase of PZ−PZN ceramics were obtained in all compositions. The phase transformation from orthorhombic to rhombohedral was observed at composition $0.2 < x < 0.3$. Furthermore, a change from antiferroelectric behavior in the PZ ceramic to normal ferroelectric behavior in PZ−PZN ceramics was observed in composition $0.1 < x < 0.2$. These results clearly show the significance of added PZN in reducing the antiferroelectric behavior in PZ ceramic.

Keywords Materials preparation; piezoceramics; lead zirconate and lead zinc niobate

PACS: 64.70.K-, 77.22.Ch, 81.05.Je, 85.80.-n and 77.84.Dy

Introduction

Since the discovery of antiferroelectricity in the perovskite structure during the 1950s, Lead zirconate oxide ($PbZrO_3$ or PZ) has been the focus of extensive experimental and theoretical studies [1]. At room temperature, PZ has an antiferroelectric phase (AFE) with an orthorhombic structure. It undergoes the AFE to a paraelectric phase (PE) and transforms from an orthorhombic structure to a cubic one at 236°C [2]. PZ was also studied for its microwave dielectric properties, but it shows a dielectric relaxation near microwave frequencies [3]. This feature of $PbZrO_3$ makes it a candidate material for energy storage applications [3]. There have been many studies concerning the solid solution of PZ and other perovskite materials such as $PbTiO_3$ [1], $BaZrO_3$, [4, 5] $PbSnO_3$ [6], $SrZrO_3$ [1]

Received August 3, 2008; in final form December 31, 2008.
*Corresponding author. E-mail: naratipcmu@yahoo.com

and $PbNi_{1/3}Nb_{2/3}O_3$ [7]. Lead zinc niobate [$Pb(Zn_{1/3}Nb_{2/3})O_3$ abbreviated as PZN] is an important relaxor ferroelectric material with a rhombohedral structure at room temperature [8, 9]. Extensive research has been carried on PZN single crystals because of their excellent dielectric, electrostrictive and optical properties [8]. Because of the partially disordered arrangement of the Zn^{2+} and Nb^{5+} cations in the B-site of the perovskite structure, a broad ferroelectric phase transition from rhombohedral (ferroelectric) to cubic (paraelectric) symmetry takes place at about 140°C, showing a very high dielectric constant maximum [10]. However, to the best of the authors' knowledge, no work has been done on the solid solution between PZ and PZN. Therefore, the objective of our present study is to investigate phase transition and dielectric properties of $(1–x)PbZrO_3– xPb(Zn_{1/3}Nb_{2/3})O_3$ (PZ-PZN) with $x = 0.00–0.30$ as a function of composition prepared by the columbite method.

Experimental Procedure

The $(1 - x)PbZrO_3–xPb(Zn_{1/3}Nb_{2/3})O_3$ ceramics, where $x = 0.00, 0.02, 0.04, 0.06, 0.08, 0.10, 0.20$ and 0.30, were prepared by a columbite precursor. First, preparation of a columbite ($ZnNb_2O_6$) precursor was carried out using reagent-grade ZnO and Nb_2O_5 in stoichiometric proportions. After mixing the powders thoroughly in a ball mill for 18 h, with a grinding medium of ethanol, the mixed powder was calcined at 1,050°C for 4 h to obtain the columbite precursor, which was mixed with PbO (99% purity) and ZrO_2 (99% purity) in different proportions to make various compositions. Each powder mix was calcined at 900°C for 4 h in order to produce the required composition of (1-x)PZ−xPZN. The lead loss during sintering was compensated for by adding two mol percent of excess PbO to all the compositions. Powders were compacted in disk form to 15 mm in diameter and 2–3 mm thickness and sintered in PbO−rich atmosphere at 1,250°C for 4 h. The sintered sample densities were measured to ∼95% of the theoretical values, and the crystal structure of the sintered pellets was determined by X-ray diffraction (XRD). An HP4284A LCR meter was used to measure the capacitance. Relative permittivity (ε_r) was calculated using the geometric area and thickness of the discs. Finally, the polarization–electric field ($P–E$) hysteresis loops were obtained at room temperature using a standardized ferroelectric tester system (RT66A) at a frequency of 4 Hz.

Results and Discussion

XRD patterns of ceramics in the (1-x)PZ−xPZN system had a fully crystallized perovskite structure for all compositions, as shown in Fig. 1, and the pyrochlore phase was not observed at all in this system. As indicated by XRD patterns of the PZ-PZN compositions, a combination between PZ and PZN patterns showed that the perovskite structure had a symmetry that varied between orthorhombic and rhombohedral types.

Ceramics with $0.02 \leq x \leq 0.20$ shared the same crystal structure with PZ, i.e., an orthorhombic unit cell at room temperature. If the XRD pattern of PZ is indexed on the basis of the pseudo-cubic cell, then ¼ ($h\,k\,l$)-type superlattice reflections representing the antiparallel shifts of Pb^{2+} ions will appear. In Fig.1, all the indices were based on the pseudo-cubic cell and the XRD patterns of the samples with $0.02 \leq x < 0.20$, which showed the presence of ¼ ($h\,k\,l$)-type superlattice reflections. According to the Glazer [11], these types of reflections represent anti-phase tilting of the oxygen octrahedra without distortion. However, samples at the composition of $x = 0.30$ had a split (1 1 1) and (2 2 0) and single (2 0 0) reflection, thus confirming that the crystal structure of composition $x =$

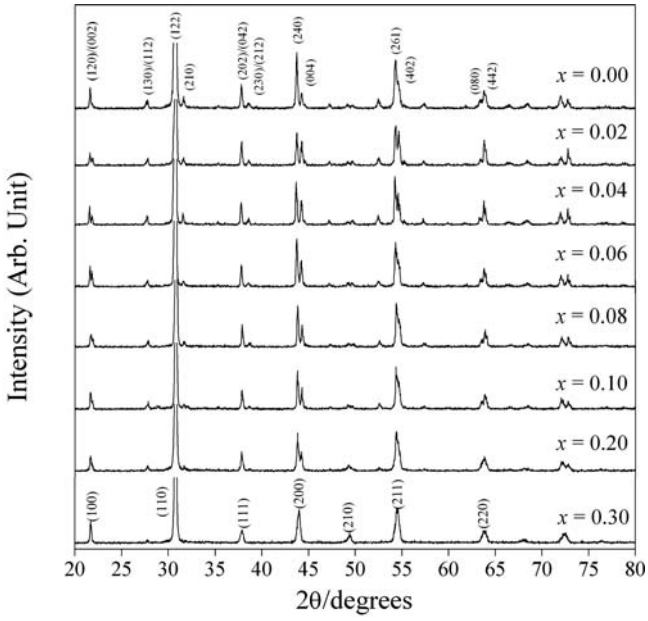

Figure 1. XRD patterns of $(1-x)PbZrO_3-xPb(Zn_{1/3}Nb_{2/3})O_3$ sintered pellets.

0.30 is a rhombohedral perovskite. Therefore, in accordance with the XRD results, the solid solution, PZ-PZN, successively transforms from orthorhombic to rhombohedral symmetry when the concentration of PZN is increased. The relative permitivity at room temperature, with all compositions of (1-x)PZ–xPZN ceramic at 100 Hz, is shown in Fig. 2. These results show that the dielectric constants of PZ-PZN ceramics at room temperature were increased with an increasing concentration of x. The effect of increasing relative permittivity at room

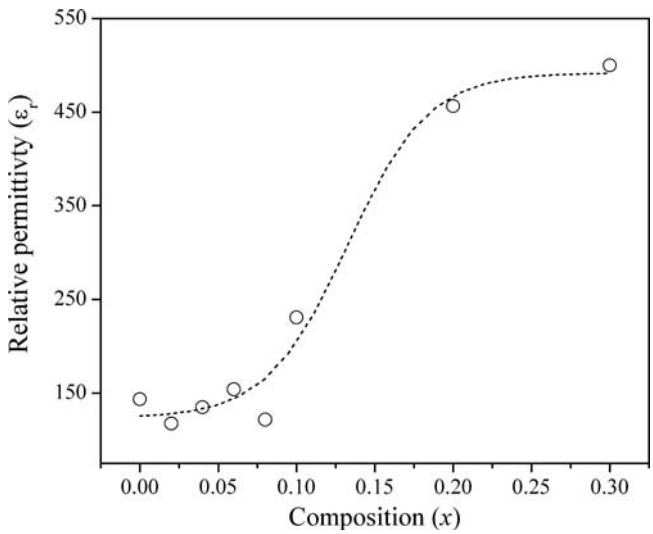

Figure 2. Variation of dielectric constant at room temperature with all compositions of $(1-x)$PZ–xPZN ceramic at 100 Hz.

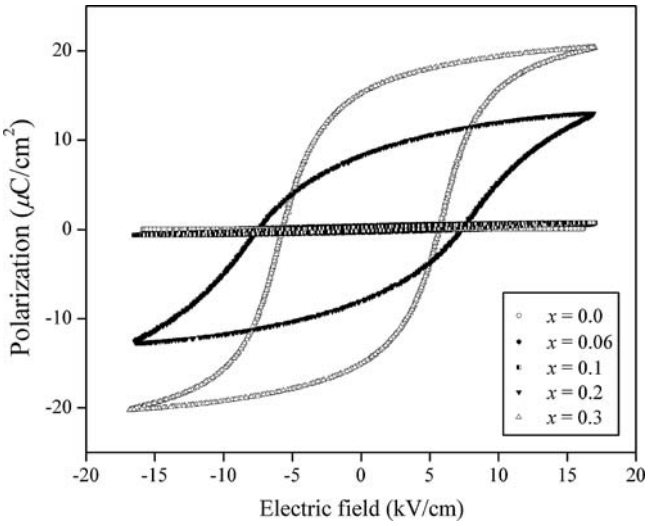

Figure 3. Effect of composition (x) on the P-E hysteresis loops of (1-x)PZ – xPZN ceramics.

temperature with increasing PZN content is interpreted to be due to the possibility of the decrease of transition temperature to near room temperature. The transition temperature of the PZ-PZN ceramics are shifted towards room temperature when PZN is added to PZ; thus increasing the dielectric properties measured at room temperature.

A series of polarization–field (P–E) hysteresis loops for the PZ-PZN ceramics is illustrated in Fig. 3, and from these loops, the remnant polarizations (P_r) and coercive field E_C (shown as an electric field required to zero polarization) are determined and listed in Table 1. The composition of $0.0 \leq x < 0.20$ ceramic, only a linear curve was observed at room temperature, which is perhaps due to the extremely high coercive field, indicating that this composition belongs to the AFE phase. No double loop was observed in the range of the applied electric field up to 20 kV/cm.

The polarization loops of 0.8PZ−0.2PZN and 0.7PZ−0.3PZN become well developed, due to the large amount of relaxor ferroelectric PZN content, showing large remnant

Table 1
Characteristics of (1–x)PZ-xPZN ceramics with optimized processing conditions (R, Rhombohedral; O, Orthorhombic)

Composition (x)	Crystal Structure	ε_r at room temperature	P_r (μC/cm^2)	E_c (kV/cm)
0.00	O	143.5	—	—
0.02	O	117.5	—	—
0.04	O	134.9	—	—
0.06	O	154.2	—	—
0.08	O	121.6	—	—
0.10	O	230.9	—	—
0.20	O	456.4	8.2	7.4
0.30	R	500.0	15.2	5.8

polarization (P_r) as shown in Fig. 3. The hysteresis loops are of a typical "square" form, as a result of domain switching in an applied field. This is a typical characteristic of a phase that contains long-range interaction between dipoles in the ferroelectric micro-domain state, and confirms that these compositions are of a normal ferroelectric phase, with rhombohedral symmetry, as indicated by XRD analysis.

Conclusions

It has been found that the crystal structure of dielectric and ferroelectric properties of PZ ceramics are strongly influenced by the addition of the relaxor ferroelectric, PZN. Data of the crystal structure obtained from XRD, show that the solid solution (1-x)PZ–xPZN, where $x = 0.00$–0.30, successively transforms from orthorhombic to rhombohedral symmetry with increased PZN concentration. The dielectric constants of PZ-PZN ceramics at room temperature were increased with an increasing concentration of x. 0.7PZ-0.3PZN induced normal ferroelectric behavior, with a high polarization value.

Acknowledgments

This work was supported by the Thailand Research Fund (TRF), and the National Nanotechnology Center (NANOTEC) NSTDA, Ministry of Science and Technology, Thailand through its program of Center of Excellence Network.

References

1. B. Jaffe and W. R. Cook, Piezoelectric ceramic: R.A.N. Publishers, 1971.
2. E. Sawaguchi, G. Shirane, and S. Hoshino, Antiferroelectric Structure of Lead Zirconate, *Phys. Rev*. **83**, 1078 (1951).
3. G. H. Haertling, Ferroelectric Ceramics: History and Technology. *J. Am. Ceram. Soc*. **82**, 797–818 (1999).
4. B. P. Pokharel and D. Pandey, Effect of Ba^{2+} substitution on the stability of the antiferroelectric and ferroelectric phases in $(Pb_{1-x}Ba_x)ZrO_3$: Phenomenological theory considerations. *Phys. Rev. B* **65**, 214108 (2002).
5. B. P. Pokharel and D. Pandey, Irreversibility of the antiferroelectric to ferroelectric phase transition in $(Pb_{0.90}Ba_{0.10})ZrO_3$ ceramics. *J. Appl. Phys*. **86**, 3327–3332 (1999).
6. Y. Xu, Ferroelectric Materials and Their Application: Elsevier Science Publishers B.V. 1991.
7. S. Wirunchit, P. Laoratanakul, and N. Vittayakorn, Physical properties and phase transitions in perovskite $Pb[Zr_{1-x}(Ni_{1/3}Nb_{2/3})_x]O_3$ ($0.0 \leq x \leq 0.5$) ceramics. *J. Phys. D: Appl. Phys*. **41**, 125406 (2008).
8. T. Takenaka, K. Muramata, and T. Fujii, Piezoelectric properties of PZN-PT prepared by HIP. *Ferroelectrics* **134**, 133 (1992).
9. Y. Yokomizo, T. Takahashi, and S. Nomura, Ferroelectric properties of PZN. *J. of Phys. Soc. Jpn*. **28**, 1278–1284 (1970).
10. M. Villegas, A. C. Caballero, C. Moure, and R. E. Newham, Influence of Processing parameters on the sintering and Electrical properties of $Pb(Zn_{1/3}Nb_{2/3})O_3$-Based Ceramics. *J. Am. Ceram. Soc*. **83**, 141 (2000).
11. A. M. Glazer, Simple ways of determining perovskite structures. *Acta Crystallogr*. **A31**, 756 (1975).

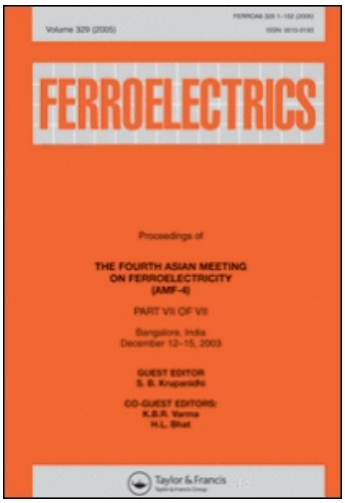

Ferroelectrics
Publication details, including instructions for authors and subscription information:
http://www.informaworld.com/smpp/title~content=t713617887

Crossover from Antiferroelectric to Normal Ferroelectric Behavior in Lead Zirconate—Lead Nickel Niobate Ceramics Prepared by the Reaction Sintering Process

Supamas Wirunchit [a]; Naratip Vittayakorn [ab]
[a] Materials Science Research Unit, Department of Chemistry, Faculty of Science, King Mongkut's Institute of Technology Ladkrabang, Bangkok, Thailand [b] College of KMITL Nanotechnology, King Mongkut's Institute of Technology Ladkrabang, Bangkok, Thailand

Online Publication Date: 01 January 2009

To cite this Article Wirunchit, Supamas and Vittayakorn, Naratip(2009)'Crossover from Antiferroelectric to Normal Ferroelectric Behavior in Lead Zirconate—Lead Nickel Niobate Ceramics Prepared by the Reaction Sintering Process',Ferroelectrics,382:1,135 — 140

To link to this Article: DOI: 10.1080/00150190902870069

URL: http://dx.doi.org/10.1080/00150190902870069

Ferroelectrics, 382:135–140, 2009

ISSN: 0015-0193 print / 1563-5112 online
DOI: 10.1080/00150190902870069

Crossover from Antiferroelectric to Normal Ferroelectric Behavior in Lead Zirconate—Lead Nickel Niobate Ceramics Prepared by the Reaction Sintering Process

SUPAMAS WIRUNCHIT[1] AND NARATIP VITTAYAKORN[1,2,*]

[1]Materials Science Research Unit, Department of Chemistry, Faculty of Science, King Mongkut's Institute of Technology Ladkrabang, Bangkok 10520, Thailand
[2]College of KMITL Nanotechnology King Mongkut's Institute of Technology Ladkrabang, King Mongkut's Institute of Technology Ladkrabang Bangkok 10520, Thailand

The lead zirconate—lead nickel niobate ceramics, (1-x)PbZrO3—xPb(Ni1/3Nb2/3)O3 (PZ-PNN) with x = 0.00–0.10, have been prepared by reaction sintering. Without any calcination involved, the mixture of raw materials was pressed and sintered directly. The PZ–PNN ceramics could be obtained after 6 h sintering at 1,100–1,250°C. The crystal structure data obtained from XRD indicate that the PZ-PNN, where x = 0.00–0.10, successively transforms from orthorhombic to rhombohedral symmetry with an increase in the PNN concentration around x = 0.08. The antiferroelectric phase (AFE) → ferroelectric phase (FE) transition occurs in compositions of 0.0 ≤ x ≤ 0.08. The AFE→FE phase transition shifts to lower temperatures with higher compositions of x. The FE phase temperature range width increases with increased PNN.

Keywords Reaction-Sintering process; Materials preparation, Lead Zirconate and Lead Nickel Niobate

PACS: 64.70.K-; 77.22.Ch; 81.05.Je; 85.80.-n and 77.84.Dy

Introduction

Lead zirconate, $PbZrO_3$ (PZ), is considered to be an excellent candidate as a key material of antiferroelectric ceramics [1–2]. At room temperature, PZ has an orthorhombic structure [3], and an antiferroelectric (AFE) phase. It undergoes the AFE to a paraelectric (PE) phase and transforms from an orthorhombic structure to a cubic structure at 236°C [3]. It is reported that a ferroelectric (FE) phase exists over a very narrow temperature range (230–233°C) [4–7]. Lead nickel niobate ($Pb(Ni_{1/3}Nb_{2/3})O_3$; PNN) has a perovskite structure and typical relaxor ferroelectric properties. It exhibits a diffuse phase transition at around −120°C, with a much lower peak permittivity of about 4000 [8]. The crystal structure of PNN at room temperature is cubic (*Pm3m*), with a lattice parameter of 4.03 Å [8]. New piezoelectric ceramics for high-frequency ultrasonic transducer application using modified

Received August 3, 2008; in final form December 31, 2008.
*Corresponding author. E-mail: naratipcmu@yahoo.com

$PbZrO_3$ ceramic compositions in the $(1\text{-}x - y)PbZrO_3 + xPb(Mg_{1/3}Nb_{2/3})O_3 + yPbTiO_3$ system, with an ferroelectric (FE) rhombohedral phase near the antiferroelectric (AFE) orthorhombic phase ($0.0 < x \leq 0.1$ and $0.0 < y \leq 0.2$), have been reported by Takeuchi et al. [9]. The anisotropy of electromechanical coupling factors (k_t/k_p ratio) was 24 for $x = 0.05$ and $y = 0.00$, which is a boundary composition between the AFE orthorhombic phase and the FE rhombohedral phase [9]. The solid solution of PZ-PNN ceramics was synthesized via the columbite precursor method, which was studied by Wirunchit et al. [10]. The columbite precursor method consists of two calcinations. The columbite precursor is formed first, followed by the formation of perovskite. Two calcinations and pulverization stages were carried out before sintering PZ-PNN ceramics. The crystal structure of the solid solution (1-x)PZ-xPNN, where $x = 0.00$–0.50, successively transforms from orthorhombic to rhombohedral to pseudo-cubic symmetry with an increase in the PNN concentration [10].

The reaction-sintering process is a simple and effective route in synthesizing ceramics. The calcination step is bypassed and the raw material mixture is pressed into pellets and sintered into ceramics directly [11]. In the present investigation, the phase transition of (1-x)PZ-xPNN ($x = 0.00$–0.10) ceramics is prepared by the reaction-sintering process.

Experimental Procedure

The perovskite structure of lead zirconate – lead nickel niobate ceramic, $(1\text{-}x)PbZrO_3 - xPb(Ni_{1/3}Nb_{2/3})O_3$ [(1-x)PZ-xPNN; x =0.0–0.1], was prepared by the reaction-sintering process via the columbite precursor method. Firstly, the columbite structure ($NiNb_2O_6$) was synthesized. Stoichiometric amounts of the precursor (NiO and Nb_2O_5) were mixed and milled in ethyl alcohol for 18 h. The mixture was dried and calcined at 1,100°C for 4 h. The calcined powder was pulverized and the appropriate amounts of PbO and ZrO_2 were then added, according to the composition of $(1\text{-}x)PbZrO_3 - xPb(Ni_{1/3}Nb_{2/3})O_3$ (PZ-PNN), $0 \leq x \leq 0.10$, with an excessive content of 2 mol% PbO. After re-milling and drying, the pulverized mixtures of $NiNb_2O_6$, PbO and ZrO_2 were pressed into pellets. Pellets of 15 mm in diameter were pressed using 5% PVA. The binder was burnt out by slowly heating to 500°C over 2 h. The samples were sintered at 1,100– 1,150°C for 6 h. Phase formation and phase transition of PZ-PNN were investigated by X-ray diffraction (XRD) and a differential scanning calorimeter (DSC).

Results and Discussion

The XRD patterns of $(1\text{-}x)PbZrO_3 - xPb(Ni_{1/3}Nb_{2/3})O_3$, $(0.00 \leq x \leq 0.10)$ ceramics, sintered at 1,150°C, are shown in Fig. 1. From the patterns, PZ powder was identified as a single-phase material with a perovskite structure having orthorhombic symmetry, which could be matched with ICDD file no. 75–1607. The XRD patterns of the PZ-PNN compositions showed a combination between PZ and PNN patterns, which indicated a perovskite structure having a symmetry that varied from orthorhombic to pseudo-cubic types. The ICDD file no. 34-0103 for PNN, with a cubic structural symmetry, showed a better comparison. The $(1\text{-}x)PbZrO_3 - xPb(Ni_{1/3}Nb_{2/3})O_3$ was orthorhombic and rhombohedral for compositions where $x = 0.00 \leq x < 0.10$ and $x = 0.10$, respectively. Figure 2 shows the density percentage of PZ-PNN ceramics as a function of composition$x$. The density percentage increases with an increase of sintering temperature and reaches 97.48% at 1,200°C. For sintering at a temperature of 1,250°C, the density percentage is lower at 1,200°C. The DSC was used to investigate the phase transition in the $(1\text{-}x)PbZrO_3 - xPb(Ni_{1/3}Nb_{2/3})O_3$ system. AFE-FE phase transition temperatures, enthalpy and paraelectric (PE) transitions are

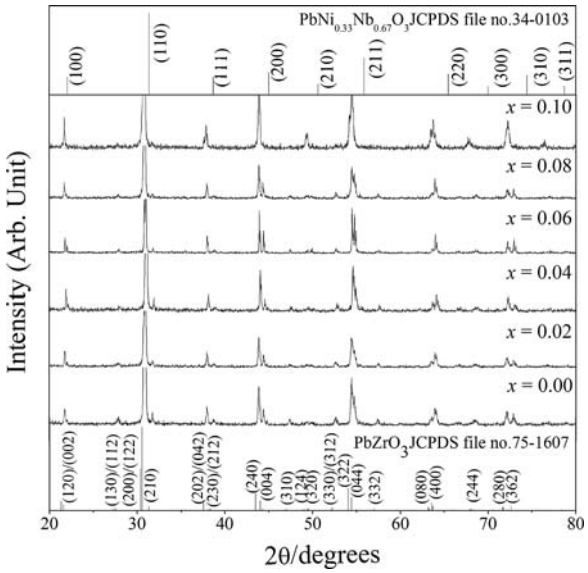

Figure 1. XRD patterns of $(1–x)PbZrO_3– xPb(Ni_{1/3}Nb_{2/3})O_3$; $x = 0.0–0.1$ ceramics.

summarized in Table 1. Figure 3 shows results of the DSC analysis of the PZ-PNN ceramics. Two distinct endothermic peaks were observed for $(1\text{-}x)PbZrO_3 - xPb(Ni_{1/3}Nb_{2/3})O_3$ samples with $0.00 < x < 0.08$. The lower temperature corresponds to the transition temperature of the AFE $\rightarrow$ FE phase transition, while the higher temperature corresponds to the FE$\rightarrow$PE phase transition. It is noteworthy that the areas under two endothermic peaks in Fig. 3 decreased with an increasing amount of PNN. Since those areas represent a free-energy difference between the two phases, this result indicated that the addition of

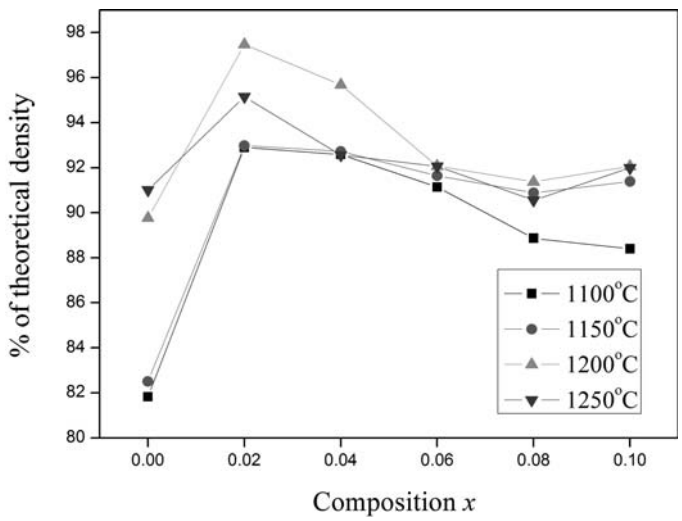

Figure 2. Variation of the density percentage with the sintering temperature of $(1–x)PbZrO_3–xPb(Ni_{1/3}Nb_{2/3})O_3$; $x = 0.0–0.1$ ceramics. (See Color Plate XXXV)

Table 1
Phase transition temperatures of $(1–x)PbZrO_3– xPb(Ni_{1/3}Nb_{2/3})O_3$; $x = 0.0–0.1$ ceramics (R, Rhombohedral; O, Orthorhombic)

Composition (x)	Crystal Structure	Phase transition Temperature (°C)		Enthalpy (J/g)	
		AFE→FE	FE→PE	AFE→FE	FE→PE
0.00	O	229.5		4.55	
0.02	O	203.1	226.2	1.34	2.29
0.04	O	175.8	218.0	1.17	2.20
0.06	O	134.1	210.9	0.87	1.89
0.08	O	80.8	204.3	0.19	1.76
0.10	R	—	196.4	—	1.34

PNN decreases stability of the orthorhombic phase. It is apparent that the replacement of the Zr^{4+} ion by Ni^{2+}/Nb^{5+} ions would decrease the driving force for the antiparallel shift of Pb^{2+} ions because they interrupt the translational symmetry. This interruption caused the appearance of a rhombohedral ferroelectric phase when the amount of PNN was more than 10 mol%.

Figure 4 illustrates the P-E curves of sample with $x = 0.00$-0.10 measured at 25 kV/cm. For the composition $0.0 \leq x < 0.08$ ceramic, only a linear curve was observed, which is perhaps due to the extremely high coercive field, indicating that this composition belongs to the AFE phase. For the composition $x \leq 0.08$, a rectangular loop characteristic

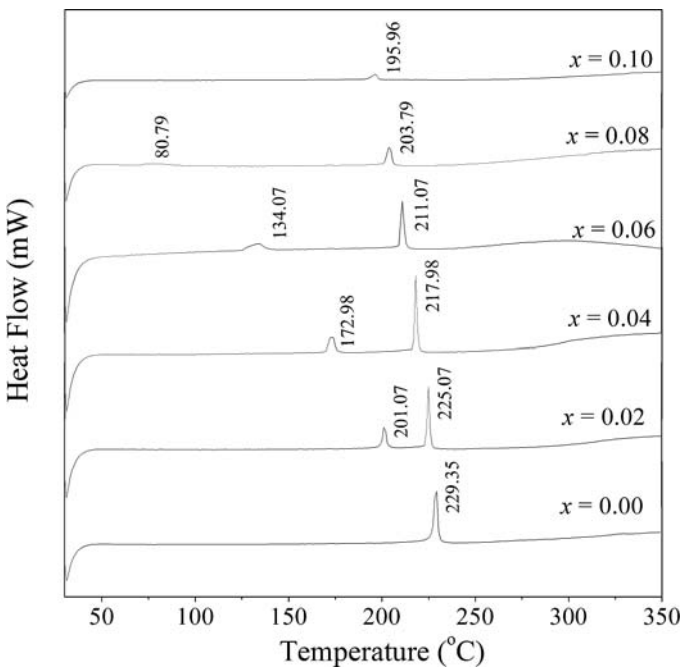

Figure 3. DSC thermographs of $(1–x)PbZrO_3– xPb(Ni_{1/3}Nb_{2/3})O_3$; $x = 0.0–0.1$ ceramics.

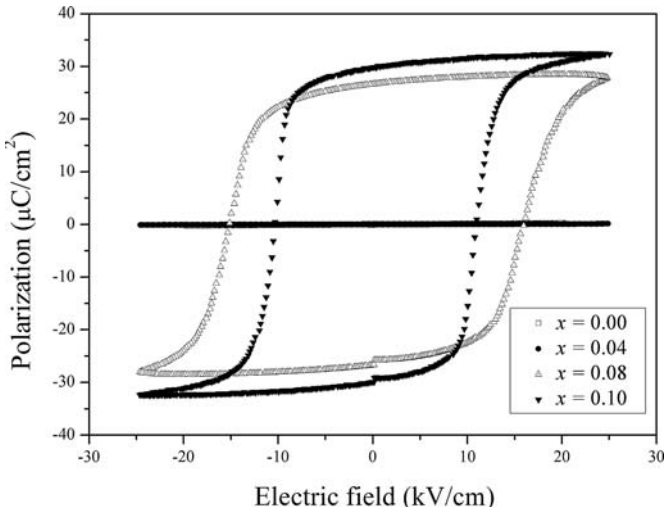

Figure 4. Hysteresis loops of the $(1–x)PbZrO_3– xPb(Ni_{1/3}Nb_{2/3})O_3$ ceramics with $x = 0.0–0.1$ measured at 25 kV/cm.

of ferroelectricity was clearly evident. The maximum value of remanent polarization $(P_r) = 31\ \mu C/cm^2$ was observed in the composition $x = 0.1$. The P-E hysteresis loop measurement demonstrated that the ferroelectric properties of the ceramics in the $(1-x)PbZrO_3 - xPb(Ni_{1/3}Nb_{2/3})O_3$ system shift gradually from antiferroelectric behavior to normal ferroelectric behavior.

Based on the results of XRD, and DSC data, the ferroelectric phase diagram for the $(1-x)PbZrO_3 - xPb(Ni_{1/3}Nb_{2/3})O_3$ binary system has been established, as shown in Fig. 5. The transition temperature decreases at approximate linearity with x. The phase

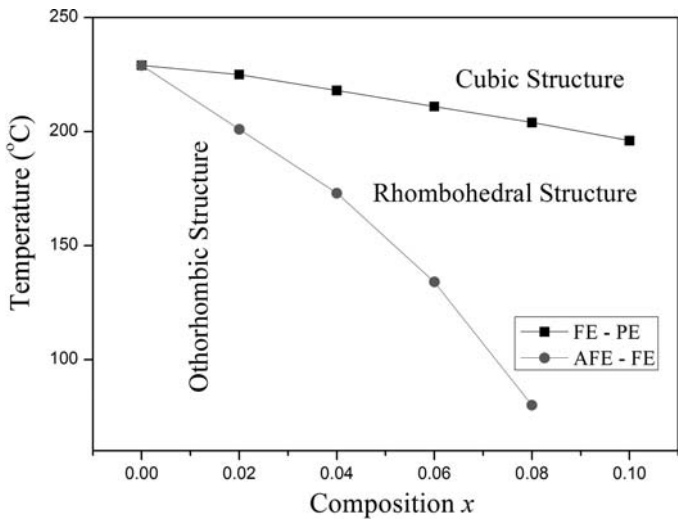

Figure 5. Ferroelectric phase diagram of the $(1–x)PbZrO_3– xPb(Ni_{1/3}Nb_{2/3})O_3$; $x = 0.0–0.1$ binary system.

diagram consists of three distinct crystallographic phases in this system; high temperature paraelectric cubic (*Pm3m*), rhombohedral (*R3m*), and ferroelectric orthorhombic [*P2cb* (no. 32)]. At low concentrations of PNN $x \leq 0.08$, the symmetry can be defined as orthorhombic. The orthorhombic symmetry transforms into rhombohedral at a composition near $x = 0.08$.

Conclusions

The perovskite (1-x)$PbZrO_3 - xPb(Ni_{1/3}Nb_{2/3})O_3$ (PZ-PNN) ceramics could be obtained successfully by the reaction-sintering process. The Structure of PZ-PNN is orthorhombic for a composition where $x = 0.00 \leq x \leq 0.08$ and rhombohedral for compositions where $x = 0.10$. Highly dense PZ-PNN ceramics with a density higher than 97.48% of theoretical density could be obtained. The AFE→FE phase transition shifts to lower temperatures with higher compositions of x. The temperature range width of FE phase increases with an increasing amount of PNN. It is apparent that replacement of the Zr^{4+} ion by Ni^{2+}/Nb^{5+} ions would decrease the driving force for the antiparallel shift of Pb^{2+} ions because they interrupt the translational symmetry. This interruption caused the appearance of a rhombohedral ferroelectric phase when the amount of PNN was more than 10 mol%.

Acknowledgments

This work was supported by the Thailand Research Fund (TRF), the Commission on Higher Education (CHE), Thailand Graduate Institute of Science and Technology (TGIST), National Research Council of Thailand (NRCT), and the National Nanotechnology Center (NANOTEC) NSTDA, Ministry of Science and Technology, Thailand through its program of Center of Excellence Network.

References

1. E. Sawaguchi, G. Shirane, and S. Hosshino, *Phys. Rev.* **83**, 1078 (1951).
2. E. Sawaguchi, G. Shirane, and Y. Takagi, *J. Phys. Jpn. Soc.* **6**, 333 (1951).
3. S. Roberts, *J. Am. Ceram. Soc.* **33**, 63 (1953).
4. L. Goulpeau, *Sov. Phys. Solid State* **8**, 1967 (1970).
5. V. J. Tennery, *J. Am. Ceram. Soc.* **49**, 483 (1966).
6. B. A. Scott and G. Burns, *J. Am. Ceram. Soc.* **55**, 331 (1972).
7. R. W. Whatmore and A. M. Glazer, Structural phase transitions in lead zirconate. *J.Phys. C: Solid State Phys.* **12**, 1505 (1979).
8. V. A. Bokov and I. E Myl'nikova, *Sov. Phys. Solid State* **3**, 631 (1961).
9. H. Takeuchi, S. Jyomura, and C. Nakaya, *Jpn. J. Appl. Phys.* **24**, 36–40 (1985).
10. S. Wirunchit, P. Laoratanakul, and N. Vittayakorn, Physical properties and phase transitions in perovskite $Pb[Zr_{1-x}(Ni_{1/3}Nb_{2/3})_x]O_3$ ($0.0 \leq \times \leq 0.5$) ceramics. *J. Phys. D: Appl. Phys.* **41,** 125406 (2008).
11. Y. C. Liou and C. T. Wu, Synthesis and diffused phase transition of $Ba_{0.7}Sr_{0.3}TiO_3$ ceramics by a reaction-sintering process. *Ceramics International*, **34**, 517–522 (2008).

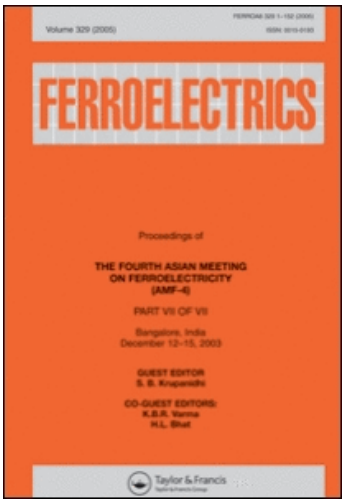

Ferroelectrics
Publication details, including instructions for authors and subscription information:
http://www.informaworld.com/smpp/title~content=t713617887

Preparation of Lead Zirconate-Lead Nickel Niobate Ceramics by the Reaction Sintering Process

Supamas Wirunchit [a]; Rangson Muanghlua [b]; Surasak Niemcharoen [b]; Wanwilai C. Vittayakorn [c]; Pitak Laoratanakul [d]; Naratip Vittayakorn [ae]
[a] Materials Science Research Unit, Department of Chemistry, Faculty of Science, King Mongkut's Institute of Technology Ladkrabang, Bangkok, Thailand [b] Department of Electronics, Faculty of Engineering, King Mongkut's Institute of Technology Ladkrabang, Bangkok, Thailand [c] Department of Physics, Faculty of Science, Chiang Mai University, Chiang Mai, Thailand [d] National Metal and Materials Technology Center (MTEC), Pathumthani, Thailand [e] College of KMITL Nanotechnology, King Mongkut's Institute of Technology, Bangkok, Thailand

Online Publication Date: 01 January 2009

To cite this Article Wirunchit, Supamas, Muanghlua, Rangson, Niemcharoen, Surasak, Vittayakorn, Wanwilai C., Laoratanakul, Pitak and Vittayakorn, Naratip(2009)'Preparation of Lead Zirconate-Lead Nickel Niobate Ceramics by the Reaction Sintering Process',Ferroelectrics,380:1,14 — 19
To link to this Article: DOI: 10.1080/00150190902869996
URL: http://dx.doi.org/10.1080/00150190902869996

Ferroelectrics, 380:14–19, 2009

ISSN: 0015-0193 print / 1563-5112 online
DOI: 10.1080/00150190902869996

Preparation of Lead Zirconate-Lead Nickel Niobate Ceramics by the Reaction Sintering Process

SUPAMAS WIRUNCHIT,[1] RANGSON MUANGHLUA,[2] SURASAK NIEMCHAROEN,[2] WANWILAI C. VITTAYAKORN,[3] PITAK LAORATANAKUL,[4] AND NARATIP VITTAYAKORN[1,5,*]

[1]Materials Science Research Unit, Department of Chemistry, Faculty of Science, King Mongkut's Institute of Technology Ladkrabang, Bangkok 10520, Thailand
[2]Department of Electronics, Faculty of Engineering, King Mongkut's Institute of Technology Ladkrabang, Bangkok Thailand 10520
[3]Department of Physics, Faculty of Science, Chiang Mai University, Chiang Mai 50200, Thailand
[4]National Metal and Materials Technology Center (MTEC), Pathumthani 12120, Thailand
[5]College of KMITL Nanotechnology, King Mongkut's Institute of Technology, Ladkrabang, Bangkok 10520, Thailand

The perovskite structure of lead zirconate – lead nickel niobate ceramics, (1-x) $PbZrO_3$–x$Pb(Ni_{1/3}Nb_{2/3})O_3$ (PZ – PNN) at x between 0.00–0.50, has been prepared by the reaction-sintering process. The specimens were prepared directly from a mixture of their constituent oxide without any calcination step. The PZ – PNN ceramics could be obtained after 6 h sintering at 1,100–1,250°C. Crystal structure and phase transition of PZ-PNN were investigated by x-ray diffraction (XRD). XRD indicated that the structure of PZ-PNN ceramics is orthorhombic for a composition where $x = 0.00$, rhombohedral for compositions where $x = 0.10 \leq x \leq 0.40$ and pseudo-cubic for a composition where $x = 0.50$. The dielectric properties of the ceramics were measured as functions of both temperature and frequency. The results indicated that the transition temperature decreases with increasing PNN concentration. Furthermore, morphology and grain size evolution have been determined via a scanning electron microscope (SEM)

Keywords Reaction-Sintering process; Materials preparation; Lead Zirconate and Lead Nickel Niobate

PACS: 64.70.K-, 77.22.Ch, 81.05.Je, 85.80.-n and 77.84.Dy

Introduction

Lead zirconate [$PbZrO_3$;PZ] is an antiferroelectric ceramic, which has an orthorhombic structure and a Curie temperature of about 230°C [1, 2]. PZ is a parent compound of $PbZr_{1-x}Ti_xO_3$ (PZT) solid solutions, which are of high scientific and technological interest

Received August 3, 2008; in final form December 31, 2008.
*Corresponding author. E-mail: naratipcmu@yahoo.com

for their ferroelectricity and piezoelectricity that have been observed over a wide range of compositions [3]. Lead nickel niobate ($Pb(Ni_{1/3}Nb_{2/3})O_3$;PNN) is a perovskite structure and has typical relaxor ferroelectric properties. It exhibits a diffuse phase transition of around $-120°C$, with a much lower peak permittivity of about 4,000 [4]. The crystal structure of PNN at room temperature is cubic (*Pm3m*) [5]. Thus, mixing PNN with PZ is expected to decrease the sintering temperature of PZ-based ceramics, which is desirable towards lower-cost electrodes [6]. In our previous work [7, 8], we studied synthesis of the solid solution of PZ-PNN ceramics via the columbite precursor method. This method consists of two calcination processes. Columbite is formed first, followed by the formation of perovskite. Two calcination and pulverization stages were carried out before sintering PZ-PNN ceramics. The crystal structure of the solid solution (1-x)PZ-xPNN, where $x =$ 0.00–0.50, successively transforms from orthorhombic through rhombohedral to pseudo-cubic symmetry with increase of the PNN concentration [9].

The reaction-sintering process is a simple and effective route in synthesizing ceramics. The calcination step is skipped and the raw material mixture is pressed into pellets and sintered into ceramics directly. The purpose of this study was to investigate the sintering behavior of (1-x)PZ-xPNN ($x = 0.00$–0.50) ceramics prepared by the reaction-sintering process. The phase transition, morphology and dielectric properties are presented and analyzed.

Experimental Procedure

The ceramics of lead zirconate – lead nickel niobate ceramics, (1-x)$PbZrO_3$-$Pb(Ni_{1/3}Nb_{2/3})O_3$ (PZ-PNN), have been prepared by the reaction-sintering process via the columbite precursor method. Firstly, the columbite structure ($NiNb_2O_6$) was synthesized. Stoichiometric amounts of the precursor (NiO, Nb_2O_5) were mixed and milled in ethyl alcohol for 18 h. The mixture was dried and calcined at 1,100°C for 4 h. Then, $NiNb_2O_6$ and ZrO_2 were mixed with PbO, according to the composition of (1-x)$PbZrO_3$-$Pb(Ni_{1/3}Nb_{2/3})O_3$ (PZ-PNN), $0 \leq x \leq 0.50$, with an excessive content of 2|mol% PbO. After re-milling and drying, the milled powders were directly pressed into 15 mm diameter pellets using 5% PVA and without calcination. The binder was burnt out by slowly heating up to 500°C for 2 h. The samples were sintered at 1,100–1,250°C for 6 h. Phase formation and phase transition of PZ-PNN were investigated by x-ray diffraction (XRD). Dielectric properties measured the ceramics by using an HP-4284A LCR meter. Ceramic morphologies were imaged, using scanning electron microscopy (SEM; JEOL JSM-840A).

Results and Discussion

The formation of the perovskite phases in the (1-x)PZ-xPNN ($x = 0.0$–0.5) specimens, produced by the reaction-sintering process, were studied and analyzed by XRD. The XRD patterns from this system are shown in Fig. 1. It can be seen that a complete crystalline solution of perovskite structure is formed throughout all of the composition ranges without the presence of pyrochlore or unwanted phases. From the patterns, PZ ceramic is identified as a single-phase material with a perovskite structure having orthorhombic symmetry, which could be matched with international center for diffraction data (ICDD) file no. 75–1607. The XRD patterns of the PZ-PNN compositions show a combination between both PZ and PNN patterns, indicating a perovskite structure having a symmetry that varies from orthorhombic to pseudo-cubic types. A better comparison is the ICDD file no. 34–0103 for PNN, with a cubic structural symmetry. The (1-x)PZ-xPNN is orthorhombic for a

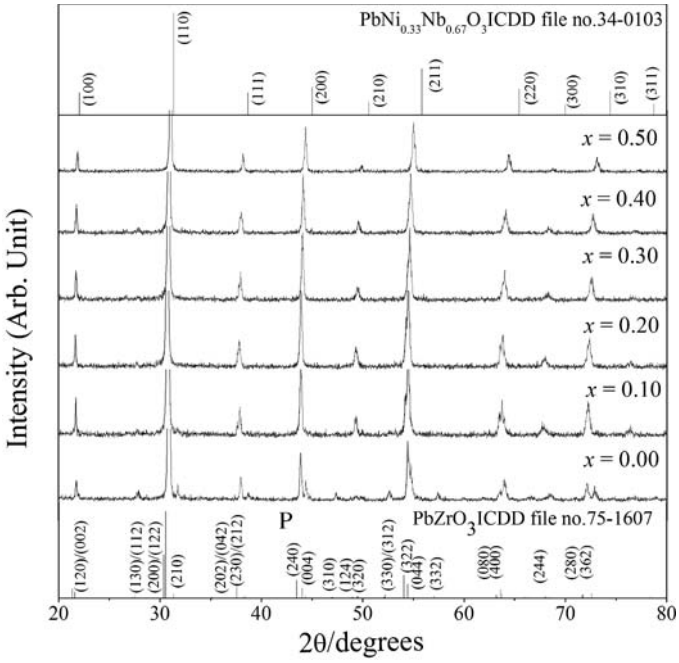

Figure 1. XRD patterns of $(1–x)PbZrO_3– xPb(Ni_{1/3}Nb_{2/3})O_3$ ceramics.

composition where $x = 0.00$, rhombohedral for compositions where $x = 0.10 \leq x \leq 0.40$ and pseudo-cubic for a composition where $x = 0.50$. It increases from 10.08 to 12.22%, 11.63 to 13.57 and 13.18 to 14.73 for $x = 0.10$, 0.20 and 0.50, respectively. The shrinkage percentages of PZ-PNN ceramics are shown in Fig. 2.

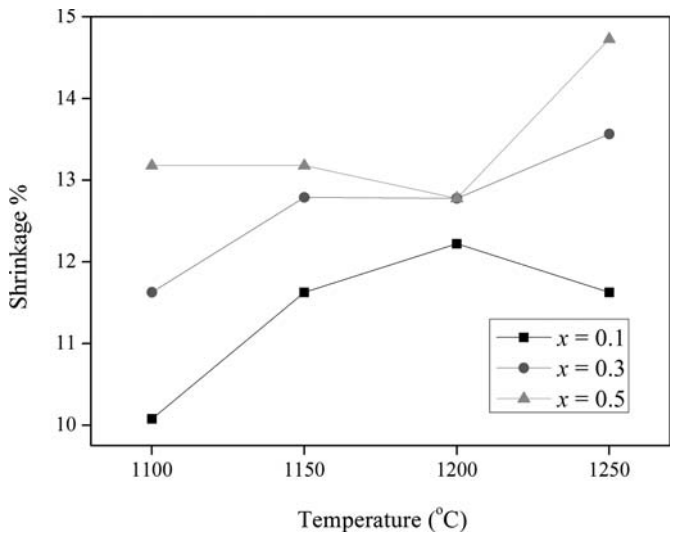

Figure 2. Shrinkage percentage of $(1–x)$PZ– PNN ceramics. (See Color Plate I)

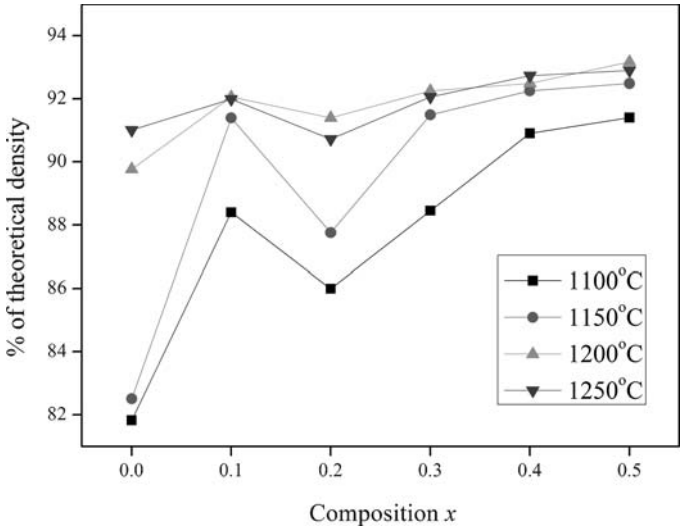

Figure 3. Variation of the density percentage with sintering temperature of (1–x)PZ–xPNN ceramics. (See Color Plate II)

Figure 3 shows the density percentage of PZ-PNN ceramics as a function of composition$x$. The density percentage increases with increasing sintering temperature and reaches 93.17% at 1,200°C. For composition $x = 0.20$, 0.30 and 0.50 at 1,250 °C, density percentages are lower than the 1,200°C sintering temperature.

The compositional dependence of the dielectric response characteristics for PZ-PNN ceramics, where the normal and relaxor ferroelectric behavior crosses over, is shown in Fig. 4 for the composition $x = 0.00$–0.50 taken at measurement frequencies of 0.1, 1, 10 and 100 kHz. For composition $x = 0.0$, the relative permittivity increased slowly until

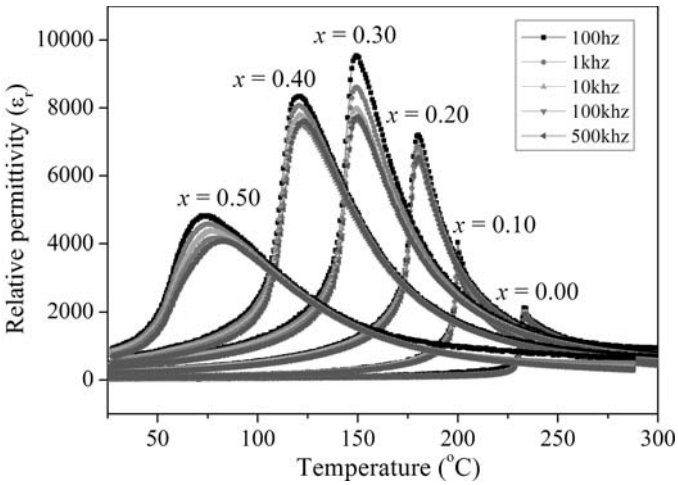

Figure 4. Temperature dependence of relative permittivity ε_r for $(1 - x)$PZ $-x$PNN; $x = 0.0$–0.5 ceramics. (See Color Plate III)

the temperature approached 230°C. At around 235°C, the relative permittivity increased greatly, passing through a maximum at about 236°C. With further heating, the relative permittivity decreased in accordance with the Curie-Weiss law, $\varepsilon_r = C/(T\text{-}T_o)$, where ε_r is the relative permittivity, T is the temperature and C and T_o are constants that, in this study, were 1.04×10^5 and 460.70 K, respectively. With increasing PNN concentration to $x = 0.3$, the relaxor-like dielectric dispersion became increasingly more pronounced by existing over a broader temperature range near T_{max}. The first-order dielectric features of the spontaneous transformation became decreasingly distinct when $x \geq 0.4$,. These results clearly show that a spontaneous crossover between relaxor and normal state exits over a relatively wide PNN content range of between $x = 0.3$ and 0.4. Upon increasing the PNN concentration to $x = 0.5$, the ceramic exhibits a broad maximum of relative permittivity with strong frequency dispersion, which is reminiscent of the relaxor ferroelectric behavior of PNN crystal. The maximum value of relative permittivity decreases with increasing frequency. The dielectric dispersion below transition temperature reflects typical relaxor ferroelectric behavior arising from the responses of polar micro-domains with a spectrum of relaxation time [10, 11].

Figure 5(a)–(d) show the scanning electron microscopy images of the fracture surfaces of $(1\text{-}x)PbZrO_3 - xPb(Ni_{1/3}Nb_{2/3})O_3$ ceramics. No plate-like grains were observed in any sample, indicating the absence of pyrochlore formation. Other compositions of the system also exhibited high density and irregular grain size and shape. By applying the linear intercept methods to these SEM micrographs, the average grain size was calculated to be between 0.91–1.74 μm for all of the samples.

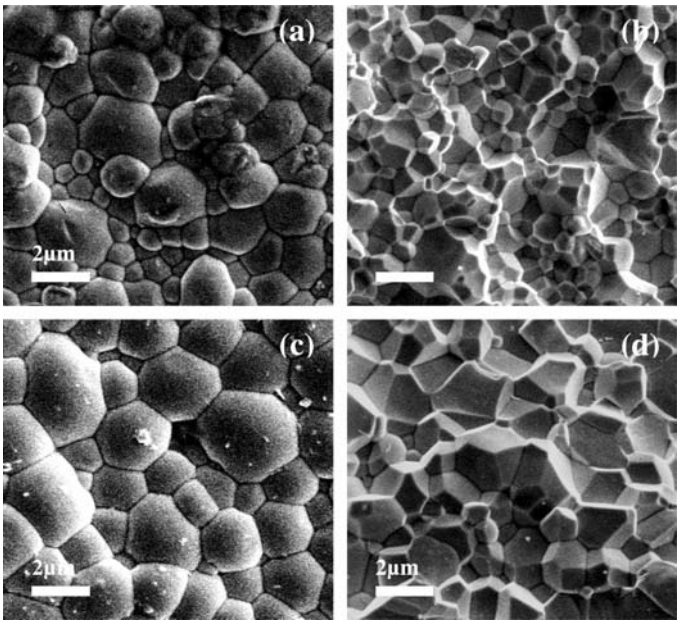

Figure 5. SEM photographs of four $(1 - x)PZ - xPNN$ ceramics; (a) and (b) $x = 0.20$, (c) and (d) $x = 0.50$.

Conclusions

The perovskite (1-x)$PbZrO_3 - xPb(Ni_{1/3}Nb_{2/3})O_3$ (PZ-PNN) ceramics could be obtained successfully by the reaction-sintering process. The structure of PZ-PNN is orthorhombic for a composition where $x = 0.00$, rhombohedral for compositions where $x = 0.10 \leq x \leq 0.40$ and pseudo-cubic for a composition where $x = 0.50$. Density of PZ-PNN ceramics higher than 85% of theoretical density was obtained. The density percentage increases with increasing sintering temperature. The dielectric constant of (1-x)$PbZrO_3 - xPb(Ni_{1/3}Nb_{2/3})O_3$ was found to increase with increased PNN concentration. The transition from the normal FE to relexor FE state was clearly observed as the mole fraction of the PNN increase.

Acknowledgments

This work was supported by the Thailand Research Fund (TRF), the Commission on Higher Education (CHE), Thailand Graduate Institute of Science and Technology (TGIST) National Research Council of Thailand (NRCT), and the National Nanotechnology Center (NANOTEC) NSTDA, Ministry of Science and Technology, Thailand through its program of Center of Excellence Network.

References

1. E. Sawaguchi, G. Shirane, and S. Hoshino, Antiferroelectric structure of lead zirconate. *Phys. Rev.* **83**, 1078 (1951).
2. F. Jona, G. Shirane, F. Mazzi, and R. Pepinsky, X-Ray and neutron diffraction study of antiferroelectric lead zirconate, PbZrO3. *Phys. Rev.* **105**, 849–856 (1957).
3. G. H. Haertling, Ferroelectric ceramics: history and technology. *J. Am. Ceram. Soc.* **82**, 797–818 (1999).
4. G. A. Smolenskii and A. L. Agranovskaya, Dielectric polarization of and lossed of some complex compounds. *Sov. Phys.-Tech. Phys.* 1380 (1958).
5. S. Sharma, R. Sati, and R. N. P. Choudhary, Relaxation beheaviour of PNN ceramics. *Can. J. Phys.* **71**, 322 (1993).
6. Y. Xu, Ferroelectric materials and their application: elsevier science publishers B.V. 1991.
7. S. Wirunchit, P. Laoratanakul, and N. Vittayakorn, Physical properties and phase transitions in perovskite $Pb[Zr_{1-x}(Ni_{1/3}Nb_{2/3})_x]O_3$ ($0.0 \leq x \leq 0.5$) ceramics. *J. Phys. D: Appl. Phys.* **41**, 125406 (2008).
8. N. Vittayakorn and S. Wirunchit, Perovskite formation, dielectric and ferroelectric properties of $PbZrO_3$–$Pb(Ni_{1/3}Nb_{2/3})O_3$ ceramics via a columbite precursor synthetic route. *Smart Mater. Struct.* **16**, 851–857 (2007).
9. S. Wirunchit and N. Vittayakorn, Structural transformation in antiferroelectric $PbZrO_3$-relaxor ferroelectric $Pb(Ni_{1/3}Nb_{2/3})O_3$ solid solution system. *J. Appl. Phys.* **104**, 024103–6 (2008).
10. X. H. Zhao, W. G. Qu, H. He, N. Vittayakorn, and X. L. Tan, Influence of cation order on the electric field-induced phase transition in Pb(Mg1/3Nb2/3)O-3-based relaxor ferroelectrics. *Journal of the American Ceramic Society.* **89**, 202–209 (2006).
11. N. Vittayakorn, S. Uttiya, G. Rujijanagul, and D. P. Cann, Dielectric and ferroelectric characteristics of 0.7PZT–0.3PZN ceramics substituted with Sr. *J. Phys. D: Appl. Phys.* **38**, 2942–2946 (2005).

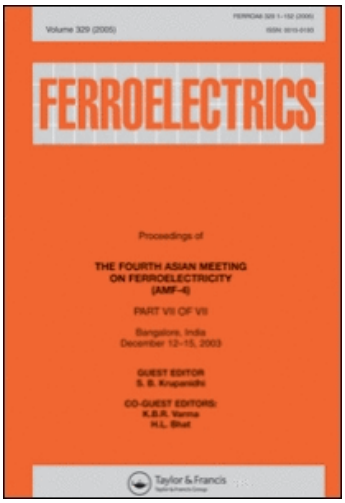

Ferroelectrics
Publication details, including instructions for authors and subscription information:
http://www.informaworld.com/smpp/title~content=t713617887

Effect of Annealing Time on Electrical and Mechanical Properties of $0.7(Pb(Zr_{1/2}Ti_{1/2})O_3) - 0.3(Pb(Zn_{1/2}Nb_{2/3})O_3$ Ceramics

G. Rujijanagul [a]; N. Vittayakorn [b]; S. Nabunmee [a]
[a] Department of Physics, Faculty of Science, Chiang Mai University, Thailand [b] Department of Chemistry, Faculty of Science, King Mongkut's Institute of Technology Ladkrabang, Bangkok, Thailand

Online Publication Date: 01 January 2009

To cite this Article Rujijanagul, G., Vittayakorn, N. and Nabunmee, S.(2009)'Effect of Annealing Time on Electrical and Mechanical Properties of $0.7(Pb(Zr_{1/2}Ti_{1/2})O_3) - 0.3(Pb(Zn_{1/2}Nb_{2/3})O_3$ Ceramics',Ferroelectrics,384:1,68 — 72
To link to this Article: DOI: 10.1080/00150190902892816
URL: http://dx.doi.org/10.1080/00150190902892816

Ferroelectrics, 384:68–72, 2009

ISSN: 0015-0193 print / 1563-5112 online
DOI: 10.1080/00150190902892816

Effect of Annealing Time on Electrical and Mechanical Properties of $0.7(Pb(Zr_{1/2}Ti_{1/2})O_3)$ – $0.3(Pb(Zn_{1/2}Nb_{2/3})O_3$ Ceramics

G. RUJIJANAGUL,[1,*] N. VITTAYAKORN,[2]
AND S. NABUNMEE[1]

[1]Department of Physics, Faculty of Science, Chiang Mai University, Thailand 50200
[2]Department of Chemistry, Faculty of Science, King Mongkut's Institute of Technology Ladkrabang, Bangkok 10520, Thailand

The solid solution between the normal ferroelectric and relaxor ferroelectric of $0.7(Pb(Zr_{1/2}Ti_{1/2})O_3) - 0.3(Pb(Zn_{1/2}Nb_{2/3})O_3$ was synthesized by the columbite method. After sintering, the ceramics were investigated as a function of annealing time. Properties of the ceramics were characterized by X-ray diffraction (XRD), scanning electron microscopy (SEM), dielectric spectroscopy, and hardness tester. The results indicated that dielectric constant of the annealed samples was enhanced. In addition, hardness values of the annealed samples were also improved.

Keywords Post-sintering annealing; dielectric constant; mechanical properties

Introduction

Lead zirconate titanate ($PbZr_{1-x}$ Ti_xO_3, PZT) is one of the most interesting perovskite ferroelectric which is host to exceptionally high dielectric and piezoelectric properties. The optimum electrical properties of PZT were reported for compositions close to the morphotropic phase boundary (MPB), i.e., $x = 0.48$ [1]. Therefore, most commercial ferroelectric ceramics are thus designed in the vicinity of the MPB with various doping schemes in order to achieve excellent properties. In order to improved the electric properties, PZT have been alloyed with several complex perovskite oxides such as $Pb(Fe_{1/2}\ Nb_{1/2})O_3$ (PFN) [2], $Pb(Mn_{1/2}\ Nb_{1/2})O_3$(PMN) [3], $Pb(Sc_{1/2}\ Nb_{1/2})O_3$ (PSN) [4], $Pb(Zn_{1/3}–Nb_{2/3})O_3$ (PZN) [5], and $Pb(Cd_{\ 1/3}\ Nb_{2/3})O_3$(PCN) [6]. Among these complex perovskite oxides, PZN was found to have an extremely high relative permittivities ∼60,000 (for single crystal).[7, 8, 9]. PZN exhibits a typical ferroelectric relaxor material with a diffuse phase transition temperature of 140°C [10]. Nanometer-level chemical heterogeneity in the form of short range order of Zn^{2+} and Nb^{5+} at B-sites was proposed to account for the observed diffuse phase transition [11, 12]. The crystal structure of PZN is rhombohedral at room temperature and transforms to cubic at high temperatures. Recent work has shown that ultrahigh piezoelectric and dielectric properties can be obtained in the binary system of

Received August 3, 2008; in final form December 31, 2008.
*Corresponding author. E-mail: rujijanagul@yahoo.com

0.7 ($Pb(Zr_{1/2}Ti_{1/2})O_3$) – 0.3 ($Pb(Zn_{1/2}Nb_{2/3})O_3$ (0.7PZT-0.3PZN[13]. Further, it is suggested that the properties of many binary systems can be improved by a thermal heat treatment [14]. In the present work 0.7PZT-0.3PZN ceramics were prepared by a columbite method. Effect of annealing time on electrical and mechanical properties of the sintered ceramics was investigated.

Experimental

The binary system solid solution of 0.7PZT-0.3PZN was synthesized by a columbite method. Reagent grade metal oxides (purity $\geq$ 98%) were used in the present work. The columbite precursor $ZnNb_2O_6$ was prepared from the reaction between ZnO and Nb_2O_5 at 975°C for 4 h. The wolframite precursor $ZrTiO_4$ was formed by reacting ZrO_2 with TiO_2 at 1400°C for 4 hours. The precursors $ZnNb_2O_6$, $ZrTiO_4$ were then mixed with PbO according to the stoichiometric ratio for the desired compositions. An excess of PbO equivalent to 2 mol% was also added to the mixed powder, to prevent PbO volatilization at high temperature. The mixed powders were calcined at temperatures ranging 900°C at a dwell time of 2 h in a double crucible configuration with a heating rate of 20°C/min. The calcined powders were isostatically cold pressed into pellets at a pressure of 100 MPa and then sintered at 1100–1300°C with a dwell time of 4 h. To determine the effect of thermal annealing, the maximum density sample was thermally annealed at 900°C in the same PbO atmosphere for various times up to 32 h. For dielectric measurement, the ceramic discs with diameter of 15 mm were polished into a thickness of 1 mm. The samples were coated with gold as electrodes for electrical contact. The dielectric properties were measured with an LCR meter utilizing an environmental chamber for the temperature measurements. The mechanical property of the samples was studied using a Vickers microhardness tester. Indentations were applied on the polished surfaces with loads in the range of 0.2–1.0 kg, and an indentation period of 15 s.

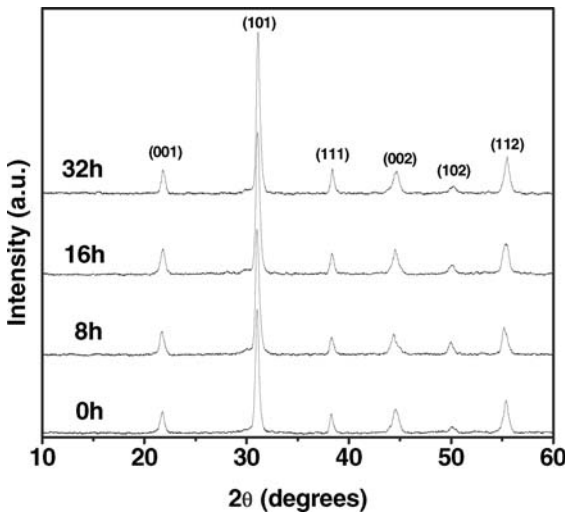

Figure 1. X-ray diffraction patterns of 0.7PZT-0.3PZN ceramics at various annealing times.

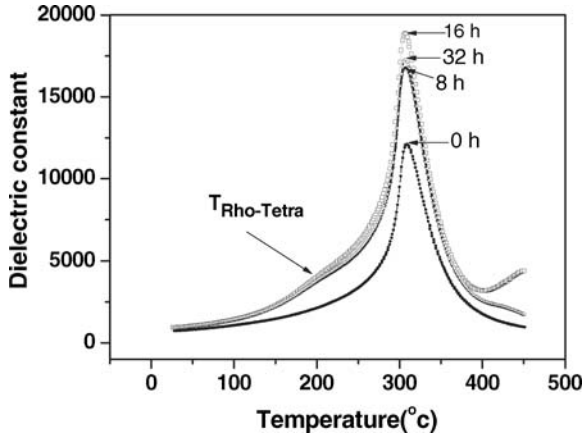

Figure 2. Temperature dependence of the dielectric constant at various annealing times for 0.7PZT-0.3PZN ceramics.

Results and Discussion

XRD patterns of as sintered and annealed samples as shown in Fig. 1, reveals that all samples have a perovskite structure. The XRD data was found to consist with rhombohedral symmetry, which is indicative of a ferroelectric phase.

The relationship between dielectric constant and temperature of the as sintered and the annealed samples are shown in Fig. 2. It is clearly seen that the annealing produced a thermally induced phase transitions. Clear shoulders at the rhombohedral to tetragonal phase transition temperature (T_{Rho}–T_{tetra}) ∼195–200°C were observed, indicates a decrease in the chemical heterogeneity of the annealed samples. The dielectric permittivity result also shows a significant improvement in the dielectric constant. However, limit of improvement was observed for the 16 h annealed sample because the longer annealing time results in a high PbO evaporation and produces defects in the samples.

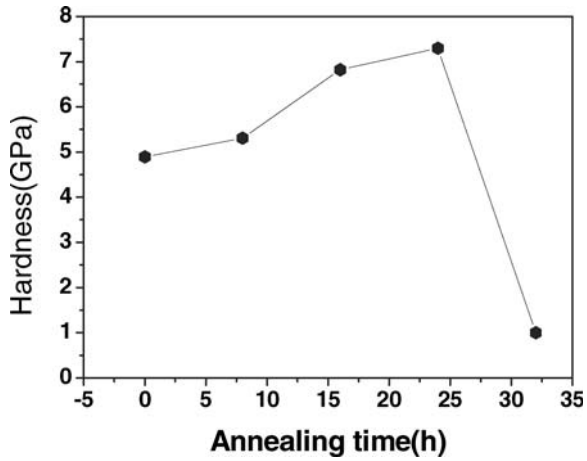

Figure 3. Vickers hardness as a function of annealing time for 0.7PZT-0.3PZN ceramics.

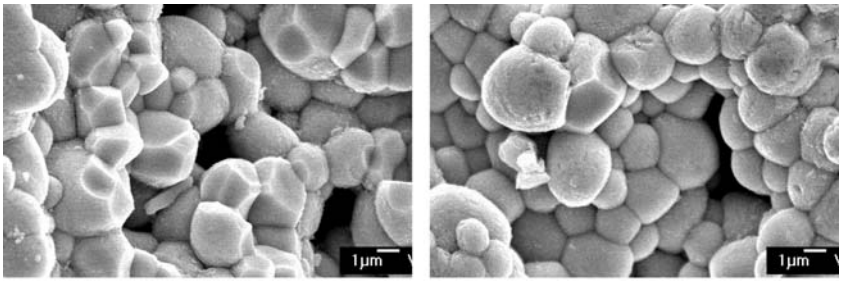

(a) (b)

Figure 4. SEM micrographs of 0.9PZT–0.1PZN ceramics before and after annealing: (a) as-sintered and (b) annealed at 900°C for 32 h.

Vickers hardness data in Fig. 3 indicates that annealing enhanced the hardness of the samples. The value of hardness was found to increase from 4.89 GPa for as sintered sample to 6.82 GPa for 16h annealed sample. However, a decrease harness value was found for the 32 h annealed sample. Scanning electron microscopy (SEM) images of the surfaces of the ceramics before annealing and after annealing for 32h are shown in Fig. 4. Compared with the as sintered sample, rounder grain shape was observed for the annealed samples. In addition, grain size of the samples was calculated to be around 2 μm (2.06–2.11 μm). This result indicates that grain size has not much influence on the trend of hardness.

For lead-based ferroelectric ceramics, many authors proposed that excess PbO has an influence on the electrical properties [14]. A liquid phase sintering is present due to low melting point of lead oxide. Thus, a small amount of excess PbO can be added to assist in the formation of the perovskite phase and for densification of the ceramic. In present work, an excess PbO was introduced into the samples. An overabundance of PbO may result in a low dielectric constant due to PbO enrichment of the grain boundary and the formation of a grain boundary layer. This layer has a low dielectric constant. Thus, thermal annealing is effective to ameliorate this effect and to increase the chemical homogeneity. However, a longer annealing time produces a loss of PbO and results a formation of defects. This made the 32 h annealed sample have a lower dielectric constant and hardness value.

Conclusions

The dielectric and mechanical properties of annealed 0.7PZT–0.3PZN ceramics formed via the columbite process were investigated. With an increase in the annealing time up to 16 h, the maximum dielectric constant increased. The clear phase transition for the rhombohedral to tetragonal phase was observed for the annealed samples, indicating a greater degree of homogeneity on the atomic scale. In addition, 16 h annealed sample showed the better mechanical property.

Acknowledgments

The authors would like to express their sincere thanks to financial support from the Thailand Research Fund, National Nanotechnology Center (NANOTEC), Faculty of Science and Graduate school, Chiang Mai University and Commission on Higher Education (CHE)

Thailand. We would also like to thank Prof. Dr. Tawee Tunkasiri for his help in many facilities.

References

1. A. J. Moulson and J. M. Herbert, Electroceramics: Materials, Properties, Appications. New York: Chapman and Hall; 1990.
2. Y. Yoshikawa, Microstructural characterizations of ferroelectromagnet lead iron niobate crystals. *J. Eur. Ceram. Soc.* **19**, 1037–1041 (1999).
3. Y. Yamashita and N. Ichinose, Can relaxor piezoelectric materials outperform PZT?. *Proc. IEEE ISAF.* **96**, 71–77 (1996).
4. V. A. Isupov, *Sov. Phys. Solid State* **136**, 5 (1958).
5. N. Vittayakorn, G. Rujijanagul, X. Tan, and D. P. Cann, Influence of processing conditions on the phase transition and ferroelectric properties of $Pb(Zn_{1/3}Nb_{2/3})O_3-Pb(Zr_{1/2}Ti_{1/2})O_3$ ceramics. *Mat. Sci. Eng. B* **108**, 258–265 (2004).
6. N. Ichinose, T. Takahashi, and Y. Tokomizo, Crystal growth of $Pb(Cd_{1/3}Nb_{2/3})O_3$ and its dielectric properties. *J. Phys. Soc. Jpn.* **31**, 1848 (1971).
7. K. Uchino, High electromechanical coupling piezoelectrics: relaxor and normal ferroelectric solid solutions. *Solid State Ionics* **108**, 43–52 (1998).
8. J. Kuwata, K. Uchino, and S. Nomura, Phase transitions in the Pb $(Zn_{1/3}Nb_{2/3})O_3$-$PbTiO_3$ system. *Ferroelectrics* **37**, 579–582 (1981).
9. M. L. Mulvihill, L. E. Cross, W. Cao, and K. Uchino, Domain-related phase transitionlike behavior in lead zinc niobate relaxor ferroelectric single crystals. *J. Am. Ceram. Soc.* **80**, 1462–1468 (1997).
10. G. A. Smolenskii and A. L. Agranovskaya, *Sov. Phys.-Tech. Phys.* 1380 (1958).
11. C. A. Randall, A. S. Bhalla, T. R. Shrout, and L. E. Cross, Classification and consequences of complex lead perovskite ferroelectrics with regard to B-site cation order. *J. Mater. Res.* **5**, 829–834 (1990).
12. C. A. Randall, A. S. Bhalla, T. R. Shrout, and L. E. Cross, Relationship between B-site order and properties in $Pb(B'B'')O_3$ perovskites. *Ferroelectrics* **11**, 103–106 (1990).
13. N. Vittayakorn, G. Rujijanagul, X. Tan, H. He, M. A. Marquardt, and D. P. Cann, Dielectric properties and morphotropic phase boundaries in the $xPb(Zn_{1/3}Nb_{2/3})O_3-(1-x)Pb(Zr_{0.5}Ti_{0.5})O_3$ pseudo-binary system. *J. Electroceram.* **16**, 141–149 (2006).
14. F. Xia and X. Yao, The role of PbO content on the dielectric and piezoelectric properties of PZN-based ceramics. *J. Mater. Sci.* **36**, 247–253 (2001).

Journal of Alloys and Compounds 486 (2009) 689–692

Contents lists available at ScienceDirect

Journal of Alloys and Compounds

journal homepage: www.elsevier.com/locate/jallcom

A simple route to synthesize new binary cobalt iron cyclotetraphosphate $CoFeP_4O_{12}$ using aqueous and acetone media

Banjong Boonchom[a,b,*], Montree Thongkam[c], Samart Kongtaweelert[c], Naratip Vittayakorn[b,d]

[a] King Mongkut's Institute of Technology Ladkrabang, Chumphon Campus, 17/1 M. 6 Pha Thiew District, Chumphon 86160, Thailand
[b] Advanced Materials Science Research Unit, Department of Chemistry, Faculty of Science, King Mongkut's Institute of Technology Ladkrabang, Bangkok 10520, Thailand
[c] Department of Chemistry, Faculty of Science, King Mongkut's Institute of Technology Ladkrabang, Ladkrabang, Bangkok 10520, Thailand
[d] College of KMITL Nanotechnology, King Mongkut's Institute of Technology Ladkrabang, Bangkok 10520, Thailand

ARTICLE INFO

Article history:
Received 30 May 2009
Received in revised form 6 July 2009
Accepted 7 July 2009
Available online 15 July 2009

Keywords:
$CoFeP_4O_{12}$
New binary cobalt iron cyclotetraphosphate
Solid state synthesis
Water–acetone media

ABSTRACT

A new binary cobalt iron cyclotetraphosphate, $CoFeP_4O_{12}$ was synthesized through solid phase reaction using cobalt carbonate, iron metal and phosphoric acid in the presence of water–acetone media with further calcinations at the temperature of 500 °C. The particle size obtained from X-ray line broadening is 65 ± 24 nm for the $CoFeP_4O_{12}$. FTIR spectrum of $CoFeP_4O_{12}$ is assigned based on the $P_4O_{12}^{4-}$ ion in the structure. The SEM micrograph of the synthesized $CoFeP_4O_{12}$ shows non-uniform microparticle, which is important for specific application. Room temperature magnetization result shows superparamagnetic behavior of the $CoFeP_4O_{12}$ powder, having no hysteresis loop in the range of ±10,000 Oe with the specific magnetization value of 14.243 emu/g. The XRD and FTIR results of the synthesized $CoFeP_4O_{12}$ appear to be very similar to that of $M_2P_4O_{12}$ (M = Co and Fe), which indicates the monoclinic phase with space group *C*2/*c*.

1. Introduction

The cyclotetraphosphates of some bivalent metals are relatively stable compounds, both thermally and chemically [1–3]. They exhibit properties of colour, anticorrosion ability and luminescence, which allow their application as special inorganic pigments [4,5]. Additionally, these compounds are valuable phosphorus (P) and micronutrient (Ca, Mg, Fe, Mn, Co, Ni) fertilizers due to their solubility in soils. The new cyclotetraphosphates of some binary divalent metals have been prepared in our laboratory and examined for many potential applications [1–3]. This work is of interest because it appears economically advantageous to substitute a portion of the divalent metal with a less costly divalent element that could also improve, in many cases, potential pigments, selective catalysts, phosphors, materials for corrosion-resistant coatings and biocompatible and biodegradable in tissue [1–3]. Such a suitable element, from our experiences, is iron, which alone does give both a cyclotetraphosphate and polyphosphate [1–5]. In addition, the binary cobalt iron cyclotetraphosphate has not been described in the literature. Consequently, it is pertinent to synthesize binary cyclotetraphosphate and its solid solution. By varying the composition of the solid solution (within its homogeneity range), one can change its useful properties. So far, other binary cyclotetraphosphates ($M_{2-x}A_xP_4O_{12}$; M and A = Mg, Ca, Mn, Co, Ni, Zn, or Cu; x = 0–2) have been synthesized by the mixture of corresponding metal cyclotetraphosphates, and then were melted together on platinum dishes in an electric furnace at high temperature (>700 °C) and long time consumption (>5 h) [5–8].

In this work, we report for the first time the synthesis of a new binary cobalt iron cyclotetraphosphate, $CoFeP_4O_{12}$ by solid state route from cobalt carbonate, iron metal and phosphoric acid in water–acetone medium. The presence of acetone reduced hot reaction and prevented the evolved H_2(g) and CO_2(g) in the precipitation process. This method is a simple, rapid, cost-effective and environmental friendly route for synthesis of $CoFeP_4O_{12}$. The synthesized sample was characterized by X-ray powder diffraction (XRD), Fourier transform infrared (FTIR), scanning electron microscope (SEM) and a vibrating sample magnetometer (VSM) techniques.

2. Experimental

In this study, $CoCO_3$ (99.99%, Merck), Fe (c; complexometric) (99.99%, Fluka), H_3PO_4 (86.4%, w/w, Merck) and acetone (99.99%, Merck) were used as starting materials. The synthetic method of $CoFeP_4O_{12}$ involves a two-step process (1–2). Beginning procedure (1), 10 mL of acetone was added to 1.1893 g of $CoCO_3$ and 0.5584 g of Fe(c) (a mole ratio corresponding to the nominal composition of Fe:Co ratio of 1.0:1.0) and this suspension referred to as suspension A. Then 5 mL of 70% H_3PO_4 (86.4%, w/w H_3PO_4 dissolved in DI water) was added to suspension A. The resulting suspension was continuously stirred at ambient temperature (10 min) and

* Corresponding author at: King Mongkut's Institute of Technology Ladkrabang, Chumphon Campus, 17/1 M. 6 Pha Thiew District, Chumphon 86160, Thailand. Tel.: +66 7750 6422x4565; fax: +66 7750 6410.
E-mail addresses: kbbanjon@kmitl.ac.th, kbbanjon@gmail.com (B. Boonchom).

0925-8388/$ – see front matter © 2009 Elsevier B.V. All rights reserved.
doi:10.1016/j.jallcom.2009.07.036

the precipitate was obtained. The prepared solid was filtered by suction pump, washed with acetone and dried in air. Final step (2), the prepared solid was heated in the furnace at 500 °C for 3 h and its final product, $CoFeP_4O_{12}$ was obtained and further investigated. The obtained compound ($CoFeP_4O_{12}$) is significantly different from that prepared from $CoCO_3$–Fe(c)–H_3PO_4 ($CoFeP_2O_7$) with water–methanol system in our previous work [9].

$$\tfrac{1}{2}CoCO_3 + \tfrac{1}{2}Fe + 2H_3PO_4 \xrightarrow{\text{acetone room temperature}} Co_{0.5}Fe_{0.5}(H_2PO_4)_2 + \tfrac{1}{2}H_2O + \tfrac{1}{2}CO_2 + \tfrac{1}{2}H_2 \quad (1)$$

$$Co_{0.5}Fe_{0.5}(H_2PO_4)_2 \xrightarrow{500\,^\circ C} \tfrac{1}{2}CoFeP_4O_{12} + 2H_2O \quad (2)$$

The cobalt and iron contents of $CoFeP_4O_{12}$ were determined by dissolving in 0.0126 M hydrochloric acid using atomic absorption spectrophotometry (AAS, PerkinElmer, Analyst100). The phosphorus content was determined by colorimetric analysis of the molybdophosphate complex. The room temperature FTIR spectrum was recorded in the range of 4000–370 cm^{-1} with 8 scans on a Perkin-Elmer Spectrum GX FTIR/FT-Raman spectrometer with the resolution of 4 cm^{-1} using KBr pellets (KBr, spectroscopy grade, Merck). The structure and crystallite size of the synthesized sample were studied by an X-ray powder diffraction using a X-ray diffractometer (Phillips PW3040, The Netherlands) with Cu Kα radiation (λ = 0.15406 nm). The Scherrer method was used to evaluate the crystallite size [10]. The morphology of the prepared sample was examined with scanning electron microscope using LEO SEM VP1450 after gold coating. The magnetic property of the $CoFeP_4O_{12}$ was examined at room temperature (20 °C) using a vibrating sample magnetometer (VSM 7403, Lake Shore, USA).

3. Results and discussion

3.1. Chemical analysis

The chemical analysis of the synthesized $CoFeP_4O_{12}$ gives 15.83 wt% Co_{total}, 14.92 wt% Fe_{total} and 33.20 wt% P_{total}, suggesting the molar ratio Co_{total}:Fe_{total}:P_{total} = 1.00:0.99:3.99. This indicates that the general formula would be $CoFeP_4O_{12}$.

3.2. FTIR spectroscopy

The FTIR spectrum of the calcined product $CoFeP_4O_{12}$ is shown in Fig. 1, which is very similar to those exhibited in $M_2P_4O_{12}$ (M = Mn, Co, Fe) [1–3]. The vibrational modes of $P_4O_{12}{}^{4-}$ ion observed in the frequency range of 370–1400 cm^{-1} are assigned according to the literature [4]. The anion contains the $PO_2{}^{2-}$ radical and the P–O–P bride, which are interpreted the FTIR spectra from viewpoint of the vibrations of these two groups. As the P–O bond strength in the P–O–P bride is weaker than in the $PO_2{}^{2-}$ radical, the stretching frequencies of the P–O–P bride are expected to be lower than those in the $PO_2{}^{2-}$ radical. The asymmetric and symmetric stretching frequencies of the $PO_2{}^{2-}$ radical are generally observed in the areas 1350–1220 and 1150–1100 cm^{-1}, respectively.

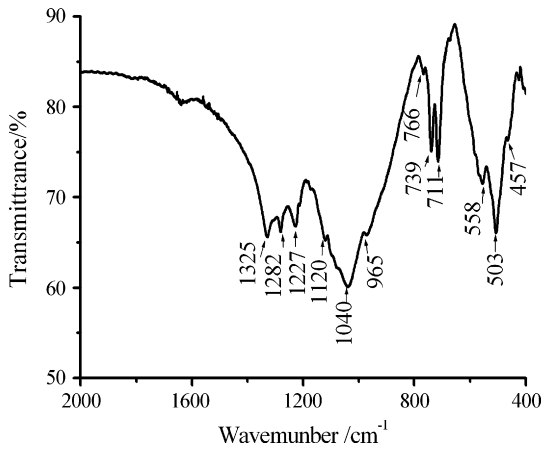

Fig. 1. FTIR spectrum of $CoFeP_4O_{12}$.

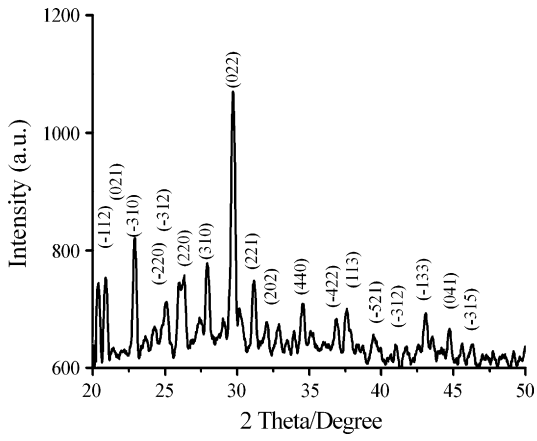

Fig. 2. XRD pattern of $CoFeP_4O_{12}$.

The P–O–P bride has its asymmetric and symmetric stretching frequencies around 1000–900 and 900–700 cm^{-1}, respectively. The bending modes are expected in the area 600–400 cm^{-1} ($PO_2{}^{2-}$ radical) and 400–370 cm^{-1} (P–O–P bride). The metal–O stretching usually appears in the bending mode region as the bending modes of the P–O–P bride and absorption bands associated with these vibrations are usually very weak. The observation of a strong ν_sPOP band is known to be the most striking feature of cyclotetraphosphate spectra, along with the presence of the $\nu_{as}OPO^-$ band. From X-ray diffraction data [11], it was shown that the crystal structure is monoclinic (space group *C*2/*c*) with a cyclic structure of the $[P_4O_{12}]^{4-}$ anion. This has been confirmed by the FTIR measurements. On the basis of above results, the FTIR spectrum of $CoFeP_4O_{12}$ is similar to those obtained from other binary $M_{1-x}A_xP_4O_{12}$ (M and A = Mg, Ca, Mn, Fe, Co; *x* = 0–1) and individual $M_2P_4O_{12}$ [1–4], which confirm their isostructural properties.

3.3. X-ray powder diffraction

The XRD pattern of $CoFeP_4O_{12}$ is similar to those obtained from the individual $M_2P_4O_{12}$ (when M = Co and Fe) in our previous works [1–3], but the intensities are slightly different (Fig. 2). In the systems of binary cobalt iron solid solutions (or cobalt iron cyclotetraphosphate), the electric charges of cations are equivalent, and the radii of cations are close to each other, so the spectrum peaks are quite similar. On the basis of above analysis, we can draw a conclusion that the synthesized $CoFeP_4O_{12}$ is solid solution and not a mixture of the individual ones. These results indicate that the binary $M_{1-x}A_xP_4O_{12}$ and the single metal $M_2P_4O_{12}$ (M = Mg, Mn, Co, Ni, Fe, Zn) types are isostructural. All the detectable peaks can be distinctly indexed as a pure monoclinic phase with space group *C*2/*c* (*Z* = 4) for $CoFeP_4O_{12}$, which note to be similar to those of the standard XRD data (PDF no. 842208 for $Co_2P_4O_{12}$ and PDF no. 782285 for $Fe_2P_4O_{12}$). The average crystallite size and lattice parameter of $CoFeP_4O_{12}$ were calculated from XRD patterns and also tabulated in Table 1. Additionally, the lattice parameters of the $CoFeP_4O_{12}$ are comparable to those of the standard data ($Co_2P_4O_{12}$ (PDF no. 842208) and $Fe_2P_4O_{12}$ (PDF no. 782285)) and the prepared single metal compounds in our previous works [1,2]. However, the crystallite size for the studied binary compound in this work is larger than those from the single metal compounds (40 ± 10 nm for $Co_2P_4O_{12}$ and 29 ± 6 nm for $Fe_2P_4O_{12}$) in our previous works [1–3].

3.4. Scanning electron microscopy

The SEM micrograph of $CoFeP_4O_{12}$ is shown in Fig. 3. The particle shape and size are changed throughout the whole decomposition

Table 1
Average particle size and lattice parameters of $CoFeP_4O_{12}$ calculated from XRD data.

Compounds	Systems	*a* (Å)	*b* (Å)	*c* (Å)	*β* (°)	Average crystallite size (nm)
$Co_2P_4O_{12}$	PDF no. 842208	11.8	8.28	9.92	118.72	–
	Ref. [2]	11.83(8)	8.22(6)	9.94(0)	118.51(1)	40 ± 10
$CoFeP_4O_{12}$	This work	11.69(3)	8.41(5)	9.77(2)	118.13(2)	65 ± 24
$Fe_2P_4O_{12}$	PDF no. 782285	11.94	8.37	9.93	118.74	
	Ref. [1]	12.80(0)	8.80(4)	10.56(0)	118.67(4)	29 ± 6

product. The morphology of $CoFeP_4O_{12}$ shows a high agglomerate of non-uniform particles, which is not similar to those of $M_2P_4O_{12}$ (M = Co or Fe) (Fig. 4b) in our previous works [1–3]. The highly agglomerate of $CoFeP_4O_{12}$ powder is possibly caused by the process of dissolution and a rapid co-precipitation as well as the decomposition process, subsequently. The different morphologies between of the single metal compounds ($M_2P_4O_{12}$, M = Co or Fe) and the binary $CoFeP_4O_{12}$ indicate the presence of Co ions in substitution position of Fe ions, which confirm the formation of new binary cobalt iron cyclotetraphosphate $CoFeP_4O_{12}$. The result of SEM experiment indicates that the grain sizes of $CoFeP_4O_{12}$ are not consistent with the crystallite sizes in the XRD analysis because the exact particle nucleation and growth mechanisms are caused.

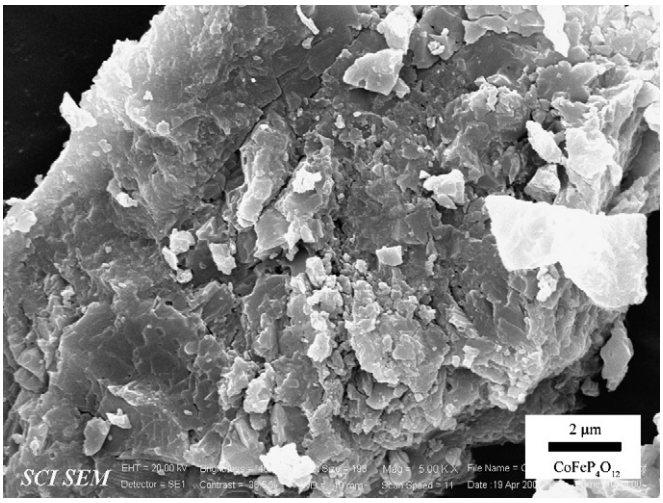

Fig. 3. SEM micrograph of $CoFeP_4O_{12}$.

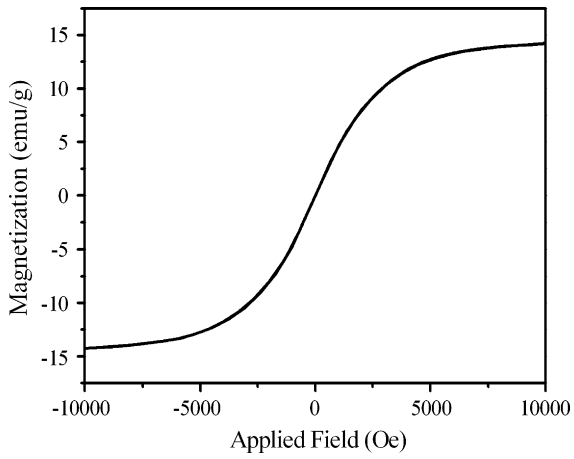

Fig. 4. The specific magnetization of $CoFeP_4O_{12}$ as a function of field, measured at 20 °C.

3.5. VSM magnetometer

The specific magnetization curve of $CoFeP_4O_{12}$ powder obtained from room temperature VSM measurement is shown in Fig. 4. This curve is typical superparamagnetic behavior without any hysteresis in the field range of ±10,000 Oe. Specific saturated magnetization (M_s) value of 14.243 emu/g was observed for the $CoFeP_4O_{12}$ powder. The result is lower than the saturated magnetization for Fe_3O_4 nanoparticles (in a range of 30–50 emu/g) [12,13]. It is seen that magnetization of the $CoFeP_4O_{12}$ is lower than that of $Fe_2P_4O_{12}$ (85.01 emu/g) but markedly distinct from the diamagnetic properties of $Co_2P_4O_{12}$ [2,3]. This result indicates that the presence of Co ions in substitution position of Fe ions has the strong effect on the magnetic behavior of $CoFeP_4O_{12}$. To our knowledge, it is worth nothing that superparamagnetic property of the $CoFeP_4O_{12}$ sample is reported for the first time in this study.

4. Conclusions

A single monoclinic phase of a new binary $CoFeP_4O_{12}$ was successfully synthesized by solid state route from cobalt carbonate, iron metal and phosphoric acid in the presence of water–acetone media. FTIR, XRD, SEM and VSM results suggested the formation of a new binary $CoFeP_4O_{12}$. The morphology of $CoFeP_4O_{12}$ shows a high agglomerate of non-uniform particles. The synthesized powder is polycrystalline, having crystallite size of 65 ± 24 nm for $CoFeP_4O_{12}$, as estimated by XRD. The synthesized $CoFeP_4O_{12}$ is superparamagnetic behavior, having no hysteresis loop in the range of $-10{,}000\ \text{Oe} < H < 10{,}000\ \text{Oe}$ with the specific magnetization of 14.243 emu/g at 10 kOe. This work presents the simple, cost-effective, rapid time consumption and environmental friendly synthetic method for the precipitation of $CoFeP_4O_{12}$. The new binary $CoFeP_4O_{12}$ powder may be useful for potential applications as super phosphate and micronutrient fertilizers, inorganic ceramic pigments and corrosion-proof compositions.

Acknowledgements

This work is financially supported by the Thailand Research Fund (TRF), the Commission on Higher Education (CHE): Research Grant for New Scholar and the National Nanotechnology Center (NANOTEC) NSTDA, Ministry of Science and Technology, Thailand.

Appendix A. Supplementary data

Supplementary data associated with this article can be found, in the online version, at doi:10.1016/j.jallcom.2009.07.036.

References

[1] B. Boonchom, C. Danvirutai, S. Youngme, S. Maensiri, Ind. Eng. Chem. Res. 47 (2008) 7642.
[2] B. Boonchom, C. Danvirutai, J. Chem. Eng. Data 54 (2009) 1225, and reference therein.
[3] B. Boonchom, S. Youngme, C. Danvirutai, Solid State Sci. 10 (2008) 129.
[4] V. Koleva, H. Effenberger, J. Solid State Chem. 180 (2007) 956, and reference therein.

[5] O.A. Lukyanchenko, V.V. Samuskevich, Thermochim. Acta 327 (1999) 181, and reference therein.
[6] M. Trojan, D. Brandová, Z. Šolc, Thermochim. Acta 110 (1987) 343, and reference therein.
[7] M. Trojan, D. Brandová, Z. Šolc, Thermochim. Acta 85 (1985) 99, and reference therein.
[8] B. Boonchom, S. Maensiri, S. Youngme, C. Danvirutai, Solid State Sci. 11 (2009) 485, and reference therein.
[9] B. Boonchom, N. Phuvongphu, Mater. Lett. 63 (2009) 1709.
[10] B.D. Cullity, Elements of X-ray Diffraction, 2nd ed., Addison–Wesley Publishing, 1977.
[11] W. Gunsser, D. Fruehauf, K. Rohwer, A. Zimmermann, A. Wiedenmann, J. Solid State Chem. 82 (1989) 43.
[12] E.H. Soumhi, I. Saadoune, A. Driss, J. Solid State Chem. 156 (2001) 364.
[13] A.K. Gupta, M. Gupta, Biomaterials 26 (2005) 3995.

Functional Materials Letters
Vol. 2, No. 4 (2009) 169–174

THE STRUCTURAL PHASE AND MICROSTRUCTURES OF PEROVSKITE $Ba(Ti_{1-x}Zr_x)O_3$ CERAMICS USING THE COMBUSTION ROUTE

NALINEE PHUNGJITT
Department of Physics, Faculty of Science
Uttaradit Rajabhat University, Uttaradit 53000, Thailand

PERAPONG PANYA and THEERACHAI BONGKARN*
Department of Physics, Faculty of Science
Naresuan University, Phitsanulok 65000, Thailand
**researchcmu@yahoo.com*

NARATIP VITTAYAKORN
Department of Chemistry, Faculty of Science
King Mongkut's Institute of Technology, Ladkrabang
Bangkok 10520, Thailand

Received 13 July 2009; Revised 17 October 2009

$Ba(Ti_{1-x}Zr_x)O_3$; BTZ ($x = 0.20$ and 0.25) ceramics are attractive candidates for dynamic random access memories, tunable microwave devices and capacitors. In this study, the preparation of BTZ powders and ceramics fabricated by the combustion method were studied in detail. The calcination and sintering conditions were performed from 600 to 900°C for 4 h and from 1300 to 1450°C for 2 h, respectively. The highest percentage of the cubic perovskite phase was found in the powders that were calcined at 800°C. A pure cubic perovskite structure was found in all ceramic samples. The average grain size increased with increasing sintering temperatures. Dielectric constant-temperature plots showed a maximum peak value of 7500 and 8300 for $x = 0.20$ and 0.25. The phase transition temperature of the BTZ ceramics occurred at 30°C and 10°C for $x = 20$ and 25, respectively.

Keywords: Ferroelectric perovskite; structural phase; barium titanate zirconate; dielectric constant.

Barium titanate zirconate ($Ba(Ti_{1-x}Zr_x)O_3$; BTZ) perovskite is a well known ferroelectric perovskite ceramic, because of its high dielectric constant, low dielectric loss, and large tunability, making it suitable for dynamic random access memories, tunable microwave devices and capacitors.[1] Brajer and Kulscar reported that, as the zirconium content increases, the orthorhombic–tetragonal phase transition temperature increases and the tetragonal–cubic phase transition temperature decreases but the rhombohedral–orthorhombic phase transition temperature remains the same.[2,3] At a Zr/Ti ratio greater than 0.10, the three dielectric constant peaks coalesce into a single broad maximum.[4] Moreover, the transition temperature of BTZ shifts to a lower temperature range with the increase of the Zr content. The dielectric study of the BTZ ceramics with $x = 0.20$ (BTZ20) and 0.25 (BTZ25) showed high tunability, a high value of figure of merit (FOM) and a normal ferroelectric with a weak diffuse phase transition behavior. These make the BTZ20 and BTZ25 ceramics promising materials for tunable capacitor applications.[5]

The conventional synthetic methods for making $Ba(Ti_{1-x}Zr_x)O_3$ include: the solid-state reaction route, the sol–gel process, and the hydrothermal technique.[6–8] The solid state reaction route shows that the calcined powders often contain large and inhomogeneous particles.[6] On the other hand, the chemical route is a costly and complicated process.[7,8] Recently, many authors have reported that the combustion route is particularly useful in the production of ultrafine ceramic powders with a small average particle size.[9] It is also a simple method with the advantage of using inexpensive precursors and highly reactive powders.[10,11] However, no researcher has reported the preparation of $Ba(Ti_{1-x}Zr_x)O_3$ ($x = 0.20$ and 0.25) by the combustion route and no one has

*Corresponding Author.

shown the results of firing conditions on phase formation and the microstructure of BTZ20 and BTZ25. Therefore, in the present work, the effects of firing temperatures on phase formation and the microstructure of BTZ20 and BTZ25 ceramics prepared via the combustion route were studied. The dielectric constant was also observed.

Barium titanate zirconate powder was synthesized by the combustion route. Mixtures of $BaCO_3$, TiO_2 and ZrO_2 powders were milled (zirconia milling media under ethanol for 24 h). Drying was carried out at 120°C for 4 h. After sieving, the powders and urea were mixed in an agate mortar. Then, the mixture was calcined at various calcination temperatures, ranging from 600 to 900 °C, with a dwell time of 4 h. The calcined powders were pressed into disks with a diameter of 15 mm at a pressure of 40 MPa. The pellets were sintered from 1300 to 1450 °C, for 2 h. X-ray diffraction was employed to identify phase formation and the optimum temperature for preparing BTZ powders and ceramics. Calcined powders and sintered ceramics morphologies were imaged using scanning electron microscopy (SEM). The morphologies of calcined powders were studied by transmission electron microscopy (TEM). The average particle size was computed from Full Width at Half Maximum (FWHM) using the Scherrer formula. Densities of sintered ceramics were measured by the Archimedes method and the average grain size was determined by using the mean linear intercept method. The capacitance was measured with a LCR meter. The dielectric constant (ε_r) was calculated using the geometric area and thickness of the discs.

The XRD patterns of the BTZ powder with $x = 0.25$ (BTZ25), calcined at various temperatures (600–900°C), are shown in Fig. 1(a). The XRD patterns could be indexed in the cubic perovskite structure and matched with JCPDS file no. 36-0019.[12] The second phase, such as $BaCO_3$, ZrO_2 and $BaTiO_3$, were found in all samples. The XRD results of the BTZ20 powders were similar with the BTZ25 powders. The highest percent perovskite phase of BTZ20 and BTZ25 were 96% and 85% obtained from powder calcined at 800°C. The particle size computed from the XRD peaks are demonstrated in Fig. 2. The nano-size of the particles was increased with the increasing of calcination temperatures.

The SEM images of BTZ20 and BTZ25 powders are shown in Fig. 3. It is clearly seen that the powders have a spongy appearance, forming agglomerates of fine particles of different shapes. When the calcination temperatures increased, the porosity of the powders decreased. These results were similar with previous research.[13]

The TEM microphotographs of BTZ25 powder are shown in Fig. 4. The average agglomerate size of the as-calcined powders was evaluated at about 220 nm by analyzing

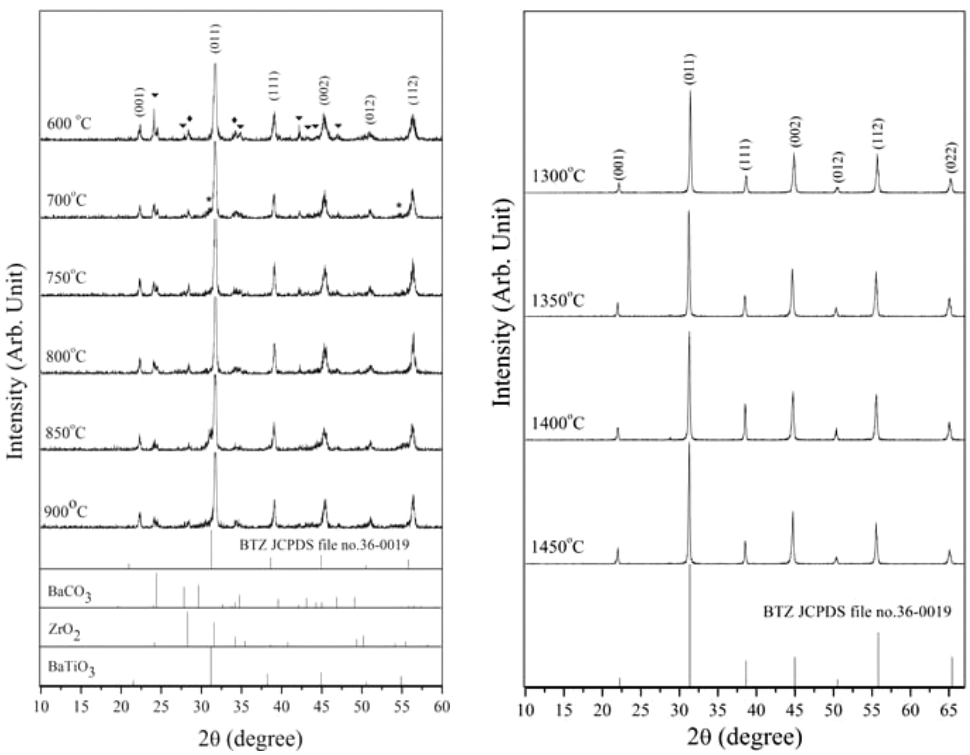

Fig. 1. XRD patterns of BTZ25 samples; (a) powders calcined at different temperatures; (▼) $BaCO_3$, (♦) ZrO_2 and (*) $BaTiO_3$; (b) ceramics sintered at different temperatures.

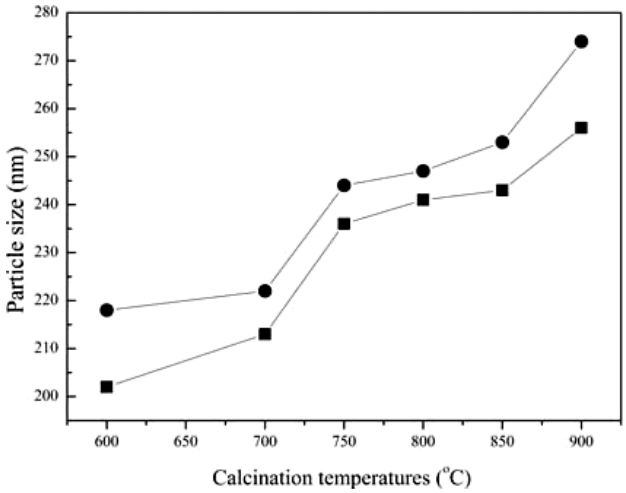

Fig. 2. The particle size of BTZ powders calcined at various temperatures; (■) BTZ20 and (●) BTZ25.

more than 300 particles observed by TEM in a low magnification (Fig. 4(a)). The details of the aggregated particles are seen in a high magnification image in Fig. 4(b). It can be seen that many fine primary particles with size from 30 to 50 nm combined to form large secondary ones. Such an appearance is consistent with SEM images. The particle size calculated from the XRD peaks was similar with the agglomerate size but higher than ∼ 5–8 times of the particle sizes obtained from TEM images. This indicated that the agglomeration affects the XRD results.

The powder calcined at 800°C was sintered at different sintering temperatures (1300–1450°C). Figure 1(b) shows the XRD traces of BTZ25 ceramics. The XRD results have a major peak at (011) and demonstrate a pure cubic perovskite structure in all samples. As the sintering temperatures increased, the lattice *a* axis was increased (Table 1). The XRD results of BTZ20 ceramics were similar to BTZ25 ceramics.

Figure 5 shows the morphological evolution of BTZ20 and BTZ25 ceramics as a function of sintering temperatures. The average grain sizes increased from 2.8 to 43.1 μm for BTZ20 and 2.4 to 41.7 μm for BTZ25 with the increase of sintering temperatures from 1300 to 1450°C (Table 1). The results also showed clear grain boundaries and it is evident that the combustion route could be used for producing good BTZ ceramics. The density of BTZ pellets increased when the sintering temperatures increased up to 1400°C then decreased with higher sintering temperatures. The densest of the BTZ20 and BTZ25 pellets were 95 and 96% from samples sintered at 1400°C (Table 1).

Figure 6 shows the temperature dependence of the dielectric constant of BTZ20 and BTZ25 pellets. The dielectric

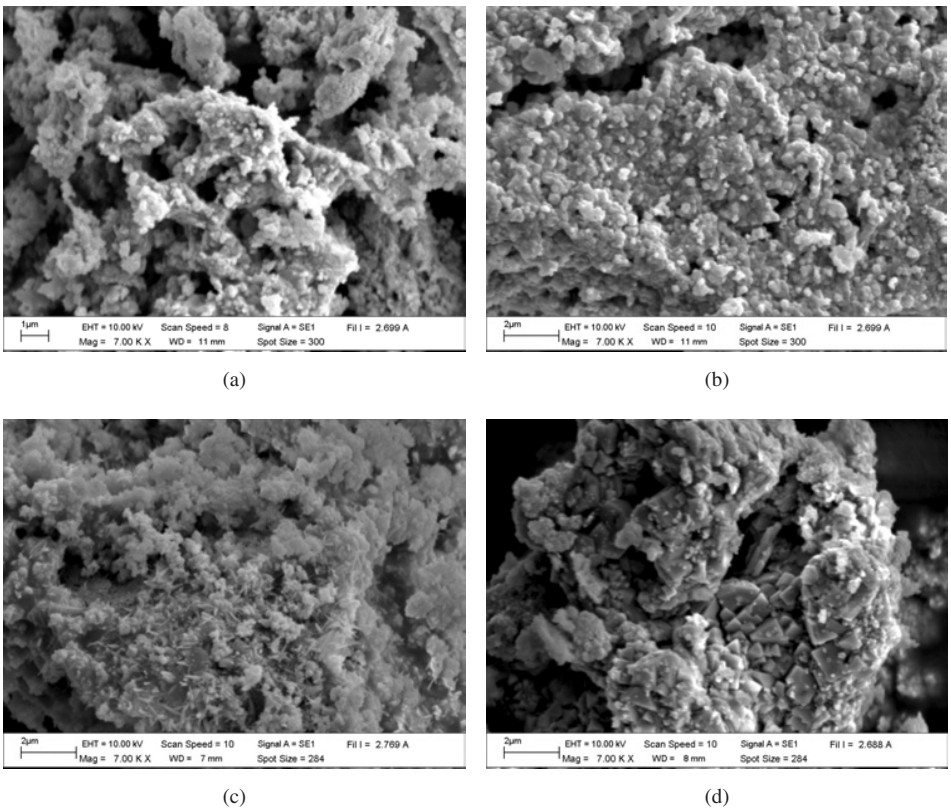

Fig. 3. SEM photographs of BTZ powders; (a) BTZ20 calcined at 600°C, (b) BTZ20 calcined at 900°C, (c) BTZ25 calcined at 600°C and (d) BTZ25 calcined at 900°C.

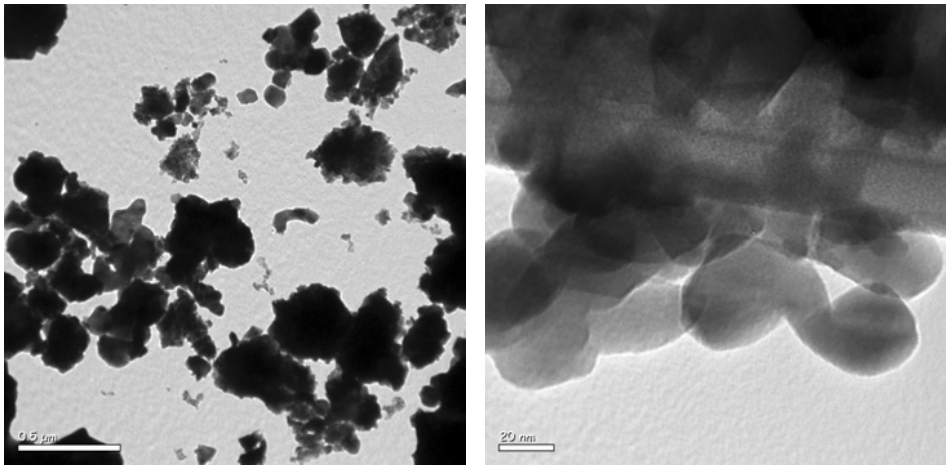

(a) (b)

Fig. 4. TEM microphotographs of BTZ25 powder calcined at 800°C; (a) low magnification and (b) high magnification.

Table 1. The lattice parameter a, grain size, density and maximum dielectric constant of BTZ ceramics.

Sintering temperatures (°C)	Lattice parameter a (Å)		Grain size (μm)		Density (g/cm^3)		Maximum dielectric constant	
	BTZ20	BTZ25	BTZ20	BTZ25	BTZ20	BTZ25	BTZ20	BTZ25
1300	4.0362	4.0361	2.8	2.4	5.57	5.64	5300	5900
1350	4.0409	4.0399	21.1	26.1	5.58	5.67	6100	7100
1400	4.0416	4.0449	38.3	37.9	5.61	5.76	7500	8300
1450	4.0427	4.0459	43.1	41.7	5.57	5.63	6500	7000

constant curve of BTZ25 is broader than the dielectric constant curves of BTZ20, which can be attributed to the diffuse nature of the ferroelectric to the paraelectric phase transition in the higher Zr content sample. This confirmed that the broadness increased when the Zr ion content increased.[4] The Curie temperature is found at about 30°C and 10°C for BTZ20 and BTZ25 respectively. The maximum dielectric constant ($\varepsilon_{r,\max}$) of the BTZ20 and BTZ25 ceramics were 7500 and 8300 and appeared from a sample sintered at 1400°C (Table 1). The dielectric constant corresponded with the density of the sintered pellets. The maximum dielectric constant of $Ba(Ti_{0.75}Zr_{0.25})O_3$ prepared via the solid state reaction route was found to be about 5600 in a sample sintered at 1350°C.[14] The dielectric loss at room temperature of BTZ25 prepared by the solid state reaction[15] and the combustion technique was 0.012 and 0.030, respectively. Although the dielectric loss in this study was higher than the solid state reaction method, it is still in the range for commercial applications. This indicated

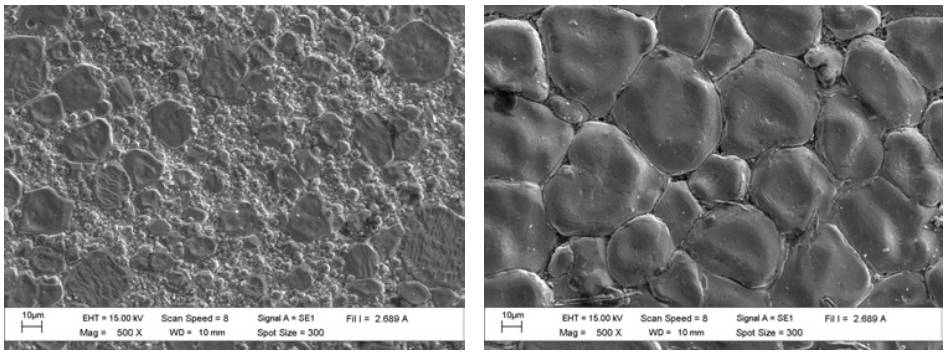

(a) (b)

Fig. 5. SEM photographs of BTZ ceramics; (a) BTZ20 sintered at 1300°C, (b) BTZ20 sintered at 1400°C, (c) BTZ25 sintered at 1300°C and (d) BTZ25 sintered at 1400°C.

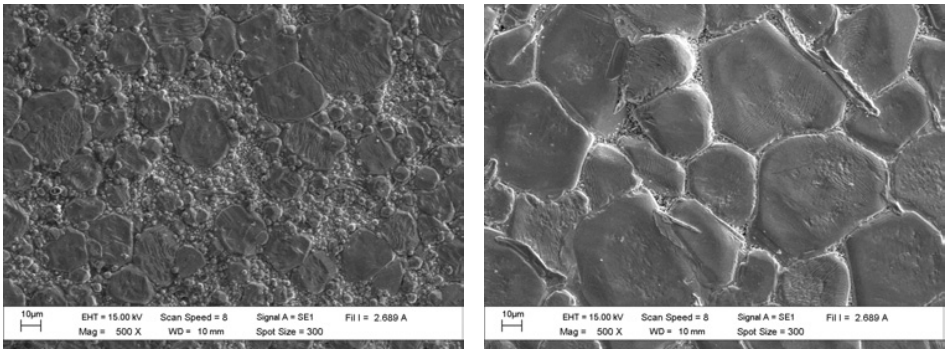

(c) (d)

Fig. 5. (*Continued*)

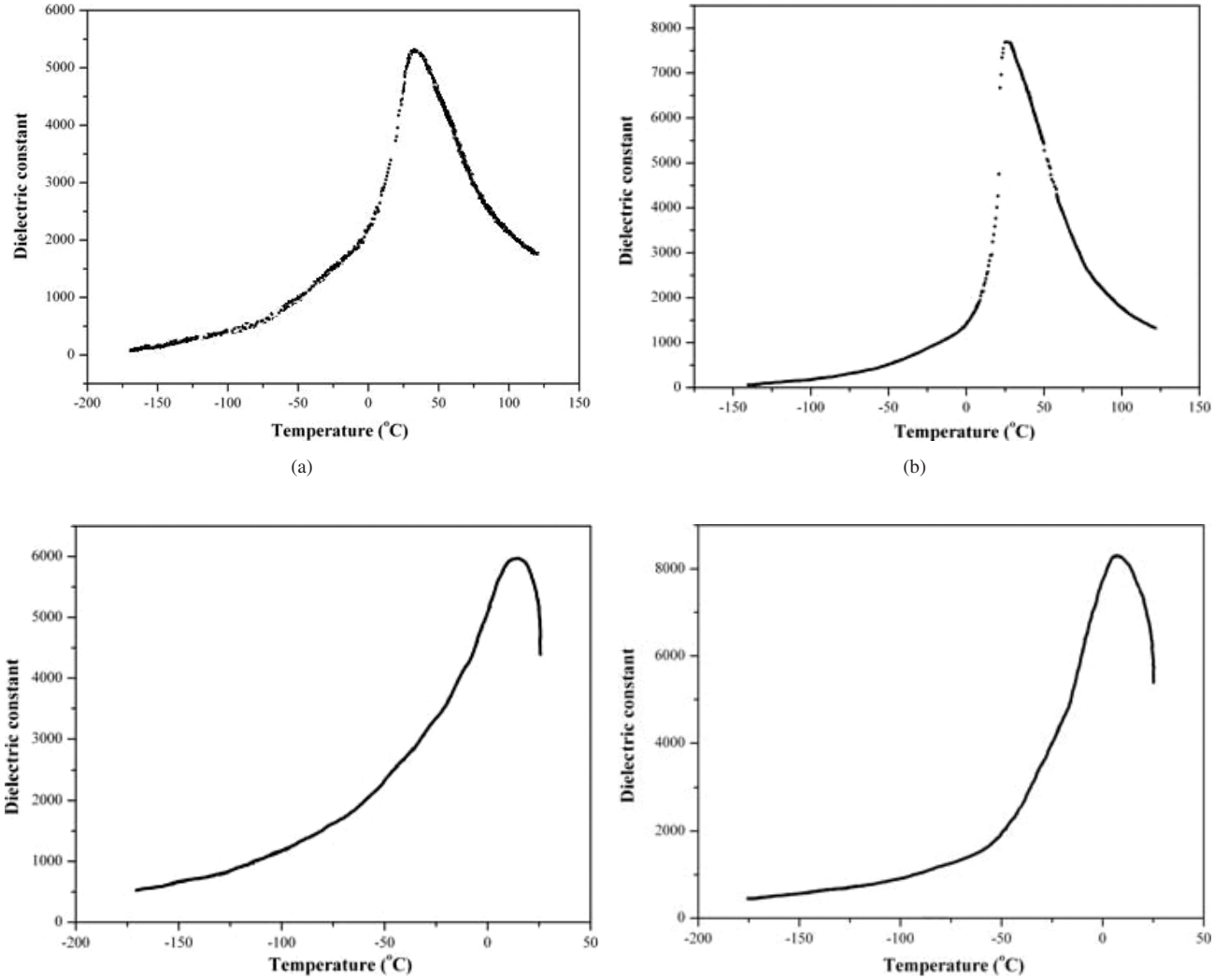

(a) (b) (c) (d)

Fig. 6. The dielectric constant of BTZ ceramics; (a) BTZ20 sintered at 1300°C, (b) BTZ20 sintered at 1400°C, (c) BTZ25 sintered at 1300°C and (d) BTZ25 sintered at 1400°C.

that the combustion route can produce good BTZ ceramics with a high dielectric constant.

The high dielectric constant of BTZ ceramics can be successfully obtained by the combustion route. The firing temperatures and Zr ion contents have a strong influence on the phase formation, microstructure, density, Curie temperatures and dielectric constant. The XRD patterns of the samples were indexed to cubic perovskite structures. The lattice parameter a and the grain size increased with the increasing of sintering temperatures. A maximum dielectric constant was obtained from the samples sintered at 1400°C.

Acknowledgments

The authors gratefully acknowledge the financial support of the Thailand Research Fund (TRF), Commission on Higher Education (CHE) and Faculty of Science, Naresuan University. Special thanks to the Uttaradit Rajabphat University and King Mongkut's Institute of Technology, Ladkrabang (KMITL) for supporting facilities. Acknowledgment is also given to Mr. Don Hindle, for his helpful comments and correction of the manuscript.

References

1. Z. Yu, R. Guo and A. S. Bhalla, *J. Appl. Phys.* **88**, 410 (2000).
2. E. J. Brajer: U.S. Patent 2, 708, 243 (1955).
3. F. Kulscar: U.S. Patent 2, 735, 024 (1956).
4. D. Hennings, A. Schnell and G. Simon, *J. Am. Ceram. Soc.* **65**, 539 (1982).
5. R. Liang, X. Dong, Y. Chen, F. Cao and Y. Wang, *Ceram. Int.* **33**, 957 (2007).
6. T. Bongkarn, N. Phungjitt and N. Vittayakorn, *Adv. Mater. Res.* **55–57**, 205 (2008).
7. A. Dixit, S. B.Majumder, A.Savvinov, R. S. Katiyar, R. Guo and A. S. Bhalla, *Mater. Lett.* **56**, 933 (2002).
8. R. Wendelbo, D. E. Akporiaye, A. Karlsson, M. Plassen and A. Olafsen, *J. Eur. Ceram. Soc.* **26**, 849 (2006).
9. K. Prabhakaran, J. Joseph, N. M. Gokhale, S. C. Sharma and R. Lal, *Ceram. Int.* **31**, 327 (2005).
10. L. A. Chick, L. R. Pederson, G. D. Maupin, J. L. Bates, L. E. Thomas and G. J. Exarhos, *Mater. Lett.* **10**, 6 (1990).
11. R. S. Guo, Q. T. Wei, H. L. Li and F. H. Wang, *Mater. Lett.* **60**, 261 (2006).
12. Powder Diffraction File No. 36-0019, International Center for Diffraction Data, Newton Square, PA, 2003.
13. L. Conceicao, N. F. P. Ribeiro, J. G. M. Furtado and M. M. V. M. Souza, *Ceram. Int.* **35**, 1683 (2009).
14. T. Badapanda, S. K. Rout, S. Panigrahi and T. P. Sinha, *Curr. Appl. Phys.* **9**, 727 (2009).
15. D. Shan, Y. F. Qu and J. J. Song, *J. Solid State Commun.* **141**, 65 (2007).

J Mater Sci (2010) 45:1443–1447
DOI 10.1007/s10853-009-4098-z

Solid-state reaction synthesis of sodium niobate ($NaNbO_3$) powder at low temperature

Nopsiri Chaiyo · Banjong Boonchom · Naratip Vittayakorn

Received: 16 September 2009 / Accepted: 30 November 2009 / Published online: 15 December 2009

Abstract A modified solid-state reaction was applied to produce lead-free piezoelectric sodium niobate ($NaNbO_3$) powders. The mixture of $Na_2C_2O_4$ and Nb_2O_5 was identified by thermo gravimetric analysis (TGA) and differential thermal analysis (DTA). The powders were characterized using a scanning electron microscope (SEM) and the X-ray diffraction technique (XRD). The SEM image suggested that the particle size of the powders obtained ranged from 180 to 360 nm. The XRD pattern showed that the pure perovskite phase of $NaNbO_3$ could be synthesized at the low temperature of 475 °C for 1 h, with an average crystallite size of 31.45 ± 5.28 nm. This temperature was about 300 °C lower than that when using the conventional solid-state method with Na_2CO_3 as reactant, which resulted in a cost-, energy-, and time-saving method.

N. Chaiyo · N. Vittayakorn
Electroceramic Research Laboratory, College of KMITL Nanotechnology, King Mongkut's Institute of Technology Ladkrabang, Bangkok 10520, Thailand

B. Boonchom
King Mongkut's Institute of Technology Ladkrabang, Chumphon Campus, 17/1 M. 6 Pha Thiew District, Chumphon 86160, Thailand

N. Vittayakorn (✉)
Advanced Materials Science Research Unit, Department of Chemistry, Faculty of Science, King Mongkut's Institute of Technology Ladkrabang, Bangkok 10520, Thailand
e-mail: naratipcmu@yahoo.com

N. Chaiyo · N. Vittayakorn
ThEP Center, CHE, 328 Si Ayutthaya Rd., Bangkok 10400, Thailand

Introduction

Alkaline niobate materials are considered a lead-free candidate for the substitution of widely used commercial lead-based piezoelectric material, based on the aim to avoid highly harmful lead compounds [1–4]. Among several compounds, sodium niobate ($NaNbO_3$) has attracted considerable attention because of its unique properties [3] and high dielectric constant (2000–3000) at Curie temperature [5]. Unlike most oxidic perovskite, $NaNbO_3$ possesses six phase transitions from the ferroelectric phase at low temperature (rhombohedral) to the antiferroelectric room temperature phase (orthorhombic) and non-polar cubic structure at 640 °C [6]. It can form solid solution with other niobate compounds, such as $LiNbO_3$ and $KNbO_3$, to acquire good ferroelectric and piezoelectric properties [7–10]. Traditionally, alkali metal niobate powders have been synthesized via the solid-state reaction of alkali metal carbonates and Nb_2O_5 [3, 11]. This method requires a high calcination temperature (about 750 °C or more) for a long period of time, possibly causing volatilization of the alkali metal and leading to poor compositional homogeneity [3, 4, 11]. The powders can be agglomerated during heating, which affects their properties [3, 12]. Thereafter, powders with high sinterability and stoichiometric control are necessary for developing $NaNbO_3$-based piezoelectric ceramics. Numerous alternative methods are used to prepare $NaNbO_3$ such as hydrothermal [13], chemical [12], and polymeric precursor processes [14], and the mechanochemical process [3, 15, 16]. Although $NaNbO_3$ was performed by mechanochemical activation after thermal treatment of a stoichiometric Na_2CO_3/Nb_2O_5 mixture at 600 °C, this procedure required a long operational period of up to 30 days [3]. Moreover, $NaNbO_3$ was also obtained at a low temperature (450 °C) by the wet-chemical method

using a water-soluble malic acid complex [17]. However, most chemical techniques require specialized experimental apparatus and high purity reactant, which are more expensive. Interestingly, sodium tantalate ($NaTaO_3$) powder, with high crystallinity has been successfully synthesized at 600 °C through a simple method called modified solid-state reaction or combustion synthesis, in which urea plays an important role. Unusual starting material ($Na_2C_2O_4$ instead of Na_2CO_3/Na_2O) has been described. This method was found to produce $NaTaO_3$ as a general route at the lower temperature of ~500–600 °C, when compared with conventional solid-state reaction [18]. On the other hand, urea, which was added as fuel in order to achieve the final product, could cause problems in this method, due to risks if performing on a large scale. Nonetheless, the aim of the present study was to produce $NaNbO_3$ using a simple, rapid, low cost, and environment friendly route, such as a solid-state reaction of $Na_2C_2O_4$ and Nb_2O_5 without the addition of any fuel.

Experiment

$NaNbO_3$ was synthesized by a solid-state reaction method. Reagent grade sodium oxalate ($Na_2C_2O_4$, 99.9%) and niobium oxide (Nb_2O_5, 99.9%) were employed as raw material. Firstly, starting materials were weighed according to the required stoichiometric ratio that related to the reaction below.

$$Na_2C_2O_{4(s)} + Nb_2O_{5(s)} \rightarrow 2NaNbO_{3(s)} + 2CO_{2(g)} \quad (1)$$

Then, raw materials were mixed together by ball-milling in ethyl alcohol using partially stabilized zirconia balls for 18 h. After drying on a hot plate by regularly stirring at about 80 °C for an approximate period, the thermal behavior during heat treatment was determined by thermo gravimetric analysis (TGA, Perkin Elmer) and differential thermal analysis (DTA, Perkin Elmer). According to TG-DTA results, the mixture was subsequently placed in a closed alumina crucible and calcined for different periods of time in air at various temperatures, ranging from 300 to 600 °C, in order to investigate the formation of $NaNbO_3$.

Afterward, calcined powders were subsequently inspected by room temperature X-ray diffraction (XRD, Advance D8), using Ni-filtered Cu K_α radiation, to examine the effect of thermal treatment on phase development and the optimal calcination condition for the formation of crystalline $NaNbO_3$ powders. Powder morphologies and particle size were figured directly using a scanning electron microscope (SEM, LEO1455 VP).

Results and discussion

The TGA and DTA of a powder mixed in the stoichiometric proportions of $NaNbO_3$ are illustrated in Fig. 1. The TG curve accordingly revealed a weight loss of 16.8%, occurring during the temperature rise from 400 to 500 °C. This observation corresponded to the endothermic peak of the DTA curve, which cantered at 484.8 °C. This endotherm may be related to the decomposition of $Na_2C_2O_4$ to Na_2CO_3, which lies on the temperature of 450–550 °C, and abruptly to the decomposition of Na_2CO_3 to Na_2O (decomposition temperature in the range of 400 °C) before releasing CO and CO_2 molecules, as revealed below [19].

$$Na_2C_2O_4 \rightarrow Na_2CO_3 + CO \quad (2)$$

$$Na_2CO_3 \rightarrow Na_2O + CO_2 \quad (3)$$

It is interesting to note that there was no weight loss or thermal effect at a temperature of about 100 °C, at which no decomposition occurrence was indicated. The endothermic peak correlates at the range of 100 °C with the release of water molecules. This confirmed that non-absorptive $Na_2C_2O_4$ raw material contrasts with Na_2CO_3, because Na_2CO_3 is the hygroscopic compound which can lead to the erroneous stoichiometric ratio. Therefore, powders with good compositional homogeneity, when comparing with the conventional solid-state method with Na_2CO_3 as reactant, may possibly be produced via this solid-state reaction.

Thus, based on TG-DTA data, the powders were calcined at temperatures ranging from 300 to 600 °C for 4 h in order to investigate the calcination temperature outcome in the development phase. The mixture of starting material was calcined in air using the steady heating/cooling rate of 20 °C at various temperatures, and followed by phase analysis using the XRD technique. Figure 2 shows the XRD pattern of the $NaNbO_3$ powders calcined at different

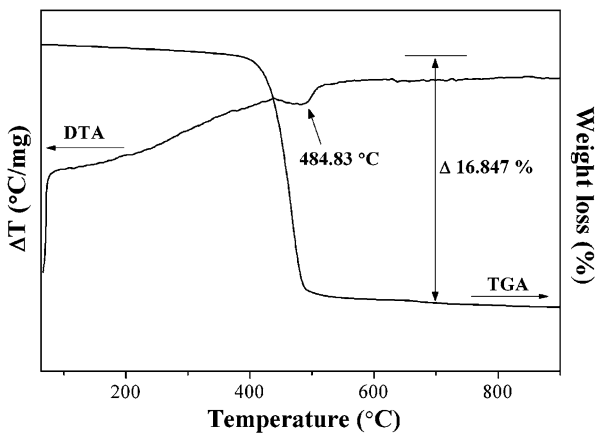

Fig. 1 TG-DTA result of an uncalcined powder mixed in the stoichiometric proportion of $NaNbO_3$

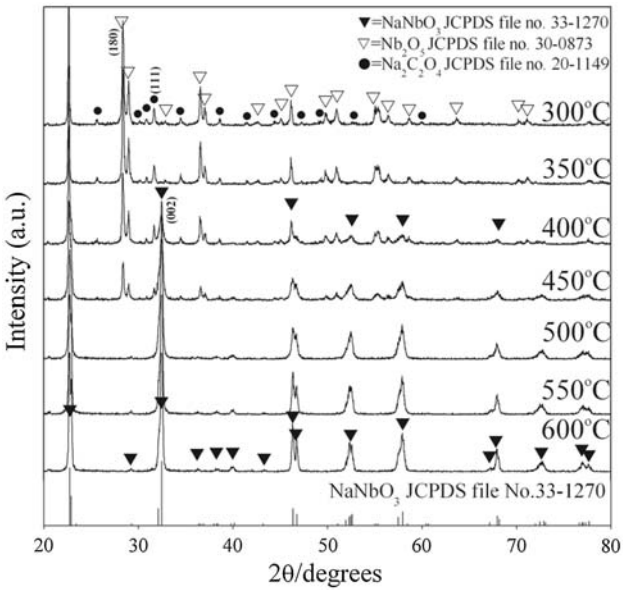

Fig. 2 XRD patterns of $NaNbO_3$ powder calcined at various temperatures for 4 h with a heating/cooling rate of 20 °C/min

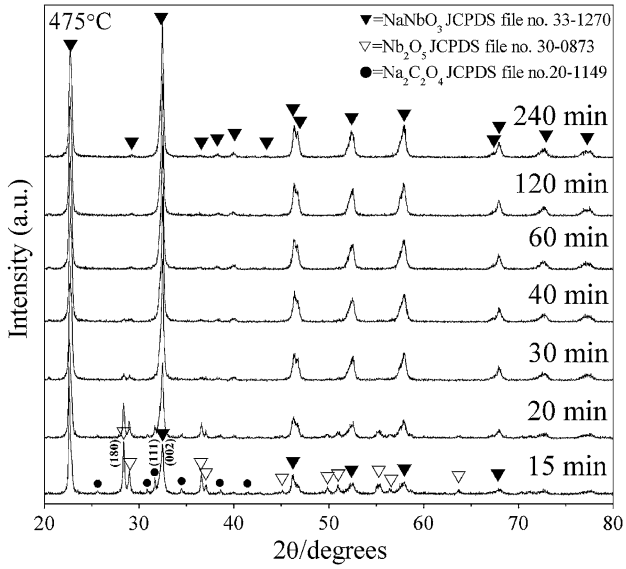

Fig. 3 XRD patterns of $NaNbO_3$ powder calcined at the calcination temperature of 475 °C for various dwell times with a heating/cooling rate of 20 °C/min

temperatures for 4 h. It can be seen that fine $NaNbO_3$ crystallites were developed at a calcination temperature as low as 400 °C, accompanied by the phase of unreacted Nb_2O_5 (JCPDS file no. 30-0873) and $Na_2C_2O_4$ (JCPDS file no. 20-1149). This observation suggests that nucleation of the perovskite $NaNbO_3$ phase did occur. In addition, the minor phase of Nb_2O_5 and $Na_2C_2O_4$ was also decreased with escalating calcination temperature, and disappeared completely after the powders were calcined at the calcination temperature of 500 °C for 4 h. Whereas, the intensity of the perovskite $NaNbO_3$ peak was enhanced further and an essentially monophasic $NaNbO_3$ perovskite phase (yield of 100% within the limitations of the XRD technique) was observed. This $NaNbO_3$ phase could be indexed according to an orthorhombic structure with the space group *Pbma* (no. 57), which was consistent with JCPDS file No. 33-1270. Although the calcination temperature rose at 550 and 600 °C, the monophasic $NaNbO_3$ perovskite phase was also obtained. There was no evidence of the pyrochlore diffraction peak. This result also correlates with the TG-DTA analysis shown above. As the calcination temperature increased, so too did the amount of the $NaNbO_3$ crystallite phase, and this can be seen as intensity of the amplified peak. Since the diffusion coefficient is a temperature dependence parameter, the higher temperature has the most intense effect on the rate of diffusion [20], and can enhance higher atomic mobility [11].

As the finest calcination temperature was established at 500 °C, a dwell time ranging from 15 min to 4 h was applied at 475 °C (instead of 500 °C). This temperature was preferred because of the rapid diffraction peak change of the powder calcined at 450 and 500 °C. The XRD pattern of the $NaNbO_3$ powders, which were calcined at 475 °C with different dwell times, is shown in Fig. 3. It was found that the single-phase of $NaNbO_3$ powder was also successfully synthesized at the calcination temperature of 475 °C, with a dwell time of 60 min or more applied. The increase in crystallinity of the $NaNbO_3$ phase was seen to relate with the escalation of dwell time. Although the calcination temperature of 475 °C was higher than the nucleation temperature of the powder obtained by a polymeric precursor [14], this was a single-step and low-cost starting material method that could save time, energy, and cost. Likewise, this temperature was much lower than the conventional solid-state reaction process with Na_2CO_3 as reactant, which was in the range of 750 °C [3]. This observation indicated that calcination temperature and dwell time might play an important role in evolution of the pure phase product and also be consistent with other systems [21].

The volume fraction of the perovskite phase formation was considered at various calcination temperatures and dwell times. These relative amounts of perovskite, $Na_2C_2O_4$ and Nb_2O_5 phases, were approximated by calculating the ratio of the main X-ray peak intensities of perovskite $NaNbO_3$, $Na_2C_2O_4$, and Nb_2O_5 phase using the following equation [22]:

$$\text{Wt\% perovskite} = \frac{I_{\text{perov}}}{I_{\text{perov}} + I_{\text{Na}_2\text{C}_2\text{O}_4} + I_{\text{Nb}_2\text{O}_5}} \times 100 \qquad (4)$$

where I_{perov}, $I_{Na_2C_2O_4}$, and $I_{Nb_2O_5}$ stand for the intensities belonging to the strongest reflection peak of (002)

Table 1 Fraction of perovskite phase formed as a function of calcination temperature and dwell time

$NaNbO_3$	Calcination temperature (°C)						
	300	350	400	450	500	550	600
%Perovskite	0	0	35.42	62.86	100.00	100.00	100.00
$NaNbO_3$	Dwell time (min) at 475 °C						
	15	20	30	40	60	120	240
%Perovskite	41.89	60.56	89.13	97.00	100.00	100.00	100.00

perovskite, (111) $Na_2C_2O_4$, and (180) Nb_2O_5, respectively. A volume fraction increase of the perovskite $NaNbO_3$ phase formation of the calcined powders, resulting from the calcinations process at various temperatures and dwell times, is shown in Table 1. As the calcination temperature rose, the yield of the perovskite phase increased significantly until the temperature reached 500 °C, and a pure phase of $NaNbO_3$ was established. Likewise, in observing powders calcined at 475 °C for different dwell times, the $NaNbO_3$ phase was enlarged as the dwell time increased up to 60 min, and the monophasic phase of $NaNbO_3$ was seen to form.

Accordingly, the Johnson–Mehl–Avrami, or JMA equation was used in the present study. This equation was found appropriate for describing a wide variety of isothermal solid-state transformations [23, 24]. It was used to study the kinetic of the reaction and mechanism involving nucleation and growth, and has the general form of:

$$x(t) = 1 - \exp[-(kt)^n]. \quad (5)$$

where x is the volume fraction of the perovskite phase formed, k the reaction rate constant, t the calcination time, and n the Avrami exponent. For analyzing the results, the relation of ln [ln $1/(1 - x)$] versus ln t was plotted. Figure 4 shows a good linear fit of the Avrami plot for $NaNbO_3$ powders calcined at 475 °C. This shows that the isothermal formation of the perovskite phase can be described accurately by the theory of phase transformations. The constant n, which can be calculated from the slope of this Avrami plot, was found to be 1.79. This indicated that the reaction of solid solution formation is diffusion controlled (n is less than 2.5) [25]. The beginning stage of transformation is a fixed number of perovskite nuclei [26].

The average crystallite size of the powders obtained can be determined from the XRD pattern according to Scherrer's equation [27]:

$$D = \frac{k\lambda}{\beta \cos \theta_B} \quad (6)$$

where D is the average crystallite size, k a constant equal to 0.89, λ the wavelength of X-ray radiation, β the full width

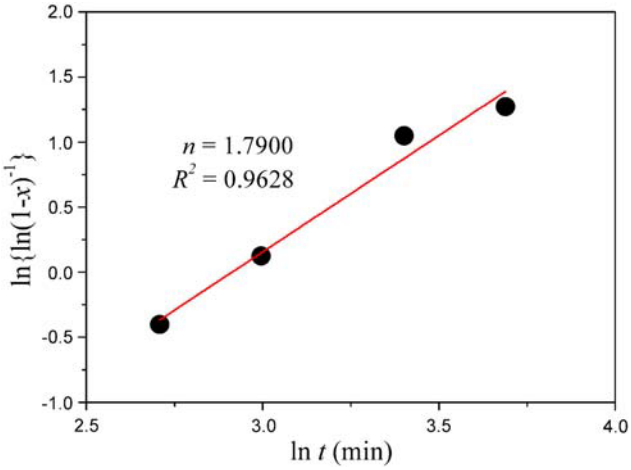

Fig. 4 Johnson–Mehl–Avrami for the formation of perovskite phase in $NaNbO_3$ powders isothermally heat treated at 475 °C

at half maximum (FWHM), and θ_B the diffraction angle. The average crystallite size of powders calcined at 475 °C for 15 min to 4 h was found to be from 21.52 to 35.56 nm, and that of powders calcined at the optimum condition (475 °C for 60 min) was about 31.45 nm. The increase in crystallinity of the $NaNbO_3$ phase was affected by increasing dwell time. This may confirm that the dwell time also plays an important role in development of the pure phase creation.

SEM micrographs of the powder calcined at 475 °C for 60 min are given in Fig. 5. The particle size, which can be estimated from these micrographs, was found to be in the range of 180 to 360 nm. This value is greater than the average crystallite size calculated from XRD patterns. The inconsistency value could point out the agglomeration

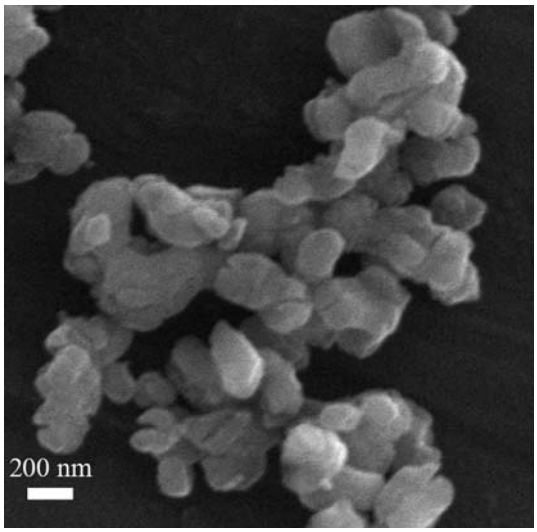

Fig. 5 SEM micrographs showing $NaNbO_3$ powders synthesized at 475 °C for 60 min, with a heating/cooling rate of 20 °C/min

of the calcined powders. No evidence of difference phase or pyrochlore phase was found. This outcome relates to the XRD result, in which the monophasic perovskite phase of $NaNbO_3$ can be established after calcination at 475 °C for 60 min.

Conclusion

Crystalline powders of sodium niobate $NaNbO_3$ were synthesized from a modified solid-state reaction of $Na_2C_2O_4$ and Nb_2O_5. This method is an excellent, simple and cost effective way to prepare stoichiometric, homogeneous, and fine powders. The perovskite phase of $NaNbO_3$ was successfully synthesized at the low temperature of 475 °C for 1 h, with an average crystallite size of 31.45 ± 5.28 nm. This temperature is about 275 °C lower than that used in the conventional method, which lies in the 750 °C range. As dwell time increased, XRD peaks became narrower, and a pattern similar to that expected for orthorhombic $NaNbO_3$ was achieved, as indicated by the separate peaks. The resulting $NaNbO_3$ powders comprised agglomerated particles of 180 to 360 nm in size.

Acknowledgements This work was supported by the Thailand Research Fund (TRF), Thailand Graduate Institute of Science and Technology (TGIST), National Research Council of Thailand (NRCT), and the National Nanotechnology Center (NANOTEC) NSTDA, Ministry of Science and Technology, Thailand through its "Center of Excellence Network" Program.

References

1. Matsubara M, Yamaguchi T, Sakamoto W, Kikuta K, Yogo T, Hirano S-I (2005) J Am Chem Soc 88:1190
2. Zhaoa P, Zhanga B-P, Lib J-F (2008) Scripta Mater 58:429
3. Hungría T, Pardo L, Moure A, Castro A (2005) J Alloys Compd 395:166
4. Ke T-Y, Chen H-A, Sheu H-S, Yeh J-W, Lin H-N, Lee C-Y, Chiu H-T (2008) J Phys Chem C 112:8827
5. Jona F, Shirane G (1993) Ferroelectric crystals. Dover Publications, New York
6. Wang X-B, Shen Z, Hu Z-P, Qin L, Tang SH, Kuok MH (1996) J Mol Struct 385:1
7. Du H, Zhou W, Luo F, Zhu D, Qu S, Li Y, Pei Z (2008) J Appl Phys 104:034104-7
8. Chang Y, Yang Z-P, Ma D, Liu Z, Wang Z (2008) J Appl Phys 104:024109-8
9. Wu J, Xiao D, Wang Y, Wu W, Zhang B, Zhu J (2008) J Appl Phys 104:024102-4
10. Lei C, Ye Z-G (2008) Appl Phys Lett 93:042901-3
11. Hsiao Y-J, Chang Y-H, Chang Y-S, Fang T-H, Chai Y-L, Chen G-J, Huang T-W (2007) Mater Sci Eng B 136:129
12. Lanfredi S, Dessemond L, Rodrigue ACM (2000) J Eur Ceram Soc 20:983
13. Goh GKL, Lange FF, Haile SM, Levi CG (2003) J Mater Res 18:338
14. de Lima Nobre MA, Longo E, Leite ER, Varela JA (1996) Mater Lett 28:215
15. Moure A, Hungría T, Castro A, Pardo L (2009) J Eur Ceram Soc 29:2297
16. Rojac T, Kosec M, Malic B, Holc J (2005) Mater Res Bull 40:341
17. Camargo ER, Popa M, Kakihana M (2002) Chem Mater 14:2365
18. Xu J, Xue D, Yan C (2005) Mater Lett 59:2920
19. McAlexander LH, Beck CM, Burdeniuc JJ, Crabtree RH (1999) J Fluorine Chem 99:67
20. Callister WD (2007) Materials science and engineering: an introduction. Wiley, New York
21. Chaiyo N, Vittayakorn N (2008) J Ceram Process Res 9:381
22. Feng G, Rongzi H, Jiaji L, Zhen L, Lihong C, Changsheng T (2009) J Eur Ceram Soc 29:1687
23. Sheibani S, Ataie A, Heshmati-Manesh S (2008) J Alloys Compd 455:447
24. Yan Z-J, Dang S-E, Wang X-H, Lian P-X (2008) Trans Nonferrous Met Soc China 18:138
25. Jang HM, Cho SR, Lee K-M (1995) J Am Ceram Soc 78:297
26. Shen Y, Hng HH, Oh JT (2004) Mater Lett 58:2824
27. Klug HP, Alexander LE (1974) X-ray diffraction procedure of polycrystalline and amorphous materials. Wiley, New York

J Mater Sci
DOI 10.1007/s10853-009-4101-8

One-step thermal synthesis of binary manganese iron cyclotetraphosphate $MnFeP_4O_{12}$

Banjong Boonchom · Naratip Vittayakorn

Received: 3 August 2009 / Accepted: 30 November 2009

Abstract The manganese iron cyclotetraphosphate ($MnFeP_4O_{12}$) was synthesized through one-step thermal synthesis at 700 °C using the mixing of manganese and iron metals and phosphoric acid in the presence of water–acetone media. Both FTIR and XRD results indicate the cyclotetraphosphate ($P_4O_{12}^{4-}$) structure and a pure monoclinic phase with space group *C2/c* ($Z = 4$). The morphology and crystallite size for the $MnFeP_4O_{12}$ obtained from SEM data and X-ray line broadening show non-uniform particles and 30 ± 9 nm, respectively. The magnetic study of the synthesized $MnFeP_4O_{12}$ shows superparamagnetic behavior, which is important for specific application. Some physical properties of the synthesized $MnFeP_4O_{12}$ powder presented for the first time are comparable with those from individual $M_2P_4O_{12}$ (M = Mn and Fe) and a binary metal compound as $CoFeP_4O_{12}$.

Introduction

The metal(II) phosphates have considerable industrial interesting properties such as ceramics, catalysts, fluorescent materials, dielectrics, metal surface treatment agents, detergents, food additives, fuel cell materials, pigment, etc. [1–4]. Metal cyclotetraphosphates $M_2P_4O_{12}$ and binary metal cyclotetraphosphates $M_{2-x}A_xP_4O_{12}$ (M and A = Mg, Ca, Mn, Co, Ni, Zn, or Cu; $0 < x < 2$), are isostructural, were examined for potential applications as special inorganic pigments [5, 6]. All these compounds have similar X-ray diffraction patterns and close unit cell parameters, which crystallize in monoclinic space group *C2/c* ($Z = 4$) [7]. They were first described by Trojan et al. [6, 8, 9] and prepared by mixing starting materials, followed by calcination, crushing, and adjusting their color [9–11]. Many methods have been employed to synthesize single or binary metal cyclotetraphosphate, including two-step thermal method [6, 8, 9], hydrothermal synthesis [5], and the condensation of binary metal(II) dihydrogenphosphate hydrates ($M_{1-y}A_y(H_2PO_4)_2{\cdot}nH_2O$ where $0 < y < 1$; $1 < n < 4$) [12, 13]. In our previous work, the $MnFeP_4O_{12}$ prepared by the calcinations of $Mn_{0.5}Fe_{0.5}(H_2PO_4)_2{\cdot}nH_2O$ at 500 °C uses several processes [12]. These previously reported methods were long time consuming (>5 h) with high temperature (800–1000 °C) and were the evolved toxic gases (NO_2 and CO_2). These works are of interest because it appears economically advantageous and environmentally friendly to substitute a portion of the divalent metal with a less costly divalent element, which influences many properties, for example, the color of pigments, thermally and chemically stable compounds [6, 8], anti-corrosion ability, and luminescence [8, 9, 14, 15]. However, it is relevant to synthesize binary cyclotetraphosphate and its solid solution because changing the metal ratio influences its useful properties.

Herein, we report for the first time the synthesis of a binary manganese iron cyclotetraphosphate, $MnFeP_4O_{12}$ by one-step thermal synthesis using solid state route of manganese and iron metals and phosphoric acid in water–acetone medium. This method is a simple, rapid, cost-effective, and environmental friendly route for synthesis of

B. Boonchom (✉)
King Mongkut's Institute of Technology Ladkrabang, Chumphon Campus, 17/1 M. 6 Pha Thiew District, Chumphon 86160, Thailand
e-mail: kbbanjon@kmitl.ac.th

B. Boonchom · N. Vittayakorn
Advanced Materials Science Research Unit, Department of Chemistry, Faculty of Science, King Mongkut's Institute of Technology Ladkrabang, Bangkok 10520, Thailand

Published online: 11 December 2009

$MnFeP_4O_{12}$, exhibiting the differences of some physical and chemical properties from those in our previously report [12, 16, 17]. The synthesized sample was characterized by X-ray powder diffraction (XRD), Fourier transform infrared (FTIR), scanning electron microscope (SEM), and a vibrating sample magnetometer (VSM) techniques.

Experimental

Reagent and apparatus

The starting reagents are Mn, Fe, H_3PO_4, and acetone. All chemicals were of p.a. quality (Merck). As metal sources we use crystalline Mn and Fe metals since they display: (i) a moderate stability at storage (with respect to bond oxidation to Fe(II) and Mn(II) and dehydration, which ensures an exact stoichiometry in the final product; (ii) appearance of reducing gaseous products (H_2, H_2O, CO, or CO_2) during the calcination process. The manganese and iron contents of $MnFeP_4O_{12}$ were determined by dissolving in 0.0126 M hydrochloric acid using atomic absorption spectrophotometry (AAS, Perkin Elmer, Analyst100). The phosphorus content was determined by colorimetric analysis. The room temperature FTIR spectrum was recorded in the range of 4000–370 cm^{-1} with 8 scans on a Perkin-Elmer Spectrum GX FT-IR/FT-Raman spectrometer with the resolution of 4 cm^{-1} using KBr pellets (KBr, spectroscopy grade, Merck). The structure and crystallite size of the product were studied by X-ray powder diffraction using a X-ray diffractometer (Phillips PW3040, The Netherlands) with Cu Kα radiation ($\lambda = 0.15406$ nm). The Scherrer method was used to evaluate the crystallite size [18]. The morphology of the product was examined with scanning electron microscope using LEO SEM VP1450 after gold coating. The magnetic study of the product was examined at room temperature (20 °C) using a vibrating sample magnetometer (VSM 7403, Lake Shore, USA).

Preparation of manganese iron cyclotetraphosphate $MnFeP_4O_{12}$

Typical procedure, 0.5494 g of Mn (c), 0.5584 g of Fe (c), and 10 mL acetone were put in a beaker with mechanical stirring. The mixture was added by 5 mL of 70% H_3PO_4 (86.4% w/w H_3PO_4 dissolved in DI water) with continuous stirring at ambient temperature (10 min). The reactant mixture was transferred to a crucible, which was heated in the furnace at 700 °C for 2 h in an air atmosphere. The obtained pale gray powder was crushed and washed repeatedly with water until no PO_4^{3-} was detected in filtrate. Then, the powder was washed again for several times with methanol and dried at room temperature. The reaction equation can be expressed as:

$$\mathrm{Mn(s)} + \mathrm{Fe(s)} + 4\mathrm{H_3PO_4(aq)} \xrightarrow{\text{Acetone, 700 °C in air atmosphere}} \mathrm{MnFeP_4O_{12}(s)} + 4\mathrm{H_2O(g)} + 2\mathrm{H_2(g)} \quad (1)$$

Results and discussion

Chemical analysis of $MnFeP_4O_{12}$

The chemical compositions of the synthesized $MnFeP_4O_{12}$ were analyzed according to the discussed methods. The data showed that manganese, iron, and phosphorus mass percentages were 14.55, 14.30, and 31.92 wt%, respectively. In other words, mole ratio of Mn:Fe:P in the synthetic product is equal to 1.03:1.00:4.02. This indicates that the general formula would be $MnFeP_4O_{12}$.

XRD analysis of $MnFeP_4O_{12}$

Figure 1 shows the XRD pattern of the product $MnFeP_4O_{12}$ obtained at 700 °C. The higher intensities of XRD peaks observed indicate crystallization as well as particle sizes of the product. On the basis of isostructural, XRD patterns of the individual $M_2P_4O_{12}$ (when M = Mn and Fe) and the binary $M_{1-x}A_xP_4O_{12}$ are quite similar due to the electric charges of cations are equivalent, and the radii of cations are close to each other. Consequently, we can draw a conclusion that the synthesized $MnFeP_4O_{12}$ is solid solution and not a mixture of the individual ones. All the detectable peaks in the figure are found to be in agreement with monoclinic phase, space group *C2/c* ($Z = 4$) from PDF card 380314 for $Mn_2P_4O_{12}$ and PDF card 782285 for

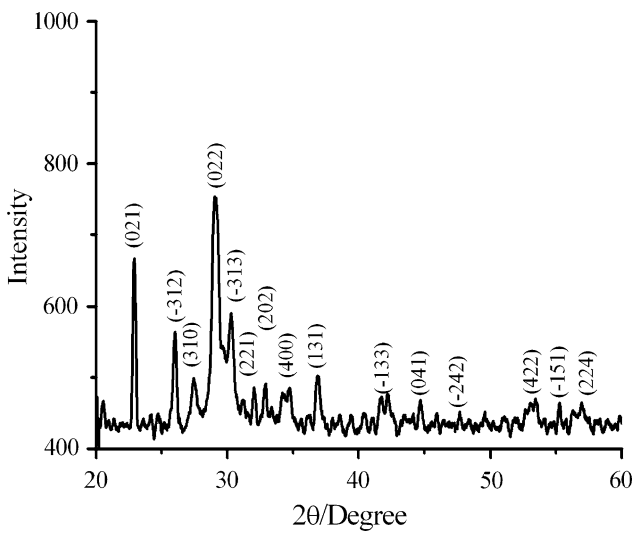

Fig. 1 XRD pattern of $MnFeP_4O_{12}$

Table 1 Average particle size and lattice parameters of $MnFeP_4O_{12}$ calculated from XRD data

Compounds	Systems	*a* (Å)	*b* (Å)	*c* (Å)	*β* (°)	Average crystallite size (nm)
$Mn_2P_4O_{12}$	PDF no 380314	11.88	8.588	10.137	119.21	–
	Ref. [16]	11.784(0)	8.913(4)	10.055(6)	119.95(3)	29 ± 9
$MnFeP_4O_{12}$	This work	12.02(0)	8.23(0)	10.57(0)	118.89(2)	30 ± 9
	Ref. [12]	12.02(8)	8.42(2)	10.10(4)	119.11(5)	69 ± 21
$Fe_2P_4O_{12}$	PDF no.782285	11.94	8.37	9.93	118.74	
	Ref. [17]	12.80(0)	8.80(4)	10.56(0)	118.67(4)	29 ± 6

$Fe_2P_4O_{12}$ and the XRD pattern of the prepared sample is in agreement with that of $MnFeP_4O_{12}$, obtained by the thermal transformation of $Mn_{0.5}Fe_{0.5}(H_2PO_4)_2{\cdot}nH_2O$ at 500 °C. According to the Scherrer formula: $D = 0.89\lambda/\beta\cos\theta$), where D is crystallite diameter, $\lambda = 0.15406$ nm (the wavelength of X-ray radiation), θ is the diffraction angle, and β is the full width at half maximum (FWHM) [18]. The crystallite size of the product are estimated from the strong peaks below 40° fro 2θ. The resulting crystallite size of the product is 30 ± 9 nm. The lattice parameters determined from the XRD spectra are very close to the standard data file (from PDF no. 380314 for $Mn_2P_4O_{12}$ and PDF no. 782285 for $Fe_2P_4O_{12}$) and $MnFeP_4O_{12}$ reported in the literature (Table 1) [12, 16, 17].

FT-IR spectroscopic analysis of $MnFeP_4O_{12}$

The FTIR spectrum of the product $MnFeP_4O_{12}$ is seen in Fig. 2. The crystal structure is a three-dimensional framework of MO_6 (M = Mn or Fe) polyhedral linked with P_4O_{12} rings by M–O–P. The vibrational modes of $P_4O_{12}{}^{4-}$ ion observed in the frequency range of 370–1400 cm^{-1} are assigned according to the literature [16, 17, 19]. The strong band at 1226 cm^{-1} is due to the asymmetric stretching frequency of the $PO_2{}^{2-}$ radical, while the bands at 1100–100 cm^{-1} to the symmetric stretching frequencies of the $PO_2{}^{2-}$ radical. The bending modes are expected in the area 600–400 cm^{-1} ($PO_2{}^{2-}$ radical) and 400–370 cm^{-1} (P–O–P bridge). The metal–O stretching usually appears in the bending mode region as the bending modes of the P–O–P bridge and absorption bands associated with these vibrations are usually very weak. One strong band at 970 cm^{-1} is assigned to the asymmetric of the P–O–P bridge. Three bands between 800 and 700 cm^{-1} are due to symmetric stretching frequencies of the P–O–P bridge. The observation of a strong ν_sPOP band is known to be the most striking feature of cyclotetraphosphate spectra, along with the presence of the $\nu_{as}OPO^-$ band, which indicate the cyclic structure of the $[P_4O_{12}]^{4-}$ anion. This FTIR result is consistent with X-ray diffraction data [5].

SEM analysis of $MnFeP_4O_{12}$

Figure 3 shows the SEM micrograph of $MnFeP_4O_{12}$ product. The whole thermal transformation phase changed

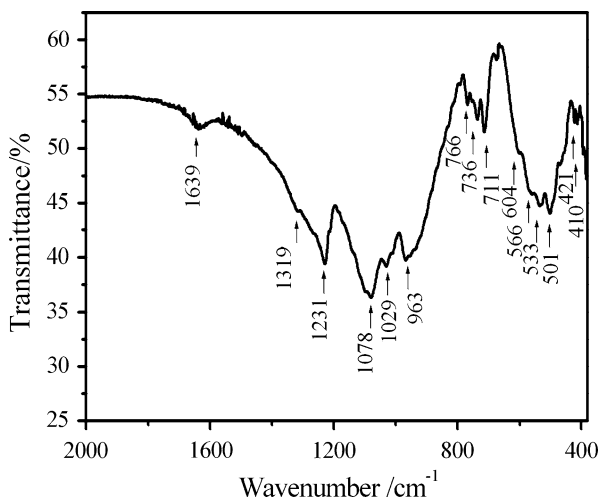

Fig. 2 FTIR spectrum of $MnFeP_4O_{12}$

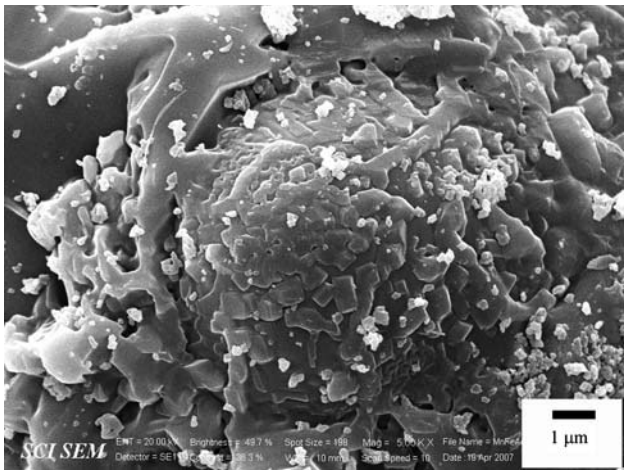

Fig. 3 SEM micrograph of $MnFeP_4O_{12}$

particle shape and size of the product composed of a high agglomerate of non-uniform particles, which is not similar to those of $M_2P_4O_{12}$ (M = Mn or Fe) (Fig. 3) and $MnFeP_4O_{12}$ obtained by thermal condensation of $Mn_{0.5}Fe_{0.5}(H_2PO_4)_2{\cdot}nH_2O$ in our previous studies [12, 16, 17] The highly agglomerate of $MnFeP_4O_{12}$ powder is possibly caused by the process of the decomposition process in acetone medium. There is strong agglomeration phenomenon among the particles of $MnFeP_4O_{12}$, which is attributed that the each other absorption exists among particles with the layered structure compound. The SEM result indicates that the grain sizes of $MnFeP_4O_{12}$ are not consistent with the crystallite sizes in the XRD analysis because the exact particle nucleation and growth mechanisms are caused.

VSM magnetometer

Magnetization curve (M–H loop) for $MnFeP_4O_{12}$ powder obtained from room temperature VSM measurement is illustrated in Fig. 4. Magnetization did not reach saturation, even at maximum applied magnetic field in range of ±10,000 Oe, and no hysteresis was found, which indicated that the studied product is superparamagnetic [20]. Specific saturated magnetization (M_s) value (14.09 emu/g) for the studied $MnFeP_4O_{12}$ powder [12] is close to that of $CoFeP_4O_{12}$ (14.24 emu/g)[15]. But the superparamagnetic property for the studied compound is significantly different from the ferromagnetic properties for $Fe_2P_4O_{12}$ (85.01 emu/g) [17] and $MnFeP_4O_{12}$ (13.14 emu/g) [12] (obtained from thermal condensation of $Mn_{0.5}Fe_{0.5}(H_2PO_4)_2{\cdot}nH_2O$ at 500 °C) and the diamagnetic property for $Mn_2P_4O_{12}$ [16]. Compared with the M_s of Fe_3O_4 bulk (92 emu/g) and Fe_3O_4 nanoparticles (in a range of 30–50 emu/g), the M_s of

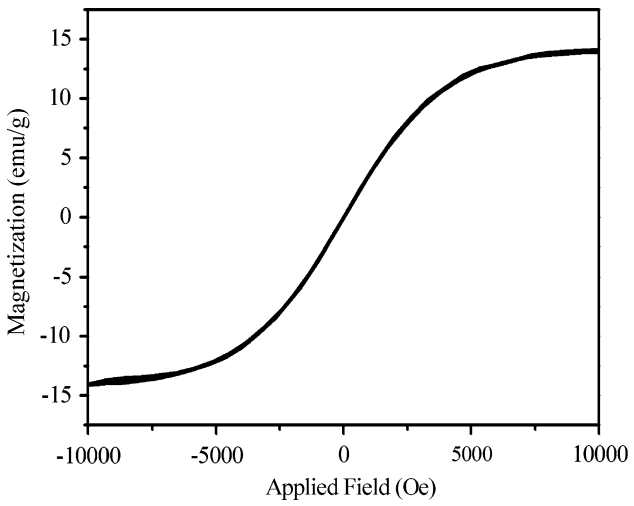

Fig. 4 The specific magnetization of $MnFeP_4O_{12}$ as a function of field, measured at 20 °C

$MnFeP_4O_{12}$ was lower, which might be attributed the nature of samples; crystal structure, shape, and particle size [21]. If Mn(II) is inserted to $Fe_2P_4O_{12}$, the magnetism would decrease significantly, since the effective metal radius of $MnFeP_4O_{12}$ was different from its core radius of $Fe_2P_4O_{12}$. This result indicates that the different magnetic property of $MnFeP_4O_{12}$ is caused by the presence of Mn ions in substitution position of Fe ions in the skeleton. This study demonstrates that the synthesized $MnFeP_4O_{12}$ is truly superparamagnetic, which is a unique feature of magnetic materials. This material may be used in modern technologies including magnetic resonance imaging contrast agents, data lifetime in high density information storage, ferrofluid technology, and magnetocaloric refrigeration [19–21].

Conclusions

This research has successfully achieved a simple one-step thermal synthesis of a monoclinic binary $MnFeP_4O_{12}$ in the presence of water–acetone media. FTIR, XRD, SEM, and VSM results suggested the formation of a binary manganese iron cyclotetraphosphate $MnFeP_4O_{12}$. The FTIR and XRD data confirmed the most feature of cyclic polyphosphate anion, which indicated the dominant cyclotetraphosphate of $P_4O_{12}^{4-}$ anion. The morphology and crystallite size of $MnFeP_4O_{12}$ show a high agglomerate of non-uniform particles and polycrystalline having crystallite size of 30 ± 9 nm, as estimated by SEM and XRD, respectively. The magnetic analysis of the synthesized $MnFeP_4O_{12}$ shows superparamagnetic property, having no hysteresis loop in the range of $-10{,}000$ Oe $< H <$ 10,000 Oe with the specific magnetization of 14.09 emu/g at 10 kOe. This research displays that the simple, cost-effective, rapid time consumption, and environmental friendly method is necessary for elaboration of technology and academic scientist to produce the cyclotetraphosphate of transition metals, which may be useful for potentially applications as super phosphate and micronutrient fertilizers, inorganic ceramic pigment, catalyst, fuel cell material and corrosion-proof compositions.

Acknowledgements This work is financially supported by the Thailand Research Fund (TRF), the Commission on Higher Education (CHE): Research Grant for New Scholar and the National Nanotechnology Center (NANOTEC) NSTDA, Ministry of Science and Technology, Thailand.

References

1. Hu X, Yan S, Ma L, Wan G, Hu J (2009) Powder Technol 192:27
2. Amri M, Zouari N, Mhiri T, Daoud A, Gravereau P (2006) J Mol Struct 782:16
3. Trojan M, Šulcová P (2000) Dyes Pigments 47:291

4. Boonchom B, Danvirutai C (2008) Ind Eng Chem Res 47:5976
5. Gunsser W, Fruehauf D, Rohwer K, Zimmermann A, Wiedenmann A (1989) J Solid State Chem 82:43
6. Trojan M, Brandová D (1985) Thermochim Acta 88:415
7. Durif A (2005) Solid State Sci 7:760
8. Trojan M, Šulcová P (2000) Thermochim Acta 343:135
9. Trojan M, Šulcová P (2000) J Therm Anal Calorim 60:215
10. Arbi K, Ben Hassen-Chehimi D, Trabelsi-Ayadi M, Silvestre JP (2000) Mater Res Bull 35:1533
11. Naïli H, Ettis H, Mhiri T (2006) J Alloys Compd 424:400
12. Boonchom B, Maensiri S, Youngme S, Danvirutai C (2009) Solid State Sci 11:485
13. Trojan M, Brandová D (1990) Thermochim Acta 161:11
14. Averbuch-Pouchat MT, Durif A (1996) Topics in phosphate Chemistry. World Scienctific, Singapore
15. Boonchom B, Thongkam M, Kongtaweelert S, Vittayakorn N (2009) J Alloys Compd 486:689
16. Boonchom B, Maensiri S, Youngme S, Danvirutai C (2008) Mater Chem Phys 109:404
17. Boonchom B, Maensiri S, Youngme S, Danvirutai C (2008) Ind Eng Chem Res 47:7642
18. Cullity BD (1977) Elements of X-ray diffraction, 2nd edn. Addison-Wesley Publishing, Massachusetts
19. Ramakrishnan V, Aruldhas G (1985) Infrared Phys 25:665
20. Ma H, Qi X-r, Maitani Y, Nagai T (2007) Int J Pharm 333:177
21. Gupta AK, Gupta M (2005) Biomaterials 26:3995

Materials Research Bulletin 44 (2009) 2206–2210

Contents lists available at ScienceDirect

Materials Research Bulletin

journal homepage: www.elsevier.com/locate/matresbu

Flower-like microparticles and novel superparamagnetic properties of new binary $Co_{1/2}Fe_{1/2}(H_2PO_4)_2{\cdot}2H_2O$ obtained by a rapid solid state route at ambient temperature

Banjong Boonchom [a,b,*], Montree Thongkam [c], Samart Kongtaweelert [c], Naratip Vittayakorn [b,d]

[a] King Mongkut's Institute of Technology Ladkrabang, Chumphon Campus, 17/1M. 6 Pha Thiew District, Chumphon 86160, Thailand
[b] Advanced Materials Science Research Unit, Department of Chemistry, Faculty of Science, King Mongkut's Institute of Technology Ladkrabang, Bangkok 10520, Thailand
[c] Department of Chemistry, Faculty of Science, King Mongkut's Institute of Technology Ladkrabang, Ladkrabang, Bangkok 10520, Thailand
[d] College of KMITL Nanotechnology, King Mongkut's Institute of Technology Ladkrabang, Bangkok 10520, Thailand

ARTICLE INFO

Article history:
Received 7 July 2009
Received in revised form 19 July 2009
Accepted 4 August 2009
Available online 12 August 2009

Keywords:
A. Inorganic compounds
Ceramics
B. Chemical synthesis
C. Infrared spectroscopy
Thermogravimetric analysis (TGA)
D. Magnetic properties

ABSTRACT

A new binary $Co_{1/2}Fe_{1/2}(H_2PO_4)_2{\cdot}2H_2O$ was synthesized by a simple, rapid and cost-effective method using $CoCO_3$–Fe(c)–H_3PO_4 system at ambient temperature. Thermal treatment of the obtained $Co_{1/2}Fe_{1/2}(H_2PO_4)_2{\cdot}2H_2O$ at 600 °C yielded as a binary cobalt iron cyclotetraphosphate $CoFeP_4O_{12}$. The FTIR and XRD results of the synthesized $Co_{1/2}Fe_{1/2}(H_2PO_4)_2{\cdot}2H_2O$ and its final decomposed product $CoFeP_4O_{12}$ indicate the monoclinic phases with space group $P2_1/n$ and $C2/c$, respectively. The particle morphologies of both binary metal compounds appear the flower-like microparticle shapes. Room temperature magnetization results show novel superparamagnetic behaviors of the $Co_{1/2}Fe_{1/2}(H_2PO_4)_2{\cdot}2H_2O$ and its final decomposed product $CoFeP_4O_{12}$, having no hysteresis loops in the range of ±10,000 Oe with the specific magnetization values of 0.045 and 12.502 emu/g at 10 kOe, respectively. The dominant physical properties of the obtained binary metal compounds ($Co_{1/2}Fe_{1/2}(H_2PO_4)_2{\cdot}2H_2O$ and $CoFeP_4O_{12}$) are compared with the single compounds ($M(H_2PO_4)_2{\cdot}2H_2O$ and $M_2P_4O_{12}$; where M = Co, Fe), indicating the presence of Co ions in substitution position of Fe ions.

1. Introduction

In recent years, a large number of inorganic natural or synthesized phosphates have the incremented use in order to supply the demands of industrial, commercial, scientific and heath sectors due to valuable physical–chemical properties and reactivity [1–4]. The metal phosphate compounds are divided by block unit as PO_4^{3-}, HPO_4^{2-}, $H_2PO_4^{-}$, $P_2O_7^{4-}$ and $P_4O_{12}^{4-}$ units, which have found widespread applications in catalysts and adsorbents, ion-exchange materials, solid electrolytes for batteries, in linear and non-linear optical components, chelating agents, tooth powder and doughs, artificial teeth and bones, corrosion-resistant coating, sewage purifying agents, glass-ceramics, refratories, fire extinguishers, cements, soap powders, biomaterials and implantates, forages for animals, superinonic conductors, piezo- and ferroelectrics, gas and moisture sensors, magnets, phosphors, detergents and high-quality fertilizers [5–11]. Synthesis of these materials by solid state reaction at ambient temperature and the morphology and architecture at microscale and nanoscale levels is a significant challenge, which attracts increased attention because of their conveniences and their strong influence on material properties.

Metal dihydrogenphosphate ($H_2PO_4^{-}$) group, one of the important metal phosphates, has found widespread applications according to above mentioned. Additionally, this metal dihydrogenphosphate group is transformed to metal cyclotetraphosphate ($P_4O_{12}^{4-}$) group by dehydration and polycondensation reactions at high temperature, which is advance material, such as ceramic pigment, catalyst and fertilizer [12–17]. Both metal dihydrogenphosphate and metal cyclotetraphosphate groups have received a great deal of attention due to simple, nontoxic and cheap synthetic routes and their friendly environment [5–11]. Consequently, in the last few years many works have been a successful attempt in the synthesis of metal (II) dihydrogenphosphate hydrates $M_{1-x}A_x(H_2PO_4)_2{\cdot}nH_2O$ (M and A = Mg, Ca, Mn, Fe, Co, Ni, Zn, or Cu; x = 0–1; n = 1–4) [12–17] and metal (II) cyclotetraphosphates $M_{2-y}A_yP_4O_{12}$ (y = 0–2) [15–17]. However, it is pertinent to synthesize binary metal dihydrogenphosphates, binary metal cyclotetraphosphates and their solid solutions. By varying the composition of the solid solution (within its homogeneity range), one can change its useful properties. So far, binary metal dihydrogen phosphates were synthesized from

* Corresponding author at: King Mongkut's Institute of Technology Ladkrabang, Chumphon Campus, 17/1M. 6 Pha Thiew District, Chumphon 86160, Thailand. Tel.: +66 7750 6422x4565; fax: +66 7750 6410.
E-mail address: kbbanjon@kmitl.ac.th (B. Boonchom).

0025-5408/$ – see front matter © 2009 Elsevier Ltd. All rights reserved.
doi:10.1016/j.materresbull.2009.08.007

corresponding metal(II) carbonates (or metal oxides) and phosphoric acid at low temperature (40–80 °C) with long time periods (>48 h) [15–17]. While binary metal cyclotetraphosphate was synthesized by mix of corresponding metal cyclotetraphosphates, then melting them together on platinum dishes in an electric furnace at high temperature (>900 °C) with long time consumption (>5 h). However, binary metal cobalt iron dihydrogenphosphate and it decomposed product has not been reported in the literature.

The purpose of this work is to prepare new binary $Co_{1/2}Fe_{1/2}(H_2PO_4)_2{\cdot}2H_2O$ by solid state reaction at ambient temperature with short time consumption (<15 min). Thermal transformation product of the synthesized sample is binary cobalt iron cyclotetraphosphate $CoFeP_4O_{12}$. The synthesized powders of $Co_{1/2}Fe_{1/2}(H_2PO_4)_2{\cdot}2H_2O$ and its thermal transformation $CoFeP_4O_{12}$ with flower-like microparticles and novel superparamagnetic properties were characterized by thermogravimetry–differential thermal gravimetry–differential thermal analysis (TG–DTG–DTA), X-ray diffraction (XRD), scanning electron microscopy (SEM), Fourier transform IR (FTIR), and vibrating sample magnetometer (VSM) techniques for the first time.

2. Experimental

2.1. Preparation

All chemicals (analytical grade or chemically pure grade) were purchased from Fluka and Merck. Following procedure, 4 mL of 70% H_3PO_4 (86.4% (w/w) H_3PO_4 dissolved in DI water) was added to 1.1893 g of $CoCO_3$ and 0.5593 g of Fe(c) (a mole ratio corresponding to the nominal composition of Fe:Co ratio of 1.0:1.0), the resulting suspension was continuously stirred at ambient temperature until CO_2(g) was completely evolved and the precipitates were obtained. For this procedure, the increasing temperature of the precipitates from exothermic process was cooled to room temperature. The nearly dry sample was obtained and then 10 mL of acetone was added to allow highly crystalline product to be developed. The prepared solid was filtered by suction pump, washed with acetone and dried in air.

2.2. Characterization

Thermal property of the studied compound was investigated on a TG–DTG–DTA Pyris Diamond Perkin Elmer Instruments. The experiment was performed in dynamic air at heating rate of 10 °C min^{-1} over the temperature range from 30 to 600 °C and the flow rate of 100 mL min^{-1}. Its final decomposition product seemed to occur at temperatures above 500 °C (Fig. 1). In order to gain its final thermal transformation product, the obtained $Co_{1/2}Fe_{1/2}(H_2PO_4)_2{\cdot}2H_2O$ was heated in the furnace at 600 °C for 3 h and the thermal transformation products was further investigated. The cobalt and iron contents were determined by dissolving in 0.0126 M hydrochloric acid using atomic absorption spectrophotometry (AAS, Perkin Elmer, Analyst100). The phosphorus content was determined by colorimetric analysis of the molybdophosphate complex. The water content was determined by TG data. The structure and crystallite size of the synthesized $Co_{1/2}Fe_{1/2}(H_2PO_4)_2{\cdot}2H_2O$ and the thermal transformation products were studied by X-ray powder diffraction using a X-ray diffractometer (Phillips PW3040, The Netherlands) with Cu Kα radiation (λ = 0.15406 nm). The Scherrer method was used to evaluate the crystallite size [18]. The morphologies were examined with scanning electron microscope (SEM) using LEO SEM VP1450 after gold coating. The room temperature FTIR spectra were recorded in the range of 4000–370 cm^{-1} with 8 scans on a Perkin-Elmer Spectrum GX FTIR/FT-Raman spectrometer with the resolution of 4 cm^{-1} using KBr pellets (KBr, spectroscopy grade, Merck). The magnetic properties were examined at room temperature (20 °C) using a vibrating sample magnetometer (VSM 7403, Lake Shore, USA).

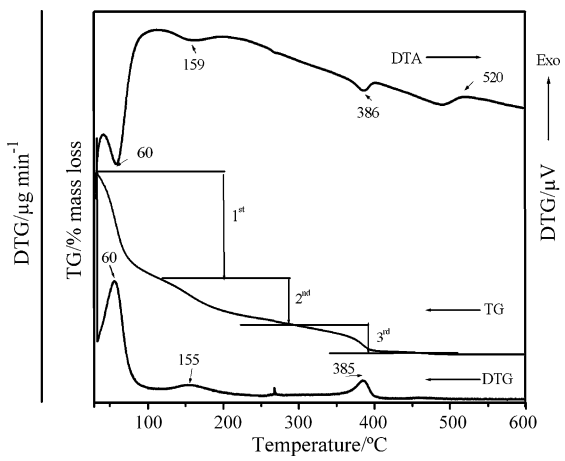

Fig. 1. TG–DTG–DTA curves of $Co_{1/2}Fe_{1/2}(H_2PO_4)_2{\cdot}2H_2O$.

3. Results and discussion

3.1. Thermal analysis

The TG/DTG/DTA curves of $Co_{1/2}Fe_{1/2}(H_2PO_4)_2{\cdot}2H_2O$ are shown in Fig. 1. The TG curve shows the mass loss between 30 and 600 °C, which is related to the elimination of water molecules in crystallization water and an intermolecular phosphate condensation. The eliminations of water were observed in three areas: 45–130, 130–300 and 300–450 °C. The mass losses in three stages are 12.80, 7.42 and 5.61%, which correspond to 2.04, 1.18 and 0.89 mol of water for $Co_{1/2}Fe_{1/2}(H_2PO_4)_2{\cdot}2H_2O$, respectively. The DTA curve shows three endothermic effects over the temperature region at 60, 159 and 386 °C whereas the DTG curve shows three peaks at 60, 155, and 385 °C. Further, a small exothermic effect at 520 °C without appreciable mass loss is observed in the DTA curve, which can be ascribed to a transition phase from of $CoFeP_4O_{12}$. The thermal decomposition of $Co_{1/2}Fe_{1/2}(H_2PO_4)_2{\cdot}2H_2O$ in the range of 30–600 °C involves the dehydration of the coordination water molecules (2 mol H_2O) and an intramolecular dehydration of the protonated dihydrogenphosphate groups (2 mol H_2O) as shown in Eqs. (1)–(3):

$$Co_{1/2}Fe_{1/2}(H_2PO_4)_2{\cdot}2H_2O \rightarrow Co_{1/2}Fe_{1/2}(H_2PO_4)_2 + 2H_2O \quad (1)$$

$$Co_{1/2}Fe_{1/2}(H_2PO_4)_2 \rightarrow Co_{1/2}(H_2PO_4)\cdot[1/4Fe_2P_4O_{12}] + 1H_2O \quad (2)$$

$$Co_{1/2}(H_2PO_4)\cdot[1/4Fe_2P_4O_{12}] \rightarrow 1/2CoFeP_4O_{12} + 1H_2O \quad (3)$$

The intermediate compounds, such as acid polyphosphate $Co_{1/2}Fe_{1/2}(H_2PO_4)_2$ and $Co_{1/2}(H_2PO_4){\cdot}[1/4Fe_2P_4O_{12}]$ and mixture of both intermediates have been registered. $Co_{1/2}(H_2PO_4){\cdot}[1/4Fe_2P_4O_{12}]$ is observed in Eq. (2) due to $Fe_2P_4O_{12}$ is formed at lower temperature than $Co_2P_4O_{12}$, which related to thermal transformation of single dihydrogenphosphate dihydrate in our previous works [19,20]. The intermediates were similarly observed with single metal dihydrogen phosphate [9,10,12–15]. The binary cobalt iron cyclotetraphosphate, $CoFeP_4O_{12}$ is found to be the final product of the thermal decomposition at $T > 500$ °C. The total mass loss is 25.83% (4.12 mol H_2O), which is in agreement with those reported for other binary dihydrogenphosphate dihydrate in the literature ($1 <$ mole of water < 4) [9,10,12–15]. The thermal stability, mechanism and phase transition temperature of the studied compound in this work are significantly different from

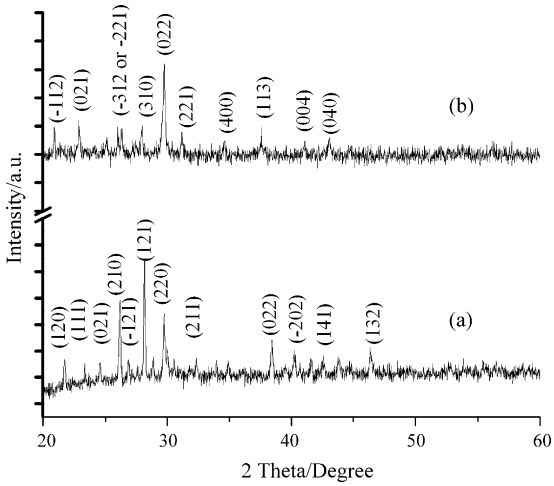

Fig. 2. XRD patterns of $Co_{1/2}Fe_{1/2}(H_2PO_4)_2{\cdot}2H_2O$ (a) and its decomposed product $CoFeP_4O_{12}$ (b).

those of the decomposition reactions of individual metal compounds ($Fe(H_2PO_4)_2{\cdot}2H_2O$ [19] and $Co(H_2PO_4)_2{\cdot}2H_2O$ [20]). These results indicate that the incorporation of Fe and Co metals in the skeleton has the effects of thermal behaviors, which support the formations of new binary dihydrogen phosphate $Co_{1/2}Fe_{1/2}(H_2PO_4)_2{\cdot}2H_2O$ and binary metal cyclotetraphosphate $CoFeP_4O_{12}$.

3.2. X-ray powder diffraction

The XRD patterns of $Co_{1/2}Fe_{1/2}(H_2PO_4)_2{\cdot}2H_2O$ and its decomposed product $CoFeP_4O_{12}$ are similar to those obtained from the individual $M(H_2PO_4)_2{\cdot}2H_2O$ and $M_2P_4O_{12}$ (when M = Co and Fe) but the intensities are slightly different (Fig. 2). The spectrum peaks for the systems of binary cobalt iron solid solution and single metal dihydrogen phosphate (or metal cyclotetraphosphate) are quite similar due to the electronic charges and the radii of cations are equivalent and close to each other, respectively [13–17]. According to the XRD analysis, we can draw a conclusion that the synthesized $Co_{1/2}Fe_{1/2}(H_2PO_4)_2{\cdot}2H_2O$ and its decomposed product $CoFeP_4O_{12}$ are solid solutions and not a mixture of the individual ones. In addition, the result confirmed that new binary metal ($Co_{1/2}Fe_{1/2}(H_2PO_4)_2{\cdot}2H_2O$ and $CoFeP_4O_{12}$) are isostructural to type series of the single metal ($M(H_2PO_4)_2{\cdot}H_2O$ and $M_2P_4O_{12}$; where M or A = Mg, Mn, Co, Ni, Fe, Zn). All the reflections can be distinctly indexed as a pure monoclinic phase with space group $P2_1/n$ ($Z = 2$) for $Co_{1/2}Fe_{1/2}(H_2PO_4)_2{\cdot}2H_2O$ and $C2/c$ ($Z = 4$) for the decomposed products $CoFeP_4O_{12}$, which noted to be similar to those of standard data of $M(H_2PO_4)_2{\cdot}H_2O$ (PDF no 390698 for Co and PDF no 751444 for Fe) and $M_2P_4O_{12}$ (PDF no 842208 for Co and PDF no 782285 for Fe), respectively. The average crystallite sizes and lattice parameters of $Co_{1/2}Fe_{1/2}(H_2PO_4)_2{\cdot}2H_2O$ and the decomposed product $CoFeP_4O_{12}$ were calculated from XRD patterns and also tabulated in Table 1. The lattice parameters of $Co_{1/2}Fe_{1/2}(H_2PO_4)_2{\cdot}2H_2O$ and the decomposed products $CoFeP_4O_{12}$ are comparable to those of the standard data of individual ones. The average crystallite sizes of $Co_{1/2}Fe_{1/2}(H_2PO_4)_2{\cdot}2H_2O$ and the decomposed product $CoFeP_4O_{12}$ were found to be 77 ± 27 and 73 ± 18 nm, respectively. However, the crystallite sizes for the obtained compounds in this work are larger than those from the single metal compounds (Table 1) in our previous works [13,14,18,19].

3.3. FTIR spectroscopy

The FTIR spectra of $Co_{1/2}Fe_{1/2}(H_2PO_4)_2{\cdot}2H_2O$ and the decomposed products $CoFeP_4O_{12}$ are shown in Fig. 3 and they are very similar to those of $M(H_2PO_4)_2{\cdot}2H_2O$ and $M_2P_4O_{12}$ (M = Co or Fe), which confirmed their isostructural. Vibrational bands are identified in relation to the crystal structure in terms of the fundamental vibrating units namely $H_2PO_4^-$ and H_2O for $Co_{1/2}Fe_{1/2}(H_2PO_4)_2{\cdot}2H_2O$ and $[P_4O_{12}]^{4-}$ ion for $CoFeP_4O_{12}$, which are assigned according to the literature [9,10,12–15,21,22].

The FTIR spectrum of $Co_{1/2}Fe_{1/2}(H_2PO_4)_2{\cdot}2H_2O$ (Fig. 3a) is very similar to those observed by Koleva et al. [10] and Boonchom et al. [19,20]. The highest site symmetry of $H_2PO_4^-$ ion is C_{2v}, in the crystallographic unit cell ($P2_1/n$, $Z = 2$) [10], but the four $H_2PO_4^-$ ions are located on the set of non-equivalent site symmetry of C_1. A pair of $H_2PO_4^-$ ions is related to each other by a center of symmetry. The four fundamental modes of the free phosphate ion undergo factor group splitting [22]. It is known that the existence of short OH···O hydrogen bonds in a variety of strongly hydrogen-bonded solids is manifested by the appearance of the characteristic *ABC* structure of the ν(OH) vibrational bands [9,10]. The problem of the origin of the *ABC* trio is discussed in many studies on acidic salts, but an explanation of this behaviour of strongly hydrogen-bonded systems is still to be found [9,10]. One of the most popular interpretations of the *ABC* trio suggests a strong Fermi resonance between the ν(OH) stretching fundamentals and the overtones [2δ(OH) and 2γ(OH)] or combinations involving the δ(OH) and γ(OH) vibrations. Usually, the *ABC* bands are very broad and consist of many ill-resolved components. Two bands centered at 3138 and 2427 cm^{-1} in the FTIR spectra are referred to as bands A and B, respectively. The third component (band C) is observed around 1749–1639 cm^{-1}. The intense band at about 1260 cm^{-1} is due to the in plane P–O–H bending (A_2), while the out of plane bending (A_1) vibration is observed at about 816 cm^{-1}. Vibrational spectra of present hydrate are assigned by factor group analysis and derived from the same mode as in free $H_2PO_4^-$ ion. A strong band at about

Table 1
Average crystallite sizes and lattice parameters of $Co_{1/2}Fe_{1/2}(H_2PO_4)_2{\cdot}2H_2O$ and its decomposed product $CoFeP_4O_{12}$ calculated from XRD data.

Compound	Method	*a* (Å)	*b* (Å)	*c* (Å)	*β* (°)	Average particle sizes (nm)
$Co(H_2PO_4)_2{\cdot}2H_2O$	PDF no 390698	7.27	9.88	5.33	94.86	
	Ref. [20]	7.21(3)	9.91(1)	5.29(5)	94.88(6)	26 ± 2
$Co_{1/2}Fe_{1/2}(H_2PO_4)_2{\cdot}2H_2O$	This work	7.30(0)	9.92(0)	5.35(1)	95.01(2)	77 ± 27
$Fe(H_2PO_4)_2{\cdot}2H_2O$	PDF no 751444	7.30	9.92	5.34	95.14	–
	Ref. [19]	7.25(1)	10.10(0)	5.32(0)	95.71(0)	28 ± 4
$Co_2P_4O_{12}$	PDF no 842208	11.8	8.297	9.923	118.72	
	Ref. [20]	11.83(8)	8.22(6)	9.94(0)	118.51(1)	40 ± 10
$CoFeP_4O_{12}$ (calcined 600 °C)	This work	11.77(3)	8.56(0)	9.63(1)	119.09(0)	73 ± 18
$Fe_2P_4O_{12}$	PDF no 782285	11.94	8.37	9.93	118.74	–
	Ref. [19]	12.80(0)	8.80(4)	10.56(0)	118.67(4)	29 ± 6

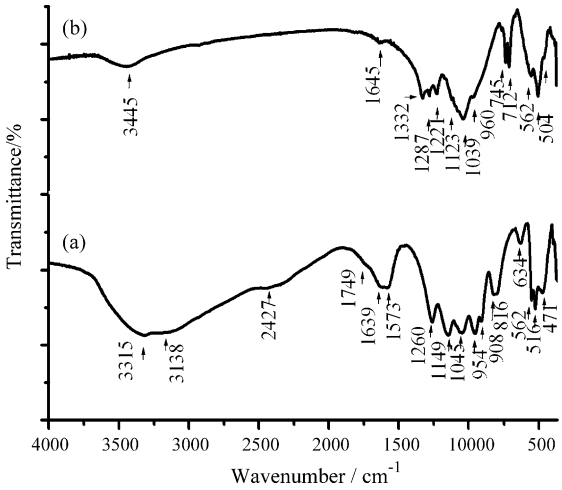

Fig. 3. FTIR spectra of $Co_{1/2}Fe_{1/2}(H_2PO_4)_2{\cdot}2H_2O$ (a) and its decomposed product $CoFeP_4O_{12}$ (b).

1149 cm^{-1} in FTIR spectra is assigned to PO_2 asymmetric stretching (B_1), while the other one at about 1045 cm^{-1} corresponds to PO_2 symmetric stretching modes (A_1). The FTIR frequency of the $P(OH)_2$ asymmetric stretching (B_2) shows the strong band at about 954 cm^{-1}. The weak band at about 908 cm^{-1} is assigned to $P(OH)_2$ symmetric stretching modes (A_1). The medium band at about 562 cm^{-1} is corresponding to PO_2 bending modes (B_1). Two strong bands appeared at about 516 and 471 cm^{-1} are attributed to PO_2 rocking modes as B_1 and A_2 vibrations, respectively. The bands of water vibrations are illustrated in Fig. 3a as a doublet bands (1639 and 1573 cm^{-1}) contribute both to the band C and to the water bending band. A weak band occurs in the FTIR spectra at approximately 634 cm^{-1} is assigned to rocking mode involving water librations. The ν_{OH} stretching modes of HOH in $Co_{1/2}Fe_{1/2}(H_2PO_4)_2{\cdot}2H_2O$ appear at 3138 cm^{-1} (ν_1 or A band) and 3315 cm^{-1} (ν_3). The bands associated with the ν_{OH} stretching frequencies in $H_2PO_4^-$ ions are observed at about 2850 and 2427 cm^{-1}.

The FTIR spectrum of the decomposed product $CoFeP_4O_{12}$ (Fig. 3b) is very similar to those obtained from the individual $M_2P_4O_{12}$ (M = Co and Fe) [13,14,18,19]. The band assignment is identified in terms of the fundamental vibrating modes of $P_4O_{12}^{4-}$ ion in the frequency range of 370–1400 cm^{-1}, which are assigned according to the literature [13,14,18,19]. The anion contains the PO_2^{2-} radical and the P–O–P bride, where are interpreted the FTIR spectra from viewpoint of the vibrations of these two groups. As the P–O bond strength in the P–O–P bride is weaker than in the PO_2^{2-} radical, the stretching frequencies of the P–O–P bride are expected to be lower than those in the PO_2^{2-} radical. The asymmetric and symmetric stretching frequencies of the PO_2^{2-} radical are generally observed in the areas 1325–1227 and 1151–1100 cm^{-1}, respectively. The P–O–P bride has its asymmetric and symmetric stretching frequencies around 1000–900 and 900–700 cm^{-1}, respectively. The bending modes are expected in the area: 600–400 cm^{-1} (PO_2^{2-} radical) and 400–370 cm^{-1} (P–O–P bride). The metal-O stretching usually appears in the bending mode region as the bending modes of the P–O–P bride and absorption bands associated with these vibrations are usually very weak. The observation of a strong ν_sPOP band is known to be the most striking feature of cyclotetraphosphate spectra, along with the presence of the $\nu_{as}OPO^-$ band. From X-ray diffraction data [10], it was shown that the crystal structure is monoclinic (space group $C2/c$) with a cyclic structure of the $[P_4O_{12}]^{4-}$ anion. This has been confirmed by the FTIR measurements.

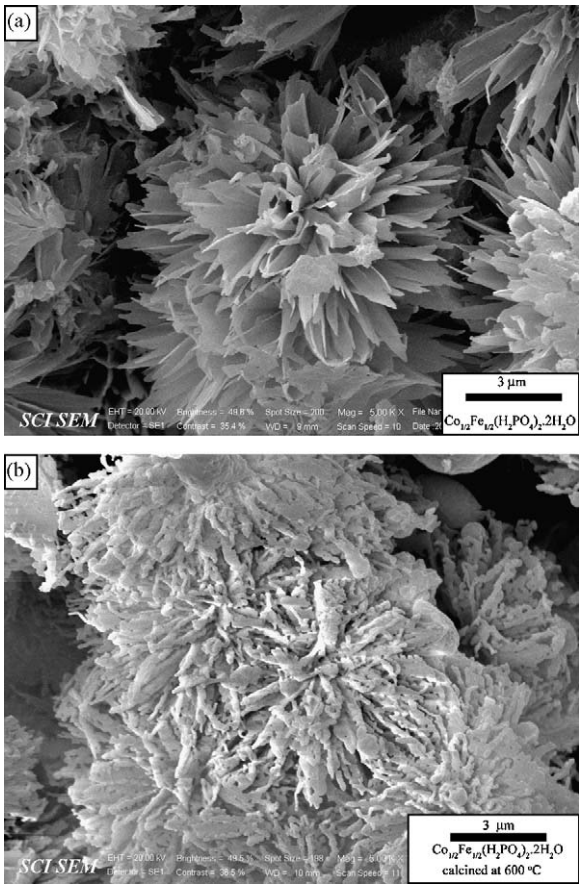

Fig. 4. SEM micrographs of $Co_{1/2}Fe_{1/2}(H_2PO_4)_2{\cdot}2H_2O$ (a) and its decomposed product $CoFeP_4O_{12}$ (b).

3.4. Scanning electron microscopy

The SEM micrographs of $Co_{1/2}Fe_{1/2}(H_2PO_4)_2{\cdot}2H_2O$ and the decomposed product $CoFeP_4O_{12}$ are shown in Fig. 4. The particle shape and size are changed throughout the whole decomposition product. The SEM micrographs of $Co_{1/2}Fe_{1/2}(H_2PO_4)_2{\cdot}2H_2O$ and the decomposed product $CoFeP_4O_{12}$ show flower-like architectures, having sizes of 15–20 μm. The morphology of $Co_{1/2}Fe_{1/2}(H_2PO_4)_2{\cdot}2H_2O$ (Fig. 4a) shows petal-bud-like microparticles, which exhibit the different features from $Co(H_2PO_4)_2{\cdot}2H_2O$ and $Fe(H_2PO_4)_2{\cdot}2H_2O$ in the our previous reports [13,14,18,19]. The morphology of the decomposed product $CoFeP_4O_{12}$ (Fig. 4b) shows filament-like structures and porosity on the filament surface, which are significant different grain from single metal cyclotetraphosphate ($M_2P_4O_{12}$; M = Mn or Fe) in our previous reports [13,14,18,19]. The different morphologies between the single metal compounds ($M(H_2PO_4)_2{\cdot}2H_2O$ and $M_2P_4O_{12}$, M = Co or Fe) and the binary metal compounds confirm the formation of $Co_{1/2}Fe_{1/2}(H_2PO_4)_2{\cdot}2H_2O$ and $CoFeP_4O_{12}$, which support the presence of Co ions in substitution position of Fe ions.

3.5. VSM magnetometer

The specific magnetization curves of $Co_{1/2}Fe_{1/2}(H_2PO_4)_2{\cdot}2H_2O$ and the decomposed product $CoFeP_4O_{12}$ obtained from room temperature VSM measurements are shown in Fig. 5. All samples demonstrate typical superparamagnetic behavior with negligible coercivity and remanence, in accordance with the theory that superparamagnetic behavior is often observed at room temperature. The specific magnetization curves are typical superparamagnetic

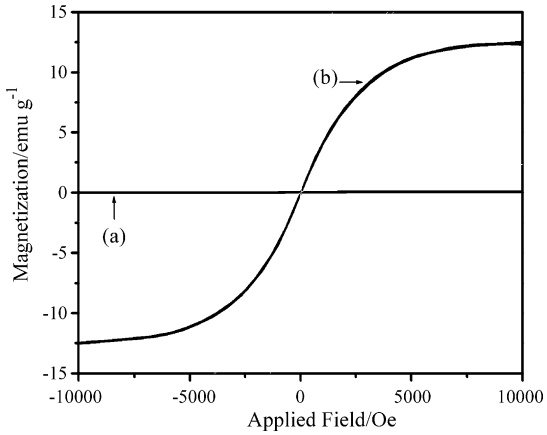

Fig. 5. The specific magnetizations of $Co_{1/2}Fe_{1/2}(H_2PO_4)_2{\cdot}2H_2O$ (a) and its decomposed product $CoFeP_4O_{12}$ (b) as a function of field, measured at 293 K.

behavior without any hysteresis in the field range of ±10,000 Oe. Specific saturated magnetization (M_s) values of $Co_{1/2}Fe_{1/2}(H_2PO_4)_2{\cdot}2H_2O$ and the decomposed product $CoFeP_4O_{12}$ are found to be 0.045 and 12.502 emu/g, respectively. It is worth nothing that these saturated magnetizations were compared with other magnetic materials (M_s of Fe_3O_4 is 10–50 emu/g) [23–25]. It is seen that magnetizations of the $Co_{1/2}Fe_{1/2}(H_2PO_4)_2{\cdot}2H_2O$ and $CoFeP_4O_{12}$ are lower than those of $Fe(H_2PO_4)_2{\cdot}2H_2O$ (96.28 emu/g) and $Fe_2P_4O_{12}$ (85.01 emu/g) [20] but markedly distinct from the diamagnetic properties of $Co(H_2PO_4)_2{\cdot}2H_2O$ and $Co_2P_4O_{12}$ [19]. To our knowledge, it is worth nothing that superparamagnetic properties of the $Co_{1/2}Fe_{1/2}(H_2PO_4)_2{\cdot}2H_2O$ and $CoFeP_4O_{12}$ samples are reported for the first time in this study.

4. Conclusion

Flower-like microparticle $Co_{1/2}Fe_{1/2}(H_2PO_4)_2{\cdot}2H_2O$ was successfully synthesized by solid state method from $CoCO_3$–Fe–H_3PO_4 system at ambient temperature with short time consumption (15 min). $Co_{1/2}Fe_{1/2}(H_2PO_4)_2{\cdot}2H_2O$ decomposes in three steps which correspond to the loss of water of crystallization in the first step, subsequently to a continuous intermolecular polycondensation and elimination of water of constituent in anion (the second and the third steps). The thermal behaviors, flower-like morphologies, particle sizes and superparamagnetic properties of $Co_{1/2}Fe_{1/2}(H_2PO_4)_2{\cdot}2H_2O$ and the thermal transformation products $CoFeP_4O_{12}$ in this work are different from single metal compounds in our previous reports. This work presents the simple, cost-effective and short time consuming method for the preparation of new binary metal $Co_{1/2}Fe_{1/2}(H_2PO_4)_2{\cdot}2H_2O$ and $CoFeP_4O_{12}$ compounds, which may be used in many important applications such as catalytic, superinonic conductors, piezo- and ferroelectrics, magnets, electrochemical, bioceramic and environmental processes.

Acknowledgements

The authors would like to thank the Chemistry Department, Khon Kaen University for facilities. This work is financially supported by the Thailand Research Fund (TRF) and the Commission on Higher Education (CHE): Research Grant for New Scholar and King Mongkut's Institute of Technology Ladkrabang Research (KMITL Research), Ministry of Education, Thailand.

References

[1] A. Durif, Solid State Sci. 7 (2005) 760.
[2] H. Onoda, K.-I. Okumoto, I. Tanaka, Mater. Chem. Phys. 107 (2008) 339.
[3] S.-L. Yang, H. Zhang, Z. Xie, D. Zhao, W.-L Zhang, W.-D. Cheng, J. Solid State Chem. 182 (2009) 855.
[4] T. Dammak, N. Fourati, Y. Abid, A. Mlayah, C. Minot, J. Mol. Struct. 852 (2008) 83.
[5] T. Kitsugi, T. Yamamuro, T. Nakamura, M. Oka, Biomaterials 16 (1995) 1101.
[6] B. Jian-Jiang, K. Dong-Wan, H. Kug Sun, J. Eur. Ceram. Soc. 23 (2003) 2589.
[7] I.-C. Marcu, I. Sandulescu, Y. Yves Schuurman, J.-M.M. Millet, Appl. Catal. A. 334 (2008) 207.
[8] M. Kaplanová, M. Trojan, D. Brandová, J. Navrátil, J. Lumin. 29 (1984) 199.
[9] B. Boonchom, S. Maesiri, S. Youngme, C. Danvirutai, Solid State Sci. 11 (2009) 485.
[10] V. Koleva, H. Effenberger, J. Solid State Chem. 180 (2007) 956.
[11] Y. Tang, H.F. Chappell, M.T. Dove, R.J. Reeder, Y.J. Lee, Biomaterials 30 (2009) 2864.
[12] M. Trojan, P. Šulcová, Dyes Pigments 47 (2000) 291.
[13] B. Boonchom, S. Maensiri, C. Danvirutai, Mater. Chem. Phys. 109 (2008) 404.
[14] B. Boonchom, C. Danvirutai, Ind. Eng. Chem. Res. 47 (2008) 2941 (and references therein).
[15] N.M. Antraptseva, L.N. Shchegrov, I.G. Ponomareva, Russ. J. Inorg. Chem. 51 (2006) 1493.
[16] M. Trojan, P. Šulcová, P. MoŠner, Dyes Pigments 44 (2000) 161.
[17] D. Brandová, M. Trojan, F. Paulik, J. Paulik, M. Arnold, J. Therm. Anal. Calorimet. 36 (1990) 881.
[18] B.D. Cullity, Elements of X-ray Diffraction, 2nd ed., Addison-Wesley Publishing, 1977.
[19] B. Boonchom, C. Danvirutai, J. Chem. Eng. Data 54 (2009) 1225.
[20] B. Boonchom, C. Danvirutai, S. Youngme, S. Maensiri, Ind. Eng. Chem. Res. 47 (2008) 7642.
[21] N.B. Colthup, L.H. Daly, S.E. Wiberley, Introduction to Infrared and Raman Spectroscopy, Academic Press, New York, 1964.
[22] G. Herzberg Molekülspektren und Molekülstruktur. I. Zweiatomige Moleküle., Steinkopff, Dresden, 1939.
[23] E.H. Soumhi, I. Saadoune, A. Driss, J. Solid State Chem. 56 (2001) 364.
[24] J. Tang, M. Myers, K.A. Bosnick, L.E. Brus, J. Phys. Chem. B 107 (2003) 7501.
[25] A.K. Gupta, M. Gupta, Biomaterials 26 (2005) 3995.

Materials Letters 64 (2010) 275–277

Contents lists available at ScienceDirect

Materials Letters

journal homepage: www.elsevier.com/locate/matlet

Synthesis and ferromagnetic property of new binary copper iron pyrophosphate $CuFeP_2O_7$

Banjong Boonchom [a,b,*], Naratip Vittayakorn [b,c]

[a] King Mongkut's Institute of Technology Ladkrabang, Chumphon Campus, 17/1 M. 6 Pha Thiew District, Chumphon, 86160, Thailand
[b] Advanced Materials Science Research Unit, Department of Chemistry, Faculty of Science, King Mongkut's Institute of Technology Ladkrabang, Bangkok 10520, Thailand
[c] College of KMITL Nanotechnology, King Mongkut's Institute of Technology Ladkrabang, Bangkok 10520, Thailand

ARTICLE INFO

Article history:
Received 28 September 2009
Accepted 26 October 2009
Available online 30 October 2009

Keywords:
$CuFeP_2O_7$
New binary pyrophosphate
Synthesis
Ferromagnetic

ABSTRACT

The pyrophosphate of $CuFeP_2O_7$ was synthesized through one step-thermal synthesis at 500 °C using the mixing of copper carbonate, iron metals and phosphoric acid. FTIR and XRD results indicate the dominant feature of pyrophosphate ($P_2O_7^{4-}$) anion and a pure monoclinic phase with space group C_{2h}^6 ($Z=4$), respectively. The crystallite size of 25 ± 9 nm for the $CuFeP_2O_7$ was estimated by X-ray line broadening. Room temperature magnetization result shows ferromagnetic behavior of the $CuFeP_2O_7$ powder, having hysteresis loop in the range of $\pm$10,000 Oe with the specific magnetization value of 1.57 emu g^{-1}. This property is important for specific application and is presented for the first time.

1. Introduction

Binary metal (II) pyrophosphates consisting of a homogeneous solid solution are characterized by high corrosion resistance, high tensile strengths, improved ductility and good malleability as compared with the corresponding single metals [1,2]. These materials are widely employed in various fields as catalysts, wastewater purification systems, ferroelectrics, lithium batteries, the steel and glass industries [2–4]. In the recent years, they have been proposed as the cathode in lithium batteries and lithium metal phosphates can be used as cathode or anode electrodes in lithium batteries because they are the next generation of positive-electrode materials for lithium batteries and offer additional advantages in practical applications due to their lower cost, safety, benign environmental properties, stability and low toxicity [5,6]. The binary metal $M_{2-x}A_xP_2O_7$ (M or A = Mg, Mn, Co, Cu, Ni, Fe, Zn; $0<x<2$) group, one of the important metal phosphates, has found widespread applications and is graining interesting according to above mentioned [7]. Because it appears economically advantageous to substitute a portion of the divalent metal with a less costly divalent element, which influences many properties, for example, the color of pigments, the relatively stable compounds—both thermally and chemically, anticorrosion ability and luminescence [1–4]. In addition, some metals, such as copper or iron, and $(P_2O_7)^{4-}$ species are lower cost, safety, benign environmental properties and low toxicity [5,7]. Therefore, our laboratory has focused on the studies of the synthesis of new binary metal pyrophosphates [8,9], which are important for the development of new inorganic functional materials.

The present paper describes the synthesis and characterization of a new binary copper iron pyrophosphate, $CuFeP_2O_7$ using powder X-ray diffraction (XRD), Fourier transform infrared (FTIR) and vibrating magnetometric (VSM) techniques. The information on the synthesis and characterization of a new binary copper iron pyrophosphate, $CuFeP_2O_7$ are reported for the first time.

2. Experimental

All the reagents used in this study were of A.R. grade. In typical procedure, $CuCO_3$ and Fe (complexometric) were mixed together with mole ratio of 1.0:1.0 and then was ground for 10 min. Subsequently, 5 mL of 70 % H_3PO_4 (86.4 %w/w H_3PO_4 dissolved in DI water) was added slowly to the mixed solid with mechanically stirring at ambient temperature (10 min). Then, the mixed suspension was evaporated by heating in the furnace at 500 °C for 2 h. The obtained gray pink precursor was crushed into powder, which was washed repeatedly by DI water until no PO_4^{3-} was detected. Finally, the powder was washed again for several times with methanol and dried at room temperature. The reaction equation can be expressed as:

$$CuCO_3(s) + Fe(s) + 2H_3PO_4(aq) \rightarrow CuFeP_2O_7(s) + 3H_2O(g) + CO(g) \quad (1)$$

The copper and iron contents of $CuFeP_2O_7$ were determined by dissolving in 0.0126 M hydrochloric acid using atomic absorption

* Corresponding author. King Mongkut's Institute of Technology Ladkrabang, Chumphon Campus, 17/1 M. 6 Pha Thiew District, Chumphon, 86160, Thailand. Tel.: +66 7750 6422x4565; fax: +66 7750 6410.
E-mail address: kbbanjon@kmitl.ac.th (B. Boonchom).

0167-577X/$ – see front matter © 2009 Elsevier B.V. All rights reserved.
doi:10.1016/j.matlet.2009.10.058

spectrophotometry (AAS, Perkin Elmer, Analyst100). The phosphorus content was determined by colorimetric analysis of the molybdophosphate complex. X-ray powder diffraction (XRD) was carried out by a Phillips PW3040 X-ray diffractometer (The Netherland) utilizing Cu Kα radiation (λ = 0.15406 nm) at 40 kV/200 mA. The Scherrer method was used to evaluate the crystallite size [10]. The room temperature FTIR spectrum in the range of 4000–370 cm^{-1} was recorded by a Perkin-Elmer Spectrum GX FT-IR/FT-Raman spectrometer with 8 scans and the resolution of 4 cm^{-1} using KBr pellets. The magnetic property was examined at room temperature (20 °C) using a vibrating sample magnetometer (VSM 7403, Lake Shore, USA).

3. Results and discussion

The XRD pattern of $CuFeP_2O_7$ is similar to those obtained from the individual $M_2P_2O_7$ (when M = Cu, Co, Mn and Fe) [1–4,11], but the intensities are slightly different (Fig. 1). The lower and higher intensities of XRD peaks indicate the differences of crystallization or amorphous phase as well as crystallite sizes of these materials. From literature, it indicates that the binary solid solutions ($M_{2-x}A_xP_2O_7$) and the single metal compounds for $M_2P_2O_7$ (M or A = Mg, Mn, Co, Cu, Ni, Fe, Zn; $0<x<2$) types are isostructural [1–4,11]. In the hypothesis of isostructural, the spectrum peaks for the systems of binary copper iron pyrophosphate (solid solution) and single metal pyrophosphate ($M_2P_2O_7$, M = Cu and Fe) are quite similar because of the equivalent electronic charges and the close radii of cations. In addition, no characteristic peaks of other impurities ($CuCO_3$ or Fe) were observed. In this respect, we can draw a conclusion that the synthesized product $CuFeP_2O_7$ is solid solution and not a mixture of the individual ones. Consequently, all reflections can be distinctly indexed based on a pure monoclinic phase with space group C2/c ($Z=4$) for $CuFeP_2O_7$, which noted to be similar to those of the standard XRD patterns of $M_2P_2O_7$ (PDF no. 79-2075 for Cu and PDF no.76-1762 for Fe), respectively. The average crystallite size of product is estimated from the strongest three diffraction peaks below 40° for 2θ and found to be 25 ± 9 nm. The lattice parameters calculated from the XRD spectra are $a=6.73$ (0), $b=8.21(1)$, $c=9.39(0)$ Å and $b=110.65(4)$ °, which are close to those of the standard data file ($a=6.89$ (5), $b=8.11(3)$, $c=9.16(4)$ Å and $b=109.62(0)$ ° from PDF no. 79-2075 for $Cu_2P_2O_7$ and $a=6.65$ (0), $b=8.48(4)$, $c=4.49(0)$ Å and $b=103.89(0)$ ° from PDF no.76-1762 for $Fe_2P_2O_7$) and the literature [11,12].

FTIR spectrum of $CuFeP_2O_7$ shown in Fig. 2 is very similar to those obtained from the single metal pyrophosphates $M_2P_2O_7$ (M = Mn, Ni, Co and Fe) [7–9,12,14]. The vibrational modes of $P_2O_7^{4-}$ ion observed in the frequency range of 370–1400 cm^{-1} are assigned according to the literature [7–9,13,14]. The anion containing the PO_3 and the P–O–P bride are interpreted the FTIR spectrum from viewpoint of the vibrations of these two groups. The asymmetric and symmetric stretching frequencies of the PO_3 are generally observed at 1097 and 1067 cm^{-1}, respectively. The bending modes of PO_3 are expected in the range of 592–518 cm^{-1}. The metal-O stretching usually appears in the bending mode region as the bending modes of the PO_3 and absorption bands associated with these vibrations are usually very weak. The bands found at 955 and 739 cm^{-1} are typical of the pyrophosphate group and correspond to the stretching and bending vibrations of the P–O–P bridge, respectively. The observation of a strong ν_{as}POP band is known to be the most striking feature of pyrophosphate spectra, along with the presence of the $\nu_{as}OPO^-$ band. The PO_3 deformation and rocking modes, the POP deformations as well as the torsional and external modes are found in the 592–410 cm^{-1} region. FTIR result is consistent with X-ray data [15], indicating that the crystal structure is monoclinic (space group C2/c) with pyrophosphate groups of the $[P_2O_7]^{4-}$ anion.

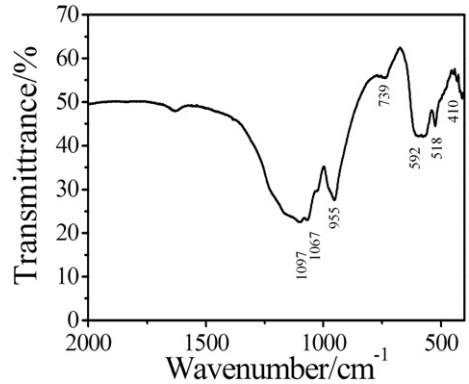

Fig. 2. FTIR spectrum of $CuFeP_2O_7$.

The specific magnetization curve of the $CuFeP_2O_7$ sample obtained from room temperature VSM measurement is shown in Fig. 3. This curve is typical for a soft magnetic material and indicates hysteresis ferromagnetism in the field range of ~ ± 10,000 Oe while outside this range the specific magnetization increases with increasing field and saturates in the field range investigated (± 10 kOe). The specific saturation magnetization (M_s) value of 1.57 emu g^{-1} was observed for the $CuFeP_2O_7$ sample. The coercive force (Hc) obtained on the increasing and decreasing filed sides (blanket) were 67.70 (−67.70) Oe for the $CuFeP_2O_7$ sample. The ferromagnetic solid solution formed in $CuFeP_2O_7$ system is different from paramagnetic for $Fe_2P_2O_7$ and diamagnetic for $Cu_2P_2O_7$. The $CuFeP_2O_7$ called pyrophosphate constitutes the largest family of condensed phosphates and contains different cations (Cu^{2+} and Fe^{2+}) [15–18]. The ferromagnetic of the studied compound originates from magnetic moment of anti-parallel spins of between Cu^{2+} (non-magnetic element) at octahedral sites and Fe^{2+} (magnetic element) at distorted octahedral coordination

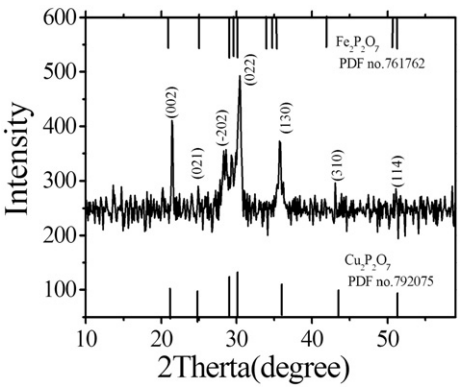

Fig. 1. XRD pattern of $CuFeP_2O_7$.

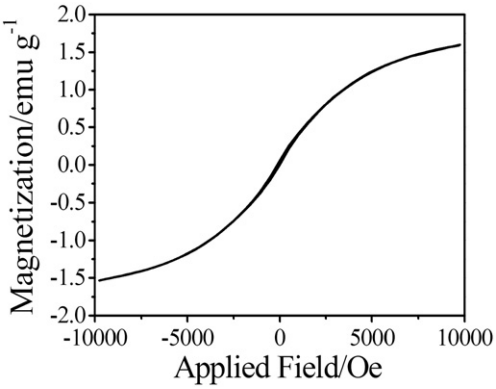

Fig. 3. The specific magnetization of $CuFeP_2O_7$ as a function of field, measured at 20 °C.

[17,18]. This should be necessary for the appearance of ferromagnetism [18]. Additionally, it found that the tendency of Ms to increase is consistent with the enhancement of crystallinity or particle sizes, and the saturation value of Ms for $CuFeP_2O_7$ is observed due to the obtained microstructure. This result has been essentially verified in a quantitative sense within the last two decades. Ferromagnetic property of the $CuFeP_2O_7$ sample reported for the first time is important for specific applications such as magnetic resonance imaging contrast agents, data lifetime in high density information storage, ferrofluid technology, lithium batteries and magnetocaloric refrigeration [15,16].

4. Conclusions

This research has successfully achieved a simple one-step thermal synthesis of a monoclinic phase of a new binary copper iron pyrophosphate $CuFeP_2O_7$. FTIR, XRD and VSM results suggested the formation of a binary metal $CuFeP_2O_7$. The FTIR and XRD data confirmed the dominant feature of pyrophosphate ($P_2O_7^{4-}$) anion indicated the formation of a binary $CuFeP_2O_7$. The crystallize size of $CuFeP_2O_7$ shows polycrystalline having crystallite size of 25 ± 9 nm, as estimated by XRD. The synthesized $CuFeP_2O_7$ shows ferromagnetic property, which has hysteresis loop in the range of $-10{,}000$ Oe $< H <$ 10,000 Oe with the specific magnetization of 1.57 emu $^{-1}$ at 10 kOe. This research displays that the simple, cost effective and rapid time consumption is necessary for elaboration of technology and academic scientist to produce the pyrophosphate of transition metals, which may be useful for potentially applications as inorganic ceramic pigment, catalyst, fuel cell material and corrosion-proof compositions.

Acknowledgement

This work is financially supported by the Thailand Research Fund (TRF) and the Commission on Higher Education (CHE):Research Grant for New Scholar, Ministry of Education, Thailand.

Appendix A. Supplementary data

Supplementary data associated with this article can be found, in the online version, at doi:10.1016/j.matlet.2009.10.058.

References

[1] Benkhouja K, Zahir M, Sadel A, Handizi A, Boukhari A, Holt EM, et al. Mater Res Bull 1995;30:49.
[2] Ishikawa M, Enomoto H, Maisuuka M, Iwakura§ C. Electrochim Acta 1995;40:1663.
[3] Masson NC, de Souza EF, Galembeck F. Colloids Surf A 1997;121:247.
[4] Masala O, Mcinnes EJL, O'Brien P. Inorg Chem Acta 2002;339:366.
[5] Masala O, O'Brien Pl, Rafeletos G. Cryst Growth Des 2003;3:431.
[6] Shepelev YF, Petrova MA, Novikova AS, Lapshin AE. Glass Phys Chem 2002;28:317.
[7] Onoda H, Yokouchi K, Kojima K, Nariai H. Mater Sci Eng B 2005;116:189.
[8] Boonchom B, Phuwongpha N. Mater Lett 2009;63:1709.
[9] Boonchom B, Danvirutai C. Ind Eng Chem Res 2008;47:5976.
[10] Cullity BD. Elements of X-ray Diffraction. 2nd ed. Addison-Wesley Publishing; 1977.
[11] Boukhari A, Moqine A, Flandrois S. J Solid State Chem 1990;87:251.
[12] Xiao ZW, Hu GR, Peng ZD, Du K, Gao XG. Chinese Chem Lett 2007;18:1525.
[13] Du Y, Xiong Y, Li J, Yang X. J Mol Catal A 2009;298:12.
[14] Steger E, Käbner B. Spectrochim Acta 1968;24A:447.
[15] Touaiher M, Rissouli K, Benkhouja K, Taibi M, Aride J, Boukhari A, et al. Mater Chem Phys 2004;85:41.
[16] Handizi A, Boukhari A, Holt EM, Aride J, Flandrois S. Mater Res Bull 1993;28:1241.
[17] Mahesh MJ, Gopalakrishna GS, Ashamanjari KG. Mater Sci Semicon Proc 2007;10:117.
[18] Ino H, Hayashi K, Otsuka T, Isobe D, Tokumitsu K, Oda K. Mater Sci Eng 2001;A304–306:972.

Powder Technology 198 (2010) 25–28

Contents lists available at ScienceDirect

Powder Technology

journal homepage: www.elsevier.com/locate/powtec

Floral-like microarchitectures of cobalt iron cyclotetraphosphate obtained by solid state synthesis

Banjong Boonchom [a,b,*], Naratip Vittayakorn [b,c]

[a] King Mongkut's Institute of Technology Ladkrabang, Chumphon Campus, 17/1 M. 6 Pha Thiew District, Chumphon, 86160, Thailand
[b] Advanced Materials Science Research Unit, Department of Chemistry, Faculty of Science, King Mongkut's Institute of Technology Ladkrabang, Bangkok 10520, Thailand
[c] College of KMITL Nanotechnology, King Mongkut's Institute of Technology Ladkrabang, Bangkok 10520, Thailand

ARTICLE INFO

Article history:
Received 5 August 2009
Received in revised form 7 October 2009
Accepted 13 October 2009
Available online 20 October 2009

Keywords:
Floral-like microparticle $CoFeP_4O_{12}$
Superparamagnetic behavior
Solid state synthesis
Inorganic ceramic pigment

ABSTRACT

Floral-like microparticle of a binary cobalt iron cyclotetraphosphate $CoFeP_4O_{12}$ was synthesized through solid phase reaction using cobalt carbonate, iron metal and phosphoric acid with further calcinations at the temperature of 500 °C. The XRD and FTIR results indicate that the prepared $CoFeP_4O_{12}$ has a pure monoclinic phase without the presence of any phase impurities. The floral-like microparticle and superparamagnetic behavior of the synthesized $CoFeP_4O_{12}$ are important properties for specific applications, which were revealed by SEM and VSM techniques, respectively. The dominant features of the synthesized $CoFeP_4O_{12}$ in this work are compared with $M_2P_4O_{12}$ (M = Co and Fe) and $CoFeP_4O_{12}$ reported in our previous works.

1. Introduction

In recent years, synthesis of the morphology and architecture of inorganic phosphates at micro-/nanoscale levels is a significant challenge, which attracts increased attention because of their strong influence on the chemical and physical properties of materials [1–3]. Morphology influences not only the intrinsic chemical, optical, and catalytic properties of micro-/nanoscale metal phosphates, but also their relevant applications in electronic, biocompartible and biodegradable in tissue [2,4]. As one of the members of phosphate material family, transition metal cyclotetraphosphate micro-/nanoparticles can be used in potential pigments, selective catalysts, phosphors, materials for corrosion-resistant coatings and biocompartible and biodegradable in tissue [5–8]. Several divalent including 3d metals, namely, Mn, Co, Fe, Zn, Cu, and Ni, are known to form the single metal cyclotetraphosphate $M_2P_4O_{12}$, where M(II) stands for a divalent metal. The binary metal cyclotetraphosphates $M_{2-x}A_xP_4O_{12}$ (M and A = Mg, Ca, Mn, Co, Ni, Zn, or Cu; $x = 0$–2), isostructural with the single metal cyclotetraphosphates $M_2P_4O_{12}$, were prepared by Trojan et al. [5–8] and Boonchom et al. [9–11]. All these compounds have similar X-ray diffraction patterns and close unit cell parameters, which crystallize in monoclinic space group C2/c (Z = 4) [12]. Various methods have been employed to synthesize binary metal cyclotetraphosphates, including two-step thermal method [5–8], hydrothermal synthesis [5] and the decomposition of binary metal (II) dihydrogenphosphates ($M_{1-y}A_y(H_2PO_4)_2$ nH_2O; where M and A = Ca, Mg, Mn, Fe, Co, Ni, Cu or Zn; $y = 0$–1; $n = 1$–4) [9–11]. This work is of interest because it appears economically advantageous to replace partially the divalent metal cations by some cheaper divalent element which could also improve special properties as above mentioned [1–4]. However, it is relevant to synthesize binary cyclotetraphosphate and its solid solution because changing the metal ratio influences its useful properties. Consequently, it is a major challenge to synthesize binary metal cyclotetraphosphate micro-/nanoparticles with its intrinsic shape-dependent properties and resulting application. Recently, cobalt iron pyrophosphate $CoFeP_2O_7$ and cobalt iron cyclotetraphosphate $CoFeP_4O_{12}$ were prepared by mixing of $CoCO_3$, Fe and H_3PO_4 in water–methanol and in water–acetone, respectively [13,14]. The difference of media (solvents) in the precipitation process leads to the obtaining different phosphates, as revealed by XRD and FTIR data. Due to its solubility in water and its ability to associate with metal ions in media, solvent has been used as a binder cum gel for shaping materials (bulk, porous, micro- or nanoparticles) and a matrix for entrapment of ions to generate a gelled precursor which resulted in obtaining different material or same material with different size and morphology after heat treatment. The results obtained are also in agreement with other phosphate group reported in literature [15,16]. In this work, we report for the first time one step thermal synthesis of floral-like microarchitectures of binary cobalt iron cyclotetraphosphate $CoFeP_4O_{12}$ by solid state reaction from cobalt carbonate, iron metal and phosphoric acid without organic media agent (or solvent). The different preparation routes of the $CoFeP_2O_7$ between this work and our previous report [14] affect the differences of some physical and chemical properties such as morphology, particle size

* Corresponding author. King Mongkut's Institute of Technology Ladkrabang, Chumphon Campus, 17/1 M. 6 Pha Thiew District, Chumphon, 86160, Thailand. Tel.: +66 7750 6422x4565; fax: +66 7750 6410.
E-mail addresses: kbbanjon@gmail.com, kbbanjon@kmitl.ac.th (B. Boonchom).

0032-5910/$ – see front matter © 2009 Elsevier B.V. All rights reserved.
doi:10.1016/j.powtec.2009.10.010

and magnetic behavior. The synthesized sample was characterized by X-ray powder diffraction (XRD), Fourier transform infrared (FTIR), scanning electron microscope (SEM) and vibrating sample magnetometer (VSM) techniques.

2. Experimental

All the reagents used in this study were of A.R. grade. A binary cobalt iron cyclotetraphosphate $CoFeP_4O_{12}$ was prepared at laboratory temperature. In typical procedure, $CoCO_3$ and Fe (complexometric) were mixed together with mole ratio of 1.0:1.0 and then was ground for 10 min. Subsequently, 5 mL of 70 % H_3PO_4 (86.4 % w/w H_3PO_4 dissolved in DI water) was added slowly to the mixed solid with mechanically stirring at ambient temperature (10 min). Then, the mixed solution was evaporated by heating in the furnace at 500 °C for 2 h. The obtained gray pink precursor was crushed into powder and was washed repeatedly by DI water until no PO_4^{3-} was detected. Finally, the powder was washed again for several times with methanol and dried at room temperature. The reaction equation can be expressed as:

$$CoCO_3(s) + Fe(s) + 4H_3PO_4(aq) \xrightarrow{500\,^\circ C} CoFeP_4O_{12}(s) + 6H_2O(g) + CO(g) \quad (1)$$

The cobalt and iron contents of $CoFeP_4O_{12}$ were determined by dissolving in 0.0126 M hydrochloric acid using atomic absorption spectrophotometry (AAS, Perkin Elmer, Analyst100). The phosphorus content was determined by colorimetric analysis of the molybdophosphate complex. X-ray powder diffraction (XRD) was carried out by a Phillips PW3040 X-ray diffractometer (The Netherland) utilizing Cu Kα radiation (λ = 0.15406 nm) at 40 kV/200 mA. The Scherrer method was used to evaluate the crystallite size [17]. The room-temperature FTIR spectrum in the range of 4000–370 cm^{-1} was recorded by a Perkin Elmer Spectrum GX FTIR/FT-Raman spectrometer with 8 scans and the resolution of 4 cm^{-1} using KBr pellets. The morphology was examined with SEM picture by LEO SEM VP1450 scanning electron microscope. The magnetic property was examined at room temperature (20 °C) using a vibrating sample magnetometer (VSM 7403, Lake Shore, USA).

3. Results and discussion

3.1. Chemical analysis

The chemical analysis data showed that the cobalt, iron and phosphorus mass percentage were 13.58%, 12.92% and 28.75%, respectively. In other words, the molar ratio of Co_{total}:Fe_{total}:P_{total} in the synthetic product is equal to 1.00:1.00:4.03, which indicates that the general formula would be $CoFeP_4O_{12}$.

3.2. X-ray powder diffraction

XRD was used to characterize the phase the crystallographic structure of the product (Fig. 1). The XRD pattern of as prepared floral-like $CoFeP_4O_{12}$ is similar to that of non-uniform particle $CoFeP_4O_{12}$ reported by our previous work [14] but the intensities are slightly different. The lower and higher intensities of XRD peaks indicate the differences of crystallization or amorphous phase as well as particle sizes of these materials. In the hypothesis of isostructural, the spectrum peaks for the systems of binary cobalt iron cyclotetraphosphate (solid solution) and single metal cyclotetraphosphate ($M_2P_4O_{12}$, M = Co and Fe) are quite similar because of the equivalent electronic charges and the close radii of cations. Consequently, all the diffraction peaks in the figure are found to be in agreement with monoclinic $M_2P_4O_{12}$ (PDF no. 842208 for $Co_2P_4O_{12}$ and PDF no.782285 for $Fe_2P_4O_{12}$), space group C2/c (Z = 4). No characteristic peaks of other impurities ($CoCO_3$ or Fe) were observed,

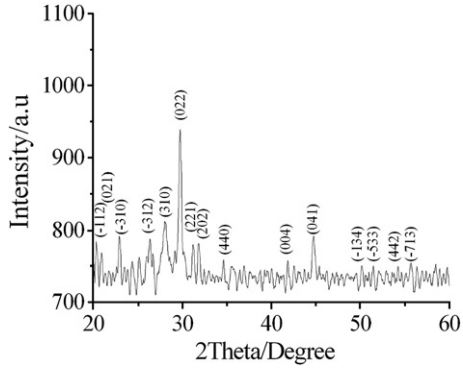

Fig. 1. XRD pattern of $CoFeP_4O_{12}$.

and all the reflections could be indexed to the pure monoclinic phase of binary cobalt iron cyclotetraphosphate $CoFeP_4O_{12}$. From XRD analysis (Fig. 1), it can conclude that the as prepared floral-like $CoFeP_4O_{12}$ is solid solution, not a mixture of the individual phases and isostructural with the single metal $M_2P_4O_{12}$ (M = Co and Fe). According to the Scherrer formula: $D = K\lambda/(\beta \cos \theta)$, where D is particle diameter, $K = 0.89$ (the Scherrer constant), $\lambda = 0.15406$ (wavelength of the X-ray used), β is the width of line at the half-maximum intensity and θ is the corresponding angle. The average crystallite size of product is estimated from the strongest three diffraction peaks below 40° for 2θ and found to be 49 ± 20 nm. This crystallite size of the prepared $CoFeP_4O_{12}$ in this work is smaller than that obtained from our previous work (65 ± 24 nm) [14] but it is larger than those for the single metal compounds (40 ± 10 nm for $Co_2P_4O_{12}$ and 29 ± 6 159 nm for $Fe_2P_4O_{12}$) in our previous studies [9–11]. The lattice parameters calculated from the XRD spectra are $a = 11.89(0)$, $b = 8.33(0)$, $c = 10.15(0)$ Å and $b = 119.09(0)°$, which are close to those of the standard data file (from PDF no. 842208 for $Co_2P_4O_{12}$ and PDF no.782285 for $Fe_2P_4O_{12}$) and the literature [9–11,14].

3.3. FTIR spectroscopy

The $CoFeP_4O_{12}$ structure is characterized by a three- dimensional framework with MO_6 (M = Co or Fe) polyhedral linked with P_4O_{12} rings by M–O–P. The basic structure unit is the centrosymmetric cyclotetraphosphate ring P_4O_{12} and therefore vibrational modes can consider it as made up of the $P_4O_{12}^{4-}$ anion. The vibrational modes of $P_4O_{12}^{4-}$ ion observed in the frequency range of 370–1400 cm^{-1} are assigned according to the literature (Fig. 2) [18–20]. The many peaks split in these regions indicate the different strength of the bond between cations (M = Co^{2+} and Fe^{2+}) and anion ($P_4O_{12}^{4-}$), which confirm the inserting different cations in the skeletal as well as the formation of binary cobalt iron cyclotetraphosphate. The anion contains the PO_2^{2-} radical and the P–O–P bridge which differ in their bond strength. As the P–O bond strength in the PO_2^{2-} radical is stronger than in the P–O–P bridge, the

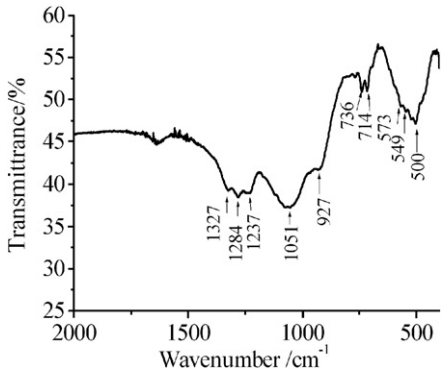

Fig. 2. FTIR spectrum of $CoFeP_4O_{12}$.

stretching frequencies of the PO_2^{2-} radical are expected to be higher than those in the P–O–P bridge. The P–O bonds in the PO_2^{2-} radical show its asymmetric and symmetric stretching frequencies around 1327–1237 and 1150–1000 cm^{-1}, respectively. The asymmetric and symmetric stretching frequencies of the P–O–P bridge are observed in the regions of 1000–900 and 800–700 cm^{-1}, respectively. The symmetric P–O–P bridge stretching modes occur at 736 and 714 cm^{-1}. These observed bands are known to be the most striking feature of cyclotetraphosphate spectra, along with the presence of the $\nu_{as}OPO^-$ band. From X-ray diffraction data [12], it was shown that the crystal structure is monoclinic (space group C2/c) with a cyclic structure of the $[P_4O_{12}]^{4-}$ anion. This has been confirmed by the FTIR measurements. The bending modes are expected in the area 600–400 cm^{-1} (PO_2^{2-} radical) and 400–370 cm^{-1} (P–O–P bride). The metal–O stretching usually appears in the bending mode region as the bending modes of the P–O–P bridge and absorption bands associated with these vibrations are usually very weak. The weak FTIR band at 400 cm^{-1} is probably due to metal–O stretching mode.

3.4. Scanning electron microscopy

SEM micrograph of $CoFeP_4O_{12}$ sample is shown in Fig. 3. It can be seen that the sample is composed of floral-like structures. There is soft agglomeration phenomenon among the particles of $CoFeP_4O_{12}$, which is attributed that the strong absorption of each other exists among particles with the layered structure compound. The floral-like morphology consists of similar petal-like flakes growing radically from the centre as can be observed under a higher magnification (inset). The different morphologies between the single metal compounds ($M_2P_4O_{12}$, M = Co or Fe) and the binary $CoFeP_4O_{12}$ indicate the presence of Co ions in substitution position of Fe ions, which confirms the formation of binary cobalt iron cyclotetraphosphate $CoFeP_4O_{12}$. The result of SEM experiment indicates that the grain sizes of $CoFeP_4O_{12}$ are not consistent with the crystallite sizes in the XRD analysis indicating the influence of media agents on particle nucleation and growth mechanisms. In addition, the floral-like morphology of the prepared $CoFeP_4O_{12}$ in this work is different from the non-uniform particles of $CoFeP_4O_{12}$ reported in our previous work [14]. These results indicate that the medium reagents for precipitation have the strong effect on the morphology of binary metal cyclotetraphosphate and are also in agreement with other reported other phosphate groups [12–15].

3.5. VSM magnetometer

The room-temperature magnetization curves of the floral-like microparticle $CoFeP_4O_{12}$ displays typical superparamagnetic behavior (Fig. 4). This curve is typical superparamagnetic behavior without any

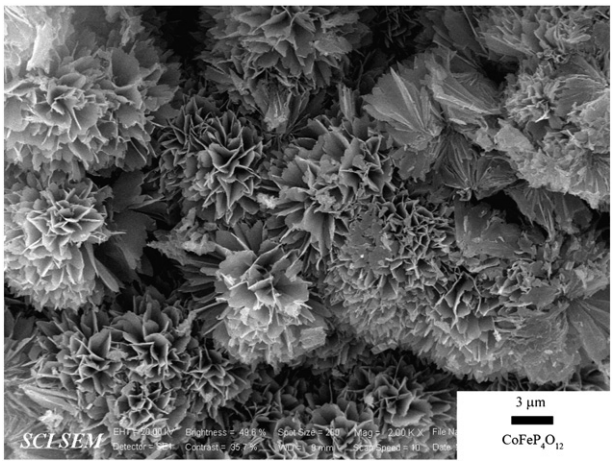

Fig. 3. SEM micrograph of $CoFeP_4O_{12}$.

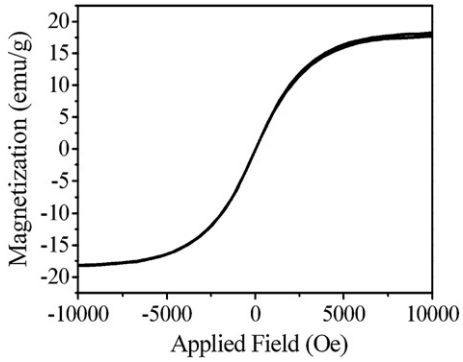

Fig. 4. The specific magnetization of $CoFeP_4O_{12}$ as a function of field, measured at 20 °C.

hysteresis in the field range of ±10,000 Oe. Specific saturated magnetization (M_s) value of the floral-like microparticle $CoFeP_4O_{12}$ (18.202 emu/g) in this work is higher than that of non-uniform microparticle $CoFeP_4O_{12}$ (14.243 emu/g) reported in our previous work [14] because of their small size. The result is lower than the saturated magnetization for Fe_3O_4 nanoparticles (in a range of 30–50 emu/g) [21,22]. It is seen that magnetization of the prepared $CoFeP_4O_{12}$ is lower than that of $Fe_2P_4O_{12}$ (85.01 emu/g) but markedly distinct from the diamagnetic properties of $Co_2P_4O_{12}$ [9,10]. This result indicates that the presence of Co ions in substitution position of Fe ions has the strong effect on the magnetic behavior of $CoFeP_4O_{12}$. This study demonstrates that the floral-like microparticle $CoFeP_4O_{12}$ is truly superparamagnetic, which is a unique feature of magnetic materials. This material may be used in modern technologies including magnetic resonance imaging contrast agents, data lifetime in high density information storage, ferrofluid technology, and magnetocaloric refrigeration [21–25].

4. Conclusions

Floral-like microparticle $CoFeP_4O_{12}$ was successfully synthesized by solid state route from cobalt carbonate, iron metal and phosphoric acid at 500 °C. The floral-like morphology and higher magnetization value of $CoFeP_4O_{12}$ in this work are different from those obtained from other works indicating that this may be caused by the media agents. The morphology of $CoFeP_4O_{12}$ shows floral-like crystals, as revealed by SEM data. The synthesized powder is polycrystalline, having crystallite size of 49 ± 20 nm for $CoFeP_4O_{12}$, as estimated by XRD. The synthesized $CoFeP_4O_{12}$ is superparamagnetic, having no hysteresis loop in the range of −10,000 Oe < H < 10,000 Oe with the specific magnetization of 18.202 emu/g at 10 kOe. The results obtained are necessary for elaboration of technology to produce the cyclotetraphosphate of transition metals, which may be useful for potentially applications as catalytic, ceramic and the biomedical materials etc.

Acknowledgements

This work is financially supported by the Thailand Research Fund (TRF), the Commission on Higher Education (CHE): Research Grant for New Scholar and the National Nanotechnology Center (NANOTEC) NSTDA, Ministry of Science and Technology, Thailand.

References

[1] H.N. Lim, A. Kassim, N.M. Huang, P.S. Khiewc, W.S. Chiu, Three-dimensional flower-like brushite crystals prepared from high internal phase emulsion for drug delivery application, Colloids Surf., A 345 (2009) 211–218.
[2] F.-H. Lin, C.-J. Liao, K.-S. Chen, J.-S. Sun, C.-P. Lin, Petal-like apatite formed on the surface of tricalcium phosphate ceramic after soaking in distilled water, Biomaterials 22 (2001) 2981–2992.
[3] L. Hong, Q. Li, H. Lin, Y. Li, Synthesis of flower-like silver nanoarchitectures at room temperature, Mater. Res. Bull. 44 (2009) 1201–1204.

[4] M.T. Averbuch-Pouchot, A. Durif, Topics in Phosphate Chemistry, World Scientific Publishing Co. Pte. Ltd., Singapore, 1996.
[5] M. Trojan, P. Šulcová, Binary Cu(II) – Mn(II) cyclo-tetraphosphates, Dyes Pigm. 47 (2000) 291–294.
[6] M. Trojan, P. Šulcová, P. Mošner, The synthesis of binary zinc(II) – nickel(II)cyclo-tetraphosphates as new special pigments, Dyes Pigm. 44 (2000) 161–164.
[7] M. Trojan, Binary cyclotetraphosphates $Zn_{2-x}Ca_xP_4O_{12}$ as new special pigments, Dyes Pigm. 13 (2000) 1–10.
[8] M. Trojan, D. Brandová, A study of the thermal preparation of c-$Cd_{4/3}Ca_{2/3}P_4O_{12}$, Thermochim. Acta 160 (1990) 349–359.
[9] B. Boonchom, S. Maensiri, S. Youngme, C. Danvirutai, A simple synthesis and room temperature magnetic properties of new binary $Mn_{0.5}Fe_{0.5}(H_2PO_4)_2$ xH_2O obtained from a rapid co-precipitation at ambient temperature, Solid State Sci. 11 (2009) 485–490.
[10] B. Boonchom, C. Danvirutai, Synthesis of $MnNiP_2O_7$ and nonisothermal decomposition kinetics of a new binary $Mn_{0.5}Ni_{0.5}HPO_4$ H_2O precursor obtained from a rapid coprecipitation at ambient temperature, Ind. Eng. Chem. Res. 47 (2008) 5976–5981.
[11] B. Boonchom, C. Danvirutai, S. Youngme, A rapid co-precipitation and non-isothermal decomposition kinetics of new binary $Mn_{0.5}Co_{0.5}(H_2PO_4)_2$ $2H_2O$, Solid State Sci. 10 (2008) 129–136.
[12] M. Bagieu-Beucher, M. Gondrand, M. Perroux, High-pressure study of tetrametaphosphates of the $M_2P_4O_{12}$ type (M = Ni, Mg, Cu, Co, Fe, Mn, Cd). Crystallographic data on all $M_2P_4O_{12}$ compounds, J. Solid State Chem. 19 (1976) 353–357.
[13] B. Boonchom, N. Phuvongpha, Synthesis of new binary cobalt iron pyrophosphate $CoFeP_2O_7$, Mater. Lett. 63 (2009) 1709–1711.
[14] B. Boonchom, M. Thongkam, S. Kongtaweelert, N. Vittayakorn, A simple route to synthesize new binary cobalt iron cycloletraphosphate $CoFeP_4O_{12}$ using aqueous and acetone media, J. Alloys Compd. 486 (2009) 689–692.
[15] S. Scaccia, M. Carewska, A. Di Bartolomeo, P.P. Prosini, Thermoanalytical investigation of nanocrystalline iron (II) phosphate obtained by spontaneous precipitation from aqueous solutions, Thermochim. Acta 397 (2003) 135–141.
[16] S. Scaccia, M. Carewska, P.P. Prosini, Thermoanalytical study of iron(III) phosphate obtained by homogeneous precipitation from different media, Thermochim. Acta 413 (2004) 81–86.
[17] B.D. Cullity, Elements of X-ray Diffraction, 2nd edAddison-Wesley Publishing, 1977.
[18] V. Ramakrishnan, G. Aruldhas, Vibrational spectra of Cu(II) and Co(II) tetrametaphosphates, Infrared Phys. 25 (1985) 665–670.
[19] E.J. Baran, R.C. Mercader, A. Massaferro, E. Kremer, Vibrational and ^{57}Fe-Mössbauer spectra of some mixed cation diphosphates of the type $M^{II}Fe_2^{III}(P_2O_7)_2$, Spectrochim Acta. 60 (2004) 1001–1005.
[20] E.H. Soumhi, I. Saadoune, A. Driss, A new organic-cation cyclotetraphosphate C10H28N4P4O12 4H2O: crystal structure, thermal analysis, and vibrational spectra, J. Solid State Chem. 156 (2001) 364–369.
[21] A.K. Gupta, M. Gupta, Synthesis and surface engineering of iron oxide nanoparticles for biomedical applications, Biomaterials 26 (2005) 3995–4021.
[22] C. Yang, J. Xing, Y. Guan, J. Liu, H. Liu, Synthesis and characterization of superparamagnetic iron nanocomposites by hydrazine reduction, J. Alloys Compd. 385 (2004) 283–287.
[23] S. Gyergyek, M. Huskić, D. Makovec, M. Drofenik, Superparamagnetic nanocomposites of iron oxide in a polymethyl methacrylate matrix synthesized by in situ polymerization, Colloids Surf. A 317 (2008) 49–55.
[24] H. Cao, J. He, L. Deng, X. Gao, Fabrication of cyclodextrin-functionalized superparamagnetic Fe_3O_4/amino-silane core–shell nanoparticles via layer-by-layer method, Appl. Surf. Sci. 255 (2009) 7974–7980.
[25] X. Li, G. Wang, Low-temperature synthesis and growth of superparamagnetic $Zn_{0.5}Ni_{0.5}Fe_2O_4$ nanosized particles, J. Magn. Magn. Mater. 321 (2009) 1276–1279.

Dielectric properties and phase transition behaviors in $(1-x)PbZrO_3-xPb(Mg_{1/2}W_{1/2})O_3$ ceramics

Naratip Vittayakorn,[1,2,3,a)] Piyanut Charoonsuk,[2] Panisara Kasiansin,[2] Supamas Wirunchit,[1,3] and Banjong Boonchom[4]
[1]*College of KMITL Nanotechnology, King Mongkut's Institute of Technology Ladkrabang, Bangkok 10520, Thailand*
[2]*Department of Chemistry, Advanced Materials Science Research Unit, Faculty of Science, King Mongkut's Institute of Technology Ladkrabang, Bangkok 10520, Thailand*
[3]*Thailand Center of Excellence in Physics (ThEP), CHE, 328 Si Ayutthaya Rd., Bangkok 10400, Thailand*
[4]*King Mongkut's Institute of Technology Ladkrabang, Chumphon Campus, 17/1 M.6 Pha Thiew District, Chumphon 86160, Thailand*

(Received 24 June 2009; accepted 1 August 2009; published online 16 September 2009)

The solid solution of lead zirconate [$PbZrO_3$ (PZ)] and lead magnesium tungstate [$Pb(Mg_{1/2}W_{1/2})O_3$ (PMW)] has been synthesized by the wolframite precursor method. The crystal structure, phase transformations, dielectric and thermal properties of $(1-x)$PZ-xPMW, where $x=0.00-0.10$, were investigated. The crystal structure of sintered ceramics was analyzed by x-ray diffraction. Phase-pure perovskite was obtained for all compositions. Furthermore, a change from orthorhombic to rhombohedral symmetry was observed as the mole fraction of increased PMW. As a result, it was found that $PbZrO_3$–$Pb(Mg_{1/2}W_{1/2})O_3$ undergoes successive transitions from the antiferroelectric phase to the ferroelectric phase to the paraelectric state. The coexistence of orthorhombic and rhombohedral phases in this binary system is located near the composition $x=0.1$. © *2009 American Institute of Physics*. [doi:10.1063/1.3212991]

I. INTRODUCTION

Antiferroelectric (AFE) materials are widely used for various devices: high charge storage capacitors, large strain actuators, and microelectromechanical systems.[1,2] The basic physics for these applications is due to the behaviors of electric-field-induced AFE to ferroelectric (FE) phase transformation. Lead zirconate [$PbZrO_3$ (PZ)] has been considered as the prototype AFE since its discovery by Sawaguchi *et al.* in 1951.[3] At room temperature, PZ has an orthorhombic structure with the lattice parameters $a=5.884$ Å, $b=11.768$ Å, and $c=8.22$ Å.[4] The orthorhombic unit cell consists of eight formula units and eight primitive cells with a tetragonal structure.[3] AFE PZ has spontaneous polarization, with adjacent rows of dipoles oriented antiparallel to each other, and no net spontaneous polarization at the equilibrium. AFE PZ has a phase transition to the paraelectric (PE) state, which occurs at approximately 236 °C. However, transition from the orthorhombic AFE to a rhombohedral FE structure, at a few degrees below the PE transition temperature, has been reported by several authors.[5,6] It is well known that the AFE to FE phase transformation in PZ ceramic requires a very strong electric field; otherwise, dielectric breakdown occurs.[3] Consequently, most commercial AFE ceramics are chemically modified by adding Ti^{4+}, Nb^{5+}, Sn^{4+}, or La^{3+} to reduce the critical field and optimize the physical and electrical properties.[7,8]

Lead magnesium tungstate [$Pb(Mg_{1/2}W_{1/2})O_3$ (PMW)] is a complex perovskite compound with Mg^{2+} and W^{6+} ordered on the B-site of the ABO_3 perovskite structure.[9] PMW-based ceramics have been known as dielectric materials possessing low dielectric loss and low sintering temperature.[10] Therefore, these materials can be used to fabricate multilayer capacitors with inner electrodes that melt in low temperature. At room temperature, PMW has an AFE phase, which has an orthorhombic structure. It undergoes a first order phase transition from an orthorhombic AFE phase to the cubic phase ($Fm3m$) at 38 °C.[9] The room temperature x-ray diffraction (XRD) pattern of PMW shows the presence of superlattice reflections due to the B-site ordering.[9]

Most studies of FE solid solutions have focused on relaxor-PT systems, such as $Pb(Mg_{1/3}Nb_{2/3})O_3-PbTiO_3$,[11] $Pb(Zn_{1/3}Nb_{2/3})O_3-PbTiO_3$,[11,12] and $Pb(Ni_{1/3}Nb_{2/3})O_3-PbTiO_3$,[13] and AFE-PT systems, for example, $PbZrO_3-PbTiO_3$.[14,15] A small number of studies have focused on AFE-AFE systems. Furthermore, the structure-property relationship between solid solution and an AFE-AFE system is still unclear.

Since PZ is an AFE with a sharp dielectric peak near $T_c \sim 236$ °C, and PMW is a B-site ordered AFE with a sharp maximum permittivity at $T_c \sim 38$ °C, the Curie temperature in the PZ-PMW system can be engineered over a wide range of temperatures by controlling the amount of PMW in the system. This study deals with the binary compound of PZ-PMW because, to the author's knowledge, there has been no detailed report on the structure and electrical properties of this entire system. In order to obtain more information about the combination of AFE and ordered AFE materials and recognize the properties of PZMW ceramics, this paper attempted to carry out synthesis of the quasibinary solid solu-

[a)]Author to whom correspondence should be addressed. Electronic mail: naratipcmu@yahoo.com. FAX: 66-2-326-4415.

tion, $Pb[Zr_{(1-x)}(Mg_{1/2}W_{1/2})_x]O_3$ with $x=0.0-0.1$, using the wolframite precursor method. This paper also reported some properties of the ceramics obtained.

II. EXPERIMENTAL PROCEDURE

Samples of $Pb[Zr_{(1-x)}(Mg_{1/2}W_{1/2})_x]O_3$, $x=0.00$, 0.02, 0.04, 0.06, 0.08, and 0.10, were synthesized from high-purity (>99%) oxides via a modified wolframite-type route. The wolframite ($MgWO_4$) was initially prepared by mixing starting magnesium oxide (MgO) and tungsten (VI) oxide (WO_3). Single phase formation of $MgWO_4$ was confirmed by XRD. The wolframite precursor was then mixed and ball milled with predetermined amounts of PbO (with 2 at. % excess) and ZrO_2 powders. The mixture was calcined in an alumina crucible at 900 °C for 2 h to form phase-pure perovskite powders. The calcined powders were milled for 6 h to reduce the particle size. After grinding and sieving, the calcined powder was mixed with a 5 wt % polyvinyl alcohol binder and uniaxially pressed into a pellet. The binder burnout occurred by slowly heating the pellets to 500 °C and holding them at that temperature for 2 h. Sintering occurred between 1100 and 1250 °C with a dwell time of 4 h depending on the composition. To mitigate the effects of lead loss during sintering, the pellets were sintered in a closed alumina crucible containing $PbZrO_3$ powder. The density of the sintered PZ-PMW pellets was measured by the Archimedes water immersion method. The relative density of all the sintered pellets was approximately 96%–97% of the theoretical density. The crystal structure of the sintered ceramics was analyzed by XRD (Bruker D8 Advance diffractometer). To determine the dielectric and FE properties, the maximum density of each composition sample was lapped on their major faces, and silver electrodes were made from a low-temperature silver paste by firing at 550 °C for 30 min to enable recording of electrical measurements. The relative permittivity (ε_r) (calculated from the capacitance using the sample dimensions and sample thickness) and dissipation factor (tan δ) of stress-free samples were measured using a precision LCR meter (HP-4284A, Hewlett-Packard, Palo Alto, CA). The capacitance and dissipation factors of the samples were measured at 100 Hz–1 MHz, the temperature varied between 25 and 300 °C, and a heating rate of 2 °C/min was used while measurements were being taken. The phase transitions were also measured by a differential scanning calorimeter (DSC 2920, TA Instrument) between ambient temperature and 350 °C at a rate of 10 °C/min. The FE polarization versus electric field (P-E) measurements were made using an RT66A standard FE test system with a frequency of about 4 Hz. The peak field was maintained at 30 kV/cm during measurement.

III. RESULTS AND DISCUSSION

A. Crystal structure

XRD patterns for the $(1-x)$PZ-xPMW, $x=0.0-0.1$, are presented in Fig. 1. The complete crystalline solutions of a perovskite structure were formed throughout the whole composition range. Evidence of the pyrochlore or other second phases was not detected in the patterns. It is believed that Mg^{2+} and W^{6+} ions diffuse into PZ lattices to form a solid solution. In general, XRD patterns of pure PZ ceramic exhibit $\frac{1}{4}$ $(h\ k\ l)$ superlattice reflections arising from the antiparallel displacements of Pb^{2+} ions. Meanwhile, XRD patterns of perovskite PMW display $\frac{1}{2}$ $(h\ k\ l)$ superlattice reflections, resulting from the ordering of B-site ions in an ABO_3 structure. Figure 1 shows that the $\frac{1}{4}$ $(h\ k\ l)$ superlattice reflections were clearly presented in all compositions. Unfortunately, the $\frac{1}{2}$ $(h\ k\ l)$ superlattice reflections were not detected, indicating that the long range Mg/W/Zr cation order was not developed. Furthermore, the intensity of $\frac{1}{4}$ $(h\ k\ l)$ superlattice reflections decreased with increased Mg^{2+}/W^{6+} content. This result indicates that the replacement of the Zr^{4+} ions by Mg^{2+}/W^{6+} ions decreases the driving force for an antiparallel shift of Pb^{2+} ions.

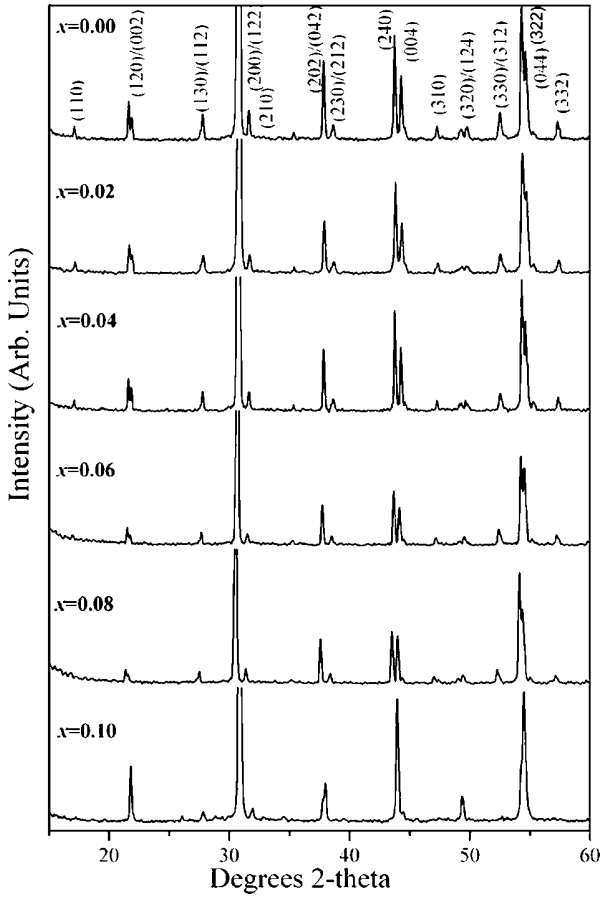

FIG. 1. XRD profiles for $(1-x)$PZ-xPMW obtained at optimum sintering temperature.

Figure 2 shows enlarged profiles of the (1 1 1), (2 4 0), and $\frac{1}{4}$ $(h\ k\ l)$ superlattice reflections for determining the crystal structure of the as-sintered ceramics. Based on the careful XRD spectra study of the $\frac{1}{4}$ $(h\ k\ l)$ superlattice reflection, (1 1 1) and (2 4 0) reflections in Fig. 2, a phase transformation from the orthorhombic to the rhombohedral structure was found to occur with increasing PMW content. The XRD data show that the $\frac{1}{4}$ $(h\ k\ l)$ superlattice reflection peak (*) and splitting of (2 4 0) peaks are clearly observed in the composition $x=0.0-0.08$, indicating that the major

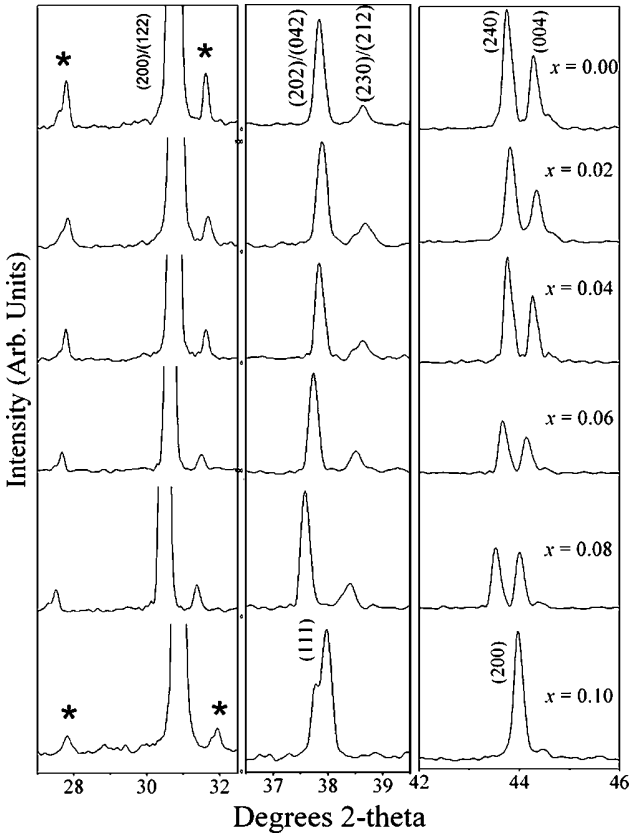

FIG. 2. XRD profiles for the $\frac{1}{4}$ $(h\ k\ l)$ superlattice reflection (*) and (200) peaks of $(1-x)$PZ-xPMW, $x=0.00-0.10$, ceramics.

phase in those compositions had an orthorhombic symmetry. At $x=0.1$ composition, the split (2 4 0) peaks from an orthorhombic symmetry were rapidly combined into a single peak, and the (1 1 1) diffraction peaks began to split, indicating that the crystal transformed into a rhombohedral symmetry. However, the $\frac{1}{4}$ $(h\ k\ l)$ superlattice reflections still remained. This indicates that both orthorhombic and rhombohedral phases coexist in this composition. Nevertheless, hysteresis loop results indicated that the $x=0.1$ composition shows an AFE phase at room temperature. We believe that this composition is within the orthorhombic-rich side of the coexistent phase. It is interesting to note that the phase evolution sequence in the present PZ-PMW system is very similar to that in the $Pb_{(1-x)}Ba_xZrO_3$,[16] $PbZrO_3-Pb(Co_{1/3}Nb_{2/3})O_3$,[17] $PbZrO_3-Pb(Ni_{1/3}Nb_{2/3})O_3$,[18–20] and $PbZrO_3-Pb(Zn_{1/3}Nb_{2/3})O_3$[21,22] systems.

B. Dielectric properties

The temperature dependencies of the relative permittivity and dielectric losses during as-sintered ceramic heating are shown in Fig. 3. A pure PZ ceramic shows the first order phase transition. The temperature dependence of relative permittivity shows discontinuities at the transitions, and the maximum relative permittivity is 3600. Above the Curie temperature, the relative permittivity follows the Curie–Weiss law, $\varepsilon_r=C/(T-T_0)$, with the Curie constant $C\sim 1.59\times 10^{-5}$ K and Curie–Weiss temperature $T_0\sim 191$ °C. The fact that the Curie–Weiss temperature T_0 is lower than the transition temperature ($T_c=231$ °C) confirms the first order type of the phase transition in $PbZrO_3$. The measured Curie

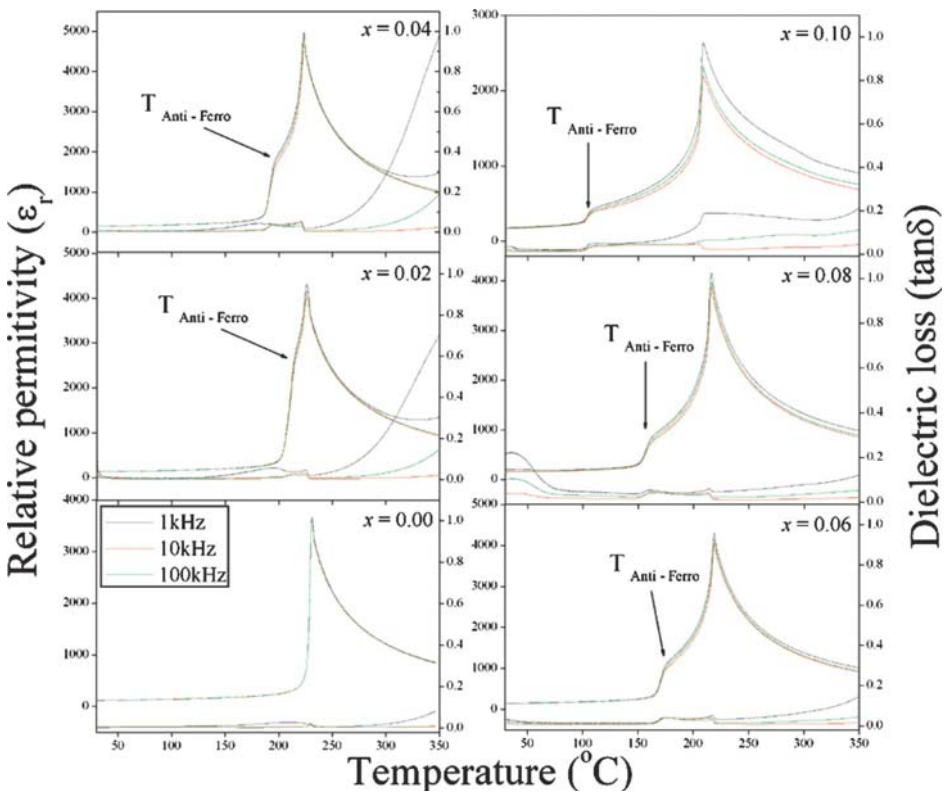

FIG. 3. (Color online) Relative permittivity (ε_r) and dielectric loss (tan δ) as a temperature function of $(1-x)$PZ-xPMW, $x=0.00-0.10$, ceramics.

TABLE I. Dielectric properties of $(1-x)$PZ-xPMW, $x=0.00-0.10$, ceramics.

Compositions	Crystal structure	$\varepsilon_{r,\mathrm{room}}$	$\varepsilon_{r,\max}$	$T_{\mathrm{AFE\text{-}FE}}$ (°C)	$T_{\mathrm{FE\text{-}PE}}$ (°C)
$x=0.00$	O	116	3670	⋯	231
$x=0.02$	O	140	4318	214	226
$x=0.04$	O	150	4836	195	222
$x=0.06$	O	155	4057	174	219
$x=0.08$	O	200	4160	160	216
$x=0.10$	O+R	180	2643	105	206

O is the orthorhombic phase and R is the rhombohedral phase.

constant and Curie–Weiss temperature are in close agreement with that reported by Sawaguchi.[18,19] For the composition $x=0.02$, there were two distinct changes in both dielectric peak and loss. The first one occurred at around 214 °C, where both relative permittivity and dielectric loss increased by one order of magnitude. This anomaly is due to the transformation from the AFE to the FE intermediate phase. Later FE data descriptions supported this assumption.

The dielectric anomaly corresponding to the AFE-FE transition was also observed at 195, 174, and 160 °C, and at 105 °C for compositions $x=0.04$, 0.06, 0.08, and 0.1. The value of relative permittivity at the AFE-FE phase transition temperature decreases with increasing PMW content from 2700 for $x=0.02$ to 400 for $x=0.1$. Crystal structure, dielectric data, and transition temperature are summarized in Table I. The temperature range width of the FE phase increases progressively with PMW content. It is interesting to note that all compositions show the AFE-FE phase transition temperature higher than room temperature, and an AFE state is expected to be observed in all compositions at room temperature.

The second abrupt change occurred at the dielectric maximum ($\varepsilon_{r,\max}$). This anomaly is linked to the transition of the FE into the cubic PE phase. Dielectric results have shown a significant difference in $\varepsilon_{r,\max}$ across the composition range. This may be due to the ionic size difference between Zr^{4+} and Mg^{2+}/W^{6+}. However, the transition temperature is well dispersed over the compositions. The FE-PE transition temperature ($T_{\mathrm{FE\text{-}PE}}$) decreases nearly linearly at the rate of 2.28 °C/mol % of PMW when compared with its value for pure PZ. It is noticeable that this rate is much less than PZ-PNN (2.81 °C/mol %).[18,19]

C. FE properties

To clarify the dielectric behavior of the FE intermediate phases further in the PZ-PMW system, electrical polarization hysteresis loop measurements were performed under a peak field of 30 kV. At 30 °C, no FE hysteresis loop was observed in the composition $0.0 \leq x \leq 0.1$. The linear polarization was observed, as a function of electric fields, in a range of up to 30 kV/cm. This could indicate that ceramics with the composition $x \leq 0.1$ have an AFE behavior at room temperature. For AFE ceramics, the net remanent polarization (P_r) is zero due to the existence of the antiparallel dipole moments. To induce an AFE-FE phase transition, an intense electric field needs to be applied to the ceramics. However, it is well known that the electric field required for inducing the AFE-FE transition at room temperature in PZ ceramics is usually higher than the breakdown strength of the ceramics. FE data support the assumption of an existing AFE stage at room temperature in dielectric results.

Figures 4(a)–4(d) show the changes in the hysteresis loop with rising temperature for the 0.9PZ-0.1PMW ceramic. The FE hysteresis loop was recorded after the temperature was stabilized for at least 5 min. As shown in Fig. 4(a), very small polarizations can be induced by the electric field applied in the ceramic at room temperature. This is typical of an AFE ceramic subjected to electric fields that are not sufficient enough to induce the AFE to FE phase transition. Such linear behavior with minimum polarization remains at temperatures of up to 100 °C [Fig. 4(b)].

When the temperature was raised to 150 °C, a regular hysteresis loop exhibiting ferroelectricity was clearly demonstrated, corresponding to the intermediate phase between 105 °C and $T_{\mathrm{FE\text{-}PE}}$ [Fig. 4(c)]. At 150 °C, the $P_r = 19.2\ \mu\mathrm{C/cm^2}$ and $E_c = 7.9$ kV/cm were observed. Above $T_{\mathrm{FE\text{-}PE}}$, a linear curve was also seen as an indication of the cubic PE phase [Fig. 4(d)].

D. Thermal properties

The DSC technique was used as the secondary tool to investigate and confirm the phase transition of PZ-PMW ceramics with increasing PMW concentration. The phase transition temperature in PZ-PMW ceramics, clearly confirmed by DSC measurement, is presented in Fig. 5, which shows that two distinct endothermic peaks were observed for PZ-PMW samples with $0.0 \leq x \leq 0.10$. The lower temperature corresponds to the transition temperature of the AFE→FE phase transition, while the higher temperature corresponds to the FE→PE phase transition. AFE→FE phase transition, FE→PE phase transition, ΔH, ΔS, and $\Delta S/T_t$ are summarized in Table II. The AFE→FE phase transition was found in the composition $0.0 \leq x \leq 0.10$. The peaks shifted to lower temperatures with higher compositions of x. In Table II, the temperature range width of progressive FE phase continuously increases with PMW content. The temperature range widths of the FE phase are around 7.5, 25, 40, 52.6, 67.5, and 80 °C for compositions $x=0.00$, 0.02, 0.04, 0.06, 0.08, and 0.10, respectively. The peak value of heat capacity became weaker, and the heat capacity anomaly gradually broader, with increasing PMW concentration. These results

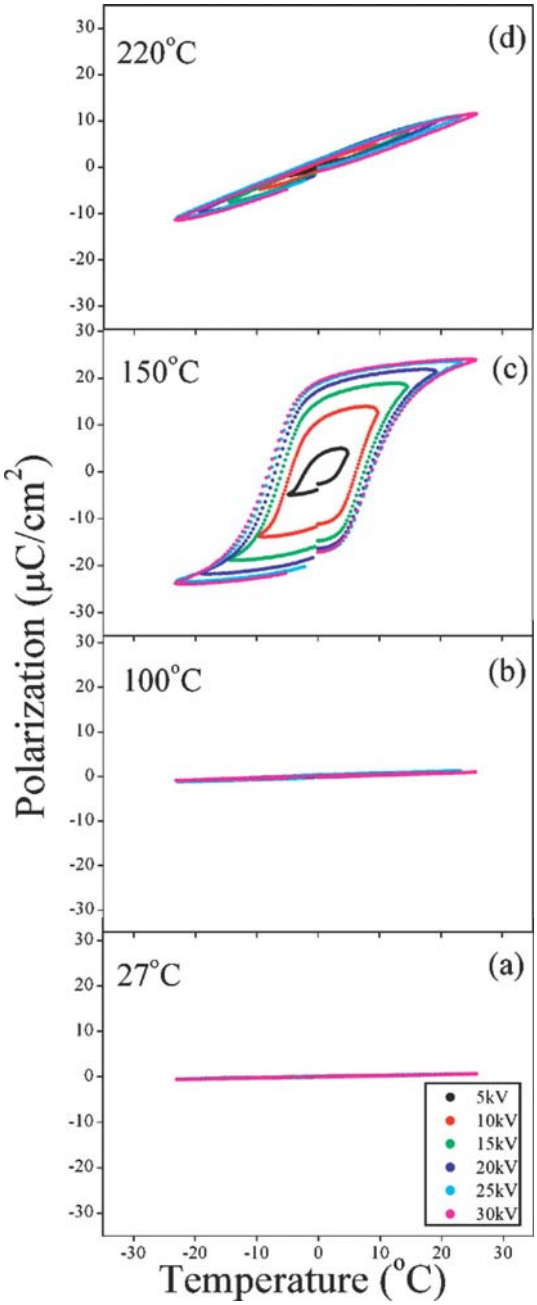

FIG. 4. (Color online) Polarization hysteresis loops recorded from 0.9PZ-0.1PMW at 4 Hz during heating at (a) 25 °C, (b) 100 °C, (c) 150 °C, and (d) 200 °C.

indicated that the phase transition deviates gradually from the first order type. Stenger and Burggraaf[23] observed that the change in entropy (ΔS) and $\Delta S/T_t$ correlates with the fluctuation probability in conjunction with a small spontaneous lattice deformation and polarization. They explained that large values of the ratio, $\Delta S/T_t$, give sharp transition and lower values, which lead to diffuse behavior. Table II shows small ΔS and $\Delta S/T_t$ values for the PMW doped sample when compared to the pure PZ sample, indicating existence of diffuseness in the phase transition behavior that increases with increased PMW content, which coincides well with the dielectric results in the composition range investigated.

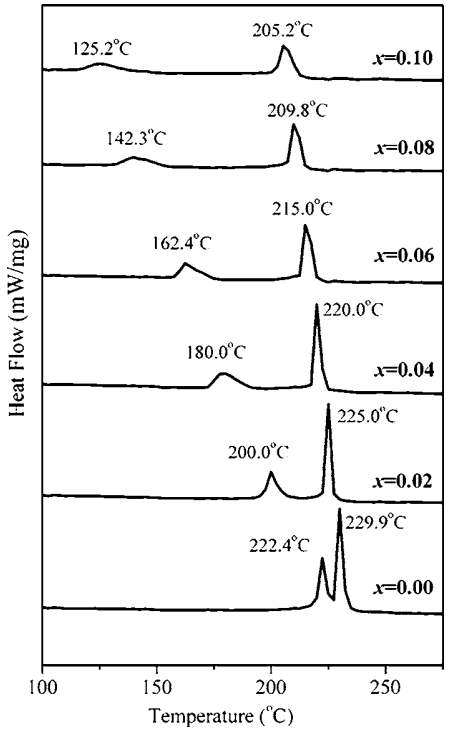

FIG. 5. Typical DSC curves for $(1-x)$PZ-xPMW, $x=0.0-0.1$, ceramics.

E. FE phase diagram

After accumulating all these data, a FE phase diagram for the $(1-x)$PZ-xPMW, $x=0.0-0.1$, was finally determined and is shown in Fig. 6. The phase diagram consists of three distinct crystallographic phases in this system: high-temperature PE cubic, FE rhombohedral, and AFE orthorhombic. At room temperature, the composition $0.0 \leq x \leq 0.08$ has an AFE orthorhombic phase. With increasing temperature, an AFE orthorhombic to a FE rhombohedral phase was observed in the samples with $0.02 \leq x \leq 0.10$. The temperature range width of the FE rhombohedral phase increases progressively with PMW content. At room temperature, the phase boundary between the AFE orthorhombic and FE rhombohedral phases was observed near $x=0.10$.

IV. CONCLUSIONS

In this work, the phase transition and dielectric properties of the solid solution between AFE PZ and AFE PMW have been investigated. AFE PMW has been found to strongly influence the phase development and physical property responses of PZ ceramics. The crystal structure data obtained from XRD indicate that the solid solution, $(1-x)$PZ-xPMW, where $x=0.0-0.1$, successively transforms from orthorhombic to rhombohedral phase with an increase in PMW concentration. The coexistence of orthorhombic and rhombohedral phases in this binary system is located near the composition $x=0.1$.

ACKNOWLEDGMENTS

This work was supported by the Thailand Research Fund (TRF), National Research Council of Thailand (NRCT), and

TABLE II. Thermal properties of $(1-x)$PZ-xPMW, $x=0.00-0.10$, ceramics.

Compositions	$T_{AFE\text{-}FE}$ (°C)	$T_{FE\text{-}PE}$ (°C)	ΔH (J g^{-1})	$\Delta S\times 10^3$ (J g^{-1} K^{-1})	$(\Delta S/T_t)\times 10^6$ (J g^{-1} K^{-2})
$x=0.00$	222	230	2.227	9.682	42.096
$x=0.02$	200	224	2.148	9.568	42.169
$x=0.04$	180	220	2.354	10.676	48.416
$x=0.06$	163	216	2.325	10.764	49.830
$x=0.08$	140	211	1.956	9.270	43.934
$x=0.10$	123	205	1.855	9.049	44.141

the National Nanotechnology Center (NANOTEC) NSTDA, Ministry of Science and Technology, Thailand through its program of Center of Excellence Network.

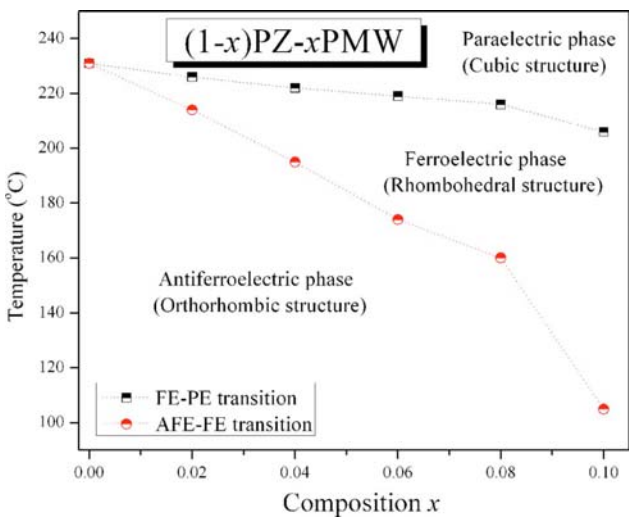

FIG. 6. (Color online) FE phase diagram of $(1-x)$PZ-xPMW, $x=0.0-0.1$, system.

[1]K. Uchino, *Ferroelectric Devices* (Dekker, New York, 2000).
[2]B. Jaffe and W. R. Cook, *Piezoelectric Ceramic* (Academic, New York, 1971).
[3]E. Sawaguchi, G. Shirane, and S. Hoshino, Phys. Rev. **83**, 1078 (1951).
[4]F. Jona, G. Shirane, F. Mazzi, and R. Pepinsky, Phys. Rev. **105**, 849 (1957).
[5]L. E. Balyunis, V. Y. Topolov, I. S. Bah, and A. V. Turik, J. Phys.: Condens. Matter **5**, 1419 (1993).
[6]B. P. Pokharel and D. Pandey, Phys. Rev. B **65**, 214108 (2002).
[7]H. He and X. Tan, Phys. Rev. B **72**, 024102 (2005).
[8]L. J. Zhou, Z. Zhao, A. Zimmermann, F. Aldinger, and M. Nygren, J. Am. Ceram. Soc. **87**, 606 (2004).
[9]G. Baldinozzi, P. Sciau, M. Pinot, and D. Grebille, Acta Crystallogr., Sect. B: Struct. Sci. **51**, 668 (1995).
[10]L. Ruan, L. Li, and Z. Gui, J. Mater. Res. **13**, 253 (1998).
[11]S.-E. Park and T. R. Shrout, IEEE Trans. Ultrason. Ferroelectr. Freq. Control **44**, 1140 (1997).
[12]T. Takenaka, K. Muramata, and T. Fujii, Ferroelectrics **134**, 133 (1992).
[13]I. A. Cornejo, B. Jadidian, E. K. Akdogan, and A. Safari, in *Proceedings of the 11th IEEE International Symposium on Applications of Ferroelectrics (ISAF 98)*, Montrex, Switzerland (Institute of Electrical and Electronic Engineers, Piscataway, NJ, 1998), pp. 337–340.
[14]E. Sawaguchi, J. Phys. Soc. Jpn. **8**, 615 (1953).
[15]G. A. Samara and E. L. Venturini, Phase Transitions **79**, 21 (2006).
[16]N. Vittayakorn, T. Bongkarn, and G. Rujijanagul, Physica B **387**, 415 (2007).
[17]W. Banlue and N. Vittayakorn, Appl. Phys. A: Mater. Sci. Process. **93**, 565 (2008).
[18]S. Wirunchit, P. Laoratanakul, and N. Vittayakorn, J. Phys. D: Appl. Phys. **41**, 125406 (2008).
[19]S. Wirunchit and N. Vittayakorn, J. Appl. Phys. **104**, 024103 (2008).
[20]N. Vittayakorn and S. Wirunchit, Smart Mater. Struct. **16**, 851 (2007).
[21]W. Banlue and N. Vittayakorn, Ferroelectrics **382**, 122 (2009).
[22]N. Vittayakorn and W. Banlue, Ferroelectrics **382**, 110 (2009).
[23]C. Stenger and A. J. Burggraaf, Phys. Status Solidi A **61**, 275 (1980).

Appl Phys A (2010) 100: 551–559
DOI 10.1007/s00339-010-5871-1

Applied Physics A
Materials Science & Processing

Antiferroelectric–ferroelectric phase transition in lead zinc niobate modified lead zirconate ceramics: crystal studies, microstructure, thermal and electrical properties

Usa Sukkha · Rangson Muanghlua · Surasak Niemcharoen · Banjong Boonchoma · Naratip Vittayakorn

Received: 11 February 2010 / Accepted: 8 June 2010 / Published online: 20 June 2010

Abstract The combination of antiferroelectric $PbZrO_3$ (PZ) and relaxor ferroelectric $Pb(Zn_{1/3}Nb_{2/3})O_3$ was prepared via the columbite precursor method. The basic characterizations were performed using X-ray diffraction (XRD), scanning electron microscopy (SEM), linear thermal expansion, differential scanning calorimetry (DSC) techniques, dielectric spectroscopy, and hysteresis measurement. The XRD result indicated that the solid solubility limit of the $(1-x)$PZ–xPZN system was about $x = 0.40$. The crystal structure of $(1-x)$PZ–xPZN transformed from orthorhombic to rhombohedral symmetry when the concentration of PZN was increased. A ferroelectric intermediate phase began to appear between the paraelectric and antiferroelectric phases of pure PZ, with increasing PZN content. In addition, the temperature range of the ferroelectric phase increased with increasing PZN concentration. The morphotropic phase boundary (MPB) in this system was located close to the composition, $x = 0.20$.

U. Sukkha · N. Vittayakorn (✉)
Electroceramic Research Laboratory, College of KMITL Nanotechnology, King Mongkut's Institite of Technology Ladkrabang, Bangkok 10520, Thailand
e-mail: naratipcmu@yahoo.com
Fax: +66-2-3264415

R. Muanghlua · S. Niemcharoen
Department of Electronics, Faculty of Engineering, King Mongkut's Institute of Technology Ladkrabang, Bangkok 10520, Thailand

B. Boonchoma
King Mongkut's Institute of Technology Ladkrabang, Chumphon Campus, 17/1M. 6 Pha Thiew District, Chumphon 86160, Thailand

N. Vittayakorn
Department of Chemistry, Faculty of Science, King Mongkut's Institute of Technology Ladkrabang, Bangkok 10520, Thailand

U. Sukkha · N. Vittayakorn
ThEp Center, CHE, 328 Si Ayutthaya Road, Bankok 10400, Thailand

1 Introduction

Ferroelectric materials are extensively used for many different electronic devices, such as actuators, transducers, and multilayer capacitors [1–3]. Study over several decades has focused mainly on the development of physical and electrical properties of ferroelectric materials [2, 3]. Many ferroelectric ceramics have been developed from binary systems containing a combination of antiferroelectric and normal ferroelectric ceramics such as $(1-x)PbZrO_3$–$xPbTiO_3$ (PZ–PT, PZT) [3, 4], and $(1-x)SrTiO_3$–$xPbZrO_3$ [4, 5]. Among them, PZT is a very famous ferroelectric ceramic, due to its exhibition of high piezoelectric coefficient and electromechanical coupling factor around the morphotropic phase boundary (MPB) [3, 4]. The combination of normal ferroelectric and relaxor ferroelectric ceramics also shows excellent piezoelectric and dielectric properties such as $Pb(Mg_{1/3}Nb_{2/3})O_3$–$PbTiO_3$(PMN–PT) [5], $Pb(Zn_{1/3}Nb_{2/3})O_3$–$PbTiO_3$(PZN–PT) [6, 7], $Pb(Zn_{1/3}Nb_{2/3})O_3$–$Pb(Zr_{1/2}Ti_{1/2})O_3$(PZN–PZT) [8], and $Pb(Ni_{1/3}Nb_{2/3})O_3$–$Pb(Zr_{1/2}Ti_{1/2})O_3$(PNN–PZT) [9]. Furthermore, PZN–PZT, PNN–PZT, and $Pb(Zr_{1/2}Ti_{1/2})O_3$–$Pb(Co_{1/3}Nb_{2/3})O_3$(PZT–PCN) [8–10] ceramics show high, relative permittivity.

Metal oxide Lead zirconate ($PbZrO_3$, PZ) is a prototype of antiferroelectric ceramics. The PZ phase changes from the orthorhombic antiferroelectric phase (AFE) to cubic paraelectric phase (PE) at 236°C, and a ferroelectric phase (FE) exists over a very narrow temperature range

(230–233°C) [11]. Stability of the ferroelectric phase can be altered by substitutions such as Ba^{2+} ions or La^{3+} ions at the A-site of the perovskite structure (ABO_3) [12–14]. Besides, PZ-based thin films are also particularly interesting because of the characteristic hysteresis loop resulting from the electric field-induced antiferroelectric-to-ferroelectric phase switching [14, 15]. Our recent work reported that the combination of antiferroelectric PZ and relaxor ferroelectric (RFE), $Pb(Co_{1/3}Nb_{2/3})O_3$ (PCoN), or $Pb(Ni_{1/3}Nb_{2/3})O_3$ (PNN) can also induce the ferroelectric phase of PZ [16, 17]. Nevertheless, due to PCoN and PNN having a low transition temperature ($T_m \sim -90$°C and ~ -120°C for PCoN and PNN, respectively), the transition temperature of PZ–PCoN and PZ–PNN systems was dramatically decreased [17, 18].

Complex metal oxide lead zinc niobate ($Pb(Zn_{1/3}Nb_{2/3})O_3$, PZN) is an RFE material with a rhombohedral perovskite structure at room temperature. A diffuse phase transition from paraelectric to ferroelectric polar state occurs at the high temperature of 140°C [6, 7]. There has been extensive research carried out on single PZN crystals because of their high relative permittivity ($\varepsilon_{r,10\,\mathrm{kHz}}$ reaching 50,000), pyroelectric constant ($P_{20°\mathrm{C}} = 7 \times 10^{-12}$ C/m^2 K) [6], high piezoelectric coefficient ($d_{33} \approx 1100$ pC/N), and high electromechanical coupling factors ($k_{33} \approx 92\%$) [7]. Single crystals of PZN can be prepared by the flux-growth method, but pure perovskite PZN ceramics are difficult to synthesize via the conventional mixed-oxide method under atmospheric pressure [19, 20]. It is well known that forming solid solutions with other perovskites such as $Ba(Zn_{1/3}Nb_{2/3})O_3$, $BaTiO_3$, and $SrTiO_3$ [20, 21] is considered an effective way to stabilize the perovskite PZN ceramic.

As both PZ and PZN have a perovskite structure, it has been suggested that PZN can be alloyed with PZ in order to stabilize the perovskite structure and find a suitable composition across the MPB. To the best of the author's knowledge, there has been no detailed report on the structure, solubility limit, dielectric properties, thermal properties, or phase transition in this system. Additionally, as PZN is a relaxor ferroelectric with broad dielectric peak near $T_m \sim 140$°C, and PZ is an antiferroelectric with sharp maximum permittivity at $T_c \sim 230$°C, the Curie temperature in the PZ–PZN system can be engineered over a wide range of temperatures via control of the PZN amount in the system. With a complementary characteristic, it is expected that excellent properties can be obtained from PZ–PZN ceramics. The relationship between the phase evolution and the properties was emphasized.

2 Experiment

The composition series of $(1-x)PbZrO_3$–$xPb(Zn_{1/3}Nb_{2/3})O_3$ ceramics, where $x = 0.00$, 0.02, 0.04, 0.06, 0.08, 0.10, 0.20, 0.30, 0.40, and 0.50 were fabricated via a columbite precursor. The reagent-grade oxide powders of PbO (99.9%, Aldrich, Milwaukee, WI, USA), ZnO (99.9%), Nb_2O_5 (99.5%), and ZrO_2 (99.6%) were used as starting raw materials. Prior to reaction with other raw materials, ZnO was reacted with Nb_2O_5 at 975°C for 4 h to form $ZnNb_2O_6$. The precursors, $ZnNb_2O_6$, ZrO_2, and PbO (with 2 mol% excess PbO), were weighed and mixed well by ball-milling in a polyethylene bottle together with methyl alcohol and partially stabilized zirconia balls. Methyl alcohol was removed by heating at 80°C for appropriate durations, and then the mixture was dried at 150°C for 24 h. After drying, the mixed powders were calcined at 750–850°C for 4 h in a covered Al_2O_3 crucible. After that, all compositions of $(1-x)$PZ–xPZN were ball-milled again for 18 h. The calcined powders were sieved and uniaxially cold-pressed at 300 MPa. The disks were sintered at 1,200–1,250°C for 4 h depending on the composition. To compensate PbO volatilization; the PbO atmosphere for the sintering was maintained using $PbZrO_3$ as the spacer powder.

The crystal structure and phase transition of the sintered pellets were characterized using an X-ray diffractometer (XRD; Bruker-AXS D8, CuKα radiation). The density of PZ–PZN ceramics was measured via Archimedes water immersion method. Scanning electron microscopy (SEM; Hitachi, s4007) was employed to investigate the microstructure of sintered pellets. The phase transition of samples was investigated using a differential scanning calorimeter (DSC 2920, TA Instrument) between room temperature and 300°C at a heating rate of 10°C/min. To confirm the phase transition of samples, the sintered pellets were measured by a dilatometer (DIL 402 PC, Netzsch) between 25–300°C at a rate of 1°C/min. For the measurement of electrical properties, both sides of the maximum density of each composition sample were polished and electroded with silver paste (C1000, Heraeus). An LCR meter (HP4284A, Hewlett-Packard, Palo Alto, CA) was used to measure the dielectric properties, and the temperature varied between 25–350°C with a heating rate of 2°C/min. The polarization–electric field (P–E) hysteresis loops were obtained at room temperature using a standardized ferroelectric tester system (RT-66A, Radiant Technologies, Albuquerque, NM) at a frequency of 4 Hz.

3 Results and discussion

3.1 Crystal structure

The XRD patterns of the sintered $(1-x)$PZ–xPZN ceramics for $0.00 \le x \le 0.50$ are shown in Fig. 1. At the composition, $0.00 \le x \le 0.40$, ceramic samples had a pure perovskite structure. Evidence for the secondary phases was

not observed in the patterns, indicating homogeneous solid solution of PZ–PZN. However, increasing the amount of PZN further to 50 mol%, gave rise to formation of the pyrochlore phase, $Pb_{1.88}Zn_{0.3}Nb_{1.25}O_{5.305}$, which could be matched with JCPDS No. 25-0446. This result could explain the larger ionic size of Zn^{2+} (0.88 Å) [22], as compared to the sixfold lattice sites formed by the oxygen octrahedra. Then, Zn^{2+} cannot enter the B-site of the perovskite structure as a replacement for Zr^{4+} (0.86 Å) ions [22]. This result indicated that the solubility limit of the $(1-x)$PZ–xPZN system was found at $x = 0.40$. Furthermore, the 1/4 (h k l)-type superlattice reflection peaks, identified with "*", arise from antiparallel displacement of Pb^{2+} cations, and this was clearly seen in all compositions. The relative intensity of 1/4 (h k l)-type superlattice reflection peaks decreased with increasing PZN, which indicated that the substitution of Zr^{4+} ions by Zn^{2+}/Nb^{5+} ions decreased the driving force for an antiparallel shift of Pb^{2+} ions.

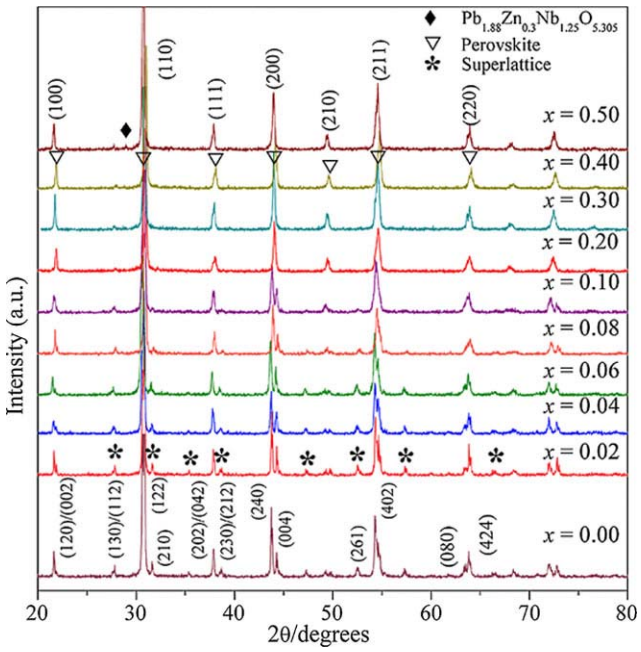

Fig. 1 XRD patterns of sintered ceramics for various compositions of $(1-x)PbZrO_3$–$xPb(Zn_{1/3}Nb_{2/3})O_3$, where $x = 0.0$–0.5

Figure 2 shows enlarged profiles of the 1/4 (h k l)-type superlattice reflections (*): (1 1 1), (2 0 0), and (2 2 0) reflections. At the composition, $0.00 \le x \le 0.10$, the XRD data exhibit the superlattice reflections and splitting of (2 4 0) peak at roughly 43°, indicating that the crystal structure of samples at the composition, $0.00 \le x \le 0.10$, are orthorhombic perovskite. Furthermore, the compositions, $0.20 \le x \le 0.50$, showed a split (1 1 1) and (2 2 0) reflection, and single (2 0 0) reflection, indicating that the crystal structure transformed into a rhombohedral structure. Moreover, the XRD patterns of $0.20 \le x \le 0.50$ compositions also showed 1/4 (h k l)-type superlattice reflections. Therefore, it could be assumed that the orthorhombic and rhombohedral phase coexist in these compositions. Consequently, the composition, $x = 0.20$, is expected to be close to the MPB, whereas the $0.30 \le x \le 0.50$ compositions are in the rhombohedral-rich region of the coexistent phase. Elu-

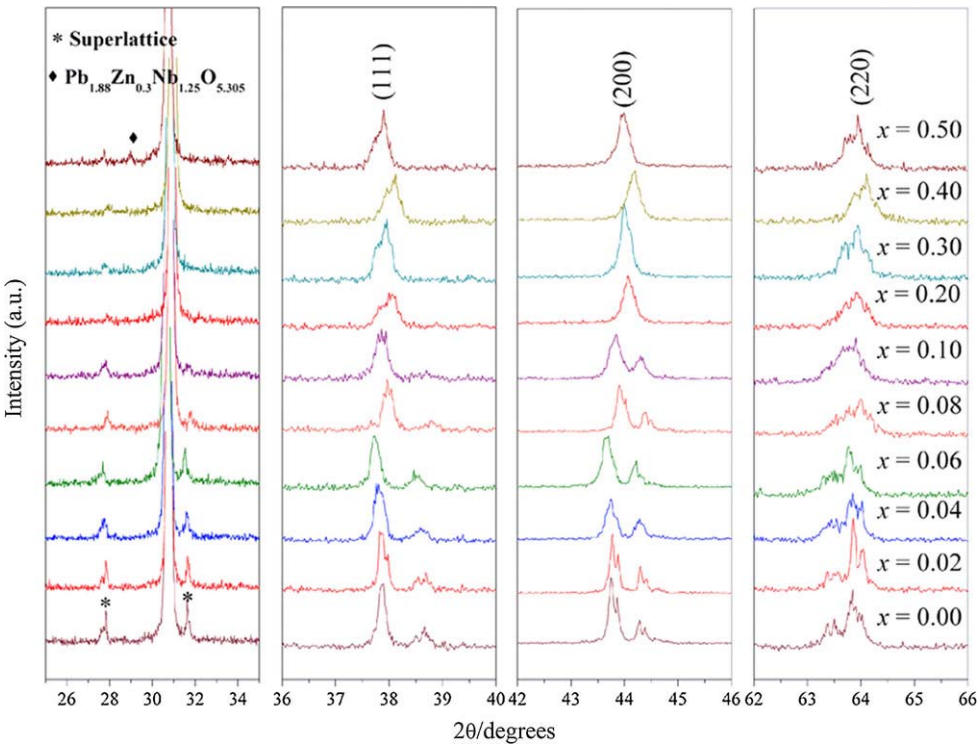

Fig. 2 XRD patterns of the 1/4(h k l)-type superlattice reflections, and the (1 1 1), (2 0 0) and (2 2 0) peaks of $(1-x)$PZ–xPZN ceramics with $x = 0.0$–0.5

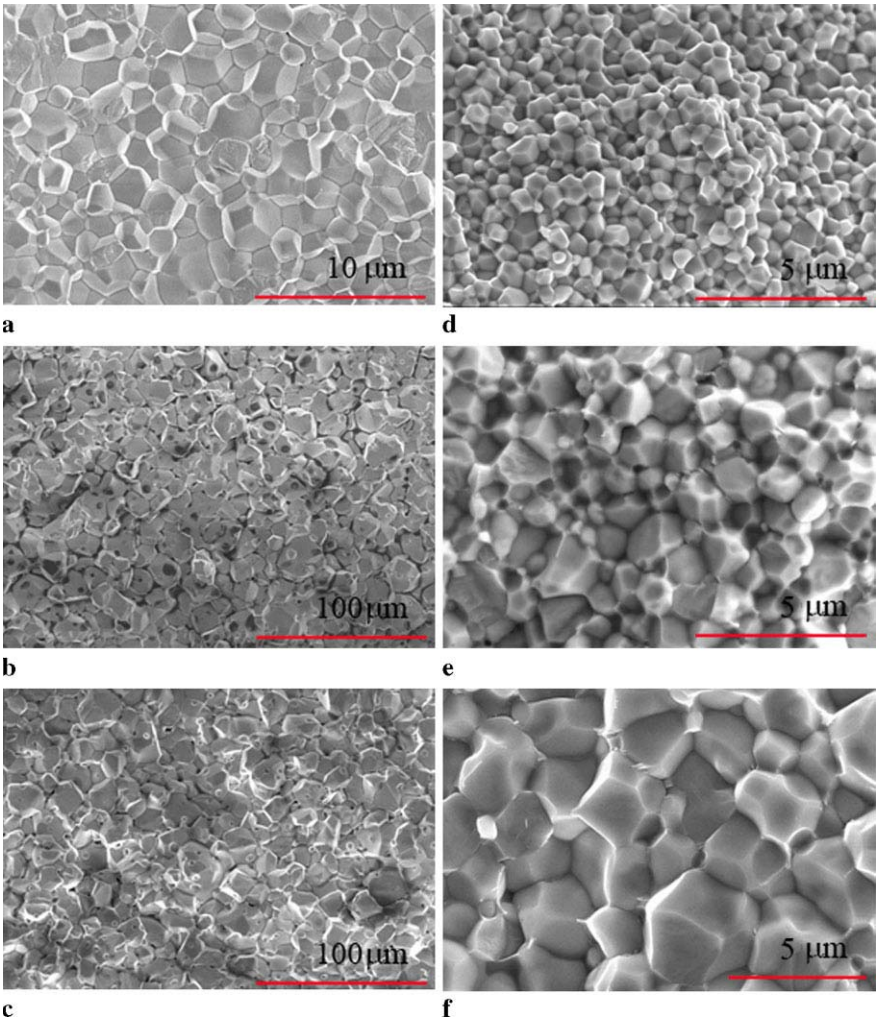

Fig. 3 SEM micrographs of the fractured surfaces of $(1-x)PbZrO_3$–$xPb(Zn_{1/3}Nb_{2/3})O_3$ with various compositions (**a**) $x = 0.00$, (**b**) $x = 0.02$, (**c**) $x = 0.04$, (**d**) $x = 0.10$, (**e**) $x = 0.30$, and (**f**) $x = 0.50$

cidated electrical property data later confirmed this assumption. It is interesting to note that the influence of additional $Pb(Zn_{1/3}Nb_{2/3})O_3$ on phase transition of the $PbZrO_3$ system was similar to that of PZ−PMW and PZ−PCoN systems [17, 23].

3.2 Microstructure

The effects of PZN amount on the microstructure of $(1-x)$ PZ–xPZN, where $x = 0.00$, 0.02, 0.04, 0.10, 0.30, and 0.50 ceramics, are shown in Fig. 3. From these micrographs, specimens show the absence of pyrochlore formation. It is interesting to note that at the composition, $x = 0.50$, the pyrochlore phase was detected by XRD but not observed from the SEM micrograph in Fig. 3(f). As the pyrochlore phase was probably located at the surface, and the scale was too small, it did not appear in the SEM micrograph of the fractured surface. This result was similar to that in the PMN system [24]. The ceramics displayed a dense microstructure, and most of the grains were fractured in an intergranular manner. The grain boundaries could be clearly observed, and then the average grain size was calculated directly by the linear interception method [25]. Physical properties of the sintered $(1-x)$PZ–xPZN ceramics are listed in Table 1. The SEM images in Fig. 3 reveal that the addition of PZN resulted in significant changes in the microstructure of the ceramics. All ceramics exhibited high density with an average grain size range of about 0.54 ± 0.09 to 17.02 ± 0.19 μm. The relative densities were obtained in the range of 90–97% of theoretical density. Additionally, shrinkage of about 11–17% of $(1-x)$PZ–xPZN ceramics could be achieved in this study. This value is consistent with other lead-based systems [26]. The average grain size dramatically increased from ∼1.80 μm in the composition, $x = 0.0$, to approximately 17.02 μm in the composition, $x = 0.06$. Conversely, in concentrations of PZN increasing to $x = 0.08$, the grain size significantly decreased with increasing PZN. From these results, it can be assumed that a small amount of PZN substitution improves the sinterability of the ceramic. While excessive PZN substitution was segregated at the grain boundary, which acts as impuri-

Table 1 Physical properties of $(1-x)PbZrO_3$–$xPb(Zn_{1/3}Nb_{2/3})O_3$ ceramics (R, Rhombohedral; O, Orthorhombic; Pyr, Pyrochlore)

Composition (x)	Crystal structure	Average grain size (μm)	Shrinkage (%)	Relative density (%)
0.00	O	1.80 ± 0.31	15.0±0.02	97.2±0.11
0.02	O	11.96 ± 0.21	11.0±0.01	89.8±0.21
0.04	O	12.22 ± 0.17	12.7±0.03	93.3±0.33
0.06	O	17.02 ± 0.19	13.5±0.03	92.5±0.30
0.08	O	1.20 ± 0.15	12.9±0.02	91.1±0.13
0.10	O	0.54 ± 0.09	13.9±0.01	94.3±0.09
0.20	O + R	0.77 ± 0.26	13.9±0.02	93.0±0.16
0.30	R-rich	0.95 ± 0.16	15.6±0.01	93.8±0.14
0.40	R-rich	1.59 ± 0.31	17.1±0.01	95.1±0.18
0.50	R-rich + Pyr	1.96 ± 0.48	17.3±0.01	94.4±0.39

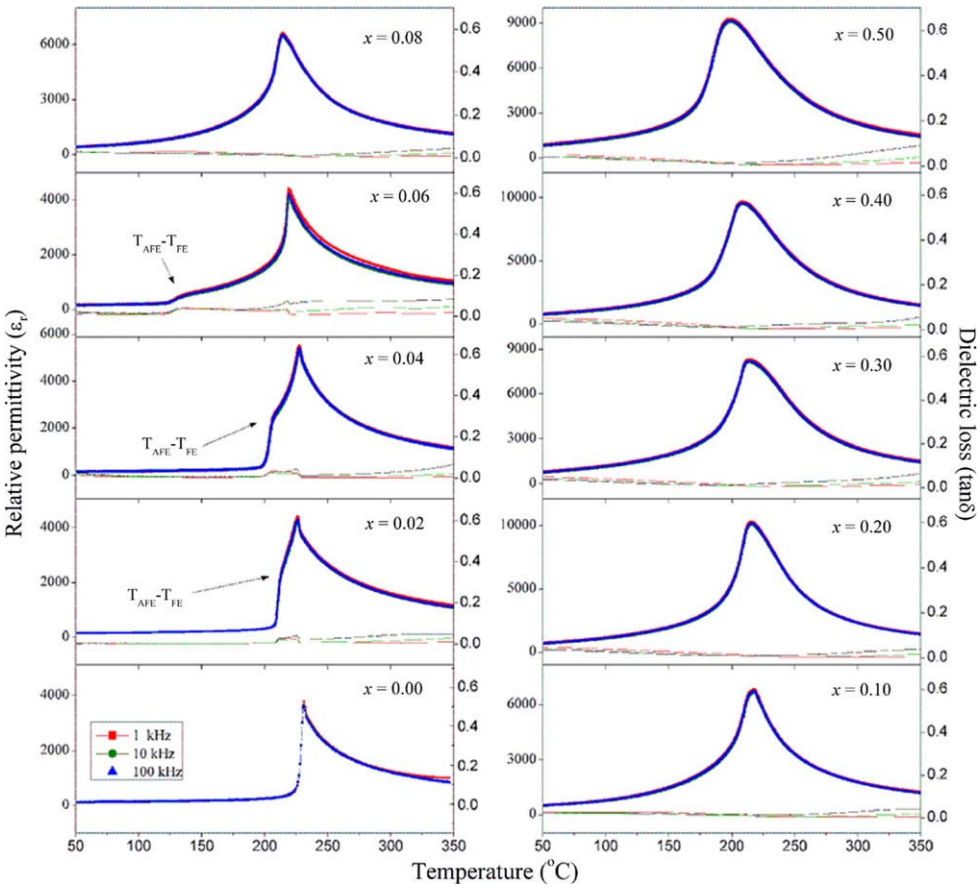

Fig. 4 Temperature dependence of dielectric properties of $(1-x)PbZrO_3$–$xPb(Zn_{1/3}Nb_{2/3})O_3$ ceramics

ties, the grain growth was inhibited. This phenomenon was similar to those in other solid solution systems [27].

3.3 Dielectric properties

The relative permittivity of $(1-x)$PZ–xPZN ceramics, as a function of temperature at differently applied frequencies between 1 and 100 kHz, are given in Fig. 4. At the composition, $0.00 < x \leq 0.06$, two distinct dielectric peaks were observed. The phase transitions at lower temperatures were due to transformation from the orthorhombic antiferroelectric phase to rhombohedral ferroelectric phase [16], while the maximum dielectric was linked with the transformation of the rhombohedral ferroelectric phase into the cubic paraelectric phase [17, 23]. Later descriptions in ferroelectric data supported this finding.

Table 2 Phase transition temperatures and enthalpy of $(1-x)PbZrO_3$–$xPb(Zn_{1/3}Nb_{2/3})O_3$ ceramics

Composition (x)	Phase transition temperature (°C)						ΔH ($J\,g^{-1}$)	$\Delta S \times 10^3$ ($J\,g^{-1}K^{-1}$)	$\Delta S/T_t \times 10^6$ ($J\,g^{-1}K^{-2}$)
	Dielectric constant		Thermal expansion		DSC				
	T_{AFE-FE}	T_{FE-PE}	T_{AFE-FE}	T_{FE-PE}	T_{AFE-FE}	T_{FE-PE}			
$x=0.00$	–	233	212	220	208.4	225.6	2.6	11.6	51.7
$x=0.02$	212	226	192	213	193.1	224.9	3.3	14.6	64.8
$x=0.04$	207	227	181	215	184.7	223.2	3.3	14.7	65.8
$x=0.06$	130	219	110	205	137.4	222.1	3.6	16.2	72.8
$x=0.08$	–	214	–	200	94.7	219.5	3.3	15.1	68.9
$x=0.10$	–	217	–	–	59.0	217.3	2.6	11.8	54.2
$x=0.20$	–	216	–	–	–	211.2	1.5	7.1	33.8
$x=0.30$	–	213	–	–	–	209.4	0.8	4.0	19.4
$x=0.40$	–	210	–	–	–	188.5	0.6	3.4	18.0
$x=0.50$	–	200	–	–	–	–	–	–	–

Phase transition temperature of $(1-x)$PZ–xPZN ceramics is summarized in Table 2. The transition temperatures of the AFE to FE phase became lower, and the temperature range width of the FE phase also increased continuously with increasing PZN. For the composition, $x \geq 0.08$, transition of the orthorhombic antiferroelectric phase to rhombohedral ferroelectric phase was not observed. As PZN concentration increased, the diffuse phase transition (DPT) behavior, with broad maximum and frequency dispersion, became more self-evident. The FE to PE transition decreased nearly linearly at the rate of 0.48°C/mol% of PZN, when compared with its value for pure PZ. Noticeably, this rate was much lower than that of PZ–PCoN (2.20°C/mol%) [17] and PZ–PNN (2.81°C/mol%) [18]. The maximum relative permittivity for all compositions is listed in Table 3. The composition, $x = 0.20$, showed the highest value of relative permittivity, and existence of the MPB near this composition was expected. This result is consistent with the X-ray diffraction finding that both orthorhombic and rhombohedral phases coexist in this composition. It was found that the addition of PZN also shifts the transition temperature (T_m) value of PZ–PZN ceramics down from 243°C (T_c for PZ) in the composition, $x = 0.0$, to 199°C in the composition, $x = 0.5$. A similar trend has also been found in the PZ–PNN [18] and PZ–PCoN system [17].

It is well known that the relative permittivity of a normal ferroelectric, which is above the maximum relative permittivity temperatures, can be described by the Curie–Weiss law [4]:

$$\frac{1}{\varepsilon_r} = \frac{T - T_0}{C}, \tag{1}$$

where T_0 is the Curie–Weiss temperature, and C the Curie constant. Above the Curie temperature, the relative permittivity of pure PZ obeys the Curie–Weiss law, with the Curie constant $C \sim 1.70 \times 10^5$°C and Curie–Weiss temperature $T_0 \sim 179$°C. However, a broad relative permittivity of relaxor ferroelectric can be described by a simple quadratic law. The relative permittivity of relaxor ferroelectric above the maximum relative permittivity temperatures can be derived via the following expression [28]:

$$\frac{\varepsilon'_m}{\varepsilon'(f,T)} = 1 + \frac{(T - T_m(f))^\gamma}{2\delta_\gamma^2} \quad (1 \leq \gamma \leq 2), \tag{2}$$

where ε'_m is the maximum value of the permittivity at $T = T_m(f)$. The value of γ expresses the degree of dielectric relaxation in the relaxor ferroelectric material, when $\gamma = 1$ (2) expresses Curie–Weiss behavior, while $\gamma = 2$ in this equation is identical to the quadratic relationship. Many relaxor ferroelectric materials can fit (2) with $\gamma = 2$ at temperatures above T_{max}. The parameter δ_γ can be used to measure the degree of diffuseness of the phase transition in mixed relaxor antiferroelectric materials. The values γ and δ_γ are both material constants depending on the structure and composition of the material. The δ_γ value can be determined from the slope of $\varepsilon'_m/\varepsilon'$ versus $(T - T_m)^2$, which should be linear. By plotting $\ln(1/\varepsilon - 1/\varepsilon_{max})$ versus $\ln(T - T_m)$, γ can be determined directly from the gradient. According to (2), the values of $\ln(1/\varepsilon - 1/\varepsilon_{max})$ for the sintered ceramics measured at 100 kHz are plotted against $\ln(T - T_m)$ in Fig. 5. As shown in the figure, the plotted lines for all samples demonstrate significantly good linearity within the measured temperature range. The intercept and gradient of lines in Fig. 5 are used to calculate and demonstrate γ and δ_γ for each sample in Table 3. The value of γ presented in Table 3 varies between 1.02 and 1.81. The δ_γ values are increased also from 11.5 to 15.6 with increasing PZN content, thus confirming that a diffuse phase transition occurs in the PZ–PZN system. Nevertheless, a minor swing of γ values

Table 3 Dielectric and ferroelectric properties of $(1-x)PbZrO_3$–$xPb(Zn_{1/3}Nb_{2/3})O_3$ ceramics

Composition (x)	T_m (°C)	$\varepsilon_{r\ max}$	δ_γ	γ	P_r (μC/cm^2)	P_s (μC/cm^2)	E_c (kV/cm)
0.00	233	2850	11.5	1.02	–	–	–
0.02	226	4400	11.6	1.02	–	–	–
0.04	227	5500	11.8	1.04	–	–	–
0.06	219	4400	11.8	1.08	–	–	–
0.08	214	6600	13.5	1.33	20.20	22.86	17.88
0.10	217	6800	12.6	1.09	22.69	25.69	19.59
0.20	216	10300	14.8	1.55	26.90	31.45	15.52
0.30	213	8300	16.0	1.81	18.59	25.66	13.34
0.4	209	9700	15.3	1.59	20.73	27.48	13.04
0.5	199	9300	15.6	1.65	19.65	26.18	14.80

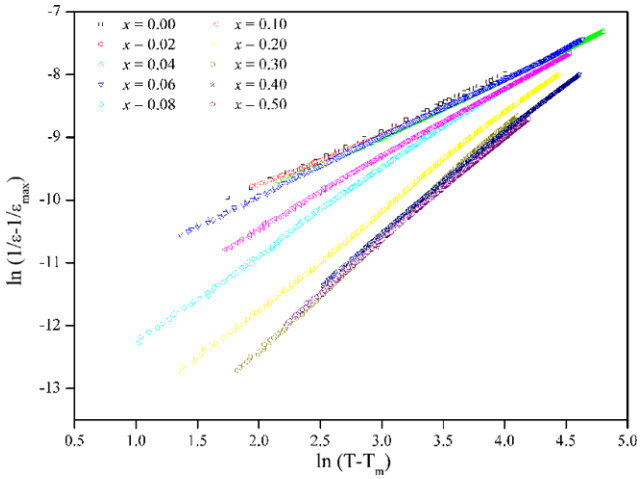

Fig. 5 The $\ln(1/\varepsilon - 1/\varepsilon_{max})$ vs. $\ln(T - T_m)$ plots for $(1-x)$PZ–xPZN ceramics with $x = 0.00$–0.50

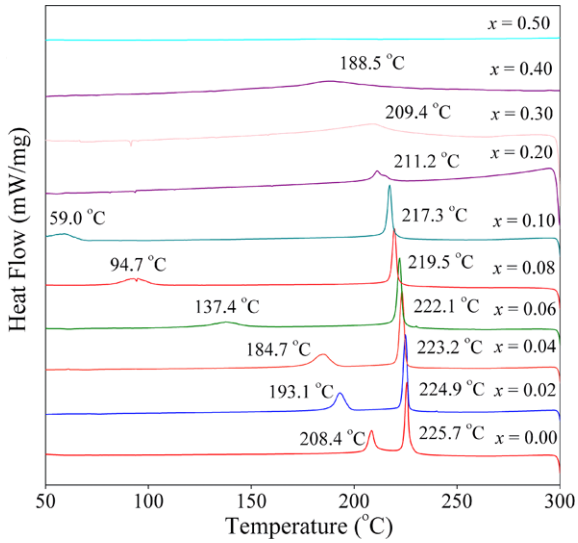

Fig. 6 Typical differential scanning calorimetry (DSC) curves for $(1-x)$PZ–xPZN ceramics with $x = 0.00$–0.50

as a function of composition was found in some compositions. For ferroelectric ceramics, it has been established that the degree of dielectric relaxation could also be caused by the decrease of grain size [29], and the observed difference of γ value could be a result of grain size variation. A similar propensity also has been detected in several prior investigations [29, 30].

3.4 Thermal properties

The DSC technique was used as a primary tool to confirm the phase transition of the PZ–PZN system. DSC analysis results of the PZ–PZN ceramics are presented in Fig. 6, in which two distinct endothermic peaks for the composition, $0.0 \le x \le 0.10$, are observed. The lower temperature corresponds to the transition temperature of the AFE→FE phase transition, while the higher temperature corresponds to the FE→PE phase transition. The AFE→FE peaks shift to lower temperatures, with a higher composition of x. This result corresponds to a decreasing AFE phase, and the temperature range width of the FE phase increases, with increasing amounts of PZN content. Moreover, the endothermic peaks become progressively broader, while the areas under these peaks (ΔH) decrease with increasing PZN content. These results indicate that phase transition diverges from the first-order type. Burggraaf et al. [31] reported that the change in entropy (ΔS) and $\Delta S/T_t$ related to fluctuation in conjunction with a small spontaneous lattice deformation and polarization. They also reported that large values of the $\Delta S/T_t$ ratio give sharp phase transition, whereas the lower values lead to diffusing phase transition. Transition temperatures and the values of ΔH, ΔS, and $\Delta S/T_t$ for all compositions are calculated and summarized in Table 2. Notably, the values of $\Delta S/T_t$ gradually reduce, which indicates that the diffuse phase transition behavior of PZ–PZN increases with increased PZN.

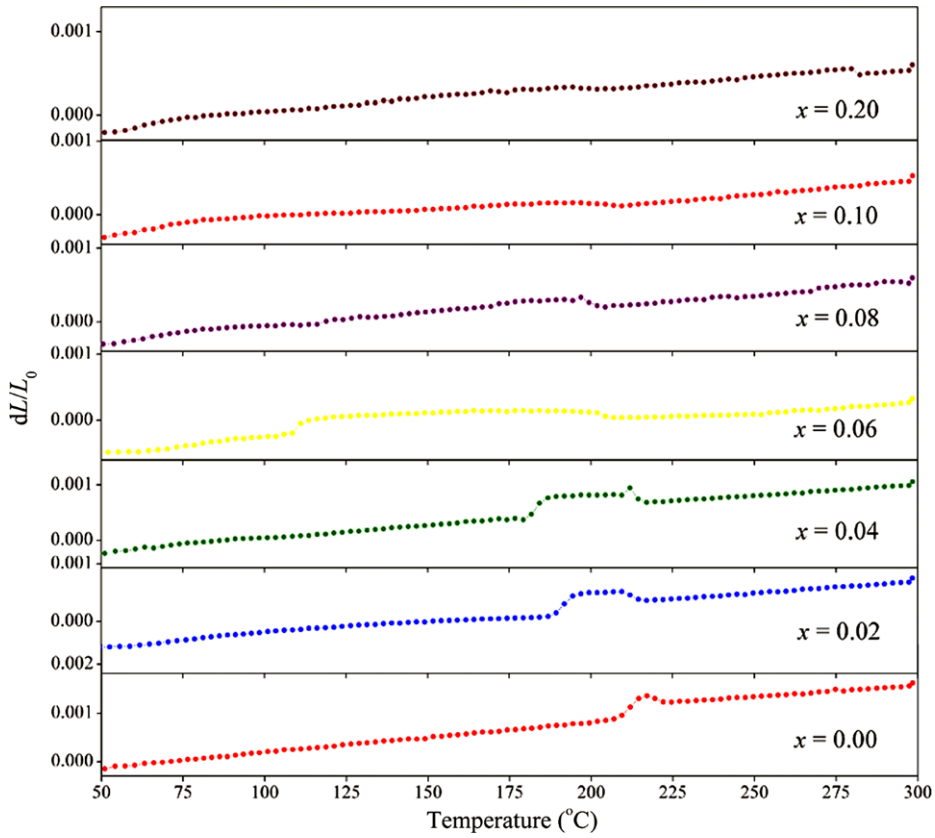

Fig. 7 Thermal expansion curves of $(1-x)PbZrO_3$–$xPb(Zn_{1/3}Nb_{2/3})O_3$ ceramics in heating

It is well known that in phase transition from AFE to FE or FE to PE the volume of material yields abrupt changes. Therefore, the thermal expansion measurement was employed as a secondary tool to confirm the phase transition sequence. Figure 7 shows thermal expansion curves for the PZ–PZN system. In the expansion curves of $0.00 < x \leq 0.06$, with rising temperature, the volume expansion that resulted from the transformation of AFE to FE, and the small volume contraction of FE to PE transition, were observed. The thermal expansion curves exhibited FE to PE phase transition only when the amount of PZN increased to $x = 0.08$; however, the transition temperature tended to decrease continuously with increasing PZN. There was no clear anomaly in the thermal expansion at transition temperature for the composition, $x \geq 0.10$, because these compositions showed the second-order phase transition, which is the behavior of relaxor-like FE [16]. This occurrence was similar to those in other researches on different solid solution systems [32]. In demonstrating phase transition of PZ–PZN ceramics by relative permittivity, DSC, and thermal expansion measurements, it is noteworthy that all compositions showed the difference of transition temperature in each technique, as listed in Table 2. This result attributed to the different heating rates used during the measurements.

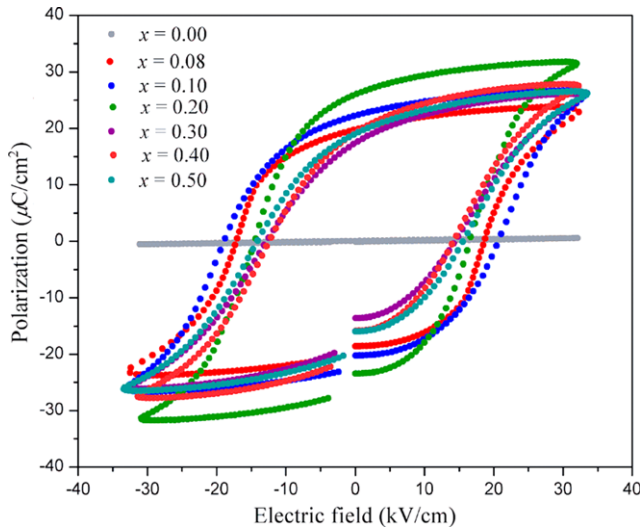

Fig. 8 Polarization–electric field hysteresis loops of $(1-x)PbZrO_3$–$xPb(Zn_{1/3}Nb_{2/3})O_3$ ceramics

3.5 Ferroelectric properties

The ferroelectric measurement was used to clarify further dielectric behavior of the FE phase in the PZ–PZN system. The P–E hysteresis loops for all composition ceramics at room temperature are shown in Fig. 8. At the composition, $0.00 \leq x \leq 0.06$, a near-linear relationship of P–E

loop is observed, due to electric fields being insufficient to switch any ferroelectric domains. It is well known that in PZ ceramics, the electric field required for inducing the AFE to FE phase transition at room temperature is higher than the breakdown strength of the ceramics [11, 33]. This result indicated that the AFE phase of pure PZ persisted in the PZ–PZN system for $x < 0.08$ at room temperature, which corresponded to the dielectric and thermal expansion results. For $0.08 \leq x \leq 0.50$, at the 35 kV/cm electric field strength, fully and symmetrical hysteresis loops were detected. The driving force for an antiparallel shift of Pb^{2+} ions was decreased, due to the replacement of the Zr^{4+} ion by Zn^{2+}/Nb^{5+} ions, which interrupted the translational symmetry. Then, the ferroelectric phase appeared when the amount of PZN was more than 6 mol%. Moreover, the hysteresis loop of ceramics at $0.08 \leq x \leq 0.50$ showed normal-like ferroelectric behavior with the square loop. The remanent polarization (P_r) and coercive field (E_c) value of ceramics at $0.08 \leq x \leq 0.50$ did not change significantly. However, the highest P_r value of this system was found in the composition, $x = 0.20$, where $P_r = 26.90$ μC/cm^2 and $E_c = 15.52$ kV/cm. The ferroelectric properties, together with the basis of XRD and dielectric measurements, led to the conclusion that the MPB of the $(1-x)$PZ–xPZN system exists at $x = 0.20$. Interestingly, the MPB of the $(1-x)$PZ–xPZN system shows higher remanent polarization and coercive field when compared to that of the PZT system [34, 35]. It is well known that the MPB and grain size effect are important parameters that strongly influence electrical properties of lead-based piezoelectric ceramics. However, this study showed that the MPB in the PZ–PZN system is more influential to electrical properties than the grain size effect. For the composition, $x = 0.50$, the value of P_r decreased to 19.65 μC/cm^2, due to the coexistence of a pyrochlore phase, as observed by the XRD technique.

4 Conclusion

The solid solubility limit of the $(1-x)PbZrO_3$–$xPb(Zn_{1/3}Nb_{2/3})O_3$ system, which was prepared via the columbite method, was about $x = 0.40$. Relaxor ferroelectric PZN was found to strongly influence crystal structure, and electrical and thermal properties of PZ ceramics. The XRD results indicate that the crystal structure of solid solution $(1-x)$PZ–xPZN, where $x = 0.00$–0.50, successively transforms from orthorhombic to rhombohedral symmetry, with increased PZN concentration. The AFE→FE phase transition shifts to lower temperatures with higher compositions of x. The temperature range width of the FE phase increases with the amount of PZN increase. The dielectric properties of PZ–PZN exhibited significant improvement with PZN loading. The MPB of the $(1-x)$PZ–xPZN system exists close to the composition, $x = 0.20$.

Acknowledgements This research was supported by a grant from the program for Strategic Scholarships for Frontier Research Network for the Join Ph.D. Program Thai Doctoral degree of the Commission on Higher Education (CHE), the Thailand Research Fund (TRF), and the National Nanotechnology Center (NANOTEC) NSTDA, Ministry of Science and Technology, Thailand, through its "Center of Excellence Network" program.

References

1. A.S. Bhalla, R. Guo, R. Roy, Mater. Res. Innov. **4**, 3 (2000)
2. G.H. Haertling, J. Am. Ceram. Soc. **82**, 797 (1999)
3. Y. Xu, *Ferroelectric Materials and Their Application* (Elsevier, Amsterdam, 1991)
4. B. Jaffe, W.R. Cook, *Piezoelectric Ceramic* (R.A.N. Publishers, 1971)
5. P. Seung-Eek, T.R. Shrout, IEEE Trans. Ultrason. Ferroelectr. Freq. Control **44**, 1140 (1997)
6. T. Takenaka, K. Muramata, T. Fujii, Ferroelectrics **134**, 133 (1992)
7. J. Kuwata, K. Uchino, S. Nomura, Ferroelectrics **37**, 579 (1981)
8. N. Vittayakorn, C. Puchmark, G. Rujijanagul, X. Tan, D.P. Cann, Curr. Appl. Phys. **6**, 303 (2006)
9. N. Vittayakorn, G. Rujijanagul, X. Tan, M.A. Marquardt, D.P. Cann, J. Appl. Phys. **96**, 5103 (2004)
10. N. Vittayakorn, T. Tunkasiri, Phys. Scr. T **129**, 199 (2007)
11. E. Sawaguchi, G. Shirane, S. Hoshino, Phys. Rev. **83**, 1078 (1951)
12. G. Shirane, Phys. Rev. **86**, 219 (1952)
13. N. Vittayakorn, T. Bongkarn, G. Rujijanagul, Physica B, Condens. Matter **387**, 415 (2007)
14. B. Xu, N.G. Pai, L.E. Cross, Mater. Lett. **34**, 157 (1998)
15. X. Hao, J. Zhai, J. Zhou, J. Yang, X. Song, S. An, J. Cryst. Growth **312**, 667 (2010)
16. S. Wirunchit, N. Vittayakorn, J. Appl. Phys. **104**, 024103 (2008)
17. W. Banlue, N. Vittayakorn, Appl. Phys. A **93**, 565 (2008)
18. S. Wirunchit, P. Laoratanakul, N. Vittayakorn, J. Phys. D, Appl. Phys. **41**, 125406 (2008)
19. A. Halliyal, U. Kumar, R.E. Newham, L.E. Cross, Am. Ceram. Soc. Bull. **66**, 671 (1987)
20. T.R. Shrout, A. Halliyal, Am. Ceram. Soc. Bull. **66**, 704 (1987)
21. J.R. Belsick, A. Halliyal, U. Kumar, R.E. Newham, Am. Ceram. Soc. Bull. **66**, 664 (1987)
22. R.D. Shannon, Acta Crystallogr. **A32**, 751 (1976)
23. N. Vittayakorn, P. Charoonsuk, P. Kasiansin, S. Wirunchit, B. Boonchom, J. Appl. Phys. **106**, 064104 (2009)
24. A.L. Costa, C. Galassi, G. Fabbri, E. Roncari, C. Capiani, J. Eur. Ceram. Soc. **21**, 1165 (2001)
25. J.C. William, *Materials Science and Engineering: An Introduction* (Wiley, New York, 2007)
26. S. Wirunchit, N. Vittayakorn, Ferroelectrics **382**, 135 (2009)
27. J. Yoo, K. Kim, C. Lee, L. Hwang, D. Paik, H. Yoon, H. Choi, Sens. Actuators A, Phys. **137**, 81 (2007)
28. K. Uchino, S. Nomura, Ferroelectr. Lett. **44**, 55 (1982)
29. V. Koval, C. Alemany, J. Briancin, H. Brunckova, J. Electroceram. **10**, 19 (2003)
30. X.J. Lu, X.M. Chen, J. Electroceram. **7**, 127 (2001)
31. C. Stenger, A.J. Burggraaf, Phys. Status Solidi **61**, 275 (1980)
32. N. Vittayakorn, D.P. Cann, Appl. Phys. A **86**, 403 (2007)
33. S. Roberts, J. Am. Ceram. Soc. **33**, 63 (1953)
34. R. Yimnirun, S. Ananta, P. Laoratanakul, J. Eur. Ceram. Soc. **25**, 3235 (2005)
35. S. Wongsaenmai, Y. Laosiritaworn, S. Ananta, R. Yimnirun, Mater. Sci. Eng. B **128**, 83 (2005)

Powder Technology 203 (2010) 310–314

Contents lists available at ScienceDirect

Powder Technology

journal homepage: www.elsevier.com/locate/powtec

Grass blade-like microparticle $MnPO_4 \cdot H_2O$ prepared by a simple precipitation at room temperature

Banjong Boonchom [a,*], Rattanai Baitahe [b,c,d], Zongporn Joungmunkong [e], Naratip Vittayakorn [b,c,d]

[a] King Mongkut's Institute of Technology Ladkrabang, Chumphon Campus, 17/1 M. 6 Pha Thiew District, Chumphon 86160, Thailand
[b] Electroceramic Research Laboratory, College of KMITL Nanotechnology, King Mongkut's Institute of Technology Ladkrabang, Bangkok 10520, Thailand
[c] Advanced Materials Science Research Unit, Department of Chemistry, Faculty of Science, King Mongkut's Institute of Technology Ladkrabang, Bangkok 10520, Thailand
[d] ThEP Center, CHE, 328 Si Ayutthaya Rd., Bangkok 10400, Thailand
[e] Faculty of Pharmaceutical Sciences, Ubon Ratchathani University, Ubonratchathani 34190, Thailand

ARTICLE INFO

Article history:
Received 4 February 2010
Received in revised form 12 May 2010
Accepted 14 May 2010
Available online 8 June 2010

Keywords:
Grass blade-like particle $MnPO_4 \cdot H_2O$
FTIR
Thermogravimetric analysis
Powder synthesis

ABSTRACT

Grass blade-like microparticle $MnPO_4 \cdot H_2O$ was synthesized by a simple precipitation at room temperature using a mixture of manganese sulphate monohydrate, phosphoric acid and water at pH = 7. The thermogravimetric study indicates that the synthesized compound is stable below 500 °C and its final decomposed product is $Mn_2P_2O_7$. The pure monoclinic phases of the synthesized $MnPO_4 \cdot H_2O$ and its final decomposed product $Mn_2P_2O_7$ are verified by XRD data. FTIR spectra indicate the presences of the PO_4^{3-} ion and water molecules in the $MnPO_4 \cdot H_2O$ structure and the $P_2O_7^{4-}$ ion in the $Mn_2P_2O_7$ structure. The thermal stability, crystallite size, and grass blade-like microparticle of $MnPO_4 \cdot H_2O$ in this work are different from previous reports, which may be caused by the starting reagents and reaction condition for the precipitation.

1. Introduction

In the recent years, a large number of inorganic natural and synthesized metal phosphates have the incremented use in order to supply the demands of industrial, commercial, agricultural, scientific and heath sectors because of their valuable physical–chemical properties and reactivity [1,2]. The metal phosphate compounds are divided by phosphate block unit as PO_4^{3-}, HPO_4^{2-}, $H_2PO_4^{-}$, $P_2O_7^{4-}$ and $P_4O_{12}^{4-}$ units [3], which have found widespread applications in laser host [4], ceramic [5], dielectric [6], electric [7], magnetic [8], fertilizer [9], and catalytic [10] processes. Synthesis of these phosphate materials by precipitation reaction at room temperature with short time consumption and the morphology and architecture at micro-/nanoscale levels have attracted the interest of many researchers due to their conveniences and their strong influence on material properties [4–10]. Compared with hydrothermal method, solid state method, and sol–gel method, the remarkable advantages of precipitation reaction are its flexibility of operation, simple and rapid route, and environmental benign and cost-effective technique [7,11–13].

Manganese phosphate monohydrate ($MnPO_4 \cdot XH_2O$, $x = 1.0$–1.7 mol), non-toxic foundational compound, has been applied widely in catalysis, fertilizer, and electrical fields, was synthesized by various methods (hydrothermal method, sol–gel method, solid state route or high-temperature method) and was also found in nature [14,15]. Christensen [16] reported for the first time the synthesis of $MnPO_4 \cdot XH_2O$ by manganese(II) nitrate–phosphoric acid system in the presence of nitric acid, which was used for the oxidation of manganese(II) nitrate. The another preparation method involved the oxidation of manganese(II) carbonate by nitric acid in the presence of phosphoric acid [17–19]. Recently, our group reported the synthesis of $MnPO_4 \cdot H_2O$ by soft solution route using manganese (II) nitrate–phosphoric acid–methanol system at 40 °C [20]. To improve its functional properties and enlarge its application, many attempts have been conducted during the last two decades, one of which is to control shaping powder material (bulk, porous, micro- or nanoparticles) [11–13,21]. So far, there have been structural and spectroscopic reports on $MnPO_4 \cdot XH_2O$ ($x = 1.0$–1.7 mol), to our knowledge, little are the morphology and architecture data available.

In this present, $MnPO_4 \cdot H_2O$ powder was prepared by simple precipitation at room temperature using manganese sulphate monohydrate, phosphoric acid and water at pH = 7. This method is simple, rapid, cost-effective and has non-toxic routes to synthesize grass blade-like microparticle $MnPO_4 \cdot H_2O$. The precipitates were characterized by TG/DTG, DSC, XRD, SEM and FTIR techniques. The data obtained will be important for further studies of the compound.

* Corresponding author. Tel.: +66 7750 6422x4565; fax: +66 7750 6411.
E-mail address: kbbanjon@kmitl.ac.th (B. Boonchom).

0032-5910/$ – see front matter © 2010 Elsevier B.V. All rights reserved.
doi:10.1016/j.powtec.2010.05.022

2. Experimental

$MnPO_4 \cdot H_2O$ crystalline powder was prepared by a solution precipitation method using $MnSO_4 \cdot H_2O$ (>99% purity, Fluka) and phosphoric acid (86.4% w/w H_3PO_4, Merck) as starting materials. Following procedure, 1.70 g of $MnSO_4 \cdot H_2O$ was dissolved in 18 mL of 1 M H_3PO_4. The pH of the manganese- and phosphate-containing solution was adjusted to 7 by the addition of NaOH, and $MnPO_4 \cdot H_2O$ was precipitated at room temperature. The powder was obtained, then isolated by filtration, washed with deionized water and dried in air. This process can be explained by the following reaction:

$$Mn^{2+}_{(s)} \rightarrow Mn^{3+} + e^- \text{(anodic)}$$

$$H^+ + e^- \rightarrow 1/2H_2\uparrow \text{(cathodic)} \rightarrow H_3PO_4 \rightarrow 3H^+ + PO_4^{3-}$$

$$Mn^{3+} + PO_4^{3-} \rightarrow Mn(PO_4)\downarrow$$

Therefore, the overall reaction can be rewritten by:

$$\text{NaOH pH} = 7 \text{ at room temperature}$$

$$Mn^{2+}SO_4 \cdot H_2O + 3H^+ + PO_4^{3-} \rightarrow Mn^{3+}PO_4 \cdot H_2O\downarrow + 1/2H_2\uparrow + 2H^+(2H_2O) + SO_4^{2-}(Na_2SO_4)$$

Thermal property of the studied compound was investigated on a TG-DTG (Thermogravimetry, TG; Derivative Thermogravimetry, DTG) Pyris One Perkin-Elmer instrument and a DSC (Differential Scanning Calorimetry) 204 F1 Phoenix Perkin-Elmer apparatus with α-Al_2O_3 powder as the reference material. On the basis of TG data, its final decomposed product seemed to occur at a temperature above 500 °C and the water content was determined. In order to gain the thermal decomposition phase, the synthesized $MnPO_4 \cdot H_2O$ was heated in a box furnace at 500 °C for 2 h. The manganese contents of the synthesized $MnPO_4 \cdot H_2O$ and its decomposed product $Mn_2P_2O_7$ were determined by dissolving in 0.0126 M hydrochloric acid using atomic absorption spectrophotometry (AAS, Perkin-Elmer, Analyst100). The phosphorus contents were analyzed by colorimetric method of the molybdophosphate complex [22]. The structure and crystallite sizes of the prepared powder and its decomposed product were studied by X-ray powder diffraction using a D8 Advanced powder diffractometer (Bruker AXS, Karlsruhe, Germany) with Cu Kα radiation ($\lambda = 0.1546$ nm). The Scherrer method was used to evaluate the crystalline size [23]. The room temperature FTIR spectra were recorded in the range of 4000–400 cm^{-1} with 8 scans on a Perkin-Elmer Spectrum GX spectrometer with the resolution of 4 cm^{-1}. The morphology was examined by SEM using Hitachi S4700 after gold coating.

3. Results and discussion

The TG/DTG curves of $MnPO_4 \cdot H_2O$ are shown in Fig. 1. The TG curve shows the weight loss between 50 and 600 °C, which is related to the elimination of crystallization water and oxygen. The first weight loss in the range of 50–320 °C was 10.80%, which corresponds to the elimination of one molecule of crystallization water. The second weight loss in the range of 320–500 °C was 5.20%, which corresponds to the consequent release of oxygen due to the reduction of manganese (III) to manganese(II) [17,18]. Total weight loss of 16.00% is close to the reported values by previous works [17–20]. The mass retained of about 84% is comparable with the value expected for the formation of $Mn_2P_2O_7$, which is verified by XRD and FTIR measurements. In the DTG curve, the corresponding peaks at 120, 190, 260 and 330 °C are observed. The overall reaction formally could be presented as:

$$MnPO_4 \cdot H_2O \; 1/2Mn_2P_2O_7 + H_2O + 1/2O_2$$

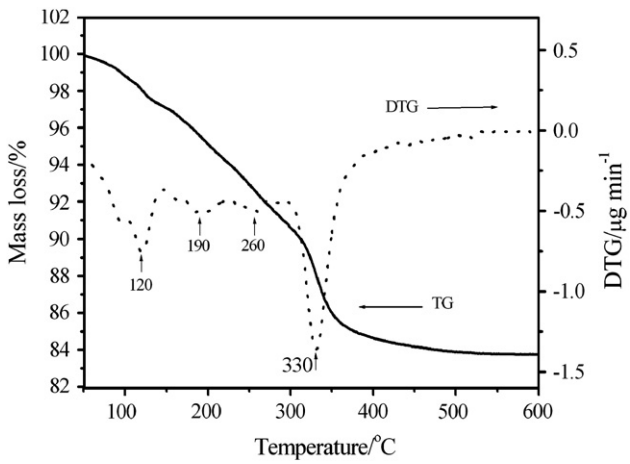

Fig. 1. TG/DTG curves of the synthesized $MnPO_4 \cdot H_2O$ at the heating range of 10 °C min^{-1}.

The temperature at which theoretical mass loss is achieved can be also determined from TG trace and considered to be the minimum temperature needed for the calcinations process. Thus, the $MnPO_4 \cdot H_2O$ powder was calcined at 500 °C for 2 h in a box furnace, which is lower temperature comparable with this phosphate reported by previous works [17–20]. The thermal behavior of the prepared $MnPO_4 \cdot H_2O$ powder in this work is significantly different from that of the decomposition reactions of $MnPO_4 \cdot H_2O$ reported in the literature [17–20]. The result indicates that starting reagent and reaction condition for the precipitation have the effects on the thermal transformation of $MnPO_4 \cdot H_2O$.

The DSC curve of $MnPO_4 \cdot H_2O$ in N_2 is shown in Fig. 2. The DSC trace shows three endothermic peaks and one exothermic peak at 130, 268, 324, and 475 °C (onset peak at 117, 250, 300, and 450 °C) which are due to two dehydration, reduction and phase transformation reactions of this compound, respectively. According to the DSC curve, the heat of two dehydration, reduction and phase transformation reactions can be calculated and were found to be 20.70, 19.65, 140.88 and −17.18 J g^{-1}, respectively. The reduction step exhibits higher heat energy in comparison with other ones. This result indicates that it occurs harder than the dehydration and phase transformation reactions.

The XRD patterns of $MnPO_4 \cdot H_2O$ and its decomposed product $Mn_2P_2O_7$ are shown in Fig. 3. The five strong peaks (2θ data) were observed at 27.898(021), 30.988(−202), 34.003(−221), 41.1204 (−311), and 55.961(042) for the $MnPO_4 \cdot H_2O$ and 28.837(111),

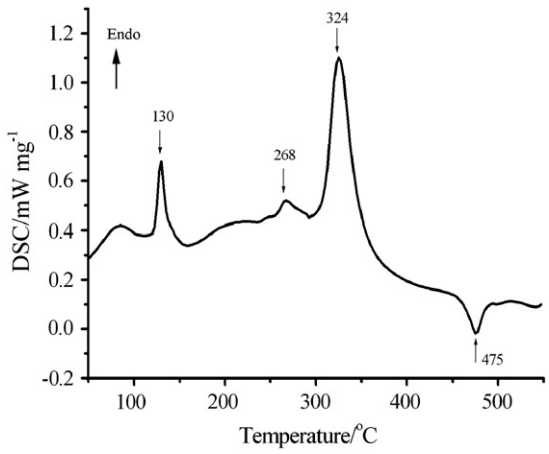

Fig. 2. DSC curve of the synthesized $MnPO_4 \cdot H_2O$ at the heating range of 10 °C min^{-1}.

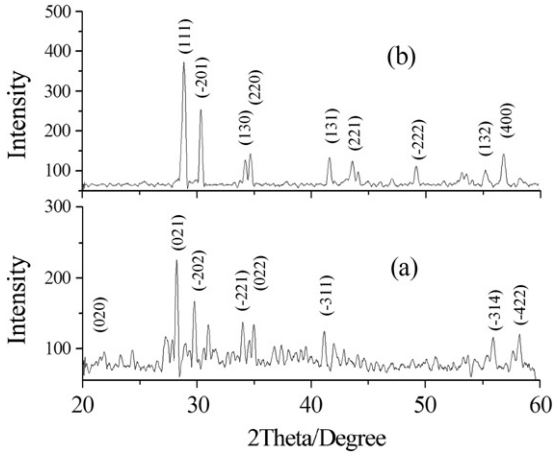

Fig. 3. XRD patterns of the synthesized $MnPO_4 \cdot H_2O$ (a) and its decomposed product $Mn_2P_2O_7$ (b).

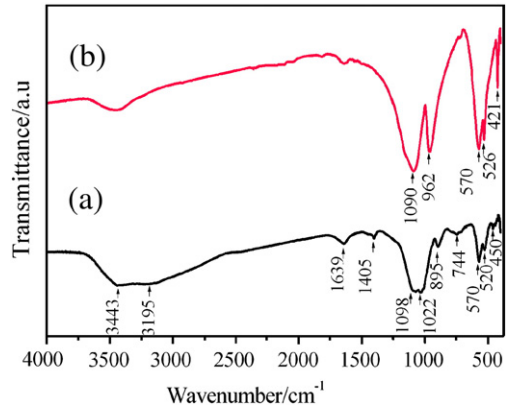

Fig. 4. FTIR spectra of the synthesized $MnPO_4 \cdot H_2O$ (a) and its decomposed product $Mn_2P_2O_7$ (b).

30.317(−201), 34.206(130), 34.661(220), and 41.657(131) for $Mn_2P_2O_7$, respectively (indices are given in parentheses). The patterns match the standard XRD data for the $MnPO_4 \cdot H_2O$ of PDF no. 511548 and for $Mn_2P_2O_7$ of PDF no. 771243. These results indicated that both crystal structures are monoclinic systems with space group C2/c ($Z=4$) for $MnPO_4 \cdot H_2O$ and C2/m ($Z=2$) for $Mn_2P_2O_7$. The average crystallite sizes and lattice parameters of the $MnPO_4 \cdot H_2O$ and the decomposed product $Mn_2P_2O_7$ were calculated from XRD patterns and also tabulated in Table 1. The lattice parameters of $MnPO_4 \cdot H_2O$ and $Mn_2P_2O_7$ are close to those of the standard data PDF no. 511548 and PDF no. 771243, respectively. However, the problem here is that the XRD patterns are very weak, so the lattice parameters obtained from these data are different from the value presented by other researchers. The result is caused by the different synthetic methods, which are in agreement with the results reported in the literature [11,12,19,20]. The average crystallite size of 41 ± 13 nm for $MnPO_4 \cdot H_2O$ sample and 38 ± 11 nm for $Mn_2P_2O_7$ in this work are smaller than those prepared from $Mn(NO_3)_2 \cdot 4H_2O$–H_3PO_4–CH_3OH system reported by Boonchom et al. (66 ± 28 nm for $MnPO_4 \cdot H_2O$ and 54 ± 18 nm for $Mn_2P_2O_7$)[20]. The crystallite size of $Mn_2P_2O_7$ in this work is close to that from $Mn_2P_2O_7$ prepared at 800 °C (31 ± 13 nm) in our previous study [24], although the $Mn_2P_2O_7$ in this work was obtained from the lower temperature (500 °C). These results confirmed that the different crystallite sizes of the synthesized $MnPO_4 \cdot H_2O$ and $Mn_2P_2O_7$ depend on the starting reagent and reaction condition for the precipitations, which is consistent with the literature [25–27].

The FTIR spectrum of the synthesized $MnPO_4 \cdot H_2O$ powder (Fig. 4a) reflects characteristic vibrations of PO_4^{3-} ion and H_2O molecules. Water bonding at 1639 cm^{-1} and O–H stretching broad band center at 3443 cm^{-1} can be observed, implying the presence of crystalline hydrate. Spectra involving phosphate vibrations center on four regions because of the idealized T_d symmetry of the phosphate ion. Vibrational bands of PO_4^{3-} ion are observed in the regions of 990–950, 1100–1020, 480–400 and 650–500 cm^{-1}, which are assigned to the symmetric stretching region (ν_1), the antisymmetric stretching region (ν_3), the symmetric bending region (ν_2), and the antisymmetric bending region (ν_4), respectively [28,29]. The several strong and sharp bands in the ranges of 1100–890 and 600–500 cm^{-1}, which split into several peaks, report complexes of stretching and bending of PO_4^{3-} group, respectively. Antisymmetric stretching and bending vibrations are found at higher wavenumbers than symmetric stretching and bending vibrations, are more intense in infrared spectroscopy and weaker in Raman spectroscopy. Hence most absorptions in the 1000–1100 cm^{-1} region are attributable to antisymmetric (ν_3) vibrations. For the synthesized $MnPO_4 \cdot H_2O$ powder strong band was observed at 1098 and 1022 cm^{-1}. Another strong band observed at 895 cm^{-1} was attributed to the symmetric stretching mode of PO_4^{3-}. Antisymmetric bending (ν_2) vibrations are observed at 570 and 520 cm^{-1}. These phosphate band positions are in excellent agreement with published data [28,29]. The weak bands at 1639 and 1405 cm^{-1} are the H–O–H bending broad. The last band is assigned to the very low bending of water molecule, which is in excellent agreement with the literature [28,29]. The middle intense bands at 3443 and 3195 cm^{-1} are assigned to the antisymmetric and symmetric stretchings of water molecule, respectively. In addition, a weak band observed at 744 cm^{-1} is assigned to water libration (rocking mode) [28,29]. There results show that only the tribasic form of PO_4^{3-} was present and some crystalline water existed in the title compound.

Table 1
Average crystallite sizes and lattice parameters of $MnPO_4 \cdot H_2O$ and $Mn_2P_2O_7$ calculated from XRD data.

Lattice parameters	$MnPO_4 \cdot H_2O$			$Mn_2P_2O_7$		
	This work	PDF #511548	DIF (This work-PDF)	This work	PDF #771243	DIF (This work-PDF)
a (Å)	7.009(0)	6.913	+0.096	6.845(0)	6.633	+0.212
b (Å)	7.666(0)	7.474	+0.192	8.651(4)	8.584	+0.067
c (Å)	7.234(0)	7.363	−0.129	4.657(0)	4.646	+0.011
β (°)	113.27(0)	112.30	+0.97	102.17(0)	102.67	−0.50
Average crystallite size (nm)	41 ± 13	–	–	38 ± 11	–	–

FTIR spectrum of the calcined $MnPO_4 \cdot H_2O$ powder at 500 °C (Fig. 4b) exhibits the same characteristic as that of $Mn_2P_2O_7$. FTIR bands are assigned according to the literature [24,30] based on the fundamental vibrating unit $P_2O_7^{4-}$ anion. One of the most noteworthy features of the spectrum is the presence of the strong bands at 1090, 962, 570, 526, and 421 cm^{-1}. These bands can be assigned to $\nu_{as}(PO_3)$, $\nu_{as}(POP)$, δ (PO_3), δ (PO_3), and ρ (PO_3), respectively. The symmetric and asymmetric vibrations of the POP bridge (ν_{as} POP and ν_s POP) observed in the range 700–970 cm^{-1} [24,30], which indicate the presence of the $P_2O_7^{4-}$ anions with a bent POP angles in this salt.

The morphologies of $MnPO_4 \cdot H_2O$ and its decomposed product $Mn_2P_2O_7$ powders are shown in Fig. 5a and b. The $MnPO_4 \cdot H_2O$ shapes in this work show well-defined grass blade-like microparticles, which are not similar to those of $MnPO_4 \cdot H_2O$ reported in previous works [18–20]. The grass blade-like morphology consists of similar leaf-like flakes growing radically from the inside. Its decomposed product $Mn_2P_2O_7$ shows high agglomerate of non-uniform polyhedral particles, which is possibly caused by the dehydration and reduction processes. The morphology of $Mn_2P_2O_7$ indicates further nucleation/growth of the nanocrystals inside the powder. This phenomenon is still not clear. The morphologies of the synthesized $MnPO_4 \cdot H_2O$ and its decomposed product $Mn_2P_2O_7$ in this work are significantly different from those of our previous reports [20,24,25]. The results indicate that the starting reagent and reaction condition of the precipitation have the strong effect in the morphologies of the studied compounds.

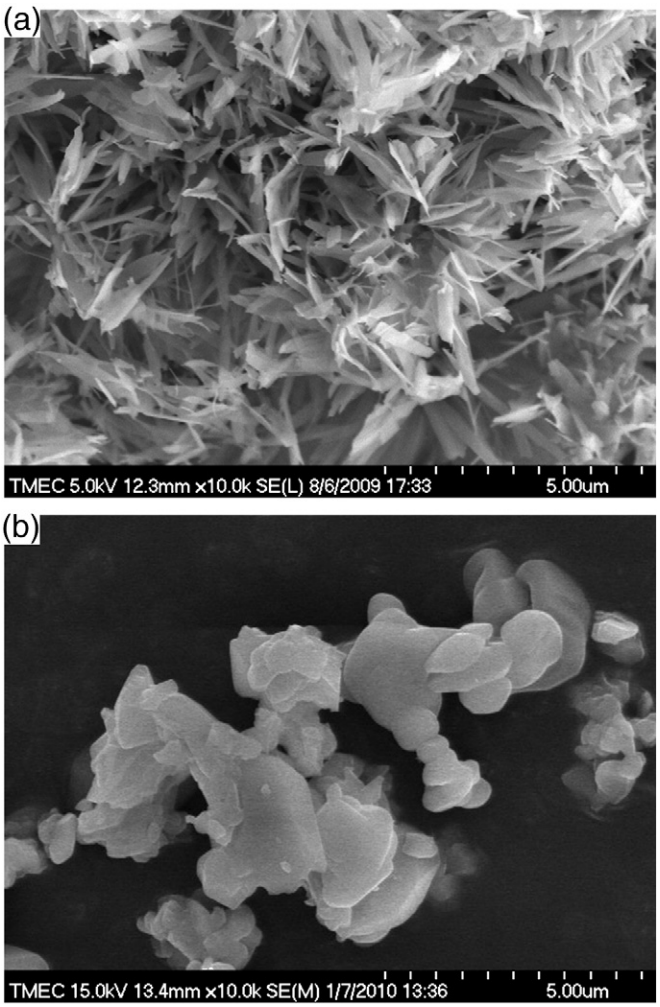

Fig. 5. SEM micrographs of the synthesized $MnPO_4 \cdot H_2O$ (a) and its decomposed product $Mn_2P_2O_7$ (b).

4. Conclusion

Grass blade-like microparticle $MnPO_4 \cdot H_2O$ was successfully synthesized by simple precipitation at room temperature using the mixture of manganese sulphate monohydrate, phosphoric acid and water at pH = 7. The $MnPO_4 \cdot H_2O$ decomposes in more complex steps which correspond to the loss of crystallization water in the first step, subsequently to the reduction of manganese(III) to manganese(II) and the consequent release of oxygen (last step). The XRD and FTIR results confirmed the formation of $MnPO_4 \cdot H_2O$ and its decomposed product $Mn_2P_2O_7$. The thermal behaviors, grass blade-like shapes, particle size and crystallite sizes of the synthesized $MnPO_4 \cdot H_2O$ and $Mn_2P_2O_7$ are different from previous reports. This is possibly due to the effects of the starting reagents and reaction condition for the precipitation. The results obtained are necessary for theoretical study, application development, and industrial production to produce the $MnPO_4 \cdot H_2O$ and $Mn_2P_2O_7$, which play potential applications as catalytic, ceramic and the biomedical materials etc.

Acknowledgments

This work was financially supported by the Thailand Research Fund (TRF), the Commission on Higher Education (CHE): Research Grant for New Scholar and the National Nanotechnology Center (NANOTEC) NSTDA, Ministry of Science and Technology, Thailand.

References

[1] G. Chen, T.J. Richardson, Thermal instability of Olivine-type $LiMnPO_4$ cathodes, J. Power Sources 195 (2010) 1221–1224.
[2] W. Massa, O.V. Yakubovich, O.V. Dimitrova, A novel modification of manganese orthophosphate $Mn_3(PO_4)_2$, Solid State Sci. 7 (2005) 950–956.
[3] M.T. Averbuch-Pouchot, A. Durif, Topics in Phosphate Chemistry, World Scientific Publishing Co. Pte. Ltd., Singapore, 1996.
[4] A. Jouini, J.C. Gâcon, M. Ferid, M. Trabelsi-Ayadi, Luminescence and scintillation properties of praseodymium poly and diphosphates, Opt. Mater. 24 (2003) 175–180.
[5] H.I. Hsiang, L.T. Mei, Y.H. Lin, Formation and growth of manganese phosphate passivation layers for NTC ceramics, J. Alloys Compd. 48 (2009) 723–728.
[6] L. Adam, A. Guesdon, B. Raveau, Unique charge ordering of manganese in a new mixed valent phosphate $K_3Mn^{II}_3Mn^{III}(PO_4)(H_{0.5}PO_4)_2(HPO_4)_2$, J. Solid State Chem. 182 (2009) 2338–2343.
[7] N.N. Bramnik, H. Ehrenberg, Precursor-based synthesis and electrochemical performance of $LiMnPO_4$, J. Alloys Compd. 464 (2008) 259–264.
[8] D. Feng, C. Wang, W. Cheng, G. Li, S. Tian, F. Liao, M. Xiong, J. Lin, Synthesis, crystal structure, and magnetic properties of $K_4Mn_3(HPO_4)_4(H_2PO_4)_2$, Solid State Sci. 11 (2009) 845–851.
[9] A. Yuan, Wu, L. Bai, S. Ma, Z. Huang, Z. Tong, Standard molar enthalpies of formation for ammonium/3d-transition metal phosphates $NH_4MPO_4 \cdot H_2O$ (M Mn^{2+}, Co^{2+}, Ni^{2+}, Cu^{2+}), J. Chem. Eng. Data. 53 (2008) 1066–1070.
[10] B.Y. Jibril, S.M. Al-Zahrani, A.E. Abasaeed, Propane oxidative dehydrogenation over metal pyrophosphates catalysts, Catal. Lett. 74 (2001) 145–148.
[11] W. Xuehang, W. Wenwei, L. Sen, F. Yanjin, L. Shushu, Preparation via solid-state reaction at room temperature and characterization of layered nanocrystalline $KMnPO_4 \cdot H_2O$, J Alloys Compd. 479 (2009) 541–544.
[12] J.K. Kim, G.S. Chauhan, J.H. Ahn, H.J. Ahn, Effect of synthetic conditions on the electrochemical properties of $LiMn_{0.4}Fe_{0.6}PO_4$/C synthesized by sol–gel technique, J. Power Sources 189 (2009) 391–396.
[13] C. Delacourt, P. Poizot, M. Morcrette, J.-M. Tarascon, C. Masquelier, One-step low-temperature route for the preparation of electrochemically active $LiMnPO_4$ powders, Chem. Mater. 16 (2004) 93–99.
[14] M.A.G. Aranda, S. Bruque, Characterization of manganese(III) orthophosphate hydrate, Inorg. Chem. 29 (1990) 1334–1337.
[15] F.W. Boyle Jr., W.L. Lindsay, Diffraction patterns and solubility product of several divalent manganese phosphate compounds, Soil Sci. Soc. Am. J. 50 (1986) 761–766.
[16] O.T. Christensen, Beiträge zur Kenntniss der Oxyde des Mangans, J Prakt. Chem. 28 (1883) 1–37.
[17] Y. Cudennec, A. Riou, Y. Gerault, Manganese(II) hydrogenphosphate trihydrate, Acta Cryst. C45 (1989) 1411–1412.
[18] P. Lightfoot, A.K. Cheetham, A.W. Sleight, Structure of manganese(3+) phosphate monohydrate by synchrotron x-ray powder diffraction, Inorg. Chem. 26 (1987) 3544–3547.

[19] T. Witzke, R. Wegner, T. Doering, H. PÖllmann, W. Schuckmann, Serrabrancaite, $MnPO_4 \cdot H_2O$, a new mineral from the Alto Serra Branca pegmatite, Pedra Lavrada, Paraiba, Brazil, Am. Min. 85 (2000) 847–849.
[20] B. Boonchom, S. Youngme, S. Maensiri, C. Danvirutai, Nanocrystalline serrabrancaite ($MnPO_4 \cdot H_2O$) prepared by a simple precipitation route at low temperature, J. Alloys Compd. 454 (2008) 78–82.
[21] B. Boonchom, N. Vittayakorn, Floral-like microarchitectures of cobalt iron cyclotetraphosphate obtained by solid state synthesis, Powder Tech. 198 (2010) 25–28.
[22] A.I. Vogel, A Textbook of Quantitative Inorganic Analysis, 3rd edn, Green and Co. Ltd, Longmans, 1969.
[23] B.D. Cullity, Elements of X-ray Diffraction, second ed, Addison-Wesley Publishing, 1977.
[24] B. Boonchom, R. Baitahe, Synthesis and characterization of nanocrystalline manganese pyrophosphate $Mn_2P_2O_7$, Mater. Lett. 63 (2009) 2218–2220.
[25] B. Boonchom, C. Danvirutai, S. Maensiri, Soft solution synthesis, non-isothermal decomposition kinetics and characterization of manganese dihydrogen phosphate dihydrate $Mn(H_2PO_4)_2 \cdot 2H_2O$ and its thermal transformation products, Mater. Chem. Phys. 109 (2008) 404–410.
[26] C. Danvirutai, B. Boonchom, S. Youngme, Nanocrystalline manganese dihydrogen phosphate dihydrate $Mn(H_2PO_4)_2 \cdot 2H_2O$ and its decomposition product ($Mn_2P_4O_{12}$) obtained by simple precipitation route, J. Alloys Compd. 457 (2008) 75–80.
[27] A. Cuneyt Tas, Monetite ($Ca(HPO_4)$ synthesis in ethanol at room temperature, J. Am. Cerm. Soc. 93 (2009) 2907–2912.
[28] G. Herzberg, Molekülspektren und Molekülstruktur. I., Zweiatomige Moleküle, Steinkopff, Dresden, 1939.
[29] N.B. Colthup, L.H. Daly, S.E. Wiberley, Introduction to Infrared and Raman Spectroscopy, Academic Press, New York, 1964.
[30] E. Steger, B. Käßner, Die infrarotspektren von wasserfreien schwermetalldiphosphaten, Spectrochim Acta 24A (1968) 447–456.

* To whom correspondence should be addressed. Tel: +66-7750-6422, ext. 4546. Fax: +66-7750-6410. E-mail: kbbanjon@kmitl.ac.th.
† King Mongkut's Institute of Technology Ladkrabang, Chumphon Campus.
‡ Advanced Materials Science Research Unit, Department of Chemistry, Faculty of Science, King Mongkut's Institute of Technology Ladkrabang.
§ Department of Chemistry, Faculty of Science, King Mongkut's Institute of Technology Ladkrabang.
|| College of KMITL Nanotechnology, King Mongkut's Institute of Technology Ladkrabang.

$$3ZnO(s) + 2H_3PO_4 + H_2O \xrightarrow[\text{ambient temperature}]{C_3H_6O,\ \text{acetone}} Zn_3(PO_4)_2{\cdot}4H_2O(s) \quad (1)$$

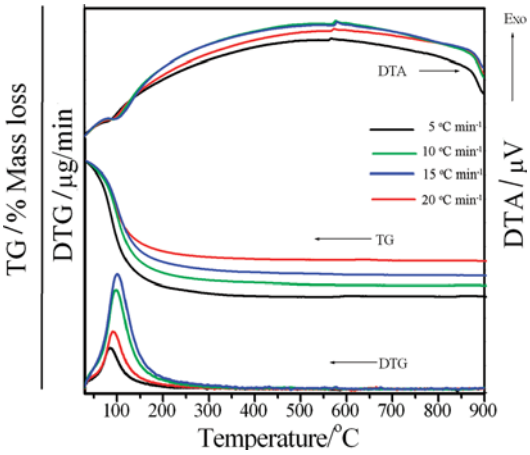

Figure 1. TG-DTG-DTA curves of $Al_{0.5}Fe_{0.5}PO_4 \cdot 2.5H_2O$ in dry air at heating rates of (5, 10, 15, and 20) °C·min^{-1}.

reaches pH 3.80. The precipitates were filtered by suction, washed by hot deionized water, and dried in air. The resultant solid was kept in a desiccator for further investigation.

2.2. Sample Characterization. Thermal analysis measurements of about (8.0 ± 0.3) mg sample mass were carried out by a Pyris1 Perkin-Elmer apparatus with an alumina crucible at heating rates of (5, 10, 15, and 20) °C·min^{-1} in dynamic air in the range of (30 to 900) °C. DSC was carried out for samples ((5 to 10) mg) in aluminum crucibles, over the temperature range of (50 to 500) °C using DSC, a Perkin-Elmer DSC 204 F1 Phoenix apparatus. The heating rate employed was 10 °C·min^{-1}. The structures of the prepared sample and its decomposed product were studied by X-ray powder diffraction using a D8 Advanced powder diffractometer (Bruker AXS, Karlsruhe, Germany) with Cu Kα radiation (λ = 0.1546 nm). The room temperature Fourier transform infrared (FTIR) spectra were recorded in the range of (4000 to 400) cm^{-1} with eight scans on a Perkin-Elmer Spectrum GX spectrometer with a resolution of 4 cm^{-1}. The morphology was examined by scanning electron microscopy (SEM) using Hitachi S4700 after gold coating.

3. Results and Discussion

3.1. Thermal Analysis. Figure 1 shows the TG-DTG-DTA curves of the thermal decomposition of $Al_{0.5}Fe_{0.5}PO_4 \cdot 2.5H_2O$ at four heating rates. TG curves of $Al_{0.5}Fe_{0.5}PO_4 \cdot 2.5H_2O$ show a single well-defined dehydration in the range of (30 to 300) °C. The water eliminated below 100 °C is related to the physical adsorbed water, whereas water eliminated at 100 °C and above (200 °C) can be considered as crystal water and coordinated water. The dehydration temperature obtained in this work suggest that the water in hydrated binary aluminum iron phosphate can be considered as physical adsorbed water and crystal water.[8,9,17,18] The peaks in the DTG and DTA curves closely correspond to the mass loss observed on the TG traces. All TG-DTG-DTA curves are approximately the same shape. However, the dehydration stage was shifted toward higher temperatures when the heating rates increase, which indicate that the mass loss is dependent on the heating rate. The average observed mass losses of four TG curves are 26.22 % by mass, which correspond to 2.51 mol of water, which is close to the theoretical value for $Al_{0.5}Fe_{0.5}PO_4 \cdot 2.5H_2O$ (26.11 %, 2.50 H_2O). An endothermic effect in the DTA curves is observed at about 100 °C that agrees with the respective DTG peak. Further, an exothermic effect at 572 °C without appreciable weight loss is observed in the DTA curve, which can be ascribed to a transition phase from an amorphous to crystalline form of $Al_{0.5}Fe_{0.5}PO_4$.[11]

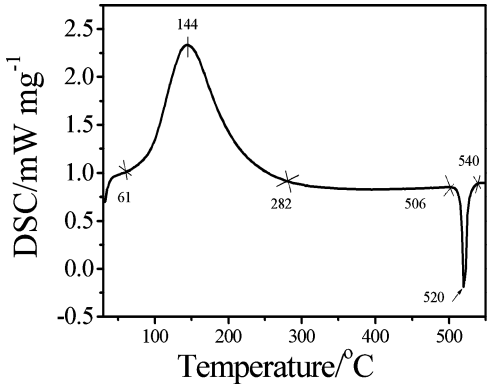

Figure 2. DSC curve of $Al_{0.5}Fe_{0.5}PO_4 \cdot 2.5H_2O$ at the heating rate of 10 K·min^{-1} in a N_2 atmosphere.

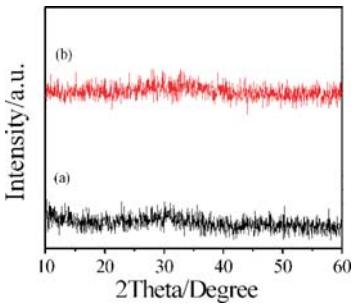

Figure 3. XRD patterns of $Al_{0.5}Fe_{0.5}PO_4 \cdot 2.5H_2O$ (a) and its decomposed product $Al_{0.5}Fe_{0.5}PO_4$ (b).

The retained mass of about 73.78 % is compatible with the value expected for the formation of $Al_{0.5}Fe_{0.5}PO_4$. The overall reaction is:

$$Al_{0.5}Fe_{0.5}PO_4 \cdot 2.5H_2O \rightarrow Al_{0.5}Fe_{0.5}PO_4 + 2.5H_2O \quad (1)$$

The binary iron aluminum phosphate, $Al_{0.5}Fe_{0.5}PO_4$, is found to be the final product of the thermal decomposition at $T > 300$ °C. The thermal stability, mechanism, and phase transition temperature of the synthesized $Al_{0.5}Fe_{0.5}PO_4 \cdot 2.5H_2O$ are lower than those of the dehydration reactions of individual metal phosphates ($AlPO_4 \cdot 2H_2O$[17] and $FePO_4 \cdot 2H_2O$[18]). On the basis of these results, we can conclude that the different thermal properties are caused by the incorporation of Fe and Al metals in the skeleton.

The DSC curve of $Al_{0.5}Fe_{0.5}PO_4 \cdot 2.5H_2O$ (Figure 2) shows an endothermic peak at 144 °C (onset peak at 61 °C) and an exothermic peak at 520 °C (onset peak at 506 °C) due to the dehydration and the transition phase from an amorphous to crystalline form of this compound, respectively. The temperatures of the DSC peaks are well in accordance with that of the DTG and DTA peaks (Figure 1), so results of the TG/DTG/DTA and DSC methods are credible.

3.2. XRD Analysis. The XRD studies of $Al_{0.5}Fe_{0.5}PO_4 \cdot 2.5H_2O$ and its dehydrated product $Al_{0.5}Fe_{0.5}PO_4$ revealed that the structures remained in the amorphous or poor crystallization phases as well as nanoparticles of these compounds (Figure 3). The problem here is that the XRD data show poorly crystalline patterns, which are no indication of $Al_{0.5}Fe_{0.5}PO_4 \cdot 2.5H_2O$ and $Al_{0.5}Fe_{0.5}PO_4$ as separated phases. The studied compounds synthesized by the precipitation route in this work were poor crystalline phases, which differ from crystallization phases of those synthesized by a hydrothermal method.[5−10] These results are in agreement with the results reported in the literature.[5−10]

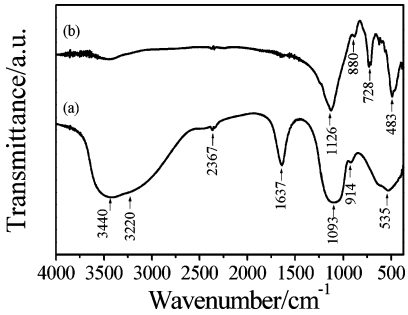

Figure 4. FTIR spectra of $Al_{0.5}Fe_{0.5}PO_4 \cdot 2.5H_2O$ (a) and its decomposed product $Al_{0.5}Fe_{0.5}PO_4$ (b).

3.3. FTIR Analysis. Figure 4 shows FTIR spectra of $Al_{0.5}Fe_{0.5}PO_4 \cdot 2.5H_2O$ and its dehydrated product $Al_{0.5}Fe_{0.5}PO_4$. The vibrational motions of $Al_{0.5}Fe_{0.5}PO_4 \cdot 2.5H_2O$ are divided into two block units of the water molecule H_2O and phosphate anion PO_4^{3-}, whereas $Al_{0.5}Fe_{0.5}PO_4$ is divided into a block unit of the only phosphate anion PO_4^{3-}. It is worth mentioning that the antisymmetric stretching (ν_{OH}), the symmetric stretching (ν_{OH}), and the bending (δ_{OH}) vibrations of water molecules are solely observed at (3440, 3220, and 1637) cm^{-1}, respectively. These bands disappear in the FTIR spectrum of $Al_{0.5}Fe_{0.5}PO_4$ (Figure 4b), implying the presence of anhydrous crystal. For the intramolecular vibrations of the PO_4^{3-} anion, we identify the symmetric stretching mode at $\nu_1 = 990$ cm^{-1}, the doublet at $\nu_2 =$ (447 to 485) cm^{-1}, the triplets ν_3 at (1000 to 1085) cm^{-1}, and the triplet ν_4 in the region (570 to 640) cm^{-1}. For condensed phosphates, the intensity of the P−O stretching IR bands near 1000 cm^{-1} are always greater than those near 880 cm^{-1}, assigned to the stretching vibration ν_{P-O-P} of P−O−P bridges. These phosphate band positions of $Al_{0.5}Fe_{0.5}PO_4 \cdot 2.5H_2O$ and $Al_{0.5}Fe_{0.5}PO_4$ are in excellent agreement with published data.[19,20]

3.4. SEM Analysis. The scanning electron micrographs of $Al_{0.5}Fe_{0.5}PO_4 \cdot 2.5H_2O$ (Figure 5a) and $Al_{0.5}Fe_{0.5}PO_4$ (Figure 5b) powders showed different uniform morphological features due to the loss of crystallization waters. It can be seen that the $Al_{0.5}Fe_{0.5}PO_4$ powders were clearly coarser than the $Al_{0.5}Fe_{0.5}PO_4 \cdot 2.5H_2O$ powders. The $Al_{0.5}Fe_{0.5}PO_4$ powders consisted of round particles near 100 nm in size along with a narrow size distribution Additionally, the SEM photographs show that both crystals have grown through a combination of surface deposition and agglomeration.

3.5. Kinetics Analysis. In the rate equation for the isothermal decomposition of a solid-state process,[21] A (solid) → B (solid) + C (gas) is often written from:

$$d\alpha/dt = A \exp(-E_a/RT) f(\alpha) \quad (2)$$

In most thermal analysis experiments, the heating rate $\beta = dT/dt$ is a constant value, so eq 2 may also lead to the corresponding equations of Ozawa[22] and Kissinger−Akahira−Sunose (KAS)[23] methods after integration.

$$\text{Ozawa equation: } \ln \beta = \ln\left(\frac{AE_\alpha}{R\, g(\alpha)}\right) - 5.3305 - 1.0516\left(\frac{E_\alpha}{RT}\right) \quad (3)$$

$$\text{KAS equation: } \ln\left(\frac{\beta}{T^2}\right) = \ln\left(\frac{AE_\alpha}{R\, g(\alpha)}\right) - \left(\frac{E_\alpha}{RT}\right) \quad (4)$$

where A (the pre-exponential factor) and E_a (the activation energy) are the Arrhenius parameters and R is the gas constant.

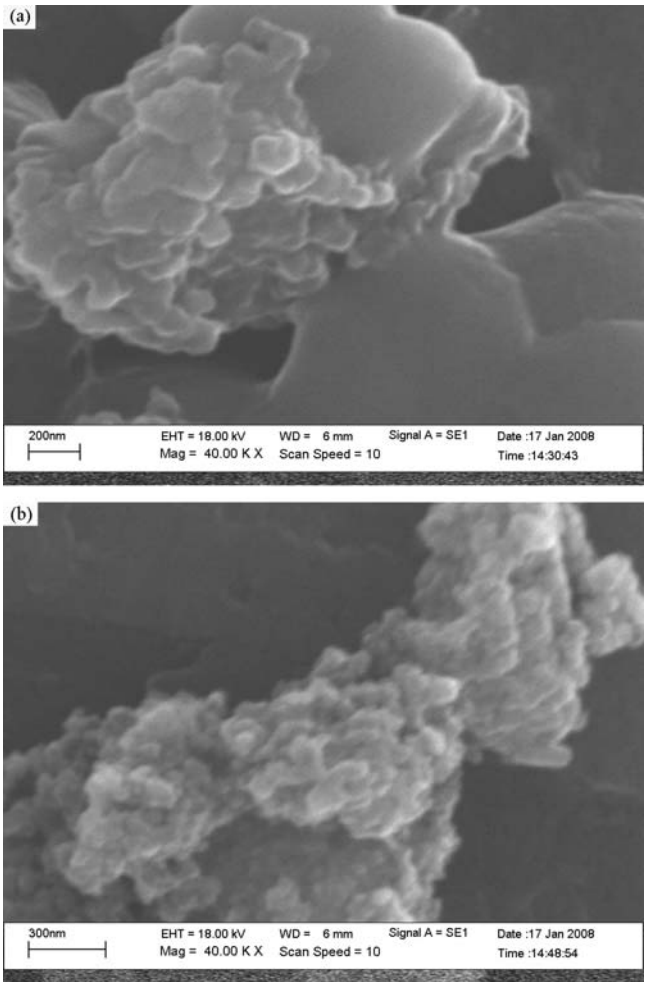

Figure 5. SEM photographs of $Al_{0.5}Fe_{0.5}PO_4 \cdot 2.5H_2O$ (a) and its decomposed product $Al_{0.5}Fe_{0.5}PO_4$ (b).

The $g(\alpha) = \int_0^\alpha (d\alpha/f(\alpha))$ is the integral form of $f(\alpha)$, which is the reaction model that depends on the reaction mechanism. The reaction can be expressed through the temperatures corresponding to fixed values of the extent of conversion ($\alpha = (m_i - m_a)/(m_i - m_f)$, where m_i, m_a, and m_f are the initial, actual, and final sample mass at time t) from experiments at different heating rates (β).

Hence, the dependences of ln β and ln β/T^2 on $1000/T$, calculated for the same α values (0.10 to 0.90) at different heating rates β ((5, 10, 15, and 20) °C·min^{-1}) can be used to calculate the activation energy, so we can obtain the activation energies through the experimental data for the dehydration of $Al_{0.5}Fe_{0.5}PO_4 \cdot 2.5H_2O$ as shown in Table 1. The activation energies E_α can be calculated from the slopes of the straight lines with a good coefficient of determination ($R^2 > 0.99$). The activation energies worked out through the Ozawa and the KAS methods vary slightly, so the results are credible. If E_α values are independent of α, the decomposition may be a simple reaction, while the dependence of E_α on α should be interpreted in terms of multistep reaction mechanisms.[24,25] From Table 1 it can be seen that the activation energies decrease first and increase at α higher than 0.6. A decreasing dependence of E_α on α is found for consecutive reactions, while an increasing dependence of E_α on α is found for competitive reactions. According to the decreasing E_α at $\alpha < 0.6$, the kinetics scheme of which corresponds to a reversible reaction followed by an irreversible one. In addition, the increasing E_α at $\alpha > 0.6$ corresponds to a two-pathway competitive reaction model.[24,25]

Table 1. Activation Energies (E_α) Versus the Coefficient of Detemination (R^2) Calculated by Ozawa and KAS Methods for the Dehydration of $Al_{0.5}Fe_{0.5}PO_4 \cdot 2.5H_2O$

	Ozawa method		KAS method	
α	E_α/kJ·mol^{-1}	R^2	E_α/kJ·mol^{-1}	R^2
0.1	231.14	0.9985	237.50	0.9985
0.2	158.58	0.9937	160.99	0.9933
0.3	136.83	0.9968	137.98	0.9965
0.4	129.85	0.9984	130.54	0.9983
0.5	126.05	0.9972	126.44	0.9970
0.6	125.90	0.9970	126.16	0.9966
0.7	136.37	0.9976	137.02	0.9974
0.8	167.18	0.9989	169.21	0.9988
0.9	275.09	0.9959	323.93	0.9957

So it is concluded that there is a fourth reaction for the dehydration reaction. Additionally, the obtained activation energy values of the dehydration reaction of the studied compound are higher than those of individual metal phosphates (69.68 ± 7 kJ·mol^{-1} (Kissinger method) for $AlPO_4 \cdot 2H_2O$[17] and 68.48 ± 1 kJ·mol^{-1} (Flynn−Wall−Ozawa method) and 65.55 ± 1 kJ·mol^{-1} (KAS method) for $FePO_4 \cdot 2H_2O$[18] reported in our previous works. As can be clearly seen, there is a direct relationship between the cation radius of Al(III) and Fe(III) and its thermal stability and activation energy of the dehydration reaction. A common conclusion is that the reason for this is the different interaction of iron and aluminum with water molecules in the structure, which supports the incorporation of Fe and Al metals in the skeleton and forms the $Al_{0.5}Fe_{0.5}PO_4 \cdot 2.5H_2O$ solid solution.

The Arvami exponent, n, can be evaluated by the Ozawa equation. First, the volume fraction of phase transition x, at the same temperature, T, from four crystallization steps under different heating rates is calculated by the ratio of partial area at T to the total area of crystallization. After plotting $\ln[-\ln(1 - x)]_T$ versus $\ln(\beta)$ and if the data can be fitted to the linear function, then the slope of the function is $-n$,[26] which is really the combined process of nucleation and growth. The most common approach used to describe the overall nonisothermal crystallization is given below:

$$-n = \frac{\mathrm{d}\ln[-\ln(1 - x)]}{\mathrm{d}\ln(\beta)} \tag{5}$$

The volumetric function of the growth mechanism directly affects the transformation rate, and the dimensionality of the transformation is reflected in the value of the Avrami exponent.[26,27] Higher dimensionality leads to a higher value of the exponent. Therefore, determination of the Avrami exponent allows one to determine which geometric model of the phase transformation is the best fit: one-, two-, or three-dimensional growth. For the dehydration step of $Al_{0.5}Fe_{0.5}PO_4 \cdot 2.5H_2O$, the Avrami exponent, n, has a value of 1.11 ($R^2 = 0.991$), indicating a one-dimensional growth mechanism. The Avrami exponent, in addition to giving information regarding the dimensionality of the growth, can also yield insight into the rate-determining step (phase boundary control or diffusion control). An analysis of the Avrami exponent suggests a phase boundary mechanism.

3.6. Thermodynamic Analysis. Thermodynamic parameters, that is, enthalpy change (ΔH^*/J·mol^{-1}), heat capacity (C_p/J·mol^{-1}·K^{-1}), entropy change (ΔS^*/J·mol^{-1}·K^{-1}), and Gibbs energy change (ΔG^*/J·mol^{-1}) were calculated from the DSC experiment. The enthalpy change was calculated directly from the amount of heat change involved in each step per unit mass of the test sample. ΔH^*, ΔS^*, and ΔG^* were calculated using the following equations:[15,16]

$$C_p = \frac{\Delta H}{\Delta T} \tag{6}$$

$$\Delta S^* = 2.303 C_p \log \frac{T_2}{T_1} \tag{7}$$

$$\Delta G^* = \Delta H^* - T_p \Delta S^* \tag{8}$$

where $\Delta T = T_2 - T_1$, T_1 is the temperature at which the DSC peak begins to depart the baseline, and T_2 is the temperature at which the peak lands. T_p is the DSC peak temperature at the corresponding stage.

The values of ΔH^*, ΔS^*, C_p, and ΔG^* were calculated and found to be 104.64 kJ·mol^{-1}, 72.40 J·K^{-1}·mol^{-1}, 290.75 J·K^{-1}·mol^{-1}, and 744.57 kJ·mol^{-1} for the dehydration reaction and −852.61 kJ·mol^{-1}, −10.74 J·K^{-1}·mol^{-1}, −968.21 J·K^{-1}·mol^{-1}, and 5.77 J·mol^{-1} for a transition form, respectively. The transition phase can be considered as the transformation of an amorphous to a crystalline form of this compound.[7,8] It is well-known that ΔS^* can be less than, equal to, or higher than zero. In the case when $\Delta S^* < 0$, the reactions are classified as "slow" and when $\Delta S^* > 0$ as "fast".[28−30] The positive value of ΔS^* indicates a malleable activated complex that leads to a large number of degrees of freedom of rotation and vibration, whereas the negative value of ΔS^* indicates a highly ordered activated complex, and the degrees of freedom of rotation as well as of vibration are less than they are in the nonactivated complex. Therefore, the dehydration reaction and a transition form of $Al_{0.5}Fe_{0.5}PO_4 \cdot 2.5H_2O$ may be interpreted as "fast" and "slow" stages, respectively.[28−30] The positive and negative values of the enthalpy ΔH^* for the dehydration reaction and a transition form are in good agreement with an endothermic and an exothermic effect in DTA and DSC data, respectively. The positive and negative values of ΔG^* indicate that nonspontaneous and spontaneous processes for dehydration and a transition form stages, respectively. The thermodynamic parameters obtained indicate that the dehydration reaction is softer than the transition phase reaction. The results obtained in this work are different from those of the individual metal phosphates ($AlPO_4 \cdot 2H_2O$[17] and $FePO_4 \cdot 2H_2O$)[18] reported in our previous work.

4. Conclusions

The results obtained in this study show that the dehydration behavior of an $Al_{0.5}Fe_{0.5}PO_4 \cdot 2.5H_2O$ solid solution varies with the function of their cations (Al(III) and Fe(III)). The feature of great interest here is that $Al_{0.5}Fe_{0.5}PO_4 \cdot 2.5H_2O$ decomposes at a relatively low temperature (< 300 °C). A fluctuating value of E for different α can be assigned to a complex multistep reaction process, which corresponds to the different interactions of iron and aluminum with water molecules in the skeleton. The thermal behavior and kinetic and thermodynamic parameters of the dehydration reaction of $Al_{0.5}Fe_{0.5}PO_4 \cdot 2.5H_2O$ are different from those of individual metal phosphates ($AlPO_4 \cdot 2H_2O$ and $FePO_4 \cdot 2H_2O$), which result from the perturbation of the molecular orbitals of the anion and cations occurring during the formation of the studied compound. The kinetic and thermodynamic data obtained from such studies can be directly applied in material science for the synthesis of various composite compounds.

Literature Cited

(1) Perri, E.; Tsamouras, D.; Dalas, E. Ferric Phosphate Precipitation in Aqueous Media. *J. Cryst. Growth* **2000**, *213*, 93.
(2) Lindsay, W. L.; Vlek, P. L. G.; Chien, S. H. Phosphate minerals. In *Minerals in soil environment*, 2nd ed.; Dixon, J. B., Weed, S. B., Eds.; Soil Science Society of America: Madison, WI, 1989; pp 1089−1130.

(3) Kniep, R.; Mootz, D.; Vega, A. Variscite. *Acta Crystallogr., Sect. B* **1977**, *33*, 263–265.
(4) Kniep, R.; Mootz, D. Metavariscite: A redetermination of its crystal structure. *Acta Crystallogr., Sect. B* **1973**, *29*, 2292–2294.
(5) Scaccia, S.; Carewska, M.; Prosini, P. P. Thermoanalytical Study of Iron(III) Phosphate obtained by Homogeneous Precipitation from Different Media. *Thermochim. Acta* **2004**, *41*, 381.
(6) Zaghib, K.; Julien, C. M. Structure and Electrochemistry of $FePO_4 \cdot 2H_2O$ Hydrate. *J. Power Sources* **2005**, *142*, 279.
(7) Song, Y.; Zavalij, P. Y.; Suzuki, M.; Whittingham, M. S. New Iron(III) Phosphate Phases: Crystal Structure and Electrochemical and Magnetic Properties. *Inorg. Chem.* **2002**, *41*, 5778.
(8) Scaccia, S.; Carewska, M.; Bartolomeo, A. D.; Prosini, P. P. Thermoanalytical Investigation of Iron Phosphate obtained by Spontaneous Precipitation from Aqueous Solutions. *Thermochim. Acta* **2002**, *383*, 145.
(9) Scaccia, S.; Carewska, M.; Bartolomeo, A. D.; Prosini, P. P. Thermoanalytical Investigation of Nanocrystalline iron(II) Phosphate obtained by Spontaneous Precipitation from Aqueous Solutions. *Thermochim. Acta* **2003**, *397*, 135.
(10) Hsu, P. H. Crystallization of variscite at room temperature. *Soil Sci.* **1982**, *133*, 305–313.
(11) Youssif, M. I.; Mohamedb, F. S.; Aziz, M. S. Chemical and physical properties of $Al_{1-x}Fe_xPO_4$ alloys Part I. Thermal stability, magnetic properties and related electrical conductivity. *Mater. Chem. Phys.* **2004**, *83*, 250–254.
(12) Siva Kumar, V.; Padmasri, A. H.; Satyanarayana, C. V. V.; Ajit Kumar Reddy, I.; David Raju, B.; Rama Rao, K. S. Nature and mode of addition of phosphate precursor in the synthesis of aluminum phosphate and its influence on methanol dehydration to dimethyl ether. *Catal. Commun.* **2006**, *7*, 745–51.
(13) Arjona, A. M.; Alario Franco, M. A. Kinetics of the thermal dehydration of variscite and specific surface area of the solid decomposition products. *J. Therm. Anal.* **1973**, *5*, 319–328.
(14) Stojakovic, D.; Rajic, N.; Sajic, S.; Logar, N. Z.; Kaucic, V. A kinetic study of the thermal degradation of 3-methylaminopropylamine inside $AlPO_4$-21. *J. Therm. Anal. Calorim.* **2007**, *87*, 337–343.
(15) Ŝesták, J. *Thermodynamical properties of solids*; Academia Publishers: Prague, 1984.
(16) Young, D. *Decomposition of Solids*; Pergamon Press: Oxford, 1966.
(17) Boonchom, B.; Danvirutai, C. Kinetics and thermodynamics of thermal decomposition of synthetic $AlPO_4 \cdot 2H_2O$. *J. Therm. Anal. Calorim.* **2009**, *98*, 771–777.
(18) Boonchom, B. Thermodynamics and kinetics of the dehydration reaction of $FePO_4 \cdot 2H_2O$. *Physica B (Amsterdam, Neth.)* **2010**, *405*, 2350−2355.
(19) Frost, R. L.; Weier, M. L. Vibrational Spectroscopy of Natural Augelite. *J. Mol. Struct.* **2004**, *697*, 207.
(20) Breitinger, D. K.; Mohr, J.; Colognesi, D.; Parker, S. F.; Schukow, H.; Schwab, R. G. Vibrational Spectra of Augelites $Al_2(OH)_3(XO_4)$ (X = P, As, V). *J. Mol. Struct.* **2001**, *563−564*, 377.
(21) Vyazovkin, S. Computational Aspects of Kinetic Analysis: Part C. The ICTAC Kinetics Project—the light at The End of The Tunnel? *Thermochim. Acta* **2000**, *355*, 155.
(22) Ozawa, T. A New Method of Analyzing Thermogravimetric Data. *Bull. Chem. Soc. Jpn.* **1965**, *38*, 1881.
(23) Kissinger, H. E. Reaction Kinetics in Differential Thermal Analysis. *J. Anal. Chem.* **1957**, *29*, 1702.
(24) Li, Z.; Shen, X.; Feng, X.; Wang, P.; Wu, Z. Non-isothermal kinetics studies on the thermal decomposition of zinc hydroxide carbonate. *Thermochim. Acta* **2005**, *438*, 102–106.
(25) Ioiţescu, A.; Vlase, G.; Vlase, T.; Doca, N. Kinetics of decomposition of different acid calcium phosphates. *J. Therm. Anal. Calorim.* **2007**, *88*, 121–125.
(26) Afify, N. A new method to study the crystallization or chemical reaction kinetics using thermal analysis technique. *J. Phys. Chem. Solids* **2008**, *69*, 1691–1697.
(27) Zhang, Y.; Lv, M.; Chen, D. D.; Wu, J. Q. Leucite Crystallization Kinetics with Kalsilite as a Transition Phase. *Mater. Lett.* **2007**, *61*, 2978–2981.
(28) Vlaev, L. T.; Nikolova, M. M.; Gospodinov, G. G. Non-Isothermal Kinetics of Dehydration of Some Selenite Hexahydrates. *J. Solid State Chem.* **2004**, *177*, 2663.
(29) Vlaev, L.; Nedelchev, N.; Gyurova, K.; Zagorcheva, M. A comparative study of non-isothermal kinetics of decomposition of calcium oxalate monohydrate. *J. Anal. Appl. Pyrolysis* **2008**, *81*, 253–262.
(30) Singh, B. K.; Sharma, R. K.; Garg, B. S. Kinetics and molecular modeling of biologically active glutathione complexes with lead(II) ions. *J. Therm. Anal. Calorim.* **2006**, *84*, 593–600.

Received for review January 29, 2010. Accepted May 16, 2010. This work is financially supported by the Thailand Research Fund (TRF), the Commission on Higher Education (CHE): Research Grant for New Scholar, and the National Nanotechnology Center (NANOTEC) NSTDA, Ministry of Science and Technology, Thailand, through its "Center of Excellence Network" program.

JE100096E

Journal of Alloys and Compounds 506 (2010) 313–316

Contents lists available at ScienceDirect

Journal of Alloys and Compounds

journal homepage: www.elsevier.com/locate/jallcom

The phase evolution with temperature in $0.94PbZrO_3$–$0.06Pb(Mg_{1/2}W_{1/2})O_3$ antiferroelectric ceramic

Piyanut Charoonsuk[a,b], Supamas Wirunchit[a,b], Rangson Muanghlua[c], Surasak Niemcharoen[c], Banjong Boonchom[d], Naratip Vittayakorn[a,b,e,*]

[a] Electroceramic Research Laboratory, College of KMITL Nanotechnology, King Mongkut's Institute of Technology Ladkrabang, Bangkok 10520, Thailand
[b] ThEP Center, CHE, 328 Si Ayutthaya Rd., Bangkok 10400, Thailand
[c] Department of Electronics, Faculty of Engineering, King Mongkut's Institute of Technology Ladkrabang, Bangkok 10520, Thailand
[d] King Mongkut's Institute of Technology Ladkrabang, Chumphon Campus, 17/1M. 6 Pha Thiew District, Chumphon 86160, Thailand
[e] Advanced Materials Science Research Unit, Department of Chemistry, Faculty of Science, King Mongkut's Institute of Technology Ladkrabang, Bangkok 10520, Thailand

ARTICLE INFO

Article history:
Received 14 May 2010
Received in revised form 28 June 2010
Accepted 30 June 2010
Available online 7 July 2010

Keywords:
Antiferroelectric
Wolframite precursor method
Lead Zirconate
Lead Magnesium Tungstate

ABSTRACT

The perovskite structure of the lead zirconate–lead magnesium tungstate ceramic, $0.94PbZrO_3$–$0.06Pb(Mg_{1/2}W_{1/2})O_3$ (0.94PZ–0.06PMW), was prepared by the wolframite precursor method. The phase evolution with temperature in the 0.94PZ–0.06PMW ceramic was investigated, with dielectric permittivity, differential scanning calorimetry and polarization measurements. The ceramic was in the antiferroelectric phase when below 177 °C, based on dielectric measurement, and an intermediate phase was detected between 177 and 219 °C. Evidence from ferroelectric data was found to suggest that this intermediate phase is ferroelectric.

1. Introduction

Active studies of antiferroelectric (AFE) materials have been recently enhanced for next-generation electronic systems, for example, microelectromechanical systems consisting of sensors and actuators and high performance energy storage devices [1,2]. The phase transition from AFE to the field-forced ferroelectric (FE) state, induced by an electric field [3,4], is characterized by typical double P–E hysteresis loops. These materials are suitable for nonlinear charge storage capacitors because a field-forced ferroelectric state releases all polarized charges and can therefore supply very high instantaneous currents at the ferroelectric to antiferroelectric reverse phase transition. Recently, AFE materials, including $Pb(Zr,Ti)O_3$, $(Pb,Ba)ZrO_3$, $(Pb,Sr)TiO_3$, $(Pb,La)(Zr,Ti)O_3$, $NaNbO_3$, and $(Bi_{0.5}Na_{0.5})TiO_3$ systems, have attracted increasing scientific attention [3–9]. Among them, lead zirconate ($PbZrO_3$; PZ) and $PbZrO_3$-based are the most attractive AFE materials, due to their high longitudinal strain response, and the latter is a proto-type of AFE ceramics that belongs to an ABO_3-type perovskite family of oxides [10,11]. At temperatures below the Curie temperature (230 °C), PZ displays an orthorhombic perovskite structure with lattice parameters of $a = 5.87$ Å, $b = 11.74$ Å and $c = 8.20$ Å [12]. This structure possesses an antiparallel shift of Pb ions along the [1 1 0], resulting in antiferroelectricity [13]. At temperatures above 230 °C, $PbZrO_3$ is in the paraelectric phase, with cubic $m3m$ symmetry [13,14]. An intermediate phase, characterized by $1/2\{1\,1\,0\}_c$-type superlattice diffractions, is in between the AFE and paraelectric phase, within a narrow temperature range of 225–230 °C [13,14]. It is well known that the AFE to FE phase transformation in PZ ceramic requires a very strong electric field; otherwise, dielectric breakdown occurs. Consequently, most commercial AFE ceramics are chemically modified by adding Ba^{2+}, Sr^{2+}, Ti^{4+} or Sn^{4+} to reduce the critical field and optimize the physical and electrical properties [3–9]. Sawaguchi [15] studied the effect of Ti^{4+} substitution in PZ on temperature variation of the P–E hysteresis loop and established the ferroelectric intermediate phase between the AFE and PE phase. Shirane [16] investigated the phase transition behavior of Ba^{2+} doping in PZ and reported that the ferroelectric intermediate phase between the AFE and PE phase for Ba^{2+} concentrations was lower than $x = 0.175$. Pokharel and Pandey [17,18] reported that relaxor ferroelectric behavior for Ba^{2+} concentrations was higher than $x = 0.25$. Recently, it was reported that antiferroelectric $(Pb_{1-x}Ba_x)ZrO_3$ (PBZ) films, with a higher barium content of more than 45 mol%, were in paraelectric state at room temperature and possessed excellent dielectric properties comparable to $(Ba,Sr)TiO_3$ [6]. On the contrary, a ferroelectric intermediate phase was not observed in lanthanum doping in PZ. Otherwise, lanthanum

* Corresponding author at: Department of Chemistry, Faculty of Science, King Mongkut's Institute of Technology Ladkrabang, Bangkok 10520, Thailand.
E-mail address: naratipcmu@yahoo.com (N. Vittayakorn).

0925-8388/$ – see front matter © 2010 Elsevier B.V. All rights reserved.
doi:10.1016/j.jallcom.2010.06.197

doping in PZ would be found to increase the stability range of the antiferroelectric phase [19,20]. Furthermore, Tan et al. [20] studied the doping effect of various metal oxide elements on field-induced polarization in PZ ceramics and found that addition of Bi^{3+} and K^{+} substantially increased stability of the antiferroelectric phase. Chen et al. [21] observed antiferroelectric-like or double hysteresis loops behavior in $(Pb,Sr)TiO_3$. However, the antiferroelectric nature is different from PZ ceramics. Rubia et al. [22] investigated the effect of Hf^{4+} substitution in PZ on phase transition, when the intermediate phase was found to increase with increasing Hf^{4+} concentrations. Up to now, scientific information about the effect of metal oxide substitution in PZ and nature of the intermediate phase is still unclear. Recently, our research work reported that the intermediate phase can also be introduced by partial replacement of Zr^{4+} ions with complex B-site ions such as Ni^{2+}/Nb^{5+} [23,24], Zn^{2+}/Nb^{5+} [25], or Co^{2+}/Nb^{5+} [26]. Furthermore, our previous study found that by adding minor amounts (2–10 mol%) of antiferroelectric $Pb(Mg_{1/2}W_{1/2})O_3$ (PMW) into antiferroelectric PZ, the temperature range expanded to an intermediate phase, which was characterized by evident frequency dispersion in dielectric permittivity [27]. As a consequence, a series of outstanding phase transitions were revealed by the dielectric measurement [27]. Nevertheless, the nature of the intermediate phase is still open for debate. The $0.94PbZrO_3$–$0.06Pb(Mg_{1/2}W_{1/2})O_3$ ceramic was selected in this study for further investigation of phase transformation sequence, while heating to 250 °C with ferroelectric measurement.

2. Experimental procedures

The perovskite structure of the lead zirconate–lead magnesium tungstate ceramic, $0.94PbZrO_3$–$0.06Pb(Mg_{1/2}W_{1/2})O_3$ (0.94PZ–0.06PMW), was prepared by the wolframite precursor method via the ball-milling technique. The wolframite structure ($MgWO_4$) was synthesized first before stoichiometric amounts of the precursor (MgO and WO_3) were mixed and milled in ethyl alcohol for 18 h. The mixture was then dried and calcined at 1100 °C for 4 h, and $MgWO_4$ and ZrO_2 were subsequently mixed with PbO. After re-milling and drying, the mixtures were calcined at 900 °C for 4 h in a closed alumina crucible. Pellets measuring 15 mm in diameter were pressed using 5% PVA, the binder was burned out slowly by heating to 500 °C over 2 h, and the samples were sintered at 1150 °C for 4 h. Phase formation of 0.94PZ–0.06PMW was investigated by X-ray diffraction (XRD). Scanning electron microscopy (SEM; Hitachi, s4007) was employed to investigate the microstructure of the sintered pellets. The major faces of the samples were lapped to determine their dielectric and ferroelectric properties, and silver electrodes were made from a low-temperature silver paste by firing at 550 °C for 30 min to enable electrical measurements to be taken. The relative permittivity (ε_r) and dissipation factor (tan δ) were measured using an HP-4284A LCR meter. The capacitance and dissipation factors of the sample were measured at 1–100 kHz, and the temperature varied between 25 and 350 °C. A heating rate of 2 °C/min was used during measurement, and the phase transitions also were measured by differential scanning calorimeter (DSC 2920, TA Instrument) between ambient temperature and 350 °C at a rate of 10 °C/min. The electrical polarization versus field hysteresis loops was recorded at a series of temperatures by a standardized ferroelectric test system (RT-66A, Radiant Technologies). The peak field was maintained at 30 kV/cm during measurement, and the ferroelectric hysteresis loop was recorded after the temperature was stabilized for at least 5 min.

3. Results and discussion

The XRD pattern of 0.94PZ–0.06PMW ceramic is presented in Fig. 1. The 0.94PZ–0.06PMW ceramic was identified from the patterns as a single-phase material with a perovskite structure having orthorhombic symmetry. Evidence of the pyrochlore or other second phases was not detected in the pattern, but the 1/4($h\,k\,l$) superstructure lines were present in the 0.94PZ–0.06PMW ceramic, indicating that the Pb^{2+} ions suffer antiparallel displacements with respect to their original position in the cubic perovskite lattice. The indexed pattern with the least number of refinement squares gave a cell with dimensions of a = 5.85(1) Å, b = 11.67(3) Å and c = 8.16(8) Å. The cell parameters of 0.94PZ–0.06PMW were close to those of the standard data: PDF#751607 [a = 5.88(4), b = 11.76(0) and c = 8.22(0)]. A 97.8% relative density of the ceramic was measured

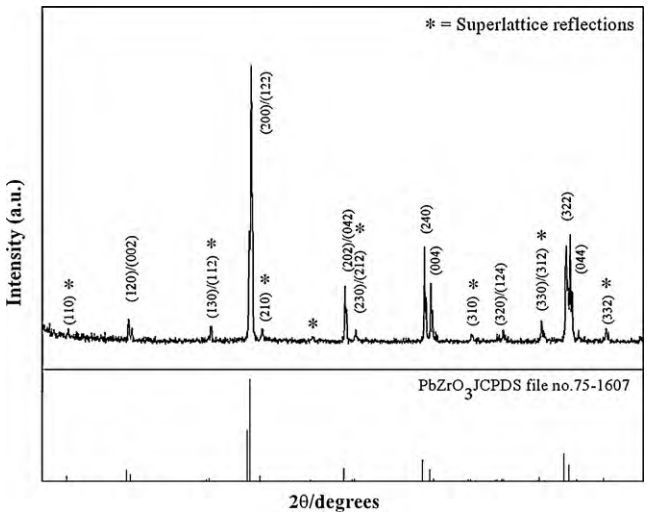

Fig. 1. XRD pattern of 0.94PZ–0.06PMW ceramic.

using the Archimedes method, and the grain size was examined by scanning electron microscopy (SEM). The fresh surface of the 0.94PZ–0.06PMW ceramic was almost free of pores, with a grain size in the range of 10–14 μm, as shown in Fig. 2.

The temperature dependence of relative permittivity and dielectric loss was measured at frequencies of 1, 10 and 100 kHz, while heating from 25 to 350 °C, and the results are displayed in Fig. 3. There were clearly two abrupt changes in both relative permittivity and dielectric loss in the 0.94PZ–0.06PMW ceramic. The first one occurred at around 177 °C, where both relative permittivity and dielectric loss increased by one order of magnitude. The other one took place at the Curie temperature of 219°C, where significant suppression of dielectric loss was seen. Therefore, the dielectric response in the 0.94PZ–0.06PMW ceramic can be divided into three stages. At temperatures below 177 °C, both the relative permittivity and the dielectric loss have low values and show negligible increases with increasing temperatures. At temperatures above 219 °C, the relative permittivity begins to decrease following the Curie–Weiss law [3,4]. In the intermediate temperature range (177–219 °C), the relative permittivity increases dramatically, while the dielectric loss remains high at around 0.08.

To elucidate further on the dielectric behavior of different phases in the 0.94PZ–0.06PMW ceramic, electrically polarized hysteresis loop measurements were performed at a series of tem-

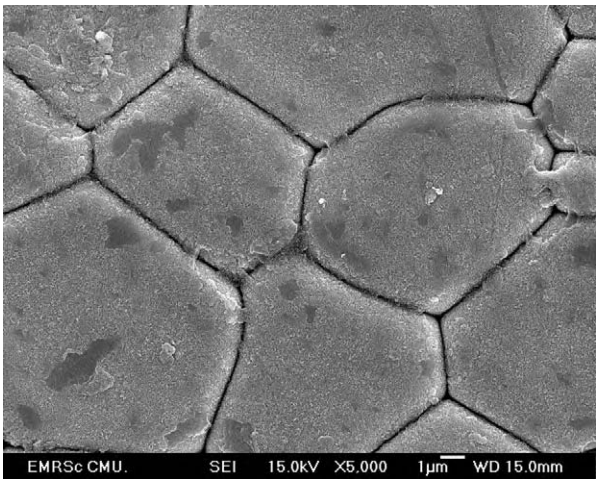

Fig. 2. SEM image of 0.94PZ–0.06PMW ceramic surfaces.

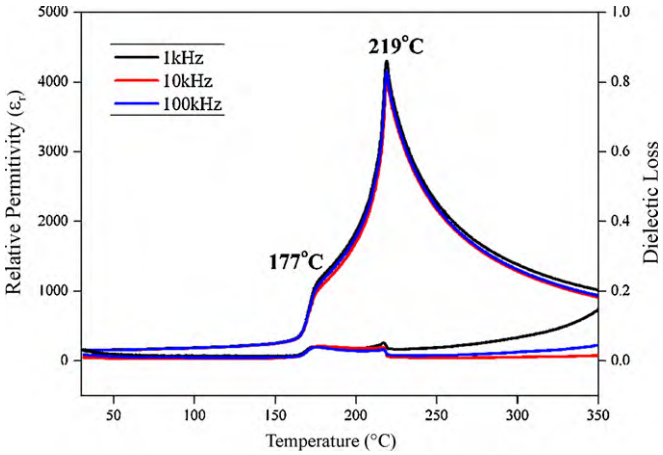

Fig. 3. Dielectric properties during heating at 1, 10 and 100 kHz in a bulk 0.94PZ–0.06PMW ceramic.

peratures under a peak field of 30 kV/cm. A circular disk specimen, with a diameter of about 10 mm and thickness of around 800 μm, was used. The loop was recorded after the temperature had been stabilized for at least 5 min. Linear polarization was displayed as a function of electric field between room temperature and 155 °C, as shown in Fig. 4(a)–(d). This could indicate that the 0.94PZ–0.06PMW ceramic has AFE behavior between room temperature and less than 150 °C [Fig. 4(a)]. Regarding bulk AFE ceramic specimens, the net remnant polarization (P_r) was zero, due to the existence of antiparallel dipole moments. To induce an AFE–FE phase transition, an intense electric field needs to be applied to the ceramics.

Hysteretic behavior starts to develop when the temperature increases to 155 °C, and a regular hysteresis loop has a coercive E_C field of 8.29 kV/cm, as shown in Fig. 4(b). However, the hysteresis loop observed does not indicate the presence of a ferroelectric phase. As seen in Fig. 4(b), close examination of the hysteresis loop at 155 °C reveals that slight distortions, which are marked by two circles, occurred at ~10 kV/cm. Similar distortions were found on the hysteresis loop in $0.98PbZrO_3$–$0.02Pb(Ni_{1/3}Nb_{2/3})O_3$ and $Pb_{0.99}Nb_{0.02}[Zr_{0.57}Sn_{0.43}]_{1-x}Ti_x]_{0.98}O_3$ ceramics, and these have been attributed to the onset of electric field-induced AFE to FE transition [28,29]. Therefore, the 0.94PZ–0.06PMW ceramic is still in the AFE phase at this temperature and it should be noted that the distortions marked at 155 °C in Fig. 4(b) indicate the AFE–FE phase transition. A regular hysteresis loop, exhibiting ferroelectricity, clearly demonstrated the intermediate phase between the AFE and PE phase when the temperature was raised to 190 °C [Fig. 4(c)]. Moreover, hysteretic behavior transition from the FE to PE phase occurred when the temperature increased to over 220 °C [Fig. 4(d)]. It is well known that the occurrence of antiferroelectricity in pure PZ is due to an antiparallel shift of Pb ions along the [1 1 0] direction and it also results in a superstructure line in the XRD pattern. It is apparent that replacement of the Zr^{4+} ion by Mg^{2+}/W^{6+} ions decreases the driving force for the antiparallel shift of Pb^{2+} ions, because they interrupt the translational symmetry. This interruption causes the appearance of an intermediate ferroelectric phase and similar behavior has been found in PZ–PNN ceramics [28].The DSC technique was used as the third tool to confirm the phase transition of PZ–PMW ceramics. Fig. 5 shows the temperature dependence of the heat flow (DSC curves) obtained when heating the 0.94PZ–0.06PMW sample at a rate of 10 °C/min. Two phase transitions in the 0.94PZ–0.06PMW ceramic were obtained with dielectric measurement and clearly confirmed by DSC measurement. The lower temperature of 163 °C corresponded to the transition temperature of the AFE → FE phase transition, while the higher one (215 °C) corresponded to the FE → PE phase transition. It is interesting to note that the difference in values of AFE–FE and FE–PE transition temperature in dielectric, ferroelectric and DSC measurement techniques is due to that in heating

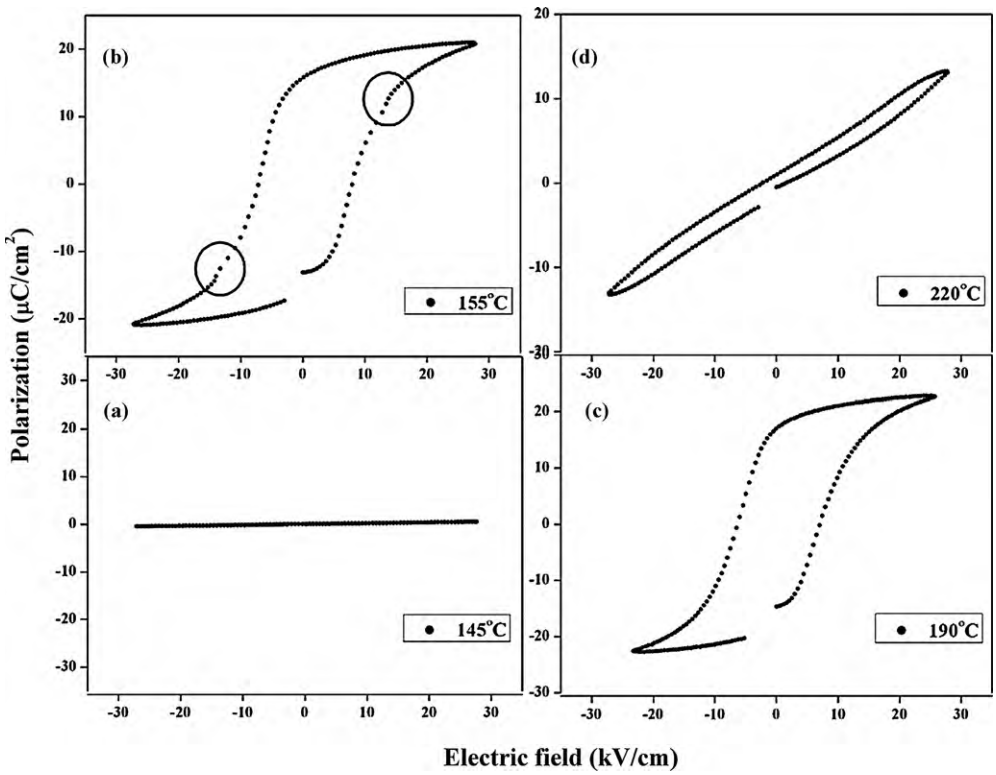

Fig. 4. Hysteresis loops of 0.94PZ–0.06PMW ceramic from temperatures of 145–220 °C.

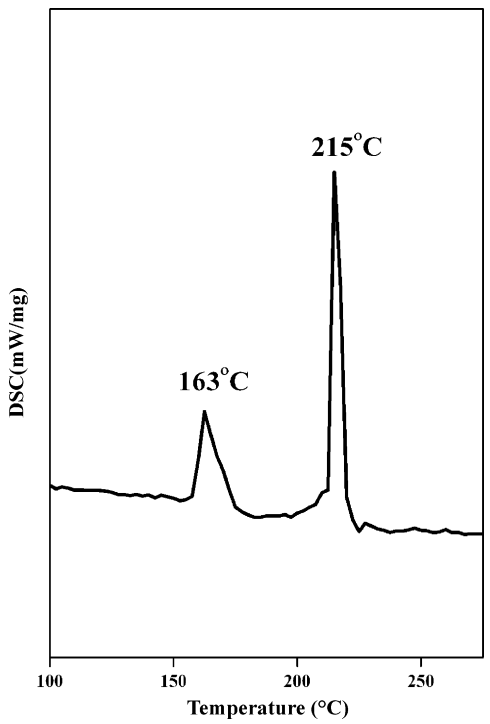

Fig. 5. DSC curves of 0.94PZ–0.06PMW ceramic.

rate and dwell time measurement. Thermodynamic parameter, enthalpy (ΔH^*/J g^{-1}), heat capacity (C_p/J g^{-1} K^{-1}), entropy change (ΔS^*/J g^{-1} K^{-1}), and Gibbs energy change (ΔG^*/J g^{-1}) were calculated from the DSC results. The enthalpy change was calculated directly from the amount of heat change involved in each step per unit mass of the sample. The ΔH^* was thus determined and implemented to calculate the specific heat capacity (C_p) using the following equation [30,31]:

$$C_p = 2.303C_p \log(T_2/T_1) \quad (1)$$

where $\Delta T = T_2 - T_1$, T_1 is the temperature at which the DSC peak begins to depart from the baseline, and T_2 is the temperature at which the peak lands. Consequently, the changes of entropy (ΔS^*) and Gibbs energy (ΔG^*) were calculated using the following equations [30,31]:

$$\Delta S* = 2.303C_p \log(T_2/T_1) \quad (2)$$

$$\Delta H* = \Delta G* - T_p \Delta S* \quad (3)$$

On the basis of DSC data, the value of ΔH^*, ΔS^*, C_p and ΔG^* for the phase transition can be calculated according to Eqs. (1)–(3), which are presented in Table 1. In terms of the activated complex theory (transition theory), the higher value of ΔS^* for the AFE to FE phase transition indicates a lower ordered activated complex. Also, the degree of rotation freedom as well as vibration is higher than that in non-activated complex antiferroelectric and paraelectric phases, which corresponds well with the formation of a non-stability phase. This means that the rate of AFE to FE phase transition is higher than that of the FE to PE phase transition of thermal transformation. Therefore, the FE to PE transformation step occurs harder than the AFE to FE transformation step. On the other hand, the thermodynamic parameter, $\Delta H^*$and ΔG^*, was calculated according to Eqs. (1)–(3) and gave the positive values for both steps, thus indicating that the AFE to FE to PE phase transitions are connected to the introduction of heat, and phase transitions are non-spontaneous processes.

Table 1
Values of thermodynamic parameters for phase transition of 0.94PZ–0.06PMW ceramics calculated from DSC data.

Temperature ranges/K	T_p/K	ΔH^*/J g^{-1}	C_p/J g^{-1} K^{-1}	ΔS^*/J g^{-1} K^{-1}	ΔG^*/J g^{-1}
431–441	436	1.207	2.768×10^{-3}	6.350×10^{-5}	1.179
487–491	488	2.325	4.764×10^{-3}	3.858×10^{-5}	2.308

4. Conclusions

The investigation of 0.94PZ–0.06PMW ceramics using XRD, dielectric behavior, differential scanning calorimetry and ferroelectric measurements has clearly shown a series of phase transitions that occur above room temperature. When the ceramic is in an antiferroelectric nature below 177 °C, both the dielectric property and the loss tangent are low and stable against temperature change. One order of magnitude increase in dielectric property occurs at around 177 °C, and loss tangent results within a narrow temperature range. The ceramic is in an intermediate phase at a temperature range of 177–219 °C, when it is believed to be ferroelectric. When the ceramic is above 219 °C, it is in the cubic paraelectric phase, with relative permittivity following the Curie–Weiss law. A thermodynamic parameter indicated that the AFE to FE to PE phase transitions are connected to the introduction of heat, and phase transitions are non-spontaneous processes.

Acknowledgements

This research was supported by a grant from the Thailand Research Fund (TRF), the Royal Golden Jubilee Ph.D. Program, and the National Nanotechnology Center (NANOTEC) NSTDA, Ministry of Science and Technology, Thailand, through its “Center of Excellence Network” program.

References

[1] G.R. Love, J. Am. Ceram. Soc. 73 (2005) 323–328.
[2] G.H. Haertling, J. Am. Ceram. Soc. 82 (1999) 797–818.
[3] Y. Xu, Ferroelectric Materials and Their Application, Elsevier Science Publishers B.V., Amsterdam, 1991.
[4] B. Jaffe, W.R. Cook, H. Jaffe, Piezoelectric Ceramics, Academic Press, London, 1971.
[5] L.B. Kong, J. Ma, W. Zhu, O.K. Tan, J. Alloys Compd. 322 (2001) 290–297.
[6] X. Hao, Z. Zhang, J. Zhou, S. An, J. Zhai, J. Alloys Compd. 501 (2010) 358–361.
[7] S.H. Leala, M.T. Escote, F.M. Pontes, E.R. Leite, M.R. Joya, P.S. Pizani, E. Longo, J.A. Varela, J. Alloys Compd. 475 (2009) 940–945.
[8] K. Bhattacharyya, A.K. Tyagi, J. Alloys Compd. 470 (2009) 580–583.
[9] L. Liu, H. Fan, S. Ke, X. Chen, J. Alloys Compd. 458 (2008) 504–508.
[10] A.S. Bhalla, R. Guo, R. Roy, Mater. Res. Innov. 4 (2000) 3–26.
[11] E. Sawaguchi, H. Maniwa, S. Hoshino, Phys. Rev. 83 (1951) 1078.
[12] S. Roberts, J. Am. Ceram. Soc. 33 (1953) 63–66.
[13] F. Jona, G. Shirane, F. Mazzi, R. Pepinsky, Phys. Rev. 105 (1957) 849–856.
[14] X. Dai, J.F. Li, D. Viehland, Phys. Rev. B 51 (1995) 2651–2655.
[15] E. Sawaguchi, J. Phys. Soc. Jpn. 8 (1951) 615–629.
[16] G. Shirane, Phys. Rev. 86 (1952) 219–227.
[17] B.P. Pokharel, D. Pandey, Phys. Rev. B 65 (2002) 214108.
[18] B.P. Pokharel, D. Pandey, J. Appl. Phys. 86 (1999) 3327–3332.
[19] B. Xu, N.G. Pai, L.E. Cross, Mater. Lett. 34 (1998) 157–160.
[20] Q. Tan, Z. Xu, D. Viehland, J. Mater. Res. 14 (1999) 4251–4258.
[21] H. Chen, C. Yang, J. Zhang, Y. Pei, Z. Zhao, J. Alloys Compd. 486 (2009) 615–620.
[22] D.L. Rubia, M.A. Alonso, R.E. Lopez-Garcia, A.R.D. Frutos, IEEE Trans. Ultrason. Ferroelectr. Freq. Control 56 (2009) 1799–1805.
[23] S. Wirunchit, P. Laoratanakul, N. Vittayakorn, J. Phys. D: Appl. Phys. 41 (2008) 125406.
[24] S. Wirunchit, N. Vittayakorn, J. Appl. Phys. 104 (2008) 024103.
[25] W. Banlue, N. Vittayakorn, Ferroelectrics 382 (2009) 122–126.
[26] W. Banlue, N. Vittayakorn, Appl. Phys. A 93 (2008) 565–569.
[27] N. Vittayakorn, P. Charoonsuk, P. Kasiansin, S. Wirunchit, B. Boonchom, J. Appl. Phys. 106 (2009) 064104.
[28] W. Qu, X. Tan, N. Vittayakorn, S. Wirunchit, M.F. Besser, J. Appl. Phys. 105 (2009) 014106.
[29] H. He, X. Tan, Phys. Rev. B 72 (2005) 024102.
[30] S.A. Halawy, N.E. Fouad, M.A. Mohamed, M.I. Zaki, J. Therm. Anal. Calorim. 82 (2005) 671–675.
[31] R.H. Abu-Eittah, N.G. Zaki, M.M.A. Mohamed, L. Kamel, J. Anal. Appl. Pyrol. 77 (2006) 1–11.

I&EC research
Industrial & Engineering Chemistry Research

ARTICLE

pubs.acs.org/IECR

Soft Synthesis Route and Characterization of Superparamagnetic $Mn_{1/2}Fe_{1/2}(H_2PO_4)_2 \cdot 2H_2O$ and Its Decomposed Product

Banjong Boonchom[*,†,‡] and Naratip Vittayakorn[‡,§,∥]

[†]King Mongkut's Institute of Technology Ladkrabang, Chumphon Campus, 17/1 M. 6 Pha Thiew District, Chumphon, 86160, Thailand
Electroceramic Research Laboratory, [‡]College of KMITL Nanotechnology, and Advanced Materials Science Research Unit,
[§]Department of Chemistry, Faculty of Science, King Mongkut's Institute of Technology Ladkrabang, Bangkok 10520, Thailand
[∥]ThEP Center, CHE, 328 Si Ayutthaya Road, Bangkok 10400, Thailand

ABSTRACT: The superparamagnetic $Mn_{1/2}Fe_{1/2}(H_2PO_4)_2 \cdot 2H_2O$ was synthesized by a soft synthesis method using a Mn(c)−Fe(c)−H_3PO_4 system in water−acetone medium at ambient temperature. The synthesized $Mn_{1/2}Fe_{1/2}(H_2PO_4)_2 \cdot 2H_2O$ decomposed through the dehydration and the phosphate condensation reactions at high temperature and yielded binary manganese iron cyclotetraphosphate $MnFeP_4O_{12}$. The XRD and FTIR results of the synthesized $Mn_{1/2}Fe_{1/2}(H_2PO_4)_2 \cdot 2H_2O$ and the decomposed $MnFeP_4O_{12}$ indicate the pure monoclinic phase with space group $P2_1/n$ and $C2/c$, respectively. The thermal behaviors and superparamagnetic properties of $Mn_{1/2}Fe_{1/2}(H_2PO_4)_2 \cdot 2H_2O$ and $MnFeP_4O_{12}$ in this work differed from the single compounds ($M(H_2PO_4)_2 \cdot 2H_2O$ and $M_2P_4O_{12}$, where M = Mn, Fe) and the binary compounds ($Mn_{0.5}Fe_{0.5}(H_2PO_4)_2 \cdot xH_2O$) reported in previous works. The kinetic and thermodynamic functions for thermal decomposition of $Mn_{1/2}Fe_{1/2}(H_2PO_4)_2 \cdot 2H_2O$ were studied and confirmed as reaction mechanisms. Vibrational frequencies of breaking bonds in two thermal transformation stages were estimated and assigned by comparison with the observed FTIR spectra.

1. INTRODUCTION

Binary metal(II) dihydrogenphosphate hydrates $M_{1-x}A_x(H_2PO_4)_2 \cdot nH_2O$ (M and A = Mg, Ca, Mn, Fe, Co, Ni, Zn, or Cu; x = 0−1; n = 1−4) have been investigated for over 30 years and have been widely applied as potential pigments, selective catalysts, phosphors, and materials for corrosion-resistant coatings, and they are biocompatible and biodegradable in tissue.[1−9] This phosphate hydrate group is transformed to binary metal(II) cyclotetraphosphate group $M_{2-y}A_yP_4O_{12}$ (y = 0−2) via the reactions of dehydration and deprotonation of dihydrogenphosphate groups as well as polycondensation at high temperatures.[10−16] Both phosphate groups are good sources for macro- and micronutrients (P, Mg, Ca, Mn, Fe, Co, Ni, Zn, Cu) required by plants.[3−13] Consequently, these phosphate materials have been become a hot research topic in materials science in recent years.

Some binary metal $M_{1-x}A_x(H_2PO_4)_2 \cdot nH_2O$ were prepared for the first time by Trojan et al. using corresponding metal carbonates and phosphoric acid at low temperature (313−353 K) with long time periods (2−60 h),[1−16] and releasing toxic gas (CO_2). Recently, $M_{1-x}Ni_x(H_2PO_4)_2 \cdot xH_2O$ (M = Mg, Mn, Fe, Co, Zn, and Cd) were prepared by corresponding metal carbonates and phosphoric acid at 293 K for 2−90 days.[9] More recently, $Mn_{1-x}A_x(H_2PO_4)_2 \cdot xH_2O$ (A = Ca, Fe, Co, Ni, and Cu) were prepared by metal sources (Mn (c; complexometric) or $MnCO_3$ and A(II) = $CaCO_3$, Fe, $CoCO_3$, $NiCO_3$, or $CuCO_3$) and phosphoric acid H_3PO_4 at ambient temperature for 20 s. These procedures were strong exothermic reactions and evolved gases (CO_2 and H_2).[17−21] However, a limited dose of $M_{1-x}A_x(H_2PO_4)_2 \cdot nH_2O$ could be synthesized without toxic gases.

Synthesis of transition phosphates by a soft solid state reaction in media agents (ethanol, acetone, and water, etc.) at ambient temperature has received a great deal of attention due to their conveniences, cost-effectiveness, and that they are environmentally benign.[22−24] Because of its solubility in water and its ability to associate with metal ions in media, solvent has been used as a binder cum gel for shaping materials (bulk, porous, micro- or nanoparticles) and as a matrix for entrapment of ions to generate a gelled precursor, which resulted in obtaining different material or the same material with different size and morphology. The presence of media agent (solvent) reduces strong exothermic reaction and protects the evolved gases, which will be necessary for elaboration of technology to produce transition metal phosphates. The use of solvent simplifies the process and would provide another alternative process for the environmental and economical synthesis of transition phosphate with different particle size and morphology.

Herein, this work reports the fabrication of $Mn_{1/2}Fe_{1/2}(H_2PO_4)_2 \cdot 2H_2O$ through a soft solid state reaction from metals of manganese and iron with phosphoric acid in water−acetone medium at ambient temperature with short time consumption (<30 min). The synthesized $Mn_{1/2}Fe_{1/2}(H_2PO_4) \cdot 2H_2O$ decomposed to binary manganese iron cyclotetraphosphate $MnFeP_4O_{12}$ at 773 K. Consequently, kinetic (E_a, A) and thermodynamic (ΔH^*, ΔS^*, ΔG^*) functions of thermal transformation of $Mn_{1/2}Fe_{1/2}(H_2PO_4)_2 \cdot 2H_2O$ playing an important role in

Received: July 4, 2010
Accepted: December 26, 2010
Revised: December 1, 2010
Published: January 19, 2011

theoretical study, application development, and industrial production have also been reported for the first time. The synthesized sample and its decomposed product were characterized by X-ray powder diffraction (XRD), Fourier transform infrared (FTIR), scanning electron microscope (SEM), and vibrating sample magnetometer (VSM) techniques. The $Mn_{1/2}Fe_{1/2}(H_2PO_4)_2 \cdot 2H_2O$ and $MnFeP_4O_{12}$ may be useful for fertilizers, (Mn- and Fe-micronutrients and P-macronutrients), ceramic pigments, magnetic materials, etc., in the future.

2. EXPERIMENTAL SECTION

2.1. Synthesis and Characterization. The starting reagents are Mn (c; complexometric) (99.99%, Merck), Fe (c; complexometric) (99.99%, Fluka), and phosphoric acid (86.4% w/w H_3PO_4, Merck). Following this procedure, 1.0988 g of Mn(c) and 1.1186 g of Fe(c) (a mole ratio corresponding to the nominal composition of Mn:Fe ratio of 1:1) were crushed into fine mixed powders using a mortar and pestle. Subsequently, 10 mL of acetone was rapidly added to the fine mixed powders, and then 10 mL of 50% H_3PO_4 (86.4% w/w H_3PO_4 dissolved in DI water) was added slowly to the resulting suspension with continuous stirring at ambient temperature until the cooled crystalline product was developed (30 min). The prepared solid was filtered by a suction pump, washed with acetone, and dried in air.

$$\mathrm{Mn(s) + Fe(s) + 4H_3PO_4 + 2H_2O \xrightarrow[\text{room temperature}]{C_3H_6O} 2Mn_{1/2}Fe_{1/2}(H_2PO_4)_2 \cdot 2H_2O(s) + 2H_2} \quad (1)$$

The water content was investigated by the TG curve in Figure 1, which reveals that its final decomposed product, $MnFeP_4O_{12}$, seemed to occur at temperatures above 673 K. The dried white gray precipitation then was calcined in a box furnace at 773 K for 3 h in air atmosphere. The manganese and iron contents of $Mn_{1/2}Fe_{1/2}(H_2PO_4)_2 \cdot 2H_2O$ and $MnFeP_4O_{12}$ were determined by dissolving in 0.0126 M hydrochloric acid using atomic absorption spectrophotometer (AAS, Perkin-Elmer, Analyst100). The phosphorus content was determined by colorimetric analysis of the molybdophosphate complex. The structure and crystallite size of the synthesized sample and its decomposed product were studied by X-ray powder diffraction using an X-ray diffractometer (Phillips PW3040, The Netherland) with Cu Kα radiation (λ = 0.15406 nm). The Scherrer method was used to evaluate the crystallite size.[25] The morphologies of the prepared samples were examined with a scanning electron microscope (SEM) using LEO SEM VP1450 after gold coating. The room temperature FTIR spectra were recorded in the range of 4000−370 cm^{-1} with eight scans on a Perkin-Elmer Spectrum GX FT-IR/FT-Raman spectrometer with the resolution of 4 cm^{-1} using KBr pellets (KBr, spectroscopy grade, Merck). The magnetic properties of the $Mn_{1/2}Fe_{1/2}(H_2PO_4)_2 \cdot 2H_2O$ and $MnFeP_4O_{12}$ were examined at room temperature (293 K) using a vibrating sample magnetometer (VSM 7403, Lake Shore, U.S.).

2.2. Kinetic and Thermodynamic Studies. To evaluate the activation energies for the thermal decomposition of $Mn_{1/2}Fe_{1/2}(H_2PO_4)_2 \cdot 2H_2O$, a TG-DTA Pyris Diamond Perkin-Elmer Instrument was used. The experiments were performed in dynamic dry air, at heating rates of 5, 10, 15, and 20 K min^{-1} over the temperature range from 303 to 673 K and the O_2 flow rate of 100 mL min^{-1}. The sample mass of about 6.0−10.0 mg

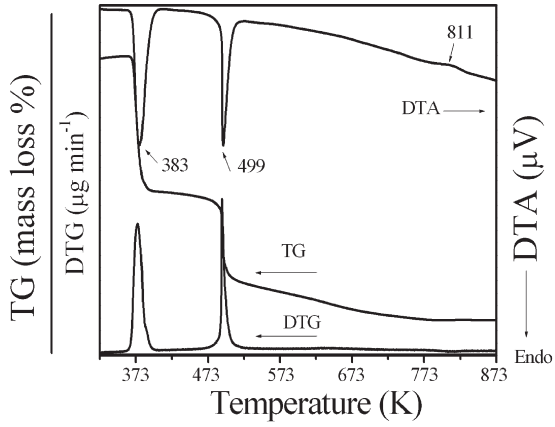

Figure 1. TG-DTG-DTA curves of $Mn_{1/2}Fe_{1/2}(H_2PO_4)_2 \cdot 2H_2O$.

was filled into an aluminum crucible without pressing. The thermogram of sample was recorded in an open aluminum crucible using α-Al_2O_3 as the reference material. Decomposition of crystal hydrates is a solid-state process of the type[26−32] A(solid) → B(solid) + C(gas). The kinetics of such reactions is described by various equations taking into account the special features of their mechanisms. The activation energies for the thermal transformation steps of $Mn_{1/2}Fe_{1/2}(H_2PO_4)_2 \cdot 2H_2O$ were calculated from two peaks on the DTA curves using the Kissinger equation:[33]

$$\ln\left(\frac{\beta}{T_p^{\,2}}\right) = -\frac{E_a}{RT_p} + \ln\left(\frac{AR}{E_a}\right) \quad (2)$$

Here, β is the DTA heating rate (K min^{-1}), E_a is the activation energy for the phase transformation (kJ mol^{-1}), R is the gas constant (8.314 J mol^{-1} K^{-1}), and T_p is the phase transformation temperature peak in the DTA curve (K). The fact that the T_p values for various heating rates can be precisely evaluated from nonisothermal data (DTA, DTG, or DSC curves) conferred to the Kissinger method to evaluate the kinetic parameters a high popularity. The plots of $\ln(\beta/T^2)$ versus $1/T_p$ should give the straight lines with the best correlation coefficients of the linear regression (R^2), which have been proved to give the values of activation energy and pre-exponential factor by the slope and the intercept for the different thermal transformation stages of $Mn_{1/2}Fe_{1/2}(H_2PO_4)_2 \cdot 2H_2O$. The advantage of Kissinger equation is that the values of E_a and A can be calculated on the basis of multiple thermogravimetric curves and do not require selection of particular kinetic model (type of $g(\alpha)$ or $f(\alpha)$ functions).[26−31] In addition, the E_a and A values obtained by this method are usually regarded as more reliable than those obtained by a single thermogravimetric curve.

The thermal decomposition mechanism could be determined from the shape factor (n) of ethe ndothermic peak represented by the following equation:[34]

$$n = \frac{2.5}{\Delta T} \cdot \frac{T_p^2}{E_a/R} \quad (3)$$

where n is the Avrami constant, and ΔT is the full width at half-maximum of the endothermic peak; T_p is the average temperature at different DTA curves; and E_a is the activation energy of the Kissinger method.

From the activated complex theory (transition state) of Eyring,[35−37] the following general equation may be written:

$$A = \left(\frac{e\chi k_B T_{ap}}{h}\right) \exp\left(\frac{\Delta S^*}{R}\right) \quad (4)$$

$$\Delta S^* = R \ln\left(\frac{Ah}{e\chi} k_B T_{ap}\right) \quad (5)$$

Because

$$\Delta H^* = E_a - RT_{ap} \quad (6)$$

$$\Delta G^* = \Delta H^* - T_{ap}\Delta S^* \quad (7)$$

where A and E_a are the pre-exponential factor and the activation energy, respectively, obtained from the Kissinger method; e = 2.7183 is the Neper number; χ is the transition factor, which is unity for monomolecular reactions; k_B is the Boltzmann constant; h is the Planck constant; and T_{ap} is the average phase transformation temperature peak in DTA curves (K). The changes of the enthalpy ΔH^* and Gibbs free energy ΔG^* for the activated complex formation from the reagent can be calculated using the well-known thermodynamic equation. In this Article, we suggest the relation between kinetic (E_a, and A) and thermodynamic (ΔH^*, ΔS^*, ΔG^*) parameters of the thermal transformation of $Mn_{1/2}Fe_{1/2}(H_2PO_4)_2 \cdot 2H_2O$ based on the Kissinger method and attract the interest of thermodynamic and kinetic scientists.

The specificity of the thermal decomposition was characterized by identification of the bonds to be selectively activated due to energy absorption at vibrational level.[28] These bonds were assigned by comparing the calculated wavenumbers with the observed wavenumbers in the IR spectra. These breaking bonds are assimilated with a Morse oscillator[28,37,38] coupled nonlinear[37,38] with the harmonic oscillators of the thermic field. Following a theoretical treatment developed by Vlase et al.,[28] the relationship between the average phase transformation temperature peak in four DTA curves (T_{ap}, K) and the wavenumber of the activated bond is given as follows:

$$\omega = \frac{k_b}{hc} T_{ap} = 0.695 T_{ap} \quad (8)$$

where c is the light velocity. Because the breaking bond has an unharmonic behavior, the specific activation is possible also due to more than one quanta, or by a higher harmonic: $\omega_{sp} = q\omega_{calc}$, $q \in N = 1, 2, 3...$, where ω_{sp} is the assigned spectroscopic number for the bond supposed to break, which relates to the evolved gas in the thermal decomposition step. In this Article, we suggested the maximum peak temperature T_{ap} in the DTA curve for the calculated wavenumbes (ω_{sp}) according to eq 8. Therefore, the use of T_p (DTA) will be an alternative method for the calculated wave numbers for identification in each thermal transition step of interesting materials.

3. RESULTS AND DISCUSSION

3.1. Synthesis and Characterization. According to the chemical analysis data, the P/(Mn + Fe) = 2.01 and H_2O/P = 1.82 molar ratios in the synthesized phosphate differed very little from those calculated for binary metal dihydrogenphosphate with the general formula $Mn_{1/2}Fe_{1/2}(H_2PO_4)_2 \cdot 2H_2O$. Similarly, the P/(Mn + Fe) = 1.98 molar ratio in the decomposed product practically corresponds to the $MnFeP_4O_{12}$ stoichiometry, where Mn(II) and Fe(II) stand for divalent cations.

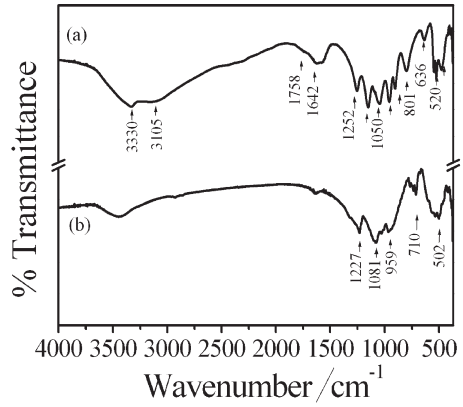

Figure 2. FTIR spectra of $Mn_{1/2}Fe_{1/2}(H_2PO_4)_2 \cdot 2H_2O$ (a) and $MnFeP_4O_{12}$ (b).

Figure 1 shows the TG-DTG-DTA curves of $Mn_{1/2}Fe_{1/2}(H_2PO_4)_2 \cdot 2H_2O$. The TG curve of $Mn_{1/2}Fe_{1/2}(H_2PO_4)_2 \cdot 2H_2O$ relating to the elimination of water molecules shows two well-defined mass loss stages in the range of 303−873 K. These two steps in the TG curve observed in the ranges of 373−423 and 473−673 K appear in the respective DTG and DTA as two endothermic peaks (383 and 499 K). The corresponding observed mass losses of 11.86 (1.89 mol of H_2O) and 11.73 (1.86 mol of H_2O) % by mass are assigned to the dehydration of coordination water molecules (eq 9) and an intramolecular dehydration of the protonated dihydogenphosphate groups (eq 10), respectively. The total mass loss of 23.58% (3.74 mol H_2O) is in agreement with those reported for other binary dihydrogenphosphate dihydrate in the literature (1 < mole of water < 4).[1−9] The thermal decomposition process of $Mn_{1/2}Fe_{1/2}(H_2PO_4)_2 \cdot 2H_2O$ could be formally presented as:

$$Mn_{1/2}Fe_{1/2}(H_2PO_4)_2 \cdot 2H_2O \xrightarrow{373-423\ K} Mn_{1/2}Fe_{1/2}(H_2PO_4)_2 + 2H_2O \quad (9)$$

$$Mn_{1/2}Fe_{1/2}(H_2PO_4)_2 \xrightarrow{473-673\ K} 1/2MnFeP_4O_{12} + 2H_2O \quad (10)$$

A stable intermediate compound, acid polyphosphate $Mn_{1/2}Fe_{1/2}(H_2PO_4)_2$, has been registered. This intermediate is similarly observed with other binary dihydrogen phosphates, as it is isostructural.[1−9] The plateau formed between 673 and 873 K on the TG curve indicated the formation of binary manganese iron cyclotetraphosphate, $MnFeP_4O_{12}$, as the final decomposed product. The thermal stability, mechanism, and phase transition temperature of the synthesized $Mn_{1/2}Fe_{1/2}(H_2PO_4)_2 \cdot 2H_2O$ in water−acetone medium of this work are significantly different from those of $Mn(H_2PO_4)_2 \cdot 2H_2O$,[40] $Fe(H_2PO_4)_2 \cdot 2H_2O$,[41] and $Mn_{0.5}Fe_{0.5}(H_2PO_4)_2 \cdot xH_2O$[18] synthesized without media agents. The obtained results are similar to those of the $Mn(H_2PO_4)_2 \cdot 2H_2O$[22] synthesized by water−acetone medium reported in our previous works. On the basis of thermal results, we can conclude that the different thermal behaviors are caused by the

different interaction and position of Mn and Fe metals in the skeleton, the medium reagents, and reaction condition for precipitation.

The FT-IR spectra of $Mn_{1/2}Fe_{1/2}(H_2PO_4)_2 \cdot 2H_2O$ (Figure 2a) and $MnFeP_4O_{12}$ (Figure 2b) are very similar to those of $M(H_2PO_4)_2 \cdot 2H_2O$ and $M_2P_4O_{12}$ (M = Mn or Fe), respectively.[1,2,18,22,40,41] The band position are shifted to the values between those of individual $M(H_2PO_4)_2 \cdot 2H_2O$ and $M_2P_4O_{12}$ (M = Mn or Fe), and sharp or weak bands are observed, indicating the inserting of different metal cations (Mn and Fe) in the skeleton. Consequently, vibrational bands are identified in relation to the crystal structure in terms of the fundamental vibrating units, $H_2PO_4^-$ and H_2O for $Mn_{1/2}Fe_{1/2}(H_2PO_4)_2 \cdot 2H_2O$ and $[P_4O_{12}]^{4-}$ ion for $MnFeP_4O_{12}$, and are assigned according to the literature.[1,2,18,42] It is known that the existence of short OH···O hydrogen bonds in a variety of strongly hydrogen-bonded solids is manifested by the appearance of the characteristic ABC structure of the ν(OH) vibration. Usually, the ABC bands are very broad and consist of many ill-resolved components. The strongest band (A) is located in the 3100−2700 cm^{-1} region, the B band appears at about 2600−2400 cm^{-1}, and the C band is around 1700−1600 cm^{-1}. The problem of the origin of the ABC trio is discussed in many studies on acidic salts, but an explanation of this behavior of strongly hydrogen-bonded systems is still to be found. One of the most popular interpretations of the ABC trio suggests a strong Fermi resonance between the ν(OH) stretching fundamentals and the overtones [2δ(OH) and 2γ(OH)] or combinations involving the δ(OH) and γ(OH) vibrations.[1,2,18,22] The second type of characteristic vibrations is associated with the phosphate groups. The stretching P−O and bending OPO vibrations of the phosphate groups appear in the ranges of 920−990 cm^{-1} (ν_1), 990−1160 cm^{-1} (ν_3), 460−375 cm^{-1} (ν_2), and 460−650 cm^{-1} (ν_4). In addition to the internal PO_4 vibrations, other vibrations involving OH motions are the characteristic of the protonated phosphate ions ($H_2PO_4^-$), both out-of-plane δ(OH) and in-plane γ(OH) bending P−O−H vibrations, which appear at 1252 and 801 cm^{-1}, respectively. The third spectra feature in the FTIR spectrum (Figure 2a) of $Mn_{1/2}Fe_{1/2}(H_2PO_4)_2 \cdot 2H_2O$ is the water molecule vibrations. The ν_{OH} stretching modes of HOH appear at 3105 cm^{-1} (ν_1 or band A) and 3330 cm^{-1} (ν_3). The doublet bands (1642 and 1570 cm^{-1}) contribute both to the band C and to the water bending band.[2] A weak band around 639 cm^{-1} could be tentatively assigned to the rocking mode involving water librations.

The vibrational modes of $P_4O_{12}^{4-}$ ion observed in the frequency range 370−1400 cm^{-1} (Figure 2b) are assigned according to the literature.[2,18,42] The $P_4O_{12}^{4-}$ anion contains the PO_2^{2-} radical and the P−O−P bridge, which are interpreted in the FTIR spectra from the viewpoint of the vibrations of these two groups. As the P−O bond strength in the P−O−P bridge is weaker than in the PO_2^{2-} radical, the stretching frequencies of the P−O−P bridge are expected to be lower than those in the PO_2^{2-} radical. The asymmetric and symmetric stretching frequencies of the PO_2^{2-} radical are generally observed in the areas of 1350−1220 and 1150−1100 cm^{-1}, respectively. The P−O−P bridge has its asymmetric and symmetric stretching frequencies around 1000−900 and 900−700 cm^{-1}, respectively. The bending modes are expected in the area of 600−400 cm^{-1} (PO_2^{2-} radical) and 400−370 cm^{-1} (P−O−P bridge). The metal−O stretching usually appears in the bending mode region as the bending modes of the P−O−P bridge and absorption

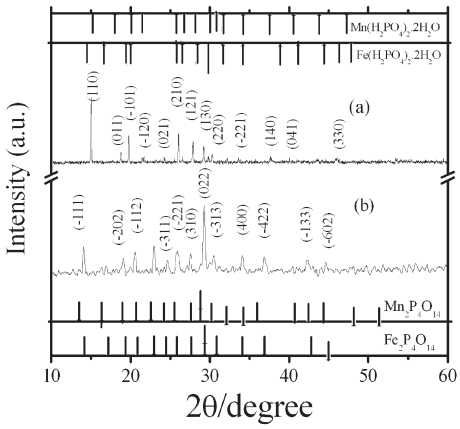

Figure 3. XRD patterns of $Mn_{1/2}Fe_{1/2}(H_2PO_4)_2 \cdot 2H_2O$ (a) and $MnFeP_4O_{12}$ (b).

bands associated with these vibrations are usually very weak. The observation of a strong ν_sPOP band is known to be the most striking feature of the cyclotetraphosphate spectra, along with the presence of the $\nu_{as}OPO^-$ band, which confirmed that the crystal structure is monoclinic (space group $C2/c$) with a cyclic structure of the $[P_4O_{12}]^{4-}$ anion.[42]

Figure 3 shows the XRD patterns of $Mn_{1/2}Fe_{1/2}(H_2PO_4)_2 \cdot 2H_2O$ and the decomposed product $MnFeP_4O_{12}$, which are similar to those obtained from the individual compounds ($M(H_2PO_4)_2 \cdot 2H_2O$ and $M_2P_4O_{12}$ (M = Mn and Fe)[1,2,22,40,41] and the binary compounds ($Mn_{0.5}Fe_{0.5}(H_2PO_4)_2 \cdot xH_2O$ and $MnFeP_4O_{12}$) in our previous work,[18] but the intensities are slightly different. The lower and higher intensities of XRD peaks indicate the differences of crystallization or amorphous phase as well as particle sizes of these materials. According to the hypothesis of isostructural, the systems of binary manganese iron solid solutions and individual metal dihydrogenphosphate (or manganese iron cyclotetraphosphate) show quite a similarity of the XRD peaks because the electronic charges of cations are equivalent and the radii of cations are close to each other. As compared to the published XRD data of the individual metal compounds ($Mn(H_2PO_4)_2 \cdot 2H_2O$ (PDF# 350010), $Fe(H_2PO_4)_2 \cdot 2H_2O$ (PDF# 390699), $Mn_2P_4O_{12}$ (PDF# 380314), and $Fe_2P_4O_{12}$ (PDF# 760223), both studied samples can be assigned to the $Mn_{1/2}Fe_{1/2}(H_2PO_4)_2 \cdot 2H_2O$ and $MnFeP_4O_{12}$ product, which are solid solutions and not a mixture of the individual ones. Consequently, all the reflections can be distinctly indexed as a pure monoclinic phase with space group $P2_1/n$ ($Z = 2$) for $Mn_{1/2}Fe_{1/2}(H_2PO_4)_2 \cdot 2H_2O$ and $C2/c$ (Z = 4) for the decomposed $MnFeP_4O_{12}$, which noted that these XRD patterns agreed well with those of standard data of $M(H_2PO_4)_2 \cdot 2H_2O$ and $M_2P_4O_{12}$ (M = Mn or Fe), respectively. The average crystallite sizes and lattice parameters of $Mn_{1/2}Fe_{1/2}(H_2PO_4)_2 \cdot 2H_2O$ and the decomposed product $MnFeP_4O_{12}$ were calculated from XRD patterns and also tabulated in Table 1. The lattice parameters of $Mn_{1/2}Fe_{1/2}(H_2PO_4)_2 \cdot 2H_2O$ are larger than those of the standard data of $Mn(H_2PO_4)_2 \cdot 2H_2O$ (PDF# 350010) and $Fe(H_2PO_4)_2 \cdot 2H_2O$ (PDF# 390699). However, the lattice parameters of the decomposed $MnFeP_4O_{12}$ are found to range between those of the standard data of $Mn_2P_4O_{12}$ (PDF# 380314) and $Fe_2P_4O_{12}$ (PDF# 760223). The average crystallite size of $Mn_{1/2}Fe_{1/2}(H_2PO_4)_2 \cdot 2H_2O$ is larger than that of the calcined $MnFeP_4O_{12}$, which resulted from two decomposition

Table 1. Average Crystallite Sizes and Lattice Parameters of $Mn(H_2PO_4)_2 \cdot 2H_2O$, $Mn_{1/2}Fe_{1/2}(H_2PO_4)_2 \cdot 2H_2O$, $Fe(H_2PO_4)_2 \cdot 2H_2O$, and the Calcined Product $MnFeP_4O_{12}$ Calculated from XRD Data

compound	*a* (Å)	*b* (Å)	*c* (Å)	*β* (deg)	average crystallite size (nm)
PDF# 350010 ($Mn(H_2PO_4)_2 \cdot 2H_2O$)	7.32	10.08	5.37	94.75	
this work ($Mn_{1/2}Fe_{1/2}(H_2PO_4)_2 \cdot H_2O$)	7.90(0)	11.03(6)	6.10 (3)	95.04 (6)	79 ± 11
PDF# 390699 ($Fe(H_2PO_4)_2 \cdot 2H_2O$)	7.31	9.94	5.37	95.24	
PDF# 380314 ($Mn_2P_4O_{12}$)	11.88	8.59	10.14	119.21	
this work ($MnFeP_4O_{12}$)	12.06(8)	8.48(2)	10.12(4)	119.12(5)	62 ± 13
PDF# 760223 ($Fe_2P_4O_{12}$)	11.94	8.37	9.94	118.77	

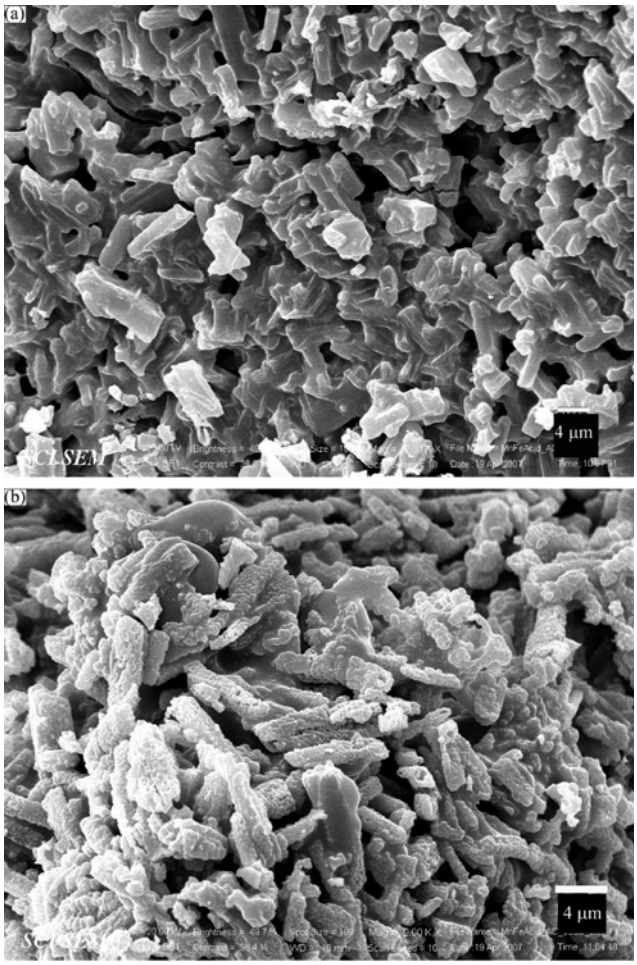

Figure 4. SEM micrographs of $Mn_{1/2}Fe_{1/2}(H_2PO_4)_2 \cdot 2H_2O$ (a) and $MnFeP_4O_{12}$ (b).

processes. The crystallite sizes of 79 ± 11 nm for $Mn_{1/2}Fe_{1/2}(H_2PO_4)_2 \cdot 2H_2O$ and 62 ± 13 nm for $MnFeP_4O_{12}$ in this work are smaller than those prepared from Mn(c)−Fe(c)−H_3PO_4 without the medium system reported by Boonchom et al. (81 ± 14 nm for $Mn_{1/2}Fe_{1/2}(H_2PO_4)_2 \cdot xH_2O$ and 69 ± 21 nm for $MnFeP_4O_{12}$).[18] However, the crystallite sizes for both binary compounds in this work are larger than those from the single

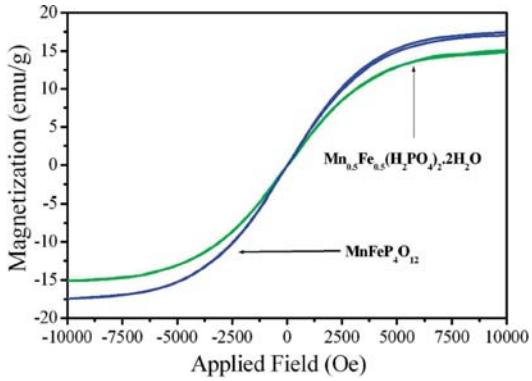

Figure 5. The specific magnetizations of $Mn_{1/2}Fe_{1/2}(H_2PO_4)_2 \cdot 2H_2O$ and $MnFeP_4O_{12}$ as a function of field, measured at 293 K.

metal compounds (52 ± 14 nm for $Mn(H_2PO_4)_2 \cdot 2H_2O$, 28 ± 4 nm for $Fe(H_2PO_4)_2 \cdot 2H_2O$, 29 ± 9 nm for $Mn_2P_4O_{12}$, and 27 ± 6 nm for $Fe_2P_4O_{12}$) in our previous studies.[22,40,41] These results confirmed that the differences in the crystallite sizes for the synthesized $Mn_{1/2}Fe_{1/2}(H_2PO_4)_2 \cdot 2H_2O$ and $MnFeP_4O_{12}$ depend on the medium, water, and metal compositions and the condition for precipitations.

The SEM micrographs of $Mn_{1/2}Fe_{1/2}(H_2PO_4)_2 \cdot 2H_2O$ and $MnFeP_4O_{12}$ are shown in Figure 4. The particle shape and size are changed throughout the whole decomposition product. The SEM micrograph of $Mn_{1/2}Fe_{1/2}(H_2PO_4)_2 \cdot 2H_2O$ (Figure 4a) shows nonuniform particles, which appear as high agglomerates. The morphology of $Mn_{1/2}Fe_{1/2}(H_2PO_4)_2 \cdot 2H_2O$ exhibits features different from those of $Mn(H_2PO_4)_2 \cdot 2H_2O$, $Fe(H_2PO_4)_2 \cdot 2H_2O$, and $Mn_{0.5}Fe_{0.5}(H_2PO_4)_2 \cdot xH_2O$ reported in our previous works.[18,40,41] The morphology of $MnFeP_4O_{12}$ shows a high agglomerate of nonuniform particles, which is not similar that for $M_2P_4O_{12}$ (M = Mn or Fe) (Figure 4b) in the work previously reported.[18,40,41] The high agglomerates of $Mn_{1/2}Fe_{1/2}(H_2PO_4)_2 \cdot 2H_2O$ and $MnFeP_4O_{12}$ powders are possibly caused by the process of dissolution and a rapid coprecipitation as well as the dehydration process.

Magnetization curves (M−H loop) of $Mn_{1/2}Fe_{1/2}(H_2PO_4)_2 \cdot 2H_2O$ and the decomposed $MnFeP_4O_{12}$ powders obtained from room temperature VSM measurements are shown in Figure 5. Both samples demonstrate typical superparamagnetic behavior with negligible coercivity and remanence, in accordance

Table 2. Values of Thermodynamics, Kinetics, and Spectroscopic Data for Two Decomposition Steps of $Mn_{1/2}Fe_{1/2}(H_2PO_4)_2 \cdot 2H_2O$

step	ΔG^*/kJ mol^{-1}	ΔH^*/kJ mol^{-1}	ΔS^*/J mol^{-1} K^{-1}	A/s^{-1}	E_a/kJ mol^{-1}	R^2	T_{ap}/K	ω_{cal}	q	$q\omega_{cal}$/cm^{-1}	band assignment
1	712.34	1119.78	105.46	3.88×10^{20}	115.19	0.9995	386	268	2	537	ν_4 (PO_4^{3-})
									3	805	γ (OH)
									4	1074	ν_{as} (PO_2)
									6	1611	ν_2 (H_2O)
									9	2416	B band ($H_2PO_4^-$)
									11	2953	A band ($H_2PO_4^-$)
									12	3222	ν_1 (H_2O)
									13	2490	ν_3 (H_2O)
2	931.60	1883.50	188.69	1.13×10^{20}	192.54	0.9971	504	350	2	701	ν (P−O_h)
									3	1051	ν_s (PO_2)
									5	1753	C band ($H_2PO_4^-$)
									7	2454	B band ($H_2PO_4^-$)
									9	3155	A band ($H_2PO_4^-$)

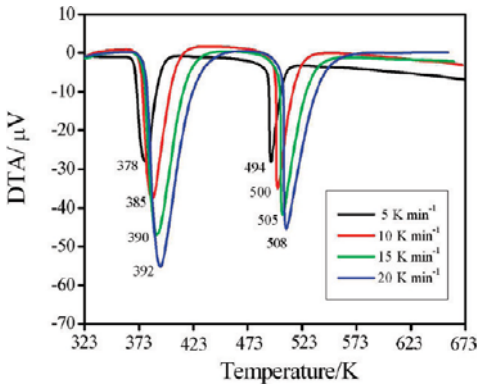

Figure 6. DTA curves of the synthesized $Mn_{1/2}Fe_{1/2}(H_2PO_4)_2 \cdot 2H_2O$ at four different heating rates (5, 10, 15, and 20 K min^{-1}).

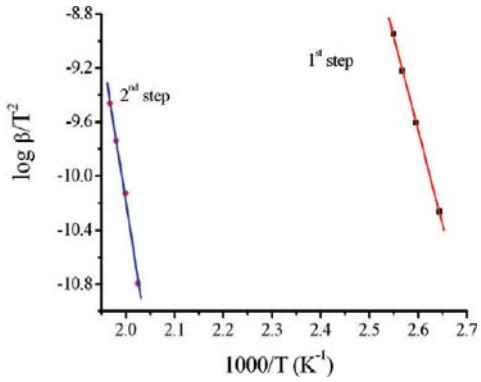

Figure 7. Kissinger plots indicating the activation energies involving two transformation steps from the synthesized $Mn_{1/2}Fe_{1/2}(H_2PO_4)_2 \cdot 2H_2O$ to $MnFeP_4O_{12}$.

with the theory that superparamagnetic behavior is often observed at room temperature.[43−45] The specific magnetization curves are typical superparamagnetic behavior without any hysteresis in the field range of ±10 000 Oe. From the magnetization curves, specific saturated magnetization (M_s) values of the $Mn_{1/2}Fe_{1/2}(H_2PO_4)_2 \cdot 2H_2O$ and $MnFeP_4O_{12}$ are 15.097 and 17.459 emu/g, respectively. The superparamagnetic solid solutions formed in $Mn_{1/2}Fe_{1/2}(H_2PO_4)_2 \cdot 2H_2O$ and $MnFeP_4O_{12}$ system in this work are different from ferromagnetic for $Fe(H_2PO_4)_2 \cdot 2H_2O$ (96.28 emu/g) and FeP_4O_{12} (85.01 emu/g),[41] and $Mn_{1/2}Fe_{1/2}(H_2PO_4)_2 \cdot xH_2O$ (25.63 emu/g) and $MnFeP_4O_{12}$ (13.14 emu/g),[18] and diamagnetic for $Mn(H_2PO_4)_2 \cdot 2H_2O$ and MnP_4O_{12}.[40] It found that the tendency of M_s to increase is consistent with the enhancement of crystallinity or particle sizes, and the saturation values of M_s for $Mn_{1/2}Fe_{1/2}(H_2PO_4)_2 \cdot 2H_2O$ and $MnFeP_4O_{12}$ are observed due to the obtained microstructure. These results indicate that the medium reagents for precipitation have the strong effect on the magnetic behaviors of $Mn_{1/2}Fe_{1/2}(H_2PO_4)_2 \cdot 2H_2O$ and $MnFeP_4O_{12}$. Superparamagnetic properties of the $Mn_{1/2}Fe_{1/2}(H_2PO_4)_2 \cdot 2H_2O$ and $MnFeP_4O_{12}$ samples reported for the first time are important for specific applications because the magnetic materials may be synthesized to have the multifunctions that can be applied in magnetic resonance imaging contrast agents, data lifetime in high density information storage, ferrofluid technology, lithium batteries, magnetocaloric refrigeration catalytic, and/or adsorption processes.[45]

3.2. Kinetic and Thermodynamic Results. The nonisothermal DTA method is desirable to analyze the reaction mechanism and calculate the activation energy of the solid state.[26−32] Several nonisothermal techniques have been proposed, which are quicker and less sensitive to previous and next transformations. The basic data of T were collected from the DTA curves of the decomposition of $Mn_{1/2}Fe_{1/2}(H_2PO_4)_2 \cdot 2H_2O$ at various heating rates (5, 10, 15, and 20 K min^{-1}) (Figure 6). Figure 7 shows the Kissinger plots of two transformation steps of the prepared $Mn_{1/2}Fe_{1/2}(H_2PO_4)_2 \cdot 2H_2O$. From the slopes of the curves (Figure 7), the activation energy values in two decomposition steps of the synthesized $Mn_{1/2}Fe_{1/2}(H_2PO_4)_2 \cdot 2H_2O$ were determined as 115.19 and 192.54 kJ mol^{-1}, respectively. The activation energies of two decompositions of $Mn_{1/2}Fe_{1/2}(H_2PO_4)_2 \cdot 2H_2O$ are different from those of $Mn(H_2PO_4)_2 \cdot 2H_2O$ (105−104 kJ/mol for the first step and 199−200 kJ/mol for the second step) and $Fe(H_2PO_4)_2 \cdot 2H_2O$ (136−137 kJ/mol for the first step). These activation energies are related to the vibrational frequencies and are the indication of the energy of the breaking bond of intermediate species. The reason may be relevant to the strengths of binding of water molecules in the crystal lattice. Hence, different dehydration temperatures and kinetic parameters are expected. The two mass loss steps

Table 3. Comparing Physical and Chemical Properties of the Studied Materials in the Present Work and in the Literature

ref no.	materials	different synthesis route
this work	$Mn_{1/2}Fe_{1/2}(H_2PO_4)_2 \cdot 2H_2O$ and $MnFeP_4O_{12}$	prepared by Mn(c)−Fe(c)−H_3PO_4 system in water−acetone medium at ambient temperature for 30 min, and its final decomposed product was obtained at 773 K
17	$Mn_{0.5}Co_{0.5}(H_2PO_4)_2 \cdot 2H_2O$ and $MnCoP_4O_{12}$	prepared by $MnCO_3$−$CoCO_3$−H_3PO_4 system at ambient temperature for 15 min, and its final decomposed product was obtained at 773 K
18	$Mn_{0.5}Fe_{0.5}(H_2PO_4)_2 \cdot 2H_2O$ and $MnFeP_4O_{12}$	prepared by Mn(c)−Fe(c)−H_3PO_4 system at ambient temperature for 30 min, and its final decomposed product was obtained at 773 K
19	$Co_{1/2}Fe_{1/2}(H_2PO_4)_2 \cdot 2H_2O$ and $CoFeP_4O_{12}$	prepared by Fe(c)−$CoCO_3$−H_3PO_4 system at ambient temperature for 15 min, and its final decomposed product was obtained at 773 K
20	$Mn_{0.5}Cu_{0.5}(H_2PO_4)_2 \cdot 1.5H_2O$ and $MnCuP_4O_{12}$	prepared by Mn(c)−CuO−H_3PO_4 system at ambient temperature for 15 min, and its final decomposed product was obtained at 673 K
21	$Mn_{0.5}Ca_{0.5}(H_2PO_4)_2 \cdot H_2O$ and $MnCaP_4O_{12}$	prepared by Mn(c)−$CaCO_3$−H_3PO_4 system at ambient temperature for 30 min, and its final decomposed product was obtained at 673 K
22	$Mn(H_2PO_4)_2 \cdot 2H_2O$ and $Mn_2P_4O_{12}$	prepared by Mn(c)−H_3PO_4 system in water−acetone medium at ambient temperature for 15 min, and its final decomposed product was obtained at 773 K
40	$Mn(H_2PO_4)_2 \cdot 2H_2O$ and $Mn_2P_4O_{12}$	prepared by Mn(c)−H_3PO_4 and $MnCO_3$−H_3PO_4 systems at ambient temperature for 15 min, and its final decomposed product was obtained at 673 K
41	$Fe(H_2PO_4)_2 \cdot 2H_2O$ and $Fe_2P_4O_{12}$	prepared by Fe(c)−H_3PO_4 system at 313 K for 30 min, and its final decomposed product was obtained at 773 K

ref no.	materials	different thermal behavior
this work	$Mn_{1/2}Fe_{1/2}(H_2PO_4)_2 \cdot 2H_2O$ and $MnFeP_4O_{12}$	well-defined two thermal transformation steps in the range of 353−873 K
17	$Mn_{0.5}Co_{0.5}(H_2PO_4)_2 \cdot 2H_2O$ and $MnCoP_4O_{12}$	four thermal transformation steps in the range of 273−873 K
18	$Mn_{0.5}Fe_{0.5}(H_2PO_4)_2 \cdot 2H_2O$ and $MnFeP_4O_{12}$	three thermal transformation steps in the range of 273−773 K
19	$Co_{1/2}Fe_{1/2}(H_2PO_4)_2 \cdot 2H_2O$ and $CoFeP_4O_{12}$	three thermal transformation steps in the range of 273−873 K
20	$Mn_{0.5}Cu_{0.5}(H2PO_4)_2 \cdot 1.5H_2O$ and $MnCuP_4O_{12}$	well-defined two thermal transformation steps in the range of 353−673 K
21	$Mn_{0.5}Ca_{0.5}(H_2PO_4)_2 \cdot H_2O$ and $MnCaP_4O_{12}$	six thermal transformation steps in the range of 353−873 K
22	$Mn(H_2PO_4)_2 \cdot 2H_2O$ and $Mn_2P_4O_{12}$	well-defined two thermal transformation steps in the range of 353−1073 K
40	$Mn(H_2PO_4)_2 \cdot 2H_2O$ and $Mn_2P_4O_{12}$	more than three thermal transformation steps in the range of 353−773 K
41	$Fe(H_2PO_4)_2 \cdot 2H_2O$ and $Fe_2P_4O_{12}$	three thermal transformation steps in the range of 353−773 K

ref no.	materials	different morphologies
this work	$Mn_{1/2}Fe_{1/2}(H_2PO_4)_2 \cdot 2H_2O$ and $MnFeP_4O_{12}$	high agglomerates of nonuniform particles for both samples
17	$Mn_{0.5}Co_{0.5}(H_2PO_4)_2 \cdot 2H_2O$ and $MnCoP_4O_{12}$	rod-like shape and nonuniform particles
18	$Mn_{0.5}Fe_{0.5}(H_2PO_4)_2 \cdot 2H_2O$ and $MnFeP_4O_{12}$	rod-like tetrahedral shape and small spherical particles with high agglomerates
19	$Co_{1/2}Fe_{1/2}(H_2PO_4)_2 \cdot 2H_2O$ and $CoFeP_4O_{12}$	flower like shape for both samples
20	$Mn_{0.5}Cu_{0.5}(H_2PO_4)_2 \cdot 1.5H_2O$ and $MnCuP_4O_{12}$	many small and some large rod like and spherical shapes
21	$Mn_{0.5}Ca_{0.5}(H_2PO_4)_2 \cdot H_2O$ and $MnCaP_4O_{12}$	roughness of many small and some large boundary surfaces and small and large spherical shapes
22	$Mn(H_2PO_4)_2 \cdot 2H_2O$ and $Mn_2P_4O_{12}$	small rod like shape and retexturing and coalescence in aggregates of irregularly shape
40	$Mn(H_2PO_4)_2 \cdot 2H_2O$ and $Mn_2P_4O_{12}$	large nonuniform polyhedral shape and retexturing and coalescence in aggregates of irregularly shape
41	$Fe(H_2PO_4)_2 \cdot 2H_2O$ and $Fe_2P_4O_{12}$	coalescence in aggregates of irregularly shapes for both samples

ref no.	materials	different magnetic properties
this work	$Mn_{1/2}Fe_{1/2}(H_2PO_4)_2 \cdot 2H_2O$ and $MnFeP_4O_{12}$	superparamagnetic properties (M_s = 15.097 emu/g for $Mn_{1/2}Fe_{1/2}(H_2PO_4)_2 \cdot 2H_2O$ and M_s = 17.459 emu/g for $MnFeP_4O_{12}$
17	$Mn_{0.5}Co_{0.5}(H_2PO_4)_2 \cdot 2H_2O$ and $MnCoP_4O_{12}$	not reported
18	$Mn_{0.5}Fe_{0.5}(H_2PO_4)_2 \cdot xH_2O$ and $MnFeP_4O_{12}$	ferromagnetic properties (M_s = 25.63 emu/g for $Mn_{0.5}Fe_{0.5}(H_2PO_4)_2 \cdot xH_2O$ and M_s = 13.14 emu/g for $MnFeP_4O_{12}$)
19	$Co_{1/2}Fe_{1/2}(H_2PO_4)_2 \cdot 2H_2O$ and $CoFeP_4O_{12}$	superparamagnetic properties (M_s = 0.045 emu/g for $Co_{1/2}Fe_{1/2}(H_2PO_4)_2 \cdot 2H_2O$ and M_s = 12.502 emu/g for $CoFeP_4O_{12}$)
20	$Mn_{0.5}Cu_{0.5}(H_2PO_4)_2 \cdot 1.5H_2O$ and $MnCuP_4O_{12}$	not reported
21	$Mn_{0.5}Ca_{0.5}(H_2PO_4)_2 \cdot H_2O$ and $MnCaP_4O_{12}$	not reported
22	$Mn(H_2PO_4)_2 \cdot 2H_2O$ and $Mn_2P_4O_{12}$	not reported

Table 3. Continued

ref no.	materials	different magnetic properties
40	$Mn(H_2PO_4)_2 \cdot 2H_2O$ and $Mn_2P_4O_{12}$	not reported
41	$Fe(H_2PO_4)_2 \cdot 2H_2O$ and $Fe2P_4O_{12}$	ferromagnetic properties (M_s = 96.28 emu/g for $Fe(H_2PO_4)_2 \cdot xH_2O$ and M_s = 37.78 emu/g for $Fe_2P_4O_{12}$)
ref no.	**materials**	**different nonisothermal decomposition kinetic data (E_a, A, n)**
this work	$Mn_{1/2}Fe_{1/2}(H_2PO_4)_2 \cdot 2H_2O$ and $MnFeP_4O_{12}$	115.19 kJ mol^{-1}, 3.88 × 10^{15} s^{-1}, 2.56 for first step and 192.54 kJ mol^{-1}, 1.13 × 10^{20} s^{-1}, 2.06 for second step
17	$Mn_{0.5}Co_{0.5}(H_2PO_4)_2 \cdot 2H_2O$ and $MnCoP_4O_{12}$	E_a values for four steps as 100.55, 88.90, 90.58, 308.58 kJ mol^{-1}, respectively
18	$Mn_{0.5}Fe_{0.5}(H_2PO_4)_2 \cdot 2H_2O$ and $MnFeP_4O_{12}$	not reported
19	$Co_{1/2}Fe_{1/2}(H_2PO_4)_2 \cdot 2H_2O$ and $CoFeP_4O_{12}$	not reported
20	$Mn_{0.5}Cu_{0.5}(H_2PO_4)_2 \cdot 1.5H_2O$ and $MnCuP_4O_{12}$	E_a and n values for two steps as 99.75, 202.84 kJ mol^{-1} and 1.34, 1.93, respectively
21	$Mn_{0.5}Ca_{0.5}(H_2PO_4)_2 \cdot H_2O$ and $MnCaP_4O_{12}$	E_a values for five steps as 147.85, 129.70, 89.41, 152.94, 236.97 kJ mol^{-1}, respectively, A values for five steps as 1.41 × 10^{20}, 6.55 × 10^{16}, 4.48 × 10^{9}, 4.04 × 10^{15}, 1.01 × 10^{20}, respectively
22	$Mn(H_2PO_4)_2 \cdot 2H_2O$ and $Mn_2P_4O_{12}$	E_a values for two steps as 86.45, 187.92 kJ mol^{-1}, respectively
40	$Mn(H_2PO_4)_2 \cdot 2H_2O$ and $Mn_2P_4O_{12}$	not reported
41	$Fe(H_2PO_4)_2 \cdot 2H_2O$ and $Fe_2P_4O_{12}$	E_a value as 136.85 kJ mol^{-1}
ref no.	**materials**	**different thermodynamic data (ΔH^*, kJ mol^{-1}; ΔG^*, kJ mol^{-1}; and ΔS^*, J mol^{-1} K^{-1})**
this work	$Mn_{1/2}Fe_{1/2}(H_2PO_4)_2 \cdot 2H_2O$ and $MnFeP_4O_{12}$	1119.78, 712, 105.46 for first step and 1883.50, 931.60, 188.69 for second step
17	$Mn_{0.5}Co_{0.5}(H_2PO_4)_2 \cdot 2H_2O$ and $MnCoP_4O_{12}$	not reported
18	$Mn_{0.5}Fe_{0.5}(H_2PO_4)_2 \cdot 2H_2O$ and $MnFeP_4O_{12}$	not reported
19	$Co_{1/2}Fe_{1/2}(H_2PO_4)_2 \cdot 2H_2O$ and $CoFeP_4O_{12}$	not reported
20	$Mn_{0.5}Cu_{0.5}(H_2PO_4)_2 \cdot 1.5H_2O$ and $MnCuP_4O_{12}$	not reported
21	$Mn_{0.5}Ca_{0.5}(H_2PO_4)_2 \cdot H_2O$ and $MnCaP_4O_{12}$	144.65, 94.38, 130.34 for first step, 126.35, 99.64, 66.18 for second step, 85.50, 119.53−72.26 for third step, 148.71, 127.80, 41.10 for fourth step, and 231.85, 155.59, 123.73 for sixth
22	$Mn(H_2PO_4)_2 \cdot 2H_2O$ and $Mn2P_4O_{12}$	not reported
40	$Mn(H_2PO_4)_2 \cdot 2H_2O$ and $Mn_2P_4O_{12}$	not reported
41	$Fe(H_2PO_4)_2 \cdot 2H_2O$ and $Fe_2P_4O_{12}$	not reported

correspond to the loss of water of coordinated water in the first steps, subsequently to a continuous intermolecular polycondensation and the elimination of water of constituent in anion in the second step.[26−28] The second step exhibits higher activation energy in comparison with the first step, and this is understandable because this step relates to true P−OH bond breaking, in connection with the polycondensation reaction.[1,2,18,40,41] These activation energies are consistent with the former hypothesis that the intermediate nucleates and crystallizes as metastable phase with adequate growth kinetics before the stable phase $MnFeP_4O_{12}$. This result is consistent with TG-DTG-DTA data as shown in eqs 9 and 10.

The pre-exponential factor (A) can be estimated from the intercept of the plots of eq 2 (Table 2). All calculations were performed using a program compiled by ourselves. The pre-exponential factor (A) values in the Arrhenius equation for solid-phase reactions are expected to be in a wide range (6 or 7 orders of magnitude), even after the effect of surface area is taken into account.[26−29] The low factors will often indicate a surface reaction, but if the reactions are not dependent on surface area, the low factor may indicate a "tight" complex. The high factors will usually indicate a "loose" complex. Even higher factors (after correction for surface area) can be obtained for complexes having free translation on the surface. Because in many cases the concentrations in solids are not controllable, it would have been convenient if the magnitude of the pre-exponential factor could provide the information for the reaction molecularity. With such bulk decomposition, any molecule is as likely to react with any others, and no preference is shown toward corners, edges, surface, defects, or sites of previous decomposition. On the basis of these reasons, the thermal decomposition reaction of $Mn_{1/2}Fe_{1/2}(H_2PO_4)_2 \cdot 2H_2O$ may be interpreted as "loose complexes" for the first and second steps, which correspond to the proposed mechanism in eqs 9 and 10.

The value of the Avrami exponent provides information regarding the morphology of the growing crystal.[17,20−22,32,34] The value of n reflects the mechanism dominating crystallization. Here, smaller n values indicate that the crystallization is dominated by a surface crystallization or that the crystallization dimension is low. On the other hand, larger n values are expected only in case of increasing nucleation rates. For $Mn_{1/2}Fe_{1/2}(H_2PO_4)_2 \cdot 2H_2O$, the n values are 2.56 for the first and 2.06 for the second decomposition steps, which are random nucleation and growth of nuclei for both decomposition steps.

As can be seen from Table 2, the entropy of activation (ΔS^*) values for all steps are positive values. It means that the corresponding activated complexes had lower degrees of arrangement than the initial state. Because the decomposition of $Mn_{1/2}Fe_{1/2}(H_2PO_4)_2 \cdot 2H_2O$ proceeds as two consecutive reactions, the formation of the second activated complex passed in situ. In terms of the activated complex theory (transition theory),[35−37] a positive value of ΔS^* indicates a malleable activated complex that leads to a large number of degrees of freedom of rotation and vibration. A result may be interpreted as a "fast" stage. On the other hand, a negative value of ΔS^* indicates a highly ordered

activated complex, and the degrees of freedom of rotation as well as of vibration are less than they are in the nonactivated complex. These results may indicate a "slow" stage.[26−30] With respect to these results, the first and second decomposed steps of $Mn_{1/2}Fe_{1/2}(H_2PO_4)_2 \cdot 2H_2O$ may be interpreted as "fast" stages. The positive values of the enthalpy ΔH^* are in good agreement with two endothermic effects in the DTA results. The positive values of ΔH^* and ΔG^* for two stages show that they are connected with the introduction of heat and are nonspontaneous processes. The results of the kinetic and thermodynamic parameters of the second steps are higher than those of the first step, which correspond to that the second step needs a higher energy pathway and a lower rate reaction than the first step.

To corroborate the calculated data with the spectroscopic ones, we drew up the FT-IR spectra of the studied compound (Figure 2). Table 2 shows the comparison of the ω_{calc} values with the ω_{sp} values determined from this compound, together with the assignments of the corresponding vibrational modes in the literature.[1,2] These wavenumbers are close to the vibrational modes of water of crystallization and dihydrogen phosphate group ($H_2PO_4^-$) reported in the literature.[20−22] The results confirm that the loss of the water of crystallization and deprotonated dihydrogen phosphate group in the first step is followed by a continuous intermolecular polycondensation for the second step.[20−22] The studied compound exhibited a very good agreement between the calculated wavenumbers from average T_p (DTA) and the observed wavenumbers from IR spectra for the bonds that were suggested to be broken.

4. CONCLUSION

The superparamagntic $Mn_{1/2}Fe_{1/2}(H_2PO_4)_2 \cdot 2H_2O$ was prepared by a soft solution solid-state reaction from the Mn(c)−Fe(c)−H_3PO_4 system in water−acetone medium at ambient temperature with short time consumption (30 min). $Mn_{1/2}Fe_{1/2}(H_2PO_4)_2 \cdot 2H_2O$ decomposes in two steps, which correspond to the loss of water of crystallization in the first step, subsequently to a continuous intermolecular polycondensation and elimination of water of constituent in anion (the second step). Thermal kinetic study results indicate the activation energies, which relate to the vibrational frequencies of the breaking bond of thermal transformation of $Mn_{1/2}Fe_{1/2}(H_2PO_4)_2 \cdot 2H_2O$. The thermal behaviors, morphologies, particle sizes, superparamagnetic properties, kinetic and thermodynamic data of $Mn_{1/2}Fe_{1/2}(H_2PO_4)_2 \cdot 2H_2O$, and its thermal transformation product ($MnFeP_4O_{12}$) in this work are different from those of single metal and binary metal compounds in our previous reports (Table 3). The study results obtained are necessary for elaboration of technology to produce the dihydrogenphosphate and cyclotetraphosphate of transition metals, which may be useful for potential applications as catalytic, ceramic, and biomedical materials, etc.

AUTHOR INFORMATION

Corresponding Author

*Tel.: +66-7750-6422 ext 4565. Fax: +66-7750-6411. E-mail: kbbanjon@gmail.com, kbbanjon@kmitl.ac.th.

ACKNOWLEDGMENT

This work is financially supported by the Thailand Research Fund (TRF) and the Commission on Higher Education (CHE): Research Grant for New Scholar and King Mongkut's Institute of Technology Ladkrabang Research (KMITL Research), Ministry of Education, Thailand.

REFERENCES

(1) Koleva, V.; Mehandjiev, D. Characterization of $M(H_2PO_4)_2 \cdot 2H_2O$ (M = Mn, Co, Ni) and their in situ thermal decomposition by magnetic measurements. *Mater. Res. Bull.* **2006**, *41*, 469.

(2) Koleva, V.; Effenberger, H. Crystal chemistry of $M[PO_2(OH)_2]_2 \cdot 2H_2O$ compounds (M = Mg, Mn, Fe, Co, Ni, Zn, Cd): Structural investigation of the Ni, Zn and Cd salts. *J. Solid State Chem.* **2007**, *180*, 966 and references therein.

(3) Antraptseva, N. M.; Shchegrov, L. N.; Ponomareva, I. G. Thermolysis features of manganese(II) and zinc dihydrogenphosphate solid solution. *Russ. J. Inorg. Chem.* **2006**, *51*, 1493.

(4) Trojan, M.; Brandová, D.; Paulik, F.; Arnold, M. Mechanism of the thermal dehydration of $Co_{1/2}Ca_{1/2}(H_2PO_4)_2 \cdot 2H_2O$. *J. Therm. Anal. Calorim.* **1990**, *36*, 929.

(5) Trojan, M.; Brandová, D. Mechanism of dehydration of $Zn_{0.5}Mg_{0.5}(H_2PO_4)_2 \cdot 2H_2O$. *Thermochim. Acta* **1990**, *159*, 1.

(6) Trojan, M.; Brandová, D. Study of thermal dehydration of $Mn_{0.5}Mg_{0.5}(H_2PO_4)_2 \cdot 4H_2O$. *Thermochim. Acta* **1990**, *161*, 11.

(7) Brandová, D.; Trojan, M.; Arnold, M.; Paulik, F. Thermal study of decomposition of $Cu_{1/2}Mg_{1/2}(H_2PO_4)_2 \cdot 0.5H_2O$. *J. Therm. Anal. Calorim.* **1990**, *36*, 677.

(8) Brandová, D.; Trojan, M.; Paulik, F.; Paulik, J.; Arnold, M. Study of the thermal dehydration of $Mn_{1/2}Ca_{1/2}(H_2PO_4)_2 \cdot 2H_2O$. *J. Therm. Anal. Calorim.* **1990**, *36*, 881.

(9) Viter, V. N.; Nagornyi, P. G. Synthesis of continuous substitutional solid solutions $M_{1-x}Ni_x(H_2PO_4)_2 \cdot 2H_2O$ with M = Mg, Mn, Co, or Zn. *Russ. J. Inorg. Chem.* **2007**, *52*, 14.

(10) Trojan, M. Double tetrametaphosphates $Mn_{2-x}Ca_xP_4O_{12}$ as special pigments. *Dyes Pigm.* **1990**, *12*, 35.

(11) Trojan, M. Binary cyclotetraphosphates $Zn_{2-x}Ca_xP_4O_{12}$ as new special pigments. *Dyes Pigm.* **1990**, *13*, 1.

(12) Trojan, M.; Šulcová, P.; Mošner, P. The synthesis of binary zinc(II)-nickel(II)cyclo-tetraphosphates as new special pigments. *Dyes Pigm.* **2000**, *44*, 161.

(13) Trojan, M.; Brandová, D. A study of the thermal preparation of c-$Cd_{4/3}Ca_{2/3}P_4O_{12}$. *Thermochim. Acta* **1990**, *160*, 349.

(14) Trojan, M.; Šulcová, P. Binary Cu(II)-Mn(II) cyclo-tetraphosphates. *Dyes Pigm.* **2000**, *47*, 291.

(15) Trojan, M.; Šulcová, P. The binary Cd(II)-Zn(II) cyclo-tetraphosphates. *Thermochim. Acta* **2000**, *343*, 135.

(16) Trojan, M.; Šulcová, P.; Skorová, L. Thermal analysis of Ba(II)-Sr(II) cyclo-tetraphosphates(V). *J. Therm. Anal. Calorim.* **2002**, *68*, 75.

(17) Boonchom, B.; Youngme, S.; Danvirutai, C. A rapid co-precipitation and non- isothermal decomposition kinetics of new binary $Mn_{0.5}Co_{0.5}(H_2PO_4)_2 \cdot 2H_2O$. *Solid State Sci.* **2008**, *10*, 129.

(18) Boonchom, B.; Maensiri, S.; Youngme, S.; Danvirutai, C. A simple synthesis and room temperature magnetic properties of new binary $Mn_{0.5}Fe_{0.5}(H_2PO_4)_2 \cdot 2H_2O$ obtained from a rapid co-precipitation at ambient temperature. *Solid State Sci.* **2009**, *11*, 485.

(19) Boonchom, B.; Thongkam, M.; Kongtaweelert, S.; Vittayakorn, N. Flower-like microparticles and novel superparamagnetic properties of new binary $Co_{1/2}Fe_{1/2}(H_2PO_4)_2 \cdot 2H_2O$ obtained by a rapid solid state route at ambient temperature. *Mater. Res. Bull.* **2009**, *44*, 2206.

(20) Boonchom, B.; Danvirutai, C. Rapid coprecipitation and non-isotheraml decomposition kinetics of new binary $Mn_{0.5}Cu_{0.5}(H_2PO_4)_2 \cdot 1.5H_2O$. *Ind. Eng. Chem. Res.* **2008**, *47*, 2941.

(21) Boonchom, B.; Danvirutai, C. Rapid synthesis, kinetics and thermodynamics of binary $Mn_{0.5}Ca_{0.5}(H_2PO_4)_2 \cdot H_2O$. *J. Therm. Anal. Calorim.* **2009**, *98*, 717.

(22) Boonchom, B.; Danvirutai, C.; Maensiri, S. Soft solution synthesis, non-isothermal decomposition kinetics and characterization of manganese dihydrogen phosphate dihydrate $Mn(H_2PO_4)_2 \cdot 2H_2O$ and its thermal transformation products. *Mater. Chem. Phys.* **2008**, *109*, 404.

(23) Boonchom, B. Parallelogram-like microparticles of calcium dihydrogen phosphate monohydrate ($Ca(H_2PO_4)_2 \cdot H_2O$) obtained by a rapid precipitation route in aqueous and acetone media. *J. Alloys Compd.* **2009**, *482*, 199.

(24) Boonchom, B.; Baitahe, R.; Kongtaweelert, S.; Vittayakorn, N. Kinetics and thermodynamics of zinc phosphate hydrate synthesized by a simple route in aqueous and acetone media. *Ind. Eng. Chem. Res.* **2010**, *49*, 3571.

(25) Cullity, B. D. *Elements of X-ray Diffraction*, 2nd ed.; Addison-Wesley Publishing: Reading, MA, 1977.

(26) Vlaev, L.; Nedelchev, N.; Gyurova, K.; Zagorcheva, M. A comparative study of non-isothermal kinetics of decomposition of calcium oxalate monohydrate. *J. Anal. Appl. Pyrolysis* **2008**, *81*, 253.

(27) Vlase, T.; Vlase, G.; Birta, N.; Doca, N. Comparative results of kinetic data obtained with different methods for complex decomposition steps. *J. Therm. Anal. Calorim.* **2007**, *88*, 631.

(28) Vlase, G.; Vlase, T.; Tudose, R.; Costişor, O.; Doca, N. Kinetic of decomposition of some complexes under non-isothermal conditions. *J. Therm. Anal. Calorim.* **2007**, *88*, 637.

(29) Vlaev, L. T.; Georgieva, V. G.; Genieva, S. D. Products and kinetics of non- isothermal decomposition of vanadium(IV) oxide compounds. *J. Therm. Anal. Calorim.* **2007**, *88*, 805.

(30) Vlaev, L. T.; Georgieva, V. G.; Gospodinov, G. G. Kinetics of isothermal decomposition of $ZnSeO_3$ and $CdSeO_3$. *J. Therm. Anal. Calorim.* **2005**, *79*, 163.

(31) Vlaev, L. T.; Tavlieva, M. P. Structural and thermal studies on the solid products in the system $MnSeO_3$-SeO_2-H_2O. *J. Therm. Anal. Calorim.* **2007**, *90*, 385.

(32) Chunxiu, G.; Yufang, S.; Donghua, C. Comparative method to evaluate reliable kinetic triplets of thermal decomposition reactions. *J. Therm. Anal. Calorim.* **2004**, *76*, 203.

(33) Kissinger, H. E. Reaction kinetics in differential thermal analysis. *J. Anal. Chem.* **1957**, *29*, 1702.

(34) Okada, K.; Kaneda, J.-I.; Kameshima, Y.; Yasumori, A.; Takei, T. Crystallization kinetics of mullite from polymeric Al_2O_3-SiO_2 xerogels. *Mater. Lett.* **2003**, *57*, 3155 and references therein.

(35) Head, C.; Smith, A. C. K. *Applied Physical Chemistry*; McMilan Press: London, 1982; p 473.

(36) Ŝesták, J. J. *Thermodynamical Properties of Solids*; Academia: Prague, 1984.

(37) Young, D. *Decomposition of Solids*; Pergamon Press: Oxford, 1966.

(38) Herzberg, G. *Molekülspektren und Molekülstruktur. I. Zweiatomige Moleküle*; Steinkopff: Dresden, 1939.

(39) Colthup, N. B.; Daly, L. H.; Wiberley, S. E. *Introduction to Infrared and Raman Spectroscopy*; Academic Press: New York, 1964.

(40) Danvirutai, C.; Boonchom, B.; Youngme, S. Nanocrystalline manganese dihydrogen phosphate dihydrate $Mn(H_2PO_4)_2 \cdot 2H_2O$ and its decomposition product ($Mn_2P_4O_{12}$) obtained by simple precipitation route. *J. Alloys Compd.* **2008**, *457*, 75.

(41) Boonchom, B.; Danvirutai, C.; Youngme, S.; Maensiri, S. Simple synthesis, magnetic properties, and nonisothermal decomposition kinetics of $Fe(H_2PO_4)_2 \cdot 2H_2O$. *Ind. Eng. Chem. Res.* **2008**, *47*, 7642.

(42) Ramakrishnan, V.; Aruldhas, G.; Bigotto, A. Vibrational spectra of Cu(II) and Co(II) tetrametaphosphates. *Infrared Phys.* **1985**, *25*, 665.

(43) Hui-li, M.; Xian-rong, Q.; Maitani, Y.; Nagai, T. Preparation and characterization of superparamagnetic iron oxide nanoparticles stabilized by alginate. *Int. J. Pharm.* **2007**, *333*, 177.

(44) Gupta, A. K.; Gupta, M. Synthesis and surface engineering of iron oxide nanoparticles for biomedical applications. *Biomaterials* **2005**, *26*, 3995.

(45) Chen, Y. H.; Franzreb, M.; Lin, R. H.; Chen, L. L.; Chang, C. Y.; Yu, Y. H.; Chiang, P. C. Platinum-doped TiO_2/magnetic poly(methyl methacrylate) microspheres as a novel photocatalyst. *Ind. Eng. Chem. Res.* **2009**, *48*, 7616–7623.

Solid State Sciences 13 (2011) 77–81

Contents lists available at ScienceDirect

Solid State Sciences

journal homepage: www.elsevier.com/locate/ssscie

A simple synthesis and characterization of binary $Co_{0.5}Fe_{0.5}(H_2PO_4)_2 \cdot 2H_2O$ and its final decomposition product $CoFeP_4O_{12}$

Banjong Boonchom [a,b,*], Chanaiporn Danvirutai [c], Naratip Vittayakorn [b,d,e]

[a] King Mongkut's Institute of Technology Ladkrabang, Chumphon Campus, 17/1 M.6 Pha Thiew District, Chumphon 86160, Thailand
[b] Advanced Materials Science Research Unit, Department of Chemistry, Faculty of Science, King Mongkut's Institute of Technology Ladkrabang, Bangkok 10520, Thailand
[c] Department of Chemistry, Faculty of Science, Khon Kaen University, Khon Kaen 40002, Thailand
[d] Department of Chemistry, Faculty of Science, King Mongkut's Institute of Technology Ladkrabang, Ladkrabang, Bangkok 10520, Thailand
[e] College of KMITL Nanotechnology, King Mongkut's Institute of Technology Ladkrabang, Bangkok 10520, Thailand

ARTICLE INFO

Article history:
Received 25 July 2009
Received in revised form
5 July 2010
Accepted 21 October 2010
Available online 29 October 2010

Keywords:
$Co_{0.5}Fe_{0.5}(H_2PO_4)_2 \cdot 2H_2O$
$CoFeP_4O_{12}$
Superparamagnetic behavior
Solid state method
Non-uniform particles

ABSTRACT

This paper reports the synthesis of binary $Co_{0.5}Fe_{0.5}(H_2PO_4)_2 \cdot 2H_2O$ by a simple, rapid and cost-effective method using $CoCO_3$–Fe(c)–H_3PO_4 system in water–acetone media at ambient temperature. Thermal transformation of the synthesized powder was investigated by TG/DTG/DTA and DSC techniques, which indicate that its final decomposed product was a binary cobalt iron cyclotetraphosphate $CoFeP_4O_{12}$. The FTIR and XRD results of the synthesized $Co_{0.5}Fe_{0.5}(H_2PO_4)_2 \cdot 2H_2O$ and the decomposed $CoFeP_4O_{12}$ indicate the pure monoclinic phases with space group $P2_1/n$ and C2/c, respectively. The morphologies of $Co_{0.5}Fe_{0.5}(H_2PO_4)_2 \cdot 2H_2O$ and $CoFeP_4O_{12}$ powders appear non-uniform particle shapes and high agglomerates, which are different from the cases of the single compounds $M(H_2PO_4)_2 \cdot 2H_2O$ and $M_2P_4O_{12}$ (where M = Co, Fe). The magnetic properties of the studied compounds are superparamagnetic behaviors, which are important for specific applications. The physical properties of the studied powders are comparable with those reported in our previous study, affected by medium and condition of preparation method.

1. Introduction

Binary metal phosphates with the general formula $M'_xM''_{1-x}(H_2PO_4)_2 \cdot nH_2O$ (M′or M″ = Mg, Ca, Ba, Mn, Co, Ni, Fe, Zn; $x = 0–1$; $n = 1–4$) have the incremented use in order to supply the demands of high modern technology [1–3]. This phosphate group is transformed to the corresponding binary metal(II) cyclo-tetraphosphate group $M'_yM''_{2-y}P_4O_{12}$ ($y = 0–2$) in the reactions of dehydration and deprotonation of dihydrogenphosphate groups at higher temperatures [4–6] Both $M'_xM''_{1-x}(H_2PO_4)_2 \cdot nH_2O$ and $M'_yM''_{2-y}P_4O_{12}$ compounds are isostructural with the single metal dihydrogenphosphate ($M'(H_2PO_4)_2 \cdot nH_2O$) and single metal(II) cyclo-tetraphosphate ($M'_2P_4O_{12}$) groups, respectively [8–10]. Consequently, they have similar X-ray diffraction patterns and close unit cell parameters, which crystallize in monoclinic space group $P2_1/n$ ($Z = 2$) for the dihydrogenphosphate group and C2/c ($Z = 4$) for cyclo-tetraphosphate group. Both binary metal phosphate groups can be used in a wide range of applications: catalysts and adsorbents, ion-exchange materials, solid electrolytes for batteries, in linear and non-linear optical components, chelating agents, tooth powder and doughs, artificial teeth and bones, corrosion-resistant coating, sewage purifying agents, glass-ceramics, refratories, fire extinguishers, cements, soap powder, biomaterials and implantates, forages for animals, superionic conductors, piezo- and ferroelectrics, gas and moisture sensors, magnets, phosphors, detergents and high-quality fertilizers [1,4,5,11,12] Therefore, the design, synthesis and characterization of the field of these phosphates have been very active during the twentieth century. However, the development of the chemistry of these phosphates was very slow, spreading along almost a century. So far, there were reports on the synthesis, the thermal analysis (TA) under quasi-isothermal and quasi-isobaric conditions of binary metal(II) dihydrogenphosphate hydrates $M'_xM''_{1-x}(H_2PO_4)_2 \cdot nH_2O$ (M′or M″ = Mg, Ca, Ba, Mn, Co, Ni, Fe, Zn; $x = 0–1$; $n = 1–4$) [1,4,5,8–12]. Recently, Viter and Nagornyi [13], Antraptseva et al. [4] and Koleva and Mehandjiev [12,14] reported the synthesis at low temperature (40–80 °C) with long time consumption (2–90 days) of $M_{1-x}Ni_x(H_2PO_4)_2 \cdot 2H_2O$ (M = Mg, Mn, Co, Zn), $Mn_{1-x}Zn_x(H_2PO_4)_2 \cdot 2H_2O$ and $M(H_2PO_4)_2 \cdot 2H_2O$ (M = Co, Ni, Mn, Fe), respectively. Most recently, our research group reported the rapid synthesis (10–20 min) of $M(H_2PO_4)_2 \cdot 2H_2O$ and $M_{1-x}A_x(H_2PO_4)_2 \cdot nH_2O$ (M and A = Ca, Mn, Fe, Cu, Co) at ambient

* Corresponding author. King Mongkut's Institute of Technology Ladkrabang, Chumphon Campus, 17/1 M.6 Pha Thiew District, Chumphon 86160, Thailand. Tel.: +66 7750 6422x4565; fax: +66 7750 6410.
E-mail address: kbbanjon@kmitl.ac.th (B. Boonchom).

1293-2558/$ – see front matter © 2010 Elsevier Masson SAS. All rights reserved.
doi:10.1016/j.solidstatesciences.2010.10.012

temperature [1,2,15,16]. However, it is obstacle to synthesize binary metal dihydrogenphosphates, binary metal cyclotetraphosphates and their solid solutions, which vary the composition of metal cations for obtaining homogeneity ranges and modified useful properties.

In this work, binary $Co_{0.5}Fe_{0.5}(H_2PO_4)_2 \cdot 2H_2O$ was prepared by solid state method at ambient temperature with short time consumption (<10 min), which is a simple and cost-effective route. Thermal transformation of $Co_{0.5}Fe_{0.5}(H_2PO_4)_2 \cdot 2H_2O$ was investigated by thermogravimetry/differential thermal gravimetry/differential thermal analysis (TG/DTG/DTA) and differential scanning calorimetry (DSC) techniques and its final decomposed product is $CoFeP_4O_{12}$. Furthermore, the synthesized $Co_{0.5}Fe_{0.5}(H_2PO_4)_2 \cdot 2H_2O$ and its decomposed product $CoFeP_4O_{12}$ were characterized by X-ray powder diffraction (XRD), Fourier transform infrared (FTIR), scanning electron microscope (SEM) and vibrating sample magnetometer (VSM) techniques.

2. Experimental

Phosphoric acid (H_3PO_4, Fluka, 86.4% w/w), cobalt carbonate ($CoCO_3$, Merck, AR grade), iron metal (Fe, Merck, AR; c; complexometric) and acetone ($CH_3CH_2OCH_3CH_2$, Merck, AR grade) were used as precursors for phosphorous, Co(II), Fe(II) and media agent, respectively. Typically process, 2.00 mL of distilled water was added to 8.00 mL H_3PO_4 and then H_3PO_4 solution was added to 2.40 g of $CoCO_3$ and 1.12 g of Fe(c) (a mole ratio corresponding to the nominal composition of Fe:Co ratio of 1.0:1.0) in the presence of 15 mL acetone. This resulting suspension was continuously stirred at ambient temperature for 10 min and the prepared solid was aged for drying at room temperature. The presence of acetone reduced strong exothermic reaction and prevented the evolved H_2(g) and CO_2(g) in the precipitation process and developed the highly crystalline product. This method is a simple, rapid, cost-effective and environmental friendly route for synthesis of $Co_{0.5}Fe_{0.5}(H_2PO_4)_2 \cdot 2H_2O$. The prepared solid was recovered by filtration (suction pump), washed with acetone, and dried in air.

Thermogravimetric analysis (TGA) and differential thermal analysis (DTA) was carried out in a flow of air (100 mL min^{-1}) with a heating rate of 10 °C min^{-1} over the temperature range from 30 to 800 °C using a TG–DTG–DTA Pyris Diamond Perkin Elmer Instruments. Its final decomposed product seemed to occur at temperatures above 600 °C, so the prepared solid was calcined at 700 °C for 3 h. Differential scanning calorimetry was carried out for a sample (5–10 mg) in an aluminum crucible, over the temperature range of 303–823 K using differential scanning calorimetry (DSC), Perkin Elmer Pyris One. The heating rate employed was 10 K min^{-1}. The cobalt and iron contents of the prepared solid and its final decomposed product were determined by dissolving in 0.0126 M hydrochloric acid using atomic absorption spectrophotometry (AAS, Perkin Elmer, Analyst100). The phosphorus content was determined by colorimetric analysis of the molybdophosphate complex. The structure and crystallite size of the synthesized sample and its decomposed product were studied by X-ray powder diffraction using an X-ray diffractometer (Phillips PW3040, The Netherlands) with Cu Kα radiation ($\lambda = 0.15406$ nm). The Scherrer method was used to evaluate the crystallite size [17]. The photographs of scanning electron microscope (SEM) were obtained by LEO SEM VP1450 after gold coating. The room temperature FTIR spectra were recorded in the range of 4000–370 cm^{-1} with 8 scans on a Perkin–Elmer Spectrum GX FT-IR/FT-Raman spectrometer with the resolution of 4 cm^{-1} using KBr pellets (KBr, spectroscopy grade, Merck). The magnetic properties of the prepared solid and its decomposed product were examined at room temperature (20 °C) using a vibrating sample magnetometer (VSM 7403, Lake Shore, USA).

3. Results and discussion

3.1. Chemical analysis

According to chemical analysis data, the P/(Co + Fe) = 2.13 and H_2O/P = 1.92 molar ratios in the synthesized phosphate differed very little from those calculated for binary metal dihydrogenphosphate with the general formula $Co_{1/2}Fe_{1/2}(H_2PO_4)_2 \cdot 2H_2O$. Similarly, the P/(Co + Fe) = 2.01 molar ratio in the decomposed product practically corresponds to the $CoFeP_4O_{12}$ stoichiometry, where Co(II) and Fe(II) stand for divalent cations.

3.2. Thermal analysis

Fig. 1 shows the TG/DTG/DTA curves of $Co_{0.5}Fe_{0.5}(H_2PO_4)_2 \cdot 2H_2O$. The TG trace shows three mass loss stages in the range of 30–600 °C. In the first stage between 45 and 140 °C, the mass loss of 11.62% corresponds to the elimination of 1.87 mol water (H_2O) of crystallization. The mass losses of 9.15% for the second stage (140–275 °C) and 5.85% for the third stage (275–600 °C) relate to the eliminations of 1.47 and 0.54 mol water of the deprotonated dihydrogenphosphate groups, respectively. Three endothermic effects in the DTA curve show over the temperature region at 119, 174 and 402 °C, which relate to three peaks in DTG curve at 114, 165, and 400 °C and closely correspond to the observed mass loss on the TG trace. Further, a small exothermic effect at 712 °C without appreciable mass loss is observed in the DTA curve, which can be ascribed to a transition phase form of $CoFeP_4O_{12}$. The thermal transformation of $Co_{0.5}Fe_{0.5}(H_2PO_4)_2 \cdot 2H_2O$ involves the dehydration of the coordination water molecule (2 mol H_2O) and an intramolecular dehydration of the protonated dihydogenphosphate groups (2 mol H_2O) as shown in Eqs. (1) and (3).

$$Co_{0.5}Fe_{0.5}(H_2PO_4)_2 \cdot 2H_2O \rightarrow Co_{0.5}Fe_{0.5}(H_2PO_4)_2 + \sim 2H_2O \quad (1)$$

$$Co_{0.5}Fe_{0.5}(H_2PO_4)_2 \rightarrow Co_{0.5}(H_2P_2O_7)_{0.5} \cdot Fe_{0.5}(H_2P_2O_7)_{0.5} + \sim H_2O \quad (2)$$

$$Co_{0.5}(H_2P_2O_7)_{0.5} \cdot Fe_{0.5}(H_2P_2O_7)_{0.5} \rightarrow 1/2CoFeP_4O_{12} + \sim H_2O \quad (3)$$

An unstable intermediate compounds, such as acid polyphosphate $Co_{0.5}Fe_{0.5}(H_2PO_4)_2$ and $Co_{0.5}(H_2P_2O_7)_{0.5} \cdot Fe_{0.5}(H_2P_2O_7)_{0.5}$ and mixtures of intermediate of both have been registered and

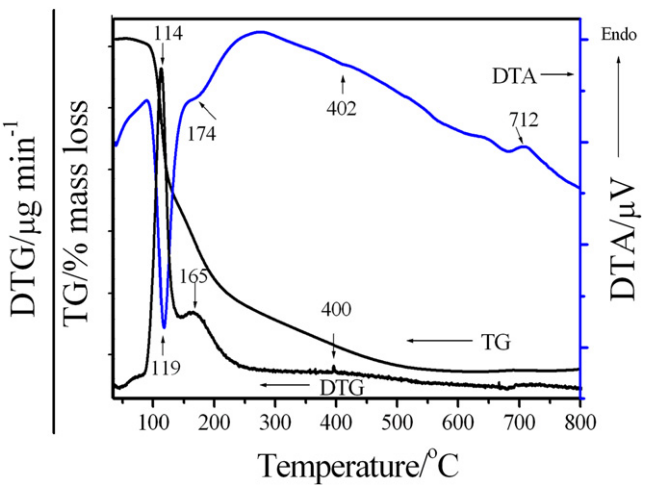

Fig. 1. TG/DTG/DTA curves of $Co_{0.5}Fe_{0.5}(H_2PO_4)_2 \cdot 2H_2O$ at the heating rate of 10 °C min^{-1} in air atmosphere.

were similarly observed with the single hydrogen phosphates and other binary metal dihydrogenphosphates [2–8]. The binary cobalt iron cyclotetraphosphate, $CoFeP_4O_{12}$ is found to be the final product of the thermal decomposition at $T > 600$ °C. The total mass loss is 26.62% (3.88 mol H_2O), which is in agreement with those reported for other binary dihydrogenphosphate dihydrate in the literature (1 < mole of water < 4) [4,12–16]. The thermal stability, mechanism and phase transition temperature of the studied compound in this work are significantly different from those from the single metal compounds ($Fe(H_2PO_4)_2 \cdot 2H_2O$ [18] and $Co(H_2PO_4)_2 \cdot 2H_2O$ [19]). The different thermal behaviors were considered to be due to the different locations of the incorporation of Fe and Co metals in the skeleton and water constitution, which affect to the strengths of water molecule bonds in the studied compound.

The DSC curve of $Co_{0.5}Fe_{0.5}(H_2PO_4)_2 \cdot 2H_2O$ (Fig. 2) shows four endothermic peaks at 121,167, 215 and 402 °C (onset peak at 98,162, 204 and 389 °C) which relate to the dehydration reactions for the first two peaks and the polycondensation reactions for the last two peaks, respectively. Three endothermic peaks at 121, 167 and 402 °C in the DSC curve are in good agreement with DTG and DTA curves as shown in Fig. 1. According to DSC experiment, the heat of dehydration reactions and the polycondensation reactions of this compound can be estimated and were found to be 154.80, 7.80, 20.98 and 34.04 J g^{-1}, respectively.

3.3. X-ray powder diffraction

Fig. 3 shows the XRD patterns of the $Co_{0.5}Fe_{0.5}(H_2PO_4)_2 \cdot 2H_2O$ sample and its final decomposed product, which are very similar to those obtained from the single metal compounds of $M(H_2PO_4)_2 \cdot 2H_2O$ and $M_2P_4O_{12}$ (when M = Co and Fe), respectively. Compared with the published XRD data of the individual metal compounds ($Co(H_2PO_4)_2 \cdot 2H_2O$ (PDF no 390698), $Fe(H_2PO_4)_2 \cdot 2H_2O$ (PDF no 751444), $Co_2P_4O_{12}$ (PDF no 842208) and $Fe_2P_4O_{12}$ (PDF no 782285)), both studied samples can be assigned to the $Co_{0.5}Fe_{0.5}(H_2PO_4)_2 \cdot 2H_2O$ and $CoFeP_4O_{12}$ products. According to hypothesis of isostructural, the systems of binary cobalt iron solid solutions and individual metal dihydrogenphosphate (or cobalt iron cyclotetraphosphate) show quite similarity of the XRD peaks because the electronic charges of cations are equivalent and the radii of cations are close to each other. Consequently, we can draw a conclusion that the synthesized $Co_{0.5}Fe_{0.5}(H_2PO_4)_2 \cdot 2H_2O$ and its

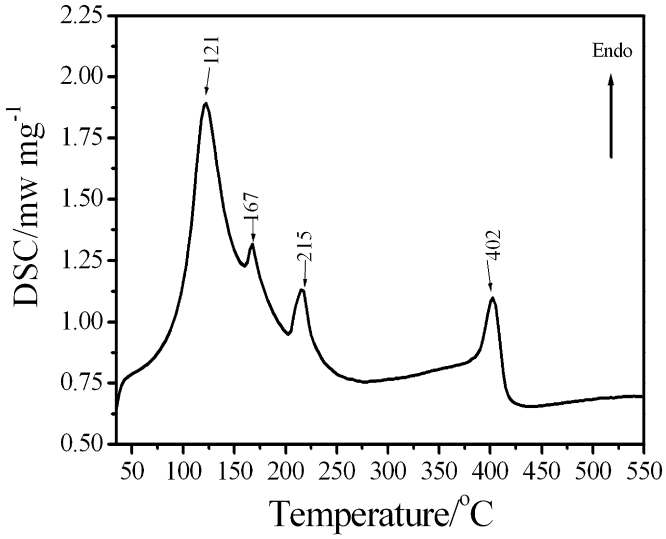

Fig. 2. DSC curve of $Co_{0.5}Fe_{0.5}(H_2PO_4)_2 \cdot 2H_2O$ at the heating rate of 10 °C min^{-1} in N_2 atmosphere.

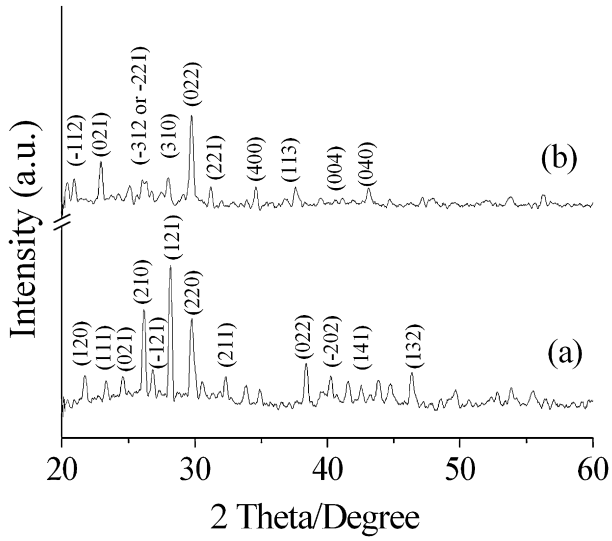

Fig. 3. XRD patterns of $Co_{0.5}Fe_{0.5}(H_2PO_4)_2 \cdot 2H_2O$ (a) and its decomposed product $CoFeP_4O_{12}$ (b).

final decomposed product are solid solutions and not a mixture of the individual ones. On the basis of XRD results, all the reflections can be distinctly indexed as pure monoclinic phases with space group $P2_1/n$ ($Z = 2$) for $Co_{0.5}Fe_{0.5}(H_2PO_4)_2 \cdot 2H_2O$ and C2/c ($Z = 4$) for $CoFeP_4O_{12}$. The average crystallite sizes and lattice parameters of both samples were calculated from the XRD patterns and were summarized in Table 1. The lattice parameters and crystallite sizes of $Co_{0.5}Fe_{0.5}(H_2PO_4)_2 \cdot 2H_2O$ and $CoFeP_4O_{12}$ are comparable to those of the single metal compounds reported in the standard data and our previous works [18,19]. As can seen from Table 1, the crystallite sizes for both binary compounds in this work are larger than those from the single metal compounds in our previous reports [18,19].

3.4. FTIR spectroscopy

The FTIR spectra of $Co_{0.5}Fe_{0.5}(H_2PO_4)_2 \cdot 2H_2O$ and its final decomposed product $CoFeP_4O_{12}$ are shown in Fig. 4. On the basis of isostructural, the FTIR spectra peaks of the binary metal and single metal of dihydrogenphosphate (or cyclotetraphosphate) are quite similar. Consequently, vibrational bands are identified in relation to the crystal structure in terms of the fundamental vibrating units namely $H_2PO_4^-$ and H_2O for $Co_{0.5}Fe_{0.5}(H_2PO_4)_2 \cdot 2H_2O$ and $[P_4O_{12}]^{4-}$ ion for $CoFeP_4O_{12}$, which are assigned according to the literature [4,12–16]. The FTIR spectrum of $Co_{0.5}Fe_{0.5}(H_2PO_4)_2 \cdot 2H_2O$ (Fig. 4a) is very similar to those observed by Koleva and Mehandjiev [12] and Boonchom et al. [18,19] The highest site symmetry of $H_2PO_4^-$ ion is C_{2v}, in the crystallographic unit cell ($P2_1/n$, $Z = 2$), but the four $H_2PO_4^-$ ions are located on the set of non-equivalent site symmetry of C_1. A pair of $H_2PO_4^-$ ions is related to each other by a center of symmetry. It is known that the existence of short OH···O hydrogen bonds in a variety of strongly hydrogen-bonded solids is manifested by the appearance of the characteristic *ABC* structure of the ν(OH) vibrational. Usually, the *ABC* bands are very broad and consist of many ill-resolved components. The strongest band (*A*) is located in the 3100–2700 cm^{-1} region, the *B* band appears about 2600–2400 cm^{-1} and the *C* band around 1700–1600 cm^{-1}. The problem of the origin of the *ABC* trio is discussed in many studies on acidic salts, but an explanation of this behavior of strongly hydrogen-bonded systems is still to be found. One of the most popular interpretations of the *ABC* trio suggests a strong Fermi resonance between the ν(OH) stretching fundamentals and the overtones [2δ(OH) and 2γ(OH)] or combinations involving the δ(OH) and γ(OH) vibrations. The IR

Table 1
Average crystallite sizes and lattice parameters of $Co_{0.5}Fe_{0.5}(H_2PO_4)_2 \cdot 2H_2O$ and its decomposed product $CoFeP_4O_{12}$ calculated from XRD data.

Compound	Method	a/Å	b/Å	c/Å	β/°	Average crystallite sizes/nm
$Co(H_2PO_4)_2 \cdot 2H_2O$	PDF no 390698	7.27	9.88	5.33	94.86	
	Ref. [19]	7.21(3)	9.91(1)	5.29(5)	94.88(6)	26 ± 2
$Co_{0.5}Fe_{0.5}(H_2PO_4)_2 \cdot 2H_2O$	This work	7.29(0)	9.90(0)	5.35(0)	95.10(0)	59 ± 13
$Fe(H_2PO_4)_2 \cdot 2H_2O$	PDF no 751444	7.30	9.92	5.34	95.14	–
	Ref. [18]	7.25(1)	10.10(0)	5.32(0)	95.71(0)	28 ± 4
$Co_2P_4O_{12}$	PDF no 842208	11.8	8.297	9.923	118.72	
	Ref. [19]	11.83(8)	8.22(6)	9.94(0)	118.51(1)	40 ± 10
$CoFeP_4O_{12}$	This work	11.62(1)	8.30(0)	9.65(2)	119.17(4)	62 ± 15
$Fe_2P_4O_{12}$	PDF no 782285	11.94	8.37	9.93	118.74	–
	Ref. [18]	12.80(0)	8.80(4)	10.56(0)	118.67(4)	29 ± 6

spectrum of $Co_{0.5}Fe_{0.5}(H_2PO_4)_2 \cdot 2H_2O$ in the region of the OH stretching modes is characterized by the appearance of a complex broad band between 3600 and 1600 cm^{-1}. Two bands centered at 3145 and 2431 cm^{-1} in the FTIR spectra are referred to as bands *A* and *B*, respectively. The third component (band *C*) is observed around 1744–1640 cm^{-1}. The intense band at about 1260 cm^{-1} is due to the in plane P–O–H bending (A_2), while the out of plane bending (A_1) vibration is observed at about 815 cm^{-1}. A strong band at about 1141 cm^{-1} is assigned to PO_2 asymmetric stretching (B_1), while the other one at about 1043 cm^{-1} corresponds to PO_2 symmetric stretching modes (A_1). The FTIR frequency of the $P(OH)_2$ asymmetric stretching (B_2) shows the strong band at about 945 cm^{-1}. The weak band at about 906 cm^{-1} is assigned to $P(OH)_2$ symmetric stretching modes (A_1). The medium band at about 560 cm^{-1} is corresponding to PO_2 bending modes (B_1). Two strong bands appeared at about 520 and 470 cm^{-1} are attributed to PO_2 rocking modes as B_1 and A_2 vibrations, respectively. The bands of water vibrations are illustrated in Fig. 4a as doublet bands (1640 and 1568 cm^{-1}) contribute both to the band *C* and to the water bending band. A weak band occurs in the FTIR spectra at approximately 638 cm^{-1} is assigned to rocking mode involving water librations. The ν_{OH} stretching modes of HOH in $Co_{0.5}Fe_{0.5}(H_2PO_4)_2 \cdot 2H_2O$ appear at 3145 cm^{-1} (ν_1 or *A* band) and 3322 cm^{-1} (ν_3). The bands associated with the ν_{OH} stretching frequencies in $H_2PO_4^-$ ions are observed at about 2929 and 2431 cm^{-1}.

The FTIR spectrum of $CoFeP_4O_{12}$ is shown in Fig. 4b, which are very similar to those obtained from the individual $M_2P_4O_{12}$ (M = Co and Fe) [18,19]. The vibrational modes of $P_4O_{12}^{4-}$ ion observed in the frequency range of 370–1400 cm^{-1} are assigned according to the literature [20,21]. One of the most noteworthy features of the spectra is the presence of strong bands in the ranges of 1332–1227, 1150–1100, 1080–959, 780–700 and 600–400 cm^{-1}. These bands can be assigned to $\nu_{as}OPO^-$, ν_sOPO^-, $\nu_{as}POP$, ν_sPOP and metal–O vibrations, respectively. The observation of a strong ν_sPOP band is known to be the most striking feature of cyclotetraphosphate spectra, along with the presence of the $\nu_{as}OPO^-$ band. From X-ray diffraction data [20,21], it was shown that the crystal structure is monoclinic (space group C2/c) with a cyclic structure of the $[P_4O_{12}]^{4-}$ anion. This has been confirmed by the FTIR measurements.

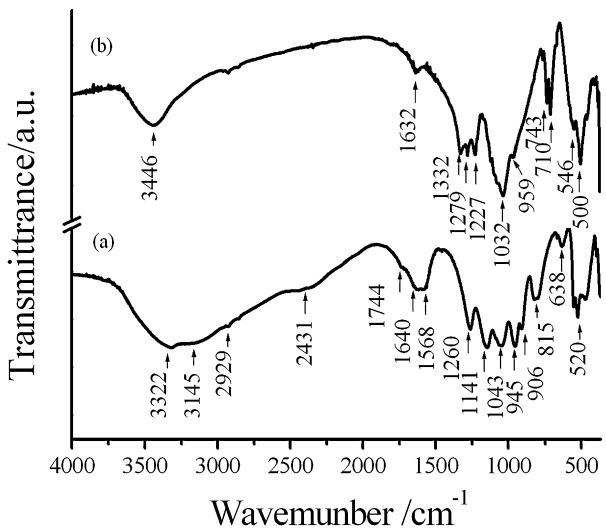

Fig. 4. FTIR spectra of $Co_{0.5}Fe_{0.5}(H_2PO_4)_2 \cdot 2H_2O$ (a) and its decomposed product $CoFeP_4O_{12}$ (b).

3.5. Scanning electron microscopy

The SEM micrographs of $Co_{0.5}Fe_{0.5}(H_2PO_4)_2 \cdot 2H_2O$ and $CoFeP_4O_{12}$ are shown in Fig. 5. The particle shape and size are changed throughout the whole decomposition product. The SEM micrographs of $Co_{0.5}Fe_{0.5}(H_2PO_4)_2 \cdot 2H_2O$ and $CoFeP_4O_{12}$ show non-uniform particles and high agglomerates, which are different from those of the single metal compounds $M(H_2PO_4)_2 \cdot 2H_2O$ and $M_2P_4O_{12}$ (M = Co or Fe) [18,19]. Additionally, the particle sizes and surface morphologies of both compounds in this work are significantly different from those of these binary compounds ($Co_{1/2}Fe_{1/2}(H_2PO_4)_2 \cdot 2H_2O$ and $CoFeP_{14}O_{12}$) reported by our previous work [22,23]. The different morphologies of the single metal compounds ($M(H_2PO_4)_2 \cdot 2H_2O$ and $M_2P_4O_{12}$, M = Co or Fe) and these binary compounds indicate the presence of Co ions in substitution position of Fe ions and the different conditions of preparation method, respectively.

3.6. VSM magnetometer

Fig. 6 shows the specific magnetization curves of $Co_{0.5}Fe_{0.5}(H_2PO_4)_2 \cdot 2H_2O$ and $CoFeP_4O_{12}$ obtained from VSM measurements measured at 20 °C. Both samples demonstrate typical superparamagnetic behavior without any hysteresis in the field range of ±10,000 Oe, which is in agreement with the theory of superparamagnetic behavior, is often observed at room temperature. Specific saturated magnetization (M_s) values of 25.61 and 11.89 emu/g are observed for the $Co_{0.5}Fe_{0.5}(H_2PO_4)_2 \cdot 2H_2O$ and $CoFeP_4O_{12}$, respectively. The superparamagnetic behaviors of the studied compounds are different from the ferromagnetic properties of Fe $(H_2PO_4)_2 \cdot 2H_2O$ and $Fe_2P_4O_{12}$ and the diamagnetic properties of Co $(H_2PO_4)_2 \cdot 2H_2O$ and $Co_2P_4O_{12}$. In addition, it is seen that magnetizations of the $Co_{0.5}Fe_{0.5}(H_2PO_4)_2 \cdot 2H_2O$ and $CoFeP_4O_{12}$ are lower than those of $Fe(H_2PO_4)_2 \cdot 2H_2O$ (96.28 emu/g) and $Fe_2P_4O_{12}$ (85.01 emu/g) [18]. The M_s of $Co_{0.5}Fe_{0.5}(H_2PO_4)_2 \cdot 2H_2O$ in this work is higher than that of $Co_{1/2}Fe_{1/2}(H_2PO_4)_2 \cdot 2H_2O$ (0.045 emu/g) prepared from other method and reported by Boonchom et al. [23]. But the M_s of

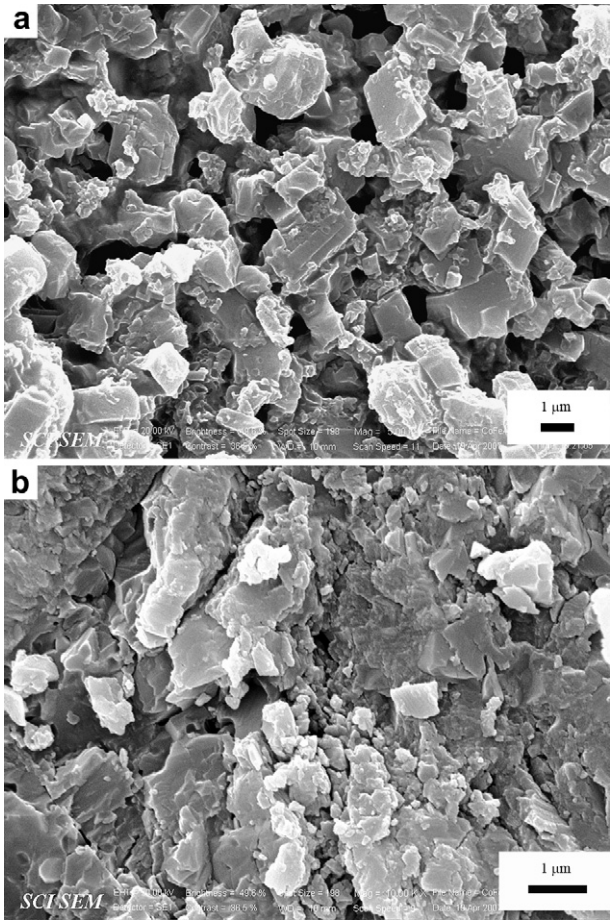

Fig. 5. SEM micrographs of $Co_{0.5}Fe_{0.5}(H_2PO_4)_2 \cdot 2H_2O$ (a) and its decomposed product $CoFeP_4O_{12}$ (b).

$CoFeP_4O_{12}$ in this work is smaller than that of the calcined $Co_{1/2}Fe_{1/2}(H_2PO_4)_2 \cdot 2H_2O$ (12.502 emu/g) precursor at 700 °C and the obtained $CoFeP_4O_{12}$ (14.243 emu/g) in our previous study [22,23]. These results confirmed that the differences in magnetic properties for the synthesized $Co_{0.5}Fe_{0.5}(H_2PO_4)_2 \cdot 2H_2O$ and $CoFeP_4O_{12}$ depend on the medium and condition for preparations.

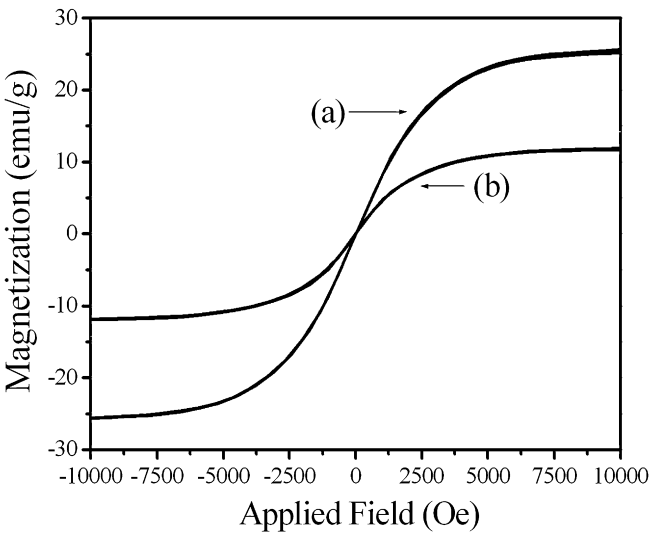

Fig. 6. The specific magnetizations of $Co_{0.5}Fe_{0.5}(H_2PO_4)_2 \cdot 2H_2O$ (a) and its decomposed product $CoFeP_4O_{12}$ (b) as a function of field, measured at 293 K.

4. Conclusion

$Co_{0.5}Fe_{0.5}(H_2PO_4)_2 \cdot 2H_2O$ was successfully synthesized by a simple solid state method using $CoCO_3$–Fe–H_3PO_4 system at ambient temperature with short time consuming (10 min). Thermal transformation of $Co_{0.5}Fe_{0.5}(H_2PO_4)_2 \cdot 2H_2O$ was investigated by TG/DTG/DTA and DSC techniques, which indicate the dehydration and the deprotonated dihydrogenphosphate reactions and its final decomposed product is $CoFeP_4O_{12}$. The structures, morphologies and magnetic properties of $Co_{0.5}Fe_{0.5}(H_2PO_4)_2 \cdot 2H_2O$ and its decomposed product $CoFeP_4O_{12}$ were investigated. The XRD patterns and FTIR spectra suggest the formation of pure monoclinic phases of $Co_{0.5}Fe_{0.5}(H_2PO_4)_2 \cdot 2H_2O$ and $CoFeP_4O_{12}$. Both samples are superparamagnetic at room temperature, having no hysteresis loop in the range of $-10{,}000\ \text{Oe} < H < +10{,}000\ \text{Oe}$. This work presents the simple, cost-effective and short time consuming method for the alternative preparation of $Co_{0.5}Fe_{0.5}(H_2PO_4)_2 \cdot 2H_2O$ and $CoFeP_4O_{12}$ compounds, which may be used in many important applications such as catalytic, superionic conductors, piezo- and ferroelectrics, magnets, ceramic and electrochemical performance.

Acknowledgements

This work is financially supported by the Thailand Research Fund (TRF) and the Commission on Higher Education (CHE) and King Mongkut's Institute of Technology Ladkrabang Research (KMITL Research), Ministry of Education, Thailand.

Appendix. Supplementary data

Supplementary data associated with this article can be found in the online version, at doi:10.1016/j.solidstatesciences.2010.10.012.

References

[1] M. Trojan, P. Šulcová, Dyes Pigments 47 (2000) 291.
[2] B. Boonchom, S. Maesiri, S. Youngme, C. Danvirutai, Solid State Sci. 11 (2009) 485.
[3] B. Boonchom, C. Danvirutai, Ind. Eng. Chem. Res. 47 (2008) 2941 and references therein.
[4] N.M. Antraptseva, L.N. Shchegrov, I.G. Ponomareva, Russ. J. Inorg. Chem. 51 (2006) 1493.
[5] M. Trojan, P. Šulcová, P. MoŠner, Dyes Pigments 44 (2000) 161.
[6] M. Trojan, D. Brandová, J. Therm. Anal. Calorim. 30 (1985) 159.
[7] M. Trojan, Dyes Pigments 12 (1990) 35.
[8] M. Trojan, Dyes Pigments 13 (1990) 1.
[9] M. Trojan, Thermochim. Acta 159 (1990) 13.
[10] M. Trojan, Thermochim. Acta 160 (1990) 361.
[11] M. Trojan, D. Brandová, Thermochim. Acta 160 (1990) 349.
[12] V. Koleva, D. Mehandjiev, Mater. Res. Bull. 413 (2006) 469.
[13] V.N. Viter, P.G. Nagornyi, Russ. J. Inorg. Chem. 52 (2007) 14.
[14] V. Koleva, H. Effenberger, J Solid Sate Chem. 180 (2007) 956.
[15] B. Boonchom, S. Youngme, C. Danvirutai, Solid State Sci. 10 (2008) 129.
[16] B. Boonchom, J. Danvirutai, J. Therm. Anal. Calorim. 97 (2009) 717.
[17] B.D. Cullity, Elements of X-ray Diffraction, second ed. Addison-Wesley Publishing, 1977.
[18] B. Boonchom, C. Danvirutai, S. Youngme, S. Maesiri, Ind. Eng. Chem. Res. 47 (2008) 7642.
[19] B. Boonchom, C. Danvirutai, J. Chem. Eng. Data 54 (2009) 1225.
[20] W. Gunsser, D. Fruehauf, K. Rohwer, A. Zimmermann, A. Wiedenmann, J. Solid State Chem. 82 (1989) 43.
[21] M. Bagieu-Beucher, M. Gondrand, M. Perroux, J. Solid State Chem. 19 (1976) 353.
[22] B. Boonchom, M. Thongkam, S. Kongtaweelert, N. Vittayakorn, J. Alloys Compd. 486 (2009) 689.
[23] B. Boonchom, M. Thongkam, S. Kongtaweelert, N. Vittayakorn, Mater. Res. Bull. 44 (2009) 2206.

Journal of Alloys and Compounds 509 (2011) 2304–2310

Contents lists available at ScienceDirect

Journal of Alloys and Compounds

journal homepage: www.elsevier.com/locate/jallcom

Effect of $BiAlO_3$ modification on the stability of antiferroelectric phase in $PbZrO_3$ ceramics prepared by conventional solid state reaction

Naratip Vittayakorn [a,b,c,*], Banjong Boonchom [d]

[a] College of KMITL Nanotechnology, King Mongkut's Institute of Technology Ladkrabang, Bangkok 10520, Thailand
[b] Department of Chemistry, Faculty of Science, King Mongkut's Technology Ladkrabang, Bangkok 10520, Thailand
[c] Thailand Center of Excellence in Physics (ThEP), CHE, 328 Si Ayutthaya Rd., Bangkok 10400, Thailand
[d] King Mongkut's Institute of Technology Ladkrabang, Chumphon Campus, 17/1 M.6 Pha Thiew District, Chumphon 86160, Thailand

ARTICLE INFO

Article history:
Received 7 September 2010
Received in revised form 28 October 2010
Accepted 28 October 2010
Available online 10 November 2010

Keywords:
Energy storage materials
Ferroelectrics
X-ray diffraction
Dielectric response

ABSTRACT

In this paper, we report on the polycrystalline $(Pb_{(1-3x/2)}Bi_x)(Zr_{1-3x/4}Al_x)O_3$ (PZO–BAO) ceramics, with $x = 0.0–0.3$, prepared by conventional solid state reaction. The crystal structure and thermal and dielectric properties of the sintered ceramics were investigated as a function of composition by means of X-ray diffraction (XRD), differential scanning calorimetry (DSC) and dielectric spectroscopy. The results indicated that the presence of $BiAlO_3$: BAO in the solid solution decreased the structural stability of the overall perovskite phase. Dielectric, thermal and P–E hysteresis results confirmed that no ferroelectric intermediate phase was seen in the PZO–BAO system. An antiferroelectric phase can be stable in a wide temperature range, indicating that BAO enhanced antiferroelectric phase stability in perovskite PZ manifests by "square" antiferroelectric behavior. Therefore, the $(Pb_{(1-3x/2)}Bi_x)(Zr_{1-3x/4}Al_x)O_3$ solid solution offers a material system for high-energy-storage capacitors and electromechanical transducers.

1. Introduction

Pure and compositionally modified lead zirconate ($PbZrO_3$; PZO) ceramics are important materials used in energy storage applications for DC fields, due its antiferroelectric (AFE) nature. PZO has an orthorhombic structure, with the lattice parameters, $a = 5.884$ Å, $b = 11.768$ Å and $c = 8.22$ Å [1]. The phase transition sequence has been found to follow the progressive heating of PZO orthorhombic AFE to rhombohedral ferroelectric (FE) ($228 < T < 230$ °C) to paraelectric (PE) cubic at $T_c = 230$ °C. The FE phase of between 228 and 230 °C is sometimes called the FE intermediate phase. The AFE-FE phase transition could occur spontaneously, due to several factors, for example, a change in stress configuration promoted by external mechanical driving fields, an increase in the amplitude of the applied AC electric field, hydrostatic pressure and/or temperature variations [2,3]. For electric field induced AFE to FE phases, transformation requires a very strong electric field in the AFE PZO, otherwise dielectric breakdown occurs instead. Therefore, most AFE ceramics are modified chemically by adding metal oxide at the A- and B-sites of the perovskite structure. The FE intermediate phase can be induced by adding Ba^{2+}, Sr^{2+}, and La^{3+} at the Pb^{2+}-site [2,4–7]. Moreover, our recent research found that the FE intermediate phase also can be induced by adding, for example, hybrid-doped Ni^{2+}/Nb^{5+}, Zn^{2+}/Nb^{5+}, Co^{2+}/Nb^{5+} and Mg^{2+}/W^{6+} at the Zr^{4+}-site [8–14].

$BiMO_3$; M = Fe^{3+}, Mn^{3+} and Nd^{3+} has received a lot of attention recently as a multiferroic, and investigation of the solid solutions, $BiMO_3$–$PbTiO_3$, has shown that they improve ferroelectric properties of $PbTiO_3$, reduce the amount of lead, and find new morphotropic phase boundary piezoelectrics [15–18]. However, very little has been known so far about experimental $BiMO_3$ with nonmagnetic ions (M = Al, Sc, Ga, and In). Furthermore, due to the relatively small size of Bi^{3+}, $Bi(M)O_3$ is not stable in perovskite form, and can be only synthesized under high pressure [19]. The smaller tolerance factor of $Bi(M)O_3$, and easily polarized Bi^{3+} ion, can enhance the transition temperature further, and with larger piezoelectric effect when solid solution with $PbTiO_3$ [15]. Crystallized $BiAlO_3$ is a noncentrosymmetric structure and isotypic with the well-known multiferroic, $BiFeO_3$. Theoretical studies by Baettig et al. [20], on a unique ferroelectric phase bismuth aluminate ($BiAlO_3$; BAO), predicted that BAO could be a promising novel candidate ferroelectric material, with a high curie temperature of ~530 °C. In 2005, Belik et al. [21] synthesized the compound of BAO by using a high-pressure, high-temperature technique at 6 GPa and 1000–1200 °C. BAO has rhombohedral (R3c) symmetry with lattice parameters given as $a = b = 5.37546(5)$ Å and $c = 13.3933(1)$ Å. Unfortunately, pure stable perovskite BAO ceramics have never been synthesized using a conventional sintering process, due to

* Corresponding author at: Department of Chemistry, Faculty of Science, King Mongkut's Institute of Technology Ladkrabang, Bangkok 10520, Thailand.
Fax: +66 2 326 4415.
E-mail address: naratipcmu@yahoo.com (N. Vittayakorn).

0925-8388/$ – see front matter © 2010 Elsevier B.V. All rights reserved.
doi:10.1016/j.jallcom.2010.10.206

the small value of t and electronegativity difference between A- and B-site cations. Zuo et al. [22] investigated the phase transitional behavior and various electrical properties of $(1-x)K_{1/2}Na_{1/2}NbO_3$; KNN–$x$BAO ceramics. The results indicate that the addition of BAO significantly influences the sintering, microstructure, phase transition and electrical properties of KNN ceramics. The identification of phase transitional behavior confirms the formation of a MPB between orthorhombic and tetragonal ferroelectric phases in the composition range of $0.005 \le x \le 0.01$. Ranjan et al. [23] studied the crystal structure and solid solubility in the $PbTiO_3$–$BiAlO_3$ system. Their study suggested that decrease in stability of the ferroelectric state, due to dilution of the Ti-sublattice by smaller sized Al^{3+} ions, was compensated for by the increase in ferroelectric stability by Bi^{3+} ions. Although the compositions of $Bi(M)O_3$–$PbTiO_3$ have been investigated widely, few reports on $Bi(M)O_3$ with other lead perovskite end members are available. To the authors' knowledge, the literature has not reported BAO as incorporated into PZO for solid solutions. Moreover, the effects of substitution in both A- and B-sites on the antiferroelectric phase stability of PZO are still unclear. The Bi^{3+} ion and Al^{3+} ion are both smaller than the Pb^{2+} and Zr^{4+} ion, respectively. Therefore, in this paper, we report on the how antiferroelectric phase stability is changed by A- and B-site substitution and determine the solubility limit of BAO in PZO.

2. Experimental procedures

2.1. Synthesis

Ceramics of $(Pb_{(1-3x/2)}Bi_x)(Zr_{1-3x/4}Al_x)O_3$, with $x = 0.0$–0.3, were synthesized using the conventional ceramic processing procedures [24]. Reagent grade oxide powders of Bi_2O_3 (≥99.9% purity, Cerac), PbO (≥99% purity, Kento), ZrO_2 (≥99.9% purity, Advance Material) and Al_2O_3 (≥99.5% purity, Fluka) were weighed according to stoichiometric formula, and ball-milled with ethanol and yttrium-stabilized zirconia media for 18 h. The dried powders were calcined in crucibles at 700–900 °C for 4 h, then ball-milled again for 6 h. The dried calcined powders were mixed with 5 wt% polyvinyl alcohol (PVA) and then pressed into pellets of 15 mm diameter and ~2 mm thickness. After burning out PVA binder at 550 °C, the pellets covered with extra powders were sintered in sealed crucibles at between 1100 °C and 1250 °C for 4 h.

2.2. Characterizations

The densities of ceramics were obtained using the Archimedes method. The density of the sintered PZO-BAO pellets was measured by the Archimedes water immersion method. The relative density of all the sintered pellets was approximately 97–98% of the theoretical density. X-ray diffraction (XRD; Bruker-AXS D8) using CuK_α radiation was utilized to determine the phases formed and optimum firing temperatures for formation of the desired phase for $0.02 \le x \le 0.3$ compositions. For measuring the dielectric and ferroelectric characteristics, the specimens were polished to 1 mm thickness using sand paper after ultrasonic cleaning in an ethanol bath. Silver-paste (Heraeus C1000) was coated on both sides of the sintered samples by the screen printing method, and then subsequently fired at 650 °C for 30 min. For investigating the dielectric properties, capacitance was measured at 1 kHz using an automated measurement system. This system consisted of an LCR meter (HP-4284, Hewlett-Packard Inc.). The dielectric constant was then calculated from $\varepsilon_r = Cd/\varepsilon_o A$, where C was the capacitance of the sample; d and A were the thickness and area of the electrode, respectively; and ε_o was the dielectric permittivity of vacuum (8.854×10^{-12} F/m). Polarizations, as a function of electric field (P–E loop) at 4 Hz of the samples, were observed using a ferroelectrics test system (RT66B; Radiant Technologies, Inc.). The peak field was maintained at 40 kV/cm during measurement.

3. Results and discussion

3.1. Crystal structure and physical properties of PZO–BAO solid solutions

The X-ray diffraction patterns of the sintered ceramics, $(Pb_{(1-3x/2)}Bi_x)(Zr_{1-3x/4}Al_x)O_3$; $x = 0.02$–0.3, at room temperature are shown in Fig. 1. The presence of diffraction peaks can be used to evaluate the structural order at long range or periodicity of the material [25]. The patterns indicate that the ceramics possess a phase of perovskite structure, and the crystalline symmetry is

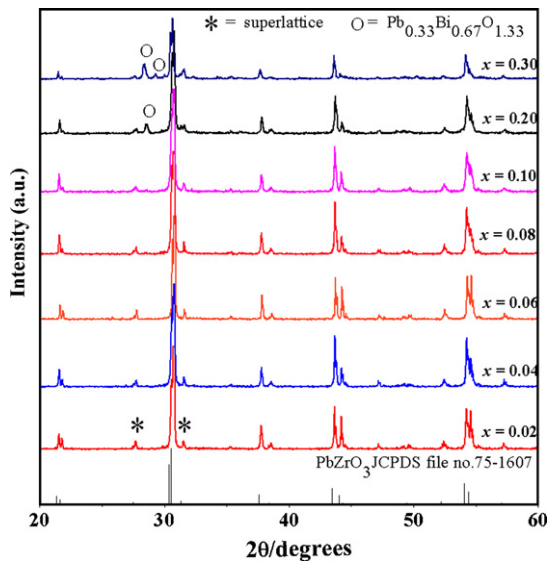

Fig. 1. XRD diffraction patterns of sintered $(Pb_{(1-3x/2)}Bi_x)(Zr_{1-3x/4}Al_x)O_3$; $x = 0.02$–0.30 ceramics.

orthorhombic. Phase-pure perovskite structures, with orthorhombic symmetry, were obtained for $x \le 0.1$; however $x \ge 0.1$, A cubic pyrochlore phase $Pb_{0.33}Bi_{0.87}O_{1.33}$ (Powder diffraction Files no. 85-0448), identified by "o", began to develop at $x \ge 0.1$, and increased in intensity with increasing BAO concentration. These results indicated that the presence of BAO in the solid solution decreases the structural stability of PZO perovskite phase, due to the instability of BAO perovskite under normal conditions and the tolerance factor. The solubility limit of $(Pb_{(1-3x/2)}Bi_x)(Zr_{1-3x/4}Al_x)O_3$ ceramics is the composition, $x = 0.1$. The peak positions shifted to higher angles, indicating a slight decrease in the lattice parameter. This phenomenon can be explained qualitatively with respect to the unit cell volume caused by the Bi^{3+} and Al^{3+} incorporation. The ionic radii of Bi^{+3} (Shannon radius = 1.17 Å for CN = 8) and Al^{+3} (Shannon radius = 0.535 Å for CN = 6) are less than those of Pb^{+2} (Shannon radius = 1.29 Å for CN = 8) and Zr^{+4} (Shannon radius = 0.72 Å for CN = 6), respectively [26]. Therefore, Bi^{3+} can enter the eight-fold coordinated A-site of the perovskite structure to substitute Pb^{2+}, and Al^{3+} can enter the six-fold coordinated B-site of the perovskite structure to substitute Zr^{4+}, due to radius matching. The lattice parameters were calculated using the least square refinement from the UNITCELL-97 program [27]. Table 1 shows the lattice parameter and cell volume of $(Pb_{(1-3x/2)}Bi_x)(Zr_{1-3x/4}Al_x)O_3$ ceramics. The substitution of the relatively smaller Bi^{3+} and Al^{3+} for the comparatively larger Pb^{2+} and Zr^{4+} led to a decrease in the unit cell volume. This seems to be the case for $x \le 0.01$ only, as composition, $x \ge 0.01$, is close to the solubility limit, but this argument does not apply due to the inhomogeneous distribution factor.

Fig. 2 shows enlarged profiles of the 1/4 (hkl) superlattice reflection (*) and (2 4 0)/(0 0 4) for determining the crystal structure of as-sintered ceramics. By increasing BAO concentration, the remaining 1/4 (hkl) superlattice reflection peaks indicated the remainder of antiparallel displacements of A-site ions in the perovskite structure. It is interesting to note that the substitution of BAO does not change the crystalline structure of PZO ceramics within the studied doping level. The influence of BAO addition on the phase structure of the PZO–BAO system is similar to that of the PT-BAO system [23,28]. The tolerance factor (t) for perovskite structure can be described by the general formula for ABO_3; $t = (R_A + R_O)/(\sqrt{2})(R_B + R_O)$, where R_A is the radius of A(CN = 8), R_B the radius of B(CN = 6) and R_O the radius of oxygen(CN = 8). When t is >1, the FE phase is stabilized, and when t is <1, the AFE phase is sta-

Table 1
Summary of the lattice parameters of $(Pb_{(1-3x/2)}Bi_x)(Zr_{1-3x/4}Al_x)O_3$; $x = 0.02–0.1$ ceramics.

Composition (x)	Lattice parameters			Volume of unit cell (Å^3)
	a	b	c	
0.00	5.8835 ± 0.0003	11.7672 ± 0.0008	8.2177 ± 0.0007	568.93
0.02	5.8629 ± 0.0207	11.7258 ± 0.0414	8.2171 ± 0.0273	564.89
0.04	5.8609 ± 0.0225	11.7221 ± 0.0453	8.2116 ± 0.0253	564.15
0.06	5.8584 ± 0.0237	11.7167 ± 0.0473	8.2023 ± 0.0195	563.01
0.08	5.8545 ± 0.0258	11.7113 ± 0.0494	8.2022 ± 0.0159	562.37
0.10	5.8522 ± 0.0275	11.7106 ± 0.0527	8.2007 ± 0.0124	562.01

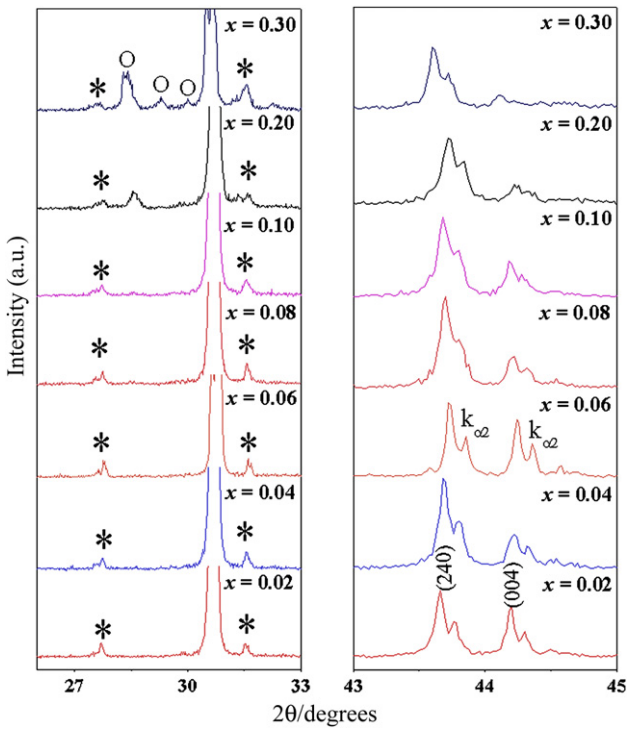

Fig. 2. X-ray diffraction profiles for the 1/4 (hkl) superlattice reflection (*), pyrochlore phase (○) and (240)/(004) peaks of $(Pb_{(1-3x/2)}Bi_x)(Zr_{1-3x/4}Al_x)O_3$; $x = 0.02–0.30$ ceramics.

bilized [29]. The average ionic radius of the A- and B-site ions in the $(Pb_{(1-3x/2)}Bi_x)(Zr_{1-3x/4}Al_x)O_3$ can be calculated from the following equation:

$$r_{\text{A-site}} = \left(1 - \frac{3x}{2}\right) r_{Pb^{2+}} + x r_{Bi^{3+}} \quad (1)$$

$$r_{\text{B-site}} = \left(1 - \frac{3x}{4}\right) r_{Zr^{4+}} + x r_{Al^{3+}} \quad (2)$$

where the ionic radii of Pb^{2+}, Bi^{3+}, Zr^{4+} and Al^{3+} are 1.29 Å, 1.17 Å, 0.72 Å and 0.535 Å, respectively [26]. The average ionic radius of the A- and B-site ions and tolerance factor in the $(Pb_{(1-3x/2)}Bi_x)(Zr_{1-3x/4}Al_x)O_3$ ceramics are shown in Table 2. The calculated tolerance factor of the $(Pb_{(1-3x/2)}Bi_x)(Zr_{1-3x/4}Al_x)O_3$; $x = 0.02–0.3$ is between 0.8904 and 0.8202, indicating that AFE behavior is expected to be seen at room temperature. Dielectric and ferroelectric properties; later explained, support this assumption. Furthermore, as expected, the stability of perovskite structure decreases with increasing BAO concentration, due to the small tolerance factor value.

3.2. Dielectric properties

Temperature dependence of relative permittivity (ε_r) and dielectric loss ($\tan\sigma$) for $(Pb_{(1-3x/2)}Bi_x)(Zr_{1-3x/4}Al_x)O_3$; $x = 0.02–0.3$ ceramics were measured at 1, 10 and 100 kHz, as shown in Fig. 3. It is well known that pure PZO has two dielectric anomaly peaks reported at 228 and 230 °C, which corresponds to the phase transitions of orthorhombic antiferroelectric (AFE) phase to rhombohedral FE intermediate phase and rhombohedral FE intermediate phase to cubic paraelectric phase, respectively. Furthermore, the FE intermediate phase can be induced easily by adding Ba^{2+}, Sr^{2+}, and Ca^{2+} at the Pb^{2+}-site [2,4–7] or Ni^{2+}/Nb^{5+}, Zn^{2+}/Nb^{5+}, Co^{2+}/Nb^{5+} and Mg^{2+}/W^{6+} at the Zr^{4+}-site [8–14]. As shown in Fig. 3, a single sharp dielectric permittivity peak arises in all ceramic samples. Interestingly, the dielectric results showed one sharp dielectric peak anomaly, indicating that the FE intermediate phase did not exist in $(Pb_{(1-3x/2)}Bi_x)(Zr_{1-3x/4}Al_x)O_3$; $x = 0.02–0.3$ samples. Increasing BAO concentration resulted in a very small decrease in transition temperature. No frequency dependence of dielectric response or shift in transition temperature with frequency was observed under transition temperature, which indicated no evidence of relaxor-like $Pb(Zr,Ni,Nb)O_3$ [8,10] or $(Pb,Ba)ZrO_3$ [5,7]. Nevertheless, at high temperature, the dielectric data revealed an enhanced dielectric loss with increasing BAO concentration. At 1 kHz measurement, frequent higher losses were found to persist to a significantly lower temperature. These results demonstrated that the enhanced dielectric losses at higher temperatures are due to a space charge mechanism [30]. For the composition, $x \geq 0.2$, the maximum relative permittivity decreases steadily with increasing BAO content (ε_r decreases from ~3700 in composition $x = 0.1$–700 in composition $x = 0.3$), and the lower value is attributed to the detrimental effect of the secondary pyrochlore phase.

Table 2
Average ionic radius of A-site, B-site ions and tolerance factor in the $(Pb_{(1-3x/2)}Bi_x)(Zr_{1-3x/4}Al_x)O_3$ ceramics.

Compositions (x)	$R_{\text{A-site}}$	$R_{\text{B-site}}$	Tolerance factor (t)
0.02	1.2747	0.7199	0.8904
0.04	1.2594	0.7198	0.8854
0.06	1.2441	0.7197	0.8804
0.08	1.2288	0.7196	0.8754
0.10	1.2135	0.7195	0.8704
0.20	1.1370	0.7190	0.8453
0.30	1.0605	0.7185	0.8202

3.3. Thermal properties

The DSC technique was used as the second tool to confirm the phase transition of PZO–BAO ceramics. Fig. 4 shows the temperature dependences of the heat flow (DSC curves) obtained when heating the $(Pb_{(1-3x/2)}Bi_x)(Zr_{1-3x/4}Al_x)O_3$; $x = 0.02–0.3$ samples at the rate of 10 K/min^{-1}. A single endothermic peak was observed for all compositions. The peaks shifted slightly to lower temperatures with increasing BAO concentrations. This transition temperature corresponds to the Curie temperature of the AFE to PE transformation. However, there is no significant difference in the temperature of AFE to PE phase transition in the composition, $x \geq 0.08$. This could be related to appearance of the pyrochlore phase. The DSC results

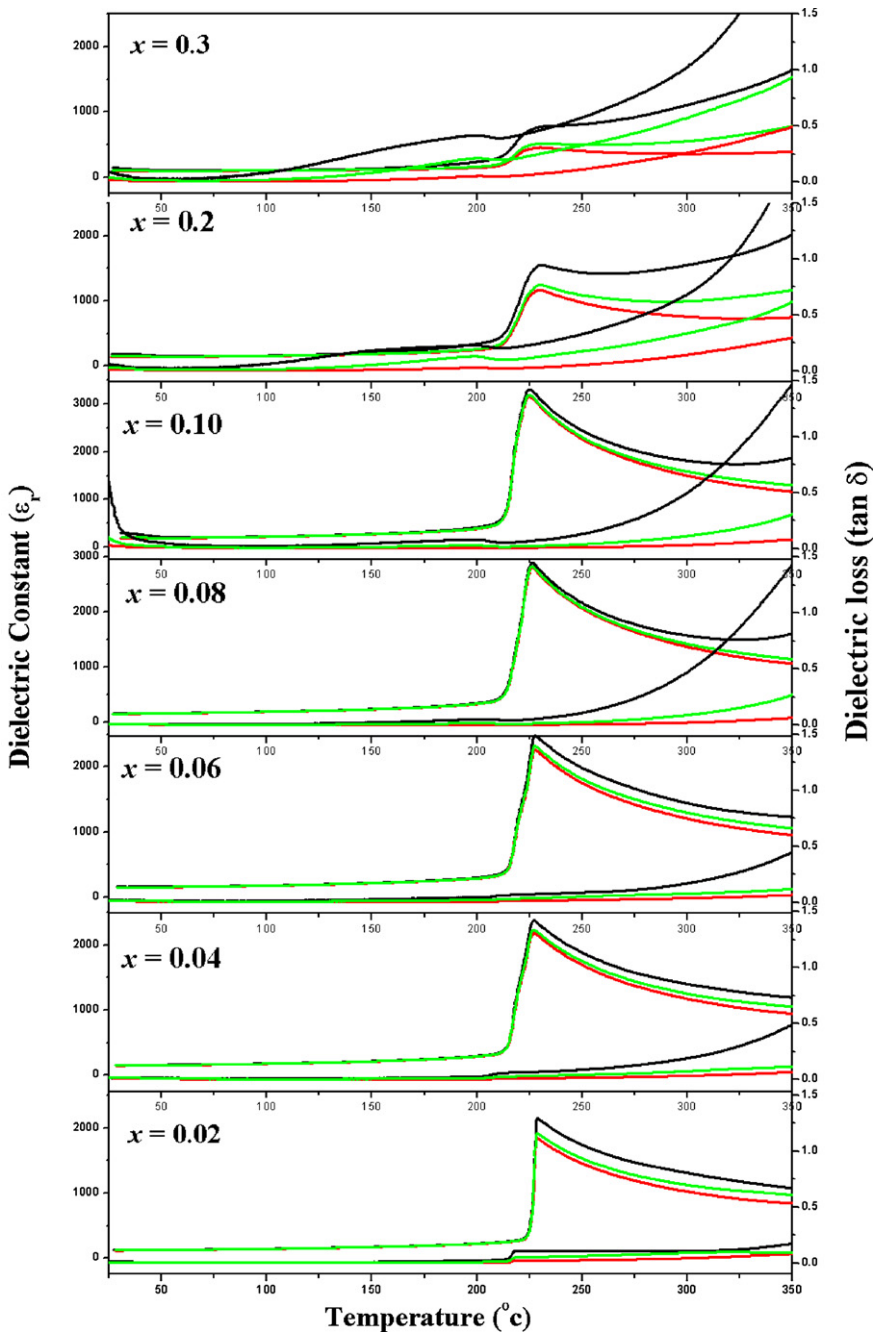

Fig. 3. Relative permittivity (ε_r) and dielectric loss (tan δ) as a temperature function of $(Pb_{(1-3x/2)}Bi_x)(Zr_{1-3x/4}Al_x)O_3$; $x = 0.02–0.3$ ceramics.

observed are consistent with dielectric measurement results. It should be pointed out that the difference in AFE-PE transition temperature values in dielectric, ferroelectric and DSC measurement techniques is due to the difference in heating rate and well time of the measurement.

Thermodynamic parameter, enthalpy (ΔH^*/J g^{-1}), heat capacity (C_p/J g^{-1} K^{-1}), entropy change (ΔS^*/J g^{-1} K^{-1}), and Gibbs energy change (ΔG^*/J g^{-1}), were calculated from the DSC results. The enthalpy change was calculated directly from the amount of heat change involved in each step per unit mass of the sample. ΔH^*, thus determined, was implemented to calculate the specific heat capacity (C_p) using the following equation [31,32]

$$C_p = \frac{\Delta H}{\Delta T} \tag{3}$$

where $\Delta T = T_2 - T_1$; T_1 is the temperature at which the DSC peak begins to depart from the baseline; and T_2 is the temperature at which the peak lands. Consequently, the changes of entropy (ΔS^*) and Gibbs energy (ΔG^*) were calculated using the following equations [31,32]

$$\Delta S^* = 2.303 C_p \log\left(\frac{T_2}{T_1}\right) \tag{4}$$

$$\Delta H^* = \Delta G^* - T_p \Delta S^* \tag{5}$$

On the basis of the DSC data, the value of ΔH^*, ΔS^*, C_p and ΔG^* for the phase transition can be calculated according to Eqs. (3)–(5), and is presented in Table 3. The peak value of heat capacity became weaker, and anomaly of heat capacity gradually broader, with increasing BAO concentration. These results indicated that the phase transition deviates gradually from the first

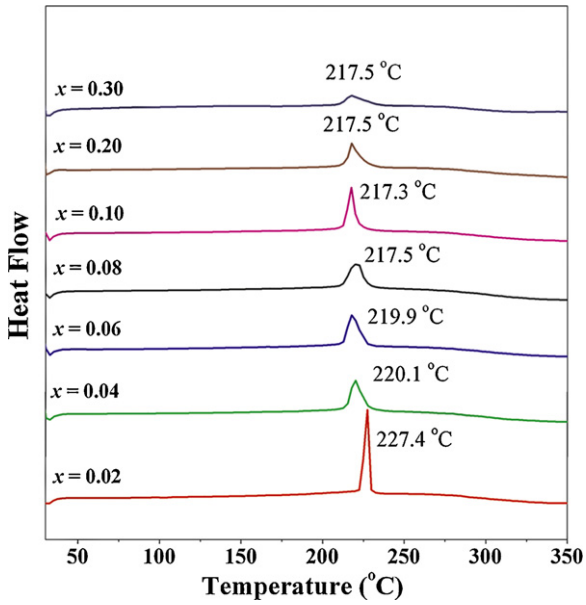

Fig. 4. Typical DSC curves for $(Pb_{(1-3x/2)}Bi_x)(Zr_{1-3x/4}Al_x)O_3$; $x = 0.02–0.3$ ceramics.

order type. Furthermore, the enthalpy (ΔH^*) continues to decrease with increasing BAO content, indicating that BAO decreases the energy requirement for transition from AFE to FE. Stenger and Burggraaf [33] observed that the change in entropy (ΔS^*) correlates with the fluctuation probability in conjunction with a small spontaneous lattice deformation and polarization. With increasing BAO content, there is no significant change in ΔS^*, indicating the stability of energy required to reorient the antiferroelectric sublattices in the PZO–BAO system [33]. On the other hand, the thermodynamic parameter, ΔH^* and ΔG^*, calculated according to Eqs. (3)–(5), gives the positive values, indicating that the AFE to PE phase transitions are connected to the introduction of heat, and phase transitions are non-spontaneous processes.

3.4. Ferroelectric properties

In order to examine how the phase transition occurs with temperature, electrical polarization hysteresis loop measurements were performed under a peak field of 40 kV/cm at a series of temperatures for $(Pb_{(1-3x/2)}Bi_x)(Zr_{1-3x/4}Al_x)O_3$ ceramics. A disk specimen, with a diameter of about 10 mm and thickness around 600 μm was used. The loop was recorded after the temperature was stabilized for at least 5 min. At 30 °C, no ferroelectric hysteresis loop was observed for any compositions ($0.0 \le x \le 0.3$). The linear polarization was observed, due perhaps to the extremely high coercive field, indicating that the composition, $x \le 0.3$, belongs to the AFE phase at room temperature. The $Pb_{0.94}Bi_{0.04}Zr_{0.97}Al_{0.04}O_3$ ceramic was selected for further investigation of the polarization behavior sequence during heating to 220 °C. The polarization behavior of $Pb_{0.94}Bi_{0.04}Zr_{0.97}Al_{0.04}O_3$ ceramic as a function of temperature is shown in Fig. 5. For the $Pb_{0.94}Bi_{0.04}Zr_{0.97}Al_{0.04}O_3$ composition, such linear behavior with minimum polarization remains at temperatures of up to 195 °C. When the temperature was raised to 200 °C, a double hysteresis loops started to develop, indicating the occurrence of electric field-induced antiferroelectric-to-ferroelectric phase transition. The transition from a minor loop at low field to a saturated double-shaped hysteresis loop at high field occurs at 205 °C by increasing the electric fields. This is expected because an antiferroelectric crystal generally has a zero net switchable dipole moment, due to the antiparallel alignment of elementary dipoles in its unit cell. When the external electric field is weak, the induced polarization is proportional to the electric field and demonstrates no macroscopic polarization hysteresis [34]. While the electric field exceeds a threshold value, called the critical field, the crystal becomes ferroelectric and the polarization displays hysteresis with respect to the field. A hysteresis loop also forms in the negative field, with the two loops being associated with antiparallel dipoles in adjacent unit-cell sublattices. As the temperature increases to 215 °C, the critical field is slowly reduced. This is caused by a higher temperature that provides higher thermal fluctuation to the polarization order parameter, which reduces the ferroelectric interaction among the dipoles.

In addition, when the temperature was increased to above 225 °C, a linear curve also was seen as an indication of the cubic paraelectric (PE) phase. Fig. 6 shows the polarization versus electric field hysteresis loops at 205 °C for the $(Pb_{(1-3x/2)}Bi_x)(Zr_{1-3x/4}Al_x)O_3$; $x = 0.02–0.08$ ceramics. The double hysteresis behavior in polarization, with an applied electric field, clearly demonstrates the antiferroelectric nature of $(Pb_{(1-3x/2)}Bi_x)(Zr_{1-3x/4}Al_x)O_3$; $x = 0.02–0.08$ ceramics. The remanent polarization, P_r, slightly decreases between $x = 0.02$ and 0.08, from 23.26 μC/cm^2 to 19.4 μC/cm^2. The AFE-FE switching field decreases for $x = 0.02$ and 0.08 from 29.23 kV/cm to13.81 kV/cm. In Berlincourt's [35] study of doped $Pb(Zr,Sn,Ti)O_3$ ceramics, two different types of AFE to FE transitions based on the character of the P–E hysteresis loop were described; the two types of double hysteresis loops have been termed "square" and "slanted". The "slanted" double hysteresis loop ceramics have far less hysteresis, small volume difference between AFE and FE phases, lower transition fields and a wider temperature range, over which the transition can be induced by electric fields. The "slanted" double hysteresis loop ceramics exhibit a small remanent polarization at zero fields, while the "square" loop ceramics do not. The P–E hysteresis loop measurements demonstrate that the ferroelectric properties of ceramics in the PZO–BAO system shift gradually from "square" to "slanted" antiferroelectric behavior, with increasing BAO concentrations. Interestingly, with increasing temperatures from room temperature to 250 °C, antiferroelectric to ferroelectric intermediate phase transition was not observed in any compositions, which indicated no ferroelectric intermediate phase in the PZO–BAO ceramics. Chu et al. [36] pointed out that the area enclosed by the decreasing field part of the polarization-electric field trace represented a stored electrical energy density. The ferroelectric results show that the PZO–BAO ceramics have large polarization at a high electric field and a large area between the polarization axis and curve. There are indications that this

Table 3
Values of thermodynamic parameters for phase transition of the $(Pb_{(1-3x/2)}Bi_x)(Zr_{1-3x/4}Al_x)O_3$ ceramics calculated from DSC data.

Compositions (x)	T_p/K	ΔH^*/J g^{-1}	C_p/J g^{-1} K^{-1}	ΔS^*/J g^{-1} K^{-1}	ΔG^*/J g^{-1}
0.02	499	3.825	7.665×10^{-3}	6.145×10^{-5}	3.856
0.04	497	3.749	7.543×10^{-3}	6.163×10^{-5}	3.795
0.06	491	3.348	6.819×10^{-3}	6.438×10^{-5}	3.382
0.08	490	2.815	5.745×10^{-3}	6.336×10^{-5}	2.849
0.10	489	2.676	5.461×10^{-3}	6.193×10^{-5}	2.901
0.20	490	2.360	4.816×10^{-3}	6.851×10^{-5}	2.408
0.30	489	1.429	2.922×10^{-3}	5.985×10^{-5}	1.455

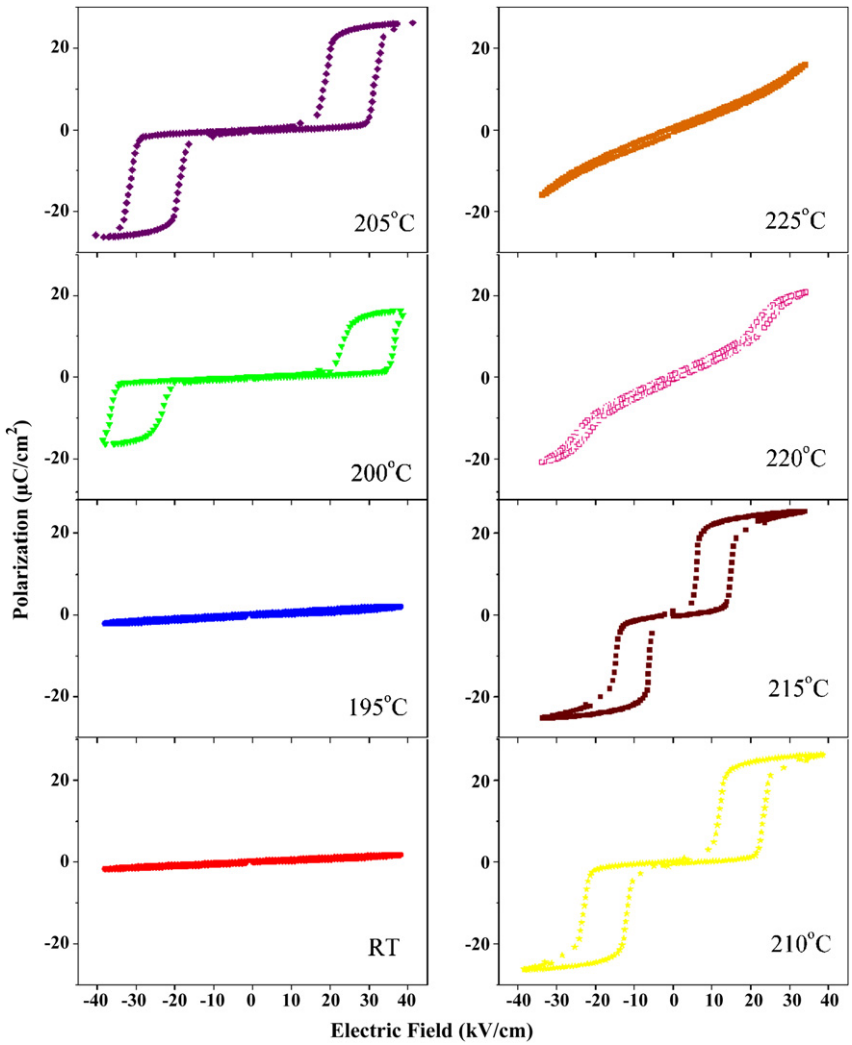

Fig. 5. Polarization hysteresis loops recorded from $Pb_{0.94}Bi_{0.04}Zr_{0.97}Al_{0.04}O_3$ ceramic at 4 Hz during heating.

material can therefore store much more energy than either the ferroelectric or linear dielectric materials.

There is good agreement between results of the three different investigation techniques. The results indicated that BAO modification can stabilize an antiferroelectric state in perovskite PZO. It is well known that the ionic size and distribution of substituent on the A- and B-site have been shown to affect antiferroelectric phase stability. If A-site ions are replaced by larger ones or a B-site ion by a smaller one, ferroelectric phase stability is enhanced. However, if A-site ions are replaced by smaller ones, or a B-site ion by a larger one, then antiferroelectric phase stability is enhanced [37]. However, in the PZO–BAO system, the ionic radius of Bi^{3+} (1.17 Å) and Al^{3+} (0.535 Å) are both smaller than Pb^{2+} (1.29 Å) and Zr^{4+} (0.72 Å), respectively. These results clearly demonstrate that the stability in antiferroelectric phase PZO, by substituting Pb^{2+} (1.29 Å) with Bi^{3+} (1.17 Å) in the A-site of the ABO_3 perovskite structure, are much more pronounced than substitution of Zr^{4+} by Al^{3+} in the B-site of the perovskite structure. This is because the decreasing average rate of radii in the A-site (0.765 Å/mol) is much higher than that in the B-site radii (0.005 Å/mol) as shown in Table 1. The decreasing average of radii in the A-site causes decreasing space in which the B-site cation is allowed to "rattle". This in turn decreases the polarizability, which facilitates a decrease in the Curie point. The results clearly demonstrated that the ionic radii of the substituent are an important factor in controlling the structure-property relations by compositional design.

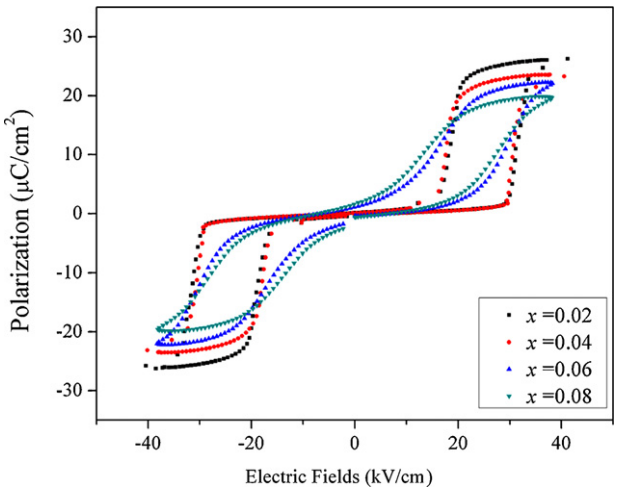

Fig. 6. Electric hysteresis loops of $(Pb_{(1-3x/2)}Bi_x)(Zr_{1-3x/4}Al_x)O_3$; $x = 0.02–0.08$ ceramics at 205 °C.

4. Conclusions

The investigation of $(Pb_{(1-3x/2)}Bi_x)(Zr_{1-3x/4}Al_x)O_3$; $x = 0.02–0.3$ using X-ray diffraction, dielectric behavior, thermal properties and ferroelectric measurements have shown clearly that phase

pure perovskite ceramics in the $(Pb_{(1-3x/2)}Bi_x)(Zr_{1-3x/4}Al_x)O_3$ system can be prepared by the solid-state reaction method with up to 10 mol% of $BiAlO_3$. Phase-pure perovskite structures with orthorhombic symmetry were obtained for $x \leq 0.1$; however $x \geq 0.1$, A cubic pyrochlore phase $Pb_{0.33}Bi_{0.87}O_{1.33}$ began to develop at $x \geq 0.1$ and increased in intensity with increasing BAO concentration. The substitution of the relatively smaller Bi^{3+} and Al^{3+} for the comparatively larger Pb^{2+} and Zr^{4+} led to a decrease in the unit cell volume. Dielectric, thermal and P–E hysteresis results confirmed that there was no ferroelectric intermediate phase in the PZO–BAO system, and only antiferroelectric to paraelectric phase transition was obtained for a wide temperature range. The results confirmed that BAO is shown to be a stable antiferroelectric state in PZO in a wide temperature range. The stability in antiferroelectric phase PZO by substituting Pb^{2+} (1.29 Å) with Bi^{3+} (1.17 Å) in the A-site of the ABO_3 perovskite structure is much more pronounced than substitution of Zr^{4+} by Al^{3+} in the B-site of the perovskite structure. The $(Pb_{(1-3x/2)}Bi_x)(Zr_{1-3x/4}Al_x)O_3$ solid solution offers a material system for possible applications in high-energy-storage capacitors and electromechanical transducers.

Acknowledgements

This research was supported by a grant from the Thailand Research Fund (TRF) National Research Council of Thailand (NRCT) and the National Nanotechnology Center (NANOTEC) NSTDA, Ministry of Science and Technology, Thailand, through its “Center of Excellence Network” program.

References

[1] F. Jona, G. Shirane, F. Mazzi, R. Pepinsky, Phys. Rev. 105 (1957) 849–856.
[2] D. Xunhu, Z. Xu, V. Dwight, J. Appl. Phys. 77 (1995) 5086–5094.
[3] X. Dai, J.F. Li, D. Viehland, Phy. Rev. B 51 (1995) 2651–2655.
[4] B.P. Pokharel, D. Pandey, J. Appl. Phys. 86 (1999) 3327–3332.
[5] B.P. Pokharel, D. Pandey, Phys. Rev. B 65 (2002) 214108.
[6] N. Vittayakorn, T. Bongkarn, G. Rujijanagul, Physica B 387 (2007) 415–420.
[7] X. Hao, Z. Zhang, J. Zhou, S. An, J. Zhai, J. Alloys Compd. 501 (2010) 358–361.
[8] S. Wirunchit, P. Laoratanakul, N. Vittayakorn, J. Phys. D: Appl. Phys. 41 (2008) 125406.
[9] N. Vittayakorn, S. Wirunchit, Smart Mater. Struct. 16 (2007) 851–857.
[10] S. Wirunchit, N. Vittayakorn, J. Appl. Phys. 104 (2008) 024103.
[11] W. Banlue, N. Vittayakorn, Ferroelectrics 382 (2009) 122–126.
[12] W. Banlue, N. Vittayakorn, Appl. Phys. A 93 (2008) 565–569.
[13] N. Vittayakorn, W. Banlue, Ferroelectrics 382 (2009) 110–114.
[14] P. Charoonsuk, S. Wirunchit, R. Muanghlua, S. Niemcharoen, B. Boonchom, N. Vittayakorn, J. Alloys Compd. 506 (1) (2010) 313–316.
[15] R.E. Eitel, C.A. Randall, T.R. Shrout, P.W. Rehrig, W. Hackenberger, S.E. Park, Jpn. J. Appl. Phys. 40 (2001) 5999–6002.
[16] C.J. Stringer, T.R. Shrout, C.A. Randall, I.M. Reaney, J. Appl. Phys. 99 (2006) 024106.
[17] M.R. Suchomel, P.K. Davies, J. Appl. Phys. 96 (2004) 4405–4410.
[18] M.R. Suchomel, P.K. Davies, Appl. Phys. Lett. 86 (2005) 262905.
[19] M.R. Suchomel, A.M. Fogg, M. Allix, H. Niu, J.B. Claridge, M.J. Rosseinsky, Chem. Mater. 18 (2006) 4987–4989.
[20] P. Baettig, C.F. Schelle, R. LeSar, U.V. Waghmare, N.A. Spaldin, Chem. Mater. 17 (2005) 1376–1380.
[21] A.A. Belik, T. Wuernisha, T. Kamiyama, K. Mori, M. Maie, T. Nagai, Y. Matsui, E. Takayama-Muromachi, Chem. Mater. 18 (2005) 133–139.
[22] R. Zuo, D. Lv, J. Fu, Y. Liu, L. Li, J. Alloys Compd. 476 (2009) 836–839.
[23] R. Ranjan, A.K. Kalyani, R. Garg, P.S.R. Krishna, Solid State Commun. 149 (2009) 2098–2101.
[24] T. Badapanda, S.K. Rout, L.S. Cavalcante, J.C. Sczancoski, S. Panigrahi, T.P. Sinha, E. Longo, Mater. Chem. Phys. 121 (2010) 147–153.
[25] L.S. Cavalcante, V.S. Marques, J.C. Sczancoski, M.T. Escote, M.R. Joya, J.A. Varela, M.R.M.C. Santos, P.S. Pizani, E. Longo, Chem. Eng. J. 143 (2008) 299–307.
[26] R.D. Shannon, Acta Cryst. A 32 (1976) 751–767.
[27] T.J.B. Holland, S.A.T. Redfern, Miner. Mag. 61 (1997) 65–77.
[28] A.K. Kalyani, R. Garg, R. Ranjan, Appl. Phys. Lett. 94 (2009) 202903.
[29] K.J. Rao, C.N.R. Rao, Phase Transitions in Solid: An Approach to the Study of the Chemistry and Physics of Solids, McGraw-Hill, New York, 1978.
[30] M.E. Lines, A.M. Glass, Principles and Applications of Ferroelectrics and Related Materials, Clarendon press, Oxford, 1977.
[31] S.A. Halawy, N.E. Fouad, M.A. Mohamed, M.I. Zaki, J. Therm. Anal. Calorim. 82 (2005) 671–675.
[32] R.H. Abu-Eittah, N.G. ZaKi, M.M.A. Mohamed, L.T. Kamel, J. Anal. Appl. Pyrol. 77 (2006) 1–11.
[33] C. Stenger, A.J. Burggraaf, Phys. Stat. Sol. 61 (1980) 275–285.
[34] F. Moura, A.Z. Simões, L.S. Cavalcante, M.A. Zaghete, J.A. Varela, E. Longo, J. Alloys Compd. 466 (1–2) (2008) L15–L18.
[35] D. Berlincourt, IEEE Trans. Sonics Ultrason. Ind. Eng. Chem. SU-13 (1966) 116–124.
[36] B. Chu, X. Zhou, K. Ren, B. Neese, M. Lin, Q. Wang, F. Bauer, Q.M. Zhang, Science 313 (2006) 334–336.
[37] Q. Tan, Z. Xu, D. Viehland, J. Mater. Res. 14 (1999) 4251.

Journal of Alloys and Compounds 509 (2011) 2445–2449

Contents lists available at ScienceDirect

Journal of Alloys and Compounds

journal homepage: www.elsevier.com/locate/jallcom

Solution combustion synthesis and characterization of lead-free piezoelectric sodium niobate ($NaNbO_3$) powders

Nopsiri Chaiyo[a,b], Rangson Muanghlua[c], Surasak Niemcharoen[c], Banjong Boonchom[d], Naratip Vittayakorn[a,b,e,*]

[a] Electroceramic Research Laboratory, College of KMITL Nanotechnology, King Mongkut's Institute of Technology Ladkrabang, Bangkok 10520, Thailand
[b] ThEP Center, CHE, 328 Si Ayutthaya Rd., Bangkok 10400, Thailand
[c] Department of Electronics, Faculty of Engineering, King Mongkut's Institute of Technology Ladkrabang, Bangkok 10520, Thailand
[d] King Mongkut's Institute of Technology Ladkrabang, Chumphon Campus, 17/1 M. 6 Pha Thiew District, Chumphon 86160, Thailand
[e] Department of Chemistry, Faculty of Science, King Mongkut's Institute of Technology Ladkrabang, Bangkok 10520, Thailand

ARTICLE INFO

Article history:
Received 20 July 2010
Received in revised form 27 October 2010
Accepted 8 November 2010
Available online 13 November 2010

Keywords:
Sodium niobate
Modified solid state reaction

ABSTRACT

Nano-crystalline sodium niobate ($NaNbO_3$) powder was synthesized by the solution combustion synthesis of sodium nitrate ($NaNO_3$) and Nb_2O_5 using glycine as the fuel. The chemical reaction, nucleation mechanisms and influence of the fuel-to-oxidizer ratio to phase formation were studied. The precursor and product powders were characterized, using thermo gravimetric analysis (TGA), differential thermal analysis (DTA), the X-ray diffraction technique (XRD), scanning electron microscope (SEM) and Fourier transform infrared (FTIR) spectroscopy. As-prepared powder possesses an orthorhombic crystal structure with an X-ray diffraction pattern that could be matched with the perovskite, $NaNbO_3$ JCPDS no. 82-0606. Perovskite $NaNbO_3$ phase, with a mean crystalline size (calculated by X-ray line broadening) ranging from 44.51 ± 11.99 nm (ratio of 0.7) to 26.11 ± 13.69 nm (ratio of 2.0) was obtained. The SEM image shows polyhedral-shaped powder with a mean particle size of 137 ± 52 nm and 226 ± 46 nm for as-prepared and calcined powder, respectively.

1. Introduction

Sodium niobate ($NaNbO_3$) is a perovskite with an inorganic complex oxide and the empirical formula, ABO_3. It is among the candidates for lead-free substances that avoid toxicity of lead-based piezoelectric materials (e.g. PZT [1,2]), and is concerned about the environment. $NaNbO_3$ has been studied widely for its unusual structural transition series [3–7]. It has a ferroelectric rhombohedral phase below −100 °C, and is antiferroelectric with orthorhombic symmetry between −100 °C and 640 °C [4]. Finally, it possesses cubic paraelectric above 640 °C [5], and in addition, its antiferroelectric, perovskite-type nature can transform into a ferroelectric one by chemical doping, i.e. K^+ [6,7] and Li^+ [8].

Generally, alkali niobate powders are synthesized by conventional solid state reaction, where alkali metal carbonate or oxide compound of starting materials are heated at high temperature (800 °C or above) for a long duration [8,9]. High calcination temperature can cause volatilization of alkali metal, thus causing this classical method difficulty in achieving a homogeneous mixture of the component [8–10]. Powder agglomeration can occur during heating, which could affect properties such as low surface area and low sinterability [10]. Thus, this method does not always allow for the production of dense, homogeneous single phase ceramics. Therefore, development of alternative methods that can produce powder with high sinterability and controlled stoichiometric composition is necessary. In recent years, ultra fine ceramic powder, which is synthesized using mechanochemical synthesis [11], polymeric precursors [12], and hydrothermal and polymerized complex methods [13], has been described in the literature to enable production of desired compositions. While synthesizing powder rapidly, with the desired composition, high porosity and high sinterability remains a challenge, combustion synthesis (CS) has been found as a potential solution for this problem.

Combustion synthesis (CS) or self-propagating high temperature synthesis (SHS) is an effective, low-cost method for producing various industrially useful materials. It has been introduced as a quick, straightforward preparation process for producing homogeneous, very fine, crystalline and unagglomerated multicomponent oxide ceramic powders, without intermediate decomposition and/or calcination steps [14,15]. The combustion synthesis technique begins with a mixture of easily oxidized reactants (such as nitrates) and a suitable organic fuel (such as urea [16], tartalic acid

* Corresponding author at: Department of Chemistry, Faculty of Science, King Mongkut's Institute of Technology Ladkrabang, Bangkok 10520, Thailand.
Fax: +66 2 326 4415.
E-mail address: naratipcmu@yahoo.com (N. Vittayakorn).

0925-8388/$ – see front matter © 2010 Elsevier B.V. All rights reserved.
doi:10.1016/j.jallcom.2010.11.043

[17], alanine [18], glycine [19], etc.), which acts as a reducing agent. The mixture is then heated until it ignites, which is when the temperature of rapid exothermal chemical reaction commences, and a self-sustaining combustion reaction starts. This highly exothermic reaction produces a high temperature and duration long enough for the synthesis to occur, even in the absence of an external heating source [20]. Ultrafine nano-sized powder also can be prepared by releasing a large amount of gas from the system. This process results in a dry, fluffy, crystalline, unagglomerated and fine oxide powder. Metal nitrate was found to be the salt preferred, due to its water solubility, and homogeneous solution could be achieved easily by melting at a low temperature [16].

However, it was reported that an exothermic redox reaction (oxidation and reduction reaction taking place simultaneously) could be initiated only when the oxidizer and fuel are mixed intimately in a fixed proportion. The basis of the combustion synthesis process derives from the thermochemical concepts used in propellant chemistry [21,22]. The method consists of establishing a simple valency balance, irrespective of whether the elements are present in the oxidizer or fuel components of the mixture, and then calculating the stoichiometric composition of the starting mixture, which is equivalent to the release of maximum energy. The assumed valencies, which are presented as usual products of the combustion reaction, consist of CO_2, H_2O and N_2. Therefore, carbon and hydrogen are considered as reducing elements with the corresponding valencies of +4 and +1, whereas oxygen is thought to be an oxidizing agent with a valency of −2, and nitrogen a valency of 0. To extrapolate the concept of combustion synthesis of ceramic oxide means considering metals as reducing agents with their valencies in the corresponding oxide or nitrate, i.e. +2 for magnesium (oxide), +3 for cerium (nitrate) and +4 for cerium (oxide). In the case of multiple valence elements, the final product is used for calculation.

The elemental stoichiometric coefficient, φ, which is the ratio between the total valencies of fuel (glycine; NH_2CH_2COOH) and that of the oxidizer (sodium nitrate), can be calculated following the method proposed by Jain et al. [21]:

$$\varphi = \frac{n(0_{(N)} + 2 \times 1_{(H)} + 4_{(C)} + 2 \times 1_{(H)} + 4_{(C)} - 2_{(O)} - 2_{(O)} + 1_{(H)})}{1_{(Na)} + 0_{(N)} + 3 \times -2_{(O)}} \quad (1)$$

where n is the mole of glycine. According to the propellant chemistry for stoichiometric redox reaction between fuel and an oxidizer, the φ ratio should be united (stoichiometric). A $\varphi < 1$ means oxidant-rich condition and $\varphi > 1$ means fuel-rich condition. To satisfy the principle in the present system, the sodium nitrate (oxidizing valency = 5−) to glycine (reducing valency = 9+) molar ratio was found to be 1:0.56. The comprehensive reaction that formed $NaNbO_3$ can be written as:

$$36NaNO_3 + 18Nb_2O_5 + 20NH_2CH_2COOH \rightarrow 36NaNbO_3 + 50H_2O + 28N_2 + 40CO_2 \quad (2)$$

It should be noted that various fuel-to-oxidizer ratios should be carried out for investigating and comparing the effect of fuel-rich/fuel-lean mixtures on the synthesis of sodium niobate powder. In this study, sodium niobate powder was synthesized via the combustion synthesis technique for the first time. This process used sodium nitrate and niobium pentoxide as starting materials, and glycine was used as fuel. The different fuel-to-oxidizer molar ratios such as fuel-deficient (<0.56), equivalent stoichiometric (0.56) and fuel-rich (>0.56) condition were applied.

2. Experimental procedure

For the combustion synthesis of perovskite sodium niobate powder, AR grade sodium nitrate ($NaNO_3$ 99.5%) and niobium pentoxide (Nb_2O_5 99.95%) were used as the oxidizer, and glycine (NH_2CH_2COOH 99.7%) as fuel. The appropriate amount of starting materials was weighed, mixed with de-ionized water in a glass beaker and stirred regularly for 30 min. The fuel (glycine) was then added and the mixture stirred for 30 min. After that, the solution precursor was boiled on a hotplate and then evaporated. Once the solution had thickened and begun to dry, the ignition took place when the temperature rapidly increased, which resulted in self-sustaining combustion with rapid evolution of a large volume of gas products, and formation of voluminous powder. For investigating thermal behavior of the precursor, the mixture of starting material was determined using thermo gravimetric analysis (TGA) and differential thermal analysis (DTA). The X-ray diffraction (XRD, Advance D8) technique was carried out on the combustion synthesized powder, using Ni-filtered CuK_α radiation for phase identification and mean crystalline size estimation. The final powder product was characterized by using the Fourier transform infrared (FTIR) technique and scanning electron microscope (SEM, Hitachi S4700).

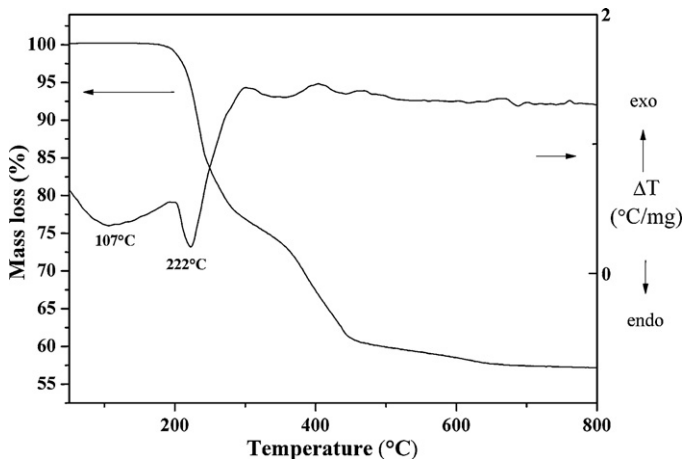

Fig. 1. TG-DTA curves of the precursor mixed in the stoichiometric proportion of $NaNbO_3$.

3. Results and discussion

Fig. 1 shows the TG/DTA plots of the stoichiometric precursor for $NaNbO_3$ powder synthesis. From observations of the TGA curve, there appeared to be three-stages of weight loss from room temperature to 800 °C. The definition of initial temperature (T_{in}) is when the sample weight starts changing rapidly during the chemical reaction [23]. As the precursor was heated, a significant weight loss was observed as the temperature reached 170 °C, indicating that the T_{in} was around this heat. The weight loss did not stop until the temperature reached 480 °C. It was indicated clearly that this reaction belongs to a multi-stage reaction. The overall weight loss was found to be about 40%, which is close to the theoretical value of 36.87% that corresponds to the release of 50 mol H_2O, 28 mol N_2 and 40 mol CO_2 related to Eq. (2). This outcome supported our conception that a hotplate can be used as a heating source because it is capable of initiating the combustion reaction at a temperature as low as that of the T_{in}.

The evolution XRD pattern of the combustion synthesized ceramic powder, with the fuel-to-oxidizer molar ratio, is illustrated in Fig. 2. The fuel-deficient (0.5) and equivalent stoichiometric ratio (0.56), were found (according to experimental observation) to have no ignition and combustion reaction in those compositions. Their XRD patterns correlated to detection results of the diffraction peaks of Nb_2O_5 (●) (JCPDS file no. 30-0873) and $NaNO_3$ (■) (JCPDS file no. 85-0859) starting materials, with no evidence of perovskite $NaNbO_3$ phase found. Although the equivalent stoichiometric ratio (0.56) was calculated for maximum energy release, auto-ignition did not occur in this study. This could indicate that oxygen deficiency in the system and its environment might lead to combustion reaction and fail to follow the theory. The fuel-to-oxidizer molar ratio was increased by using the fuel-rich condition (>0.56), which was found to produce the perovskite $NaNbO_3$ ceramic powder, due to its diffraction peaks being detected for all different fuel contents

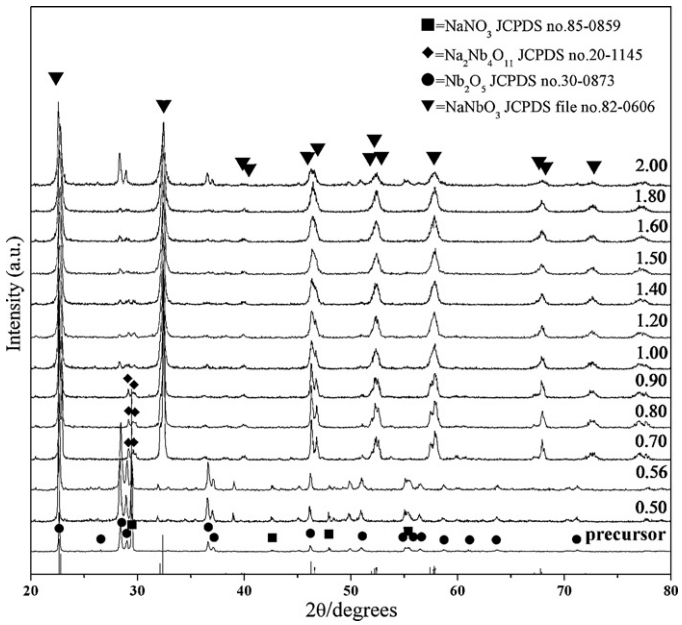

Fig. 2. X-ray diffraction patterns of $NaNbO_3$ powder obtained from various fuel-to-oxidant molar ratios.

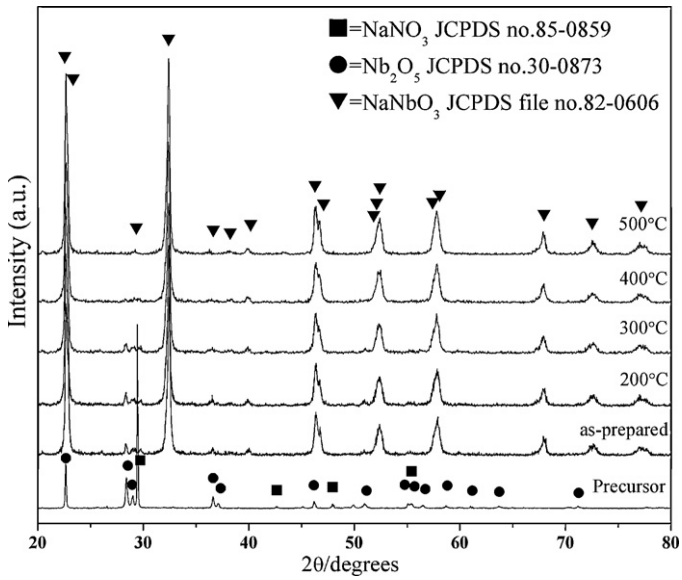

Fig. 3. X-ray diffraction patterns of $NaNbO_3$ powder (obtained from the fuel-to-oxidant molar ratio of 1.0) calcined at various temperatures for 4 h with a heating/cooling rate of 20 °C/min.

(fuel-to-oxidizer molar ratio ranging from 0.7 to 2.0). This $NaNbO_3$ phase (▼) was consistent with JCPDS file no. 82-0606, which corresponded to an orthorhombic structure with the space group, $P2_1ma$ (26). For a fuel-rich condition (fuel-to-oxidizer molar ratio of 0.7, 0.8 and 0.9), the $NaNbO_3$ phase (▼) was detected with the accompanying pyrochlore phase of $Na_2Nb_4O_{11}$ (♦), which matched JCPDS file no. 20-1145. No evidence of unreacted Nb_2O_5 and/or $NaNO_3$ diffraction peak was found. As fuel content increased from the fuel-to-oxidizer molar ratio of 1.0–2.0, unreacted Nb_2O_5 (●) (JCPDS file no. 30-0873) was found together with a majority of $NaNbO_3$ diffraction peaks. From the reflection peak, the average crystalline size (D) of $NaNbO_3$ powders was considered as a function of fuel content by using X-ray line broadening through Scherrer's equation [24]:

$$D = \frac{k\lambda}{\beta \cos \theta_B} \quad (3)$$

where D is the average crystalline size, k a constant taken as 0.89, λ the wavelength of X-ray radiation, β the full width at half maximum (FWHM) and θ_B the diffraction angle. The consequent values are reported in Table 1. As the fuel content increased, the average crystalline size (D) was found to decreased from 44.51 ± 11.99 nm (ratio of 0.7) to 26.11 ± 13.69 nm (ratio of 2.0). This suggested that elevated fuel content could lead to the production of a smaller crystalline size (related to a small particle size) of powder. Nevertheless, as a consequence of additional cost and more carbon residual, an extremely high fuel-to-oxidizer molar ratio (fuel-rich ratio) did not always result in the desired production of powder [25].

Therefore, from findings on the fine nucleation condition of monophasic $NaNbO_3$ phase, the fuel-to-oxidizer molar ratio of 1.0 was selected to investigate the effect of calcination temperature. From this ratio, the volume fraction of the perovskite phase formation (%perovskite) of as-prepared powder was found to be as high as 93%. This relative value was considered by approximately calculating the ratio of the main X-ray peak intensities of $NaNbO_3$ and Nb_2O_5 phases [26], according to the following equation; $\%\ \text{perovskite} = (I_{\text{perovskite}}/(I_{\text{perovskite}} + I_{Nb_2O_5})) \times 100$. Thus, the as-prepared powder was calcined at different temperatures for 4 h with a heating/cooling rate of 20 °C/min. The X-ray diffraction (XRD) patterns of sodium niobate ($NaNbO_3$) powder, calcined for 4 h at different temperatures, are illustrated in Fig. 3. As the XRD pattern of as-prepared powder was composed of a slight Nb_2O_5 (●) (JCPDS file no. 30-0873) phase, the intensity of that phase was found to decrease with increasing calcination temperature. The diffraction peak corresponded to the Nb_2O_5, which disappeared after calcination at 400 °C for 4 h, whereas monophasic perovskite $NaNbO_3$ phase was obtained. This result suggested that the perovskite $NaNbO_3$ powder could be synthesized by using the combustion synthesis process and calcinations at 400 °C for 4 h. This process was found to be a simple, rapid and cost-effective method when compared with the traditional solid-state reaction, which takes longer time and requires higher temperature [8,9]. In addition, the mean crystalline size (D), which is reported in Table 1, was not significantly varied between as-prepared powder (29.28 ± 5.29 nm) and increasing calcination temperatures of up to 400 °C (27.84 ± 7.12 nm). It can be suggested that calcina-

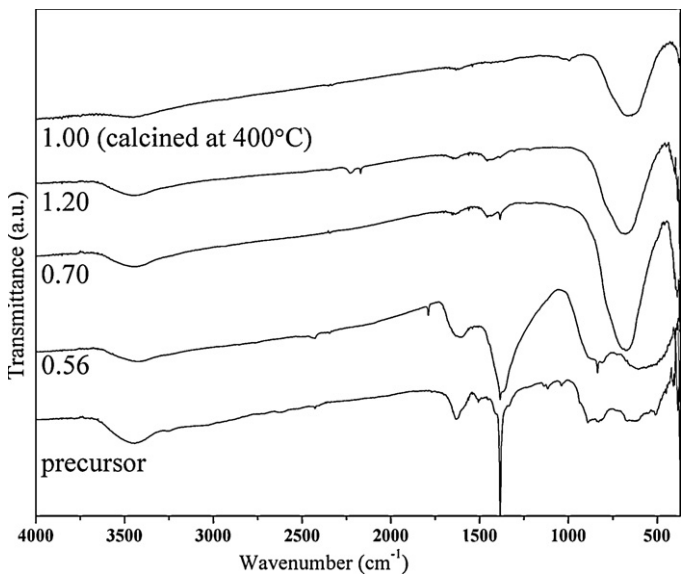

Fig. 4. FT-IR spectra of the precursor mixed in the stoichiometric proportion of $NaNbO_3$ powder obtained from various fuel-to-oxidant molar ratios and after the calcination step.

Table 1
Mean crystalline size, *D*, of $NaNbO_3$ powder obtained from various fuel-to-oxidant molar ratios.

	Fuel-to-oxidant molar ratios								
	0.7	0.8	0.9	1.0	1.2	1.4	1.6	1.8	2.0
As-prepared	44.51 ± 11.99	42.59 ± 11.54	37.31 ± 8.54	29.09 ± 5.29	27.45 ± 5.86	26.29 ± 5.97	24.40 ± 4.92	23.79 ± 5.52	26.12 ± 13.69
	Calcination temperature (°C)								
	200 °C	300 °C	400 °C	500 °C	600 °C	700 °C	800 °C	900 °C	
Calcined powder	29.95 ± 4.51	31.51 ± 4.02	27.84 ± 7.12	30 ± 82 ± 5.43	38.84 ± 8.09	60.72 ± 8.09	70.87 ± 9.22	85.27 ± 15.65	

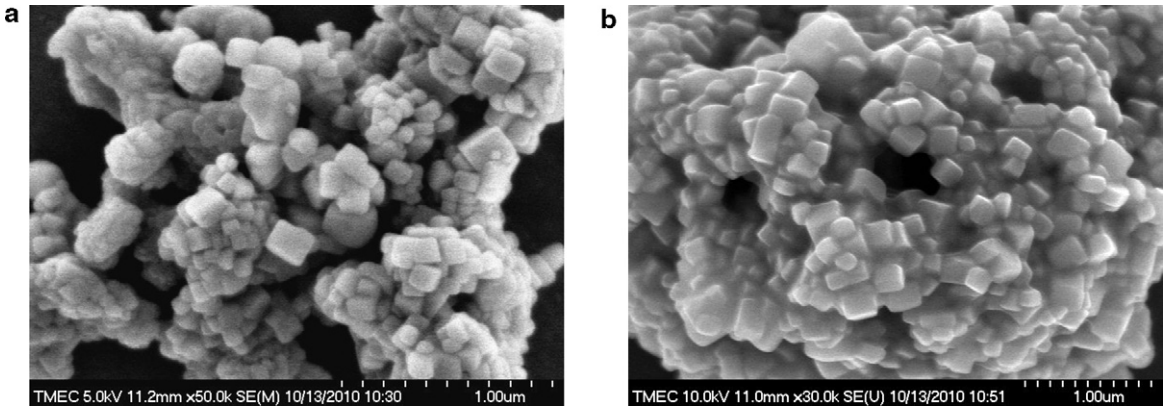

Fig. 5. SEM micrograph showing as-prepared $NaNbO_3$ powder synthesized using the fuel-to-oxidant molar ratio of 1.0 (a) and powder calcined at 400 °C for 4 h (b).

tions at this low temperature also produced a lower crystalline size when compared with the traditional solid state reaction method.

Fig. 4 shows the FT-IR spectroscopic studies of the crystalline $NaNbO_3$ obtained after combustion synthesis, its precursor without heat treatment and powder calcined at 400 °C for 4 h. For all powder, an IR band of around 3400 cm^{-1} was assigned to O–H asymmetric stretching (ν_3) [27], and on observation, it related to the moisture content of KBr. Regarding the precursor of $NaNbO_3$ powders without heat treatment, and as-prepared powder with a stoichiometric ratio (0.56), the IR spectrum indicated peaking of the characteristic band at ~1612, ~1385 and ~890 cm^{-1}, which corresponded to the anti-symmetric carboxyl group stretching vibration, anti-symmetry $NO_3{}^{-1}$ stretching and bending vibration, respectively [28]. This result proved existence of the carboxyl and $NO_3{}^{-1}$ group (belonging to the starting material) in those samples. With regard to fuel-rich ratios (0.7 and 1.2), the new broad absorption bands appeared after combustion at a low wave number of ~673 cm^{-1}, suggesting that the Nb–O bond formation did occur. This Nb–O bond was believed to be the vibration (ν_3) mode in the corner-shared NbO_6 octahedron, according to reported IR spectra of niobate glass ceramics [28]. This result led to the assumption that the perovskite $NaNbO_3$ phase was synthesized (which correlated to XRD analysis). However, the IR band of anti-symmetric COO^- and that of anti-symmetry $NO_3{}^{-1}$ stretching vibration also were observed. This clearly indicated traces of existent carboxyl group and nitrate in as-prepared $NaNbO_3$ powder, which cannot be detected when using the XRD technique. For powder calcined at 400 °C for 4 h, the spectra band of vibration (ν_3) mode belonging to the Nb–O bond was found without observation of any starting material band. This can indicate that monophasic perovskite $NaNbO_3$ has been synthesized successfully after calcination at a temperature as low as 400 °C for 4 h. Fig. 5 shows an SEM micrograph of the as-prepared $NaNbO_3$ powder using the fuel-to-oxidizer molar ratio of 1.0 (a) and powder calcined at 400 °C for 4 h (b). The powder was found to be polyhedral in shape, with uniform features. No evidence of a different or pyrochlore phase was found, which suggested the homogeneous character of the prepared powder. The average particle size, which can be estimated from micrographs, was found to be 137 ± 52 nm and 226 ± 46 nm for as-prepared and calcined powder, respectively. These particle size values are greater than the average crystalline size calculated from X-ray line broadening because a particle can be formed generally of many crystallites [29–31]. The particle growth for calcined powder seemed to be detected. It can be said that the firing process tends to produce agglomerated particles and grain growth, as reported by other works [32,33].

4. Conclusions

Crystalline $NaNbO_3$ powder, with a volume fraction of the perovskite phase formation (% perovskite) as high as 93%, was synthesized directly via the solution combustion process using $NaNO_3$, Nb_2O_5 and glycine. Monophasic perovskite $NaNbO_3$ powder was obtained after calcination at 400 °C for 4 h. The fuel-to-oxidizer molar ratio was found to affect the combustion reaction and character of the powder obtained. The average crystalline size (*D*) was found to decrease from 44.51 ± 11.99 nm (ratio of 0.7) to 26.11 ± 13.69 nm (ratio of 2.0). This method is a simple, rapid, cost- and time-saving way of synthesizing stoichiometric, homogeneous and fine $NaNbO_3$ powder with a low calcination temperature. The powder obtained was found to be a uniform soft agglomerated particle.

Acknowledgements

This work was supported by the Thailand Research Fund (TRF), Thailand Graduate Institute of Science and Technology (TGIST), King Mongkut's Institute of Technology Ladkrabang Research (KMITL Research), and the National Nanotechnology Center (NANOTEC) NSTDA, Ministry of Science and Technology, Thailand through its "Center of Excellence Network" Program.

References

[1] B. Jaffe, W.R. Cook Jr., H. Jaffe, Piezoelectric Ceramics, Academic Press, New York, 1971.
[2] B. Jaffe, R.S. Roth, S. Marzullo, J. Appl. Phys. 25 (1954) 809–810.
[3] N. Chaiyo, B. Boonchom, N. Vittayakorn, J. Mater. Sci. 45 (2010) 1443.
[4] H.D. Megaw, Ferroelectrics 7 (1974) 87–89.
[5] L.E. Cross, B. Nicholson, J. Phil. Magn. Ser. 46 (1955) 453–466.
[6] G. Shirane, B. Newnham, R. Pepinsky, Phys. Rev. 96 (1954) 581–588.
[7] Y. Shiratori, A. Magrez, C. Pithan, J. Eur. Ceram. Soc. 25 (2005) 2075–2079.
[8] T. Nitta, J. Am. Ceram. Soc. 51 (1968) 626–629.
[9] T. Rojac, O. Masson, R. Guinebretière, M. Kosec, B. Malič, J. Holc, J. Eur. Ceram. Soc. 17 (2007) 2265–2271.
[10] C.C. Hwang, T.Y. Wu, J.S. Tsai, Mater. Sci. Eng. B 111 (2004) 49–56.
[11] T. Rojac, M. Kosec, B. Malič, J. Holc, Mater. Res. Bull. 40 (2005) 341–345.
[12] M.A.L. Nobre, E. Longo, E.R. Leite, J.A. Varela, Mater. Lett. 28 (1996) 215–220.
[13] G. Li, T. Kako, D. Wang, Z. Zou, J. Ye, J. Phys. Chem. 69 (2008) 2487–2491.
[14] K.C. Patil, S.T. Aruna, S. Ekambaram, Curr. Opin. Solid State Mater. Sci. 2 (1997) 158–165.
[15] K.C. Patil, S.T. Aruna, T. Mimani, Curr. Opin. Solid State Mater. Sci. 6 (2002) 507–512.
[16] D.A. Fumo, M.R. Morelli, A.M. Segadães, Mater. Res. Bull. 31 (1996) 1243–1255.
[17] M.A. Raza, I.Z. Rahman, S. Beloshapkin, J. Alloys Compd. 485 (2009) 593–597.
[18] M.W. Raja, S. Mahanty, P. Ghosh, R.N. Basu, H.S. Maiti, Mater. Res. Bull. 42 (2007) 1499–1506.
[19] S.V. Chavan, P.U.M. Sastry, A.K. Tyagi, J. Alloys Compd. 456 (2008) 51–56.
[20] N.P. Bansal, Z. Zhong, J. Power Sources 158 (2006) 148–153.
[21] S.R. Jain, K.C. Adiga, V.R.P. Verneker, Combus. Flame 40 (1981) 71–79.
[22] S.S. Manoharan, K.C. Patil, J. Am. Ceram. Soc. 75 (1992) 1012–1015.
[23] L.A. Chick, L.R. Pederson, G.D. Maupin, J.L. Bates, L.E. Thomas, G.J. Exarthos, Mater. Lett 10 (1990) 6–12.
[24] H.P. Klug, L.E. Alexander, X-ray Diffraction Procedure of Polycrystalline and Amorphous Materials, Jonh Wciley & Sons, New York, 1974.
[25] A. Civera, M. Pavese, G. Saracco, V. Specchia, Catal. Today 83 (2003) 199–211.
[26] G. Feng, H. Rongzi, L. Jiaji, L. Zhen, C. Lihong, T. Changsheng, J. Eur. Ceram. Soc. 29 (2009) 1687–1693.
[27] C. Weifan, L. Fengsheng, L. Leili, L. Yang, J. Rare Earths 24 (2006) 782–787.
[28] S.H Xiao, W.F. Jiang, L.Y. Li, X.J. Li, Mater. Chem. Phys. 106 (2007) 82–87.
[29] M.L. Lavčević, A. Turković, Scripta Mater. 46 (2002) 501–505.
[30] W.-N. Wang, W. Widiyastuti, T. Ogi, I.W. Lenggoro, Chem. Mater. 19 (2007) 1723–1730.
[31] N. Izu, W. Shin, I. Matsubara, N. Murayama, Sens. Actuators B 94 (2003) 222–227.
[32] Y. Terashi, A. Purwanto, W.N. Wang, F. Iskandar, K. Okuyama, J. Eur. Ceram. Soc. 28 (2008) 2573.
[33] R. Wongmaneerung, W. Chaisan, O. Khamman, R. Yimnirun, S. Ananta, Ceram. Int. 34 (2008) 813.

Synthesis of potassium niobate (KNbO3) nano-powder by a modified solid-state reaction

Journal of Materials Science
Full Set - Includes

ISSN 0022-2461
Volume 46
Number 6

J Mater Sci (2010)
46:1585-1590
DOI 10.1007/
s10853-010-4967-5

J Mater Sci (2011) 46:1585–1590
DOI 10.1007/s10853-010-4967-5

Synthesis of potassium niobate ($KNbO_3$) nano-powder by a modified solid-state reaction

Nopsiri Chaiyo · Anucha Ruangphanit · Rangson Muanghlua · Surasak Niemcharoen · Banjong Boonchom · Naratip Vittayakorn

Received: 20 July 2010 / Accepted: 29 September 2010 / Published online: 15 October 2010

Abstract Crystalline lead-free piezoelectric potassium niobate ($KNbO_3$) powders have been synthesized through a modified solid-state reaction method. The thermal behavior of the $K_2C_2O_4{\cdot}H_2O$ and Nb_2O_5 raw material mixture was investigated by thermogravimetric analysis (TGA) and differential thermal analysis (DTA). The X-ray diffraction technique (XRD) was used to investigate the phase formation and purity. The morphology of the powder obtained was characterized using a scanning electron microscope (SEM). The XRD pattern showed that the monophasic perovskite phase of $KNbO_3$ could be synthesized successfully at a temperature as low as 550 °C for 240 min, with an average crystallite size of 36 ± 8 nm. The SEM images suggested that the average particle size of the powder obtained was 278 ± 75 nm.

N. Chaiyo · N. Vittayakorn
Electroceramic Research Laboratory, College of KMITL Nanotechnology, King Mongkut's Institute of Technology Ladkrabang, Bangkok 10520, Thailand

N. Chaiyo · N. Vittayakorn
ThEP Center, CHE, 328 Si Ayutthaya Rd, Bangkok 10400, Thailand

A. Ruangphanit
Thai Micro Electronics Center (TMEC), National Electronics and Computer Technology Center, Chachoengsao, Chachoengsao, Thailand

R. Muanghlua · S. Niemcharoen
Faculty of Engineering, Department of Electronics, King Mongkut's Institute of Technology Ladkrabang, Bangkok 10520, Thailand

B. Boonchom
King Mongkut's Institute of Technology Ladkrabang, Chumphon Campus, 17/1 M. 6 Pha Thiew District, Chumphon 86160, Thailand

N. Vittayakorn (✉)
Faculty of Science, Department of Chemistry, King Mongkut's Institute of Technology Ladkrabang, Bangkok 10520, Thailand
e-mail: naratipcmu@yahoo.com

Introduction

Lead zirconate titanate (PZT) ceramics are used widely in piezoelectric applications, due to their superior piezoelectric properties near the morphotropic phase boundary (MPB) [1, 2]. However, more than 50% of the lead-based piezoelectric material contains poisonous lead, which is a major drawback [3]. It has been reported that the use of lead-based ceramics causes serious environmental problems and numerous physical symptoms [3]. Furthermore, EU legislation will enforce draft directives for waste from electrical and electronic equipment (WEEE), and restrictions on the use of certain hazardous substances in electrical and electronic equipment (RoHS) and end-of life vehicles (ELV) [4–6]. According to these issues, lead and other heavy metals should be phased out, and alternative lead-free piezoelectric materials are receiving considerable attention.

Among various alternative families, perovskite type (ABO_3) ceramics have attracted much consideration. Among alkali metal niobates, potassium niobate ($KNbO_3$) is a well-known perovskite oxide that possesses attractive physical and piezoelectric properties [6–9]. Furthermore, the electromechanical coupling factor of the thickness-extensional mode, k_t, was reported to reach as high as 0.69 for the 49.5°-rotated X-cut on the Y-axis. This value of k_t is the highest among current lead-free piezoelectrics [10]. However, the main hindrance regarding this alkali niobate-based material lies in the difficulty of preparing dense and stoichiometric controlled ceramics using the conventional

solid-state reaction and ordinary air sintering methods [11, 12]. These difficulties are caused by potassium volatility at high temperatures and excessive reactivity with moisture [13, 14]. Thus, different additive methods, hot pressing and spark plasma sintering have been used to improve ceramic densification [12, 15–19].

Several alternative ways for preparing alkali niobates have been investigated and developed: the hydrothermal [20] and hydrothermal-assisted sol–gel method [22], and glycothermal [23], nitrate–tartarate precursor technique [21], etc. However, most chemical synthesis routes require high purity reactants, which are more expensive and demand complicated procedures and specific apparatus. A modified solid-state reaction method has been used to synthesize the $NaTaO_3$ perovskite type material successfully, with reduced reaction temperature [24]. In this method, the carbonate compound was replaced by oxalate, and the addition of urea played an important role. Recently, this method also has been applied to synthesize lead-free sodium niobate ($NaNbO_3$) powders (without fuel) [25]. By replacing sodium carbonate using oxalate as the raw material, a lower calcination temperature and fine powders with an average crystallite size of 31.45 ± 5.28 nm were achieved.

In this study, a modified solid-state reaction method, with an expected lower reaction temperature, was used to synthesize $KNbO_3$ particles, using potassium oxalate as raw material without the addition of any fuel. Effects of the calcination conditions on the $KNbO_3$ phase development were investigated by the X-ray diffraction technique (XRD) and a scanning electron microscope (SEM).

Experiment

$KNbO_3$ was synthesized by a modified solid-state reaction method. Reagent-grade potassium oxalate monohydrate ($K_2C_2O_4{\cdot}H_2O$, 99.9%) and niobium oxide (Nb_2O_5, 99.9%) were employed as the starting material. The raw materials were weighed in stoichiometric quantities following the equation below.

$$K_2C_2O_4 \cdot H_2O_{(s)} + Nb_2O_{5(s)} \rightarrow 2KNbO_{3(s)} + CO_{2(g)} + CO_{(g)} + H_2O \quad (1)$$

These starting materials were mixed by the ball-milling method using ethyl alcohol and partially stabilized zirconia balls for 18 h. Then, the mixture was dried on a hot plate with regular stirring for a suitable period. After drying, the precursor mixture was determined by thermo gravimetric analysis (TGA, Perkin Elmer) and differential thermal analysis (DTA, Perkin Elmer) for investigating the thermal behavior during heat treatment and finding the appropriate calcination temperature. Based on TG–DTA results, the mixture was placed subsequently in a closed alumina crucible, and calcined for different periods of time at various temperatures ranging from 300 to 700 °C, to investigate formation of the $KNbO_3$ phase.

Subsequently, calcined powders were inspected by room temperature X-ray diffraction (XRD, Advance D8), using Ni-filtered CuK_α radiation to examine the effect of thermal treatment on the phase development and optimal calcination condition of crystalline $KNbO_3$ powder formation. The room temperature FTIR spectra were recorded in the range of 4,000–400 cm^{-1} (Perkin-Elmer, Spectrum GX spectrometer), with eight scans and a resolution of 4 cm^{-1} using KBr pellets. Powder morphologies and particle size were figured directly using a scanning electron microscope (SEM, Hitachi S4700).

Results and discussion

Figure 1 shows the TG–DTA curves of the stoichiometric precursor of $KNbO_3$. The thermogravimetric (TG) curve of the $KNbO_3$ precursor shows three stages of weight loss from room temperature to 1,300 °C. Four endothermic peaks at 123, 398, 524 and 1,066 °C were observed in the differential thermal analysis (DTA) curve. Three weight-loss steps were observed in the ranges of 50–121, 121–172, and 416–532 °C. The corresponding weight losses seen were 3.92, 1.07, and 16.00%. The overall weight loss was found to be about 21%, which is close to the theoretical value of 20.01%, and corresponds to the release of 1 mol H_2O, 1 mol CO, and 1 mol CO_2 related to Eq. 1. In the temperature range from 50 to 121 °C (first stage), the initial weight loss of 3.92% showed decomposition of the oxalate molecule releasing water molecules (0.98 mol

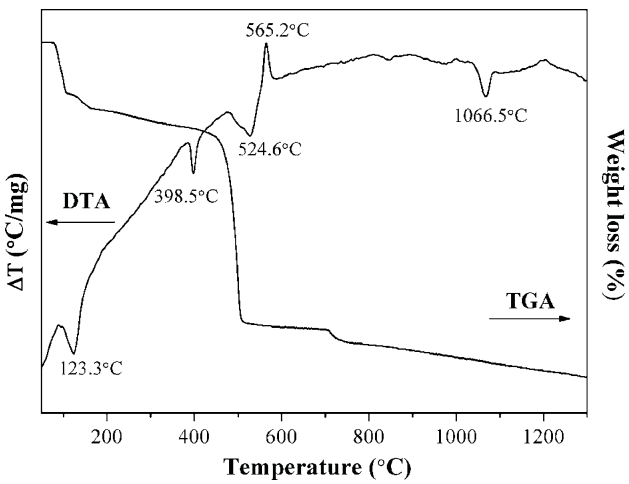

Fig. 1 TG–DTA curves of an uncalcined powder mixed in the stoichiometric proportion of $KNbO_3$

H_2O), which concurred with the theoretical value for releasing 1.00 mol H_2O (4.00%). This weight-loss corresponded to the endothermic peak, centered at 123 °C.

The second and third weight-loss steps illustrated the highest weight loss (~17%), which indicated a large elimination of organic compound that could be related to the release of CO and CO_2 by combustion reactions according to Eqs. 2 and 3 (16% theoretically). In the temperature range from 121 to 532 °C, the DTA curve shows corresponding endothermic peaks (398 and 524 °C) that agree with the TG result.

$$K_2C_2O_4 \rightarrow K_2CO_3 + CO \quad (2)$$

$$K_2CO_3 \rightarrow K_2O + CO_2 \quad (3)$$

However, an exothermic DTA peak was found centered at 565 °C. This implied that the third decomposition stage could lead to the formation of potassium niobate compound, which could be expected from the exothermic peak at 565 °C (as confirmed by XRD analysis in Fig. 2). As the temperature increased to 695 °C, weight loss was found to start again in the TGA curve, which could be correlated to the decomposition of the activated-K_2CO_3 residue. It is well known that $K_2C_2O_4$ decomposes to K_2CO_3 at a higher temperature; however, this carbonate residue could decompose at a lower temperature when its degree of arrangement is lower than its initial state [26]. When heating further, an endothermic peak (without the observed weight-loss stage) could correspond to the phase transformation at 1,066 °C. Therefore, temperatures from the above TG–DTA analysis, which ranged from 300 to 700 °C, were selected for calcinations and investigation of the phase formation. The mixture of raw materials in the required stoichiometric ratio was calcined in air using a heating/cooling rate of 20 °C/min at various temperatures and followed by the phase analysis using an X-ray diffractometer.

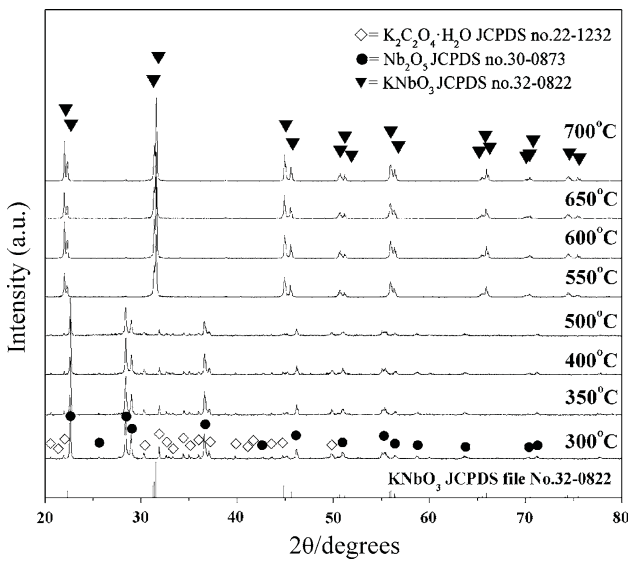

Fig. 2 X-ray diffraction patterns of $KNbO_3$ powder calcined at various temperatures for 4 h with a heating/cooling rate of 20 °C/min

The X-ray diffraction (XRD) patterns of potassium niobate ($KNbO_3$) powders, calcined for 4 h at different temperatures, are illustrated in Fig. 2. The diffraction pattern of the powder calcined at 300 °C suggests a composition of potassium oxalate (◇) (JCPDS no.22-1232) and niobium oxide (●) (JCPDS no.30-0873) raw materials. No evidence of the $KNbO_3$ perovskite phase was found. As calcination temperatures increased to 500 °C, diffraction peaks of un-reacted raw materials were also found, but with lower intensity. This could demonstrate that the completed reaction cannot occur at such a low temperature range. As the diffusion coefficient is a temperature dependent parameter, the rate of diffusion is affected greatly by higher temperatures [27], which also could improve higher atomic mobility [28]. Nonetheless, the powders calcined from 550 to 700 °C showed diffraction peaks that could correspond to the orthorhombic potassium niobate perovskite phase ($KNbO_3$) JCPDS no.32-0822 (▼). Amplified peak intensities can be seen after calcinations at increased temperatures. However, this result indicates the formation of $KNbO_3$ perovskite phase powder, which passes through the calcination temperatures from 550 to 700 °C in 4 h. These temperatures were lower than those in the chemical synthesis of $KNbO_3$, which used the polymerized complex method (PC method). This technique achieved the $KNbO_3$ compound after the calcination step at 900 °C [29], or once the citrate precursor route had obtained $KNbO_3$ nanopowder after heat treatment at 800 °C [30]. In addition, other chemical methods always require high purity reagent, which is more expensive, and involves complex procedures.

For a verdict on fine $KNbO_3$ nucleation condition, a temperature of 550 °C was chosen to find the effect of calcination dwell time. The mixture of raw material powder was calcined at 550 °C for 15–360 min. The XRD analysis of calcined powder, with a different dwell time (Fig. 3), revealed an amorphous phase for a calcination period of 15 min, and no distinct crystalline phase could be detected. The absence of reflection peaks that correspond to $K_2C_2O_4{\cdot}H_2O$ and Nb_2O_5 indicated the amorphous nature of the powder obtained. The presence of reflection peaks for the XRD pattern of powder calcined at 550 °C for 20 min or longer could be ascribed to the crystalline phase of the sample. The different diffraction pattern of the powder, calcined for 20 min, suggests the nucleation condition of the $KNbO_3$ phase, which was confirmed by further soaking time. After the calcination step at 550 °C for 20 min or longer, the powder showed an XRD pattern that could be matched with the perovskite potassium niobate (KN) phase

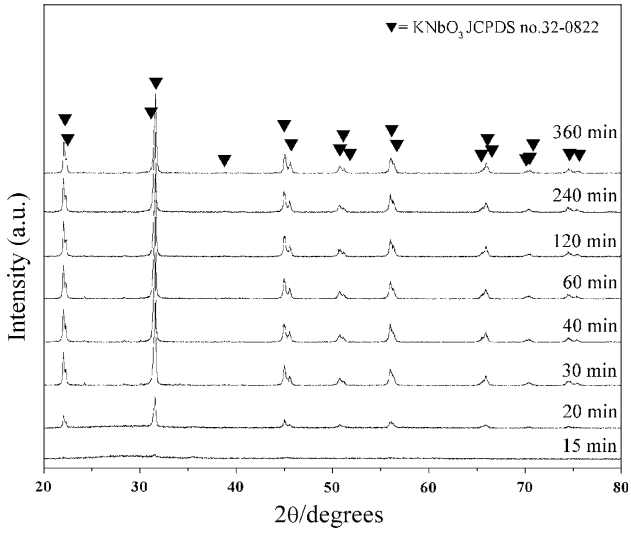

Fig. 3 X-ray diffraction patterns of $KNbO_3$ powder calcined at the calcination temperature of 550 °C for various dwell times with a heating/cooling rate of 20 °C/min

JCPDS no.32-0822. These XRD analyses agreed with the TG–DTA analysis, in which crystallization of the $KNbO_3$ phase was found around the previously mentioned temperature range. During the course of calcinations, the rise in calcination temperature and dwell time resulted in increased diffraction peak intensities, which related to higher crystallinity of the powder. This was supported by the increase in lattice parameters and average crystallite size, as revealed below. Nevertheless, it has been confirmed that this modified solid state reaction method can synthesize pure $KNbO_3$ phase powder by using potassium oxalate monohydrate as starting material at the calcination temperature of 550 °C for 20 min. This calcination temperature is much lower than that used in a mixed oxide powder process, which lies in the range of 800 °C [9, 11, 13, 31, 32], or solution process (sol–gel and precipitation methods) that requires calcination temperatures of over 600 °C [33, 34]. Since XRD analysis suggested an orthorhombic crystal structure for preparing $KNbO_3$ powder, lattice parameters of the sample could be deliberate by means of the UnitCell program package (ftp://rock.esc.cam.ac.uk/pub/minp/UnitCell/). The corresponding cell parameters, which are close to those reported from JCPDS file No.32-0822 ($a = 5.695$ nm, $b = 5.721$ nm, and $c = 3.973$ nm) are given in Table 1. The suggested orthorhombic crystal structure, obtained from matching with the JCPDS file, could be supported by this correlation of lattice parameters.

The average crystallite size of $KNbO_3$ powders was considered as a function of calcination temperature, and time for broadening the X-ray line of the reflection peak using Scherrer's equation [35]: $D = k\lambda/\beta\cos\theta_B$, where D is the average crystallite size, k a constant taken as 0.89, λ the wavelength of X-ray radiation, β the full width at half maximum (FWHM), and θ_B the diffraction angle. The corresponding values are reported in Table 2. The average crystallite size of powders, calcined from 550 to 700 °C for 4 h, was found to be about 36 ± 8 to 58 ± 6 nm. As the dwell time increased, it was found that the average crystallite size of calcined powders was increasing from 33 ± 9 to 36 ± 8 nm. The low D values suggest that the surface area of calcined powder was high enough to support high sinterability sufficiently [36]. The increase in crystallinity of the $KNbO_3$ phase was affected by increasing dwell time and calcination temperature. This consequence may confirm that the dwell time and calcination temperature also play an important role in developing the pure phase creation.

Figure 4 shows the FT-IR spectroscopic studies of the crystalline potassium niobate ($KNbO_3$) before and after the calcination step. The IR band for the uncalcined precursor was observed at 3,253 cm^{-1}, due to O–H asymmetric

Table 1 Lattice parameters of the $KNbO_3$ powder calcined at various calcination temperatures for 4 h

$KNbO_3$	Calcinations temperature (°C)			
Lattice parameter	550	600	650	700
a	5.6929 ± 0.0005	5.6876 ± 0.0070	5.7019 ± 0.0022	5.6952 ± 0.0028
b	5.6989 ± 0.0080	5.6994 ± 0.0048	5.7153 ± 0.0108	5.6980 ± 0.0060
c	3.9802 ± 0.0005	3.9768 ± 0.0006	3.9912 ± 0.0155	3.9777 ± 0.0030

Table 2 Mean crystalline size, D, of the $KNbO_3$ powder calcined at different temperatures for 4 h and for a different dwell time at 550 °C

$KNbO_3$	Calcination temperature (°C)			
	550	600	650	700
D	36.40 ± 8.25	41.46 ± 8.84	53.59 ± 6.56	57.81 ± 6.31

550 °C	Dwell time (min)					
	20	30	40	60	120	240
D	33.15 ± 9.22	34.36 ± 7.92	34.54 ± 8.128	35.30 ± 8.30	35.97 ± 6.47	36.40 ± 8.25

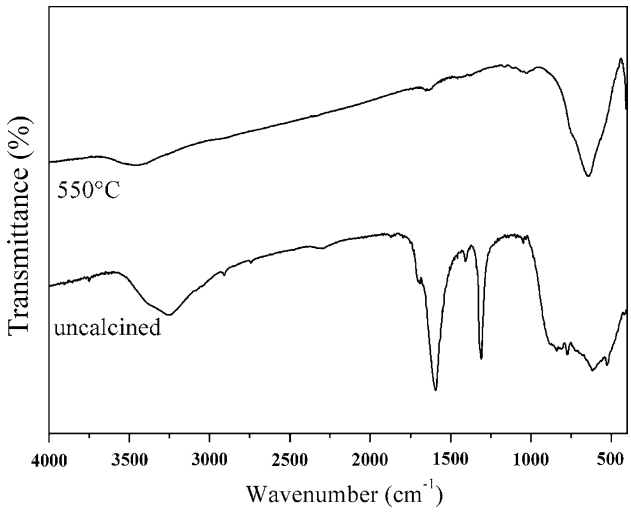

Fig. 4 FT-IR spectra of an uncalcined powder mixed in the stoichiometric proportion of $KNbO_3$ and $KNbO_3$ particles calcined at 550 °C

stretching (v_3), which related to the moisture content of the KBr pellet and scissor bending mode (v_2) of HO–H at 1,600 cm^{-1} and 1,310 cm^{-1}. When $KNbO_3$ powders were calcined at 550 °C for 4 h, the absorption of bands at a low wave number range of 620 cm^{-1} suggested occurrence of Nb–O bond formation, which was believed to be the vibration (v_3) mode in the corner-shared NbO_6 octahedron, according to the reported IR spectra of niobate glass ceramics [37]. This result shows that the perovskite $KNbO_3$ phase was synthesized, which correlated with other results. The TG result indicated that the mass loss in the TG curve at around 700 °C could be the result of the K_2CO_3 residue decomposition, however, the FTIR band corresponding to the C–O stretching mode of carbonate at 1,450 cm^{-1} [38] was not found in $KNbO_3$ powders calcined at 550 °C for 4 h. This observation could be described as the effect of dwell time.

Figure 5 shows SEM micrographs of $KNbO_3$ powder prepared using a modified solid state reaction method at 550 and 700 °C for 240 min. The $KNbO_3$ powder was found to be polyhedral in shape, with uniform features. The secondary phase could not be observed, which suggested the homogeneous character of the powder prepared. The mean particle sizes, which can be estimated from the micrographs, were found to be 278 ± 75 and 341 ± 80 for powder obtained at 550 and 700 °C, respectively. Particle growth was detected in powder calcined at a higher temperature. This value is greater than the average crystallite size, calculated from X-ray line broadening. It was believed that this contradictory value could indicate the agglomerate of the calcined powders. As reported by other studies [39, 40], the firing process tends to produce agglomerated particles and grain growth. No evidence of a different or pyrochlore phase was found. This outcome relates to the XRD result, in which the monophasic perovskite phase of $KNbO_3$ can be established after calcinations at 550 °C for 240 min.

Conclusion

Crystalline $KNbO_3$ powder was prepared from a modified solid state reaction of $K_2C_2O_4{\cdot}H_2O$ and Nb_2O_5. The final product was confirmed by XRD and SEM techniques. This is a simple cost- and time-saving method for synthesizing stoichiometric, homogeneous, and fine $KNbO_3$ powder, with a low calcination temperature of 550 °C for 240 min. This temperature is about 250 °C lower than others used, even in conventional methods. The powder obtained was found to be a uniform agglomerated particle that possesses an average crystallite size (defined by XRD) of between 36 ± 8 and 58 ± 6 nm, and a mean particle size (defined by SEM micrograph) of 278 ± 75 nm.

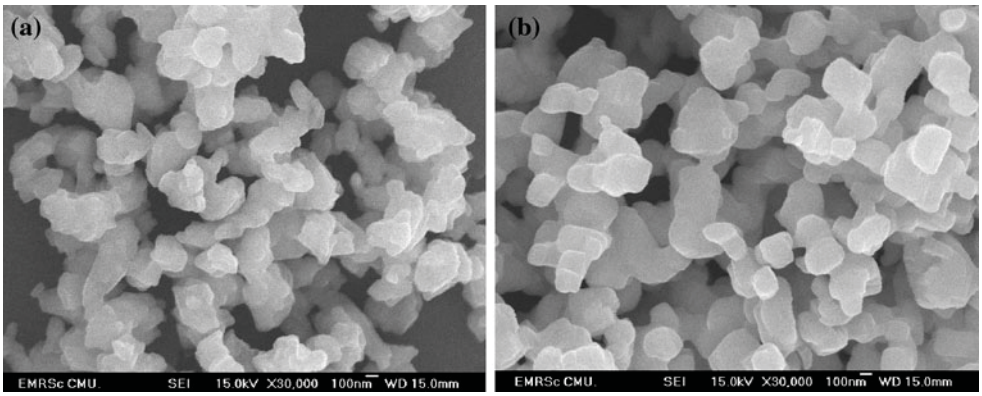

Fig. 5 SEM micrographs showing $KNbO_3$ powder synthesized at 550 °C (**a**) and 700 °C (**b**), for 4 h with a heating/cooling rate of 20 °C/min

Acknowledgements This study was supported by the Thailand Research Fund (TRF), Thailand Graduate Institute of Science and Technology (TGIST), and the National Nanotechnology Center (NANOTEC) NSTDA, Ministry of Science and Technology, Thailand, through its "Center of Excellence Network" Program.

References

1. Miclea C, Tanasoiu C, Miclea CF, Amarande L, Gheorghiu A, Spanulescu I, Plavitu C, Miclea CT, Cioangher MC, Trupina L, Iuga A (2007) J Eur Ceram Soc 27:4055
2. Setter N (2002) Piezoelectric materials in devices. Ceramic lab, EPFL, Switzerland
3. Lead and you: a guide to working safely with lead (2003) HSE (UK Health and Safety Executive). http://www.hse.gov.uk/pubns/indg305.pdf. Accessed 25 Apr 2004
4. Commission of the European Communities (2003) Directive 2002/96/EC of the European Parliament and of the Council of 27 January 2003 on waste electrical and electronic equipment (WEEE). Off J Eur Union, L37, 46:24
5. Commission of the European Communities (2003) Directive 2002/95/EC of the European Parliament and of the Council of 27 January 2003 on the restriction of the use of certain hazardous substances in electrical and electronic equipment. Off J Eur Union, L37, 46:19
6. Ichiki M, Zhang L, Tanaka M, Maeda R (2004) J Eur Ceram Soc 24:1693
7. Liu J-F, Li X-L, Li Y-D (2003) J Cryst Growth 247:419
8. Paula AJ, Parra R, Zaghete MA, Varela JA (2008) Mater Lett 62:2581
9. Yamanouchi K, Odagawa H, Kojima T, Matsumura T (1997) Electron Lett 33:193
10. Nakamura K, Kawamura Y (1999) Proc IEEE Ultrason Symp 2:1013
11. Matsumoto K, Hiruma Y, Nagata H, Takenaka T (2008) Ceram Int 34:787
12. Makovec D, Pribošič I, Drofenik M (2008) Ceram Int 34:89
13. Lu CH, Lo SY, Lin HC (1998) Mater Lett 34:172
14. Muthurajan H, Kumar HH, Samuel V, Gupta UN, Ravi V (2008) Ceram Int 34:671
15. Kim MS, Lee DS, Park EC, Jeong SJ, Song JS (2007) J Eur Ceram Soc 27:4121
16. Mgbemere HE, Herber R-P, Schneider GA (2009) J Eur Ceram Soc 29:1729
17. Wang R, Xie R, Sekiya T, Shimojo Y, Akimune Y, Hirosaki N, Itoh M (2002) Jpn J Appl Phys 41:7119
18. Ahn ZS, Schulze WA (1987) J Am Ceram Soc 70:18
19. Jaeger RE, Egerton L (1962) J Am Ceram Soc 45:209
20. Chang Y, Yang Z, Wei L, Liu B (2006) Mater Sci Eng A 437:301
21. Bhattacharyya K, Tyagi AK (2009) J Alloys Compd 470:580
22. Amini MM, Mirzaee M (2009) Ceram Int 35:2367
23. Lu C-H, Lo S-Y, Wang Y-L (2002) Mater Lett 55:121
24. Xu J, Xue D, Yan C (2005) Mater Lett 59:2920
25. Chaiyo N, Boonchom B, Vittayakorn N (2010) J Mater Sci 45:1443. doi:10.1007/s10853-009-4098-z
26. Vlaev L, Nedelchev N, Gyurova K, Zagorcheva M (2008) J Anal Appl Pyrolysis 81:253
27. Hsiao Y-J, Chang Y-H, Chang Y-S, Fang T-H, Chai Y-L, Chem G-J, Huang T-W (2007) Mater Sci Eng B 136:129
28. Callister WD (2007) Materials science and engineering: an introduction. Wiley, New York
29. Pribošič I, Makovec D, Drofenik M (2005) J Eur Ceram Soc 25:2713
30. Kakimoto K, Ito T, Ohsato H (2008) Jpn J Appl Phys 47:7669
31. Malic B, Bernard J, Bencan A, Kosec M (2008) J Eur Ceram Soc 28:1191
32. Chang Y, Yang Z-P, Ma D, Liu Z, Wang Z (2008) J Appl Phys 104:024109
33. Amini MM, Sacks MD (1991) J Am Ceram Soc 74:53
34. Kim KJ, Matijevic E (1992) J Mater Res 7:912
35. Klug HP, Alexander LE (1974) X-ray diffraction procedure of polycrystalline and amorphous materials. Wiley, New York
36. Lanfredi S, Dessemond L, Rodrigue ACM (2000) J Eur Ceram Soc 20:983
37. de Andrade JS, Pinheiro AG, Vasconcelos IF et al (1999) J Phys Condens Matter 11:4451
38. Böke HA, Akkurt S, Özdemir S, Göktürk EH, Saltik ENC (2004) Mater Lett 58:723
39. Terashi Y, Purwanto A, Wang WN, Iskandar F, Okuyama K (2008) J Eur Ceram Soc 28:2573
40. Wongmaneerung R, Chaisan W, Khamman O, Yimnirun R, Ananta S (2008) Ceram Int 34:813

Current Applied Physics 11 (2011) 434–437

Contents lists available at ScienceDirect

Current Applied Physics

journal homepage: www.elsevier.com/locate/cap

Phase transition behaviour and electrical properties of lead-free $(K_{0.5}Na_{0.5})NbO_3$–$LiNbO_3$–$LiSbO_3$ piezoelectric ceramics

Rangson Muanghlua [a], Surasak Niemcharoen [a], Manoon Sutapun [b,e], Banjong Boonchom [c], Naratip Vittayakorn [b,d,e,*]

[a] Department of Electronics, Faculty of Engineering, King Mongkut's Institute of Technology Ladkrabang, Bangkok 10520, Thailand
[b] Electroceramic Research Laboratory, College of KMITL Nanotechnology, King Mongkut's Institute of Technology Ladkrabang, Bangkok 10520, Thailand
[c] King Mongkut's Institute of Technology Ladkrabang, Chumphon Campus, 17/1M. 6 Pha Thiew District, Chumphon 86160, Thailand
[d] Department of Chemistry, Faculty of Science, King Mongkut's Institute of Technology Ladkrabang, Bangkok 10520, Thailand
[e] ThEP Center, CHE, 328 Si Ayutthaya Rd., Bangkok 10400, Thailand

ARTICLE INFO

Article history:
Received 28 September 2009
Received in revised form
21 July 2010
Accepted 18 August 2010
Available online 9 September 2010

Keywords:
Lead-free piezoelectric
Dielectric properties
Perovskite structure
$(K_{0.5}Na_{0.5})NbO_3$
$LiNbO_3$
$LiSbO_3$

ABSTRACT

The ternary system of $0.945(K_{0.5}Na_{0.5}NbO_3)$–$(0.055-x)LiNbO_3$–$xLiSbO_3$ [0.945KNN–$(0.055-x)$LN–xLS]; $x = 0.0$–0.055 lead-free piezoelectric ceramics was fabricated by the conventional mixed oxide method with normal sintering. The crystal structure was studied by means of X-ray diffraction (XRD). The results of XRD patterns show that complete solid solutions of the mixed phase between the orthorhombic and tetragonal perovskite phase were observed. The DSC and dielectric data show that the amount of $LiSbO_3$ in $K_{0.5}Na_{0.5}NbO_3$–$LiNbO_3$ solid solution slightly decreases the paraelectric cubic-ferroelectric tetragonal phase transition (T_C) to a low temperature. Furthermore, good dielectric and piezoelectric properties were observed at composition, $x = 0.03$. The polymorphic phase transition between the orthorhombic and tetragonal phases plays a very important role in enhancement of the piezoelectric properties of KNN–LN–LS ceramics.

1. Introduction

Lead-based piezoelectric materials such as $Pb(Zr,Ti)O_3$ (PZT) ceramics are the most widely used, due to their superior piezoelectric performances [1]. However, the toxicity of lead oxide, which contains more than 60 wt%, can cause damage to the kidney, brain and nervous system [2]. In recent years, many countries have required that all electronic equipment be lead-free for human health and environmental protection. Therefore, urgent development of lead-free piezoelectric ceramics, with outstanding properties for replacing lead-based ceramics, is necessary, and recent attention on this topic has been paid to $(K,Na)NbO_3$ and (KNN)-based ceramics, due to their good piezoelectric properties and high Curie temperature [3]. It is well known that not only the morphotropic phase boundary (MPB) between orthorhombic and tetragonal phase, but also the polymorphic orthorhombic and tetragonal phase transition temperature play an important role in the electrical properties of KNN-based ceramics [4,5]. It was reported that the polymorphic orthorhombic-tetragonal phase transition temperature (PPT) strongly affects the electrical properties of KNN-based ceramics, and a PPT near room temperature would be helpful in obtaining enhanced electrical properties. Recently, Guo et al observed excellent electrical properties in the $(1-x)(K_{0.5}Na_{0.5})NbO_3$–$xLiNbO_3$ system [6]. The coexistence of orthorhombic-tetragonal phase was found at $0.05 < x < 0.07$. Excellent piezoelectric and electromechanical responses; $d_{33} = 235$ pC/N, $k_p = 44\%$, and $k_t = 48\%$, were obtained as samples, with the composition, $x = 0.052$. Recent studies have also found that the binary system of $(1-x)K_{0.5}Na_{0.5}NbO_3$–$x$-$LiSbO_3$; [$(1-x)$KNN–$x$LS] at the composition, $x \sim 0.052$, exhibited good piezoelectric properties at room temperature, with electromechanical coupling factors of $k_{33} \sim 62\%$ and $k_{31} \sim 30\%$, and piezoelectric coefficients of $d_{33} \sim 265$ pC/N and $d_{31} \sim -116$ pC/N [7]. The piezoelectric, electromechanical, and elastic properties were determined as a function of temperature, showing anomalous behaviour at around room temperature, which related to the orthorhombic to tetragonal polymorphic phase transition (PPT) [7]. Since both the 0.945KNN–0.055LN [6] and 0.948KNN–0.052LS [7]

* Corresponding author. Department of Chemistry, Faculty of Science, King Mongkut's Institute of Technology Ladkrabang, Bangkok 10520, Thailand. Fax: +66 2 3264415.
E-mail address: naratipcmu@yahoo.com (N. Vittayakorn).

1567-1739/$ – see front matter © 2010 Elsevier B.V. All rights reserved.
doi:10.1016/j.cap.2010.08.015

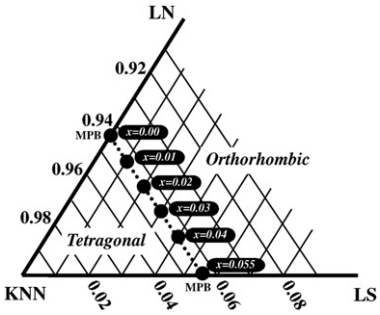

Fig. 1. Composition studied in the $0.945K_{0.5}Na_{0.5}NbO_3$–$(0.055-x)LiNbO_3$–$xLiSbO_3$ ternary solid solution.

compositions have excellent electrical properties; the combination of these two systems to form a KNN–LN–LS ternary solid solution is very interesting. In this study, the ternary solid solution of 0.945KNN–$(0.055-x)$ LN–xLS, where $x = 0$–0.055, was synthesized. To obtain a homogeneous perovskite solid solution and better electrical properties, the samples were prepared by a conventional solid state reaction process. Fig. 1 schematically shows the composition range that was studied in this work. In this study, the influence of $LiNbO_3$ (LN) and $LiSbO_3$ (LS) addition on phase transitions, and electrical properties of KNN ceramics are also reported.

2. Experiment

The sample, 0.945KNN–$(0.055-x)$LN–xLS, where $x = 0.00$, 0.01, 0.02, 0.03, 0.04 and 0.055, was prepared using the conventional solid state reaction process with normal sintering. Reagent-grade oxide and carbonate powders of K_2CO_3 (99.0%), Na_2CO_3 (99.5%), Li_2CO_3 (99.9%), Nb_2O_5 (99.5%) and Sb_2O_3 (99.9%) were used as starting raw materials. The powders were weighed according to the stoichiometric formula and ball milled in absolute ethanol for 24 h. The dried slurries were calcined at 850 °C for 4 h, then ball milled again for 24 h. The granulated powders were pressed into disks of 15 mm diameter and 1 mm thickness and then pressed using a cold isostatic pressing (CIP) technique under 300 MPa. These disks were sintered in air at 1030–1070 °C for 2 h. The density of the fired samples was determined by Archimedes method and found to be greater than 95% theoretical. Silver paste (Heraeus C1000) was fired on both sides of the samples at 550 °C for 10 min, as electrodes for dielectric measurements. The crystal structures were determined by X-ray diffraction (XRD) analysis obtained by using CuKα radiation (Bruker-D8 Advance). The temperature dependence of the samples' dielectric constant was examined using a programmable furnace with an LCR analyzer (HP-4284, Hewlett–Packard Inc.). A differential scanning calorimeter (DSC) was used to follow the phase transitions of sintered ceramics. The ceramics were poled for piezoelectric measurement in a silicone oil bath at room temperature for 30 min and field strength of 3–4 kV/mm. The piezoelectric coefficient, d_{33}, of the samples, which were left for 24 h after poling, was measured using a d_{33} meter (Model 8000, Penne baker). The planar electromechanical coupling factor, k_p, was calculated from the resonance and anti-resonance frequencies, based on IEEE standards.

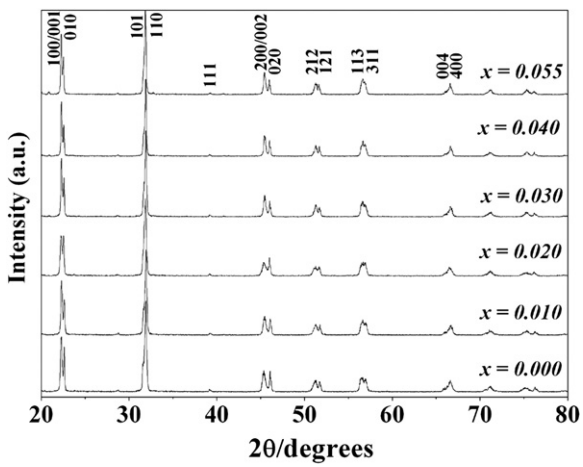

Fig. 2. XRD patterns of $0.945K_{0.5}Na_{0.5}NbO_3$–$(0.055-x)LiNbO_3$–$xLiSbO_3$ ceramics at room temperature.

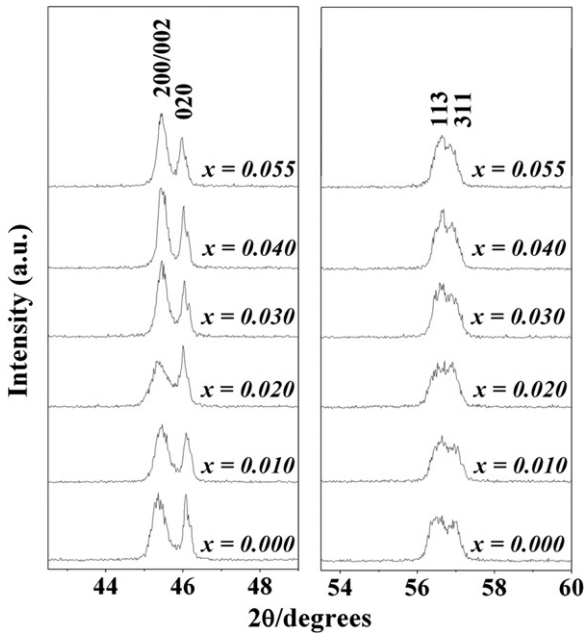

Fig. 3. XRD patterns of the (200) and (113) peaks of $0.945K_{0.5}Na_{0.5}NbO_3$–$(0.055-x)LiNbO_3$–$xLiSbO_3$ ceramics.

3. Results and discussion

Fig. 2 displays the XRD pattern of 0.945KNN–$(0.055-x)$LN–xLS ceramics sintered at 1050 °C. A series of continuous solid solutions between KNNLN and KNNLS was clearly formed. The phase structure in all samples was a pure perovskite phase and no secondary

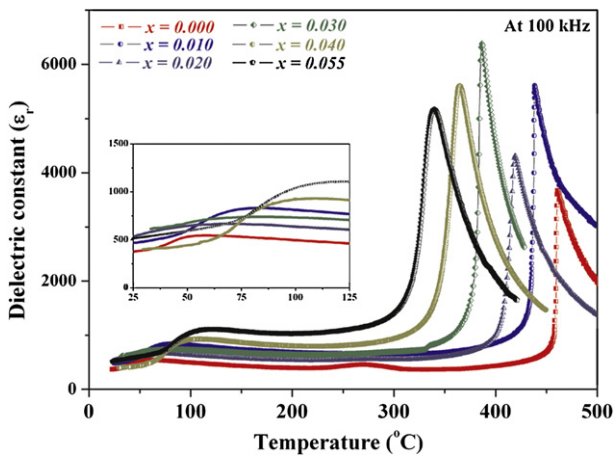

Fig. 4. Temperature dependence of the dielectric constant (ε_r) at 100 kHz of $0.945K_{0.5}Na_{0.5}NbO_3$–$(0.055-x)LiNbO_3$–$xLiSbO_3$ ceramics as a function of x.

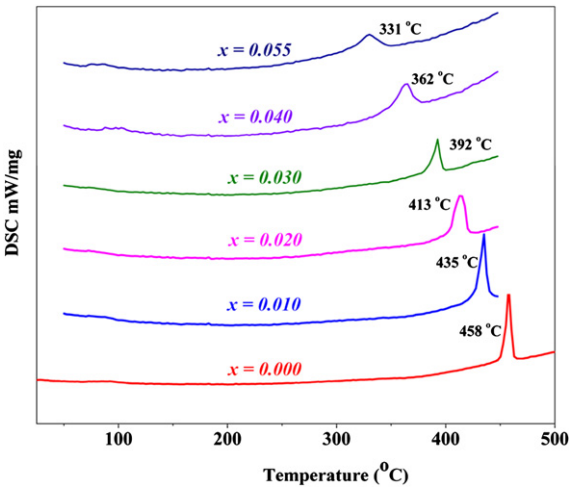

Fig. 5. DSC heating curves of $0.945K_{0.5}Na_{0.5}NbO_3$–$(0.055-x)LiNbO_3$–$xLiSbO_3$ ceramics as a function of x.

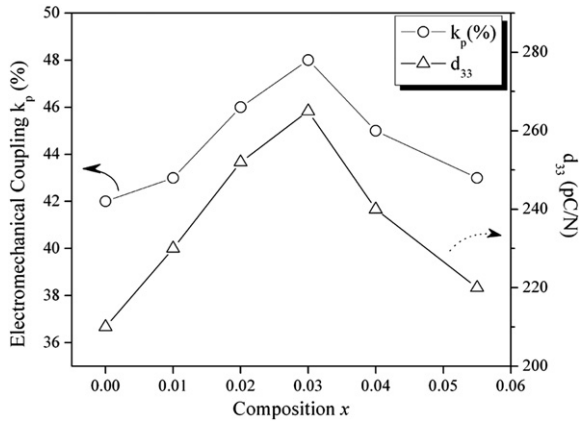

Fig. 6. Planar electromechanical coefficient and piezoelectric constant of $0.945K_{0.5}Na_{0.5}NbO_3$–$(0.055-x)LiNbO_3$–$xLiSbO_3$ ceramics as a function of x.

impurity could be certified. The result indicated that the dopants were completely diffused into the $(K_{0.5}Na_{0.5})NbO_3$ lattices, with Li^+ entering the $(Na_{0.5}K_{0.5})^+$ sites and Sb^{5+} occupying the Nb^{5+} sites, to form a new solid solution in all compositions. Fig. 3 shows the XRD patterns of 0.945KNN–$(0.055-x)$LN–xLS ceramics in the 2θ range of 43–48° and 54–60°. The compositions in this study were selected across the orthorhombic–tetragonal coexistence region between the KNN–LS and KNN–LN system. As expected, coexistence of the orthorhombic–tetragonal phase was observed in all compositions. Interestingly, with an increasing x value, the diffraction peaks located at a higher angle, and (113) and (311) peaks near $2\theta = 57°$, tended to merge into a single peak, which indicated that the crystalline structure varied from the orthorhombic–tetragonal phase to the orthorhombic-rich phase. Similar behaviour was observed in the $xPb(Zn_{1/3}Nb_{2/3}O_3)$–$(0.2-x)Pb(Ni_{1/3}Nb_{2/3})O_3$–$0.8Pb(Zr_{1/2}Ti_{1/2})O_3$ ternary system [8].

The temperature dependence of the dielectric constant, (ε_r) of 0.945KNN–$(0.055-x)$LN–xLS ceramics, at the frequency of 100 kHz is shown in Fig. 4, together with the temperature dependence of ε_r for all ceramic samples; showing two phase transitions that correspond to those of ferroelectric tetragonal to paraelectric cubic (T_C) and polymorphic ferroelectric orthorhombic to tetragonal ferroelectric (T_{O-T}) for high and low transition temperatures, respectively. The T_c decreases with increased composition x, however; T_{O-T} tends to decrease with increasing composition x up to 0.03 and continues to increase with a further increase of x. The T_{O-T} was approximately 52, 53, 49, 48, 85 and 95 °C for compositions $x = 0.00$, 0.01, 0.02, 0.03, 0.04 and 0.055, respectively. Interestingly, the T_{O-T} phase transition temperature for the composition, $x = 0.03$, is close to room temperature and this composition is expected to attribute to high piezoelectric responses. The phase transition temperature; clearly confirmed by DSC measurement, is presented in Fig. 5. At the composition, $x = 0.00$, a sharp peak was observed near the ferroelectric tetragonal to paraelectric cubic phase transition temperature, and the transition is of the first order, due to its association with a significant value of ΔH. The transition temperature defined by maximum heat capacity, which closely followed the ferroelectric to paraelectric transition temperature revealed by the dielectric measurement, is shown in Fig. 4. The peak value of heat capacity became weaker, and heat capacity anomaly gradually broader, with increasing LS concentration. These results indicated that the phase transition deviates gradually from the first order type. Stenger and Burggraaf et al. [9] observed that the change in entropy (ΔS) and $\Delta S/T_t$ correlates with the fluctuation probability in conjunction with a small spontaneous lattice deformation and polarization. They explained that large values of the ratio, $\Delta S/T_t$, give sharp transition and lower values, which lead to diffuse behaviour. Table 1 shows that the ΔS and $\Delta S/T_t$ values are small for the LS doped sample, when compared to the KNN–LN sample. This indicates the existence of diffuseness in the phase transition behaviour, which increases with increasing LS content, and coincides well with the dielectric results in the composition range investigated. This behaviour can originate from the more complex occupation of the A and B sites in an ABO_3 perovskite structure and heterogeneous compositions, which also give rise to random fields that tend to make the phase transition "diffuse" instead of sharp, as in a normal ferroelectric. Fig. 6 shows the piezoelectric constant, d_{33}, and planar electromechanical coupling factor, k_p, of polarized 0.945KNN–$(0.055-x)$LN–xLS ceramics as a function of $LiSbO_3$ concentration. It can be seen that the property exhibits a compositional dependence when d_{33} and k_p of the composition, $x = 0.00$, show values of 210 pC/N and 0.42, respectively, with increasing x, d_{33} and k_p to the maximum values of 265 pC/N and 0.48 at $x = 0.03$. As expected, the composition, $x = 0.3$, shows the maximum d_{33} and k_p value in the KNN–LN–LS system. Therefore, it can be concluded that the polymorphic phase transition between the orthorhombic and tetragonal phases plays a very important role in enhancement of the piezoelectric properties of KNN–LN–LS ceramics. Similar behaviour was observed in the KNN–LN [6] KNN–LT [10] and KNN–LT–BNT–BT [11] system. The KNN–LN–LS samples showed good piezoelectric properties when compared with the KNN–LN [6] and KNN–LS system [7].

Table 1
The values of ε_{max}, T_{max}, T_t, ΔH, ΔS and $\Delta S/T_t$ of KNN–LN–LS ceramics.

Compositions	ε_{max}	T_{o-T} (°C)	T_{max} (°C)	T_t (°C)	ΔH (J g^{-1})	$\Delta S \times 10^3$ (J g^{-1} K^{-1})	$(\Delta S/T_t) \times 10^6$ (J g^{-1} K^{-2})
$x = 0.000$	4800	52	460	458	4.174	9.114	19.900
$x = 0.010$	5750	53	439	435	3.471	7.979	18.343
$x = 0.020$	4400	49	419	413	2.858	6.920	16.755
$x = 0.030$	6700	48	388	392	1.800	4.592	11.714
$x = 0.040$	5700	85	363	362	0.987	2.727	7.533
$x = 0.055$	5250	95	340	331	0.014	0.042	0.127

4. Conclusion

In this study, $0.945K_{0.5}Na_{0.5}NbO_3$–$(0.055-x)LiNbO_3$–$xLiSbO_3$ ceramics were prepared by the conventional solid state reaction process with normal sintering. All ceramics with a perovskite structure are mixed phase of orthorhombic and tetragonal phase. The phase transition temperature of tetragonal–cubic (T_C) was

decreased with increasing x. Furthermore, good dielectric and piezoelectric properties were observed at composition, $x = 0.03$. The polymorphic phase transition between the orthorhombic and tetragonal phases plays a very important role in enhancement of the piezoelectric properties of KNN–LN–LS ceramics.

Acknowledgements

This work was supported by the Thailand Research Fund (TRF), and the National Nanotechnology Center (NANOTEC) NSTDA, Ministry of Science and Technology, Thailand, through its "Center of Excellence Network" program.

References

[1] B. Jaffe, W.R. Cook, H. Jaffe, Piezoelectric Ceramics. Academic, USA, 1971.
[2] Y. Saito, H. Takao, T. Tani, T. Nonoyama, K. Takatori, T. Homma, T. Nagaya, M. Nagamura, Nature 432 (2004) 84.
[3] T.R. Shrout, S.J. Zhang, J. Electroceram. 19 (2007) 113.
[4] G.H. Haertling, J. Am. Ceram. Soc. 50 (1967) 329.
[5] K. Kakimoto, I. Masuda, H. Ohsato, J. Eur. Ceram. Soc. 25 (2005) 2719.
[6] Y. Guo, K. Kakimoto, H. Ohsato, Appl. Phys. Lett. 85 (2004) 4121.
[7] S. Zhang, R. Xia, T.R. Shrout, J. Appl. Phys. 100 (2006) 104108.
[8] S. Nabunmee, G. Rujijanagul, N. Vittayakorn, D.P. Cann, J. Appl. Phys. 102 (2007) 094108.
[9] C. Stenger, A.J. Burggraaf, Phys. Stat. Sol. 61 (1980) 275.
[10] Y. Dai, X. Zhan, G. Zhou, Appl. Phys. Lett. 90 (2007) 26290.
[11] Y. Dai, X. Zhang, J. Eur. Ceram. Soc. 28 (2008) 3193.